NANOSTRUCTURED NONLINEAR OPTICAL MATERIALS

Studies of Clusters, Quantum Dots and Nanoparticles

Rashid Ganeev

Nanostructured Nonlinear Optical Materials

Nanostructured Nonlinear Optical Materials:

Studies of Clusters, Quantum Dots and Nanoparticles

By

Rashid A. Ganeev

Cambridge Scholars Publishing

To my parents, wife, son and daughter

TABLE OF CONTENTS

PREFACE

The great attention associated with nanoscience developments in different directions is related to the potential applications of small-sized objects in different areas of science. Among those areas, the nonlinear optics and morphology studies of such objects attracted the efforts of numerous research groups. The significance and timeliness of these topics are the applications in the formation of the efficient sources of coherent extreme ultraviolet radiation, as well as the potential use of non-spherical nanostructured species in optics and optoelectronics.

There are not many books on this topic field and certainly none with the detailed level of research comprising different topics of these studies. My previous book on those topics (R. A. Ganeev, "Nanostructured Nonlinear Optical Materials: Formation and Characterization," Elsevier, 2018) served as an introduction in the field of the optical nonlinearities of nanostructures. The present book ("Nanostructured Nonlinear Optical Materials: Studies of Clusters, Quantum Dots and Nanoparticles") comprises further consideration of novel approaches developed in this area during the last three years. This book can be considered as a continuation of the above publication, which comprises main topics and most recent advances in the optical and nonlinear optical science of different nanostructures. The major difference in the case of the proposed book with respect to previous publications is related to the broader consideration of different aspects of light-nanostructure interactions. Particularly, it contains the collection of most recent studies of the non-spherical nanoparticles and quantum dots, as well as their applications for the analysis of the lower- and higher-order nonlinear optical processes. The necessity in this collection of various studies is related to the compilation of various nanomaterials studies disseminated in different journals. The collection of these studies in a single book helps the reader to learn about the most recent achievements in the morphological, optical, and nonlinear optical features of different nano-species possessing advanced properties. The book describes the advantages achieved during the last few years in the studies of different nanomaterials for nonlinear optical applications involving laser-nanostructure interactions. This book helps to provide an insight into the complex field of nonlinearities in nanostructures. It would

certainly help the audience be able to quickly become involved in this field and could also help as a reference book for certain topics.

This book, apart from the above-mentioned advantages, has the following attractive features:

i.   Highly topical: focuses on the novel applications of laser-plasma physics such as the development of ultrashort-wavelength coherent light sources based on nanoparticles applications

ii. Balanced coverage: the consideration starting from the smallest species consequently moves towards the largest nanoparticles

iii. Detailed description of methods and approaches: this book details the experimental aspects of nanostructures formation, morphology characterization, optical and nonlinear optical application of nanostructures in liquids, and plasmas.

iv. Interdisciplinary: useful for physicists, material scientists, and engineers interested in the nanomaterials used in plasma physics, laser technology, and spectroscopy.

This book is aimed to support researchers and other readers in their development of useful nanostructures-based optoelectronic devices, as well as in the advanced studies of nanoparticles for the formation of new sources of radiation in different short-wavelength spectral ranges. The researchers involved in the development of new methods in optics and nonlinear optics will be benefited by finding the most recent novelties in this field. The undergraduate students can find interesting information about recent findings of plasma harmonic research. Additionally, the usefulness of the book could be proven by potential applications of the new knowledge developed during the recent times for ultrafast pulses generation using the proposed schemes of plasma-light interaction. Thus the audience may also include those researchers involved in the state-of-art developments of attophysics.

The primary groups of readers comprise researchers in the fields of nanomaterial science and nonlinear optics. The book would be interesting for both academics and professionals in the applied fields, as well as for the high education students and postdocs, who are aimed at further development of their career in the fields of laser-matter interaction. Additionally, any professionals interested in material science could be also benefited from updating their knowledge of new methods of material studies using high-order nonlinear spectroscopy. The potential collective users could be the numerous universities and scientific institutes where the nonlinear optical studies have the connection with plasma physics,

ultrashort pulses generation, coherent processes analysis, and laser-matter interactions.

The results presented in this book comprise studies during the last few years. All these amendments of the nanoscience studies could not be realized without the fruitful collaboration of different groups involved in similar research activities. I would like to thank H. Kuroda, T. Ozaki, P. D. Gupta, P. A. Naik, J. P. Marangos, J. W. G. Tisch, M. Castillejo, H. Zacharias, G. S. Boltaev, V. V. Kim, O. V. Ovchinnikov, A. I. Zvyagin, N. V. Kamanina, C. Guo, K. Zhang, Y. Fu, W. Yu, and A. S. Alnaser for the long-lasting collaboration.

The inspirers of this activity are my wife Lydia, son Timur and daughter Dina, who help me overcome various obstacles of life.

<div align="right">

Rashid A. Ganeev
Riga, Latvia
March 2022

</div>

INTRODUCTION

The small-sized objects for a long period attracted great attention associated with nanoscience developments in different directions. Numerous journal articles and tens of books appear yearly to maintain the science of nanomaterials at the highest state of development. Each of the new books comprises some particular aspects since it is hard to imagine how the whole area of this enormously broadened field of science can be compiled in a single publication. These monographs or collections of chapters restrict the topics of nanoscience subjects. In the present book, we also follow those principles and describe a few groups of studies, which for a long time attracted the attention of this author.

There is a classical book relevant to the nonlinear optical processes in gaseous media [1]. Another book [2] is related to the spectroscopic details of nonlinear optical studies. Separate chapters of the book [3] were also related to the above-described processes. Some details of plasma properties relevant to those at which the resonance processes play an important role are discussed in [4]. Other related titles relevant to some topics considered in the present book include [5-7]. However, neither of them covers a broad area of the optical nonlinearities of different nanostructures.

There are not many books on this topic field and certainly none with this detailed level of research. The only book that covers some of these parts is [8]. However, ten years from the publication of this book, many new approaches emerged, which are discussed in the present book. Some low-order nonlinear optical studies of nanoparticles are collected in [9].

Finally, the previous book of this author [10] served as an introduction in the field of nanostructures, as well as the optical and nonlinear optical research involving nanomaterials. The present book comprises further consideration of novel approaches developed in this area during the last three years. This book can be considered as a continuation of the above publication and contains main topics and most recent advances in the optical and nonlinear optical science of different nanostructures. The major difference in the case of this book with respect to previous publications is related to the broader consideration of different aspects of light-nanostructure interactions. Particularly, it comprises the collection of most recent studies of the non-spherical nanoparticles (NP) and quantum

dots, as well as their applications for the analysis of the lower- and higher-order nonlinear optical processes.

This book contains the analysis of recent studies of the morphological, optical, and nonlinear optical properties of nanostructured materials. It compiles studies of large molecules, thin films, clusters, quantum dots (QDs), and NPs reported during the last three years. The book is structured by dividing the text into nine chapters, each containing the characterization of dyes, fullerenes, and perovskites, morphology and optical properties of elliptical, triangular, and cube-like nanoparticles, analysis of the nonlinearities of oxidized nanostructures, studies of third-harmonic generation in nanoparticles, and analysis of the high-order harmonics produced in nanostructures, like clusters and quantum dots.

The important topics include the studies of small-sized nanoparticles (quantum dots) as the sources of coherent extreme ultraviolet radiation, analysis of their low-order nonlinear optical properties, formation and characterization of non-spherical nanoparticles (i.e. triangles, ellipsoids, and square-like species) during laser ablation of different materials in liquids. Other important topics include the comparison of the optical and nonlinear optical responses of various nanostructured species. Below we briefly describe the structure and basic principles of the collection in this book the reported studies of nonlinear optical properties of nanostructured materials. The detailed references to the topics of those studies will be presented in the corresponding chapters. Here we just underline the basic principles of our analysis of different materials and processes under consideration.

Dyes. The high-frequency Kerr effect, two-photon absorption (2PA), saturated absorption (SA), multi-photon absorption, and reverse saturated absorption (RSA) are the main nonlinear optical processes during the propagation of ultra-short laser pulses through large-sized molecules like dyes. Variations of the nonlinear optical characteristics of dyes depend on such factors as the intensity of probe pulse, solvents, temperature, etc. The irreversible changes in dyes lead to variations of their nonlinear optical parameters, such as saturation intensities, nonlinear absorption coefficients, etc. To analyze the complex behaviour of the dyes one has to measure the nonlinear optical parameters, such as the 2PA, SA, RSA, and in some cases the nonlinear refraction using various laser sources. The latter process (high-frequency Kerr effect induced nonlinear refraction) rarely plays a decisive role compared to other nonlinear optical processes, while the SA was frequently realized in many dyes. The dynamics of singlet-singlet ($S_1 \rightarrow S_0$) relaxation of dye solutions is determined by the features of dye and solvent. The population of dye molecules to higher singlet

states S_n ($n > 2$) opens decay channels mainly to the S_1 state, S_0 state, triplet states, and molecular decomposition. Frequently, as a consequence, the bleaching of dyes is observed due to SA of the intermediate state.

Thin NP-contained films. Thin-film materials have gained great attention due to their various potential applications. Particularly, the unique properties of low-dimensional materials necessitated analysis of the optical and nonlinear optical features of thin films, which could be useful in various fields of optoelectronics and laser physics. The availability of laser sources with ultra-short pulse duration allowed a considerable increase in the laser intensities used in those experiments, therewith presenting the opportunity to investigate thin materials close to their optical breakdown intensities (10^{12}-10^{13} W cm^{-2}). Particularly, the results of nonlinear refraction studies of C_{60} thin (100 nm) films have shown that their large third-order susceptibility causes strong self-focusing with a nonlinear refractive index (γ) exceeding 2×10^{-9} cm^2 W^{-1}. Notice that fullerenes dissolved in toluene at a similar concentration showed two orders of magnitude less nonlinear susceptibility. Chalcogenide films also demonstrate considerable values of optical nonlinearities. Studies of the nonlinear absorption coefficients (β) of $As_{20}S_{80}$ (3×10^{-6} cm W^{-1} at the wavelength $\lambda = 532$ nm) and $3As_2S_3/As_2Se_3$ (10^{-7} cm W^{-1} at $\lambda = 1064$ nm) have shown that some thin (200 nm) chalcogenide films possess large third-order nonlinear susceptibility. Even in the case of thick media containing thin layers of active elements, such as nanoparticles, these layers have demonstrated enhanced nonlinear absorption and refraction. In particular, thin (60 nm) layers of copper nanoparticles implanted in silica glass caused strong nonlinear absorption ($\sim10^{-6}$ cm W^{-1}). Furthermore, the nonlinear refraction of CdS thin films at $\lambda = 532$ nm was measured to be –5.2×10^{-11} cm^2 W^{-1}, while the measured value of the nonlinear refractive index of bulk CdS in this spectral region was reported to be –6×10^{-13} cm^2 W^{-1}, i.e. two orders of magnitude smaller than former structure. A considerable increase in the nonlinearity of thin films in those and other studies makes their nonlinear optical features close to those of nanoparticles.

The quantum confinement effect allows distinguishing the parameters of nanoparticles with regard to the bulk materials. A further search of prospective materials in nanoparticle form, their preparation, and application of quantum confinement are of considerable importance. Meantime, the unique properties of low-dimensional materials have ignited numerous studies of their characteristics. The investigations of these films have shown their prospects as optical limiters. One can investigate thin (of the order of a hundred nanometres) films. Particularly, gold nanocomposites

have tremendous applications in various fields due to the influence of their surface plasmon resonance (SPR) on optical properties. In the past decade, researchers have demonstrated the potential applications of gold NPs using different lasers.

During the last decade, there has been an interest in the nonlinear optical features of chalcogenide thin films. Significant efforts have been made in the syntheses of metal chalcogenide nanocrystals (NCs) due to their attractive size-tuneable optical properties and possible applications in various technological fields including light-emitting diodes, photovoltaic devices, and fluorescent biological labels. Several other sulphide precursors were subsequently reported, but elemental sulphur has been the most widely used as a less air-sensitive precursor in the syntheses of metal sulphide NCs. Decreasing the size of such materials allow to tune their physical properties and observe new phenomena. Taking this into account, newly synthesized semiconductor nanoparticles should be studied under different conditions to understand the nonlinear optical mechanisms and use their attractive properties for practical applications. Further analysis of linear and nonlinear optical features of the thin films comprising metal sulphide NCs is important for their possible use in various fields of optoelectronics and laser physics. To verify the generalized effective-medium theories for linear and nonlinear optical properties of metal sulphide NPs and QDs one has to analyze the linear and nonlinear susceptibilities of the constituent materials. Ag_2S QDs are non-cadmium and non-lead fluorescent nanomaterials developed in recent years, and Ag_2S QDs are known for displaying large optical nonlinearities. Ag_2S QD thin films can have even higher nonlinearities.

Perovskites. Due to its unique crystal and electronic structure, the large molecular ABX_3 materials have excellent photoelectric properties, which can be applied to a series of research optoelectronic devices such as solar cells, light-emitting diodes, lasers, field-effect transistors, and photodetectors. The perovskite materials appeared as polycrystalline thin films, nanowires, nanosheets, nanorods, quantum dots, and single crystals. In the above morphology, the perovskite crystal has more excellent electron transport properties due to its own fewer defects and grain boundaries, which reveals that the application of such material would be a promising way to improve the performance of devices such as solar cells and detectors. Moreover, many studies have shown that the quantum yield of perovskite material can reach 70-90%, indicating that it also has good luminescent properties.

In recent years, organo-lead halide perovskites, such as methylamino lead halide perovskites (MAPbX$_3$, MA=CH$_3$NH$_3^+$, X=Cl$^-$, Br$^-$, or I$^-$) have

attracted widespread attention due to their attractive optical and low-temperature solution processibility. MAPbBr$_3$ and MAPbI$_3$ used for high-efficiency solar cells or optoelectronic devices have been widely studied due to their narrow band gap and wide adsorption range located at visible or even near IR range. Compared to those two materials, MAPbCl$_3$ was rarely studied due to its wide band gap and specific adsorption properties. Most research on MAPbCl$_3$ was mainly focused on the growth of single crystals, the structural characterization, and phase transitions with the change of the environment. Meanwhile, the single-crystal MAPbCl$_3$ demonstrates its attractiveness due to its intrinsic structural features. Until recently, the study of perovskite materials by Raman method mainly focused on its structure properties or phase transitions, and Raman spectroscopy only plays a role in the structural characterization of the perovskite materials. However, Raman technique is a very significant method in the interfacial charge transfer property studies and the intensive exploration of the correlation between the interfacial optical or photo-electronic and Raman properties of the perovskite materials must be crucial for applying perovskite materials in photo-electronic devices.

Optical nonlinearities of NPs. The study of optical limiting with metallic nanoparticles has attracted a considerable amount of attention because of the increasing demand for protection against laser threats to sensors and human eyes. One major approach to be through the use of optical limiters. Metal NPs and QDs have attracted much attention due to their high surface-to-volume ratio and small particle effect. These nanocomposites have special nonlinear optical behaviour as compared to the bulk materials. For instance, optical nonlinearities and optical limiting (OL) effects of the nanocomposites of the metals can be significantly enhanced by increasing the number density and low size of metal particles. These particles display a drastic optical extinction due to nonlinear scattering. Among metal nanoparticle limiters, gold and silver nanoparticles have received special attention because they both show a broad SPR absorption band in the visible region, which is substantially different from the absorption of the corresponding bulk metals in this region. One can anticipate that variations of the sizes of NPs can significantly enhance OL. OL behaviour of silver nanoparticles with different sizes and shapes was investigated and compared to the optical limiting performance of conventional carbon black suspension. It was found that the optical limiting effect is strongly particle size-dependent and the best performance is achieved with the smaller particles.

The majority of studies have been based on the formation of various NPs by focusing the laser pulses on the metal targets immersed in liquids.

Due to the resonance effect arising from the SPR of some NPs their size and shape can be controlled by laser irradiation in various solvents. Advantages of this method are the high purity of the NPs, variety of materials, and the in-situ dispersion of NPs in different liquids tolerating safe and stable control of the colloids. Also, the solvent molecules surrounding NPs can protect them in some cases from aggregation due to their viscosity and other properties. One can anticipate the crucial influence of the wavelength and pulse duration of laser radiation on the size and shape of produced NPs.

Different mechanisms are responsible for the nonlinear optical properties of small-sized species, which include saturable absorption, two-photon absorption, optical limiting, and optical Kerr nonlinearities. SA has a profound influence on the overall nonlinear optical response at sufficiently high power of employed laser pulse. Another phenomenon called reverse saturable absorption may counteract the absorption saturation processes. RSA occurs as a result of large absorption by the nonlinear absorber at high laser energy via excited-state absorption because of the depletion of the ground state with the increase of the incident laser energies. The performance of small-sized nonlinear materials is limited by the accompanying linear absorption at low input energy. In this case, the incident photons may be further absorbed by excited states when their population gets large enough in an excited state. These processes not only depend on the intensity of the incident photon but also on the frequency of the incident photon, which plays an important role in their nonlinear optical properties depending on the resonant or nonresonant transitions. Apart from nonlinear optical properties of nanomaterials, many-body interactions in condensed matter and molecular systems have been of great concern because the properties like electrical, thermal conduction, superconductivity to Raman scattering, polaron formation are highly affected by an ultrafast process such as electron-phonon interactions. There has been a great advancement to understand the role of electron-phonon interaction on the properties of low-dimensional systems. A vast literature is presented on electron-phonon interaction in NPs. The interaction of NPs with short laser pulses undergoes various ultrafast processes such as electron-electron coupling, electron-phonon coupling, and phonon-phonon coupling. Thus many studies have focused on the dissipation of the acoustic vibration in noble NPs based on the size, shape, and surrounding mediums.

The performance of materials at the nanoscale is totally different from their macroscopic behaviour. Many factors, such as laser pulse duration and fluence, type of surrounding media, the temperature of the liquid, and

characteristics of irradiated targets, influence the properties of NPs. It was shown that the morphology and size of synthesized particles can cause variations of different macroscopic properties of NP-containing substrates and suspensions. Besides that, the formation mechanism of Al NPs should be investigated under different regimes of the bulk target ablation.

Non-spherical NPs. The oxide of copper, cupric oxide (CuO), and cuprous oxide (Cu_2O) are typical representatives of such species. Compared to macro-targets, the properties of ellipsoidal micro/nano-sized CuO/Cu_2O are quite different due to the increase of surface/volume ratio and the influence of the quantum size effect. As a semiconductor material, CuO is environmentally friendly, low-cost, and has numerous applications in the field of photovoltaics because of its high absorption of the solar spectrum and high carrier concentration. In addition, applications based on CuO/Cu_2O micro/nanoparticles and micro/nanostructures, electrochemical materials, and super-capacitors have received a great amount of attention, also. Triangles of Al NPs have a role in propellants and pyrotechnics because they can provide additional heat release during exothermic oxidation. The optical character of Al spherical and triangle NPs also contributes to their application for solar cells, optoelectronic devices, metal-enhanced fluorescence devices, and broad-band wire-grid polarisers. The interest in the study of the optical and structural properties of non-spherical ZnO nanostructures is due to the low cost, nontoxicity, and stability of the ZnO nanomaterials. The second- and third-order nonlinear optical properties of ZnO NPs have been applied in biomarkers and optical imaging. The noncentrosymmetric structures of ZnO NPs can exhibit relatively strong second harmonic generation (SHG). The SHG in nanocrystallites can be used in laser spectroscopy, frequency converters, and LEDs, as well as in bioimaging, and chemical sensing. Additionally, the enhancement of the third-order nonlinearity of ZnO nanorods with regard to the bulk and thin films was observed. Laser ablation is useful for the preparation of non-spherical nanoparticles from bulk metal or semiconductor targets. Particularly, the influence of surrounding liquid media and the ablating conditions resulted in the fabrication of Cu nanoparticles (NPs) in acetone and CuO NPs in chloroform, which demonstrated the urchin-like shapes.

Quantum dots. The quantum dots of semiconducting materials took attention due to their potential applications as biomarkers and sensors in medicine, as well as in the processes of photosynthesis. The optical properties of II-IV semiconductor nanoparticles (i.e. nanosized crystallites, QDs), as well as the quantum confinement effect, were observed in semiconductor QDs. The propagation of laser radiation through the

materials containing Ag_2S QDs induces various nonlinear optical processes, which could be useful in photonics. It has been reported that the visible light being transmitted through such structures becomes limited particularly due to RSA caused by two-photon optical transitions that involve excitation of the energy levels of Ag_2S photoluminescence centres. The presence of thermal lens in the case of long probe pulses significantly complicated the whole pattern of nonlinear optical properties of these species, while short laser pulses caused the two-photon absorption. Note that the sole role of RSA in the observed nonlinear absorption still remains disputable since the direct 2PA could also be properly matched with the probe pulse wavelength and band gap of Ag_2S QDs. Particularly, in the case of some other QD sulphides, such as ZnS nanocrystallites, the observed nonlinear absorption has resulted from 2PA. Femtosecond pump-probe studies show the two-photon absorption above 630 nm and slow-decaying excited state absorption below 600 nm. In experiments, open-aperture z-scans demonstrate strong 2PA at the wavelength of $\lambda = 532$ nm, with a nonlinear absorption coefficient of ZnS QDs in the range of 10 to 100 cm GW^{-1}. Transient absorption and open-aperture z-scan data have shown both RSA and strong 2PA in the case of Ag_2S nanocrystallites as well. In the nanosecond timescale, a large enhancement of 2PA was observed with the growth of Ag_2S nanoparticles concentration. Similarly to ZnS, it was suggested that for $\lambda > 670$ nm one can expect a larger influence of 2PA, while for $\lambda < 670$ nm the RSA could play the dominant role in nonlinear absorption.

One of the perspective semiconductor-based materials for these tasks is the silver sulphide, which initially was applied as a photosensitizer in photography. Silver sulphide QDs primarily attractive due to their potential application in different photovoltaic devices, photoconductors, and electrochemical storage cells. These QDs belong to the class of nanocrystallites with a lattice distance of ~0.3 nm. The colloidal Ag_2S QDs dispersed in gelatine are characterized by the formation of crystal nuclei with the size of ~2.0 nm and a shell of gelatine and its complexes with various components, such as dyes. Silver is not a toxic metal unlike many other heavy metals hence Ag_2S QDs are suitable for applications in the biomedical field. The use of Ag_2S QDs would for instance enable one to image and treat cancerous cells simultaneously. This should drastically reduce the time and number of invasive procedures. Note that the sole role of RSA in the observed nonlinear absorption still remains disputable since the direct two-photon absorption (2PA) could also be properly matched with the probe pulse wavelength and band gap of some QDs. Particularly, in the case of some other QD sulphides, such as ZnS nanocrystallites, the

observed nonlinear absorption has resulted from 2PA. It can be assumed that for $\lambda > 860$ nm one can expect a larger influence of three-photon absorption (3PA) in ZnS QDs, while for $\lambda < 860$ nm the RSA could play the role in nonlinear absorption, while the consideration of the role of 2PA could be also reasonable.

Third harmonic generation. There are several reports on the use of THG as a characterization scheme for generated mono- and nanoparticles in plasma. This was achieved by changing the arrival time of the excitation pulses relative to the heating pulses. Measurements based on the time delay of the third harmonic radiation showed the presence of large aggregates formed by laser ablation, which can also be further analyzed when they are deposited on nearby substrates. The plasma created during laser ablation contains electrons, atoms and molecules, ions, neutrals, clusters, quantum dots, and NPs. Ni plasma formation in the air can serve, particularly, as a nonlinear medium for harmonic generation in the plasma containing NPs. The formation of NPs during plasma formation in ablation plume has been shown to significantly influence the efficiency of high-order harmonic generation. At the same time, Ni NPs can be applied to study the low-order harmonic generation in cuboids structures. Increasing the pulse energy (i.e. the number of photons in the pulse) to 10 mJ allows the generation of harmonics with pulse energy up to several tens of μJ at a laser repetition rate of 10 Hz. Alternatively, using a large number of photons per second (i.e., a high pulse repetition rate) at low pulse energy can also lead to an increase in the number of coherent photons in the UV range. In particular, 100 kHz class lasers produce ~100 W of the average power of femtosecond pulses, which in turn can be converted to a third harmonic with an average power of 0.1 W.

High-order harmonic generation in NP-contained media. Nanostructured and ion-implanted semiconductor targets paved a path to produce strong high-order harmonics as compared to un-patterned samples. The dynamics of plasma formation, in that case, can be considered as follows. The material directly surrounding the NPs is a polymer (epoxy glue), which has a considerably lower ablation threshold than the metallic materials. The NPs absorb the laser pulse energy and pass the thermal energy to the surrounding media. Therefore, the NPs-carrying polymer begins to ablate at relatively low intensities, resulting in the lower laser fluence required for the preparation of the appropriate nonlinear medium for the high-order harmonic generation (HHG). This feature allowed for easier creation of the optimum plasma conditions, which resulted in better HHG conversion efficiency, particularly, from the Au NPs-containing plume compared to the plasma from the bulk target.

The application of different pumps of plasmas allows exploring various new schemes of high-order harmonic generation using ultrashort laser pulses. Particularly, the application of mid-infrared femtosecond pulses for HHG in laser-induced plasmas (LIP) using a two-colour pump allows further filling of the extreme ultraviolet range with odd and even harmonics. In the case of HHG in gases, this approach has been demonstrated in numerous studies using 800-nm-class lasers. Another approach, which considers harmonic generation as a method of nonlinear spectroscopy, has recently been emerged in the case of HHG in narrow and extended LIPs. Further developments of plasma HHG using this approach could be related to the search of single harmonic enhancement and application of nanoparticle-containing plasmas.

Among different methods of harmonic enhancement, one can admit the formation of the quasi-phase-matching (QPM) conditions between the driving and generating waves during HHG in NP- and QD-contained plasmas. This mechanism has been originally demonstrated in the visible range using solid materials. Application of this concept in the case of the shorter-wavelength region requires the conditions when the absorption of generating harmonic waves becomes insignificant with regard to the enhancement of this radiation at the conditions when the transfer of energy from driving to harmonic waves occurs at similar phase velocities.

Generation of harmonics using quantum dots. Quantum dots play an important role in different technological fields. One interesting application is the formation of QD-containing media for frequency conversion of ultrashort laser pulses from the IR towards the extreme ultraviolet range. Previous studies on HHG after ablation of small-sized nanoparticle-containing targets have revealed the advantages of such species for frequency conversion in the XUV range. A larger cross-section of recombination and the possibility of recombination of an accelerated electron with the parent particle through either recombination with the same or a neighbouring atom, or with the multi-atomic particle as a whole, were considered as the most probable reasons for the growth of HHG yield in such plasmas. One explanation was based on the disintegration of larger species into small clusters, which probably could reach the interaction area at the short delays employed. However, no sufficient confirmation of this assumption has been provided. Taking into account the anticipated velocities of atoms, molecules, and ions ($\sim 1 \times 10^4$ m s^{-1}), QDs ($\sim 1 \times 10^3$ m s^{-1}) and nanoparticles [$(1\text{-}5) \times 10^1$ m s^{-1}] of the same material one can expect their arrival in the region of the femtosecond laser beam propagation a few tens of nanosecond, a few hundreds of nanosecond, and a few tens of microsecond from the beginning of ablation, respectively. Small-sized

aggregates subject to intense laser pulses produce a strong low-order nonlinear optical response (e.g., nonlinear refraction and nonlinear absorption), as well as the emission of coherent extreme ultraviolet radiation through the harmonic generation. Previous studies of the HHG from such objects were limited to the clusters of Ar and Xe being formed in high-pressure gas jets due to rapid cooling by adiabatic expansion, as well as to the relatively large nanoparticles ablated from the bulk surfaces.

Concluding the introduction to this book the author would like to underline a few features of this collection, which can be useful in different fields of science. The academic audience of this book is likely works in the field of nanostructures and optical nonlinearities. This is a very broad field, with many researchers have published journal articles on this subject. The novelty in laser-nanoplasma interaction shown in this book would attract various groups of researchers, particularly those involved in applications of lasers and the development of short-wavelength coherent sources.

This book is organized as follows. In Chapter 1, we analyze the saturated and two-photon absorption of various classes of large molecules like heterocyclic dyes, as well as nanostructured dye suspensions. Nonlinear absorption of thiazine, xanthene, and carbocyanine dyes, peculiarities of the nonlinear optical absorption of methylene blue and thionine in different solvents, nonlinear optical characterization of colloidal solutions containing dyes and Ag_2S quantum dot associates, and nonlinear optical absorption in mixtures of dye molecules and ZnS nanoparticles among the topics of a few sections. Nonlinearities of thin films containing complex and nanostructured materials comprise the content of Chapter 2. Among the subjects under consideration, the strong nonlinear absorption in perovskite films, the nonlinear optical studies of gold nanoparticle films, and the low- and high-order nonlinear optical properties of Ag_2S quantum dot thin films. Chapter 3 formulates the principles of characterization of the nonlinear optical properties of perovskites. We discuss the charge transfer effects on resonance-enhanced Raman scattering for molecules adsorbed on single crystalline perovskite, femtosecond laser-induced micro- and nano-structures with significantly enhanced fluorescence on $MAPbBr_3$ single crystal surface, and provide the comparative analysis of optical limiting effects in metal nanoparticles and perovskite nanocrystals. Laser-synthesized nanoparticles formation and characterization is the main subject described in Chapter 4. We will consider the strong third-order optical nonlinearities of Ag nanoparticles synthesized by laser ablation of bulk silver in water and air, laser ablation-induced synthesis and nonlinear optical characterization of titanium and

cobalt nanoparticles synthesized by laser ablation of bulk materials, the effect of nanoparticle sizes on the saturable absorption and reverse saturable absorption in silver nanostructures, and discuss the mechanism of laser-assisted generation of aluminium nanoparticles, their wettability and nonlinearity properties.

Chapter 5 describes the morphological and optical characteristics of nanoparticles. Among the topics considered here are the structural variations during the aging of the particles synthesized by laser ablation of copper in water, pulse duration and wavelength effects of laser ablation on the oxidation, hydrolysis, and aging of aluminium nanoparticles in water, formation, aging, and self-assembly of regular nanostructures from laser ablation of indium and zinc in water, and effect of different hardness and a melting point of the metallic surfaces on structural and optical properties of synthesized nanoparticles. In Chapter 6, we focus on the size- and shape-dependent properties of nanoparticles. Among them are the size-dependent off-resonant nonlinear optical properties of gold nanoparticles and demonstration of efficient optical limiting, nonlinear optical characterization of copper oxide nanoellipsoids, and low-order nonlinear optical studies of ZnO nanocrystals, nanoparticles, and nanorods. Third harmonic generation in nanoparticle-contained media is considered in Chapter 7. We analyze the reports on the ablated nickel nanoparticles and third harmonic generation and optical nonlinearities in those species, as well as third and fifth harmonics generation in air and nanoparticle-containing plasmas using 150 kHz fibre laser. Chapter 8 collects the most recent studies of the high-order harmonics generation in nanoparticles. Among them are the high-order harmonic generation in Ag, Sn, fullerene, and graphene nanoparticle-containing plasmas using two-color mid-infrared pulses, high-order harmonic generation in Au nanoparticle-contained plasmas, and effects of laser-plasma formation on quasi-phase-matching of high-order harmonics from nanoparticles and atoms. High-order harmonics generation in the smallest structures (clusters and quantum dots) is discussed in Chapter 9. Those studies include the analysis of the role of carbon clusters in high-order harmonic generation in graphite plasmas, effective high-order harmonic generation from metal sulphide quantum dots, and high-order harmonic generation using quasi-phase-matching and two-colour pump in the plasmas containing molecular and alloyed metal sulphide quantum dots. Finally, a summary of discussed issues presents the whole pattern of the studied areas.

References to Introduction

[1].   J. Reintjes, "Nonlinear optical parametric processes in liquids and gases," Academic press (1984).

[2].   S. Mukamel, "Principles of nonlinear optical spectroscopy," Oxford University Press (1999).

[3].   "Nonlinear optical properties of matter," M. G. Papadopoulos, A. J. Sadlej, and J. Leszczynski, eds. Springer (2006).

[4].   R. Hippler, H. Kersten, M. Schmidt, "Low temperature plasmas: fundamentals, technologies and techniques," Wiley-VCH (2008).

[5].   V. N. Ochkin and S. Kittell, "Spectroscopy of low temperature plasma," Wiley-VCH (2009).

[6].   M. Pelton and G. W. Bryant, "Introduction to metal-nanoparticle plasmonics," Wiley (2013).

[7].   G. I. Stegeman and R. A. Stegeman, "Nonlinear optics: phenomena, materials and devices," Wiley (2012).

[8].   Ying Fu, "Nonlinear optical properties of nanostructures," Pan Stanford Publishing Pte Ltd (2011).

[9].   R. A. Ganeev, "Nonlinear optical properties of materials," Springer (2013).

[10].   R. A. Ganeev, "Nanostructured nonlinear optical materials: formation and characterization," Elsevier (2018).

CHAPTER 1

OPTICAL NONLINEARITIES OF LARGE DYE MOLECULES AND NANOSTRUCTURED DYE SUSPENSIONS

Dyes have found their applications in various areas of laser physics. These include frequency conversion of laser radiation in dye vapours, Q-switching and mode-locking in various lasers, the study of bleaching effects under the action of pulses of different duration, analysis of lasing, etc. The lasing using dyes was one of the preferable applications of these media. All these applications assume that the optical and nonlinear optical properties of dyes play an important role during their interaction with laser pulses. The nonlinear absorptive features of dyes find the application in the formation of ultrashort pulses, while the concurrence of various types of these processes may lead to different scenarios during propagation of short or long laser pulses through such media.

Nonlinear optical properties of organic dye vapours were studied for the first time more than forty years ago using benzene vapours (C_6H_6) wherein frequency conversion was carried out [1], as well as in acetylene vapours (C_2H_2) wherein third harmonic generation in ultraviolet range was realized [2]. It was shown that the nonlinear susceptibilities of organic dye molecules with double-conjugated bonds and delocalized π-electrons are comparable with the resonance-enhanced nonlinear susceptibilities of atoms [3,4]. Such molecules with double-conjugated bonds are highly attractive as nonlinear media. The calculations reported earlier have shown that some organic dyes (tetracene, paraterphenyl, pentacene) possess considerable third-order susceptibilities [5].

There is also interest in the studies of the nonlinear refraction and nonlinear absorption in the associates of the dyes of different classes (xanthenes, thiazines, carbocyanines, quinolines) and the metal sulphides quantum dots (QDs) stabilized in gelatin using pulses of different duration. The interest in sulphide-based QDs (ZnS, As_2S_3, CdS, ZnSe, CdSe, Ag_2S, etc.) was due to the high third-order nonlinearities they possess. The dependence of optical absorption in QD-contained solutions demonstrates

a considerable departure from the Lambert law. Particularly, in the case of some other QD sulphides, such as ZnS nanocrystallites, the observed nonlinear absorption resulted from 2PA. It can be assumed that for $\lambda >$ 860 nm one can expect a larger influence of three-photon absorption in ZnS QDs, while for $\lambda <$ 860 nm the RSA could play the role in nonlinear absorption, while the consideration of the role of two-photon absorption (2PA) could be also reasonable.

In this chapter, we analyze the studies of different dyes possessing strong nonlinear optical responses. We also discuss the comparative studies of the associates of dyes and quantum dots.

1.1 Nonlinear absorption of thiazine, xanthene, and carbocyanine dyes

There is a group of dyes, which can be analyzed from the point of view of the concurrence of two or more nonlinear absorptive processes, while some of those processes become suppressed. Those dyes belong to different classes [thiazine (thionine), xanthene (erythrosine), and carbocyanine (3,3'-di-(γ-sulphopropyl)-4,4',5,5'-dibenzo-9-ethylthiacarbocyaninebetaine   pyridinium salt, DEC)].

Those dyes have different chemical structures and absorption in the near-infrared, visible, and ultraviolet ranges (see Fig. 1.1 showing their absorption spectra in different ranges, the corresponding images of the cells filled with those dyes, and the structural formulas of dyes). Particularly, the structures of thionine existing in different solvents were characterized using spectroscopic methods in Ref. [6]. The wavelengths of the peaks of optical absorption of thionine and erythrosine differ from each other, particularly due to the tendency in formation of the dimers (D) [7], while DEC may form the D- и J-aggregates [8]. There are different conditions for the formation of triplet states in the case of monomers and dimers of these dyes, while the cross-sections of transitions and the lifetimes of excited singlet and triplet states differ from each other.

Meanwhile, no systematic studies of the nonlinear optical properties of those dyes except erythrosine were reported. Erythrosine has a quantum yield of triplet state almost equal to unity and is expected to undergo the following photophysical processes. Absorption of optical energy from the probe pulses produces excited singlet states, which then relax completely into the triplet manifold through the intersystem crossing. The metastable T_1 state has a lifetime ranging from less than 1 ms to several hundred ms depending on the solvent and the dye concentration [9]. Previously, nonlinear optical absorption effects in erythrosine were analyzed using the

pulsed-laser thermal lens spectrometry of this dye solution [10]. Notice that photothermal spectroscopy is an indirect method for measuring nonlinear absorbance. The probe beam was a He–Ne laser, which did not allow the analysis of the short-lasting nonlinear optical processes of absorption.
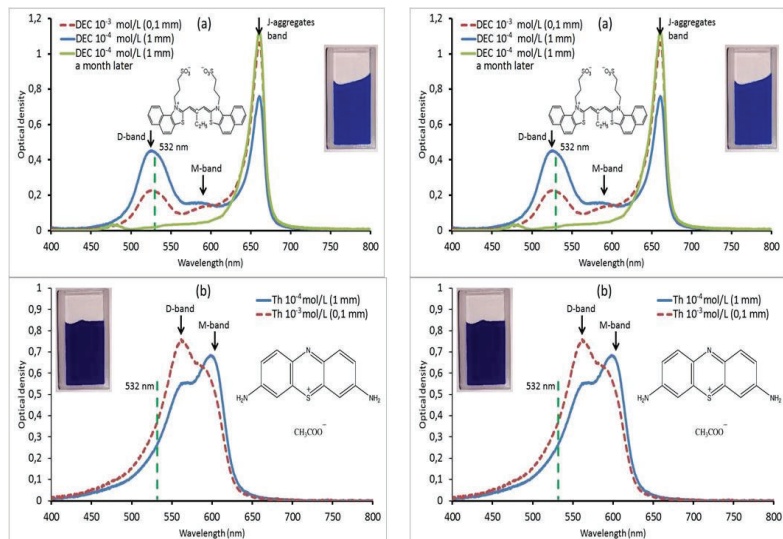
Fig. 1.1. Optical absorption spectra of (a) DEC, (b) thionine (Th), and (c) erythrosine (Ery) dyes. The inserted pictures show the corresponding images of the cells filled with those dyes. The structural formulas of dyes are shown as well. (d) UV absorption spectra of DEC, thionine, and erythrosine. Double dashed line corresponds to the doubled energy of 532 nm photons. Reproduced from [11] with permission from Elsevier.

The interest in these dyes is caused by their applications as the components of hybrid associates with different colloidal quantum dots (Ag$_2$S, ZnS, etc.). In this subsection, we discuss the studies of the nonlinear absorptive characteristics of this group of organic dyes (thionine, erythrosine, and DEC) using relatively short and long pulses in different spectral ranges. We analyze the nonlinear absorption properties of those dyes using the 40 ps and 10 ns pulses at two wavelengths (532 and 1064 nm). We also discuss the concurrence of saturable absorption (SA) and 2PA in the case of some dyes using the 532 nm pulses of different intensities and discuss a few models of SA [11].

1.1.1. Experimental arrangements and basic principles and relations of the nonlinear absorption

The measurements of the nonlinear optical properties of dyes were carried out by applying the standard z-scan technique. The Nd:YAG laser generated the single pulses (τ = 40 ps) at a 2 Hz repetition rate. This radiation (λ = 1064 nm), or its second harmonic (λ = 532 nm) generated in KDP crystal, was focused by a 500-mm focal length lens (Fig. 1.2). The beam waist diameters of probe pulses were 65 μm and 60 μm in the case of fundamental and second harmonic radiation, respectively. The laser pulse energy was measured by a calibrated photodiode and then registered by a digital voltmeter.

The 3-mm-thick quartz cells containing dye solution were moved along the z-axis through the focal plane of probe pulse using a translating stage controlled by a computer. The intensities of the optical breakdown of dye solutions by 40 ps pulses were measured to be ~1×10^{12} Wcm^{-2} (1064 nm) and 7×10^{11} Wcm^{-2} (532 nm) at the dye concentrations of $C = 10^{-3}$ and $C = 10^{-4}$ mol/L. The intensities used in the experiments did not exceed 7×10^{11} Wcm^{-2} (1064 nm) and 1×10^{11} Wcm^{-2} (532 nm). The confocal parameters of the focused 1064 and 532 nm radiations were 6 and 12 mm respectively. This experimental setup has previously been used for the measurements of the optical nonlinearities of nanoparticles, fullerenes, colloidal solutions, etc. [12].
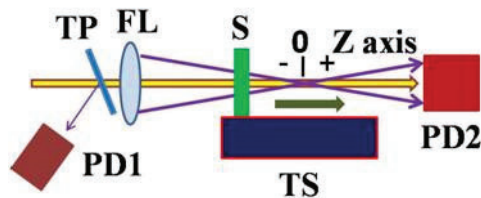
Fig. 1.2. Open-aperture z-scan scheme. TP, thin plate; FL, focusing lens; S, sample; TS, translating stage; PD1, PD2, photodiodes. Reproduced from [11] with permission from Elsevier.

In the case of closed-aperture (CA) z-scans, a 1-mm aperture was fixed at a distance of 1500 mm from the focal plane. The second photodiode was kept behind this aperture to measure the propagated radiation. The ratio of the transmitted radiation registered by a second photodiode and the incident radiation registered by the first photodiode was used as a normalized

transmittance to avoid the influence of laser radiation instability on the measured results. Each point on the experimental graphs corresponds to the averaging of 20 measurements. The CA scheme allowed defining the sign and magnitude of the nonlinear refractive index and nonlinear absorption coefficient (β) of the dye solutions.

The open-aperture (OA) z-scan scheme, i.e. the one without aperture in front of the second photodiode, was used for the measurements of β to compare with the measurements of this parameter using the CA scheme. The second detector in that case was kept at such a distance from the focal plane that allowed measuring all transmitted radiation to determine the dependence of the normalized transmittance on the position of the sample on the z-axis. Note that most experiments were carried out using the OA z-scan scheme.

The measurements of nonlinear optical characteristics using 10 ns probe pulses (1064 and 532 nm, 1 Hz pulses repetition rate) were carried out using a similar z-scan configuration. This radiation was focused using a 300-mm focal length lens. In these experiments, the 1-mm-thick cells filled with dye solutions were propagated through the focal plane. The energy and intensity characteristics of 10 ns pulses are presented throughout the description of experimental results.

Thionine, erythrosine, and DEC were chosen due to different absorption at the wavelength of the second harmonic radiation (532 nm) of Nd:YAG laser (Fig. 1.1). The insets in Fig. 1.1 show the colours of dye-filled cells. The used concentrations (10^{-4} and 10^{-3} mol/L) were sufficient for observation of the nonlinear optical response of the dyes under consideration.

The wavelengths of the maximum absorption of dyes and the ability to absorption of 532 nm radiation in these solutions were as follows. The thionine monomers showed the peak of absorption at 600 - 608 nm (M-band) and characteristic peculiarity at 560 nm attributed to the appearance of the structure corresponding to the electron transition band (Fig. 1.1b). Such spectra of the thionine solutions are the characteristic peculiarity at the $\leq 10^{-4}$ mol/L concentration in water solvent and at any concentration in the ethanol solvent. The growth of thionine concentration in water solvents up to 10^{-3} mol/L and higher led to the formation of dimers the absorption band of which (D-band) was peaked at 560 nm (Fig. 1.1b). The wavelength of probe pulse at two used concentrations of thionine coincided with the short-wavelength edge of absorption the origin of which depended on the dye concentration. Contrary to that, erythrosine did not demonstrate self-association. The optical absorption spectrum of this dye showed a single peak (~520 nm, Fig. 1.1c) and was close to the wavelength of the

probe pulse (532 nm). The most sophisticated pattern of absorption was in the case of DEC (Fig. 1.1a). At each concentration of the water solution of this dye, the weak M-band in the vicinity of 580 nm attributed to the monomers and a stronger shorter-wavelength D-band attributed to the dimers of this dye was observed. The maximum of the latter band almost coincided with the pump wavelength (532 nm). The J-aggregate induced absorption band of DEC (660 nm) was notably stronger while being far from the 532 nm wavelength of pump radiation. However, the absorption band of J-aggregates, as a rule, demonstrated a short-wavelength component, which was attributed to the defects of the formation of these aggregates. Thus at the conditions of the formation of J-aggregates in DEC solutions, one can also expect the absorption at the 532 nm wavelength. Neither of these dyes demonstrated notable absorbance at 1064 nm.

The analysis of experimental data (z-scans) was performed using the basic principles of nonlinear optical absorption in multi-level molecular systems. The most probable mechanisms of this process were chosen to be the 2PA and SA rather than reverse saturable absorption (RSA). The explanation of the insignificant role of the latter process will be discussed in the following section.

In contrast with SA, when the absorptive properties of the material possessing SA fade with increasing intensity due to depletion of the ground state, RSA can result in large absorption by the nonlinear absorber at high incident laser energies and low absorption at low laser energies. Contrary to RSA, the 2PA is a simultaneous absorption of two photons of identical or different frequencies in order to excite a molecule of dye from the ground state to a higher energy electronic state. The energy difference between the involved lower and upper states of the molecule in that case should be lower or equal to the sum of the energies of the two photons.

A five energy level model can be used, alongside other models, to interpret RSA. Such absorption in the medium requires the fulfilment of the group of basic criteria. Firstly, the material must have an excited-state absorption cross-section larger than the ground-state absorption cross-section. Secondly, the lifetime of the excited state should be long enough in comparison with the pulse duration of the laser radiation. Later, we discuss the fact that, depending on the properties of dyes, the RSA may overpass 2PA or vice versa.

In order to understand the effects of various contributing photo-physical processes, detailed beam propagation models have been developed. These approaches have been usually concentrated on modeling the interaction of a weakly focused laser beam with a thin sample but more recent interest in the low threshold tight focusing geometry has increased.

The β measurements of species were carried out using the OA z-scan technique. The normalized transmittance for the OA scheme is given as

$$T(z) = q^{-1} \ln(1 + q), \tag{1.1}$$

where $q = \beta I_0 L_{eff}/(1+z^2/z^2_0)$, $z_0 = 0.5k(w_0)^2$ is a Rayleigh length equal to $0.5b$ (b is a confocal parameter of focused radiation), $k = 2\pi/\lambda$ is a wave number, w_0 is a beam radius at the $1/e^2$ level of the spatial intensity distribution in the focal plane, λ is a probe radiation wavelength, I_0 is a laser radiation intensity in the focal plane, $L_{eff} = [1-\exp(-\alpha_0 L)]/\alpha_0$ is an effective length of the sample, α_0 is a linear absorption coefficient, and L is a thickness of the sample. Equation 1.1 was fitted to some of the OA z-scans.

The imaginary part of the third-order susceptibility of various dyes ($Im\chi^{(3)} = 10^{-7}c^2n^2_0\beta/96\pi^2\omega$) was calculated using the measured values of β. Here c is the light velocity in cm s^{-1}, ω is the laser radiation frequency in cycles s^{-1}, β is the nonlinear absorption coefficient in cm W^{-1}, and n_0 is the linear refractive index. Since, as it will be shown below, the nonlinear refraction was rather weak or even not detected during discussed experiments, the absolute values of third-order susceptibility mostly depended on the nonlinear absorptive properties of the dyes and were defined by the above relation.

Notice that, for a simple two-level system, the light excites the molecules, which induced the population change. The simplest phenomenological model is often used when the SA is considered in terms of depletion of the ground state concentration due to the high fluence of radiation. It can be described by the relation

$$(z) = \alpha_0/[1 + I(z)/I_{sat}], \tag{1.2}$$

where $\alpha(z)$ is the absorption coefficient varying along *z-axis*, $I(z)$ and I_{sat} are the laser radiation intensity and saturation intensity.

The absorption coefficient in the case of the two-level system possessing heterogeneously broadened states can also be written as

$$\alpha(z) = \alpha_0/[1 + I(z)/I_{sat}]^{0.5} . \tag{1.3}$$

Another model that can be expressed empirically as

$$\alpha(z) = \alpha_0/\{1 + [I(z)/I_{sat}]^{0.5}\} \tag{1.4}$$

was also used for the analysis of SA. Finally, Eq. (1.1) could also be considered as the simplified analytical absorption model assuming the negative sign of the nonlinear absorption coefficient.

1.1.2. Comparison of the optical nonlinearities of different dyes

As it was mentioned, dyes possess various types of optical nonlinearities. Meanwhile, the dyes under consideration did not show the nonlinear refractive properties, which can be distinguished from the overwhelming influence of different mechanisms of nonlinear absorption. The conclusion on that matter was drawn from CA z-scans, which demonstrated an extremely weak positive nonlinear refraction of dyes. The shapes of z-scans, in that case, were slightly asymmetric with regard to the focal plane of the focusing lens, when the post-focal region showed stronger normalized transmittance compared with the pre-focal region at the highest energies of probe pulses. Below we analyze the nonlinear absorptive properties of the dyes using relatively high energies of both 40 ps and 10 ns pulses of 1064 and 532 nm radiation.

The characteristic peculiarity of studied dyes was the observation of nonlinear optical effect at this wavelength in the case of the 40 ps pulses propagating through the thionine and erythrosine dye solutions. Meanwhile, the DEC solution did not show the nonlinear absorption at these conditions. Figure 1.3 comprises a group of z-scans using this wavelength of 40 ps radiation. Z = 0 in this and other figures corresponds to the position of the focal plane on the z-axis. The relatively stronger infrared pulses (1064 nm) caused a larger decrease of normalized transmittance in the vicinity of the focal plane compared with weaker probe radiation.

One has to note that, in the case of 1064 nm pulses (E_{1064nm} = 1.17 eV), the only mechanism, which could be responsible for the observed z-scan dependences, is a 2PA. There are no energy states allowing the linear absorption of 1064 nm photon in thionine and erythrosine once one considers the spectral properties of these dyes. However, the energy of two photons is sufficient for the S→S* transitions. The best approach to the resonance conditions was fulfilled for the monomers of erythrosine and dimers of thionine, while monomers of thionine did not satisfy the two-photon transitions (Fig. 1.1). The transitions of DEC dimers could be responsible for 2PA. However, the peculiarity of this dye is a notably smaller β compared with thionine and erythrosine at λ = 1064 nm.
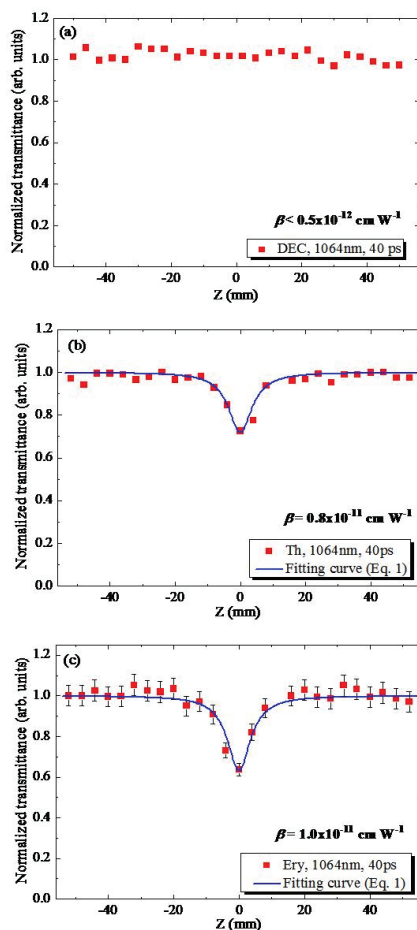
Fig. 1.3. Z-scans of (a) DEC, (b) thionine, and (c) erythrosine using the 1064 nm, 40 ps pulses and 10^{-3} mol/L concentrations of dyes in water. The confocal parameter of focused radiation and the focal area were 6 mm and 3.5×10^{-5} cm^2 respectively. The respective nonlinear absorption coefficients attributed to TPA were defined from the fitting curves of Eq. 1 and are shown in each of panels. Reproduced from [11] with permission from Elsevier.

The fitting curves shown in some graphs [Figs. 1.3(b) and 1.3(c)] allow defining the β of thionine и erythrosine solutions, which was carried out for each sample. The values of nonlinear absorption coefficients are shown

in the graphs demonstrating this process. They were of the order of 10^{-11} cm W^{-1}.

While the thionine, and especially erythrosine, demonstrated relatively strong 2PA, the DEC did not show these properties or showed extremely weak 2PA at maximal used energy of 40 ps pulses (1.2 mJ), which was close to the optical breakdown of this dye solution. The value of β in the DEC was below the threshold of registration of this parameter (0.5×10^{-12} cm W^{-1}). As already mentioned, the OA z-scans demonstrated a monotonic increase of $|\Delta T = T_{out} - T_{foc}|$ with the growth of pulse energy, thus indicating the absence of saturation until the maximal used intensity (7×10^{11} W cm^{-2}) of 1064 nm radiation for thionine and erythrosine. Here T_{out} and T_{foc} correspond to the normalized transmittances far from the focal plane and in the focal plane respectively (T_{out} is always equal to 1). The decrease of molar concentration led to a gradual decrease of $|\Delta T|$ until the entire disappearance of the valley in the $T(z)$ dependence. The error bars [$\pm 5\%$, Fig. 1.3(c)] of these and other measurements of dyes were the same during the whole set of experiments. The error bars of the definition of the absolute values of nonlinear absorption coefficients were estimated to be $\pm 30\%$ due to uncertainty in the measurements of the intensity of laser pulses in the focal plane and deviation of the spatial distribution of laser beams from the Gaussian shape.

The application of longer pulses (10 ns) at this wavelength (1064 nm) led to a significant decrease in the nonlinear optical response of the dyes. Actually, no nonlinear absorption in these dyes using the highest used concentrations of dyes and highest pulse energies was observed. Notice that maximal used intensity in the focal plane, in that case, was 1.2×10^{10} W cm^{-2}, which was lower than the one used in the experiments with picosecond probe pulses at which the nonlinear absorptive processes were detected.

At a shorter wavelength (i.e. for 532 nm photons, $E_{532nm} = 2.34$ eV), the radiation could be absorbed either through 2PA or through the excitation of intermediate states, which could further cause the additional absorption. This mechanism includes the involvement of RSA, the process when SA cannot be further realized due to saturation of the intermediate states. In some cases, one can expect negative nonlinear absorption (SA), i.e. growth of transmittance with the approach of the sample close to the focal plane in the z-scan scheme, alongside the positive nonlinear absorption (RSA and/or 2PA).
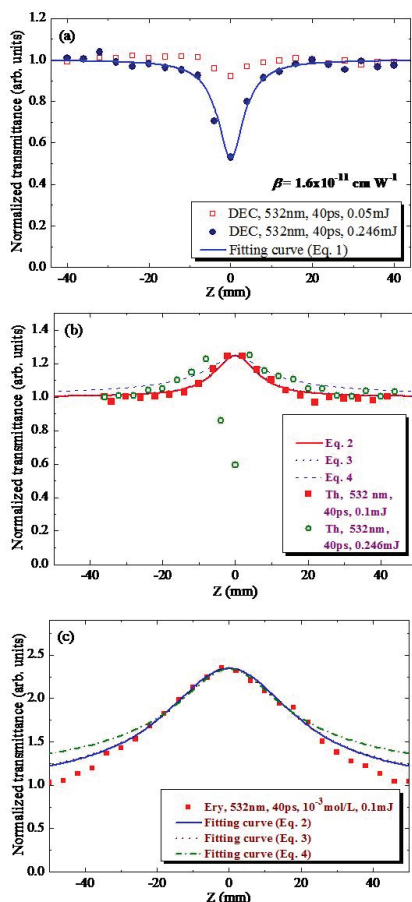
Fig. 1.4. Z-scans of (a) DEC, (b) thionine, and (c) erythrosine using 532 nm, 40 ps pulses and 10^{-3} mol/L concentrations of dyes in water. The confocal parameter of focused radiation and the area of focusing were 12 mm and 3×10^{-5} cm^2 respectively. The respective nonlinear absorption coefficient related with RSA was defined from the fitting curves and is shown in upper panel. Reproduced from [11] with permission from Elsevier.

During OA z-scans using 532 nm pulses the following dependencies were observed (Figs. 1.4 and 1.5). Figure 1.4 presents the z-scans in the case of different energies of the probe 40 ps, 532 nm pulses propagating

through the DEC, erythrosine, and thionine dye solutions. Figure 1.5 shows the z-scans of DEC, erythrosine, and thionine dye solutions in the case of the 10 ns, 532 nm pulses. In the case of thionine and DEC, predominantly decreased transmittance of dye samples was observed, while thionine also demonstrated the SA in the vicinity of the focal plane. The erythrosine showed predominantly SA in two cases (40 ps and 10 ns).

The valleys and peaks were symmetric with respect to the focal plane in the case of CA z-scans, which points out the insignificant role of the nonlinear refraction in these dyes at 532 nm. Actually, in the case of the CA z-scans of these samples at moderate energies of 40 ps, 532 nm pulses, the nonlinear refraction was below the level of registration. The CA z-scans in those cases were almost similar to the OA ones at the maximally used energies of 532 nm pulses, which points out the negligible values of the nonlinear refractive indices of dye solutions. Larger energies of pulses caused the optical breakdown of solutions. Similar behaviour of CA z-scans was observed in the case of 10 ns, 532 nm pulses.

The OA z-scans of DEC water solution using 532 nm picosecond pulses are shown in Fig. 1.4(a) for the pulse energies of 0.05 and 0.246 mJ. The decrease of transmittance of this dye in the vicinity of the focal plane was observed. DEC solution did not demonstrate the SA features.

In the case of thionine water solution, the SA observing at weaker pulses (filled squares) was followed with the prevailing influence of the positive nonlinear absorption at stronger probe pulses (empty circles) leading to the appearance of the valley in the z-scan [Fig. 1.4(b)]. The $|\Delta T|$ of the peak of z-scan increased with the growth of 532 nm probe pulse energy, with some saturation of this process ($|\Delta T|_{max} \approx 0.35$) at the pulse energies of ~0.19 mJ (not shown in this figure). Further growth of pulse energy (0.246 mJ) led to the appearance of the valley due to the prevailing influence of the mechanism of positive nonlinear absorption, which will be discussed in subsection 1.1.3.

In the case of erythrosine solution, the application of 0.1 mJ, 40 ps pulses led to the sole influence of the strong negative absorption attributed to the SA in this dye (Fig. 1.4c). The $|\Delta T|$ of the peak increased up to 2.5 with the growth of probe pulse energy from 0.1 to 0.2 mJ (not shown in this figure). The growth of pulse energy above 0.15 mJ led to the appearance of the small valley centred in the focal plane, which indicated the influence of an additional process (RSA or 2PA).

In the case of 10 ns pulses, both similarities and differences in the z-scans of the same dyes with regard to the 40 ps pulses were observed. Figure 1.5 presents the normalized transmittances of DEC, thionine, and erythrosine using different energies of probe pulses and 1×10^{-4} mol/L

concentrations. DEC solution being prepared immediately before the measurements did not show the nonlinear optical properties at the used probe pulse energy of 0.02 mJ. At a concentration of 1×10^{-3} mol/L, the linear absorption of these relatively long pulses caused the formation of the cloud of disintegrated species in the area of the focal spot. The z-scans of this dye solution were measured only at 0.02 mJ and concentration of 10^{-4} mol/L and did not observe the nonlinear optical features of this material [Fig. 1.5(a), empty squares]. Then the conditions for DEC solution formation at which the positive nonlinear absorption dominated at the energy of 0.32 mJ were defined [Fig. 1.5(a), filled circles].
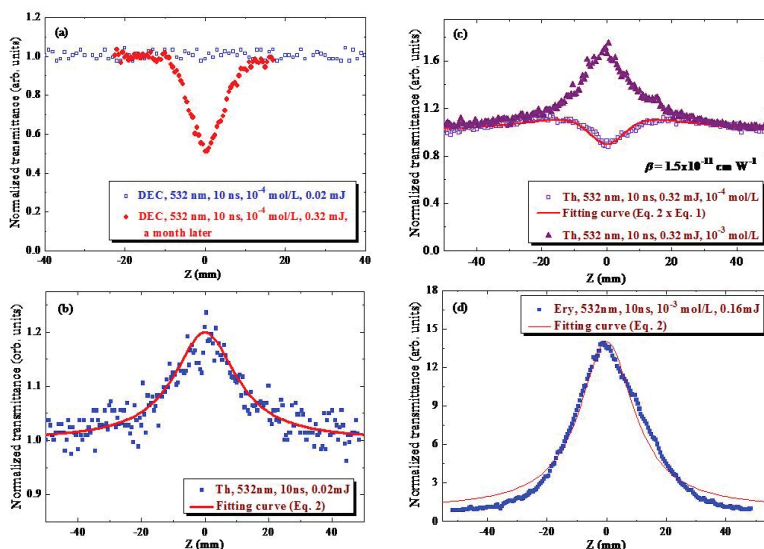
Fig. 1.5. (a) Z-scans of DEC solutions measured using 532 nm, 10 ns pulses at two conditions (see text). The corresponding energies and concentrations are shown on the graphs. (b) Z-scan of thionine solution (10^{-4} mol/L) using 532 nm, 10 ns, 0.02 mJ pulses. (c) Z-scans of thionine solution using 532 nm, 10 ns, 0.32 mJ pulses and different concentrations (10^{-3} and 10^{-4} mol/L). (d) Z-scan of erythrosine solution at concentration of 1×10^{-3} mol/L using 532 nm, 10 ns, 0.16 mJ pulses. Best fit corresponds to the phenomenological model. Reproduced from [11] with permission from Elsevier.

The samples of this solution showed a minimal concentration of DEC dimers and consisted dominantly of the J-aggregates [Fig. 1.1(a), solid green curve]. Such samples were prepared by maintaining DEC solution (10^{-4} mol/L) within one month. They did not disintegrate under the action of 0.32 mJ, 10 ns pulses. Meanwhile, the DEC dimers were unstable under the irradiation of these pulses. Additionally, the dimers probably do not have the appropriate resonance levels for RSA. This peculiarity may lead to the cancellation of SA at 532 nm and 2PA at 1064 nm. In the meantime, the optical density in the vicinity of 532 nm for the samples where one can expect the positive nonlinear absorption can be caused by the DEC J-aggregates, which can be attributed to the self-trapping defects. Most probably such structural and optical peculiarity induces positive nonlinear absorption.

The interesting dependence of the concurrence of these two processes was observed at different concentrations of thionine [Figs. 1.5(b) и 1.5(c)]. The growth of molar concentration led to the disappearance of the influence of positive nonlinear absorption [Fig. 1.5(c)]. The relative weight of SA at $C = 10^{-3}$ mol/L was significantly larger compared with the negative nonlinear absorption, while the latter process played an important role at $C = 10^{-4}$ mol/L.

Finally, the erythrosine solution demonstrated extremely strong SA properties [Fig. 1.5(d)]. $|\Delta T| = 13.7$ at the concentration of 10^{-3} mol/L and using the 0.16 mJ, 532 nm, 10 ns pulses was obtained, which is the highest relative growth of transmittance among the studied samples. The best fit corresponded to Eq. 1.2.

1.1.3. Analysis of dyes' nonlinearities

The direct single-photon absorption of 1064 nm radiation is forbidden in the case of used dyes since the photon energy is less than the absorption band energies of the samples under investigation (see Fig. 1.1 showing the absorption spectra). The nonlinear absorption of 1064 nm pulses could be attributed to the 2PA since no intermediate energy levels exist in these dyes, which could be responsible for the growth of the population and SA. Notice that extremely strong SA in erythrosine observed using both short and long 532 nm pulses correlated with the coincidence of the probe wavelength with the area of strong linear absorption (Fig. 1.1).

The values of β in the case of dyes were distinguished by a factor of two to four from each other. The difference in β at similar concentrations of dyes was attributed to a different cross-section of 2PA at $\lambda = 1064$ nm. The more sophisticated two-photon transitions in dyes through various

channels of the exchange of excitation could also play a role in this process. The nonlinear refractive indices of dyes were less than the minimal value registered by the used scheme (1×10^{-16} cm^2 W^{-1}).

The SA curves shown in Fig. 1.4(c) for erythrosine were fitted using different models described by Eqs. 1.2-1.4. The corresponding normalized transmittances in these models can be presented as $T(z) = 1+I_0/I_{sat}\times(1+z^2/z_0^2)$, $T(z) = [1+I_0/I_{sat}\times(1+z^2/z_0^2)]^{0.5}$, and $T(z) = 1+[I_0/I_{sat}\times(1+z^2/z_0^2)]^{0.5}$ for the phenomenological, two-level, and empirical models respectively. Corresponding fitting curves are presented in this figure as the solid, dotted, and dash-dotted curves. The fitting procedure comprised the coincidence of the maximal values of T and best fits with other parts of experimental data. One can see almost the same fitting curves in the case of phenomenological and two-level models, while the empirical model showed broader wings of $T(z)$ distribution. The requirement for the reasonable coincidence of theory and experiment is a definition of the same confocal parameter (or Rayleigh length z_0) for the measurements using the same wavelength and focusing optics. Initially, the Rayleigh length of the focused 532 nm radiation of 40 ps pulses was defined to be 6 mm. Meanwhile, the best fits allowed defining this parameter as 22, 18, and 14 mm, i.e. much larger than the same parameter calculated from the fitting of Eq. 1.1 and experimental data of the 2PA for DEC [Fig. 1.4(a)]. Notice that the calculations of this parameter from the data using 1064 nm radiation revealed two times shorter Rayleigh length (z_0 = 3.1 mm), which is reasonable taking into account the relation $z_0 = \pi(w_0)^2/\lambda$. A significant deviation of the calculated data of z_0 from the data depicted using 2PA fittings was caused by the "saturation" of the SA curve, shown in Fig. 1.4(c). The experimental data showed that while the maximum value of T for erythrosine saturated at $\sim$ 2.5 the wings of this $T(z)$ curve became significantly broadened, which caused the incorrect results for z_0.

To accurately fit the experimental data of SA one has to choose the conditions when this process appears at an unsaturated regime (such as those shown in Fig. 1.4(b) in the case of thionine at 0.1 mJ pulse energy). These SA data (filled squares) were fitted with three models. The phenomenological model (solid curve) revealed the Rayleigh length of focused radiation to be 7 mm, which is reasonably close to the one (6 mm) defined from other fits of z-scans. The ratio of the maximum intensity of probe pulse and saturated intensity was defined from this fit to be I_0/I_{sat} = 0.25. From this relation and assuming the maximal intensity of 532 nm pulse in the focal plane (8×10^{10} W cm^{-2}) used in this experiment one can define the I_{sat} to be 2.4×10^{11} W cm^{-2}.

By definition, saturation intensity is the one at which the absorbance of the medium drops by a factor of two. The two-level model (dotted curve) is also well fitted with experimental data and almost coincided with the fitting curve of the phenomenological model. However, the saturation intensity, in that case, was defined to be almost two times larger than the maximum intensity in the focal plane ($I_0/I_{sat} = 0.55$), which contradicts the definition of this parameter. It is obvious from the presented results that the growth of laser intensity by a factor of two does not cause the growth of the normalized transmittance on the focal plane from the present 1.2 [Fig. 1.4(b)] to 2. Thus the two-level model could not be considered in that case as the one describing the observed peculiarities of $T(z)$ dependence. The empirical model (Eq. 1.4, dash-dotted curve) did not match with the experimental data by its notably broader wings of $T(z)$ dependence. Moreover, at the calibrated maximal normalized transmittance (~1.2), the ratio of the maximum intensity of probe pulse and saturation intensity was defined to be $I_0/I_{sat} = 0.06$. This is the extremely low ratio, which gives the unrealistically high saturation intensity ($I_{sat} = 1.4 \times 10^{12}$ W cm^{-2}).

At low energy of 532 nm pulses [0.02 mJ, Fig. 1.5(b)], the SA was a dominant nonlinear optical process. As in the case of shorter pulses [Fig. 1.4(b)], the normalized transmittance initially increased up to 1.2 once the cell approached the focal plane and then decreased to the normal conditions ($T = 1$). These experimental data were fitted using the phenomenological model, which is well suited with the maximal normalized transmittance (solid curve). The ratio of maximal intensity and saturation intensity was defined from the best fit to be 0.2. From this fitting curve, the Rayleigh length (11 mm) of the focused radiation of this nanosecond laser, focal area (6×10^{-5} cm^{-2}), and intensity of 0.02 mJ pulses (3×10^7 W cm^{-2}) were defined. One can see that even at this small intensity the SA plays important role in the thionine solution. The corresponding saturation intensity was calculated to be 1.5×10^8 W cm^{-2}. Notice that in the case of 40 ps pulses $I_0/I_{sat} = 0.25$ was defined for the focal intensity of 7×10^{10} W cm^{-2} [Fig. 1.3(b)] in the case of the same dye solution. Thus in the case of short pulses, the saturation intensity was 2.8×10^{11} W cm^{-2}. These calculations point out the importance of the energy fluence rather than intensity as a crucial parameter influencing the nonlinear optical properties of the dyes. Moreover, the lifetime of the trap and intermediate states play important role in the saturation of different processes. The ratio of ~10^3 between saturation intensities indicates that the temporal characteristics of probe pulses and lifetimes of the states responsible for these processes are the crucial parameters varying the nonlinear optical response of this medium.

The third-order susceptibilities of dyes were entirely defined by the imaginary parts of these parameters. The $\text{Im}\chi^{(3)}$ for two wavelengths were in the range of 1×10^{-14} esu to 1×10^{-13} esu depending on the dyes and their molar concentrations. The maximal values of third-order nonlinear susceptibilities at the wavelengths of 1064 and 532 nm were obtained in the case of DEC dye (1×10^{-13} esu). The best fits with experimental results for most dyes showing this process were observed using the phenomenological model when the saturation is considered in terms of depletion of the ground-state concentration in the case of low intensities and low fluencies and the two-level model considering the heterogeneously broadened states at high intensities. Saturation intensities were derived from these fits. Notice that the former model is better fitted to the conditions when the population relaxation time is shorter than the duration of the probe pulses, which is the case of 10 ns, 532 nm radiation.

Meanwhile, the SA can be considered as a negative nonlinear absorption. The nonlinear absorption coefficient of erythrosine [Fig. 1.5(d)] in that case could be estimated from the comparison with the thionine being influenced by SA and positive nonlinear absorption [presumably 2PA; Fig. 1.5(c) bottom curve, $\beta = 1.5\times10^{-11}$ cm W^{-1}]. In these two cases $|\Delta T|$ in the focal area were equal to 13.7 and 0.8 respectively. Correspondingly, erythrosine showed largest value of nonlinear absorption ($|\beta| = 2.5\times10^{-10}$ cm W^{-1}). The corresponding $|\chi^{(3)}|$ was calculated to be 1.3×10^{-13} esu at $C = 1\times10^{-3}$ mol/L. Thus in the case of this species, the nonlinear susceptibility per molar unit was $\sim 1\times10^{-10}$ esu L mol^{-1}.

The data for erythrosine obtained using 532 nm radiation corroborate with the spectral and kinetic characteristics of this dye. The maximum of the absorption band of the water solution of this dye is centred at 521 - 526 nm. The molar extinction coefficient is equal to $\varepsilon = 32000$ L mol^{-1} cm^{-1}, while the effective cross-section of absorption $\sigma_{S0->S1} = 5.4\times10^{-16}$ cm^2. These values correspond to the singlet-singlet transition in erythrosine molecules. Meanwhile, efficient RSA could be observed at $\sigma_{12} > 5.4\times10^{-16}$ cm^2. The triplet-triplet absorption in the vicinity of 532 nm could be the second option for efficient absorption.

Almost all molecules will be excited to the T$_1$ triplet state under the action of 10 ns pulses since the constant rate for S$_1$->T$_1$ corresponds to $k_{isc} = (1.6 - 2.8)\times10^{9}$ sec^{-1}. In the case of 40 ps pulses, this parameter is significantly lower. Only a small part ($\sim$ 6-11%) of excited molecules translates on the triplet state during this time. Thus triplet-triplet absorption plays an important role only in the case of relatively long ($\tau > 0.5$ ns) pulses. However, even for these pulses, the main condition for

RSA ($\sigma_{12} > 5.4\times10^{-16}$ cm^2) is not fulfilled, since for these dyes $\sigma_{12}(\sigma_{T1->T2})$ $< 1/8\times\sigma_{S0->S1}$. Similar results were reported in Ref. [13] where, for the time interval of 0 - 1500 ps, they observed the bleaching band in the spectral range of 480 - 550 nm. This bleaching band was also observed for the time scale of 200 - 2000 ns [14]. One can note that RSA can be achieved in the erythrosine solutions for the wavelengths shorter than 480 nm, as well as in the 615 - 780 nm range where the effective cross-section of the triplet absorption is larger than the one of the single-singlet transition [15]. The results obtained in discussed work corroborate with those reported in Ref. [16] and explain their observations. Meanwhile, there is a probability of 2PA in erythrosine [Fig. 1.1(d)]. However, this process wasn't observed during those experiments, which points out the low value of the β attributed to the 2PA in this dye.

The behavior of thionine in the case of the 532 nm pump is rather complex. The decrease of normalized absorption in the vicinity of the focal plane was observed simultaneously with the SA. The former process could be attributed to the RSA based on the five-level scheme comprising singlet and triplet states. The absorption of this radiation corroborates with the nonforbidden transitions since the effective cross-section in that case $\sigma_{S0->S1} = 9.2\times10^{-16}$ cm^2. Taking into account the lifetime of excited singlet state and constant of interspin conversion ($k_{isc} \sim 10^9$ sec^{-1}) one can assume that triplet-triplet absorption would play an important role only for the 10 ns pulses. At the same time, a similar peculiarity was observed for the 40 ps probe pulses. Additionally, the data obtained in the literature point out that, at the wavelength of 532 nm, the induced triplet-triplet absorption of this dye is smaller than the ground state bleaching, while being larger in the 400-500 and 650-850 nm ranges. In the meantime, the water solutions of thionine demonstrate the absorption band centred at 275 nm, which can be induced by singlet-singlet transitions. This absorption band could be responsible for the 2PA under the action of 40 ps and 10 ns pulses. Thus all these assumptions can be considered as the manifestation of SA+2PA rather than SA+RSA processes.

The most sophisticated case to interpret the effects of nonlinear absorption was the observation of the valley at the focal plane during z-scan of DEC [Figs. 1.4(a) and 1.5(a)]. As already mentioned, the optical density in the vicinity of 532 nm is defined by the edge of the absorption band of J-aggregates centred near 660 nm (Fig. 1). This extended short-wavelength tail of the narrow peak of J-aggregates is caused by the defects of the packing of these aggregates. The linear absorption at 532 nm attributed to the presence of dimers should not lead to the notable nonlinear absorption. Unfortunately, there is no data in the literature

regarding the triplet-triplet transitions in monomers and dimers of DEC. Because of this one cannot define the probability of the RSA in DEC at 532 nm in the frames of the five-level scheme based on the triplet-triplet states. However, these dye solutions showing the dominantly strong J-band of DEC aggregates also possess the absorption in the region of 266 nm [Fig. 1.1(d)]. Taking into account the decrease of normalized transmittance of these species in the vicinity of the focal plane using 40 ps and 10 ns pulses of 532 nm radiation, as well as the strong intensity dependence of this process, one can attribute the observed nonlinear absorption to the 2PA through the singlet-singlet transitions.

1.2. Peculiarities of the nonlinear optical absorption of methylene blue and thionine in different solvents

Various types of dyes took attention due to their specific nonlinear optical properties [17]. At present, the physicochemical properties of thiazine dyes are being actively studied. Particular attention is paid to photophysics and photochemistry of cationic dyes of methylene blue (MB^+) and thionine (TH^+). The structural formulas of these thiazine dyes are shown in Fig. 1.6. These dyes are interesting from the point of view of creating photosensitizers of singlet oxygen, photobactericidal, and photocatalytic systems.

In particular, the molecules of MB^+ and TH^+ have some peculiar spectral properties. They absorb light in the 550 - 680 nm region. They also demonstrate a low-lying triplet state (0.3 - 0.4 eV below the first excited singlet state, and an appreciable level of triplet yields for MB^+ and TH^+ of 0.4-0.5. At relatively low intensities of the exciting radiation, these dyes are able to transform into a colourless leucoform (MB^++H$^+$+2e$^-$ →MBH), particularly through protonation from the triplet state and the attachment of electrons. The dimers of these dyes have other properties and play a negative role in the photosensitization of singlet oxygen. To diminish such processes and enhance the unique photosensitizing properties of MB^+ and TH^+, attempts are made to interface them with semiconductor quantum dots and metal nanoparticles [18].

In most cases, the laser radiation was used for the probe experiments of these dyes. This requires a detailed analysis of the response caused by the action of pulsed laser radiation. The linear absorption properties for these dyes are the most studied. At the same time, there are practically no systematic studies of the optical nonlinearities of MB^+ and TH^+ molecules. In particular, there are no data on the processes determining such nonlinear optical response as nonlinear absorption. In this section, we discuss the

studies of the nonlinear absorptive characteristics of some cationic organic thiazine dyes in aqueous and ethanol solution using 10 ns pulses at the wavelength of 532 nm (methylene blue and thionine) [19]. We analyze the 2PA, SA, and RSA of these dyes. We also demonstrate the RSA in the case of MB^+ and the concurrence of SA and TPA in the case of TH^+ using different concentrations of dye aqueous and ethanol solutions.

1.2.1. Characterization of the optical spectra of dye solutions

The measurements of the nonlinear optical properties of dyes were carried out by applying the standard z-scan technique presented in section 1.1. The Nd:YAG laser generated the single pulses ($\lambda = 1064$ nm, $\tau = 10$ ns) at a 1 Hz repetition rate. The probe second harmonic ($\lambda = 532$ nm) of this radiation generated in KDP crystal was focused by a 300-mm focal length lens. The organic dyes (MB^+ and TH^+) were selected due to different absorption near the wavelength of the probe radiation (532 nm, Fig. 1.6). The experiments were carried out using aqueous and ethanol solutions. For the concentrations of 10^{-4} M and 10^{-3} M, a noticeable linear transmittance at 532 nm characterizes these dyes. Meanwhile, the optical density of the solutions of these dyes was sufficient to record the nonlinear response under z-scan conditions.

The wavelengths of the maximum absorption of dyes and the ability in the absorption of 532 nm in these species were as follows. The MB^+ monomers (M-forms) have an optical absorption peak at 664 and 655 nm for aqueous and ethanol solutions (M-band), as well as a characteristic feature at 610 - 620 nm caused by the vibrational structure of the corresponding electronic transition band (Fig. 1.6a). Such spectra are characteristic for low-concentration aqueous solutions of this dye (in particular, for concentrations below 10^{-4} M, as well as at any concentrations of the ethanol solutions of MB^+ (Fig. 1.6a). Another characteristic feature of the aqueous solutions of MB^+ at concentrations of 10^{-4} M and higher is the appearance of yet another absorption band having a peak at 604-607 nm (Fig. 1.6a) belonging to the dimers of MB^+ (D-forms).

Spectral properties of TH^+ are qualitatively similar to MB^+ and differ to a greater extent in the position of the corresponding absorption peaks, which turned out to be shifted to the short-wavelength range by 50 - 60 nm. The TH^+ M-forms have an optical absorption peak at 599 - 603 nm (M-band) and a characteristic feature at 560 nm caused by the manifestation of the vibrational structure of the corresponding electronic transition band (Fig. 1.6b). Such spectra are characteristic for aqueous

solutions of this dye at concentrations of 10^{-4} M and lower, as well as at any concentrations of ethanol solutions of TH^+. With an increase in the concentration of TH^+ (10^{-3} M and higher), the appearance of D-forms is a characteristic of aqueous solutions, the absorption band of which has a peak at 560 nm (D-band) (Fig. 1.6b).
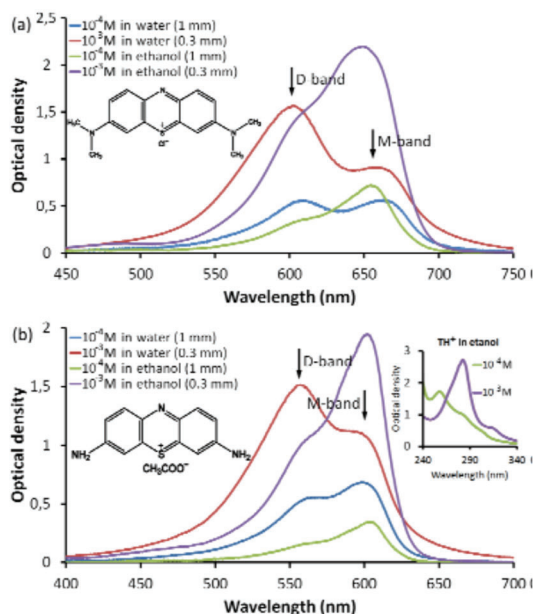
Fig. 1.6. Absorption spectra in the visible range of the aqueous and ethanol solutions of $MB+$ (a) и $TH+$ (b) using the 1- and 0.3-mm thick cells. Inset to Fig. 1.6b shows the absorption spectrum of the ethanol solution of TH^+ in the ultraviolet range. Reproduced from [19] with permission from Elsevier.

For the investigated concentrations of TH^+, the wavelength of the probe pulse falls on the short-wavelength edge of the corresponding M-band and is close to the D-band, the presence of which is determined by the concentration of TH^+ solution. For the MB^+ dye, the probe pulse wavelength is at the edge of the M-band and to a lesser extent belongs to the edge of the D-band.

1.2.2. Z-scans of dyes

The 532 nm radiation could be absorbed either through the 2PA or through the excitation of the intermediate states, which could further cause different types of absorption. In some cases, one can expect negative nonlinear absorption (SA), i.e. growth of transmittance of the sample moving close to the focal plane in the z-scan scheme, alongside the positive nonlinear absorption (RSA and/or 2PA). Figures 1.7 and 1.8 present the groups of z-scans showing the manifestation of the effects of nonlinear absorption of light in aqueous and ethanol solutions of MB^+ and TH^+ dyes having different ratios of monomers and dimers. 532 nm, 10 ns, 0.32 mJ pulses were used as the probe radiation of different concentrations of dyes in both cases.
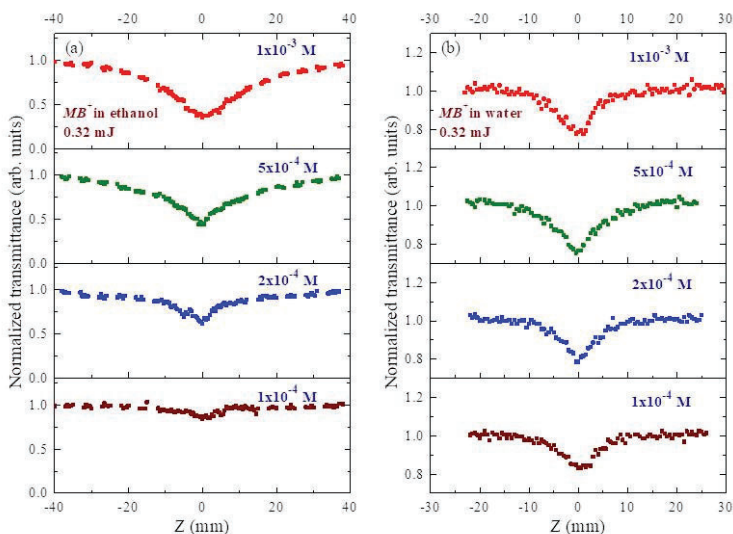
Fig. 1.7. Z-scans of (a) ethanol and (b) aqueous solutions of MB^+ at different concentrations of dye. Reproduced from [19] with permission from Elsevier.

Note that, in the case of the closed-aperture z-scans of these samples at the moderate energies of 10 ns, 532 nm pulses, the nonlinear refraction was below the level of registration. The closed-aperture z-scans in those cases were almost the same as the OA ones, which points out the

negligible values of nonlinear refractive indices of these dye solutions at the wavelength of 532 nm in the case of 10 ns pulses.
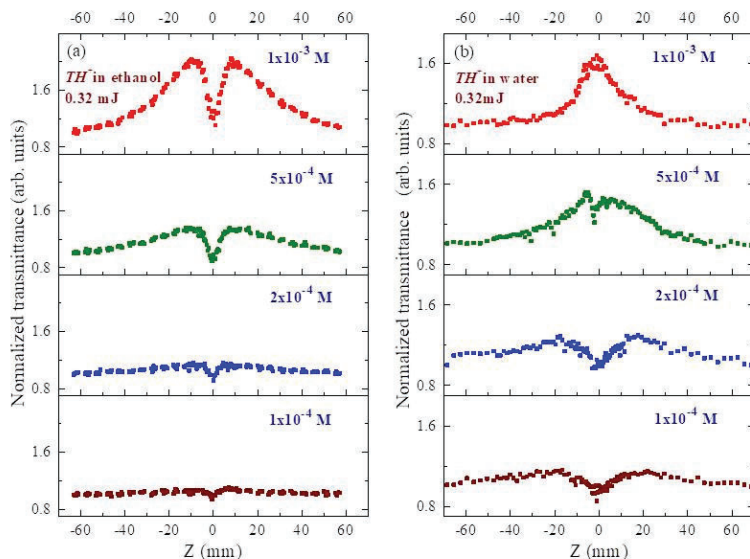
Fig. 1.8. Z-scans of (a) ethanol and (b) aqueous solutions of TH^+ at different concentrations of dye. Reproduced from [19] with permission from Elsevier.

The OA z-scans of aqueous and ethanol solutions of MB^+ using 532 nm nanosecond pulses are shown in Fig. 1.7 for the pulse energies of 0.32 mJ. The main observed regularities consisted in the formation of a symmetric z-profile, which shows a decrease in the transmission as the sample approaches the focal plane. This process was observed for MB^+ almost immediately after the start of the z-scan and gradually increased as the sample approached the focal plane (Figs. 1.7a and 1.7b).

The $|\Delta T_{max}|$ of the valley of z-scans was $|\Delta T_{max}| \approx 0.65$ at C = 1×10^{-3} M of MB^+ in the ethanol solution (Fig. 1.7a, upper panel). In that case, the nature of the nonlinear response is primarily due to the presence of the M-forms of MB^+. $|\Delta T_{max}|$ drops down to 0.15 with the concentration of the dye in the ethanol solution decreasing from 10^{-3} to 10^{-4} M. In the case of MB^+ aqueous solutions, the shape of the z-scan did not change qualitatively. However, the $|\Delta T_{max}|$ of the peak of z-scan increased with the growth of concentration lesser than in the former case, with some saturation of this

process ($|\Delta T_{max}| \approx 0.2 - 0.3$, Fig. 1.7b). Moreover, the dependence of this parameter on the concentration of aqueous solutions of MB^+ was significantly weaker compared with the ethanol solution. The observed dependences indicate that the symmetrical z-profiles of scans can be mainly attributed to the M-forms of MB^+. At the same time, the presence of dimers is indicated by the optical absorption spectra of this solution (Fig. 1.6a). However, their presence does not give a noticeable nonlinear response.

Figure 1.8 shows similar dependencies in the case of the aqueous and ethanol solutions of TH^+. In the case of the ethanol solution of TH^+ (Fig. 1.8a), SA was observed simultaneously with a decrease in the transmission (RSA) as the sample approached the focal plane of the lens. Meanwhile, for TH^+ water solution, the RSA observed at smaller concentrations was replaced by the prevailing effect of the negative nonlinear absorption (SA) at the higher concentrations of this dye. The growth of the molar concentration led to a decrease of the positive nonlinear absorption (compare four z-scans from the bottom to the upper panels of Fig. 3b). The relative weight of SA at $C = 10^{-3}$ M was significantly larger compared with RSA, while the latter process played an important role at $C = 10^{-4}$ M. The concurrence of these two processes was observed at different concentrations of TH^+, which was clearly manifested in the case of highest concentration of this dye in ethanol solution (Fig. 1.8a, upper panel).

The analysis of z-scans was performed using the basic principles of nonlinear optical absorption in the multi-level molecular systems. Most probable mechanisms of this process were chosen to be RSA and SA. The explanation of the insignificant role of the latter process will be discussed in the following section. In contrast with SA, when the absorptive properties of the material possessing SA fade with increasing the intensity due to depletion of the ground state, RSA can result in large absorption by the nonlinear absorber at high incident laser energies and low absorption at low laser energies. A five energy level model could be used to interpret RSA. Such absorption in the medium requires the fulfilment of the group of basic criteria. Firstly, the material should have an excited-state absorption cross section larger than the ground-state absorption cross section. Secondly, the lifetime of the excited state should be long enough (in comparison with the pulse duration of the laser radiation).

The nonlinear absorption coefficient (β) measurements of species were carried out using the normalized transmittance for the OA scheme (Eq. 1.1). The 532 nm ($E_{532nm} = 2.34$ eV) radiation could be absorbed either through 2PA or through the excitation of intermediate states, which could further cause the additional absorption. The latter mechanism also includes

the involvement of RSA, the process when SA cannot be further realized due to saturation of the intermediate states. In some cases, one can expect negative nonlinear absorption (SA), i.e. growth of transmittance with the approach of the sample close to the focal plane in the z-scan scheme, alongside the positive nonlinear absorption (RSA). Figures 1.7 and 1.8 just demonstrate different effects of the nonlinear absorption of dyes in water and ethanol showing different relations between dimers and monomers.
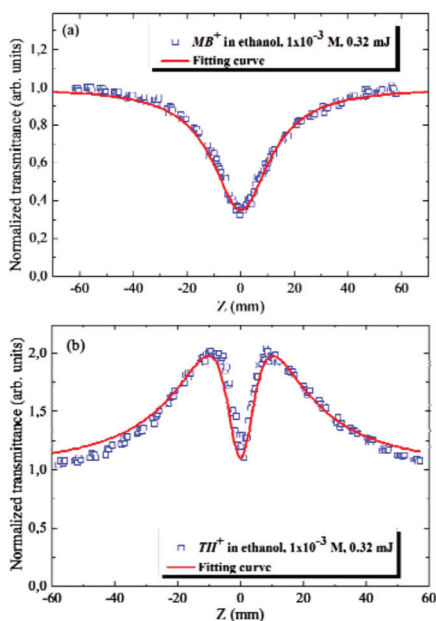
Fig. 1.9. Fitting of the OA z-scans of the (a) MB^+ and (b) TH^+ ethanol solutions using Eqs. (1) and (3). Reproduced from [19] with permission from Elsevier.

Figure 1.9 shows the fitting curves for the highest concentrations of dyes in ethanol (10^{-3} M). MB^+ demonstrated the RSA along a whole set of the variations of concentrations. The fitting of Eq. 1.1 with experimental data (solid curve in Fig. 1.9a) allowed the definition of the positive nonlinear absorption of this sample related with RSA ($\beta = 7 \times 10^{-11}$ cm W^{-1}) in the case of 532 nm, 10 ns, 0.32 mJ probe pulses. The ethanol solution of TH^+ demonstrated a rather sophisticated behaviour of z-scan (Fig. 1.9b). The fitting of these experimental data was based on the joint influence of

RSA (or 2PA) and SA (solid curve in Fig. 1.9b). These assumptions can be considered as either SA+2PA or SA+RSA processes. The saturation intensity and nonlinear absorption of this sample were calculated to be $\sim 2\times10^8$ W cm^{-2} and 1.0×10^{-11} cm W^{-1}, respectively.
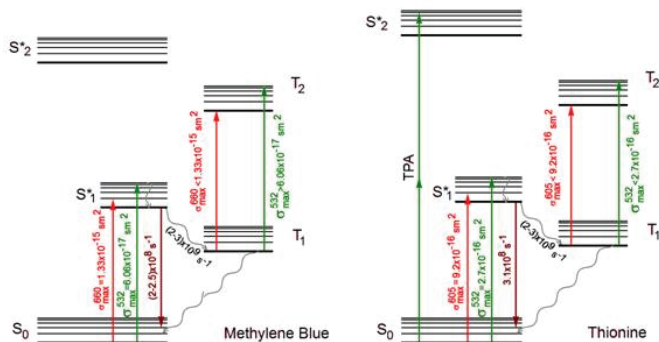
Fig. 1.10. Empirical schemes of transitions in the molecules of MB^+ and TH^+ clarifying the mechanisms of optical nonlinearities under the action of 10 ns, 532 nm pulses. Reproduced from [19] with permission from Elsevier.

The data for aqueous and ethanol solutions of MB^+ (M-forms) obtained by the action of 532 nm pulses are consistent with the spectral and kinetic data [20]. In this case, the molar extinction coefficient ε = 80,000 l·mol^{-1}·cm^{-1} and the effective absorption cross-section at the 664 nm will be σ_{01} = 1.33×10^{-15} cm^2. These quantities correspond to allowed singlet-singlet ($S_0 \rightarrow S_1$) resolved transitions of the $\pi \rightarrow \pi^*$ type in the MB^+ molecules. At a wavelength of 532 nm, the cross-section is much lower and is about σ_{01} = 6×10^{-17} cm^2. On the other hand, the requirement for RSA is the excess of the effective absorption cross-section for the second stage, i.e. $\sigma_{12} > 6\times10^{-17}$ см^2. In the case of the triplet-triplet absorption, whose wide band has a maximum of about 532 nm, a second transition (σ_{12}) for MB^+ can be applicable for the RSA (Fig. 1.10). Since the interspin conversion rate constant for the $S_1 \rightarrow T_1$ transition in MB^+ is k_{isc} = $(2 - 3)\times10^9$ sec^{-1} [21], then in the case of ns pulse durations (i.e. longer than a few hundred picoseconds, which is a case of used experimental conditions) practically all excited molecules will be in the triplet state T_1. This conclusion corroborates with the data of the yield of triplets for this dye, which is about 0.5.

The main condition for RSA ($\sigma_{12} > 6 \times 10^{-17}$ cm^2) is apparently fulfilled for MB^+. This conclusion corroborates with the data of Ref. [22]. In the case of MB^+, this condition is observed due to a strong detuning of the resonance of the optical absorption of the M-forms of MB^+ from the wavelength of the probe pulse. In addition, the data available in the literature indicate that, in the case of MB^+, at a wavelength of 532 nm the level of induced triplet-triplet absorption is higher than the corresponding ground state bleaching signal [23].

The values of $|\Delta T_{max}|$ for ethanol and aqueous solutions are also quite understandable within the RSA model. Here the main role is played by the difference in the positions of the optical absorption maxima for aqueous and ethanol solutions (Fig. 1.6). The main absorption peak is most strongly shifted to the long-wavelength region for the MB^+ aqueous solution ($\sim$ 9-10 nm), and the value of σ_{01} at the 532 nm wavelength is smaller than in the case of the ethanol solution. For triplet-triplet absorption, a shift of 10 nm does not give a significant change in σ_{12}. Therefore, for aqueous solutions MB^+, the values of $|\Delta T_{max}|$ are noticeably larger than for ethanol ones.

For solutions of TH^+ (M-forms), the z-scans obtained at a wavelength of 532 nm are much more complicated. Along with the effect of SA, a decrease in the transmission was observed as the sample approached the focal plane, which could be attributed to RSA under conditions of a five-level scheme involving singlet and triplet levels. However, the data available in the literature make it clear that at $\lambda = 532$ nm the induced triplet-triplet absorption in TH^+ is lower than the corresponding ground state bleaching [24]. It is higher in regions of 400-500 nm and 650-850 nm. A similar result was also obtained in the studies in which a bleaching band in the spectral range of 480-550 nm was observed up to 1500 ps from the beginning of excitation. In the case of a longer time interval (200-2000 ns) a bleaching band was observed in the range of 480-550 nm. Thus, the experimentally observed SA is not accidental. It should be noted that RSA can be detected in the TH^+ solutions but only in the spectral region shorter than 480 nm, and also in the region of 615 - 780 nm, where the triplet absorption band has an effective cross-section larger than for the singlet-singlet transition. There seems to be a possibility for 2PA in the TH^+ solutions (Fig. 1b). However, this process does not manifest itself due to the noticeable competition of RSA with the participation of triplet-triplet transitions. At the same time, for aqueous solutions of TH^+ there is a band with a maximum of 275 nm caused by the $\sigma \rightarrow \sigma^*$ type singlet-singlet transitions ($\varepsilon = 32000$ l·mol^{-1}·cm^{-1}). This transition is quite suitable for the realization of 2PA under the action of 10 ns pulses at a wavelength of 532

nm. Thus the results of z-scans for solutions of TH^+ could be interpreted by the joint influence of SA and 2PA (Fig. 1.10).

The observed differences in the contribution of SA for ethanol and aqueous solutions (Fig. 1.8) can be attributed to the substantial contribution to this process of the D-forms of TH^+. The maximum of absorption band of D-forms at 565 nm is closest to the wavelength of the laser pulse. Apparently, the same reason causes the absence in the z-scan of a valley for an aqueous solution with the largest content of dimers (10^{-3} M) (Fig. 1.8b, upper panel).
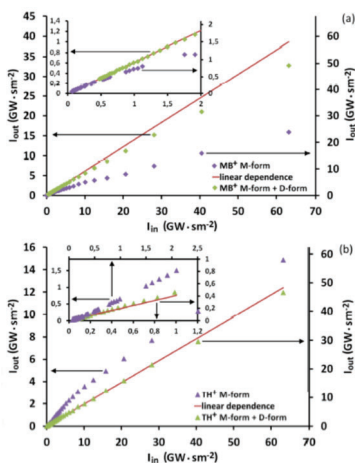
Fig. 1.11. Optical limiting curves of (a) MB^+ M-form (10^{-3} M in ethanol), MB^+ M-form + D-form (10^{-4} M in water) and (b) TH^+ M-form (10^{-3} M in ethanol), TH^+ M-form + D-form (10^{-4} M in water) with 10 ns pulse laser at 532 nm. Reproduced from [19] with permission from Elsevier.

Analysis of the z-scans results in the possibility of observing the effective optical limiting properties in MB^+ solutions. This conclusion was experimentally confirmed (Fig. 1.11). The dependence of the laser power passing through the sample on the incident power shown in Fig. 6a demonstrates that only samples containing predominantly MB^+ M-forms are suitable for the optical limiting. Reducing the concentration of the M-forms of MB^+, particularly by changing the solvent from ethanol to water and also by increasing the concentration of the dye in an aqueous solution, weakens the optical limiting effect. For TH^+, in spite of the similarity of its structure with MB^+, it is typical to bleach the medium in the first stage and then reduce this effect to the level of linear transmission (Fig. 1.11b).

1.3. Nonlinear optical characterization of colloidal solutions containing dye and Ag₂S quantum dot associates

In quantum dots containing materials, the optical limiting was observed at the wavelengths of 532 and 1064 nm at the fluencies of $1 - 2$ J cm^{-2} and pulse durations varying between 30 fs to 10 ns [25,26]. The studies of optical limiters in various materials open new opportunities for their applications as the ultrafast nonlinear optical switching systems to protect eyes and sensitive registrars from intense radiation. The mechanisms that cause optical limiting have different origins depending on the materials. The nonlinear refraction causes optical limiting in a number of inorganic clusters [27]. 2PA is responsible for optical limiting in semiconductor structures. RSA, which takes place due to high absorption from excited states, is often referred to as responsible for the optical limiting in colloidal metal compounds and fullerenes. Thus the excited state-induced nonlinearity is one of the main sources of optical nonlinearities, which has potential applications for optical limiting [28]. The availability of RSA and TPA in Ag₂S suggests that silver sulphide quantum dots (QDs) could be a very promising nonlinear medium for nonlinear photonic devices in different time scales provided these semiconductor nanocrystallites being incorporated in the appropriate media retain the attractive features of both components.

Most of the previous nonlinear optical studies of sulphide-based QDs were devoted to the analysis of nonlinear absorption for the laser pulses with the duration of a few tens of nanoseconds. It would be interesting to analyze this and other nonlinear optical processes using shorter (e. g. picosecond) pulses since no thermal lens effect can be expected at these conditions and low pulse repetition rate, which allows separation of fast- and slow-range nonlinear optical processes. In this section, we discuss the studies of the nonlinear refraction and nonlinear absorption in the associates of the dyes of different classes (xanthenes, thiazines, carbocyanines, quinolines) and the Ag₂S QDs stabilized in gelatin using 40 ps pulses [29].

The single-beam z-scan method offers a number of advantages over interferometric and other methods of measurements of the nonlinear optical parameters of various media. Investigations of QD solutions were carried out at the wavelengths of 1064 nm and 532 nm, applying the standard z-scan technique. The Nd:YAG laser generated a single pulse ($\tau = 40$ ps) at a 2 Hz repetition rate. This radiation ($\lambda = 1064$ nm), or its second harmonic ($\lambda = 532$ nm) generated in KDP crystal, was focused by a 25-cm focal length lens. The 3-mm-thick quartz cells containing QDs solution were moved along the z-axis through the focal point using a movable table

controlled by a computer. The intensities of the optical breakdown of QD solutions were measured to be 5×10^{11} W cm^{-2} and 1.5×10^{11} W cm^{-2} at the wavelengths of the fundamental and second harmonic radiation, respectively. The intensities used in the experiments did not exceed 1×10^{11} W cm^{-2} (1064 nm) and 4×10^{10} W cm^{-2} (532 nm).

Table 1.1. The wavelengths of maximum absorption of dyes and Ag$_2$S QDs and the ability of absorption of 532 nm radiation in these species Reproduced from [29] with permission from Springer.

Triquinolil-methane	DEC	erythrosine	thionine	Ag$_2$S QDs
622 nm (weak absorption at 532 nm)	658 nm (weak absorption at 532 nm)	540 nm (strong absorption at 532 nm)	609 nm (weak absorption at 532 nm)	425 nm (strong absorption at 532 nm)

The technology of colloidal Ag$_2$S QD preparation, as well as the morphology and absorption properties of the dye solution and QDs dispersed in gelatine, was as follows. Two solutions (AgNO$_3$ and Na$_2$S) were used for the preparation of Ag$_2$S QDs as the sources of Ag$^+$ and S^{2+} ions. The mixture of two solutions was performed by slow rinsing in the cell containing 2% water solution of photographic gelatine at 70 ºC. The mean sizes of QDs in gelatine were 3 nm. They showed strong absorption in the 2.90 - 3.00 eV region and notably weaker absorption in the 1.6 - 2.5 eV region. Three concentrations of dyes were used: 1×10^{-2}, 3×10^{-2}, and 1×10^{-1} moles of dye in one mole of Ag$_2$S QD + gelatine solution (in other words, molar fractions, m. f.) The used range of dye concentrations corresponded to the ratios of the dye molecules and Ag$_2$S QDs varying in the range between 2:1 and 20:1. The preparation of the dye and silver sulphide quantum dot associates was performed by the addition of water solution of different dyes to the solution of Ag$_2$S QDs. The preparation of the mixture of Ag$_2$S QDs and thioglycolic acid was performed using the technique described in [30]. Briefly, 100 ml of the water solution of AgNO$_3$ at 2×10^{-3} M l^{-1} was mixed with 2×10^{-4} M of thioglycolic acid. Then the pH of the solution was adjusted to 10 using 1 M solution of NaOH and mixed with 2×10^{-4} M of Na$_2$S. The final solution had the browned colour thus indicating the formation of Ag$_2$S, which was confirmed using TEM measurements.

Four dyes of different classes were used: quinoline (6-[Bis-(1,2,2,4)-tetramethyl-1,2,3,4-tetrahydro-quinolin-6-yl)-methylene]-1,2,2,4-tetramethyl-2,3,4,6-tetrahydro-quinolinium chloride; further this dye will

be dubbed as triquinolilmethane dye), carbocyanine (3,3'-di-(γ-sulphopropyl)- 4,4',5,5'-dibenzo-9-ethylthiacarbocyaninebetaine pyridinium salt; further this dye will be dubbed as DEC), thiazine (thionine) и xanthene (erythrosine) dyes. These dyes were chosen due to the different absorption of these species near the wavelength of the second harmonic (532 nm) of Nd: YAG laser (see Table 1.1). One can see that some of them strongly absorb at 532 nm. No absorption of 1064 nm radiation was in either of these dyes. The influence of dyes nonlinearities on the whole pattern of the z-scans of QD solution, as well as the application of different molar fractions of dyes in QD solutions and variable intensities of probe radiation (1064 nm and 532 nm) will be analyzed and discussed in the following subsection.

1.3.1. Z-scan measurements

Dyes themselves possess various types of optical nonlinearities (nonlinear refraction, saturated absorption, reverse saturated absorption, two-photon absorption, etc.). Thus their associates with QDs would result in the joint manifestation of the optical nonlinearities of two components. Prior to the analysis of Ag_2S QD and dye associates, the z-scans of Ag_2S QD solution with the solvent were measured, which did not show the nonlinear optical features. This allowed excluding the influence of dye's nonlinearities and analyzing the nonlinear optical effects attributed exclusively to QDs. Below we analyze the z-scans of the QDs prepared in gelatine and of the QDs prepared in thioglycolic acid (TGA).

OA z-scans showed that gelatine and TGA did not demonstrate the nonlinear optical features being without the QDs once one uses either 532 or 1064 nm pulses. Once QDs became embedded in gelatine the samples start to show the nonlinear absorption using 1064 nm (Fig. 1.12a, open squares) and 532 nm (Fig. 1.12a, filled circles) pulses. Z = 0 in this and other figures corresponds to the focal plane on the z-axis. One can see that stronger infrared pulses (1064 nm, 0.29 mJ) cause a lesser decrease of normalized transmittance in the vicinity of the focal plane compared with weaker visible probe radiation (532 nm, 0.16 mJ). The basic theoretical relations and numerical calculations of the nonlinear absorption and nonlinear refraction will be described in the following sections. Here various experimental options are considered allowing demonstration of the nonlinear optical features of the QDs dispersed in gelatine and QDs capped TGA.

The band gap energy of bulk Ag_2S is 1.0 eV, which points out the probability of single-photon absorption in the case of 1064 nm pulses

($E_{1064nm} = 1.17$ eV). However, in the case of QDs, the effective band gap showed a strong blue shift. In the case of used Ag$_2$S QDs the energy of exciton transition corresponds to 2.9 eV, which can be seen in the absorption spectra. Below this energy, the absorption of these QDs became notably lesser though not negligible. The absorption in this spectral region can be caused by the presence of large nanocrystallites. Also, notice that this spectral range is responsible for the IR luminescence of Ag$_2$S QDs through the trap states.
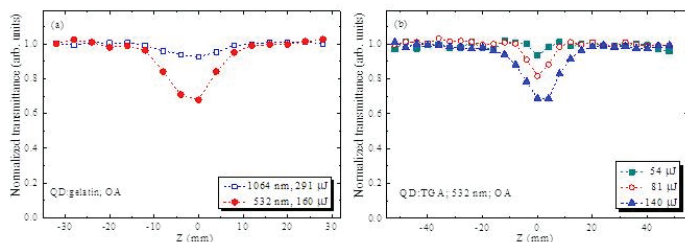
Fig. 1.12 (a) Normalized transmittances of the Ag$_2$S QDs dispersed in gelatine (QD:gelatine) using OA z-scan scheme and pulses of different wavelengths (1064 nm, 0.29 mJ and 532 nm, 0.16 mJ). (b) Normalized transmittances of Ag$_2$S QDs capped thioglycolic acid (QD:TGA) using OA z-scan scheme and 532 nm pulses of different energies (0.05, 0.08, and 0.14 mJ). The experimental data in these and other graphs were connected with each other using dotted lines for better viewing of analyzed dependencies. Reproduced from [29] with permission from Springer.

In the case of 4 nm Ag$_2$S QDs the effective band gap is 1.7 eV. For the 3 nm QDs Ag$_2$S used in present studies the effective band gap was significantly larger (2.9 эВ) due to the quantum confinement effect. The two- and three-photon absorption of 1064 nm photons explains the nonlinear absorption through the trap states or direct transition of the used QDs. As for 532 nm photons ($E_{532nm} = 2.34$ eV), they could be absorbed either through 2PA above effective band gap or through the excitation of trap states, which could further cause the additional absorption. The second option characterizes the saturated absorption in the first stage of laser-matter interaction followed by the reverse process of such kind of absorption, i.e. reverse saturated absorption. The probability of 2PA+RSA for 532 nm photons is reasonably larger compared with 2PA for 1064 nm photons, thus allowing the observation of a deeper valley in the z-scans for the former radiation even in the case of lower pulse energies (compare two valleys of the graphs shown in Fig. 1.12a).

These two mechanisms of the nonlinear absorption of 532 nm radiation in Ag_2S QDs have variable influence depending on the effective band gaps, QD size distribution, used solvents, a cross-section of the excited states population, energy transition between the absorber and the surrounding medium, etc. A lack of knowledge of most of these parameters makes it difficult to distinguish the relative role of 2PA and RSA in such solutions in the case of visible probe pulses. As already mentioned, the band gap of Ag_2S QDs strongly depends on the sizes of nanocrystallites. The reported experimental results differ from each other. Particularly for 3.3 nm QDs, the measured effective band gap is 1.8 eV. These sizes of QDs are close to those used in present studies, thus one can anticipate a larger probability of RSA compared with 2PA in discussed experimental conditions.

Figure 1.12b presents three OA z-scans in the case of different energies of the probe 532 nm pulses propagated through the QD:TGA solution. Similar to QDs dispersed in gelatine, one can speculate about the relative role of two processes of nonlinear absorption.

In the case of CA z-scans of two samples (QDs in gelatine and QDs in TGA) the nonlinear refraction was below the level of registration. The CA z-scans in those cases were similar to the OA ones, which points out the negligible value of nonlinear refractive indices of the used QDs sample and at the maximally used energies of 532 and 1064 nm pulses (0.2 and 0.3 mJ).

Below we analyze the behaviour of the associates of Ag_2S QDs with various dyes in the field of picosecond pulses.

QDs:erythrozine. CA z-scan showing normalized transmittance (T) of 532 nm pulses in the case of QDs with erythrosine is presented in Fig. 1.13a. One can see the prevalence of nonlinear absorption over nonlinear refraction, when valley ($|\Delta T = T_{out} - T_{foc}| \approx 0.4$) was notably larger than the peak ($|\Delta T| \approx 0.1$) of the $T(z)$ dependence. Here T_{out} is the normalized transmittance far from the focal plane ($T_{out} = 1$) and T_{foc} corresponds to the normalized transmittance of the sample placed in the focal plane ($T_{foc} \approx 0.6$ in the present case).

The wavelength and maximal intensity of probe beam, pulse energy, and molar fraction of dye in QD solution corresponding to the experiment shown in Fig. 1.13a were 532 nm, 2×10^{10} W cm^{-2}, 0.16 mJ, and 1×10^{-1} m. f. respectively, and are also shown in most of following figures. This QD solution showed positive nonlinear refraction, with valley preceding peak of CA z-scan. As it was mentioned in the case of QDs dispersed in gelatine, no nonlinear refraction was attributed to QDs at similar experimental conditions thus pointing out the influence of erythrosine on the whole pattern of CA z-scan. It will be shown in the following results

with other dyes that weak nonlinear refraction is a less influential
nonlinear optical process compared with nonlinear absorption.
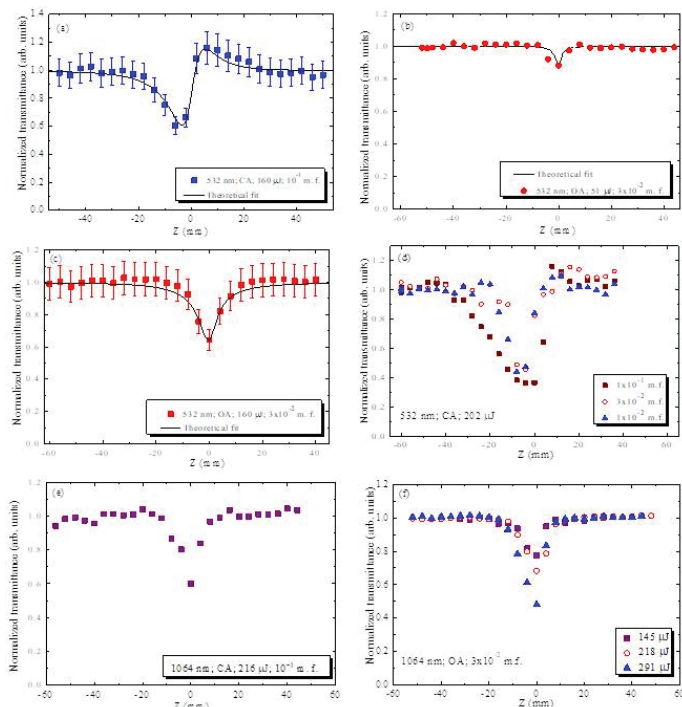
Fig. 1.13. Z-scans of QD:erythrozine samples. (a) CA z-scan using 532 nm
pulses. (b) OA z-scan using 0.05 mJ, 532 nm pulses. (c) OA z-scan using
0.16 mJ, 532 nm pulses. (d) CA z-scans using 0.2 mJ, 532 nm pulses and
different molar fractions of dye. (e) CA z-scan using 1064 nm pulses. (f)
OA z-scan using 1064 nm pulses of different energy. Solid curves show the
theoretical fits. The details of experimental conditions used during these
experiments and of theoretical fits are described in text, similarly to other
figures. Reproduced from [29] with permission from Springer.

The OA z-scans of QD: erythrosine solution are shown in Figs. 1.13b
and 1.13c for the pulse energies of (b) 0.05 and (c) 0.16 mJ. The error bars
($\pm 10\%$) of these and other OA and CA measurements of QD:erythrosine
are shown in Figs. 1.13a and 1.13c and were the same along the whole set
of experiments. The $|\Delta T|$ of valley increased with the growth of 532 nm
probe pulse energy, with some saturation of this process at the pulse

energies above 0.19 mJ. In the case of 0.2 mJ, 532 nm pulses the $|\Delta T|$ was saturated at ~0.6.

The variation of dye concentration between 1×10^{-2} and 1×10^{-1} m. f. in the case of CA z-scan showed some similarities of graphs in the case of 0.2 mJ, 532 nm pulses (Fig. 1.13d). The asymmetry of CA z-scan curves indicates the appearance of weak nonlinear refraction due to the influence of dye's nonlinearity. This component of the nonlinearities of QD:erythrosine solution was suppressed compared with nonlinear absorption during the growth of pulse energy (compare Figs. 3a and 1.13d). Probably, at a higher concentration of dye the rate of free erythrosine molecules in solution increases. Those free molecules do not interact with Ag_2S QDs and do not influence the nonlinear refraction.
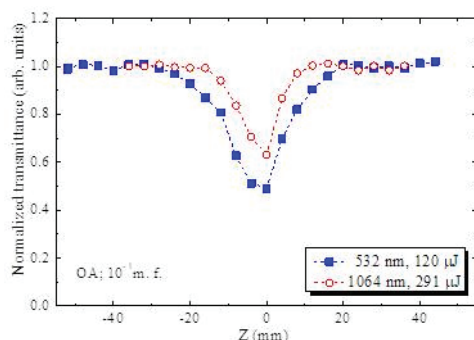
Fig. 1.14. OA z-scan of QD:thionine solutions using 532 nm (0.12 mJ) and 1064 nm (0.29 mJ) pulses. Reproduced from [29] with permission from Springer.

The application of 1064 nm pulses led to the entire disappearance of nonlinear refraction even at larger pulse energies (see CA z-scans in the case of 1064 nm, 0.22 mJ pulses and highest used concentration of dye, Fig. 1.13e). The CA curve was almost symmetric with regard to the focal plane. The OA z-scans demonstrated monotonic growth of $|\Delta T|$ with the increase of pulse energy (Fig. 1.13f), thus indicating the absence of saturation until the maximal used intensity (1.5×10^{11} W cm^{-2}). No absorption was observed at this wavelength either in erythrosine or in QDs. The nonlinear absorption in erythrosine could be only through the 2PA. The excited state of this dye can play some role in the case of QD:erythrosine solution.

QDs:thionine. In this sample, the nonlinear refraction was absent, which again points out the absence of this process in Ag$_2$S QDs. The experiment clearly showed the prevailing influence of QDs nonlinearities on the whole z-scan pattern. Meanwhile, separate OA measurements of pure thionine showed weak nonlinear absorption ($|\Delta T| \approx 0.06$) at similar parameters of laser pulses.

OA z-scans of QDs:thionine were carried out using 1064 nm, 0.29 mJ, and 532 nm, 0.12 mJ pulses (Fig. 1.14). Similar to QDs in gelatin, weaker 532 nm pulses caused larger nonlinear absorption compared with stronger IR pulses.
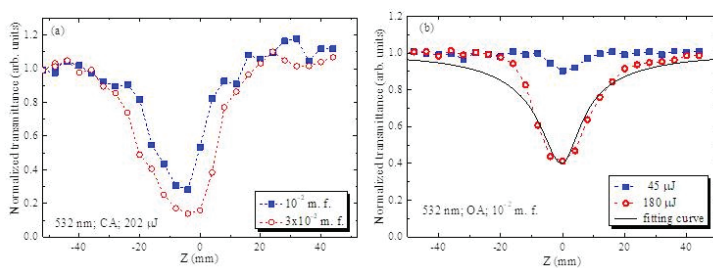
Fig. 1.15. Z-scans of QD:DEC samples. (a) CA z-scans using 532 nm pulses and different molar fractions of dye. (b) OA z-scans using 0.045 and 0.16 mJ pulses of 532 nm radiation. Solid curve corresponds to the theoretical fit (see text). Reproduced from [29] with permission from Springer.

*QD*s*:DEC*. The CA z-scans of this solution showed weak positive nonlinear refraction manifested by the asymmetry of the curve with regard to the focal plane (Fig. 1.15a). One can see the saturation of these curves at $|\Delta T| \approx 0.8$ manifested with the notable broadening of the valley. The growth of dye concentration (from 10^{-2} to 3×10^{-2} m. f.) caused the disappearance of the asymmetry of z-scans, thus indicating the entire prevalence of nonlinear absorption over nonlinear refraction in this sample. The OA z-scans using 532 nm pulses at different energies (0.045 and 0.18 mJ, Fig. 1.15b) also demonstrated the unsaturated growth of $|\Delta T|$ until maximally used intensities of 532 nm pulses. The z-scans in the case of 1064 nm pulses were similar to those of the two above QD:dye solutions.
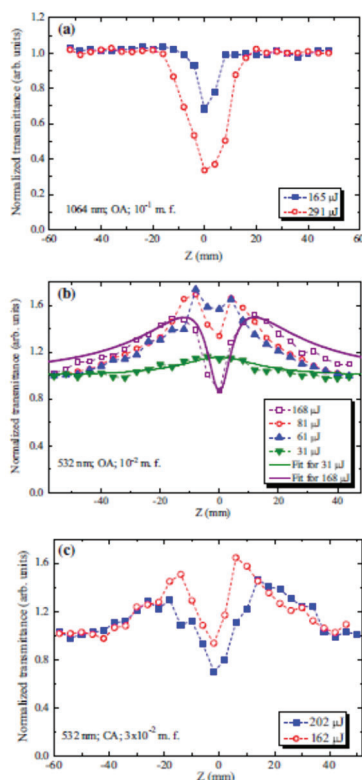
Fig. 1.16. Z-scans of QD:triquinolilmethane samples. (a) OA z-scans using 1064 nm pulses of different energies. (b) OA z-scans using 532 nm pulses of different energies. Fitting curves are shown for smallest and largest energies of 532 nm pulses assuming influence of sole saturated absorption of the dye and joint influence of saturated absorption and nonlinear absorption respectively (see text). (c) CA z-scans using 532 nm pulses of different energies. Reproduced from [29] with permission from Springer.

*QD*s:*triquinolilmethane*. These QD:dye associates demonstrated a significant influence of the nonlinear optical features of dye on the whole nonlinear optical response of the medium. Figures 1.16a and 1.16b show two sets of OA z-scans in the case of two probe pulses ((a) 1064 nm and (b) 532 nm). The application of IR pulses led to the featureless OA z-scant varying with the growth of pulse energy (Fig. 1.16a), similarly to other solutions. An entirely different pattern was observed in the case of 532 nm

pulses (Fig. 1.16b). One can see the joint influence of the saturated absorption originated from triquinolilmethane and the nonlinear absorption originated from QDs. The variation of pulse energy (from 0.04 to 0.2 mJ) showed the dominance of the latter process originated from nanocrystallites. In the case of the largest pulse energy of 532 nm radiation (0.2 mJ) the growth of transmittance far from the focal plane changes to the appearance of the valley centred in the focal point. In the meantime, the application of 0.04 mJ pulses led to the sole influence of the negative absorption attributed to the dye's nonlinearity.

Thus at low intensities of probe 532 nm pulses, the characteristic dependence of saturated absorption was observed showing the transmission increasing with the growth of pulse intensity. With further increase of pulse intensity, the $T(z)$ dependence was broadened and, at the highest intensities, the influence of additional nonlinear optical process was observed that can be attributed to both RSA and 2PA of QDs. The RSA can also play some role in the whole pattern of z-scans at the highest used pulse energies. These z-scans were fitted at weak and strong energies of 532 nm pulses assuming various saturated absorption models of dyes. The best fit with experimental results for QD:triquinolilmethane (solid thin curve for 0.03 mJ pulses, Fig. 1.16b) were observed using the kinetic model when the saturation is considered in terms of depletion of the ground-state concentration in the case of low intensities of 532 nm pulses. The fitting curve at the highest pulse energy (solid thick curve for 0.17 mJ pulses, Fig. 1.16b) comprises two processes, saturated absorption in dye based on the kinetic model and nonlinear absorption in QD.

Most of the dyes in the visible range do not show nonlinear refraction, while the weak positive γ has been reported in a few of them. The CA z-scans of QDs:triquinolilmethane demonstrated weak nonlinear refraction alongside the two types of nonlinear absorption (Fig. 1.16c). The asymmetry of the curves with regard to the focal plane (Fig. 1.16c) points out the positive sign of nonlinear refraction, similarly to the case of QDs:erythrosine.

1.3.2. Calculations of the nonlinear optical parameters of QD:dye suspensions

One of the advantages of the z-scan technique is the possibility of separation of the contributions of several nonlinearities when they are presented simultaneously. In general, when both nonlinear refraction and absorption are presented, the normalized transmittance of samples along the z-axis in the case of the CA scheme can be written as follows:

$$T(z) = 1 + \frac{4x}{(x^2+9)(x^2+1)} \Delta\Phi_o - \frac{2(x^2+3)}{(x^2+9)(x^2+1)} \Delta\Psi_o$$

$$(1.5)$$

where $x = z/z_0$, $z_0 = 0.5k(w_0)^2$, $k = 2\pi/\lambda$, w_0 is the beam radius at the $1/e^2$ level of the spatial intensity distribution in the focal plane, λ is the radiation wavelength, $\Delta\Phi_0$ and $\Delta\Psi_0$ are the parameters determining phase shift near the focal point as a result of nonlinear refraction and nonlinear absorption respectively, $\Delta\Phi_0 = k\gamma I_0 L_{eff}$, $\Delta\Psi_0 = \beta I_0 L_{eff}/2$, I_0 is the laser radiation intensity in the focal plane, $L_{eff} = [1-\exp(-\alpha_0 L)]/\alpha_0$ is the effective length of the sample, α_0 is the linear absorption coefficient, and L is the sample length. Introducing the coupling factor ρ, which is the ratio of imaginary ($\mathrm{Im}\chi^{(3)} = 10^{-7}c^2n^2_0\beta/96\pi^2\omega$) to real ($\mathrm{Re}\chi^{(3)} = 10^{-6}cn^2_0\gamma/480\pi^2$) parts of the third-order susceptibility ($\rho = \beta/2k\gamma$), one can get the relation between $\Delta\Phi_0$ and $\Delta\Psi_0$ ($\Delta\Psi_0 = \rho\Delta\Phi_0$). Here c is the light velocity in cm s^{-1}, ω is the laser radiation frequency in cycles s^{-1}, β is the nonlinear absorption coefficient in cm W^{-1}, n_0 is the linear refractive index, and γ is the nonlinear refractive index in cm^2 W^{-1}. Equation (1.5) in that case can be rewritten in the following form:

$$T = 1 + \frac{2(-\rho x^2 + 2x - 3\rho)}{(x^2+9)(x^2+1)} \Delta\Phi_o$$

$$(1.6)$$

The theoretical $T(z)$ curves were fitted to the experimental data using Eq. (1.6). In particular, the best fitting for QDs:erythrosine (Fig. 1.13a) was observed at $\rho = 0.21$ and $\Delta\Phi_0 = 0.65$. After fitting of ρ and $\Delta\Phi_0$ with experimental data the values of γ and β were consequently found ($\gamma = 4\times10^{-16}$ cm^2 W^{-1}, $\beta = 8\times10^{-11}$ cm W^{-1}). The same calculations were carried out for other samples.

The β measurements of these species were also carried out using the OA z-scan technique. The normalized transmittance for the OA scheme is given by Eq. 1.1. One can obtain the γ and β of samples in some particular cases from the CA z-scans. The OA z-scans can be performed to test the results obtained from the fitting of Eq. (1.6) with CA data. The theoretical fits were applied to all experimental data, while the fitting curves are shown only in a few graphs (Figs. 1.13a-1.13c, 1.15b, 1.16b) to not overload the figures.

The direct two-photon absorption of 1064 nm radiation is forbidden in the case of Ag$_2$S QDs since the photon energy (1.17 eV) is less than half

of the effective band gap energy of these quantum dots (~2.9 eV). One can expect the presence of large nanocrystallites in the used colloidal solutions. Thus the weak absorption in the range of 1.6 - 2.5 eV could be attributed to those species. In that case, the nonlinear absorption of 1064 nm pulses could be attributed to the TPA. However, the rate of those large nanocrystallites seems small. On other hand, there is a probability of three-photon absorption in small nanocrystallites. Note that the wavelength of 1064 nm is close to the spectral region of the excitation of IR luminescence of Ag_2S QDs (1200-1250 nm).

Such consideration should lead to variations of β with the growth of intensity in the form of $\beta = \beta_{2\omega} + \beta_{3\omega}I$ ($\beta_{2\omega}$ and $\beta_{3\omega}$ are the two- and three-photon absorption coefficients, respectively). The calculations of nonlinear optical parameters were carried out using Eqs (1.1, 1.6). Taking into account that $\beta_{2\omega}$ is insignificant compared with the third-order component, one can assume that the measured value of β of this solution at highest energies of 1064 nm pulses (5×10^{-12} cm W^{-1}) is equal to $\beta_{3\omega}\times I$. The corresponding value of the three-photon absorption coefficient of this solution was calculated to be $\beta_{3\omega} = \beta/I \approx 5\times10^{-23}$ cm^3 W^{-2}. The values of β in the case of QDs with dye associates were two to four times larger than those measured in QDs dispersed in gelatine and QDs dispersed in TGA. This difference in β at similar concentrations of QDs was attributed to the two-photon absorption in dye. The more sophisticated two-photon transitions in QD:dye associates through various channels of the exchange of excitation could also play role in this process. No nonlinear refraction was observed at this wavelength in any of the studied samples (both dye-contained and dye-free QD solutions). The nonlinear refractive index at 1064 nm was less than the minimal value registered by the used scheme (1×10^{-16} cm^2 W^{-1}).

Rather complex processes occur in the case of 532 nm pulses. It was demonstrated that surrounding medium can add their own nonlinearities to the original nonlinear optical properties of QDs. The nonlinear refraction and, notably, negative absorbance (i.e. saturated absorption) are among them. To define the parameters characterizing the latter process in dyes one has to know the saturated intensities of these species, cross-sections of various excited states of dyes responsible for excited-state absorption, etc. The relevant values of RSA in QDs and dyes also have to be taken into consideration. The above assumptions point out the complexity of the joint influence of QDs and dyes nonlinearities. That is why the analysis of the z-scans of QDs:gelatine and QDs:TGA may reveal the values of γ and β attributed entirely to nanocrystallites of Ag_2S. The β in the case of QDs dispersed in gelatine and TGA were measured to be 7×10^{-11} cm W^{-1} and

8×10^{-11} cm W^{-1} using 532 nm pulses, i.e. same as in the case of QDs:erythrosine samples at a similar concentration of nanocrystallites. Those results showed negligible nonlinear absorption in erythrosine at this wavelength and used intensities of laser pulses. The error bars of the measured values of the nonlinear absorption coefficient were 40%.

The values of β in the case of 532 nm probe pulses and QDs:thionine, QDs:DEC, and QDs:erythrosine, were close to those defined using QDs:gelatine and QDs:TGA, while in the case of QDs:triquinolilmethane it was not possible to retrieve the data for β of nanocrystallites due to strong influence of the saturated absorption of this dye. The high-frequency Kerr effect, reverse saturated absorption, multi-photon absorption, and saturated absorption are the main nonlinear optical processes during the propagation of ultrashort laser pulses through various dyes. The last process plays a crucial role in achieving the passive mode-locking for ultrafast pulses generation. As already mentioned, the nonlinear refraction of QDs:erythrosine was measured to be $\gamma = 4 \times 10^{-16}$ cm^2 W^{-1} and attributed to the Kerr nonlinearity of this dye.

One of the mechanisms of nonlinear absorption in QDs is RSA. Previously, a five energy level model has been used to interpret this process. Such absorption in the medium requires the fulfillment of the group of basic criteria. Firstly, the material must have an excited-state absorption cross-section larger than the ground-state absorption cross-section. Secondly, the lifetime of the excited state must be long enough (in comparison with the pulse duration of the laser radiation).

One has to take into account that, for some associates (QDs:thionine and QDs:DEC), the photosensibilization of IR luminescence of QDs by molecules of dyes was observed. The dyes play the role of the donors of electronic excitation for the centres of luminescence of QDs. One can consider the RSA through the five-level scheme taking into account the fact that the lifetime of excited centres of luminescence is larger than the pulse duration.

Large nanocrystals (>20 nm) show the optical absorption close to that of bulk crystalline material. However, small nanocrystals (2 - 5 nm), which could be dubbed as QDs, show a large blue shift in the absorption edge that leads to the growth of the effective band gap. These observations can be understood as quantum size effects resulting from the confinement of an electron and a hole in a small volume. Associated with the change in the absorption spectrum, and hence effective band gap, there is a change in the refractive index and nonlinear absorption. In the discussed case, the excitonic peak in the absorption spectrum was not exactly resolved,

probably due to the relatively broad size distribution and the small concentration of dyes in Ag_2S QD solution.

The third-order susceptibilities of QDs:dye, QDs:gelatine, and QD:TGA were mostly defined by the imaginary part ($Im\chi^{(3)} = 10^{-7}c^2n^2{}_0\beta/96\pi^2\omega \approx 2.8\times10^{-14}$ esu in the case of 3×10^{-2} m. f. of thionine in QD solution and 0.2 mJ, 532 nm pulses), excluding triquinolilmethane, since the real part of susceptibility ($Re\chi^{(3)} = 10^{-6}cn^2{}_0\gamma/480\pi^2 \approx 0.4\times10^{-14}$ esu at similar experimental conditions) attributed to erythrosine and DEC was rather small. Notice that actual values of the nonlinear susceptibilities of QDs are considerably higher than those of QD:dye solutions due to the small fraction of nanocrystals in the whole volume of solvent. A simple and well-established method for the estimation of the nonlinear susceptibilities of nanoparticles is to divide the nonlinear susceptibility of the compound by the volume part of QDs. In fact, the $\chi^{(3)}$ values of composites are enhanced by the local field factor as

$$\chi^{(3)} = p|f|^2 f^2 \chi^{(3)}{}_n, \qquad (1.7)$$

where $\chi^{(3)}{}_n$ is the third-order nonlinear susceptibility of nanoparticles, f is the local field factor, which in the case of Ag_2S QDs was analyzed in [31], and p is the volume fraction of nanoparticles.

1.3.3. Discussion

To consider the origin of the nonlinear processes observed in those studies, various possible mechanisms were analyzed. Among them was the thermal effect, which is dominant for long pulses and takes place due to heat transfer from QDs to the environment. However, it might be considerable for pico- or even femtosecond pulses as well in the case of a high pulse repetition rate. Similar scans were performed with single shots. No difference was found with respect to 2 Hz pulse repetition rate studies, indicating that the thermal phenomena were negligible at the used experimental conditions. It is known that the appearance of the thermal effect is connected with acoustic wave propagation. The time required for density reduction is determined by a ratio of the beam waist radius to the velocity of sound (V_s) in the surrounding material ($\tau = w_0/V_s$). Taking into account the experimental conditions ($w_0 = 75$ μm at the wavelength of 1064 nm, $V_s \sim 1500$ m s^{-1}), one could find $\tau \sim 50$ ns, i.e. the influence of the thermal effect should be neglected for the 40 ps pulses.

The viscosity of water, which was the main material surrounding QDs, does not allow the fast orientation of nanocrystals during the propagation

of picosecond pulses. Thus the most important component of Kerr-induced nonlinearity (i.e. molecular-like orientational Kerr-induced nonlinearity) in that case becomes insignificant, while the ultrafast component of Kerr nonlinearity (i.e. electronic Kerr nonlinearity) was rather small to be registered at the used concentrations of QDs.

The used Ag_2S QD solution nonlinearly absorbs 1064 nm radiation due to 2PA, while the nonlinear absorption of 532 nm pulses occurs through both RSA and 2PA mechanisms. Thus the application of these two wavelengths leads to the involvement of different nonlinear optical processes. One can distinguish their relative weight in the whole response of the QD solution. On another hand, the 1064 nm and 532 nm waves are easily available in most Nd:YAG laser configurations. Thus the choice of these two wavelengths of probe pulses allows defining the influence of RSA on the whole pattern of the nonlinear optical response of the medium, while some other processes, such as fluorescence, can simultaneously occur during laser-cluster interaction.

In accordance with the commonly accepted definition, fluorescence is the emission of light by a substance that has absorbed some electromagnetic radiation, which can be considered a form of luminescence. Fluorescence occurs when an orbital electron of a molecule, atom, or nanostructure, relaxes to its ground state by emitting a photon from an excited singlet state. A molecule in the first (electronically) excited singlet state can relax by various competing pathways. It can undergo non-radiative relaxation in which the excitation energy is dissipated as heat (vibrations) to the solvent. Excited organic molecules can also relax via conversion to a triplet state, which may subsequently relax via phosphorescence, or by a secondary non-radiative relaxation step. In most cases, the emitted light has a longer wavelength, and therefore lower energy, than the absorbed radiation; this phenomenon is known as the Stokes shift. However, when the absorbed electromagnetic radiation is intense, it is possible for one electron to absorb two photons; this two-photon absorption can lead to the emission of radiation having a shorter wavelength than the absorbed radiation.

Meanwhile, 2PA is the simultaneous absorption of two photons of identical or different frequencies in order to excite a molecule or cluster from one state (usually the ground state) to a higher energy electronic state. The energy difference between the involved lower and upper states of the molecule or cluster is equal to the sum of the energies of the two photons. 2PA is a third-order process, which is several orders of magnitude weaker than linear absorption at low light intensities. It differs from linear absorption in that the atomic transition rate due to 2PA

depends on the square of the light intensity, thus it is a nonlinear optical process, and can dominate over linear absorption at high intensities.

Thus, these two processes can simultaneously follow during the interaction of the strong electromagnetic wave with the matter. Particularly, during propagation of 1064 or 532 nm pulses through the medium containing clusters, the 2PA (or RSA) follows with some emission of longer wavelength light, which can be associated with the fluorescence. However, the value of 2PA does not affect by fluorescence.

References to Chapter 1

[1]   K. K. Innes, B. P. Stoichef, S. C. Wallace, Four-wave sum mixing (130–180 nm) in molecular vapors, Appl. Phys. Lett. 29 (11) (1976) 715-717.

[2]   M. N. R. Ashfold, C. D. Heryet, J. D. Prince, Competition between resonance-enhanced multiphoton ionisation and third-harmonic generation in acetylene vapour, Chem. Phys. Lett. 131 (4-5) (1986) 291-297.

[3]   V. F. Lukinykh, S. A. Myslivets, A. K. Popov, V. V. Slabko, Ninth-order nonlinear polarization and vuv generation in Hg vapor, Appl. Phys. B 34 (3) (1984) 171-173.

[4]   R. A. Ganeev, R. I. Tugushev, A. A. Ishchenko, N. A. Derevyanko, A. I. Ryasnyansky, T. Usmanov, Characterization of nonlinear optical parameters of polymethine dyes, Appl. Phys. B 76 (6) (2003) 683-686.

[5]   R. A. Ganeev, A. I. Ryasnyansky, M. K. Kodirov, T. Usmanov, Nonlinear susceptibilities of vapors and solutions of organic dyes, Opt. Spectrosc. 91(6) (2001) 878-882.

[6]   V. E. Nicotra, M. F. Mora, R. A. Iglesias, A. M. Baruzzi, Spectroscopic characterization of thionine species in different media, Dyes and Pigments 76 (2) (2008) 315-318.

[7]   W. C. Lai, N. S. Dixit, R. A. Mackay, Formation of H aggregates of thionine dye in water, J. Phys. Chem. 88 (22) (1984) 5364-5368.

[8]   T. D. Slavnova, H. Gorner, A. K. Chibisov, J-aggregation of anionic ethyl meso- thiacarbocyanine dyes induced by binding to proteins, J. Phys. Chem. B 111 (33) (2007) 10023-10031.

[9]   R. Brennetot, J. Georges, Transient absorption of the probe beam by the erythrosine triplet in pulsed-laser thermal lens spectrometry: The influence of the solvent, oxygen and dye concentration, Chem. Phys. Lett. 289 (1) (1998) 19-24.

[10] R. Brennetot, J. Georges, Investigation of non-linear absorption effects in pulsed-laser thermal lens spectrometry of dye solutions, Spectrochim. Acta A 55 (2) (1999) 381-395.

[11] R. A. Ganeev, G. S. Boltaev, A. I. Zvyagin, M. S. Smirnov, O. V. Ovchinnikov, Nonlinear absorption of some thiazine, xanthene, and carbocyanine dyes, Optik 157 (3) (2018) 113-124.

[12] R. A. Ganeev, Nonlinear refraction and nonlinear absorption of various media, J. Opt. A 7 (12) (2005) 717.

[13] M. A. Jhonsi, V. Srinivasan, A. Kathiravan, Light induced behavior of xanthene dyes with benzyl viologen, Synthetic Metals 196 (2014) 131-138.

[14] T. Tachikawa, Y. Kobori, K. Akiyama, A. Katsuki, U. E. Steiner, S. Tero-Kubota, Spin dynamics and zero-field splitting constants of the triplet exciplex generated by photoinduced electron transfer reaction between erythrosin B and duroquinone, Chem. Phys. Lett. 360 (1-2) (2002) 13.

[15] H. Eipper, M. H. Abdel-Kader, H. E. A. Karemer, U. E. Steines, Thionine triplet relaxation in pyridine : a completely time-resolved förster cycle, J. Photochem. 28 (3) (1985) 433.

[16] O. Berndt, F. Bandt, I. Eichwurzel, H. Stiel, Picosecond transient absorption of xanthene dyes, Acta Physica Polon. 95 (2) (1999) 207.

[17] R. A. Ganeev, R. I. Tugushev, A. A. Ishchenko, N. A. Derevyanko, A. I. Ryasnyansky, T. Usmanov, Characterization of nonlinear optical parameters of polymethine dyes, Appl. Phys. B 76 (5) (2003) 683-686.

[18] O. V. Ovchinnikov, T. S. Kondratenko, I. G. Grevtseva, M. S. Smirnov, S. I. Pokutnyi, Sensitization of photoprocesses in colloidal Ag2S quantum dots by dye molecules, J. Nanophot. 10 (3) (2016) 033505.

[19] R. A. Ganeev, A. I. Zvyagin, O. V. Ovchinnikov, M. S. Smirnov, Peculiarities of the nonlinear optical absorption of Methylene blue and Thionine in different solvents, Dyes & Pigments 149 (2018) 236-241.

[20] S. P. Pitre, C. D. McTiernan, J. C. Scaiano, Library of cationic organic dyes for visible-light-driven photoredox transformations, ACS Omega 1 (2016) 66-76.

[21] J. C. Dean, D. G. Oblinsky, S. Rafiq, G. D. Scholes, Methylene blue exciton states steer nonradiative relaxation: ultrafast spectroscopy of methylene blue dimer, J. Phys. Chem. B 120 (2016) 440–454.

[22] J. Chen, T. C. Cesario, P. M. Rentzepis, Effect of pH on methylene blue transient states and kinetics and bacteria photoinactivation, J. Phys. Chem. A 115 (2012) 2702-2707.

[23] S. Jockusch, H. J. Timpe, W. Schnabel, N. J. Turro, Photoinduced energy and electron transfer between ketone triplets and organic dyes, J. Phys. Chem. A 101 (1997) 440-445.

[24] B. Patrick, P. V. Kamat, Photoelectrochemistry in semiconductor particulate systems. 17. Photosensitization of large-bandgap semiconductors: charge injection from triplet excited thionine into zinc oxide colloids, J. Phys. Chem. 96 (1992) 1423-1428.

[25] G. S. Boltaev, D. J. Fu, B. R. Sobirov, M. S. Smirnov, O. V. Ovchinnikov, A. I. Zvyagin, R. A. Ganeev, Optical limiting, nonlinear refraction and nonlinear absorption of the associates of $Cd_{0.5}Zn_{0.5}S$ quantum dots and dyes, Opt. Express 26 (11) (2018) 13865-13875.

[26] J. Wang, W. J. Blau, Inorganic and hybrid nanostructures for optical limiting, J. Opt. A 11 (2) (2009) 024001.

[27] Z. R. Chen, H. W. Hou, X. Q. Xin, K. B. Yu, S. Shi, A half-open cage-shaped cluster, (NEt4)3[WOS3(CuBr)3(.mu.2-Br)].cntdot.2H2O: synthesis, structure, and nonlinear optical properties, J. Phys. Chem. 99 (21) (1995) 8717-8721.

[28] L.W. Tutt, T. Boggess, A review of optical limiting mechanisms and devices using organics, fullerenes, semiconductors and other materials, Prog. Quantum Electron. QE-17 (4) (1993) 299-338.

[29] G. S. Boltaev, B. Sobirov, S. Reyimbaev, H. Sherniyozov, T. Usmanov, M. S. Smirnov, O. V. Ovchinnikov, I. G. Grevtseva, T. S. Kondratenko, H. S. Shihaliev, R. A. Ganeev, Nonlinear optical characterization of colloidal solutions containing dye and Ag2S quantum dot associates, Appl. Phys. A 122 (12) (2016) 999.

[30] A. Aboulaich, D. Billaud, M. Abyan, L. Balan, J.-J. Gaumet, G. Medjadhi, J. Ghanbaja, R. Schneider, One-pot noninjection route to CdS quantum dots via hydrothermal synthesis, ACS Appl. Mater. Interfaces 4 (5) (2012) 2561-2569.

[31] F. Nan, F.-M. Xie, S. Liang, L. Ma, D.-J. Yang, X.-L. Liu, J.-H. Wang, Z.-Q. Cheng, X.-F. Yu, L. Zhou, Q.-Q. Wang, J. Zeng, Growth of metal-semiconductor core-multishell nanorods with optimized field confinement and nonlinear enhancement, Nanoscale 8 (23) (2016) 11969.

CHAPTER 2

NONLINEARITIES OF THIN FILMS CONTAINING COMPLEX AND NANOSTRUCTURED MATERIALS

In this chapter, we analyze the strong nonlinear absorption in perovskite films. We discuss the systematic comparative studies of the nonlinear optical properties of Br-, I-, and Cl-containing $CH_3NH_3PbX_3$ perovskite films using near-infrared (800 nm) femtosecond radiation of frequently used Ti:sapphire lasers. We analyze the photoluminescence emission from MAPbBr$_3$ film and demonstrate the two-photon absorption mechanism of this process. We also discuss the nonlinear optical studies of gold nanoparticle films. Finally, we discuss the variations of the optical nonlinearities of Ag_2S quantum dot thin films of different thicknesses. We also analyze the ablation of Ag_2S quantum dot films for efficient emission of high-order harmonics of femtosecond pulses. The temporal evolution of probe pulse transmittance through the Ag_2S films is discussed.

2.1. Strong nonlinear absorption in perovskite films

Perovskite films took large attention due to various potential applications of these structures. Rapid progress in perovskite solar cells allowed power conversion efficiency to reach 22% [1]. The attractive photovoltaic properties of perovskites, such as strong optical absorption, simplicity of processing, long carrier diffusion length, tolerance to defects, high radiative efficiency, band gap tunability, etc., can also be applied for other optoelectronic fields. By introducing suitable interlayers at the perovskite/electrode interfaces, the performance of the photodetectors improved significantly, which was attributed to the improved charge carrier collection efficiency. Perovskite materials such as methylammonium lead halides are inexpensive to produce and simple to manufacture. The most studied perovskite absorbers are methylammonium lead trihalides ($CH_3NH_3PbX_3$, where X is a halogen atom such as iodine, bromine or chlorine), with an optical band gap between 1.5 and 3.2 eV depending on

halide content. These methylammonium lead trihalide perovskites are commonly dubbed as MAPbI₃, MAPbBr₃, and MAPbCl₃. Thin perovskite films are also attracting increasing interest, particularly as solution-processable, white-light emissive materials [2].
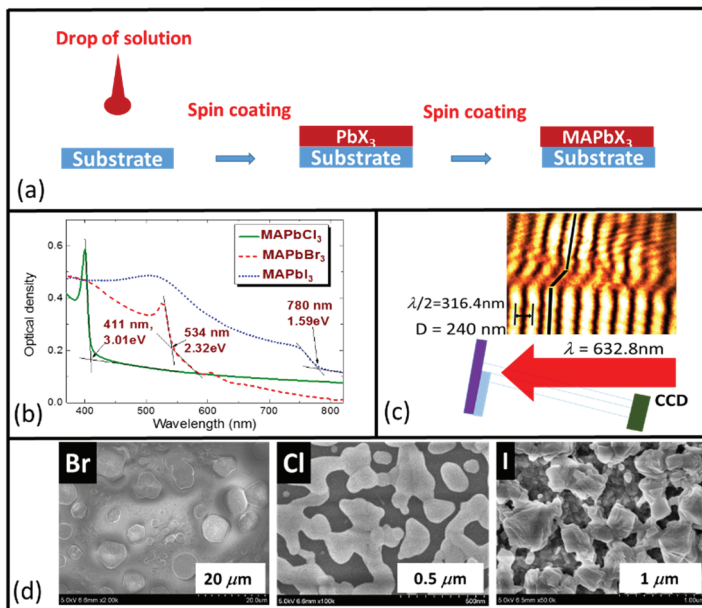
Fig. 2.1. (a) Schematic of films preparation. (b) Absorption spectra of MAPbI₃, MAPbBr₃, and MAPbCl₃ films in the near infrared, visible and UV ranges. The bandgaps of above films were defined to be 1.59, 2.32, and 3.01 eV respectively. (c) Measurement of MAPbBr₃ film thickness using Tolansky interferometer. The shift of interference strips at the border of "perovskite-glass" shown on the CCD image is caused by phase shift, from which the thickness of film was calculated to be 240 nm. (d) SEM images of (from left to right) the MAPbBr₃, MAPbCl₃, and MAPbI₃ films. White lines correspond to 20 μm (MAPbBr₃), 0.5 μm (MAPbCl₃), and 1 μm (MAPbI₃). Reproduced from [5] with permission from Optical Society of America.

Confining the organic molecules in the inorganic framework improves the nonlinear optical response of the organic-inorganic hybrids because the inorganic framework restricts the motion of the organic molecules and prevents randomization of molecular orientation due to thermal relaxation. The organic-inorganic and all-inorganic perovskites have attracted the

attention of the optical community, partially due to their exciting optical properties in addition to the potential applications in photovoltaic systems [3]. The first observation of nonlinear optical effects, such as two-photon absorption (2PA) in organometallic bromide perovskites, was reported in Ref. [4].

In this section, we discuss the systematic comparative studies of the nonlinear optical properties of Br-, I-, and Cl-containing $CH_3NH_3PbX_3$ perovskite films using near-infrared (800 nm) femtosecond radiation of frequently used Ti:sapphire lasers. Following analyzing the nonlinear absorption and nonlinear refraction of $MAPbBr_3$, $MAPbCl_3$, and $MAPbI_3$ thin (~200 nm) films using 40 fs, 800-nm pulses, it is found that these films possess strong nonlinear absorption comparable to the highest reported values for all thin structures. We also analyze the photoluminescence emission from $MAPbBr_3$ film and demonstrate the 2PA mechanism of this process [5].

The Ti:sapphire laser provided 40 fs, 800 nm pulses at 1 kHz pulse repetition rate. The standard z-scan scheme [6] was applied in these studies. Laser radiation was focused by a 400-mm focal length spherical lens and was measured by a power meter. An open-aperture (OA) scheme with a fully opened iris aperture placed in front of the power meter allowed measurement of the nonlinear absorption coefficient (β) of perovskite films during their propagation through the focal plane. When the aperture was closed to restrict the propagation of ~10% of input radiation (closed-aperture scheme) the measurements of propagated radiation allowed determination of the nonlinear refractive index (γ) of samples. The normalized transmittances of samples were measured using both OA and closed-aperture (CA) schemes to calculate their β and γ respectively.

The schematic of films preparation is shown in Fig. 2.1(a). The perovskite thin films were prepared by a two-step method. PbX_2 (X = Cl, Br, I) (1 M, in N，N-dimetylformamide for Cl, Br or γ-Butyrolactone for I) were resolved in solvents and stirred overnight. Then, PbX_2 (X = Cl, Br, I) solution was spin-coated on the cleaned glass slides with 3000 rpm for 50 s. Once the films were fully dried, MAX (X = Cl, Br, I) solution (15 mg/ml in isopropanol) was dropped onto the PbX_2 films. After waiting for 30 s, the solution was spin-coated to dry and rinsed with isopropanol. The films were then put on a hot plate for 2 min ($MAPbCl_3$ at 60 ^{0}C, $MAPbBr_3$ at 80 ^{0}C, and $MAPbI_3$ at 100 ^{0}C) to complete the preparation of samples before further optical experiments.

The UV and visible absorption spectra of the perovskite thin films were measured using a spectrophotometer. They demonstrated growth of

linear absorption at ~405, 540, and 780 nm in the case of MAPbCl$_3$, MAPbBr$_3$, and MAPbI$_3$ films respectively [Fig. 2.1(b)]. The corresponding bandgaps (E$_g$) of these films were defined as 3.01, 2.32, and 1.59 eV respectively. The inorganic layers in the conventional two-dimensional perovskites behave as a quantum well in which the organic layers play the role of the barrier, which causes sharp variations in the absorption and photoluminescence (PL) spectra. The PL spectra of perovskite films were measured using a fiber spectrometer. Particularly, PL spectrum of MAPbBr$_3$ was analyzed to determine the mechanism of this process in the case of 800 nm probe radiation.

The thickness and homogeneity of perovskites were measured using atomic force microscopy and Tolansky interferometry. The film thickness (<300 nm) was significantly less than the Rayleigh length of focused radiation to fulfil the thin sample approximation condition, which allows the application of z-scan relations to fit with the experimental results. The shift of the interference pattern in Tolansky interferometry during the reflection of the HeNe laser beam defined the roughness and the thickness of films. Particularly, the thickness of MAPbBr$_3$ film was measured from those interference images to be 240 nm [Fig. 2.1(c)]. Other films had a thickness of 225 nm (MAPbCl$_3$) and 150 nm (MAPbI$_3$).

SEM studies of the surfaces of perovskites were performed to analyze the structural properties of films. These images [Fig. 2.1(d)] showed the irregularities of surface structure, which is characteristic of polycrystalline perovskites.

CA z-scan allows distinction of the two abovementioned processes (nonlinear absorption and nonlinear refraction) when they are presented simultaneously. In the general case of the joint contribution of both those processes, the variation of normalized transmittance of samples along the z-axis, T, can be presented as follows [7]:

$$T = 1 + \frac{4x}{(x^2+9)(x^2+1)}\Delta\Phi_0 - \frac{2(x^2+3)}{(x^2+9)(x^2+1)}\Delta\psi_0 ,$$

(2.1)

where x=z/z$_0$, z$_0$=k(w$_0$)^2/2 is the Rayleigh length, k=2π/λ is the wave number, w$_0$ is the beam waist radius at the 1/e^2 level of intensity distribution, and $\Delta\Phi_0$=kγI$_0$L$_{eff}$ and $\Delta\psi_0$=βI$_0$L$_{eff}$/2 are the phase changes due to nonlinear refraction and nonlinear absorption, respectively. Here I$_0$ is the laser radiation intensity in the focal plane, L$_{eff}$=[1-exp(-α$_0$L)]/α$_0$ is the effective length of the medium, α$_0$ is the linear absorption coefficient, and L is the thickness of samples.

By making the substitution $\rho = \beta/2k\gamma$, one can determine the relation between $\Delta\Phi_0$ and $\Delta\psi_0$ ($\Delta\psi_0 = \rho\Delta\Phi_0$). Thus, Eq. 2.1 can be re-written as follows:

$$T = 1 + \frac{2(-\rho x^2 + 2x - 3\rho)}{(x^2 + 9)(x^2 + 1)}\Delta\Phi_o$$

(2.2)

This equation was used for fitting theoretical dependences with measured normalized transmittances taking into account the experimental conditions. After fitting ρ and $\Delta\Phi_0$ one can consequently find γ and β. The β measurements of these films were also carried out using OA z-scan technique. One can get the data on nonlinear refraction and nonlinear absorption coefficients of materials in some particular cases from the CA z-scan. OA z-scan can be performed to test the results of nonlinear absorption measurements obtained from the fitting of the nonlinear curve using Eq. 2.2. Notice that uncertainty in the calculation of the nonlinear absorption coefficients using OA z-scans was smaller compared with CA Z-scans, thus prompting to analyze this process using the former configuration.
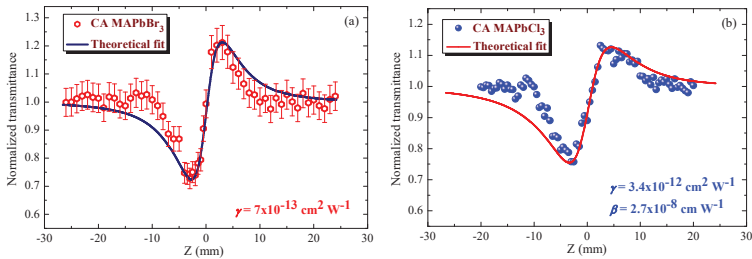
Fig. 2.2. Closed-aperture Z-scans of (a) MAPbBr$_3$ and (b) MAPbCl$_3$ films. The corresponding nonlinear optical parameters are shown on the graphs. The fitting curves correspond to Eq. (2.2). (a) The intensity of 800 nm radiation in the focal plane was 7×10^{11} W cm^{-2} ($E = 1 \times 10^{-6}$ J). The corresponding $\Delta\Phi_0$ was found to be 0.76. (b) The intensity of 800 nm radiation in the focal plane was 1.7×10^{11} W cm^{-2} ($E = 0.25 \times 10^{-6}$ J). The corresponding $\Delta\Phi_0$ and ρ were found to be 0.9 and 0.05. Reproduced from [5] with permission from Optical Society of America.

Z-scan measurements were calibrated using a 1-mm-thick fused silica plate. The calculations using the fitting procedure allowed measurement of the nonlinear refractive index of this material using 800 nm, 40 fs pulses,

which was found to be $(3.0\pm0.5)\times10^{-16}$ cm^2 W^{-1}. This value is similar to earlier reported measurements of the γ of fused silica (3×10^{-16} cm^2 W^{-1} [8], $(2.7\pm0.3)\times10^{-16}$ cm^2 W^{-1} [9]).

Figures 2.2(a) and 2.2(b) show the CA z-scans of MAPbBr$_3$ and MAPbCl$_3$ films. Several data acquisitions were performed and compared with each other at the same point of the sample in order to ensure that no sample degradation occurs during the experiment. The characteristic valley followed by the peak in the dependence of the normalized transmittance of films on their position on the z-axis indicated the positive nonlinear refraction in those two films. MAPbI$_3$ film did not show the nonlinear refractive properties until the intensities reached the optical damage threshold of this sample (4×10^{12} W cm^{-2}).

The fitting procedure of CA Z-scans (solid curves in Fig. 2.2) allowed calculation of the γ of MAPbBr$_3$ and MAPbCl$_3$ films to be $(7\pm2)\times10^{-13}$ cm^2 W^{-1} and $(3.4\pm0.8)\times10^{-12}$ cm^2 W^{-1}, respectively. Asymmetry was observed in CA data for MAPbCl$_3$ films. The reason for this asymmetry is the influence of 2PA on the CA curve. One can estimate from presented CA data the β of this film (2.7×10^{-8} cm W^{-1}). Notice that the estimates of β from these CA Z-scans were larger than those obtained from the fitting of the OA Z-scans (1.5×10^{-8} cm W^{-1}).

Figures 2.3(a) and 1.2.3(b) show the OA Z-scans of MAPbCl$_3$ and MAPbBr$_3$ and their fitted curves. As the pump power is increased, a decrease in the normalized transmittance was observed. The normalized transmittance for the OA z-scan is given as follows [10]:

$$T = q^{-1}\times\ln(1+q), \tag{2.3}$$

Here $q = \beta I_0 L_{eff}/(1+z^2/z_0^2)$. The fitting of Eq. (2.3) to the experimental data is depicted in Fig. 2.3 by the solid curves. The theoretical dependences of T calculated using the two-photon absorption model (2.3) coincided with the experimental data of OA Z-scans of films (Fig. 2.3). This coincidence confirms the prevailing influence of the third-order nonlinearities over the higher-order nonlinear optical processes (in particular, three-photon absorption). Indeed, the absorption spectra [Fig. 2.1(b)] show that the decrease in the propagation of the 800 nm radiation through these films can be explained by the 2PA mechanism.

The ratio between E_g and photon energy of radiation used (1.55 eV) lies in the range between 1 and 2 at which the probability of three-photon absorption in most cases is smaller as compared to the 2PA process. Meanwhile, if 2PA at 800 nm is possible then the three-photon absorption is also possible, and very little can be said about the relative magnitude of

the cross-sections. There are no reported data on that matter. In the meantime, it is a common case when the three-photon absorption cross-section is smaller than the same for 2PA. Obviously, for some specific cases, three-photon absorption can overpass the 2PA cross-section, however, it is a rare case.
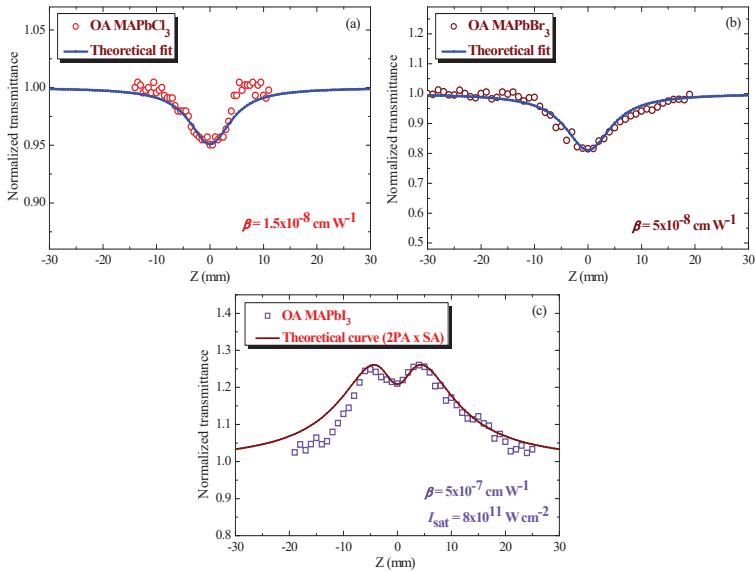
Fig. 2.3. Open-aperture z-scans of (a) MAPbCl$_3$, (b) MAPbBr$_3$, and (c) MAPbI$_3$ films. The corresponding nonlinear optical parameters are shown on the graphs. The fitting curves correspond to Eq. (2.3) describing TPA and phenomenological model of saturable absorption. (a) The intensity in the focal plane was 3.5×10^{11} W cm^{-2} ($E = 0.5 \times 10^{-6}$ J). q was found to be 0.105. (b) The intensity in the focal plane was 5.2×10^{11} W cm^{-2} ($E = 0.75 \times 10^{-6}$ J). q was found to be 0.5. (c) The intensity in the focal plane was 2×10^{11} W cm^{-2} ($E = 0.32 \times 10^{-6}$ J) and $q = 2$. I_{sat} was found to be 8×10^{11} W cm^{-2}. Reproduced from [5] with permission from Optical Society of America.

The 2PA-induced nonlinear absorption coefficients under 800 nm, 40 fs pulse excitation were determined through the fitting procedure to be $\beta = (1.5 \pm 0.4) \times 10^{-8}$ cm W^{-1} and $(5 \pm 1.2) \times 10^{-8}$ cm W^{-1} for MAPbCl$_3$ and MAPbBr$_3$ films respectively. Different intensities were used to analyze the variation of β in those films. This parameter remained almost unchanged

until the optical breakdown intensities for MAPbBr$_3$ and MAPbCl$_3$ films (5×10^{12} W cm^{-2} and 3×10^{12} W cm^{-2} respectively) were reached.

The OA z-scan of MAPbI$_3$ film showed the joint influence of two types of nonlinear absorption, 2PA and saturable absorption (SA). The absorption spectrum of MAPbI$_3$ shows a peak near 750 nm. The bandwidth of the 800 nm pulse was 26 nm, thus the wing of the spectral distribution of the laser pulse centred at 800 nm was partially overlapped with the absorption edge, which led to the absorption of the shorter-wavelength part of the laser pulse at 780 nm (E$_g$ = 1.59 eV). Probably, this overlap was the reason for the SA in MAPbI$_3$, since linear absorption at the excitation wavelength is needed if the SA effect is the one responsible for the observed bleaching of the film.

To fit the z-scan of MAPbI$_3$ film comprising simultaneous influence of SA and 2PA [Fig. 2.3(c)], one has to multiply the normalized transmittance induced by the 2PA described by Eq. (2.3) and the normalized transmittance induced by SA. There are different models of SA. The simplest phenomenological model is often used when the SA is considered in terms of depletion of the ground state concentration due to high fluence of radiation. It can be described by relation [11]

$$\alpha(z) = \alpha_0/[1 + I(z)/I_{\text{sat}}], \tag{2.4}$$

where $\alpha(z)$ is the absorption coefficient varying along the z-axis, $I(z)$ and I_{sat} are the laser radiation intensity and saturation intensity. I_{sat} is related to the concentration of the active centres in the medium, the effective cross-sections, and the lifetimes of the transitions populated upon the excitation.

The absorption coefficient in the case of the two-level system possessing heterogeneously broadened states can also be written as [12]

$$\alpha(z) = \alpha_0/[1 + I(z)/I_{\text{sat}}]^{0.5}. \tag{2.5}$$

Another model that can be expressed empirically as

$$\alpha(z) = \alpha_0/\{1 + [I(z)/I_{\text{sat}}]^{0.5}\} \tag{2.6}$$

was also used for the analysis of SA [13]. Finally, Eq. (2.3) could also be considered as the simplified analytical absorption model assuming the negative sign of the nonlinear absorption coefficient. The corresponding normalized transmittances can be presented as $T(z) = 1+I_0/I_{\text{sat}}\times(1+z^2/z_0^2)$, $T(z) = [1+I_0/I_{\text{sat}}\times(1+z^2/z_0^2)]^{0.5}$, and $T(z) = 1+[I_0/I_{\text{sat}}\times(1+z^2/z_0^2)]^{0.5}$ for the phenomenological, two-level, and empirical models respectively.

Most materials demonstrate SA using short pulses, but often only at very high optical intensities (*i.e.* close to the optical damage). At sufficiently high incident light intensity, atoms in the ground state of a saturable absorber material become excited into an upper energy state at such a rate that there is insufficient time for them to decay back to the ground state before the ground state becomes depleted, and the absorption subsequently saturates. The discussed experimental conditions were better fitted by the phenomenological model.

To accurately fit the experimental data of joint influence of SA and 2PA, one has to choose the conditions when these processes are clearly distinguished from each other like as shown in Fig. 2.3(c). At the larger intensity of 800 nm pulses, one can get a purely 2PA pattern, when the SA-related growth of transmittance becomes fully masked by the strong 2PA. In that case, it is impossible to determine the influence of SA on the whole pattern of the z-scan curve. Another extreme is relatively small energy of 800 nm pulses when only SA plays dominating role, i.e. when only bleaching process, without the decrease of transmittance at the focal plane related with the influence of 2PA, appears. At such conditions, one cannot properly determine the 2PA parameters.

The ratio of the maximum intensity of probe pulse and saturation intensity was calculated from the fit shown in Fig. 2.3(c) to be $I_0/I_{sat} = 0.25$. One can calculate the I_{sat} to be 8×10^{11} W cm^{-2} assuming the maximal intensity of 800 nm pulse in the focal plane (2×10^{11} W cm^{-2}) used in this experiment. The nonlinear absorption coefficient of MAPbI$_3$ film was deduced from this fitting procedure to be $\beta = (5 \pm 1.2) \times 10^{-7}$ cm W^{-1}. This value of nonlinear absorption is one of the largest reported for thin films.

The reason for the relatively large nonlinearity attributed to 2PA is probably related to the large cross-section of absorption. It is difficult to estimate the cross-section of this process due to the absence of pump-probe measurements of this process. The fitting of the OA curve for MAPbI$_3$ film showed that the 2PA becomes stronger than SA at relatively large energy of pulses. One can anticipate that, with the growth of laser energy, the SA will be totally suppressed by 2PA leading to domination of the positive nonlinear absorption.
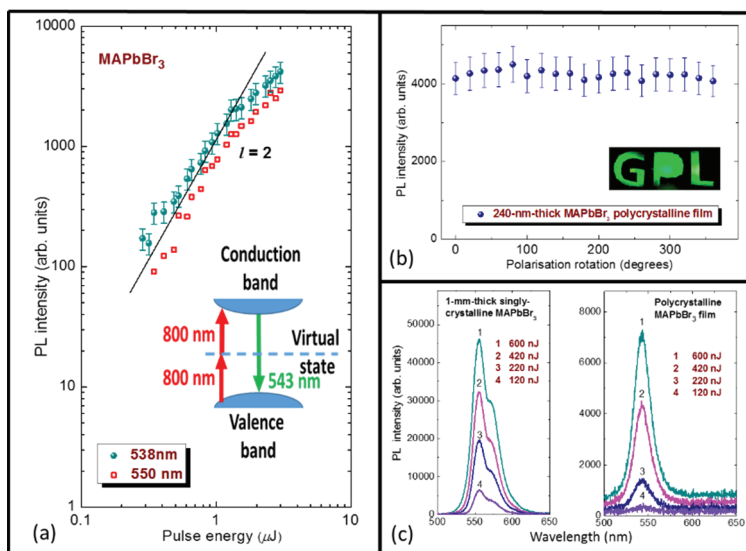
Fig. 2.4. Photoluminescence from MAPbBr$_3$ film. (a) Dependence of the PL intensity on the laser pulse energy. This dependence shows the almost quadratic slope ($l \approx 2$) up to the pulse energy of ~1 μJ for different components of a broad PL spectrum centred at 543 nm. Inset shows the band structure of perovskite. (b) Dependence of PL intensity on the rotation of polarization angle of laser radiation in the case of MAPbBr$_3$ polycrystalline film by pumping with 400 nJ, 800 nm, 40 fs pulses. Inset shows the photoluminescence of thin film during illumination through the mask containing the acronym for Guo Photonics Laboratory. (c) PL spectra observed from singly-crystalline (left side) and polycrystalline (right side) MAPbBr$_3$ perovskites using different energies of 800 nm pulses. Reproduced from [5] with permission from Optical Society of America.

Below we address the mechanism of photoluminescence in perovskite film. The PL in MAPbBr$_3$ was direct evidence that studied samples absorb the 800 nm radiation through 2PA since the band gap of this perovskite (2.32 eV) is larger than photon energy (1.55 eV). Figure 2.4(a) shows the dependence of PL emission on the exciting pulse energy. One can see an almost quadratic slope of this dependence for the PL spectral components (538 and 550 nm) until 1 μJ pulse energy, which confirms the 2PA mechanism of the formation of this emission.

The inset to this figure shows the band structure of MAPbBr$_3$ demonstrating the scheme of PL emission centred at 543 nm. The electrons in the valence band can absorb two photons at the same time and transmit

to the conduction band. The intensity of PL emission did not depend on the polarization of 800 nm radiation [Fig. 2.4(b)], which is the expected result, taking into account the polycrystalline structure of this film. The PL emission spectrum showed a peak at 543 nm using variable probe pulse energy [right side of Fig. 2.4(c)]. Here also presented the PL spectrum produced by 1-mm-thick single-crystalline MAPbBr$_3$ sample [left side of Fig. 2.4(c)]. The broader PL spectrum in the latter case was centered at 555 nm and showed an asymmetric shape.

The useful parameter for the determination of the order of nonlinearity using the z-scan technique is a valley-to-peak distance of the normalized transmittance (ΔZ_{vp}). This parameter is equal to $1.7z_o$ in the case of the third-order nonlinear optical processes and $1.2z_o$ in the case of the fifth-order ones. In described experimental conditions (λ = 800 nm, w_o = 34 μm), the Rayleigh length z_o was calculated to be 4.5 mm. In that case, a distance between the valley and peak of the T(z) dependence should be equal to 7.65 and 5.4 mm in the case of the third- and fifth-order nonlinear optical refraction processes, respectively. The experimental valley-to-peak distance in these experiments was $\Delta Z_{vp} \approx 7.4$ mm [Figs. 2.2(a) and 2.2(b)], in good agreement with the theoretical consideration of the third-order nonlinear optical processes involved at the pulse intensities used. Notice that the measurements of the nonlinear optical characteristics of perovskites were carried out up to intensities of $\sim 3 \times 10^{11}$ W cm^{-2}, i.e. below the optical damage thresholds of these films using 40 fs pulses. Nevertheless, no fifth-order processes were observed at these conditions.

Among a variety of third-order nonlinear optical processes (intermolecular interaction, molecular reorientational Kerr effect, electronic Kerr effect, etc.) contributing to the nonlinear addition of the perovskite films' refractive index, the electronic Kerr effect seems to be the most important mechanism in the case of short (femtosecond) pulses. Meanwhile, the attempts to observe the nonlinear optical effects in perovskites using long (200 ps) pulses did not show any of these processes due to the relatively small intensity (1×10^{10} W cm^{-2}) of picosecond pulses that could be applied to the films without degradation and damage. Further growth of focused picosecond radiation intensity led to the optical damage of thin films, probably due to the accumulative effect of heating even with small absorption of 800 nm radiation using a 1 kHz pulse repetition rate. The measured thresholds of optical damage of these films in the case of 200 ps pulses were 3×10^{10} W cm^{-2} (MAPbBr$_3$), 6×10^{10} W cm^{-2} (MAPbI$_3$), and 2×10^{10} W cm^{-2} (MAPbCl$_3$), while the same in the case of 40 fs pulses were 5×10^{12} W cm^{-2} (MAPbBr$_3$), 4×10^{12} W cm^{-2} (MAPbI$_3$), and 3×10^{12} W cm^{-2} (MAPbCl$_3$).

Below we discuss the sign of the nonlinear refractive index of investigated films. An important characteristic of the most commonly used perovskites, the methylammonium lead halides, is a band gap controllable by the halide content. The analysis of nonlinear refraction of the $MAPbBr_3$ and $MAPbCl_3$ films at $I_0 = 3 \times 10^{11}$ W cm^{-2} showed that they demonstrate self-focusing properties [Fig. 2.2(a)]. The nonlinear Kramers–Kronig relations predict the self-focusing in semiconductors for which the relation $\hbar\omega/E_g < 0.69$ takes place [14]. Here $\hbar$ is Planck's constant and ω is the frequency of laser radiation. As already mentioned, the values of E_g for $MAPbBr_3$ and $MAPbCl_3$ films were estimated from the absorption curves to be 2.32 and 3.01 eV, respectively. The corresponding $\hbar\omega/E_g$ values for the films at $\lambda = 800$ nm were calculated to be 0.67 ($MAPbBr_3$) and 0.51 ($MAPbCl_3$). Thus, one can expect a positive sign of γ in these two films, which was confirmed in discussed experiments [Fig. 2.2]. Note that the analysis of nonlinear optical properties of such materials using the Kramers–Kronig transformations is possible only when the photon energy is less than the band gap energy ($\hbar\omega < E_g$), which corresponds to the case for $MAPbBr_3$ and $MAPbCl_3$ films. The reason for the relatively small values of nonlinear refractive indices of perovskite films at 800 nm was related to the closeness of their $\hbar\omega/E_g$ values to 0.69 where the sign of γ changes from positive to negative.

Those studies of perovskites have demonstrated the domination of nonlinear absorption over nonlinear refraction. The Stegeman figure of merit $T_S = |2\beta\lambda/\gamma|$ [15] for the studied samples also shows the prevailing influence of nonlinear absorptive properties of used perovskites over their nonlinear refraction ($T_S \approx 7$ and 300 in the case of $MAPbBr_3$ and $MAPbCl_3$, respectively).

Finally, we address the applicability of studied samples. Either γ or β can be utilized for specific purposes, but their coexistence in a single material often causes undesirable effects that limit the performance. For instance, a large γ is required for self-focusing applications but an inherently related large β value lowers the laser-induced damage threshold, which ultimately leads to optical damage of the material via efficient 2PA. In discussed case (large nonlinear absorption and relatively moderate nonlinear refraction), the utilization of perovskite films is possible in the case of optical limiters and optical switchers. Such a perspective has recently been discussed in Ref. [16]. Besides that, the application of TPA-induced PL spectroscopy can be considered as a powerful tool for the characterization of organic-inorganic halide perovskites [17].

2.2. Nonlinear optical studies of gold nanoparticle films

In this section, we analyze the third-order nonlinear optical properties and transient absorption of gold NP thin film [18]. Figure 2.5(a) shows the scheme for the synthesis of Au NPs in solution by irradiation of the bulk gold target immersed in deionized water using 800 nm, 200 ps, 1 kHz pulses. The laser beam was focused by a 100 mm focal length lens on the bulk gold. Typically, the energy density of laser radiation on the metal surface was of the order of 10 J/cm^2. The irradiation of the metal surface resulted in the fast removal of the material confined to the laser spot. The sample was displaced with regard to the laser beam, using a translating stage to avoid the formation of deep holes. The ablation was done for 10 minutes at continuous steering. The Au film was prepared by evaporation of the aqueous suspension containing gold nanoparticles and then used as the target to perform the experiments. The thickness of the thin film was examined by scanning electron microscope (SEM) to be approximately 100 nm.
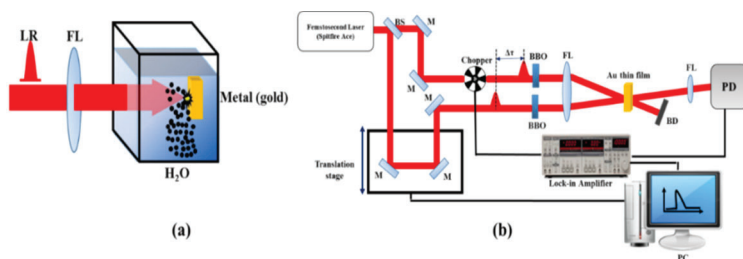
Fig. 2.5. (a) Schematic of laser ablation. LR, Laser radiation; FL, Focal lens. (b) Schematic of the transient absorption measurements. BS, Beam splitter; M, Mirrors; FL, Focal lenses; PD, Photo diode; BD, Beam dumper; BBO, Barium borate crystal; PC, Personal computer. Reproduced from [18] with permission from MDPI.

A noncollinear degenerate pump-probe technique was employed to measure the transient absorption (TA) in Au NPs film (Fig. 2.5b). TA study was performed using the 400 nm radiation obtained by second harmonic generation of 800 nm, 30 fs pulses using a 2 mm thick BBO crystal. Prior to the conversion of 800 nm to 400 nm, the laser pulse was split into two pulses using a 30:70 beam splitter. Pump and probe pulses were focused on the sample using a 300 mm focal length lens. The transmitted probe radiation was detected by ultrafast Si photodiode

connected to lock-in-amplifier to measure the transmittance of the probe pulse with respect to the position of the motorized stage. Lock-in-amplifier was externally triggered by the optical chopper running at 300 Hz. The z-scan scheme, which was used to measure the third-order nonlinear optical effects in Au NPs thin film, was similar to the one described in section 2.1.SEM images and histograms of the Au NPs prepared by ablation of bulk gold using picosecond pulses are presented in Fig. 2.6(a). The inset in Fig. 2.6(a) shows the size distribution of Au NPs, which covers the 10-90 nm range with a mean size of 30 nm. The absorption spectrum of the thin film was analyzed in the range of 400 to 800 nm. The absorbance measurements were made using a 100 nm thin film. Figure 2.6(b) shows the absorption spectrum of Au NPs-containing thin film. The observed SPR of Au NPs was at 520 nm.
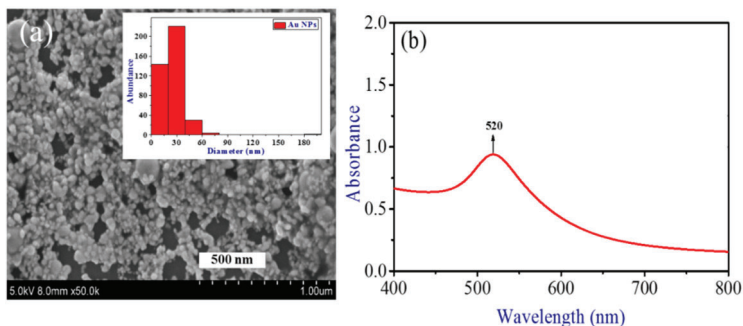
Fig. 2.6(a). SEM and size distribution of Au NPs. (b) Absorption spectrum of Au NP thin film. Reproduced from [18] with permission from MDPI.

The investigation of the nonlinear optical characteristics of Au NP thin film was carried out using the CA and OA Z-scans under excitation by 400 nm, 30 fs probe pulses at the same pulse energy (30 nJ). Figure 2.7(a) shows the OA and CA z-scan curves of the thin film. In the case of OA, the Au NP thin film showed SA, while close to the focal area it demonstrated the reverse saturable absorption (RSA). The measured saturated intensity was 1.3×10^{10} W cm^{-2}. β_{RSA} was calculated from the fitting curve to be 8.9×10^{-6} cm W^{-1}. This value is one of the largest reported in the case of thin films measurements using different materials. In the case of CA measurements, self-focusing was observed. The nonlinear refractive index was calculated to be 2.6×10^{-11} cm^2 W^{-1}.

Time evolution of the absorption of probe pulses in presence of pump pulses in the Au NPs film at 400 nm is shown in Fig. 2.7(b). Prior to the TA measurements of the Au NP film deposited on the glass slide, the TA measurements of the pure glass slide were performed to separate its contribution from the former TA data. The pump-probe profile for thin film indicated the process of photo bleaching due to excitation of the NPs under irradiation of 52 nJ, 400 nm pump pulses. This behaviour was attributed to the generation of hot electrons upon interaction with femtosecond pump pulses.
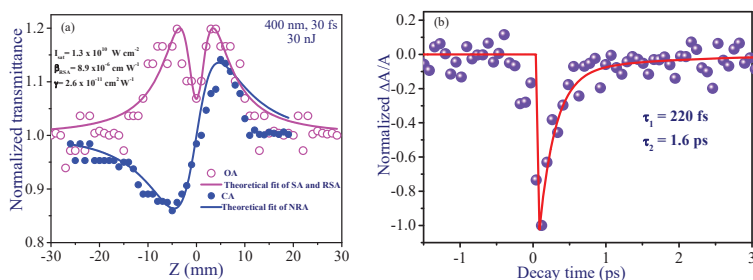
Fig. 2.7. (a) OA and CA z-scan curves of thin film measured using the 400 nm, 30 fs pulses. (b) Pump-probe dynamics of Au NPs thin film at 400 nm. Reproduced from [18] with permission from MDPI.

This study at 400 nm is considered to be out from the maximum of SPR. Experimental data were fitted with the phenomenological response function of $f(x) = (1 - exp\,(-t/\tau_1))\,(exp\,(-t/\tau_2))$, where τ_1 and τ_2 are related to the electron thermalization process and electron energy transfer to the lattice. The fitting of TA profile (solid line) allowed determining the time constants (τ_1= 220 fs and τ_2= 1.6 ps) at 400 nm. The relaxation time constant τ_1 was found to be comparable with the reported TA recovery time constant associated with the electron thermalization process in Au NPs [19]. The relaxation time constant τ_2 can be directly related to the cooling of the thermalized electron system through the electron-phonon coupling.

2.3. Low- and high-order nonlinear optical properties of Ag$_2$S quantum dot thin films

Here we discuss the variations of the optical nonlinearities of Ag$_2$S QD thin films of different thicknesses. We also analyze the ablation of Ag$_2$S

QD films for efficient emission of high-order harmonics of femtosecond pulses [20].

In the typical process of synthesis 17 g of $AgNO_3$ were dissolved in 100 mL tri-n-octyl-phosphine (TOP) to obtain the 1 M Ag-TOP. 6.4 mL of oleic acid, 5.4 g of 1-octadecylamine (ODA), and 12.8 mL of 1-octadecene were mixed in a 100 mL round-bottom flask under N_2 flushing three times to remove the water and oxygen and heated up to 70 °C. With the continuous N_2 supply and stirring, 72 mg of sulphur powder was added into the flask immediately and heated to the temperature of 190 °C. Then 4 mL of Ag-TOP was quickly injected in the flask, and the reaction was allowed to proceed for 5 min at 160 °C. 10 ml of N-butyl alcohol was injected to provide solidification from ODA. The synthesized QDs were isolated by precipitation with methyl alcohol and redispersed in methylbenzene. This process was repeated three times to ensure a clean product. The obtained QDs were dispersed in hexane or toluene and rinsed by the ultrasonic process to achieve better dispersion of QDs. The Ag_2S QD solution was then spin-coated on the glass slides to produce films of different thicknesses (80 and 500 nm).
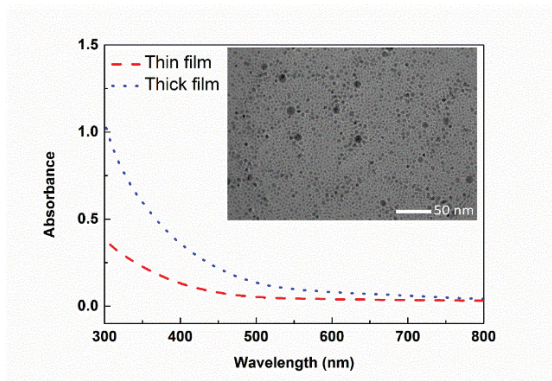
Fig. 2.8. Absorption spectra of thin (80 nm) and thick (500 nm) Ag_2S films. Inset: TEM image of synthesized silver sulphide QDs. Reproduced from [20] with permission from Walter de Gruyter GmbH & Science Wise Publishing.

In order to study the low-order nonlinear optical properties of these two films the earlier described single-beam z-scan technique was employed. Ti:sapphire laser (800 nm wavelength, 30 fs pulse duration, 1 kHz repetition rate) was used in these studies. The nonlinear optical properties of films were also analyzed using the second harmonic of this radiation (λ=400 nm). Before z-scan measurements, the spatial characteristics of the

probe beam were measured using a CCD camera. It was confirmed that the beam profile in the focal area was close to Gaussian, which is a prerequisite for the analysis of z-scan traces using the relations developed for this technique. The full width of focused femtosecond beams at $1/e^2$ level of intensity distribution was measured to be 72 μm.
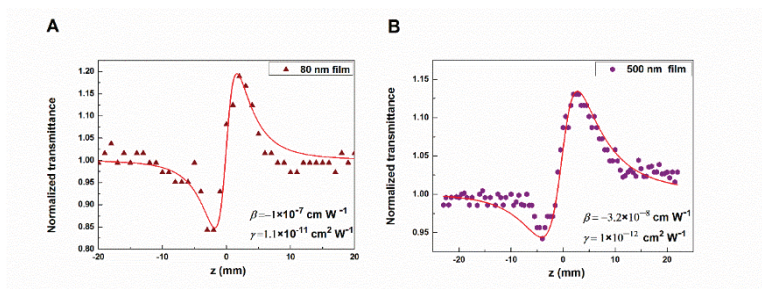
Fig. 2.9. Z-scan measurements at 800 nm. CA z-scans of (a) 80 nm and (b) 500 nm thick films. Solid curves show the fits using Eq. (2.2). Reproduced from [20] with permission from Walter de Gruyter GmbH & Science Wise Publishing.

The transient absorption measurements were carried out using the noncollinear pump-probe technique at λ=400 nm, similar to studies shown in Fig. 2.5(b). Femtosecond pulse (λ=800 nm, t=30 fs) was split at the ratio of 30:70 for the pump and probe pulses. The BBO crystals were used to generate the 400 nm pump and probe radiation. These two pulses were focused on the Ag_2S QD thin film using a 300 mm focal length lens. The energies and beam waists of the pump and the probe pulses at the focus were adjusted to be 10:1 and 1:2 respectively to match the condition required for observation of TA. In order to introduce the delay in arrival time of probe pulses with respect to pump pulses, the former radiation was reflected by a pair of mirrors mounted on the motorized translational stage. The arrival time of probe pulses with respect to pump pulses was controlled by moving the motorized translational stage connected to the motion controller. The fast photodiode and lock-in-amplifier were used to measure the transmittance of the probe pulses with respect to the position of the motorized stage. Lock-in-amplifier was externally triggered by an optical chopper running at 300 Hz.

Figure 2.8 shows the absorption spectra of two QD films of different thicknesses (80 and 500 nm). The inset shows the TEM image of Ag_2S QDs. The average size of QDs was ~4 nm. Figure 2.9 shows the CA z-

scans of two Ag$_2$S QD films using 30 fs pulses at λ=800 nm. The pulse energy was 0.36 μJ. The maximum fluence at the beam waist during these z-scans was 7×10^{-3} J cm^{-2} and the peak intensity was I_0=2×10^{11} W cm^{-2}.

The thinner film had higher values of γ and β. The β of the 80 and 500 nm films was measured to be -1×10^{-7} and -3.2×10^{-8} cm W^{-1}. The negative nonlinear absorption was attributed to SA. The nonlinear refractive index of the thicker film (γ =1×10^{-12} cm^2 W^{-1}) was 11 times smaller than that of the thin film (γ =1.1×10^{-11} cm^2 W^{-1}). Notice that the z-scan measurements of the dissolved in the hexane Ag$_2$S QDs showed that the nonlinear absorption coefficient of this suspension at λ=800 nm was 8.8×10^{-12} cm W^{-1}, and the nonlinear refractive index was 3×10^{-16} cm^2 W^{-1} [21] that was correspondingly 10^4 and 10^5 times smaller than the same parameters of 80 nm film.
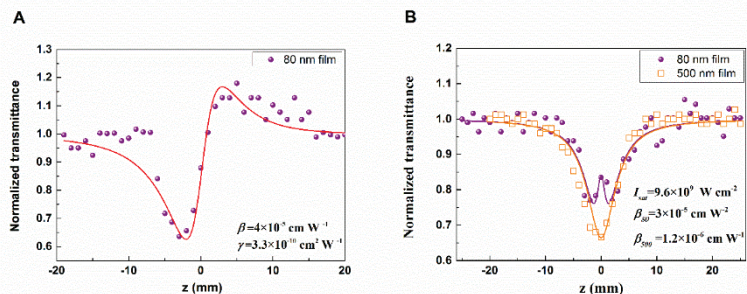
Fig. 2.10. Z-scan measurement at 400 nm. Normalized transmittances in the case of (a) CA z-scan of 80 nm film and (b) OA z-scans of 80 nm and 500 nm films measured using the 400 nm, 35 fs pulses. Reproduced from [20] with permission from Walter de Gruyter GmbH & Science Wise Publishing.

In the case of 400 nm, 35 fs probe pulses the nonlinear refraction was larger than in the case of 800 nm pulses. The CA z-scan of 80 nm film showed the positive nonlinear refraction and positive nonlinear absorption when the valley was deeper than the peak (Fig. 2.10(a)). The nonlinear refraction index of this thin film was calculated to be γ = 3.3×10^{-10} cm^2 W^{-1}, while in the case of the thicker film (500 nm) it was 25 times smaller (γ = 1.3×10^{-11} cm^2 W^{-1}).

In the case of low intensity, the SA at λ=800 nm dominated over other nonlinear optical processes in the used samples. Contrary to the 800 nm probe pulses, the use of 400 nm radiation led to a change of nonlinear

absorption from SA to RSA. The CA measurements revealed the high value of nonlinear absorption coefficient in the case of 80 nm film (β =4×10^{-5} cm W^{-1}). An almost similar value was obtained during the OA z-scan of this film (β =3×10^{-5} cm W^{-1}, Fig. 2.10(b)). Note that simultaneously with this process the growth of normalized transmittance at the highest intensities was observed that can be attributed to the higher-order SA effect (see the variation of normalized absorption in the vicinity of z=0, Fig. 2.10(b)). The nonlinear absorption in thicker (500 nm) film (β =1.2×10^{-6} cm W^{-1}, in the case of OA z-scan, and β =1.6×10^{-6} cm W^{-1}, in the case of CA z-scan) was 25 times smaller compared with the β of the thin film.
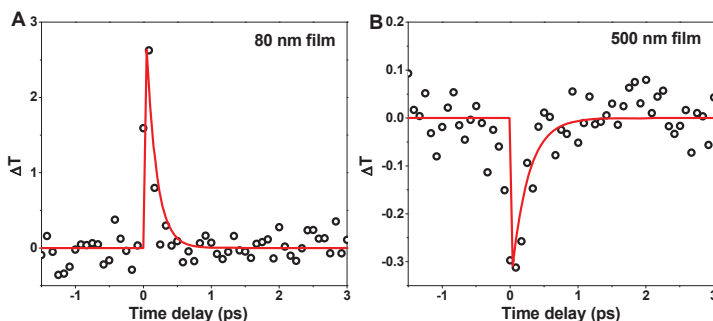
Fig. 2.11. Temporal evolution of probe pulse transmittance through the Ag_2S films in the case of 400 nm, 30 fs pulses. (a) 80 nm thick film and (b) 500 nm thick film. Reproduced from [20] with permission from Walter de Gruyter GmbH & Science Wise Publishing.

There are various reports on the TA phenomenon in the Ag_2S QDs and nanocrystals measured in the near IR region [22,23], which was attributed to the Auger recombination process. Meantime, the decay time constant for Ag_2S QDs has been reported neither at 800 nm nor at 400 nm wavelength regions. TA was measured in the 80 nm and 500 nm thin films containing the Ag_2S QDs deposited on the glass substrates using the 400 nm, 30 fs pulses. The energy of the pump pulse was used to be 35 nJ to excite the films. Prior to the measurements of the TA of films, similar measurements of the glass substrate were performed, to separate its contribution from the TA data obtained in the case of Ag_2S QD thin films, which showed the absence of the change in transmittance with time delay in the case of substrates.

Figure 2.11(a) shows the temporal evolution of transmittance in the case of the 80 nm Ag_2S QD thin film. The TA profile demonstrated the transient bleaching due to SA as compared to the reverse process in the 500 nm thick Ag_2S QD film (Fig. 2.11(b)). In the case of 500 nm Ag_2S QD film, transient transmittance decreases with delay time, which is due to RSA during the temporal overlap of pump and probe pulses. In order to confirm the RSA at 400 nm wavelength, the OA Z-scans of these two films (Fig. 2.10(b)), which depicted the positive nonlinear absorption at employed pulse energy and at the area out from the maximal intensity region (i.e. out from the focal area), were analyzed. However, as already mentioned, in the vicinity of the focal area, the transmittance of laser pulses increased for 80 nm Ag_2S QD thin film, which is probably due to the dominance of SA phenomenon over RSA, contrary to the case of the 500 nm film showing the RSA at these conditions. Thus the TA measurements (Fig. 2.11) were found to be consistent with the OA z-scan studies of two films. The decay time constants were determined to be 150 and 245 fs in the case of 80 and 500 nm films respectively. The difference in the decay times for these two films was attributed to different lifetimes of excited states and absorption probabilities in the case of thin and thick Ag_2S QD films.

References to Chapter 2

[1]   E. Zheng, B. Yuh, G. A. Tosado, Q. Yu, Solution-processed visible-blind UV-A photodetector based on CH3NH3 PbCl3 perovskite thin films, J. Mater. Chem. C 5 (15) (2017) 3796-3806.

[2]   D. Cortecchia, J. Yin, A. Bruno, S.-Z. A. Lo, G. G. Gurzadyan, S. Mhaisalkar, J. L. Brédas, C. Soci, Polaron self-localization in white-light emitting hybrid perovskites, J. Mater. Chem. C 5 (11) (2017) 2771-2780.

[3]   V. P. Gonzalez-Pedro, E. J. Juarez Perez, W. S. Arsyad, E. M. Barea, F. F. Santiago, I. M. Sero, J. Bisquert, General working principles of CH3NH3PbX3 perovskite solar cells, Nano Lett. 14 (2) (20140 888-893.

[4]   G. Walters, B. R. Sutherland, S. Hoogland, D. Shi, R. Comin, D. P. Sellan, O. M. Bakr, E. H. Sargent, Two-photon absorption in organometallic bromide perovskites, ACS Nano 9 (9) (2015) 9340-9346.

[5]   R. A. Ganeev, K. S. Rao, Z. Yu, W. Yu, C. Yao, Y. Fu, K. Zhang, C. Guo, Strong nonlinear absorption in perovskite films, Opt. Mater. Express 8 (6) (2018) 1472-1483.

[6]   M. Sheik-Bahae, A. A. Said, T.-H. Wei, D. J. Hagan, E. W. Van Stryland, Sensitive measurement of optical nonlinearities using a single beam, IEEE J. Quantum Electron. 26 (4) (1990) 760–769.

[7]   X. Liu, S. Guo, H. Wang, L. Hou, Theoretical study on the closed-aperture
      Z-scan curves in the materials with nonlinear refraction and strong nonlinear
      absorption, Opt. Commun. 197 (4-6) (2001) 431-437.

[8]   K. Dota, J. A. Dharmadhikari, D. Mathur, A. K. Dharmadhikari, Third-order
      nonlinear optical response in transparent solids using ultrashort laser pulses,
      Appl. Phys. B 107 (3) (2012) 703-709.

[9]   D. Blömer, A. Szameit, F. Dreisow, T. Schreiber, S. Nolte, A. Tünnermann,
      Nonlinear refractive index of fs-laser-written waveguides in fused silica, Opt.
      Express 14 (6) (2006) 2151-2157.

[10]   P. B. Chapple, J. Staromlynska, J. A. Hermann, T. J. Mckay, R. G. McDuff,
      Single-beam z-scan: measurement techniques and analysis, J. Nonlin. Opt.
      Mater. Phys. 6 (3) (2017) 251-263.

[11]   L. Yang, R. Dorsinville, Q. Z. Wang, P. X. Ye, R. R. Alfano, R. Zamboni, C.
      Taliani, Excited-state nonlinearity in polythiophene thin films investigated
      by the z-scan technique, Opt. Lett. 17 (5) (1992) 323-325.

[12]   G. A. Swartzlander, H. Yin, A. E. Kaplan, Continuous-wave self-deflection
      effect in sodium vapor, J. Opt. Soc. Am. B 6 (7) (1989) 1317-1325.

[13]   M. Samoc, A. Samoc, B. Luther-Devies, H. Reisch, U. Scherf, Saturable
      absorption in poly(indenofluorene): A picket-fence polymer, Opt. Lett. 23
      (16) (1998) 1295-1297.

[14]   M. Sheik-Bahae, D. C. Hutchings, D. J. Hagan, E. W. van Stryland,
      Dispersion of bound electron nonlinear refraction in solids, IEEE J. Quant.
      Electron. 27 (6) (1991) 1296–1309.

[15]   L. Brzozovski, E. H. Sargent, Azobenzenes for photonic network
      applications: Third-order nonlinear optical properties, J. Mater. Sci. Electron.
      12 (9) (2001) 483-489.

[16]   T.-C. Wei, S. Mokkapati, T.-Y. Li, C.-H. Lin, G.-R. Lin, C. Jagadish, J.-H.
      He, Nonlinear absorptionapplications of CH3NH3 PbBr3 perovskite crystals,
      Adv. Funct. Mater. 28 (18) (2018) 1707175.

[17]   H. Linnenbank, M. Saliba, L. Gui, B. Metzger, S. G. Tikhodeev, J. Kadro, G.
      Nasti, A. Abate, A. Hadfeldt, M. Graetzel, H. Giessen, Temperature
      dependent two-photon photoluminescence of CH3NH3 PbBr3: structural
      phase and exciton to free carrier transition, Opt. Mater. Express 8 (3) (2018)
      511-521.

[18]   A. Rout, G. S. Boltaev, R. A. Ganeev, Y. Fu, S. K. Maurya, V. V. Kim, K. S.
      Rao, C. Guo, Nonlinear optical studies of gold nanoparticle films,
      Nanomater. 9 (2) (2019) 291.

[19]   O. P. Varnavski, T. Goodson, M. B. Mohamed, M. A. El-Sayed,
      Femtosecond excitation dynamics in gold nanospheres and nanorods, Phys.
      Rev. B 72 (23) (2005) 1–9.

[20]   Y. Fu, R. A. Ganeev, G. S. Boltaev, S. K. Maurya, V. V. Kim, C. Zhao, A.
      Rout, C. Guo, Low- and high-order nonlinear optical properties of Ag2S
      quantum dot thin films, Nanophoton. 8 (5) (2019) 849-858.

[21]   Y. Fu, R. A. Ganeev, C. Zhao, K. S. Rao, S. K. Maurya, W. Yu, K. Zhang, C.
      Guo, Ag2S quantum dots in the fields of picosecond and femtosecond UV

and IR pulses: optical limiting, nonlinear absorption and refraction
properties, Appl. Phys. B 125 (1) (2019) 1.

[22] J. Sun, W. Yu, A. Usman, T. T. Isimjan, E. Alarousu, K. Takanabe, O. F.
Mohammed, Generation of multiple excitons in Ag2S quantum dots: single
high-energy versus multiple-photon excitation, J. Phys. Chem. Lett. 5 (4)
(2014) 659-665.

[23] S. Chand, E. Sharma, P. Sharma, Phase change induced quantization in NIR
emitting Ag2S nanocrystals: Structural and optical response for solar energy
applications, J. Alloy Compd. 770 (2019) 1173-1180.

CHAPTER 3

CHARACTERIZATION OF THE NONLINEAR OPTICAL PROPERTIES OF PEROVSKITES

In this chapter, we analyze an interface based on 4-mercaptopyridines (MPY) and MAPbCl$_3$ single crystal system. We discuss a strong Surface-enhanced Raman Scattering (SERS) signal of the MPY molecules adsorbed on this single crystal surface. The mechanism of this SERS enhancement is attributed to the charge transfer resonance at the interface of the MPY-modified single crystal. Additionally, a photo-electronic response effect under 532 nm irradiation is discussed in this single crystal system. This new phenomenon demonstrates a great advantage for practical application in photodetector based on single-crystal perovskites. We analyze the femtosecond laser-induced micro- and nanostructures with significantly enhanced fluorescence on MAPbBr$_3$ single crystal surface. Finally, we analyze the optical limiting effects in metal nanoparticles and perovskite nanocrystals.

3.1. Charge transfer effects on resonance-enhanced Raman scattering for molecules adsorbed on single crystalline perovskite

Surface-enhanced Raman Scattering (SERS) has been a widely used spectroscopic technique since it was first discovered on silver electrodes in the mid-1970s due to its unique characteristics, such as its non-destructive nature, ultra-high sensitivity, and abundant molecular fingerprint information [1]. The materials for SERS studies are mainly focused on noble metals (Au, Ag, and Cu) and gradually extended to other materials, such as some alkali metals (Na, K, and Li), transition metals, semiconductor materials, and organic semiconductor materials. Most of the observed semiconductor-enhanced Raman scattering phenomena have been explained by the charge-transfer (CT) mechanism, which inspired the development of a novel field in exploring chemical mechanisms of SERS [2].

Compared to metals, semiconductor materials contain more controllable properties that are beneficial for SERS mechanism studies, such as tuneable band gap and photoluminescence properties, high stability, and resistance to degradation. Until recently, a large number of semiconductor materials have been discovered for CT-induced SERS studies, including metallic oxides, metal sulphides, silver compounds, and semiconductor nanomaterials [3]. Under certain conditions, the chemical binding takes place between the adsorbed molecules and the atomic sites of the semiconductor substrates, and the adsorbent-adsorbate interaction rebuilds the band gap at the interface between the adsorbed molecules and the semiconductor materials. Under these conditions, the band energy at the interface will become closer to the photon energy of the excitation laser, which leads to the occurrence of a resonance Raman scattering-like effect. Previous studies of some molecule-modified metal oxides have shown this kind of resonance Raman scattering-like effect in SERS studies using semiconductors, such as pyridine modified TiO_2 and NiO [4]. In these cases, the CT enhancement mechanism is believed to have a major contribution to the observed high SERS signals. With the continued development of SERS study, the used semiconductor materials expand from metal oxides to other nanomaterials, including single elemental semiconductors (such as graphene, Si, and Ge) and some 2D materials (such as MoS_2), which have been proven to be capable of providing Raman enhancement based on the CT mechanism. Until now, the SERS property based on perovskites materials as a substrate has never been studied.

Here, we analyze a molecule-single crystal interface SERS study based on 4-mercaptopyridines (MPY) and $MAPbCl_3$ single crystal system [5]. We discuss a strong SERS signal of the MPY molecules adsorbed on this single crystal surface. The mechanism of this SERS enhancement is attributed to the charge transfer resonance at the interface of the MPY-modified single crystal. Additionally, an obviously photo-electronic response effect under 532 nm irradiation was found at this MPY-modified single crystal system. This new phenomenon extends the CT-induced SERS study to the single-crystalline materials and it demonstrates a great advantage for practical application in photodetector based on single-crystal perovskites.

4-Mercaptopyridine (MPY), dichloromethane, N,N-Dimethylformamide (DMF), dimethyl sulfoxide (DMSO), and lead chloride ($PbCl_2$) were used in these studies. MACl was synthesized as follows: Firstly, the mixed solution with 1.2 M methylamine and 1 M hydrochloride acid was stirred for 2h under an ice bath condition and then dried in a vacuum at 50°C for

2 h. After that, the sample was dissolved in ethanol and then filtered using a 0.2 μm PTFE filter. Diethyl ether was then added to the filtered solution to get the MACl powder followed by vacuum drying at 60°C. A 1M MAPbCl$_3$ solution in DMSO-DMF (1:1 by volume) was prepared by dissolving equimolar amounts of MACl and PbCl$_2$. The solution was then filtered using PTFE filter with 0.2 μm pore size. Then the precursor solution was kept in an oil bath at the temperature of 50°C for 6 h. The single crystal MAPbCl$_3$ surface modified with MPY molecules was achieved as follows: the single crystal was immersed in 10^{-3} mol/L MPY solutions (dissolved in CH$_2$Cl$_2$) and 6 h later, the sample was cleaned by CH$_2$Cl$_2$ and dried by N$_2$ flow. The 100 nm Au electrodes were deposited on the bulk single crystal and MPY modified single crystal surfaces by thermal evaporation. Raman spectra were collected using LabRAM HR Evolution Raman spectrometer. The UV-Vis spectral measurements were carried out using Cary 5000 UV-Vis-NIR spectrometer. SEM and EDS analysis were carried out by the scanning electron microscope. The *I-V* curves were collected by 4200A-SCS Parameter Analysis. The photo-electronic detection system was constructed with 532 nm and 633 nm irradiation light.
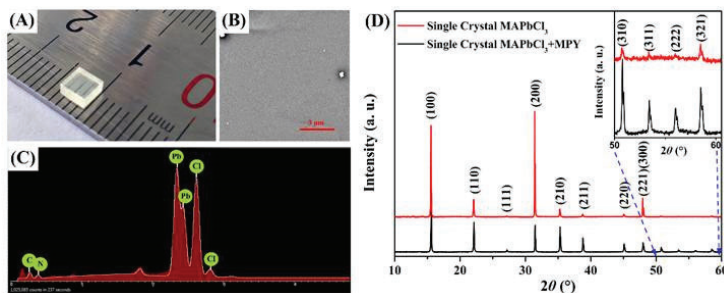
Fig. 3.1. (A) Optical image, (B) SEM, (C) EDS analysis and XRD spectra of the single crystal. Insert shows the enhanced spectrum of XRD in the range of 50 to 60°. Reproduced from [5] with permission from ACS Publications.

Figure 3.1a shows a cubic single crystal, while Figure 3.1b exhibits the surface state of the crystal by SEM. EDS confirmed the elemental content of this crystal (Fig. 3.1c). The as-prepared single-crystal MAPbCl$_3$ was then characterized by Power X-ray diffraction (Fig. 3.1d), which confirmed that the crystal possessed the single-phase cubic structure with the lattice parameter a=5.68 Å. Meanwhile, the MPY-modified single

crystal showed the same characteristic peaks compared to the pure single crystal MAPbCl₃. It indicates that the adsorption of MPY did not destroy the lattice structure of the materials substrate and maintain the intrinsic property of the single crystal.

UV-Vis spectroscopy was used to analyze the optical properties of the MAPbCl₃ single crystal after the adsorption of MPY molecules. Figure 3.2a shows the UV-Vis spectra of MPY (dissolved in CH_2Cl_2) and single-crystal MAPbCl₃ before and after the adsorption of MPY molecules. The single crystal MAPbCl₃ is transparent close to 428 nm and its colour changes from colourless (Fig. 3.1a) to yellow (Fig. 3.2a) after the adsorption of MPY molecule. The latter process leads to the formation of a new interfacial transition state. The bulk crystal showed quite a steep slope at 428 nm, which indicated that the band energy of the crystal is about 2.89 eV. After the adsorption of MPY, a notable longer wavelength absorbance occurred compared with that of unmodified crystal, and the band energy decreased to 2.32 eV. This interfacial photoabsorption can be attributed to the interaction between the adsorbed molecule and the single crystal.
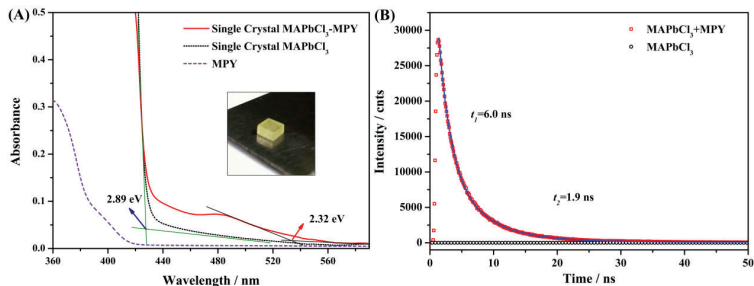
Fig. 3.2. UV-Vis spectra of the MPY molecule, single crystal MAPbCl₃ and the MPY-modified single crystal (A). The insert image shows the MPY modified single crystal; Time-resolved PL decay curves for the MAPbCl₃ single crystal before (black curve) and after (red curve) the modification of MPY molecules under excitation at 481 nm (B). Reproduced from [5] with permission from ACS Publications.

To further demonstrate the formation of the new interfacial transition state, we analyze the recombination property of the single crystal under the excitation at 481 nm. Figure 3.2b shows the PL lifetime results for the MAPbCl₃ single crystal before and after the modification of MPY molecules. The MPY modified single crystal exhibits double components

of the carrier dynamics (t_1=6 ns and t_2 =1.9 ns) with a biexponential fit of the curve. These two components are likely attributed to the interface and the bulk of the crystal respectively. As for the $MAPbCl_3$ single crystal, there is no PL response under 481 nm excitation. One can thus conclude that the modification of MPY molecule results in the formation of a new interfacial transition state.
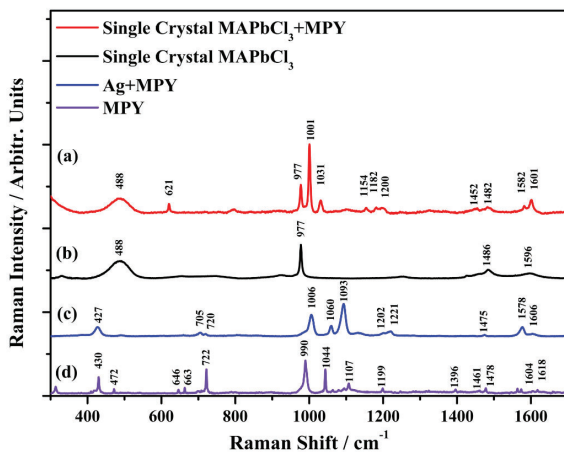
Fig. 3.3. Raman spectra of MPY molecule adsorbed on the single crystal (a), single crystal $MAPbCl_3$ (b), MPY molecule adsorbed on Ag (c), and MPY powder (d). The spectra were collected under 532 nm laser excitation. Raman spectra shifted compared each other along the Y axis for better viewing. Reproduced from [5] with permission from ACS Publications.

Figure 3.3 shows the Raman spectra of (a) MPY molecule adsorbed on the single crystal surface, (b) $MAPbCl_3$ single crystal, (c) MPY molecule adsorbed on Ag surface, and (d) MPY powder under 532 nm laser excitation. In Figure 3.3a, several observable bands located at 488 cm^{-1} and 977 cm^{-1}are attributed to the crystal mode (Figure 3b) while the 621 cm^{-1} (C–C–C/N–C=C out-of-plane bend), 1001 cm^{-1} (Ring breathing), 1031 cm^{-1} (C–H in-of-plane bend), 1182 cm^{-1} (C–H in-of-plane symmetric bend), 1200 cm^{-1} (C–H in-of-plane anti-symmetric bend), 1582 cm^{-1} (C-C stretch with deprotonated nitrogen) and 1602 cm^{-1} (C-C stretch with protonated nitrogen) are intrinsic to MPY.

As Figure 3.3c shows, the SERS spectrum of MPY adsorbed on Ag surface exhibits several characteristic peaks located at 427 cm^{-1}, 705 cm^{-1},

720 cm^{-1}, and 1093 cm^{-1}, which differs from the SERS spectrum of MPY molecule adsorbed on the single crystal MAPbCl$_3$. The difference in the characteristic bands of these two spectra could be attributed to different adsorption modes of the MPY molecules on the surface of different materials. As is well known, the -SH group can be easily combined with Ag to form S-Ag coordinate bond. Therefore, the bands at 427 cm^{-1} (ring reformation with C-S/C-C-C stretch), 720 (C-C/C-S stretch), and 1093 cm^{-1} (Trigonal ring breathing with C-S), which were correlated with the C-S mode, can be clearly observed. As for the single-crystal MAPbCl$_3$, the MPY molecule tends to adsorb on its surface through the N atom in the pyridine ring, which results in the disappearance of these two C-S mode-related Raman peaks. Moreover, the adsorption of MPY through the N atom results in the disappearance or intensity decrease of other related bands compared with the SERS spectrum of MPY on Ag surface, such as the bands at 705 cm^{-1}.
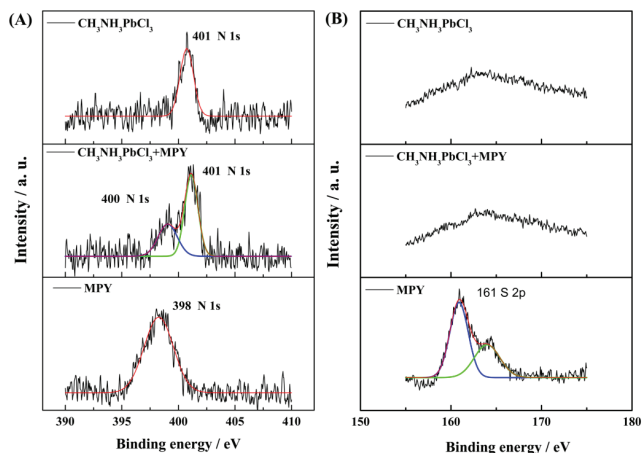
Fig. 3.4. XPS result for the N and S atoms in the three samples: CH$_3$NH$_3$PbCl$_3$, CH$_3$NH$_3$PbCl$_3$+MPY and MPY. Reproduced from [5] with permission from ACS Publications.

Figure 3.4 shows the XPS results of the N and S atom in three samples: MAPbCl$_3$, MAPbCl$_3$+MPY, and MPY. As Figure 3.4a shows, the peak for the N atom of the MPY molecule shows a 2 eV shift after being adsorbed on the single crystal surface, which can be attributed to the bonding formation between the N atom of MPY and the single crystal, while the

peak for the N atom of the MAPbCl$_3$ shows nearly no change. As for the S atom (Fig. 3.4b), only MPY molecule shows obviously characteristic peak. We can thus conclude that the MPY molecule adsorbed on the crystal surface through the N atom.

In the discussed case, the single crystal MAPbCl$_3$ does not possess surface plasmons along the excitation region of the lasers' lines used in these experiments (473 nm, 532 nm, and 785 nm), which indicates that the electromagnetic mechanism cannot be the dominant contribution to the surface-enhanced Raman signal of the MPY modified single crystal MAPbCl$_3$. The observed SERS signal can be explained by the CT mechanism. As described above, the adsorption of the molecule will lead to a red shift of the UV-Vis spectra. The band-band transition energy of the interface between a single crystal and MPY molecule can be calculated as 2.32 eV (Fig. 3.2a). This energy excellently fits with the excitation laser energy at 532 nm wavelength. Under these conditions, when the excitation light (532 nm) irradiates the sample surface, a CT resonance will take place in the energies of the single crystal/MPY interface. This resonance process is mainly due to the modification of the energy band gap from 2.89 eV to 2.32 eV, which matches the 532 nm excitation laser well. As a result, the Raman signal of the adsorbed MPY molecule was enhanced.

The evidence for the chemical enhancement mechanism is strongly associated with individual modes of the adsorbed molecules. Compared to those in the SERS spectrum of MPY adsorbed on Ag and its bulk Raman signal, there is a greater enhancement of several bands, such as 1001 and 1031 cm^{-1} bands, in the SERS spectrum of the MPY modified single crystal. Some weaker bands at 621 cm^{-1}, 1452 cm^{-1} and 1582 cm^{-1}, assigned to the b$_2$ mode of the MPY molecules, were also observed, which can only be selectively enhanced by the CT mechanism through Herzberg-Teller contributions. The additional SERS enhancements from the MPY single-crystal complex, particularly the enhancement of the b$_2$ mode result from the new band level formation at the interface of the complex and could be ascribed to the charge transfer between the single crystal and the MPY molecules.

3.2. Femtosecond laser-induced micro- and nanostructures with significantly enhanced fluorescence on MAPbBr$_3$ single crystal surface

Compared with the chemical method that controls the related parameters in the process of synthesizing process, the inherent uncontrollability of the common MAPbBr$_3$ (MA=CH$_3$NH$_3{}^+$) single crystal (MBSC) materials

becomes the main limiting factor. However, the physical processing of MBSC can be used to improve its fluorescence, which could be controlled in real-time and achieve dynamic monitoring.
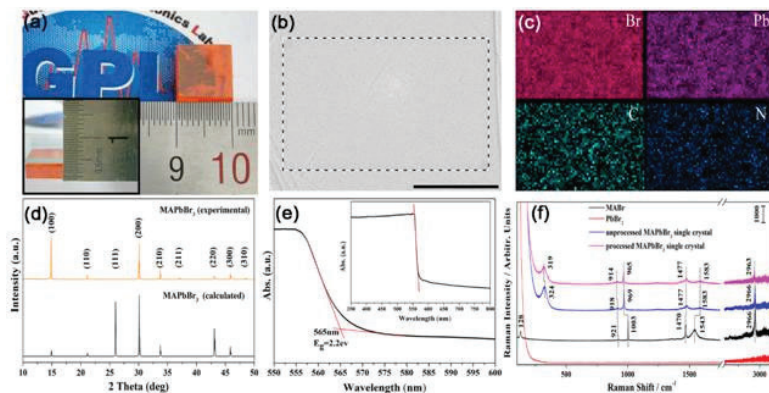
Fig. 3.5. a) Optical photography of MBSC synthesis by inverse temperature crystallization (ITC) method. The dimension is 10 mm×10 mm×4 mm; b) Scanning electron microscopy (SEM) image of single crystal surface, which shows almost no grain boundaries on surface and the scale is 10 μm; c) EDS mapping of the MBSC shows uniform elemental distribution of bromide, lead, carbon and nitrogen, respectively. d) Calculated and experimental powder X-ray diffraction pattern for MBSC; e) Partial absorption spectra of MBSC with Band gap energy. Inset: whole absorption spectra. f) Partial Raman spectra of MABr, $PbBr_2$, MBSC and femtosecond laser processed MBSC without any spectral correction or normalization. All samples were placed in air at room temperature for measurements. The laser intensity is kept at 56 W/cm^2 at 785nm. Reproduced from [6] with permission from Wiley-VCH.

Up until now, various approaches such as LIGA, electron beam lithography techniques, nano-imprint lithography techniques, and masking techniques have been developed for material modification. However, in the modification process, these techniques will inevitably include solution, direct contact, development, etch-back, stripping, and other links, resulting in perovskite single-crystal degradation and destruction, which is not adapted to improve the MBSC fluorescence. In order to avoid perovskite being broken and decomposition in solution-based or contact node fabrication processing, the femtosecond laser micro-machining technology as a new method can directly process MBSC and improve the fluorescence because of its non-contact processing, high processing precision, massless

3D processing, negligible thermal diffusion effect, a wide range of processing materials and many other advantages.

Here, we discuss that femtosecond laser micromachining technology is applied to the surface modification of MBSC material to achieve fluorescence enhancement [6]. Firstly, we analyze the effects of different laser scanning speeds (from 2.5 mm/s to 0.01 mm/s) on the surface morphology of MBSC (stripes, micro/nanoprotrusions, micro/nanorods, etc.) and analyze its mechanism. We show that the fluorescence of the laser processing region significantly enhances. Finally, we discuss the experimental observation showing that the femtosecond laser processed region on MBSC exhibits significant fluorescence enhancement both in the machined surface and in the machined interior, in air and nitrogen without affecting the morphology respectively. The results of this study show that the femtosecond laser micromachining technology could enhance the fluorescence of MBSC effectively without changing the material itself. This study provides technical support for the application of MBSC in light-emitting devices, such as LED.

MBSC grow from 1.5 molar solution containing $PbBr_2$ and MABr in DMF used inverse temperature crystallization (ITC) method. The femtosecond laser micromachining system, where a chirped-pulse amplification of Ti: sapphire laser system was adopted as a light source, delivers linearly polarized 35 fs laser pulse trains at a repetition rate of 1 kHz with the central wavelength λ=800 nm and maximum average power of $\approx$7 mJ.

MBSC grown from inverse temperature crystallization (ITC) method is shown in Fig. 3.5a, whose dimension is 10 mm×10 mm×4 mm. In Fig. 3.5b, the Scanning Electron Microscopy (SEM) images of the MBSC show good surface crystallization without any grain boundaries, indicating the single-crystalline nature. Energy Dispersive Spectrometer (EDS) mapping of the as-grown MBSC corresponding to the area selected by the dotted line in SEM image showed the uniform elemental distribution of bromide, lead, carbon, and nitrogen, respectively in Fig. 3.5c. Powder X-ray diffraction of the ground MBSC crystals demonstrate pure perovskite phase for MBSC and showed a good match with calculated XRD patterns from the MBSC model in Fig. 3.5d.

The absorption spectrum of the MBSC showed absorption cut-off around 565nm with a steep descending edge, and the band gap energy (E_g) could be calculated at the falling corners and the calculated E_g is 2.2 eV, which indicates this MBSC sample has a good quality in Fig. 3.5e. Raman spectroscopy is a powerful tool for identifying the crystalline phase of material and for measuring lattice strain. Figure 3.5f shows the normal

Raman spectra of MABr, PbBr$_2$, MBSC before and after femtosecond laser processed. For MABr, several characteristic peaks, such as 128, 921, 1003, 1470, 1543, and 2966 cm^{-1}, are observed in the MABr spectrum. When MBSC was synthesized from these two materials by the ITC method, the single characteristic peaks in MABr and PbBr$_2$ did not appear in the characteristic peaks of MBSC, 324, 918, 969, 1477, 1583, and 2966 cm^{-1}, which indicated that MABr and PbBr$_2$ had reacted completely. All of the tests on the MBSC showed good intrinsic properties.

3.2.1. Femtosecond laser micromachining and discussion of processing parameters for multiple micro- and nanostructures

A horizontal linear polarization laser with 5.4 mW was chosen for MBSC micro-machining, which allowed the investigation of the effect of laser intensity and defocus distance on dot diameter and surface ablation. All experiments are carried out under common room temperature conditions in the air.
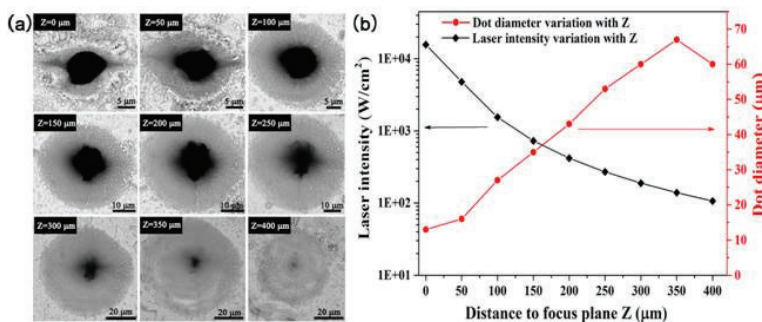
Fig. 3.6. a) SEM images of the dot diameter variation with distance, which indicates the position of sample surface is before the focus plane, Z (μm) ranging from 0 μm to 400 μm at 5.4 mW laser power. b) Relationship between both laser intensity and dot diameter with Z (μm) at 5.4 mW laser power. Reproduced from [6] with permission from Wiley-VCH.

Figure 3.6a shows the SEM images of the dot diameter with different Z, which was conducted by placing the sample before the focal plane of the objective lens (4×, N.A=0.1), and the distance between objective lens and sample surface can be controlled by the three-dimensional (x-y-z) translation stage.
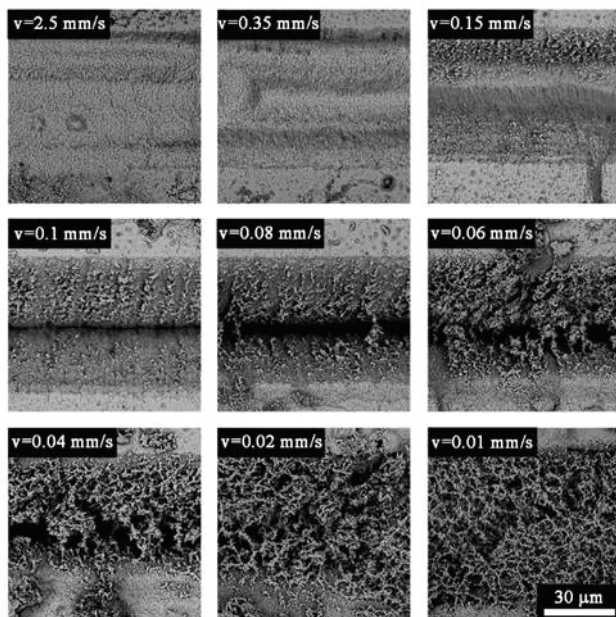
Fig. 3.7. SEM images of the laser treatment regions at scanning speeds v ranging from 2.5 mm/s to 0.01 mm/s. The laser intensity is kept at 84.4 W/cm^2 and the scale bar is applied in all images. Reproduced from [6] with permission from Wiley-VCH.

The dot diameter is minimized in SEM images when put the sample on the focal plane. Then with increasing distance Z from 0 μm to 350 μm, the dot diameter in the entire ablation area increases linearly and the middle black spot diameter shows a decrease with increasing distance Z. This behaviour results from the variation of the laser intensity as show the relationship between laser intensity and distance Z (μm) in Figure 3.6b, which shows that the focus spot size on the sample surface would gradually increase with Z increasing and begin to drop after Z=350 μm, and the laser intensity focus on the sample surface would gradually decrease. When the laser intensity drops to a threshold value that could ablate MBSC to produce round holes, the middle black hole would disappear and the entire dot diameter change to reduce because the femtosecond laser energy decreases progressively from spot centre to the edge because of the Gaussian distribution.

In order to avoid destructive ablation on the surface of MBSC like middle black spot, the sample was installed at the location of Z=450 μm, which corresponds to a laser intensity of 84.4 W/cm^2, to explore how the femtosecond laser scanning speed influences the surface morphology. As shown in Fig. 3.7, with the gradually reduced laser scanning speed v (from 2.5 mm/s to 0.01 mm/s), the thermal effect will be more obvious on the MBSC surface to produce a series of morphological changes because of the accumulation of laser energy on the sample surface.

When v is set up for 2.5 mm/s, the femtosecond laser sweeping area will only appear vertical and horizontal ripples. As the v slows to 0.35 mm/s, the edge of the processed region will appear small micro/nanoprotrusions which become more and more intensive at 0.15 mm/s. When continually reducing v to 0.1 mm/s, obvious cracks appear in the ablation area centre and clustered micro/nanoprotrusion distributes on both sides. The width of the crack increases with decreasing v from 0.08 mm/s to 0.04 mm/s and much more micro/nanorods appeared and gradually overlaid above the crack. When v=0.02 mm/s, the crack was completely covered by slender micro/nanostructures that continue to grow much more slender like micro/nano networks at v=0.01 mm/s in Fig. 3.7. This series of morphological changes are mainly due to the scanning speed changing the laser energy accumulation, and one could achieve multiple morphologies such as flat surface, ripples, micro/nanoprotrusions, micro/nanorods, or network on the MBSC surface by controlling different laser scanning speed at 84.4 W/cm^2 laser intensity.

According to Wagner's theory [7], the formation of various morphologies at different laser scanning speeds is mainly due to the diffusion process of atoms or ions, which could be described as grain boundary diffusion at low temperature, and transformed to sub-boundaries (dislocations) diffusion at middle temperature. Corresponding to the formation of different morphology in the laser ablation area, firstly the thermal effect of the laser reached the melting point of the MBSC, which caused the material to melt and generate ripples. Then with the temperature increasing, micro/nanoprotrusions appeared on the edge of the laser processed region and became much more as a result of the grain boundary diffusion dominated. Finally, most micro/nanoprotrusions began to tend to become micro/nanorods and staggered distribution into a network structure, covering the burned marks above, because of the sub-boundary (dislocation) diffusion.

In addition, a simple and fast ablation process could be achieved on the surface of MBSC by femtosecond laser direct ablating. As shown in Fig. 3.8, which are the optical microscopy image, SEM image, and fluorescent

image for the word "CIOMP" with laser intensity kept at 84.4 W/cm^2 and scanning speeds kept at 0.2 mm/s, common patterns such as different words could be ablated simply and fast without any damage out of processing area just because of the negligible thermal-diffusion effect.
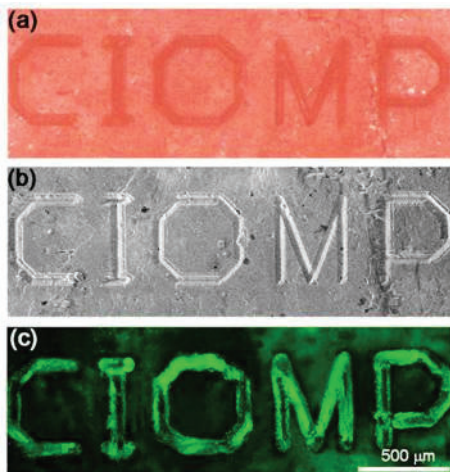
Fig. 3.8. a) Optical microscopy image for word "CIOMP" (the abbreviator for Changchun Institute for Optics, Fine Mechanics, and Physics) . b) SEM image for word "CIOMP". c) Fluorescent image for word "CIOMP". The laser intensity is kept at 84.4 W/cm^2, and scanning speed is kept at 0.2 mm/s. The scale bar is applied in all images. Reproduced from [6] with permission from Wiley-VCH.

It is understood that after the femtosecond laser ablation, the electron distribution requires hundreds of femtosecond to achieve thermal equilibrium. Consequently, according to the electron-phonon coupling intensity of the material, the energy transfer time (induced heat) from the electronic subsystem to the lattice is in the order of 1 to 100 ps, which is much longer than the time required for the electron to reach the thermal equilibrium. When the laser pulse width is much smaller than the electron-phonon coupling time interacting with the laser and the material, only a small fraction of the laser energy is converted to heat, thus achieving negligible thermal diffusion in the vicinity of the femtosecond laser processing area. The MBSC would produce green fluorescence at the excitation light of 488 nm and a noteworthy phenomenon is that the green fluorescence in the laser ablation area is much brighter than that of the

untreated region at the same laser power irradiation, which indicates that the femtosecond laser ablation process can significantly improve the fluorescence intensity of the MBSC.

After femtosecond laser treatment, a red shift occurred at several feature peaks (319, 914,965 and 2963 cm^{-1} corresponding to torsional mode [τ(MA)], rocking modes [ρ(MA)], stretching mode [ν(C−N)] and symmetric stretching mode [ν$_s$(NH$_3^+$)] respectively) in the Raman spectra of MBSC in Fig. 3.5f, which indicates that the thermal effect of laser energy changed the molecular pattern of MA, C-H, and NH$_3^+$, and influenced the original cubic phase lattice model of MBSC surface without change composition of MBSC.

3.2.2. Photoluminescence characterization of MBSC before and after femtosecond laser processing

In order to know exactly the ablation depth and the edge morphology of the MBSC under 84.4 W/cm^2 laser intensity and 0.01 mm/s scanning speed, a three-dimensional topography test on the laser processed region was performed. It was concluded that the overall ablation area by femtosecond laser processing is V-shaped, with a large number of micro/nanoprotrusions on the edge. The effective ablation depth can reach up to about 35 μm, and the micro/nanostructures that grow on the edge of the processing area can exceed the unprocessed area approach to 10 μm. The SEM image of MBSC clearly shows the micro/nanostructures distributed like coral and almost completely covered the V-shaped grooves produced by femtosecond laser ablation. Through the distribution of photoluminescence intensity (PL) at different depths, the distribution trend of green fluorescence on the MBSC surface (D=0 μm) corresponds to the distribution of micro/nanostructures in the SEM image, and the fluorescence in the laser processing area is obviously stronger than that in the untreated area. Fluorescence enhancement in the processed region can still be seen at D=-20 μm, which is still under laser ablation, except that the overall fluorescence intensity is significantly weaker; as the depth of investigation continues to increase, fluorescence has become very weak at D=-40 μm to -80 μm and the effect of laser processing is significantly diminished, which can be derived from the fluorescence intensity scale. The above results indicated that under the same excitation, on the one hand, the fluorescence intensity on the MBSC surface is generally greater than that in the body, mainly due to the MBSC surface absorbing more energy of the excitation laser because it is more consumed and scattered in the body and the surface fluorescence would radiate to the outside more easily than

the fluorescence in the body due to material dissipating. On the other hand, it can also be seen that the micro- and nanostructures produced by femtosecond laser micro-machining show an obvious fluorescence enhancement phenomenon.

In order to further clarify the effect of micro/nanostructures on fluorescence enhancement, the MBSC surface layer (from D=0 μm to -1.5 μm) was selected to detect and analyze the fluorescence intensity. From left to right in Figure 3.9a is the SEM image and different layer Photoluminescence (PL) intensity distribution image of the area, respectively. It can be drawn obviously that the PL intensity in the laser ablating region is much higher than the unprocessed region in a different layer, which also could be directly drawn according to the fluorescent brightness contrast. Moreover, with the depth of the focus plane ranging from 0 to -1.5 μm, the fluorescent bright area gradually extended to the entire laser ablation area, which may result from the accumulation of fluorescence result from the micro/nanostructures which is above the 0 μm plane from Fig. 3.9b.

To prove the existence of the fluorescence accumulation effect, a series of positions located in the processing and unprocessed area were selected to measure the fluorescence intensity with different depths ranging from 10 to -50 μm by setting the unprocessed area plane as 0 μm. The PL intensity of the processed and unprocessed region showed a downward trend after rising firstly with the focal plane position gradually down. This is because when the excitation laser is focused above D= 0 μm plane, the unprocessed area does not block the laser transmission and the excitation laser continues to travel down the MBSC surface. As the focal plane gradually approaches 0 μm, the fluorescence is stimulated when the excitation intensity exceeded a threshold, and the area of the excitation laser stimulating is gradually reduced with the focus plane continuing to move downward.

Although the intensity of the excitation light is the strongest at the 0 μm plane, the area of the luminescent material is the smallest, resulting in the maximum of total fluorescence intensity appearing above the 0 μm. Gradually focusing on the material, the fluorescence is significantly weakened due to scattering and loss of material. However for the laser processing area, the micro/nanostructures are generally higher than the 0 μm plane and less than 10 μm, so when the fluorescence intensity in the processing area from 0 to -1.5 μm was detected, in fact, the fluorescence of the micro/nanostructures above the 0 μm plane is mainly detected. From D=0 μm to -1.5 μm, as the luminescent material is sufficient and the excitation threshold is satisfied, the fluorescence intensity in the

processing area shows an additive phenomenon and the fluorescence becomes stronger and stronger.
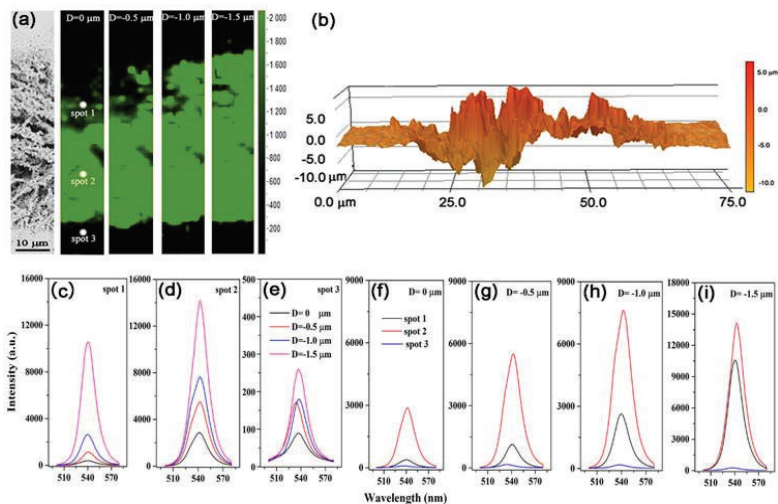
Fig. 3.9. a) SEM image and different layer (ranging from 0 to -1.5 μm) Photoluminescence (PL) intensity distribution image on MBSC including laser treatment regions and unprocessed regions in air at room temperature. The excitation laser intensity is kept at 2.55 mW/cm^2. b) Three-dimensional image of the depth variation of the selected area. The micro/nanostructures could cover the upper part of the trench and beyond the unprocessed area about 7 μm. c-e) PL spectra for each spot in different layer. All spots were spot1, spot 2 and spot 3 in a) corresponding to c), d), e), respectively. f-i) PL spectra in different layer with three spots. The depth is 0, -0.5, -1.0, and -1.5 μm corresponding to f), g), h), i), respectively. Reproduced from [6] with permission from Wiley-VCH.

As shown in Fig. 3.9c-e, the PL intensity of each selected point in Fig. 3.9a gradually increases with the focus plane down, which is inconsistent with the accumulation of fluorescence. One can conclude that the PL intensity in the processed region is two orders of magnitude higher than that in the unprocessed region from Fig. 3.9f-i for each depth on the surface region. Taking into account the influence of fluorescence accumulation, although the fluorescence intensity of a specific monolayer was difficult to be simply calculated by addition and subtraction, one still could conclude that the enhancement of the fluorescence intensity is due to the existence of the micro/nanostructures induced by femtosecond laser

and the PL of this structure is generally much higher than the original single crystal surface. It is worth noting that no obvious displacement of the fluorescence central wavelength of the micro/nanostructures formed after laser processing, which shows that the laser ablation does not change the material composition.
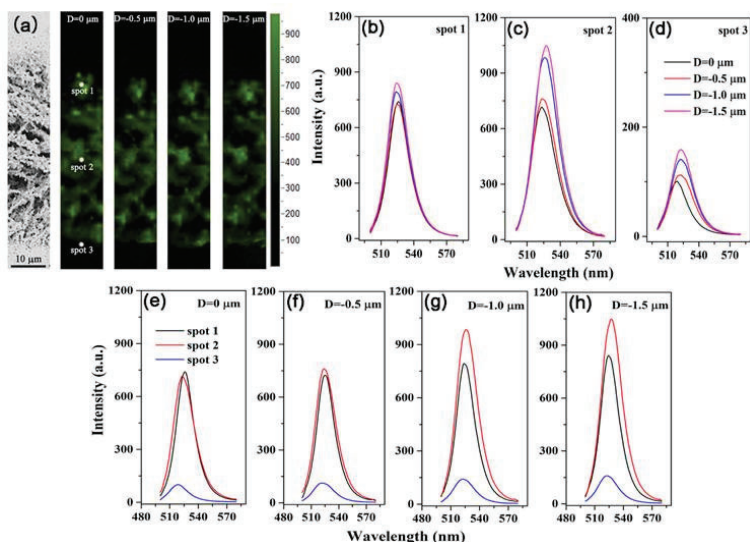
Fig. 3.10. a) SEM image and different layer (ranging from 0 to -1.5 μm) PL intensity distribution image on MBSC including laser treatment regions and unprocessed regions. The excitation laser intensity is kept at 2.55 mW/cm^2 at 473nm in N_2 at room temperature. b-d) PL spectra for each spot in different layer. All spots were spot1, spot 2 and spot 3 in a) corresponding to b), c), d), respectively. e-h) PL spectra in different layer with three spots. The depth is 0, -0.5, -1.0, and -1.5 μm corresponding to e), f), g), h), respectively. Reproduced from [6] with permission from Wiley-VCH.

To confirm that the micro/nanostructure formed by femtosecond laser ablation is stable and contributes to fluorescence enhancement, its PL intensity in a nitrogen atmosphere was retested and the results are shown in Fig. 3.10. Fluorescent brightness was significantly brighter in the laser-processed areas even under a nitrogen atmosphere, and the distribution of the fluorescence was in agreement with the microstructure distribution in the SEM image, demonstrating that the micro/nanostructure contributes to fluorescence enhancement. By measuring the PL intensity of the selected

three points, it still shows that the PL intensity gradually increases with the focused plane down in Fig. 3.10b-d, but the enhancement tendency is not particularly obvious, indicating that the fluorescence accumulation effect exists but performance is weaker in a nitrogen atmosphere.
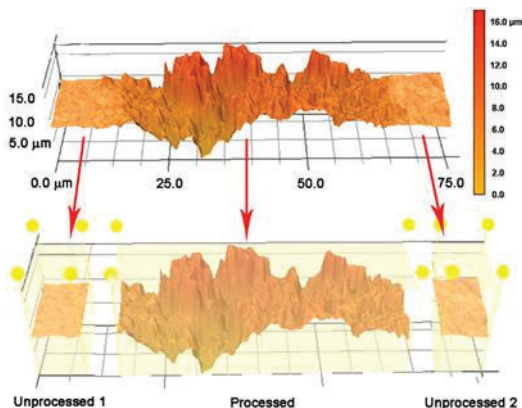
Fig. 3.11. 3D distribution image of the topography depth changes in processed and unprocessed area. Reproduced from [6] with permission from Wiley-VCH.

Figure 3.10e-h shows that PL intensity in the processed region is two to three times smaller than that in the unprocessed region in each focused layer, and the overall PL intensity in nitrogen is significantly weaker than that in air. Based on the previously reported articles' conclusion, it can be concluded that the surface fluorescence of MBSC is related to water and oxygen in the air supplying electrons to Pb^{2+} on the surface because MA^+ easily lacking. So the main reason for the weaker fluorescence in nitrogen is the lack of water and oxygen that supply electron density to Pb^{2+}, which greatly reduces the overall PL intensity. However, the micro/nanostructure in the processed region showing better fluorescence enhancement is mainly due to the rapid increase of the specific surface area.

In Figure 3.11, the previously selected area is decomposed into three parts of the two unprocessed areas on the edge and one intermediate processing area. Then the measurement of the ratio of the surface area to the volume of each area was carried out. Due to the high refractive index of perovskite materials and the uniform surface of a single crystal, most fluorescence in the internal is totally reflected by the interface between material and air and could not radiate to the outside free space, absorbed

and dissipated by the material itself, which is one of the important factors limiting the fluorescence intensity of perovskite single-crystal material [8].
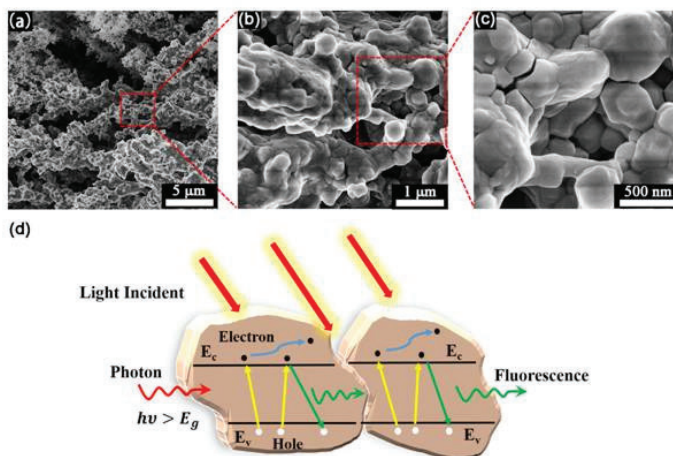
Fig. 3.12. (a-c) SEM images of the micro/nanostructures produced by femtosecond laser with 84.4 W/cm^2 laser intensity and 0.01 mm/s scanning speed in different scale. (d) Schematic diagram of the principle for fluorescence enhancement due to the micro/nanostructures formation. Reproduced from [6] with permission from Wiley-VCH.

From the SEM image of the micro/nanostructures produced by the femtosecond laser in Fig. 3.12a-c, one can clearly obtain that the micro/nanostructures like the coral group had radial growth accompanied by different degrees of crossover overlapping. Around each micro/nanorods, there are different sizes of the nanoprotrusions . Due to the existence of the above micro/nanostructures, on one hand, the diameter of the micro/nanoprotrusions was reduced to the nanoscale range. On the other hand, the surface roughness in the processed region is significantly increased and it reduced the total reflection of the incident excitation light to make more photons could be absorbed by the MBSC, which also increased emission randomness of fluorescence on the interface to make sure that more fluorescence can be detected. In addition, femtosecond laser ablation promotes the formation of micro/nanoprotrusions, which introduced more grains and grain boundaries and break the path for continuous charge transport. As shown in Figure 3.12d, when the photon energy than the band gap entered the material (red line), the electron in the valence band would absorb energy and jump to the conduction band (yellow line). After

a short period of time, most electrons in the excited state would jump to the valence band and issue fluorescence through spontaneous emission (green line) and only fewer electrons continue to transfer (blue line) due to the existence of the grain boundary, which would reduce carrier diffusion and promote the generation of fluorescent radiation.

Based on the above studies, it is shown that the micro/nanostructures on the surface of MBSC prepared by femtosecond laser micromachining technology could achieve significant fluorescence enhancement whether in the air or nitrogen atmosphere and its fluorescence enhancement effect does not appear irreversible chemical changes by changing environment alternately. It is also proved that the fluorescence emission of the MBSC surface is related to the physical adsorption of water and oxygen in the air. This provides a promising possibility for fabricating MBSC light-emitting devices.

3.3. Comparative analysis of optical limiting effects in metal nanoparticles and perovskite nanocrystals

The optical limiting is one of the potential applications of the materials' optical nonlinearities. It is aimed at protecting eyes and sensitive registration devices from damage. The aim of these studies was the comparative analysis of the optical limiting effect based on the nonlinear optical characteristics of materials. The laser ablation technique was used for the preparation of NP liquid solution. One benefit of laser ablation is that it can be conducted using both a pulsed wave and continuous wave laser, although the former is the primary method as a high level of intensity is needed with the laser beam being used. This technique allows the synthesis of pure NPs solutions depending on the purity of the target which is used for laser ablation compared to chemical methods. Pulsed laser ablation in a liquid environment provides a green, safe and efficient synthesis compared to the chemical reduction method. Moreover, it can be used to synthesis the NPs easily from different hardness and melting points of the metallic surfaces [9]. In the case of silver NPs, the optical limiting effect was compared in the suspension of silver NPs prepared by the chemical reduction method and laser ablation technique [10]. Moreover, in both cases, the shapes of absorption curves and peak positions of surface plasmon resonance (SPR) were similar to each other. These results are discussed in this subsection. The optical limiting was analyzed in NPs suspension with various sizes and properties, quantum dots, and perovskite nanocrystals using 800 nm and 400 nm 60 fs

laser pulses. Here we also discuss the advantages of the application of gold NPs as optical limiting materials for 60 fs, 800 nm pulses [11].

The study of OL of laser radiation in various metallic NPs, QDs, and perovskites opens the possibility of using these materials as laser shutters for protection against intense laser radiation and is also important in investigating the fundamental properties of nonlinear optical media. The OL mechanisms have different origins. In molecules, the OL mechanism is reverse saturable absorption (RSA) due to the large cross-section of the absorption from excited levels. Two-photon absorption (2PA) is responsible for OL in Al, Ti, Co, Ni, Zn, Ag, Sn, In, W, Au nanoparticles, and Ag_2S quantum dots as well as $CsPbBr_3$ and $CsPbI_2Br$ perovskites.
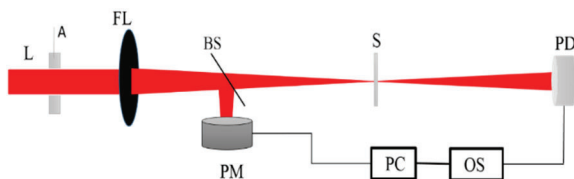
Fig. 3.13. Experiment layout for optical limiting studies. L: laser, 800 nm, 60 fs, 1 kHz, A: attenuator, FL: focal lens, f=400 mm, S: sample, BS: beam splitter, PM: power meter, PD: photodiode, PC: personal computer, OS: oscilloscope. Reproduced from [11] with permission from Elsevier.

The experimental setup for OL is shown in Fig. 3.13. The sample (colloidal solutions put in a 2 mm cell) is moved along the propagation direction of the focused beam. At the focal point, the sample experiences maximal pump intensity, which gradually decreases in either direction from the focus. A lens with a focal plane f=400 mm was used during the discussed studies. The OL properties of the reported sample suspensions were characterized by fluence-dependent transmittance measurements using 800 nm laser pulses with a pulse duration of 60 fs and a repetition rate of 1 kHz obtained from a Ti: sapphire laser. The values of $1/e^2$ beam waist at focus are 38 μm and the corresponding peak intensities are $\sim 10^{11}$ W cm^{-2}.

The reported NPs suspensions were prepared by chemical reduction and laser ablation methods using different pulse durations and wavelengths. In brief, Ag and Au NPs as well as Ag_2S QDs (0.375mg/ml), $CsPbBr_3$, and $CsPbI_2Br$ perovskites are prepared by chemical reduction method. The Al and Ag NPs are prepared by ablation bulk target using nanoseconds (ns) pulses of wavelength 1064 nm, pulse duration 6 ns, at

pulse energy 2 mJ and 5 mJ, respectively. Ni, Ti, Co, Zn, Sn, In, and W NPs were produced during the laser ablation of bulk targets using 800 nm, 200 ps pulses at pulse energy 550 µJ. These NPs were produced during the ablation time of 30 min in deionised water. Once the solution of NPs became prepared, the UV visible absorption spectroscopy and scanning electron microscopy (SEM) were performed to characterize the suspensions in terms of their SPR bands, size, and shape measurements, respectively. The shape of all the prepared NPs was spherical, except In NPs, which showed a cubic shape.

There are two major nonlinear absorption mechanisms employed for OL. One of them is the RSA and the other is 2PA. 2PA as the OL mechanism exhibits the advantage of (i) negligible linear absorption loss for weak signal, (ii) extremely fast temporal response, and (iii) retaining high beam quality of the transmitted signal. For these reasons, 2PA based devices are suitable not only for OL but also for other applicable purposes, such as optical power stabilization, optical pulse reshaping, optical spatial field reshaping, etc. The observations of the OL in reported NPs and perovskites were mostly attributed to the 2PA at the wavelength of 800 nm. Some of the NPs possess the saturable absorption (SA) and RSA nonlinear processes at lower and higher input energies. RSA generally arises in a molecular system when the excited state absorption cross-section is larger than the ground state cross-section [12]. The process can be understood by considering a system that is modelled using three vibronically broadened electronic energy levels.

In this section, we analyze the optical limiting effect of various transition (Au, Ag, Ti, Co, Ni, W, Zn) and post-transition (Al, Sn, and In) metal NPs. Metallic NPs with sizes smaller than the wavelength of light show strong dipolar excitations in the form of localized surface plasmon resonances (LSPR). LSPRs are non-propagating excitations of the conduction electrons of metallic NPs coupled to the electromagnetic field. The resonance condition is established when the frequency of light matches the natural frequency of valence electrons oscillating against this restoring force. Au and Ag NPs possess strong plasmonic resonance in the visible region of the electromagnetic spectrum. The other metal NPs such as Ti, Co, Ni, W, Zn, Sn, and In NPs possess LSPR in the UV region. The UV-visible absorption spectra are shown in the following section. The SPR is a result of the interactions between the incident light and surface electrons in a conduction band. This interaction produces coherent localized plasmon oscillations with a resonant frequency that strongly depends on the composition, size, geometry, dielectric environment, and particle-particle separation distance of NPs.

3.3.1. Characterization and optical limiting properties of noble metal non-reactive nanoparticles

Here the absorption spectra, SEM images, and the results of OL properties of noble metal non-reactive NPs such as Al, Ag, Au NPs, Ag_2S QDs and W, Sn, Zn, and In NPs suspensions are analyzed. The optical, nonlinear optical, and OL properties of these NPs suspensions strongly depend on their size and shape. Figure 3.14a - 3.14d shows the SEM images and size distribution of Ag, Al, and Au NPs, whereas Fig. 3.14e shows the TEM image of Ag_2S QDs. Figure 3.14g shows the absorption spectra for these NPs suspensions. The optical properties of Ag:chemical, Ag:ablation, Au NPs, and Ag_2S QDs characteristic absorption dominated by SPR peaks 400, 402, 527, and 403 for particle sizes of 13, 8, 17, and 4 nm respectively (Fig. 3.14g).

In the case of Ag NPs, the width and position of SPR were varied as the functions of particle size and shape. As has been previously pointed out in a number of studies, the absorption spectra of Ag and Au NPs can be controlled, to a considerable extent, by the parameters and methods of preparation of the nanoparticle-contained solutions. Al NPs show the absorption SPR bands near to UV region. Figure 3.14h shows the results of OL properties of Al, Ag, Au NPs, Ag_2S QDs. When the incident energy of 800 nm pulses was increased above the limiting threshold, the transmitted energy tended to approach a steady value. In addition, the ratio of linear transmittance with respect to water to the NPs transmittance (nonlinear attenuation factor (N_{af}) before the limiting threshold was measured.
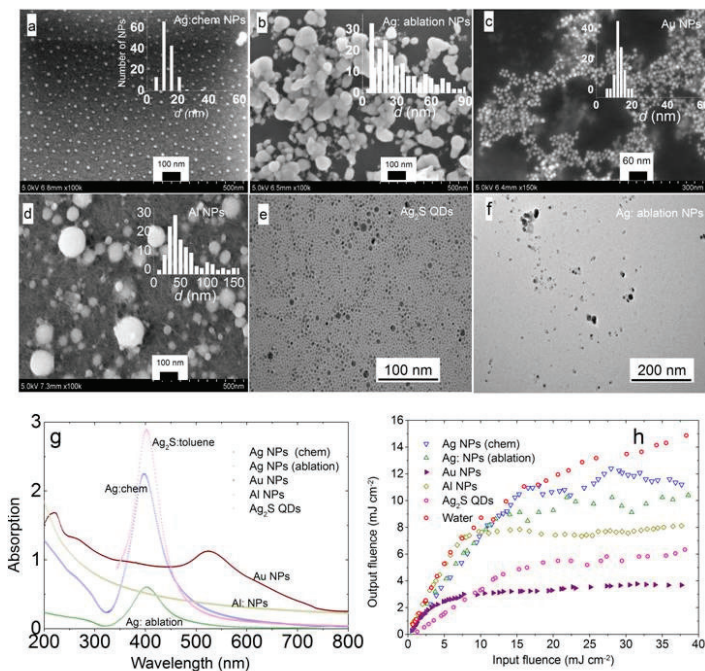
Fig. 3.14. SEM images and size distribution (x-axis: diameter (*d*) of NPs, Y-axis: Number of NPs) of (a) Ag;chem NPs, (b) Ag: ablation NPs, (c) Au NPs, (d) Al NPs. TEM image of (e) Ag₂S QDs, and (f) Ag: ablation NPs, (g) UV absorption spectra, and (h) optical limiting of Ag, Au and Al NPs suspensions in water and Ag₂S QDs. Reproduced from [11] with permission from Elsevier.

OL thresholds (OL$_T$), N$_{af}$, size distribution, mean size of reported NPs suspensions, and the corresponding nonlinear processes are comprised in Table 3.1. Ablated Ag NPs have higher particle size distribution i.e. 5-90 nm, and contain a larger number of smallest nanoparticles with a mean size of 8 nm. Whereas, Ag:chemical NPs have a size distribution of 8-18 nm, at a mean size of 13 nm. It was observed that ablated Ag NPs possess higher OL properties compared to the chemically synthesized NPs, it might be due to the contribution of the smallest NPs (~8 nm) of ablated Ag NPs. The TEM analysis is shown in Fig. 3.14f. Therefore, the metal nanoparticles were synthesized by the laser ablation method. Gold nanoparticles possess high OL properties as compared to Ag NPs, whereas

Al NPs show high OL compared to Ag NPs. This might be due to the concentration of Al NPs being larger than the Ag NPs. However, the N_{af} of Al NPs is lower than the N_{af} of Ag NPs. Among Ag NPs, ablated NPs have the highest value of N_{af} (1.17) compared to chemically prepared ones (1.09).

Table 3.1. OL thresholds, nonlinear attenuation factors (N_{af}) and responsible nonlinear optical processes. Reproduced from [11] with permission from Elsevier.

NPs	NPs SD (nm)	Mean (nm)	OL_T (mJ cm^{-2})	N_{af}	NP
Nonmagnetic NPs					
Ag: chemical	8-18	13	16.5	1.09	2PA+SA
Ag: ablation	5-90	8	12.1	1.17	2PA
Au: chemical	10-30	17	3.26	1.39	2PA
Al: ablation	10-150	35	7.33	0.87	2PA
W	4-22	8	13.4	1.75	2PA
Sn	3-12	7	12.4	2.07	2PA
Zn	5-30	20	18.8	1.36	2PA+SA
In	20-120	50	16.8	1.74	2PA+SA
Magnetic NPs					
Ni	15-250	96	10	1.35	2PA
Ti	25-250	125	7.6	1.07	SA
Co	5-200	90	8	1.99	2PA
QDs and perovskites					
Ag$_2$S QDs	3-6	4	10.2		2PA
CsPbBr$_3$			6.2		2PA+SA
CsPbI$_2$Br			13.2		2PA

From Fig. 3.14h, it can be seen that the OL curve for Ag$_2$S, Al NPs, Ag NPs (ablation) shows similar trends. However, Ag NPs (chemical) show a similar trend to Ag NPs (ablation) up to 12.6 mJ cm^{-2}. Beyond this fluence, the output fluence increases. This is probably due to the influence of the size of NPs which is smaller for the case of Ag NPs prepared from the ablation method. Among the Ag NPs (prepared by chemical, ablation) and Ag$_2$S QDs, even though these have nearly SPR peaks (Fig. 3.14g), Ag$_2$S QDs shows higher OL efficiency increased as compared to Ag NPs, due to the small size distribution of Ag$_2$S QDs (Fig. 1.3.14e). Another reason for the change in the OL profile is the process of saturable absorption at fluence higher than 23 mJ cm^{-2}.

Fig. 3.15. SEM images and size distribution of (a) W NPs, (b) Sn NPs, (c) Zn NPs, (d) In NPs. (e) UV absorption spectra, and (f) optical limiting curves for Zn, Sn, In, and W NPs suspensions. Reproduced from [11] with permission from Elsevier.

The OL efficiency is increased with small-sized NPs like Ag_2S QDs. Au NPs having a size distribution range of 10-20 nm and a mean size of 17 nm possess a smaller OL threshold (3.26 mJ cm^{-2}) compared to other metal NPs. Also, it might be due to excitation wavelength much closer to the Au SPR bands as compared to SPR bands of other nanoparticles. The linear dependence between input and output pulses was sustained up to the OL threshold of the fluence of the propagated laser radiation. The OL thresholds for these NPs are comprised in Table 3.1. The absence of SPR in Al NPs suspensions, as shown in Fig. 3.14g, results in a similar profile

of the OL curves (Fig. 3.14h) of water up to 8 mJ cm^{-2}. However, a further increase of laser fluence can lead to a multi-photon absorption process, which can eventually lead to a decrease in the output laser fluence, which shows the OL behaviour.

Figure 3.15(a-d) shows the SEM images and size distribution of W, Sn, Zn and In NPs, whereas Fig. 1.3.15e indicates the UV absorption spectra. The SPR peaks for these NPs are located near 322, 245, 236, and 252 nm, respectively. Among all, Sn NPs have the smallest size distribution lying between 3-12 nm, with a mean size of 8 nm.

Figure 3.15f shows the OL curves for W, Sn, Zn, and In NPs prepared by laser ablation using ps pulses. Zn and In NPs show different OL behaviour (i.e. the influence of SA beyond the input fluence of 25 mJ cm^{-2}) as compared to W and Sn NPs. Consequently, Sn NPs show higher optical nonlinearity as compared to that of W, ZN, and In NPs suspensions, due to their small particle size (~6 nm). The W and Sn NPs have a lower limiting threshold than the W and Sn (see Table 3.1).

3.3.2. Characterization and optical limiting in Ni, Ti, and Co NPs suspensions

Figure 3.16d demonstrates the UV-visible absorption spectra of Ti and Co NPs ablated in water. The Ti NPs have a characteristic SPR peak at ~280 nm. Ti NP suspension initiates to absorb at ~ 500 nm. Synthesis of pure titanium nanoparticles in liquid by laser ablation method is not a simple task because titanium is an active material. For the preparation of pure titanium NPs one has to add some chemical active component as a polyvinylpyrrolidone against to aggregation of titanium nanoparticles with oxide in water solution. The self-aggregation process of TiO depends on the type of liquid. The case of ablation of Ti target in dichloroethane through chemical reaction formation of TiC was demonstrated in Ref. [13]. In discussed case, the fresh ablated suspension was used to study the optical limiting effect in pure Ti NPs.

The Co NPs in water show some absorption peaks at 400 nm and 700 nm, respectively. Earlier studies demonstrated that some contradicting results on the position of SPRs of Co NPs, which probably can be attributed to different methods of NP formation and different spatial shapes of these small-sized species. The absorption spectra of Ni NPS show strong absorption near to 200 nm with the beginning of the broad absorption bands around 400 nm. Earlier, several efforts have been made for an explanation of the appearance of the absorption band at 400 nm, which is assigned to the SPR in Ni NPs [14,15]. It has been explicitly

shown the presence of two absorption bands in Ni NPs absorption spectra centred at 345 nm and 217 nm which were assigned to the SPR of Ni and interband *d–d* transition in Ni, respectively.
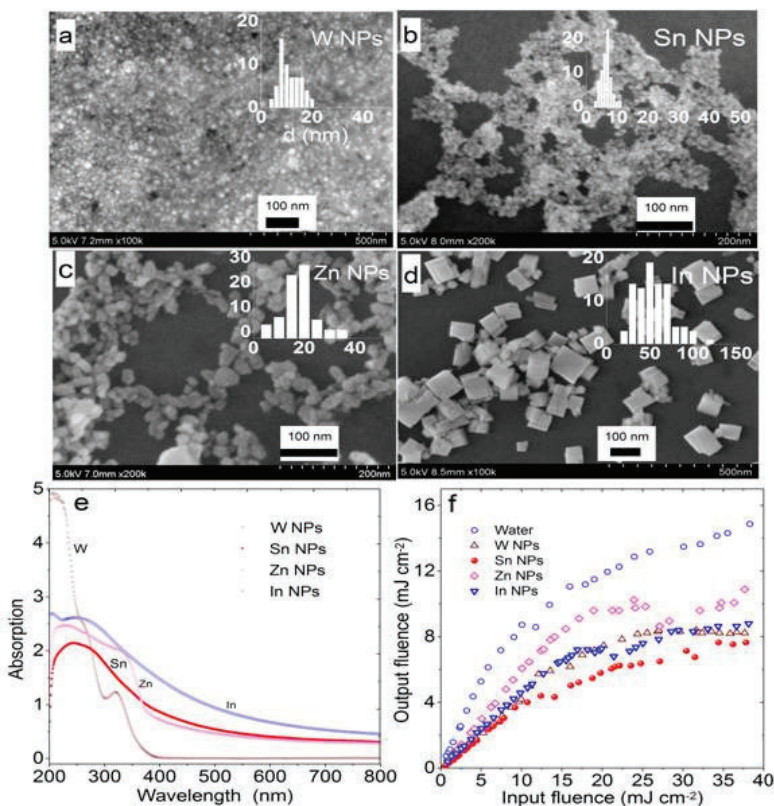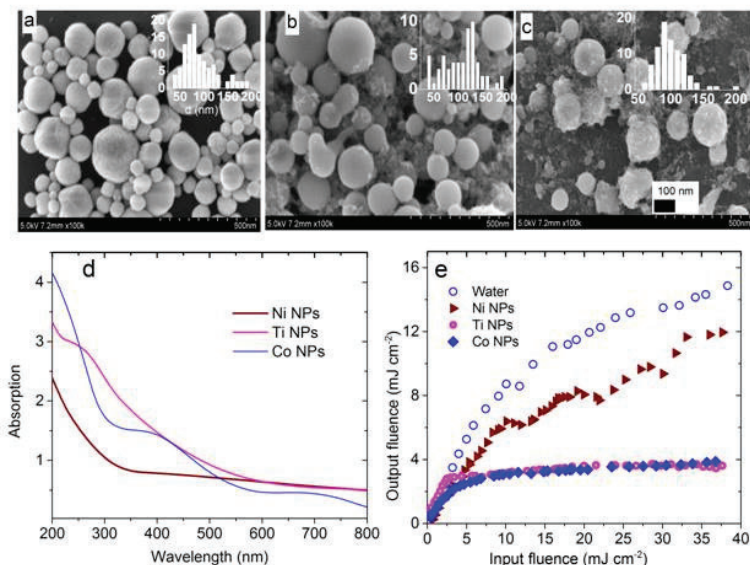

Fig. 3.16. SEM images and size distribution of (a) Ni NPs, (b) Ti NPs, (c) Co NPs. (d) UV absorption spectra, (e) optical limiting curves for these NPs suspensions. Reproduced from [11] with permission from Elsevier.

Figures 3.16a – 3.16c shows the SEM images and size distributions of the Ni, Ti, and Co NPs, the corresponding size distribution of lied between 30-200, 30-250, and 50-200 nm ranges at the mean size of 75, 125 and 90 nm, respectively. Figure 3.16e shows the results of OL properties of Ni, Ti, and Co NPs. Ti and Co NPs in water show high OL limiting properties compared to Ni NPs. The transmittance of Ni NPs suspension remained unchanged up to the input fluence of 10 mJ cm^{-2}. Then the transmittance decreased upon the increase of input fluence above the OL threshold. This observation led to the conclusion that, at the higher input fluence or intensity, the NPs suspension exhibits 2PA. Similar to the Ni NPs, Co NPs possess 2PA, whereas Ti NPs show SA in deionised water at a lower fluence of 800 nm pulses. However, the Ti NPs show comparatively higher OL property compared to Ni NPs and similar response with the Co NPs. The OL thresholds for Ni, Ti, and Co NPs in water are 10, 7.6, and 8

mJ cm^{-2} respectively. Ti and Co NPs in water show higher nonlinearity compared to Ni NPs.

3.3.3. Characterization and optical limiting in CsPbBr$_3$, and CsPbI$_2$Br perovskite nanocrystals

Figures 3.17a and 3.17b show the SEM images, while Fig. 3.17c shows the UV-visible absorption spectra of CsPbI$_2$Br and CsPbBr$_3$ perovskite nanocrystals. The rise in the absorption initiated in the case of CsPbI$_2$Br and CsPbBr$_3$ is 650 nm and 530 nm, respectively. These perovskite nanocrystals possess the cubic shape, CsPbI$_2$Br having the smaller size compared to CsPbBr$_3$ is shown in Fig. 3.17(a,b). The OL behaviour of perovskites nanocrystals is high compared to pure toluene (Fig. 3.16d, open triangles). However, QDs (Ag$_2$S QDs, Fig. 3.14h) have higher OL properties compared to perovskite nanocrystals (Fig. 3.17d). The OL$_T$ of Ag$_2$S QDs is 10.2 mJ cm^{-2}. CsPbI$_2$Br and CsPbBr$_3$ perovskites have 6.2 and 13.2 mJ cm^{-2} thresholds, respectively.

It was observed that, under higher laser fluence, CsPbBr$_3$ has the highest value of OL$_T$, even though it has a higher volume of nanocrystals. OL in the case of CsPbI$_2$Br shows conventional behavior compared to CsPbBr$_3$. Up to laser fluence of 12.5 mJ cm^{-2}, the OL curve of CsPbBr$_3$ is similar to CsPbI$_2$Br. Beyond 12.5 mJ cm^{-2}, the effect of saturation of 2PA was observed in the case of CsPbBr$_3$. However, under high laser fluence CsPbBr$_3$ shows high OL behaviour. The 2PA in metal NPs, Ag$_2$S QDs, and perovskites is known to be accompanied by the formation of free carriers, which also contribute to the nonlinear character of light propagation in these media. The interaction of the propagating radiation with these newly formed charge carriers can result in self-defocusing. One should distinguish the third-order nonlinearities caused by cumulative processes of absorption and free-carriers generation from those caused by electronic processes.

The perfect OL materials should have a high transmission for low energies of radiation and limited transmission for higher energies. Since the optical limiters are based mainly on two effects, 2PA and RSA, the real conditions of their application become the determining factor. The 2PA is a function of the radiation intensity, while the RSA depends on the energy density of radiation. Thus, if one needs to limit the femtosecond, as well as the picosecond, radiation, the 2PA is preferable and, conversely, materials exhibiting the RSA will be more efficient if one needs to limit longer pulses i.e. nanosecond to microsecond radiation.
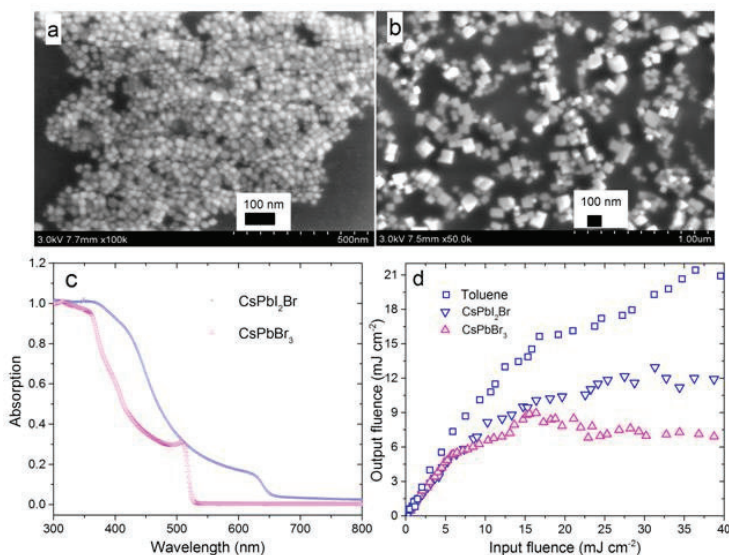
Fig. 3.17. SEM images of (a) CsPbI₂Br (b) CsPbBr₃. (c) UV absorption spectra, and (d) optical limiting in CsPbBr₃ (upper open triangles) and CsPbI₂Br (lower open triangles) perovskites and pure toluene (open squares) Reproduced from [11] with permission from Elsevier.

References to Chapter 3

[1]   M. D. Sonntag, J. M. Klingsporn, A. B. Zrimsek, B. Sharma, L. K. Ruvuna, R. P. Van Duyne, Molecular plasmonics for nanoscale spectroscopy, Chem. Soc. Rev. 43 (4) (2014) 1230-1247.

[2]   J. R. Lombardi, R. L. Birke, A unified view of surface-enhanced Raman scattering, Accounts Chem. Res. 42 (6) (2009) 734-742.

[3]   X. X. Han, W. Ji, B. Zhao, Y. Ozaki, Semiconductor-enhanced Raman scattering: active nanomaterials and applications, Nanoscale 9 (15) (2017) 4847-4861.

[4]   C. P. Leon, L. Kador, B. Peng, M. Thelakkat, Characterization of the adsorption of Ru-bpy dyes on mesoporous TiO₂ films with UV-Vis, Raman, and FTIR spectroscopies, J. Phys. Chem. B 110 (17) (2006) 8723-8730.

[5]   Z. Yu, W. Yu, J. Xing, R. A. Ganeev, W. Xin, J. Cheng, C. Guo, Charge transfer effects on resonance-enhanced Raman scattering for molecules adsorbed on single crystalline perovskite, ACS Photonics 5 (5) (2018) 1619-1627.

[6]   J. Xing, X. Zheng, Z. Yu, Y. Lei, L. Hou, Y. Zou, C. Zhao, B. Wang, H. Yu, D. Pan, Y. Zhai, J. Cheng, D. Zhou, S. Qu, J. Yang, R. A. Ganeev, W. Yu, C.

Guo, Dramatically enhanced photoluminescence from femtosecond laser induced micro-/nanostructures on MAPbBr3 single crystal surface, Adv. Optical Mater. 6 (20) (2018) 1800411.

[7]   C. Wagner, Beitrag zur theorie des anlaufvorgangs, Zeitschrift Für Physikalische Chemie 21B (1) (1933) 25-29.

[8]   A. B. Wong, M. L. Lai, S. W. Eaton, Y. Yu, E. Lin, L. Dou, A. Fu, P. D. Yang, Core–shell CdS–Cu_2S nanorod array solar cells, Nano Lett. 15 (8) (2015) 5519-5524.

[9]   K. Zhang, R.A. Ganeev, G.S. Boltaev, P. V. Redkin, C. Guo, Effect of different hardness and melting point of the metallic surfaces on the structural and optical properties of synthesized nanoparticles, Mater. Res. Express 6 (4) (2019) 045027.

[10] G.S. Boltaev, R.A. Ganeev, P.S. Krishnendu, S.K. Maurya, P. V. Redkin, K.S. Rao, K. Zhang, C. Guo, Strong third-order optical nonlinearities of Ag nanoparticles synthesized by laser ablation of bulk silver in water and air, Appl. Phys. A 124 (2018) 766.

[11] K. S. Rao, R. A. Ganeev, K. Zhang, Y. Fu, G. S. Boltaev, S. K. Maurya, C. Guo, Comparative analysis of optical limiting effect in metal nanoparticles and perovskites nanocrystals, Opt. Mater. 92 (2) (2019) 366-372.

[12] G.S. Boltaev, D. J. Fu, B. R. Sobirov, M. S. Smirnov, O. V. Ovchinnikov, A. I. Zvyagin, R. A. Ganeev, Optical limiting, nonlinear refraction and nonlinear absorption of the associates of $Cd_{0.5}Zn_{0.5}S$ quantum dots and dyes, Opt. Express. 26 (11) (2018) 13865–13875.

[13] S.I. Dolgaev, A. V Simakin, V. V Voronov, G.A. Shafeev, F. Bozon-Verduraz, Nanoparticles produced by laser ablation of solids in liquid environment, Appl. Surf. Sci. 186 (1-4) (2002) 546–551.

[14] T. Isobe, S.Y. Park, R.A. Weeks, R.A. Zuhr, The optical and magnetic properties of Ni^+-implanted silica, J. Non. Cryst. Solids. 189 (1-2) (1995) 173–180.

[15] H. Amekura, H. Kitazawa, N. Umeda, Y. Takeda, N. Kishimoto, Nickel nanoparticles in silica glass fabricated by 60 keV negative-ion implantation, Nucl. Instruments Methods Phys. Res. B 222 (1-2) (2004) 114–122.

CHAPTER 4

LASER- AND CHEMICALLY-SYNTHESIZED NANOPARTICLES

In this chapter, we discuss the results of systematic studies of the ablation-produced Ag nanoparticles prepared by 5 ns, 200 ps, and 60 fs pulses at the wavelengths of 1064 and 800 nm. The analysis of optical limiting in Ag nanoparticle suspension induced by different nonlinear optical processes is presented. We discuss the results of nonlinear refraction and nonlinear absorption studies using different wavelengths and pulse durations of laser radiation. We analyze the calculations of laser ablation of bulk Ag in liquid demonstrating nanoparticles formation. We also discuss the ablation of titanium and cobalt using picosecond laser pulses and the formation of Ti and Co nanoparticles in three liquids. The results of measurements of the nonlinear refractive indices, nonlinear absorption coefficients, and saturated intensities of these nanoparticles are analyzed. We analyze the impact of the size of Ag nanoparticles on the saturable absorption and two-photon absorption using femtosecond pulses at 400 nm and 800 nm. The studies of ultrafast dynamics of silver nanoparticles are discussed. We analyze the observation of the presence of acoustic vibration in Ag nanoparticles upon excitation with the resonant wavelength. Finally, we analyze the ability of Al nanoparticles to modify the wettability of surfaces and the nonlinear optical properties of surfaces, suspensions, and plasmas. We analyze the variations of wettability of the glass surfaces under the deposition of nanoparticles produced during laser ablation of aluminium in water, as well as during direct deposition of laser-generated nanoparticles and ablation debris on the substrates in a vacuum. The nonlinearities of the Al-based nanoparticles produced in water by nano-, pico-, and femtosecond pulses are determined.

4.1. Strong third-order optical nonlinearities of Ag nanoparticles synthesized by laser ablation of bulk silver in water and air

Silver nanoparticles took special attention among numerous small-sized species due to their use in imaging, biosensors, photovoltaic devices, solar cells, light-emitting devices, catalysis, etc. Silver nanoparticles (Ag NPs) have unique optical, electrical, and thermal properties and are already found applications being incorporated into products that range from photovoltaics to biological and chemical sensors. Examples include conductive inks, pastes, and fillers which utilize Ag NPs for their high electrical conductivity, stability, and low sintering temperatures. Additional applications include molecular diagnostics and photonic devices, which take advantage of the novel optical properties of these nanomaterials. Ag NPs are extraordinarily efficient at absorbing and scattering light and, unlike many dyes and pigments, have a colour that depends upon the size and the shape of the particle. The strong interaction of the Ag NPs with light occurs because the conduction electrons on the metal surface undergo a collective oscillation when excited by light at specific wavelengths. The advantages of Ag NPs include monodisperse distribution in the surrounding environment without agglomeration and aggregation, comprehensive characterization including TEM and UV-Vis, good stability, and long lifetime. A unique property of spherical Ag NPs is that their surface plasmon resonance (SPR) can be tuned from 400 nm to 530 nm by changing the particle size and the local refractive index near the particle surface. Even larger shifts of resonance peak towards the IR region can be achieved by producing silver nanoparticles with rod or plate shapes.

Different physical and chemical techniques are used for the preparation of metallic NPs with variable morphology and sizes. Among them, laser ablation of bulk material has been proven to be a simple method for the synthesis of spherical Ag NPs in various liquids. In many cases, distilled water is used during the laser ablation of silver. The preparation of NPs in various solutions has many applications. For example, Ag NPs prepared during ablation in water are useful for surface-enhanced Raman scattering spectroscopy [1]. Preparation of colloidal Ag NPs in aqueous gelatine solution using nanosecond pulses of Nd:YAG laser at the wavelength of 532 nm was reported in Ref. [2]. They have shown the influence of the pulse repetition rate on the morphology and optical properties of samples. Synthesis of Ag NPs in ethanol by laser ablation using the photoacoustic pulsed technique was reported in Ref. [3]. The application of the

photoacoustic technique allowed controlling the production rate per laser pulse, and the concentration of synthesized Ag NPs.

Modification of Ag NPs size distribution by laser irradiation of their water suspensions was reported in Ref. [4]. The change of the nanoparticles' characteristics caused by variable laser fluence and duration of irradiation was observed. A considerable narrowing (by a factor of three) of the SPR bandwidth was achieved, which is evidence of narrowing of the particles size distribution. Time-dependent preparation of gelatine-stabilized Ag NPs was demonstrated in Ref. [5]. The mean diameter of Ag NPs decreased with increasing the ablation time of the silver target. Ag NPs with sizes of 8 nm have been synthesized in ethanol [6]. The SPR of these NPs has shown maximum absorption at 422 nm.

The third-order optical nonlinearity, which is responsible for nonlinear refraction and nonlinear absorption of Ag NPs in aqueous solutions, is analyzed in Ref. [7]. They have shown the dependence of the nonlinear response on the nanoparticles' filling factor. The conventional z-scan technique was employed, using 80 fs laser pulses at 800 nm, at the regimes of high and low pulse repetition rate. The thermo-optic nonlinear response of silver colloids containing Ag NPs of different sizes was reported in Ref. [8]. The colloidal nanoparticles were synthesized by laser ablation of bulk Ag in acetone using nanosecond pulses. The self-defocusing was the main process at the lowest power of laser radiation. An increase in the concentration of nanoparticles in acetone led to an increase in the nonlinear refraction index, while the threshold power of optical limiting (OL) was decreased. The thermal-induced self-defocusing and Kerr-induced self-focusing in the Ag NP suspension prepared by laser ablation were investigated using femtosecond and nanosecond laser pulses at the wavelengths of 397.5, 532, and 795 nm [9]. The thermal-induced self-defocusing dominated at a high pulse repetition rate as well as in the case of nanosecond probe pulses. In the case of low pulse repetition rate, the self-focusing and saturable absorption (SA) of picosecond and femtosecond pulses were observed in these colloidal solutions. The SA and reverse saturable absorption (RSA) influence the transient absorption spectroscopy of Ag NPs. These processes play an important role while analyzing the properties of synthesized NPs in different spectral ranges [10].

Another nonlinear process which actively pursued using different NPs is the frequency conversion of strong laser field in the plasmas containing such species. The low-order nonlinearities of NPs, which are responsible for third harmonic generation in laser-induced plasmas (LIP), were studied in Ref. [11]. The LIPs are also considered as the attractive nonlinear media

for conversion of the frequency of ultrashort infrared laser pulses towards the ultraviolet and extreme ultraviolet ranges [12]. The advantages of using *in situ* produced Ag NPs for high-order harmonic generation (HHG) due to the large nonlinear optical response of Ag NPs in the field of femtosecond probe pulses were analyzed in Ref. [13]. The spectral characteristics of harmonics from nanoparticles produced *in situ* were compared with the HHG from atomic plasma and with the HHG from preformed nanoparticle-containing plasma.

Meanwhile, no systematic studies which combine the analysis of nonlinear absorption/refraction and lowest order harmonic generation in the same nanoparticle medium were reported so far. Each of the above-mentioned studies was focused on the particular properties of Ag NPs related to different components of their third-order nonlinear susceptibilities. Particularly, nobody analyzed in-depth the correlation between different components of those susceptibilities. Here we discuss those groups of studies to demonstrate the fact that exceptionally strong nonlinearities (particularly, nonlinear absorption) out of the SPRs of nanoparticles strongly correlate with highly efficient third harmonic generation in Ag NPs. These studies show the way to explain the earlier reported exceptionally strong HHG conversion efficiency in Ag NP plasma by the specific properties of those particles related with involvement of their plasmonic properties in the enhancement of nonlinear optical response in the extreme ultraviolet range.

In this section, we analyze the results of the systematic studies of the ablation-produced Ag NPs prepared by 5 ns, 200 ps, and 60 fs pulses at the wavelengths of 1064 and 800 nm [14]. We discuss the OL in Ag NP suspension induced by two-photon absorption (2PA) and RSA at the wavelengths of 800 and 355 nm, respectively. We analyze the results of nonlinear refraction and nonlinear absorption studies using different wavelengths and pulse durations of laser radiation. Third harmonic generation (THG) in the plasmas containing Ag NPs is analyzed. We discuss the calculations of laser ablation of bulk Ag in liquid demonstrating NPs formation. We also discuss the advantages in the application of small (8 nm) Ag NPs for low- and high-order harmonic generation of ultrashort laser pulses.

4.1.1. Experimental arrangements for ablation and synthesis of Ag NPs in water and characterization of their nonlinear optical parameters

The Ag NPs were synthesized by ablation of bulk silver in water using a nanosecond laser. Laser radiation (wavelength: 1064 nm, pulse duration: 5 ns, pulse repetition rate: 10 Hz, pulse energy: 40 mJ) was focused by a 100 mm focal length lens on the surface of silver target immersed in deionised water [Fig. 4.1(a)]. The target sizes were $5\times5\times2$ mm^3. The purity of the bulk silver target was 99.9%. The silver target was moved by a two-coordinate translating stage during laser ablation. The ablation was carried out for 30 min. The colour of the suspension was changed during laser ablation until became a yellow shade.

The nonlinear optical parameters of Ag NP suspension were investigated using the z-scan technique described in previous chapters. Different conditions were used for comparative analysis of the nonlinear optical parameters of suspensions. The nonlinear optical studies of Ag NP suspensions were carried out using nanosecond and femtosecond laser pulses at four different wavelengths (1064, 800, 400, and 355 nm). The closed-aperture (CA) and the open-aperture (OA) z-scan schemes were used for the nonlinear optical characterization of samples. The radiation of the Nd:YAG laser (λ=1064 nm, τ=5 ns) or its third harmonic (λ=355 nm) was focused by a 200 mm focal length lens [Fig. 4.1(b)]. The beam waist diameters were 81 and 39 μm (at $1/e^2$ level of the spatial distribution at the focal plane) in the case of fundamental and third harmonic radiation respectively. The energy of laser radiation was varied using neutral filters. The propagated pulses were detected by a large aperture photodiode.

The 2-mm-thick fused silica cell containing Ag NP suspension was moved along the z-axis through the focal point using a translating stage. Attention was given to prevent the optical breakdown of the studied medium. The intensities of the optical breakdown of suspensions in the case of nanosecond laser pulses were measured to be 6.4×10^9 and 1×10^9 W cm^{-2} at the wavelengths of fundamental and third harmonic radiation respectively, while the maximally used intensities of probe radiation in the experiments did not exceed 1.6×10^9 (λ=1064 nm) and 6×10^8 W cm^{-2} (λ=355 nm). Ti:sapphire laser provided 60 fs, 800 nm or 210 ps, 800 nm pulses at 1 kHz pulse repetition rate. The intensities of used femtosecond pulses (τ=60 fs) did not exceed 2×10^{10} (λ=800 nm) and 1.6×10^{10} W cm^{-2} (λ=400 nm). This z-scan scheme was calibrated using the known values of the nonlinear optical parameters of 1-mm-thick fused silica slides. The OL study was carried out by varying the energy of the pulses propagating

through the quartz cell containing Ag NP suspension, which was installed in the focal plane. The stability of morphology was controlled by analyzing the position of SPR for three months. Additionally, TEM and SEM studies confirmed the conclusion about the good stability of synthesized NPs.
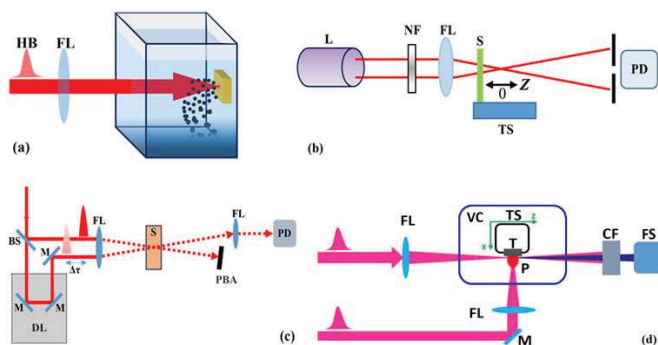
Fig. 4.1 (a) Experimental setup for laser ablation in liquid. HB: heating beam, FL: focusing lens. (b) Experimental setup for z-scan studies. L: Q-smart 850 nanosecond laser or Ti:sapphire femtosecond laser, NF: neutral filters, FL: focusing lens, S: sample, TS: translating stage, PD: photodiode. (c) Experimental setup for pump-probe studies. BS: beam splitter, M: mirrors, S: sample, FL: focusing lenses, PD: photodiode, DL: delay line, PBA: pump beam absorber. (d) Experimental scheme for third harmonic generation in laser plasma. FL: focusing lenses, M: mirror, VC: vacuum chamber, TS: translating stage, T: target, P: plasma, CF: colour filters, FS: fibre spectrometer (USB2000). Reproduced from [14] with permission from Springer.

A noncollinear degenerate pump-probe technique was applied to study the transient absorption (TA) in Ag NPs. Laser radiation (λ=400 nm, τ=60 fs) was split into two parts using a beam splitter. One part was used as pump radiation and another part was used as probe radiation, which was passed through the delay line to control the time separation between pump and probe pulses during their propagation through Ag NP suspension [Fig. 4.1(c)]. Relative intensities and beam diameters of pump and probe pulses were adjusted to be ~ 15:1 and 1:2. This study was performed at the wavelength of 400 nm obtained by doubling the frequency of fundamental radiation (800 nm) using barium borate (BBO) crystal. The pump pulse energy of 0.22 μJ was used for the TA study.

In the case of THG studies the laser radiation (λ=800 nm, τ=60 fs) was focused by a 400 mm focal length lens on the LIP [Fig. 4.1(d)]. The beam waist radius of the focused radiation was 38 μm. The spectral characteristics of third harmonic radiation (λ=266 nm) were analyzed by a spectrometer. To create a plasma plume, a pulse was split from the Ti:sapphire laser by a beam splitter before the compression of the fundamental uncompressed pulse. The heating pulse duration was 210 ps. This radiation was focused on the target to heat it and produce LIP in the air conditions [Fig. 4.1(d)]. The area of ablation was adjusted to be approximately 0.25 mm. A delay between fundamental and heating pulses was adjusted to be 38 ns. Different pressures of air were also used by a variable pumping vacuum chamber.

4.1.2. Morphology and nonlinear optical characterization of silver ablated in water

TEM and SEM images and histograms of the Ag NPs prepared by ablation of bulk silver using pulses of different duration are presented in Figs. 4.2(a), 4.2(b) and 4.2(c). The linear absorption spectra of Ag NP suspensions [Fig. 4.2(d)] were measured using a spectrophotometer (Agilent Technologies). The SPRs of Ag NPs in two cases of ablation were observed at 402 nm. In the case of picosecond ablation, the linear absorption coefficient of Ag NPs at λ>450 nm was larger compared to the case of nanosecond ablation. The sizes of NPs were measured to be 8 and 50 nm, by using the 5 ns and 210 ps pulses for laser ablation.

Optical limiting is the important aspect for the application of nanostructured materials in nonlinear optics and laser physics particularly to protect sensitive systems and eyes from high-power laser radiation. Earlier the optical limiting using Ag NPs was reported in Ref. [15]. It was shown that OL in these NPs in the field of nanosecond laser pulses at λ=532 nm is much stronger than in other materials such as C_{60} and chloroaluminum phthalocyanine. Below we analyze the OL using 800 nm, 60 fs, and 355 nm, 5 ns laser pulses, which propagated through the suspension of Ag NPs in deionised water. The suspension was obtained during the ablation of bulk silver using nanosecond laser pulses. This suspension was placed at the focal plane of a 400 mm focal length lens.
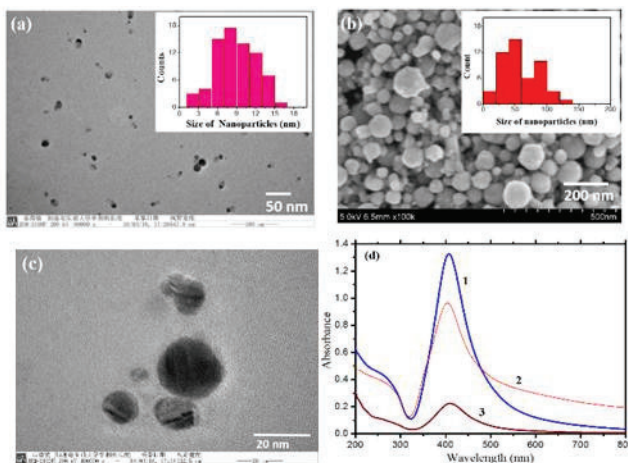
Fig. 4.2. (a) TEM image and histogram of size distribution of Ag NPs in the case of ablation in water using 1064 nm, 5 ns pulses, (b) SEM image and size distribution of Ag NPs ablated in water using 800 nm, 200 ps pulses, (c) TEM image of Ag NPs in the case of ablation in water using 800 nm, 60 fs pulses. (d) Absorption spectra of Ag NPs suspensions in case of ablation using (1) 1064 nm, 5 ns, (2) 800 nm, 200 ps and (3) 800 nm, 60 fs pulses. Reproduced from [14] with permission from Springer.

The linear dependence between input and output 800 nm, 60 fs pulses was maintained up to the input pulse energy of ~ 0.6 μJ [Fig. 4.3(a), filled triangles]. Further growth of input pulse energy led to OL of propagated laser radiation due to 2PA. This process was maintained up to the energy of 800 nm pulses of ~ 2.0 μJ, which allowed stabilization of output energy at the level of 0.5 μJ along while using the 0.6 – 2.2 μJ energy range of input pulses. The OL in pure water was also studied in this energy range of propagated laser pulses. The slope of linear fitting for pure deionised water at small input pulse energies was equal to 1.0, while the slope of linear fitting of Ag NPs was equal to 0.7. The latter slope corresponded to the initial transmittance of the suspension containing Ag NPs in deionised water. In the case of water, the inclination of I_{out}/I_{in} from the linear dependence due to white light generation was observed [Fig. 4.3(a), empty circles].
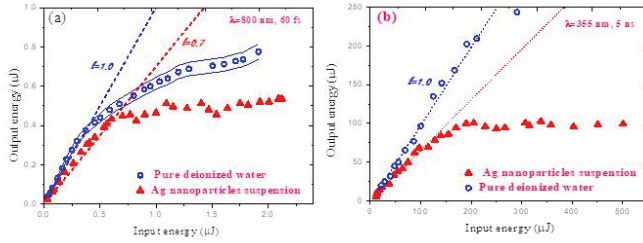
Fig. 4.3. Optical limiting in the aqueous suspension of Ag NPs (filled triangles) and pure water (empty circles) using (a) 60 fs, 800 nm, and (b) 5 ns, 355 nm probe pulses. Dotted lines show the linear dependences between output and input pulse energies at the lower energy ranges of input pulses. Reproduced from [14] with permission from Springer.

In the case of nanosecond laser pulses, RSA led to the OL of 355 nm laser radiation. This process was analyzed in the range of energies between 150 to 600 μJ [Fig. 4.3(b)]. One can see that Ag NP suspension demonstrated excellent OL properties in the case of nanosecond UV pulses. The observations of the optical limiting in silver nanoparticles suspension were attributed to 2PA and RSA at the wavelengths of 800 nm and 355 nm probe pulses, respectively. During these experiments, the OL was analyzed by either increasing or decreasing the energy of laser pulses. In these two cases, similarities with the same threshold energy for OL were observed.

The dependences of refractive indices and absorption coefficients of materials on the laser intensity are presented as

$$n=n_0+\gamma\times I \text{ and } \alpha=\alpha_0+\beta\times I. \tag{4.1}$$

Here n_0 is the linear refractive index, I is the intensity of laser beam, γ and β are the nonlinear refractive index and nonlinear absorption coefficient of media, and α_0 is the linear absorption coefficient. The determination of γ and β of materials can be accomplished using the analysis of z-scan curves. The z-scan curves in the cases of CA and OA schemes for the bulk silver ablated in deionised water using nanosecond and picosecond pulses are shown in Fig. 5. Circles and squares represent the experimental data and solid lines are the theoretical fits. In the case of the CA z-scan scheme, the normalized transmittance [$T(z)$] is related to the nonlinear refractive index by

$$T(z)=1+4\Delta\Phi_0 x/(x^2+1)(x^2+9). \tag{4.2}$$

Here $x=z/z_0$, $z_0=0.5kw_o^2$ is the Rayleigh length, $k = 2\pi/\lambda$ is the wave number, w_o is the beam waist radius of the focused beam and $\Delta\Phi_0$ is the phase change. The nonlinear refractive index is related to the phase change as $\gamma = \Delta\Phi_0/kL_{eff}I_0$, where $L_{eff}=[1-exp\ (-\alpha_0L)]/\alpha_0$ is the effective length of the nonlinear medium, I_0 is the intensity of laser beam at the focal plane of focusing lens, and L is the sample thickness. The normalized transmittance curves were fitted with the CA experimental data. In the case of OA z-scans, the photodetector measured the whole transmittance of propagated radiation. Figures 4.4(a)-4.4(d) show the 2PA-induced OA z-scans (empty circles). In that case, the normalized transmittance of laser pulses can be described by

$$T(z) \approx 1 - q_0/2\sqrt{2}. \tag{4.3}$$

Here, $q_0(z) = I_0\ \beta\ L_{eff}\ /[1 + z^2/(z_0)^2]$. Equation (13) was fitted with the OA data presented in Fig. 4.4.

The nonlinear optical parameters were studied in the field of nanosecond and femtosecond laser pulses. The thermal induced self-defocusing was observed in the case of 1064 nm, 5 ns probe pulses [Fig. 4.4(d), filled squares]. The reverse process was observed in the case of 800 nm, 60 fs pulses at 1 kHz repetition rate [Fig. 4.4(a-c), filled squares]. This regime of the interaction of femtosecond laser pulses with Ag NP suspension led to self-focusing, which is due to the electronic response of nanoparticles. The corresponding nonlinear optical parameters of 8 nm sizes Ag NPs in the case of 1064 nm, 5 ns probe laser pulses were: $\beta_{2PA}=3.0\times10^{-10}$ cm W^{-1}, and $\gamma=1.2\times10^{-14}$ cm^2 W^{-1}. At 800 nm, 60 fs probe pulses $\beta_{2PA}=1.0\times10^{-10}$ cm W^{-1}, and $\gamma=2.0\times10^{-15}$ cm^2 W^{-1}.

The Kerr-induced mechanism of self-defocusing for analysis of colloidal silver in the field of picosecond pulses has been considered in Ref. [16]. The thermal-induced effects can dominate over the fast Kerr-induced electronic contribution when the probe pulse duration becomes longer than the thermal conductivity relaxation time of small-sized Ag NPs. Hence, the duration of laser pulses is a critical parameter for the evaluation of third-order nonlinear response, especially nonlinear refraction.
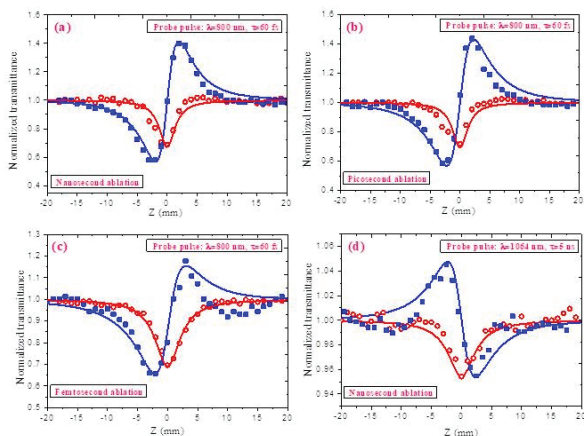
Fig. 4.4. OA and CA z-scans of Ag NP suspensions prepared by laser ablation of solid target using (a) 5 ns, 1064 nm, (b) 200 ps, 800 nm, and (c) 60 fs, 800 nm laser pulses. 60 fs, 800 nm pulses were used as a probe radiation in the (a), (b), and (c) cases. (d) OA and CA curves in the case of 5 ns, 1064 nm probe pulses. Ag NPs were prepared using 5 ns, 1064 nm pulses. Solid curves are the fits to experimental data (see text). Reproduced from [14] with permission from Springer.

The dependences of OA and CA normalized transmittances of Ag NP suspensions at the wavelength of 400 nm femtosecond laser pulses are shown in Fig. 4.5. The 2PA, SA, and RSA parameters of used suspension at this wavelength were calculated by fitting the experimental data with the Eq. (4.3) and the relation describing SA:

$$T_{SA}(z) = 1 + \frac{I_o}{I_{sat}(x^2+1)}, \tag{4.4}$$

where I_{sat} is the saturated intensity of the medium.
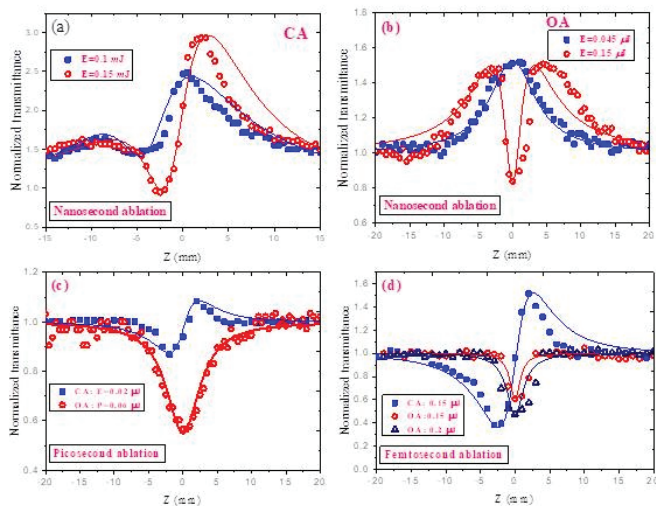
Fig. 4.5. Measurements using 400 nm, 60 fs pulses. (a) CA, and (b) OA z-scans of Ag NP suspension produced by 5 ns, 1064 nm pulses at different energies of probe pulses. (c) OA and CA z-scans of Ag NP suspension produced by 200 ps, 800 nm pulses. (d) OA and CA z-scans of Ag NP suspension produced by 60 fs, 800 nm pulses. Reproduced from [14] with permission from Springer.

Figure 4.5(a) demonstrates three processes: SA, RSA, and self-focusing in silver nanoparticles suspension at 400 nm, 60 fs probe pulses. These studies showed the dominance of the self-focusing process at higher energies of probe pulses. These data were fitted using the equation for three processes: SA, RSA, and self-focusing.

The results of similar OA studies of Ag NP suspension ablated by nanosecond radiation using 355 nm, 5 ns probe pulses are shown in Fig. 4.6(a). The corresponding nonlinear absorption coefficients of the studied samples at λ=355 nm were as: β_{SA}=-3×10^{-11} cm W^{-1}, and β_{RSA}=2×10^{-10} cm W^{-1}.
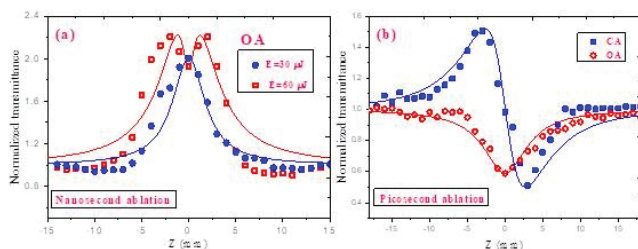
Fig. 4.6. (a) SA and RSA in Ag NP suspensions prepared by ablation using nanosecond pulses at different energies of 355 nm, 5 ns probe pulses: (filled circles) 30 μJ, and (empty squares) 60 μJ. (b) Self-defocusing and 2PA using 355 nm, 5 ns laser pulses (E=50 μJ) in the case of the suspension prepared by picosecond pulses. Reproduced from [14] with permission from Springer.

Figure 4.6(b) shows self-defocusing and 2PA of 355 nm laser radiation in Ag NP suspension ablated by picosecond laser pulses. The nonlinear optical parameters of the Ag NP suspensions measured at different experimental conditions are collected in Table 4.1. Notice that the concentration of Ag NPs in the case of femtosecond ablation was notably smaller than the concentration of the NPs produced during ablation using picosecond and nanosecond pulses due to less efficient ablation in the former case. Because of this, the nonlinear optical response of these species under the action of nanosecond probe pulses was at the threshold of registration.

Notice that actual values of the nonlinear susceptibilities of NPs are considerably larger than those of NP suspensions due to the small fraction of nanoparticles in the whole volume of solvent. A simple and well-established method for estimation of the nonlinear susceptibilities of nanoparticles is to divide the nonlinear susceptibility of the compound by the volume or weight part of NPs. In fact, the third-order nonlinear susceptibilities [$\chi^{(3)}$] of composites, and correspondingly, γ and β, are also depend on the local field factor as

$$\chi^{(3)} = p|f|^2 f^2 \chi_{NPs}^{(3)}. \tag{4.5}$$

Here $\chi_{NPs}^{(3)}$ is the third-order nonlinear susceptibility of NPs, f is the local field factor, and p is the filling factor (i.e., volume or weight part). The enhancement due to the local field factor is insignificant in the case of metal NPs far from their SPRs. In particular, the insignificant

enhancement of local field factor for Mn nanoparticles suspension was reported in Ref. [17]. In the case of Ag NPs $|f|^2$ is in the range of 0.1 and 1 in non-resonance conditions (i.e. at the wavelengths of 800, 1064, and 355 nm). In the resonance conditions, the local field factor increases and becomes equal to 3.6 at 400 nm. The f of small-sized Ag NPs at different wavelengths was estimated in Ref. [18] where the influence of the local field factor on the power of probe pulse, particle size, and photon energy around the SPR was analyzed.

Third-order nonlinear susceptibilities in media having nonlinear absorption and refractive index can be considered to be a complex quantity

$$\chi^{(3)} = Re\chi^{(3)} + iIm\chi^{(3)} \qquad (4.6)$$

where the imaginary part is related to the nonlinear absorption coefficient through

$$Im\chi^{(3)} = \frac{n^2 \varepsilon_0 c\lambda\beta}{2\pi} \qquad (4.7)$$

and the real part is related to γ through

$$Re\chi^{(3)} = 2n^2\varepsilon_0 c\gamma \qquad (4.8)$$

Here ε_0 is the permittivity of free space. For the presentation of $\chi^{(3)}$ in esu units, the relation $\chi^{(3)}[\text{esu units}] = (9 \times 10^8/4\pi)\chi^{(3)}[\text{SI units}]$ was used. $\chi^{(3)}$ of NP suspensions were calculated and included these results in Table 4.1.

It was reported in [19] that the nonlinear refraction index in larger-sized NPs is higher than in small NPs. The authors of this paper have also shown that the nonlinear refractive index is larger for 17 nm Ag NPs with regard to 13 nm Ag NPs. Switching from SA at lower intensities to RSA at higher intensities is explained through the transitions of conduction band electrons to higher excited states. In the discussed case, the switching of SA to RSA and self-focusing was observed at the highest used intensities of 400 nm, 60 fs laser pulses.

The parameters shown in Table 4.1 are attributed to the suspensions of Ag NPs. The estimates show that the volume fraction of NPs in suspensions was in the range of 10^{-3}. The values of γ and β of Ag NPs with 8 nm sizes can be multiplied by a factor of 1.0×10^5 for 1064 nm (i.e. far from SPR) and 11.0 for 400 nm pulses (i.e. in the resonance conditions) to determine these parameters attributed to Ag NPs taking into account the f

defined from Ref. [18]. In particular, β of suspension measured by 1064 nm, 5 ns, and 400 nm, 60 fs probe pulses was 3.0×10^{-10} cm W^{-1} and 8.6×10^{-10} cm W^{-1}. One can estimate β of NPs at these conditions to be 3.0×10^{-5} cm W^{-1}, and 9.4×10^{-9} cm W^{-1} respectively.

Table 4.1. Nonlinear optical parameters of Ag NP suspensions. Reproduced from [14] with permission from Springer.

		Ag NPs (8 nm)	Ag NPs (50 nm)	Ag NPs (15 nm)
		Parameters of heating pulses		
		λ=1064 nm, τ=5 ns, E=40 mJ	λ=800 nm, τ=200 ps, E=0.56 µJ	λ=800 nm, τ=60 fs, P=0.96 µJ
800 nm, 60 fs	β (cm^2 W^{-1})	2.0×10^{-15}	3.4×10^{-15}	1.9×10^{-15}
	β_{2PA} (cm W^{-1})	1.0×10^{-10}	0.9×10^{-10}	0.9×10^{-10}
	$\chi^{(3)}$(esu units)	1.8×10^{-9}	2.6×10^{-9}	1.6×10^{-9}
400 nm, 60 fs	γ (cm^2 W^{-1})	2.1×10^{-15}	1.5×10^{-15}	3.2×10^{-15}
	β (cm W^{-1})	RSA: $8.6.\times10^{-10}$	RSA: 5.5×10^{-10}	2PA: 5.5×10^{-10}
	β_{SA} (cm W^{-1})	-1.9×10^{-10}	-	-
	$\chi^{(3)}$(esu units)	3.6×10^{-9}	2.8×10^{-9}	3.3×10^{-9}
1064 nm, 5 ns	γ (cm^2 W^{-1})	-1.2×10^{-14}	-	-
	β_{2PA} (cm W^{-1})	3.0×10^{-10}	-	-
	$\chi^{(3)}$(esu units)	0.6×10^{-9}	-	-
355 nm, 5 ns	γ (cm^2 W^{-1})	-	-2.5×10^{-15}	-
	β_{RSA} (cm W^{-1})	2.0×10^{-10}	9.0×10^{-10}	-
	β_{SA} (cm W^{-1})	-3.0×10^{-11}	-	-
	$\chi^{(3)}$(esu units)	-0.2×10^{-9}	0.8×10^{-9}	-

During these studies, the 2PA cross-section of Ag NPs was calculated. The β_{2PA} values of Ag NPs were used for the determination of the 2PA cross-section (σ_{2PA}) using the following relation

$$\sigma_{2PA}=(10^3\times h\nu\times\beta_{2PA})/N_A V \tag{4.9}$$

where h is Planck's constant, v is the frequency of light, N_A is the Avogadro's number, and V is the volume fraction of nanoparticles. The value of the 2PA cross-section for the 2PA absorption coefficient of the Ag NPs at 800 nm, 60 fs probe pulses was calculated to be 3.6×10^{-47} cm^4 s/photon.

4.1.3. Measurements of transient absorption and third harmonic generation in laser-produced plasmas

Figure 4.7 shows the pump-probe data for 8 nm Ag NPs prepared by ablation using nanosecond pulses in deionised water. The TA curve for Ag NPs in water was fitted with a single exponential fit (solid curve). The profile of the pump-probe signal of Ag NPs in deionised water indicates the process of photo-bleaching due to the resonant excitation at 400 nm [see also Fig. 4.5(b), filled squares]. The lifetime of excited plasmon for Ag NPs at 400 nm was measured to be 2.5 ps, which can be assigned to the electron-phonon relaxation time. There was no similar response in the case of 50 nm Ag NPs at the wavelength of 400 nm. This behaviour could be explained by the size dependence and the nonlinear optical response of electron-phonon interaction dynamics of the Ag NPs.
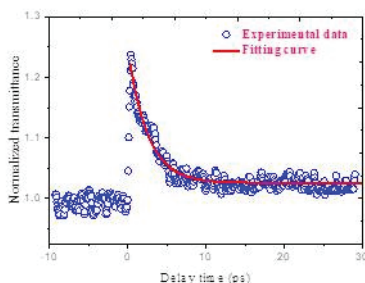
Fig. 4.7. Pump-probe measurements of Ag NP suspension at the wavelength of 400 nm using 60 fs laser pulses. Reproduced from [14] with permission from Springer.

For understanding the dynamics of electron relaxation in excited Ag NPs at resonance conditions the z-scan and pump-probe data were used. One can determine the cross-section of bleaching of the Ag NPs by equation [20]:

$$\sigma_{12} = h\nu/(2I_{sat} \times t_{12}) \qquad\qquad (4.10)$$

where σ_{12} is the absorption cross-section of Ag NPs and t_{12} is the relaxation time of electron-phonon interaction. Using this equation and values of saturation intensities $I_{sat}=6.3\times10^8$ W cm^{-2} at 355 nm, 5 ns, and $I_{sat}=2.4\times10^{10}$ W cm^{-2} at 400 nm, 60 fs probe pulses the excited state

absorption cross-sections at the wavelengths of 355 nm and 400 nm were calculated as 6.7×10^{-16} and 8×10^{-17} cm^2 respectively.
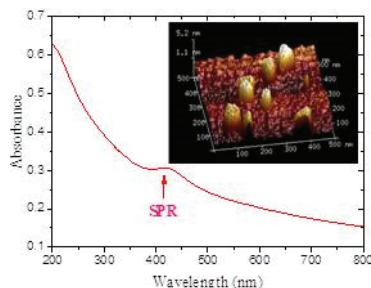
Fig. 4.8. Absorption spectra of the deposited silver on the surface of quartz substrate using 800 nm, 200 ps heating laser pulses. Inset: AFM of deposited films showing presence of Ag NPs on the deposited surfaces of quartz substrate. Reproduced from [14] with permission from Springer.

Prior to the THG studies the structural and optical properties of deposited thin films on the surfaces of quartz and silicon substrates were analyzed to prove the presence of Ag NPs during ablation of the silver target in the air. The absorption spectrum of the deposited thin films showed the appearance of SPR at 415 nm due to the formation of Ag NPs (Fig. 4.8). The atomic force microscopy (AFM) of the deposited silver films showed a broad distribution of NPs' sizes. Laser ablation facilitates the condensation of metal atoms into clusters and rapid growth of the atomic clusters into nanoparticles with maximum sizes barely exceeding 10 nm. The NPs with large sizes at around 100 nm did not contribute to the low-order harmonic process. The velocity of nanoparticles depends on the mass and fluence of the heating beam. Only small clusters appear in the area of interaction at the moment of femtosecond pulse arrival (i.e. 38 ns from the beginning of ablation). Thus these species are responsible for harmonic generation in present conditions.

Some previous studies using the atomic plasmas produced on the surfaces of bulk silver target and the plasmas containing Ag NPs have shown relatively high conversion efficiency of harmonics generated in such media [21]. The usefulness in application Ag NPs for enhancement of HHG in the extreme ultraviolet range has also been demonstrated in Ref. [22].
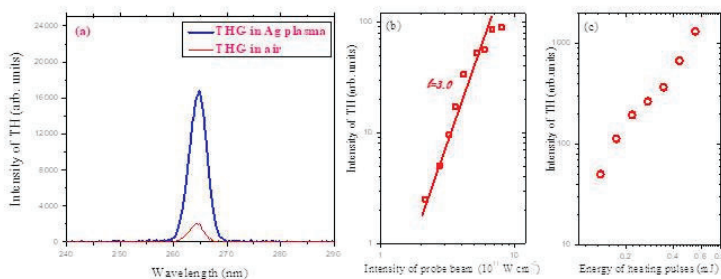
Fig. 4.9. (a) Spectra of the third harmonic generation in the plasma containing Ag NPs (thick curve) and in the air (thin curve). (b) Dependence of the intensity of TH on the intensity of femtosecond laser pulses in silver plasma. (c) Dependence of the intensity of TH on the energy of heating picosecond laser pulses. Reproduced from [14] with permission from Springer.

Figure 4.9 presents the spectra and the intensity of the third harmonic (TH) as a function of the probe and the heating pulse intensity in the plasma plumes containing Ag NPs. One can see a six-fold enhancement of TH efficiency in the case of air conditions compared with the THG in air. TH yield was also analyzed at the air pressure of 1.3 kPa. In that case, the 20× enhancement of TH yield from Ag plasma with regard to residual air was obtained. A slope of the fitting line in Fig. 4.9(b) corresponds to 3, which is the indication of the expected cubic dependence between fundamental and harmonic pulses in the case of THG. Figure 4.9(c) shows the dependence of TH yield on the heating pulse energy. No saturation of THG was observed at the highest used energy of heating picosecond pulses (0.5 mJ).

Figure 4.10(a) shows the dependence of the TH yield at different angles of rotation of the quarter-wave plate, which caused variation of the polarization of driving radiation from linear (at 0^0) to circular (at 45^0). A deviation from linear polarization led to a decrease of TH intensity, which is typical for low- and high-order harmonics. The application of circularly polarized laser pulses led to the complete disappearance of harmonic emission, as it should occur assuming the origin of the harmonic generation process.
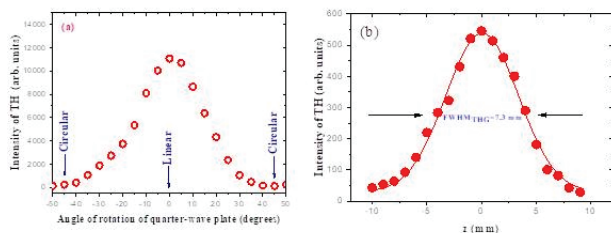
Fig. 4.10. (a) Dependence of TH intensity on the angle of rotation of the quarter-wave plate. (b) Dependence of THG on the position of plasma plume with regard to the focal plane of probe pulses. The intensity of laser beam in the focal plane was 1.2×10^{11} W cm^{-2}. Reproduced from [14] with permission from Springer.

Figure 4.10(b) shows the z-scan of THG performed for Ag plasma by changing the position of the focusing lens of the probe pulses. These measurements were carried out at 1.2×10^{11} W cm^{-2} intensity of probe pulses in the focal plane. Further increase of intensity of femtosecond pulses in the focal position led to the decrease of THG at z=0 position of plasma plumes. This behaviour can be explained by phase mismatch of interacting waves due to the growth of concentration of the electrons in the interaction zones.

The conversion towards 266 nm radiation in the case of plasma plume was notably stronger compared with THG in air. The THG conversion efficiencies in air and Ag NP plasmas were defined to be 1×10^{-3} and 4×10^{-3} in the case of 800 nm, 60 fs driving pulses. The value of conversion efficiency in the air was comparable with earlier reported studies carried out at similar conditions [23,24]. The TH enhancement was attributed to the involvement of small silver clusters in the harmonic generation.

4.2. Laser ablation-induced synthesis and nonlinear optical characterization of titanium and cobalt nanoparticles synthesized by laser ablation of bulk materials

Among numerous NPs the titanium (Ti) and cobalt (Co) species attracted interest due to their various potential applications. The titanium in its metallic form is not only strong and lightweight but also highly resistant to corrosion. Therefore, it is often used in aerospace and military applications. Ti NPs allow improvement of the radiation resistance. Ti NPs

are used in different industrial applications, disease diagnostics, medical imaging, and other fields [25]. They have high transparency in the visible range and high UV absorption. Co NPs can be used in medical sensors, coatings, plastics, nanofibers, nanowires, textiles, and high-performance magnetic recording materials. Cobalt oxide NPs can also be used in military applications due to their strong absorption of visible, infrared, and millimetre waves.

Earlier, researchers ablated the bulk Ti rods using nanosecond and femtosecond pulses to produce NPs [26]. The results of studies of various titanium-based NPs formation by laser ablation of Ti rods in a liquid environment comprising water, ethanol, 2-propanol, and n-hexane were also reported in Ref. [27]. They have shown the effect of laser fluence on NP characteristics by ablation using a 532 nm Nd: YAG nanosecond laser operating at 10 Hz. In particular, it has been demonstrated that mean particle size and the size distribution increase with growing laser intensity. Ti shows the presence of oxygen in its NPs, which comprised the combination of TiO and TiO_2. Previously, TiO_2 NPs have shown the reverse saturable absorption (RSA) at the wavelength of $\lambda=780$ nm [28], and the giant nonlinear optical response at $\lambda=1064$ nm related with two-photon absorption (2PA) [29]. The mixed two- and three-photon absorption in bulk rutile TiO_2 at $\lambda=800$ nm was observed using the open-aperture (OA) z-scan technique [30]. The formation of Co NPs has been earlier achieved with laser ablation using nanosecond pulses at 355, 532, and 1064 nm [31,32]. Despite those previous works, there have been no reports on the nonlinear absorption and refraction coefficients of Ti and Co NPs at 800 and 400 nm wavelengths measured using femtosecond pulses.

Both Ti and Co are transition metals from the fourth period. Elements in the same period show trends in atomic radius, ionization energy, electron affinity, and electronegativity. Moving left to right across a period, atomic radius usually decreases. This decrease in atomic radius also causes the ionization energy to increase when moving from left to right across a period. Ti and Co have comparable boiling (3287 and 2927 ^{0}C) and melting (1660 and 1495 ^{0}C) temperatures, while different densities (4.54 and 8.9 g/cm^3). Their main thermal properties are similar. Apart from the above-mentioned interest in Ti and Co NPs the search of peculiarities in the nonlinear optical response can give additional information about their structural properties.

In this section, we discuss the ablation of titanium and cobalt using picosecond laser pulses and the formation of Ti and Co NPs in three liquids [33]. Three solvents such as deionised water, toluene, and ethylene

glycol (EG) were chosen to create the NPs of Ti and Co and control their sizes and shapes. We analyze the observation of the fact that the size and shape of NPs vary in different surrounding liquids at similar laser ablation conditions. The results of measurements of the nonlinear refractive indices, nonlinear absorption coefficients, and saturated intensities of these NPs at the wavelengths of 800 nm and 400 nm (at a pulse duration of t=60 fs), as well as 355 nm (t=5 ns) are analyzed. We also discuss studies of optical limiting (OL) in the suspensions containing these NPs.
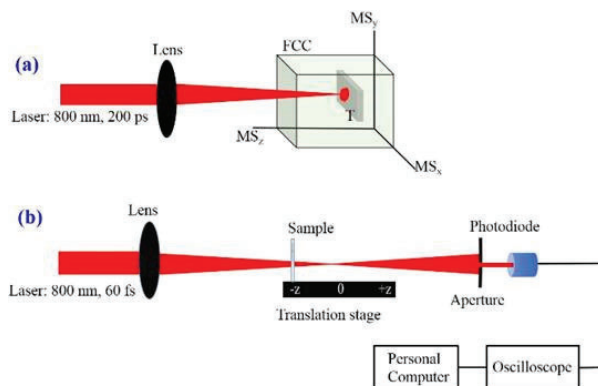
Fig. 4.11. (a) Schematic layout for ablation of titanium and cobalt in different liquids. Laser: (800 nm, 200 ps, 1 kHz), Lens: f=100 mm, FCC: fused silica cell, T: target metal, MS_{xyz}: moving stage. (b) z-scan scheme. Reproduced from [33] with permission from Springer.

The nanoparticles were formed via laser ablation of the Ti and Co sheets immersed in a liquid-containing fused silica cell. The experimental arrangement for laser ablation is shown in Fig. 4.11(a). The incident light was focused on the 1-mm-thick metal sheet using a 100 mm focal length spherical lens, while the 20 mm thick cell was moved along two directions (X and Y) at a velocity of 0.01 mm s^{-1}. The ablation was performed using uncompressed radiation of Ti: sapphire laser (200 ps, 800 nm) at 1 kHz repetition rate during 20 to 30 min.

Once the solution of NPs became prepared, the UV-visible absorption spectroscopy and scanning electron microscopy (SEM) were performed to characterize the suspensions. The UV and visible absorption spectra of NPs were measured using the spectrophotometer. The SEM studies were carried out using the scanning electron microscope (SEM).

Figure 4.11(b) shows the standard z-scan scheme, which was used in these studies and described in previous subsections. Ti: sapphire laser

provided 60 fs, 800 nm pulses at 1 kHz repetition rate. These pulses were focused by a 400-mm focal length spherical lens. The thickness of fused silica cells filled with NP suspensions was 2 mm.

The normalized transmittances of samples were analyzed using the standard fitting procedure to determine their nonlinear absorption coefficients (β) and nonlinear refractive indices (γ). Prior to z-scan measurements the probe beam was characterized using a CCD camera and confirmed that the beam profile in the focal area was close to Gaussian, which is a prerequisite for the analysis of the z-scan traces using the relations developed for this technique. The corresponding full widths of focused beam at half maximum and $1/e^2$ maximum of intensity distribution were measured to be 42 and 76 μm, respectively. For z-scan studies the 400 nm radiation from the same laser was used by converting 800 nm, 60 fs pulses to the second harmonic in the barium borate (BBO) crystal, as well as 355 nm, 5 ns pulses from Nd:YAG laser. For OL studies, the samples were kept at the focal area of laser beams and measured the transmitted energy as a function of input energy.

4.2.1. Ablation and characterization of samples

The ablation of bulk materials and formation of NPs in the surrounding media like liquids are the complex processes requiring the analysis of the size-dependent spectral properties of synthesized NPs. Ablation of materials by laser pulses can be considered as a several stage process with different relaxation times. Initially, laser energy is absorbed by electrons in the bulk target. This process is almost instantaneous as the only element governing it is the long-range Coulomb force of the laser field and the charged particles. Then the heated electrons give their energy to ions, which is a longer process involving the electron-phonon coupling of the material. This process is also relatively fast as compared to atom-atom collisions which redistribute the energy across the volume of the bulk target, melt it, and lead to actual material removal if the energy acquired by the particle is sufficient to leave the surface of the target. Certainly, it can happen that more atoms tend to split off together resulting in the direct removal of NPs from the surface. The next stage is the interaction of the ablated material with the laser pulses and the surrounding medium.

In general, interaction with the laser radiation follows the same stages and leads to further fragmentation of NPs. However, the particles have quite different sizes, so their spectral properties are altered greatly, and the destruction of smaller NPs can go slower. The effect of interaction with the surrounding dense medium is twofold. From one hand, the speed of the

particles is greatly reduced compared with ablation in air and vacuum, resulting in longer times of exposition to laser radiation. As a result of friction in the medium the temperature on the surface of ablated NPs increases. On the other hand, the NPs quickly transfer heat to the surrounding medium via heat conductivity, so the actual temperature dynamics may be complicated. Also, the agglomeration of NPs and deposition of particles on NPs can occur with much greater probability in the surrounding medium than in vacuum or air.
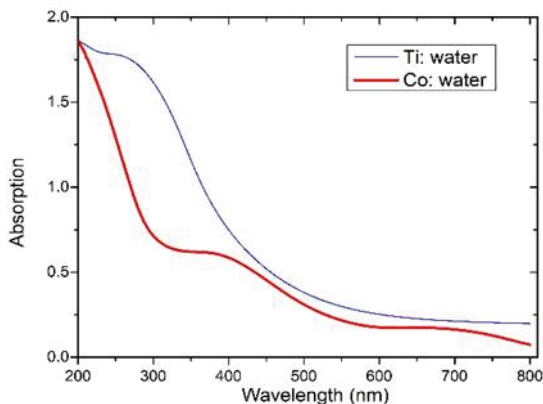
Fig. 4.12. UV-visible absorption spectra of Ti and Co NPs' suspensions. Reproduced from [33] with permission from Springer.

Ti NPs were synthesized by laser ablation of bulk material in water (H_2O), ethylene glycol (C_2H_2), and toluene (C_7H_8), whereas Co NPs were produced in water and toluene. Ti NPs produced in ethylene glycol (EG) and toluene solvents might contain carbon. Ablation in water led to varying the amount of oxygen incorporation and titanium oxides formation. Very stable and large size NPs were produced due to the high pressures and temperatures of the reaction conditions. After initial analysis, the solutions of NPs were stored in vials. The NPs were analyzed over a period of one month and showed stability with some minor fluctuations in sampling. There was no deviation in the composition. The NPs did not undergo further modification within this time. Some of the largest NPs precipitated and a faint deposit was visible on the bottom of the vials. UV absorption spectra and SEM analysis of the solution revealed that NPs became suspended in solutions without deposition and

aggregation. A similar procedure of NPs formation was maintained during bulk Co ablation.
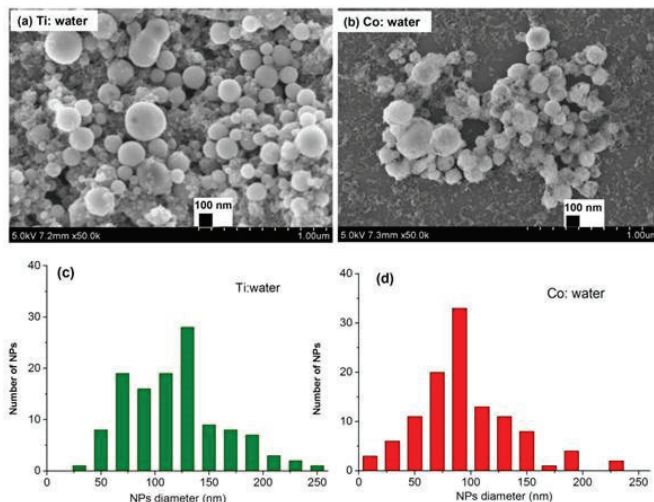
Fig. 4.13. (a, b) SEM images and (c, d) histograms of size distribution of the Ti (a,c) and Co (b,d) NPs synthesized during ablation in water. Reproduced from [33] with permission from Springer.

Figure 4.12 shows the UV-visible absorption spectra of Ti and Co NPs ablated in water. The Ti NPs show the SPR (Fig. 4.12, thin curve) at ~280 nm. However, the absorbance of Ti NPs suspension starts to increase at $\lambda \leq 500$ nm. Ti NPs have the absorption peak at 530 nm after being ablated by 355 nm, 150 ps pulses in water [34]. The Co NPs in water show some absorption peaks at 400 nm and 700 nm respectively (Fig. 4.12, thick curve). Earlier, it was shown that SPR for Co/C was red shifted to 424 nm due to the surface carbon layer [35]. From Mie theory, the plasmon resonance in Co is expected in the UV range. Notice that different studies report some contradicting results on the position of SPRs, which probably can be attributed to different methods of NPs formation.

Figure 4.13 shows the SEM images and size distributions of the Ti and Co NPs ablated in water using pulse energy of 550 μJ. The size distribution of Ti NPs in water lay between 30 and 250 nm at the mean size of 125 nm. The size distribution of Co NPs synthesized in water was centred at 90 nm. It is important to analyze the processes that determine the morphology of synthesized NPs to control the mean diameter and size distribution of the resulting particles by changing the solvent and pulse

energy. Particularly, the sizes of Ti and Co NPs synthesized in water were larger than those prepared in toluene and EG. The surface shape of spherical Ti and Co NPs in water was smooth. Water is a highly polar liquid, and the presence of oxygen leads to the formation of the oxides of Ti and Co NPs during laser ablation.

The liquid bubbles were produced during the ablation of Ti and Co sheets that indicated the vaporization of solvents. The superheated bubbles serve as reaction vessels during NP formation. Atomic and molecular ions most likely come from both the solvent and the Ti/Co during ablation, whereby ion-ion, ion-radical, and ion-molecule interactions take place to form new species. The solvent plays an important role in the variety of produced NPs.

Laser ablation is very efficient in the preparation of the NPs and strongly influences the SPRs compared to the chemical methods of NPs' formation. One should take into account the high oxidization of NPs when treating the role of solvent because oxide shell changes the effects of plasmon resonances' formation. Such oxide shells are difficult to be destroyed, so small core-shell NPs appear to be stable enough. Additionally, the decrease of geometrical cross-section due to fragmentation results in a decrease in equilibrium temperature. On the other hand, the melting temperature for smaller NPs is lower than that of the bulk targets and is shape-dependent, so the fragmentation or aggregation of such particles continues during further irradiation of NP-containing suspensions.

4.2.2. Nonlinear optical characterization of samples

OL of propagating radiation by metal NPs is attractive due to various applications. Previously, considerable efforts have been focused on the investigation of the relationship between the OL and nonlinear optical properties of NPs as well as their sizes and shapes. In the following subsections we will analyze how, in the case of nanosecond and femtosecond probe pulses, the Ti and Co NPs can exhibit intensity-dependent transformation from saturable absorption (SA) to RSA. Thus, such NPs may demonstrate strong OL properties in the case of both relatively long and short laser pulses.

In discussed studies, OL was analyzed using the 800 nm, 60 fs pulses propagating through the suspensions containing Ti and Co NPs in water. Below we discuss the OL data for Co NPs suspension, while similar behaviour was observed for Ti NPs suspension as well. The Co NPs suspension was placed close to the focal plane of the 400 mm focal length lens. The energy of 800 nm pulses was gradually increased and then the

output radiation, which propagated through the 2-mm-thick cell containing the NP suspension, was measured. The linear dependence between input and output pulses was maintained up to the input pulse energy of ~0.08 μJ [Fig. 4.14(a), filled triangles]. The corresponding laser intensity at which OL started to play an important role was 3×10^{10} W cm^{-2}. Further growth of input pulse energy led to the OL of the energy of propagated laser radiation.
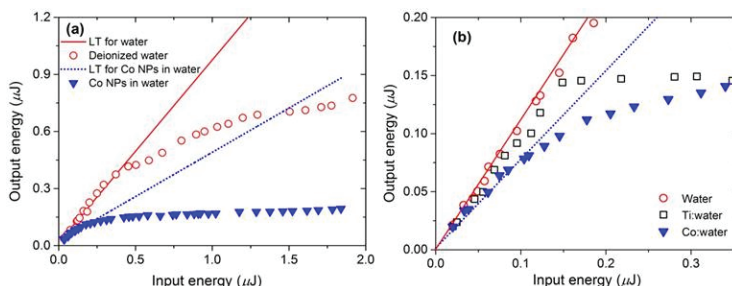
Fig. 4.14. (a) Optical limiting in Co NPs suspended in water. Filled triangles correspond to Co NPs, and empty circles correspond to pure water. (b) Different behaviour of Ti (empty squares) and Co (filled triangles) NPs at relatively small pulse energies during OL studies. Solid and dotted lines correspond to linear transmittance (LT) for water and Co NPs in water. Reproduced from [33] with permission from Springer.

The output energy was stabilized at 0.15 μJ. This process was maintained up to the input energy of 1.8 μJ, above which stronger impeding processes worsened the propagation of laser pulses. A similar study in pure water showed no declination from the linear dependence up to E_{output}~0.35 μJ of output radiation [Fig. 4.14(a), empty circles]. At these conditions, the coefficient of OL-induced suppression of propagating radiation was measured to be ~2.2. Further growth of input energy (i.e. above E_{input}=0.4 μJ) in pure water led to white light generation and declination of E_{input}/E_{output} ratio from the linear dependence. Nevertheless, at the highest input energy used ($E_{input}\approx1.85$ μJ) the ~3.7 fold suppression of output pulses was achieved in Co NPs suspension compared to pure water.
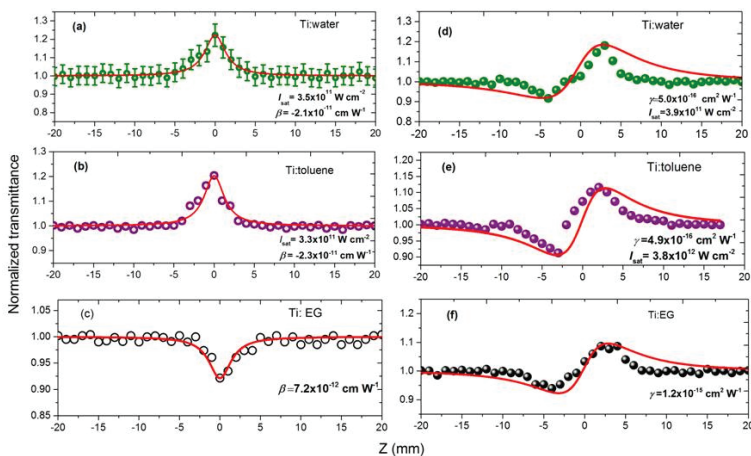
Fig. 4.15. (a-c) OA, and (d-f) CA z-scans of Ti NPs in different liquids measured using 800 nm radiation. The probe pulse intensities for each of these measurements are presented in Table 4.2. Reproduced from [33] with permission from Springer.

Meanwhile, considering a similar process in Ti NPs suspended in water an increase of transmittance at the initial stages of this E_{output} (E_{input}) dependence was observed [Fig. 4.14(b), empty squares]. This process was attributed to the SA, which with further growth of pulse energy was transformed to the RSA. Then the latter process became responsible for OL in this NP suspension.

To analyze the nonlinear optical processes responsible for OL the systematic studies of these suspensions were carried out to determine their γ and β. Figure 4.15 shows the z-scans of Ti NPs measured using 800 nm, 60 fs pulses, as well as the solid curves corresponding to theoretical fits of experimental data. Figures 4.15(a-c) and 4.15(d-f) show the OA and CA z-scan data corresponding to the Ti NPs in water, toluene, and EG, respectively. Similarly, Figure 4.16 presents the z-scans and theoretical fits in the case of 400 nm, 60 fs probe pulses. The nonlinear optical parameters of Ti NPs at 800 and 400 nm calculated using the equations (1-4) are comprised in Table 4.2. At the 800 nm probe wavelength, the Ti NPs in both water and toluene solutions showed the SA [β=-2.1×10^{-11} and β=-2.3×10^{-11} cm W^{-1}, respectively; Figs. 4.15(a) and 4.15(b)]. In the case of CA, the combined processes of NR and SA were observed in these suspensions. They were manifested by larger peaks compared with preceding valleys [Figs. 4.15(d) and 4.15(e)]. Meanwhile, the influence of

SA in Ti NPs in the case of ablation in EG has diminished due to high positive nonlinear absorption of pure solvent [Figs. 4.15(c) and 4.15(f)]. The negative nonlinear absorption attributed to Ti NPs was smaller compared to the positive nonlinear absorption attributed to EG.
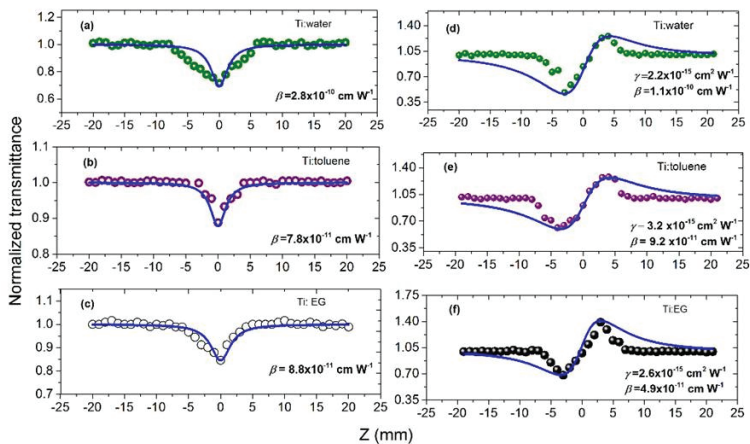
Fig. 4.16. (a-c) OA and (d-f) CA z-scans of Ti NPs suspensions obtained using 400 nm radiation. $I_0=1.5\times10^{10}$ W cm^{-2}. Reproduced from [33] with permission from Springer.

Overall, the Ti NPs suspended in EG showed positive nonlinear absorption in the OA scheme. The corresponding nonlinear absorption coefficient in this suspension was $\beta=7.2\times10^{-12}$ cm W^{-1}. In the case of the CA scheme, the Ti NPs in EG demonstrated pure self-focusing [$\gamma=1.2\times10^{-15}$ cm^2 W^{-1}, Fig. 4.15(f)], whereas in water and toluene solutions these particles showed the NR+SA processes ($\gamma=5\times10^{-16}$ cm^2 W^{-1}, $I_{sat}=3.9\times10^{11}$ W cm^{-2}, and $\gamma=4.9\times10^{-16}$ cm^2 W^{-1}, $I_{sat}=3.8\times10^{11}$ W cm^{-2} respectively). These OA z-scans demonstrated that the Ti NPs possess SA at 800 nm in the case of 60 fs probe pulses. The values of nonlinear refraction and absorption coefficients of Ti NPs in water were slightly higher compared to Ti NPs in toluene. These studies showed that, at relatively small intensities (7×10^{10} W cm^{-2}), SA is the prevailing process of nonlinear absorption that confirms the behaviour of OL curve for Ti NPs suspension at small pulse energies [Fig. 4.14(b)]. Then, with the growth of laser intensity i.e. at $I_0>10^{11}$ W cm^{-2}, the SA process became replaced by RSA leading to OL in this suspension.

In the case of 400 nm probe pulses, the Ti NPs in three solvents showed stronger nonlinear absorption and refraction compared to 800 nm pulses [Fig. 4.16] due to the closeness of probe pulses to the SPR of Ti NPs. Ti NPs in water demonstrated the largest nonlinear absorption at λ=400 nm compared to the other two solvents [compare the data for β, Figs. 4.16(a-c)]. Both 2PA and RSA could be responsible for positive nonlinear absorption in these conditions. The nonlinear optical characteristics comprised in Table 4.2 show that the values of nonlinear absorption coefficients for the Ti NPs in these solvents followed the relation $\beta_{water} > \beta_{EG} > \beta_{toluene}$ at λ=400 nm. In the meantime, the nonlinear refraction indices of Ti NPs suspensions did not follow this rule and were roughly equal to each other [Figs. 4.16(d-f)].
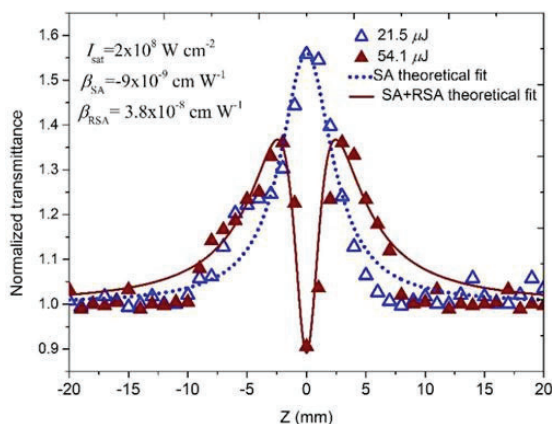
Fig. 4.17. OA z-scans of aqueous Ti NPs suspension using two energies of 355 nm, 5 ns pulses (21.5 μJ, empty triangles and 54.1 μJ, filled triangles). Fitted curves correspond to the SA (dotted curve) and joint influence of SA and RSA (solid curve). Reproduced from [33] with permission from Springer.

Previously, 2PA, SA, and RSA in nanostructured Ni-Ti alloys were investigated at 532 and 1064 nm using nanosecond pulses [36]. The dependences of nonlinear absorption on the intensities of laser pulses and sizes of Ni-Ti nanostructures were analyzed. The normalized variation of transmitted radiation in the case of the Ti NPs suspended in water was also measured using 355 nm, 5 ns probe pulses. At small energies (E=21 μJ) only the SA occurred in the aqueous suspension containing Ti NPs [Fig. 4.17, empty triangles]. The growth of pulse energy (E=54 μJ) led to the

change of the sign and magnitude of nonlinear absorption of this suspension in the vicinity of the focal plane [Fig. 4.17, filled triangles]. Further growth of the energy of 355 nm pulses (E>0.1 mJ) led to the entire disappearance of SA over-passed by RSA.

The nonlinear absorption at λ = 355 nm in the cases including SA and RSA can be analyzed by the relation $\alpha(I)=\alpha_0 \times I/(1+I/I_{sat})+\beta \times I=\alpha_{SA}+\alpha_{RSA}$ for intensity-dependent absorption coefficient. Here I is the intensity of the laser pulse variable along the z-axis. The nonlinear absorption coefficient consists of two parts: one related to saturable absorption (α_{SA}) and another related to reverse saturable absorption (α_{RSA}). Using this model one can find the saturation intensity ($I_{sat}=2\times10^8$ W cm^{-2}) for the Ti NPs aqueous suspension studied in the case of nanosecond UV pulses (5 ns, 355 nm).

Table 4.2. Nonlinear optical parameters of Ti NP suspensions calculated using 800 and 400 nm, 60 fs radiation. Reproduced from [33] with permission from Springer.

NPs suspension	I_0 (W cm^{-2}) $\times10^{10}$	γ (cm^2 W^{-1}) $\times 10^{-16}$	β (cm W^{-1}) $\times10^{-11}$	I_{sat} (W cm^{-2}) $\times 10^{11}$	
		CA	OA	OA	CA
Measurements using 800 nm radiation					
Ti: water	7.9	5	-2.1	3.5	3.9
Ti: toluene	6.6	4.9	-2.3	3.3	3.8
Ti: EG	10	12	0.72		
Measurements using 400 nm radiation					
Ti: water	1.6	22	28		
Ti: toluene	1.6	32	7.8		
Ti: EG	1.6	26	8.8		

The nonlinear absorption coefficient of this suspension associated with RSA was calculated to be $\beta_{RSA}=3.8\times10^{-8}$ cm W^{-1} (at λ=355 nm), while the negative nonlinear absorption associated with SA was calculated to be $\beta_{SA}=-9\times10^{-9}$ cm W^{-1}. The RSA in the medium requires the fulfilment of the following basic criteria: firstly, the material should have an excited-state absorption cross-section larger than the ground-state absorption cross-section, and secondly, the lifetime of the excited state must be long enough. Probably, Ti NPs satisfy the criteria which allow observation of

such variations of normalized transmittance using relatively long laser pulses.
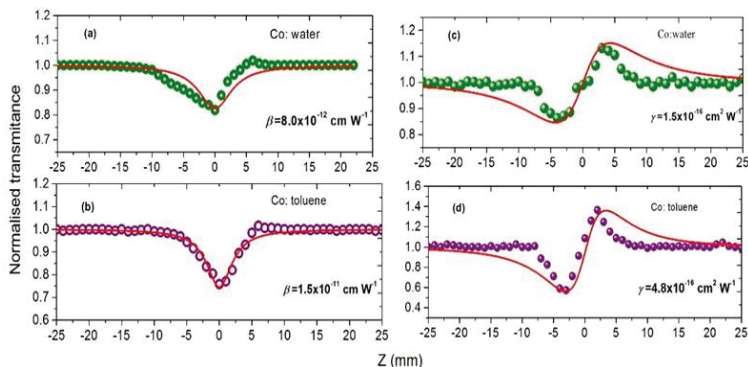
Fig. 4.18. (a,b) OA, and (c,d) CA z-scans (800 nm, 60 fs) of the Co NPs obtained during ablation in water (a,c) and toluene (b,d) respectively. The corresponding nonlinear optical parameters are shown on the graphs. Reproduced from [33] with permission from Springer.

SA has been observed previously in various media (glasses doped with semiconductor nanoparticles, dyes, thin polythiophene films, etc.) using long laser pulses in the IR, visible, and UV ranges. This process was observed at two wavelengths and different pulse durations (800 nm, 60 fs, and 355 nm, 5 ns) in the case of suspension containing Ti NPs. The appearance of SA in these studies is attributed to bleaching of the ground state at moderate intensities.

Figures 4.18 and 4.19 show the OA and CA z-scans of the Co NPs ablated in water and toluene in case of probe 800 and 400 nm, respectively. The corresponding nonlinear optical processes and their parameters are shown on the graphs and comprised in Table 4.3.

In the case of OA z-scans, the Co NPs in water and toluene demonstrated the 2PA or RSA (800 nm) and RSA (400 nm), whereas the CA scheme revealed the nonlinear refraction and absorption. The values of γ and β for Co NPs in toluene were higher than those for Co NPs in water (Table 4.3), which indicates the influence of the nonlinearities of toluene. The nonlinear absorption studies of Co NP suspensions showed that this process was observed at both wavelengths (800 nm and 400 nm).
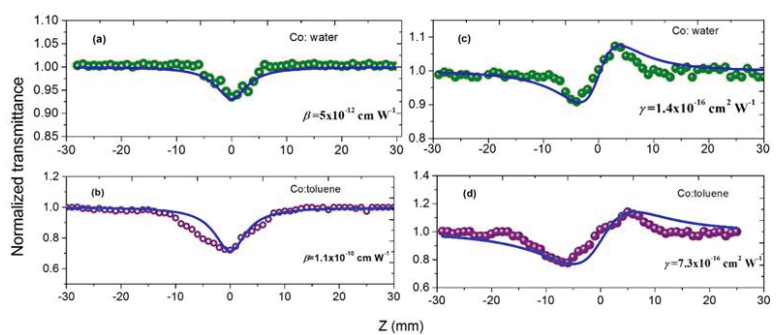
Fig. 4.19. (a,b) OA and (c,d) CA z-scans (400 nm, 40 fs) of Co NPs in water (a,c) and toluene (b,d) respectively. The corresponding nonlinear optical parameters are shown on the graphs. Reproduced from [33] with permission from Springer.

Table 4.3. Nonlinear optical parameters calculated from the z-scans (800 nm, 400 nm) of Co NPs in water and toluene. Reproduced from [33] with permission from Springer.

NPs suspension	I_0 (W cm^{-2}) $\times 10^{11}$	γ (cm^2 W^{-1}) $\times 10^{-16}$	β (cm W^{-1}) $\times 10^{-12}$
Measurements using 800 nm radiation			
Co:water	2.7	1.5	8
Co:toluene	2.5	4.8	15
Measurements using 400 nm radiation			
Co:water	2.2	1.6	5.0
Co:toluene	0.3	7.3	110

As it is shown in Fig. 4.12 the absorption peak of Co NPs demonstrates the SPR at 400 nm. These NPs have stronger linear absorption at 400 nm compared to 800 nm. In discussed case, at both 800 and 400 nm wavelengths, the Co NPs in toluene showed self-focusing while using short (60 fs) pulses. The nonlinear optical parameters of Co NPs in water have higher values at 800 nm compared to 400 nm and contrary to the Co NPs in toluene. These measurements of the nonlinearities of the Co NPs suspended in different liquids show that, in some cases, they possess strong nonlinear refraction and absorption at 400 nm.

4.3. Effect of nanoparticle sizes on the saturable absorption and reverse saturable absorption in silver nanostructures

Among various metal NPs, silver (Ag) NPs possess unique optoelectronic and thermal properties which lead to efficient use in a wide range of technological advancements such as molecular diagnostics and photonic devices based on their optical properties. Ag NPs exemplify amazingly efficient optical properties, which depend on the size and the shape of the particle. There have been several reports on the presence of SA and TPA in Ag NPs depending on the excitation wavelength [37,38]. At the same time, Ag NPs have been studied in order to observe ultrafast dynamics depending on their size and shape [39,40]. However, there are few reports on a systematic study in ultrafast dynamics depending on the size and shape of Ag NPs [41,42]. The important objective is to investigate the NLO properties and ultrafast dynamics associated with Ag NPs under SPR resonance which can effectively provide the correlation of NLO properties and ultrafast dynamics with the size of NPs.

Below we discuss the results of systematic studies of the chemically prepared Ag NPs which can efficiently provide the variation in the size of the prepared NPs [43]. We analyze the impact of the size of Ag NP on the SA and 2PA using femtosecond pulses at 400 nm and 800 nm. The studies of ultrafast dynamics of chemically prepared Ag NPs using femtosecond 400 nm are discussed. We analyze the observation of the presence of acoustic vibration in Ag NPs upon excitation with the resonant wavelength. The effect of the size of NPs on acoustic oscillations and associated damping time constants were discussed in detail.

Ag NPs were prepared by chemical reduction of sodium nitrate ($AgNO_3$) from sodium borohydride (SBH) in an aqueous medium. In order to prepare Ag NPs in deionised water, at First, 0.043 g $AgNO_3$ was dissolved in 50 mL deionised water, and 0.012 g SBH was dissolved in 150 mL deionised water respectively with constant stirring. The 3 ml of aqueous $AgNO_3$ solution was dripped slowly into 10 ml of aqueous SBH solution at three different temperature conditions of 0℃, 25℃, and 60℃. This mixture was stirred for a few seconds, which allowed $AgNO_3$ and $NaBH_4$ to react completely. With the addition of $AgNO_3$, the solution gradually turns yellow, light gray, and dark grey colour which indicates that Ag NPs were formed. From here onward, Ag NPs suspensions represented as S1, S5, and S9 prepared by addition of $AgNO_3$ solution to SBH solution by the dripping method at 0℃, 25℃, and 60℃, respectively, are distinguished. Whereas NPs suspensions represented as S3, S7 and

S11 were prepared by fast mixing of AgNO$_3$ and SBH solution at 0°C, 25°C, and 60°C, respectively. Thus the Ag NPs prepared by these methods yield different sizes of the NPs. Prepared Ag NPs were characterized by UV-Visible spectrometer and scanning electron microscope.

Under the assumption that the optimal packing efficiency of Ag atoms under spherical NPs was estimated to be 74%, the concentration of Ag NPs suspension was calculated by using the mean sizes of Ag NPs measured from SEM images. The concentrations of NPs suspensions were determined to be 1.7, 2.4, 1.6, 2.4, 1.7, and 2 nmol/L for S1, S3, S5, S7, S9, and S11 respectively. The synthesized Ag NPs suspensions were found to be stable up to 30 days which was confirmed by their UV-Visible spectroscopy measurements and SEM images. NLO studies were performed at low and high concentrations of Ag NPs suspension. The change of the Ag NPs concentration in deionised water was achieved through the dilution of synthesized Ag NPs using water as a solvent.

The conventional z-scan technique was employed to study the NLO properties of the prepared Ag NPs in deionised water. A conventional noncollinear degenerate pump-probe technique was employed to observe the transient absorption (TA) in chemically prepared Ag NP in deionised water at different temperatures.

4.3.1. Linear and nonlinear optical properties of chemically prepared Ag NPs

The optical absorption spectra of Ag NPs suspensions in deionised water were measured using a UV-visible spectrophotometer. From Fig. 4.20, one can observe distinctive surface plasmon resonance at 389 nm for S1 and S3, 381 nm at S5 and S7 nm, and 385 nm for S9 and S11. The emergence of these peaks was the direct consequence of the size of Ag NPs. The SPRs of Ag NPs prepared at 0 ºC exhibit an absorption band at 389 nm with an additional absorption band at 433 nm. These absorption peaks around 390 nm in all Ag NPs are the result of direct transition from occupied *sp* to unoccupied *sp* transition. This observation shows the emergence of the absorption band at 430 nm in prepared Ag NPs at 0 ºC and 25 ºC whereas the emergence of the absorption peak at 350 nm was observed at 60 ºC. The emergence of these absorption bands can be attributed to the Ag NPs distortion which results in the formation of prolate and oblate spheroid NPs. These distorted NPs are responsible for the emergence of the SPR band at 350 and 430 nm due to the high multipolar excitation.
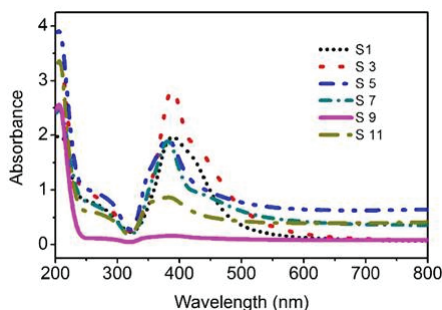
Fig. 4.20. Optical absorption spectra of chemically prepared NPs in deionised water. Reproduced from [43] with permission from Hindawi.
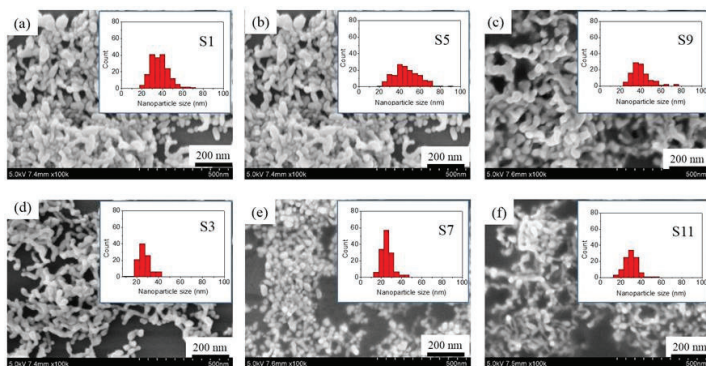
Fig. 4.21. SEM image of chemically prepared Ag NPs in deionised water by dripping aqueous AgNO₃ in SBH slowly at (a) 0ºC, (b) 25ºC, (c) 60ºC, whereas (d) 0ºC, (e) 25ºC, (f) 60ºC represents the Ag NPs prepared by mixing aqueous AgNO₃ and SBH instantaneously. Reproduced from [43] with permission from Hindawi.

SEM images and their respective histograms of prepared Ag NPs at different temperatures are shown in Fig. 4.21a–f. It is evident from the SEM images that the shape of the prepared Ag NPs is distorted. Size and its distribution Ag NPs associated with S3, S7, and S11 are observed to be similar and narrow as compared to S1, S5, and S9, respectively. As mentioned in the experimental setup, S1, S5, and S9 were prepared using the slow addition of aqueous AgNO₃ in an aqueous SBH solution.

The mechanism of creation of NPs involves the reduction of metal ions by reducing agent which is followed by the nucleation process of clustering of reduced metal that acts as a seed to grow the different sizes of NPs. Under the dripping method of addition, first smaller-sized aggregates are mostly formed which upon further addition of metal ions, reduced metal ions can aggregate on the surface of small-sized NPs. This process leads to bigger size NPs compared to NPs prepared by mixing metal ions and reducing agents instantaneously. Their nucleation process limits the sizes of NPs.
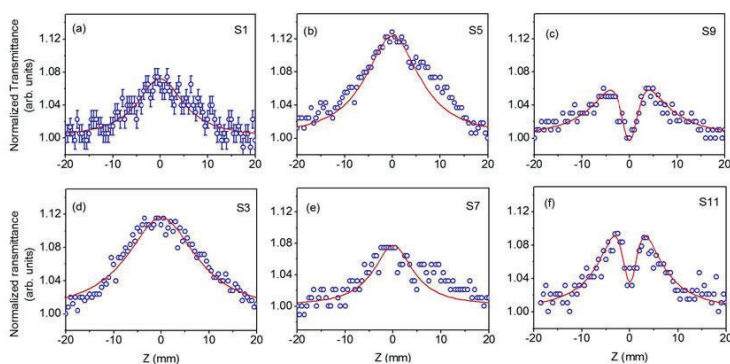
Fig. 4.22. Open aperture z-scan trace for chemically prepared Ag NPs with a peak intensity of 9.9×10^{10} W cm^{-2} at 400 nm. (a) S1, (b) S5, (c) S9, (d) S3, (e) S7 and (f) S11. The open circle represents the experimental data and the solid line represents the theoretical fit. Reproduced from [43] with permission from Hindawi.

NLO properties of chemically prepared Ag NPs in deionised water were investigated using the technique with amplified femtosecond pulses at resonant 400 nm and nonresonant 800 nm. Prior to the z-scan measurement, the open aperture was measured for deionised water, which exhibits negligible optical nonlinearity with a maximal applied peak intensity of 1.2×10^{11} W cm^{-2} at 400 nm and 2.5×10^{11} W cm^{-2} at 800 nm. Figure 4.22 shows the open aperture trace of all NPs (S1, S3, S5, S7, S9, and S11) at the peak pulse intensity of 9×10^{10} W cm^{-2} at 400 nm. As shown in Fig. 4.22, all prepared Ag NPs show the increase in the transmittance of 400 nm wavelength as the sample approaches the focal point, which indicates that all materials exhibit SA at 400 nm. OA z-scan data were analyzed by fitting the standard transmittance equation of SA. The estimated values of I_{Sat} were tabulated in Table 4.4 for respective

nanoparticle suspension. The saturable absorption for all NPs suspensions can be explained by the presence of SPR resonance at 400 nm which resulted in the increase of transmittance through Ag NPs suspensions.
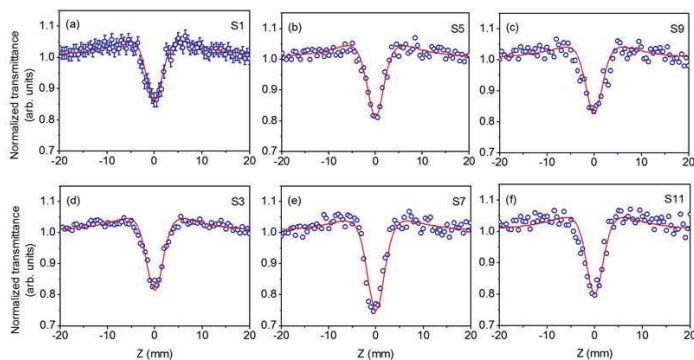
Fig. 4.23. Open aperture z-scan trace for chemically prepared Ag NPs with a peak intensity of 2.7×10^{11} W cm^{-2} at 800 nm. (a) S1, (b) S5, (c) S9, (d) S3, (e) S7 and (f) S11. The open circle represents the experimental data and the solid line represents the theoretical fit. Reproduced from [43] with permission from Hindawi.

Figure 4.23 shows the open aperture z-scan at 800 for each Ag NPs. Similar to the z-scan profile at 400 nm, S1, S3, S5, and S7 exhibit saturation absorption with I_{Sat} of 3.3×10^{12} W cm^{-2}, 2.1×10^{11} W cm^{-2}, 1.9×10^{10} W cm^{-2}, and 3.1×10^{10} W cm^{-2}, respectively. On the other hand, S9 and S11 exhibit two-photon absorption in addition to saturable absorption at the peak intensity of 2.7×10^{11} W cm^{-2}. The estimated value of I_{Sat} and β are 8.3×10^{11} W cm^{-2} and 1.7×10^{-11} cm^{-1}W for S9, and 2.7×10^{11} W cm^{-2} and 4.6×10^{-11} cm^{-1}W for S11.

The NLO response of prepared Ag NPs was also measured with 30 time's lower concentration at 400 nm. At a resonant wavelength of 400 nm with a low concentration of Ag NPs, the RSA was observed with absorption saturation (see Fig. 4.24). The estimated values of I_{Sat} were 1.4×10^{11} W cm^{-2}, 1.1×10^{11} W cm^{-2}, 1.4×10^{10} W cm^{-2}, 1.3×10^{10} W cm^{-2}, 1.3×10^{11} W cm^{-2}, and 1.1×10^{11} W cm^{-2} for S1, S3, S5, S7, S9 and S11, respectively. Whereas, the corresponding β value were 1.1×10^{-10} cmW^{-1}, 1.3×10^{-10} cm W^{-1}, 1.2×10^{-10} cm W^{-1}, 1.4×10^{-10} cm W^{-1}, 1.1×10^{-10} cm W^{-1}, and 1.3×10^{-10} cm W^{-1} for S1, S3, S5, S7, S9 and S11, respectively.
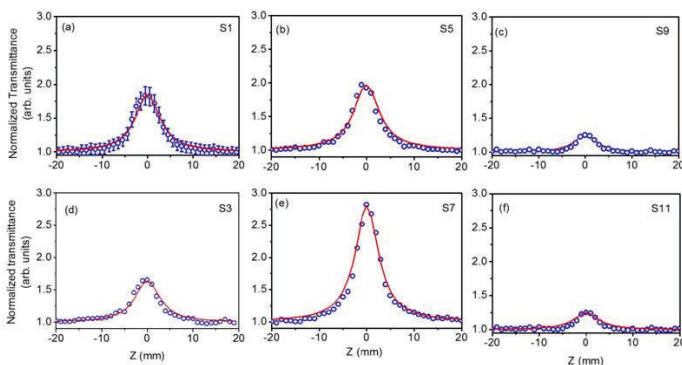
Fig. 4.24. Open aperture z-scan trace for chemically prepared Ag NPs at low concentration with a peak intensity of 1.2×10^{11} W cm^{-2} at 400 nm. (a) S1, (b) S5, (c) S9, (d) S3, (e) S7 and (f) S11. The open circle represents the experimental data and the solid line represents the theoretical fit. Reproduced from [43] with permission from Hindawi.
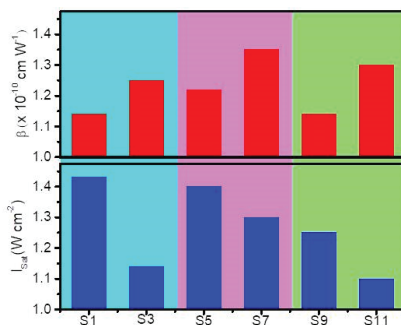
Fig. 4.25. Comparison of I_{Sat} and RSA coefficient of all prepared Ag NPs at 400 nm femtosecond laser pulses. Reproduced from [43] with permission from Hindawi.

It was observed that RSA value is higher for S7 compared to other NPs which can be attributed to the smaller size of Ag NPs. It is evident from the calculated value of I_{SA} and β that I_{SA} decreases and β increases as the sizes of the Ag NPs increase as shown in Fig. 4.25. It was observed that under resonant excitation SA can dominate over two photon absorption. The estimated values of nonlinear absorption for all samples are represented in Table 4.4.

Table 4.4. The NLO and decay time characteristic of chemically prepared Ag NPs in deionised water. Reproduced from [43] with permission from Hindawi.

	Size (nm)	Nonlinear absorption				
		400 nm			800 nm	
		High concentration	Low concentration		Low concentration	
		I_{sat}, 10^{10} Wcm^{-2}	I_{sat}, 10^{11} Wcm^{-2}	β 10^{-10} cmW^{-1}	I_{sat} 10^{10} Wcm^{-2}	β 10^{-11} cmW^{-1}
S1	37	10±1	1.4±0.1	1.1±0.2	330±40	-
S3	25	13±2	1.1±0.2	1.3±0.1	21±4	-
S5	38	8.8±1	1.4±0.2	1.2±0.2	1.9±0.3	-
S7	25	4.7±1	1.3±0.2	1.4±0.2	3.1±0.4	-
S9	30	34±4	1.4±0.2	1.1±0.2	83±6	17±4
S11	37	34±5	1.1±0.2	1.3±0.2	27±4	46±5

4.3.2. Pump-probe study of chemically prepared Ag NPs suspensions

The degenerate pump-probe measurement of the chemically prepared Ag NPs in deionised water was performed at 400 nm with 35 fs pulses. The intensity of the pump and probe pulses was 17 GW cm^{-2} and 1 GW cm^{-2}, respectively. Here, all NPs suspensions exhibit photobleaching effect evident of saturable absorption as shown in the z-scan profile of Ag NPs at 400 nm. Figure 4.26 shows the temporal evolution of change in transmittance of probe pulses. The energy relaxation upon excitation from pump pulses is generally described as a series of relaxation processes which include electron-electron scattering, electron-phonon coupling, and heat dissipation through the surrounding.

Apart from these relaxation processes, the particle can go under acoustic vibrations through two distinct excitation mechanisms. First is the creation of pressure on the surface of the particle due to a sudden surge in electron temperature and second is the energy transfer from the electron to the lattice leading to the increase in the equilibrium interatomic distance by thermal expansion. The acoustic vibration time scale is longer than the electron-lattice relaxation time. Thus, the particles are brought out of

equilibrium leading to mechanical oscillations which are responsible for the periodic change in size and shape of NPs. These periodic oscillations are easy to probe by wavelength closer to plasmonic resonance. In particles, the fundamental mode of vibration involves radial breathing mode (RBM) which depends on both bulk and searing elastic modulus.
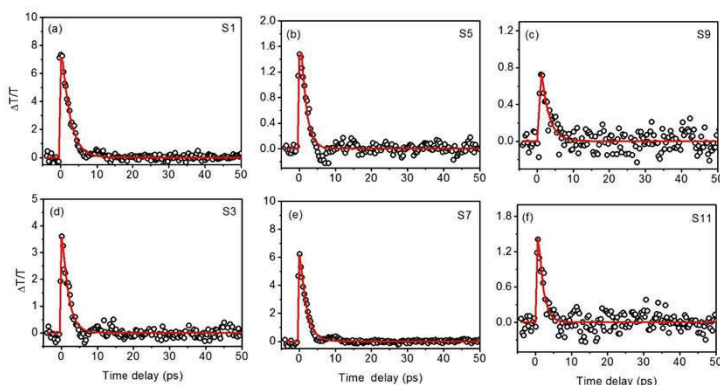
Fig. 4.26. TA profile chemically prepared Ag NPs (a) S1, (b) S5, (c) S9, (d) S3, (e) S7 and (f) S11 NPs at 400 nm. The open circle represents the experimental data and the solid line represents the theoretical fit. Reproduced from [43] with permission from Hindawi.

In chemically prepared Ag NPs, distinct damped oscillation in probe pulse transmittance was observed for S1, S3, S5, and S7 due to acoustic vibration, which is superposed with the exponentially decaying back of the excited Ag NPs to its ground state through cooling of the hot lattice. However, this acoustic vibration was not observed for S9 and S11. As seen in Fig. 4.26 (c,f), the signal-to-noise ratio is poor as compared to the other transmission profiles which can be directly correlated to the impact of the low concentration of the Ag NPs in S9 and S11. The damping in the acoustic vibration was witnessed which is associated with the damping time of the breathing mode due to the effect of the surrounding solvent. These oscillations were observed within 20 ps after the 0-time delay between pump and probe pulses.

4.4. Mechanism of laser-assisted generation of aluminium nanoparticles, their wettability, and nonlinearity properties

The studies of the low- and high-order nonlinear optical properties of Al NPs are driven by the practical and fundamental principles of applications of the small-sized aggregates in different fields of nonlinear optics. These aggregates being formed during laser-induced ablation of metal surfaces serve as an efficient medium for high-order harmonics generation in the extreme ultraviolet range. The approach of creating efficient sources of coherent short-wavelength radiation has been demonstrated using different nanoparticles. However, those nanoparticles were initially formed by chemical methods and attached to the substrates for ablation and NP plasma formation [22,44]. Here we analyze the *in-situ* formation of Al NPs followed by propagation of driving pulses through the cloud of synthesized nanoparticles resulting in enhanced harmonic yield compared to the application of aluminium atoms and ions.

The potential application of NPs, which is of great interest, is the modification of the wettability of the materials covered by such nanostructures. NPs were proposed as alternative agents to chemical coating in changing the wettability of the surfaces [45]. In this connection, the deposition of the thin layers of Al NPs on different surfaces can alter the contact angle of the water on this surface. Therefore, it is technologically relevant to analyze different methods of Al NPs deposition on the substrates (e.g. the laser-induced deposition of ablation debris in a vacuum and the deposition of Al NPs from the suspensions on the glass surfaces).

In this section, we analyze the ability of Al NPs to modify the wettability of surfaces and the nonlinear optical properties of surfaces, suspensions, and plasmas [46]. We analyze the variations of wettability of the glass surfaces under the deposition of NPs produced during laser ablation of aluminium in water, as well as during direct deposition of laser-generated NPs and ablation debris on the substrates in a vacuum. The nonlinearities of the Al-based NPs produced in water by nano-, pico-, and femtosecond pulses are determined.

4.4.1. Characterization of ablation

Al-based NPs were synthesized by ablation of the bulk aluminium block immersed in deionised water using laser pulses of 1064 nm wavelength, 10 ns pulse duration, and 10 Hz repetition rate at a pulse

energy of 4 mJ. The laser beam was focused by a 100 mm focal length lens. The ablation of bulk Al in a vacuum was carried out using the same laser. The 10 ns pulses were focused inside a vacuum chamber on the surface of the aluminium target. The debris from the ablated material was deposited on the nearby glass and silicon substrates. The ablation lasted for 30 min. The femtosecond pulses (300 fs, 1030 nm, 100 kHz, 0.5 mJ) were also used to ablate the aluminium target in water and vacuum.

The morphology of deposited particles during ablation by 10 ns pulses in vacuum and water was analyzed using a scanning electron microscope (SEM). The SEM images of Al-based NPs produced by nanosecond pulses in vacuum and water are shown in Figs. 4.27(a) - (c). NP sizes were determined to be 55 and 34 nm, respectively, Figs. 4.27(d) and 4.27(e). To qualitatively relate the effect of water on the NPs size distribution these two cases were compared. It was found that size distribution was narrower in the case of ablation in water. Based on the theoretical study above, the NPs size distribution is also narrowed due to the thermal and mechanical action of a dense liquid environment (water). The process of NPs formation can be affected by either the spallation mechanism of the material ejection (mechanical damage regime) or explosive boiling mechanism (thermal damage regime) or a mixture of them for the sufficiently high value of the absorbed laser energy (fluence).

Thus, the water environment results in more narrow and uniform size distribution of NPs as compared to that in vacuum [47-49], which was also supported by the experimental and modelling results. Unlike the NPs generation in a vacuum, where the NPs are segregated along the ablation plume by their size and velocity, the water environment, due to its significant density and mechanical resistance, compresses the ablation plume causing more active nucleation of the metal atoms from a vapour state into clusters. However, depending on particular irradiation conditions and the environment, other mechanisms of the NPs generations can be involved that can affect their size distribution. The sizes and shape of particles significantly changed after one month of ablation. Triangle shapes of aggregated particles were observed [Fig. 4.27(c)]. In the case of aged NPs in water, the sizes of aggregated pyramids and triangles were found to be approximately $200 \times 200 \times 200$ nm^3.

The absorption spectrum of the Al-based NP suspension produced by nanosecond pulses is shown in Fig. 4.27(f). The peak of absorption spectrum at ~275 nm, corresponding to the surface plasmon resonance of the spherical Al-based NPs and is similar to the one reported in [50], was measured immediately after ablation. The colloidal solution was further

analyzed as a nonlinear optical medium to determine its nonlinear refraction and nonlinear absorption properties.
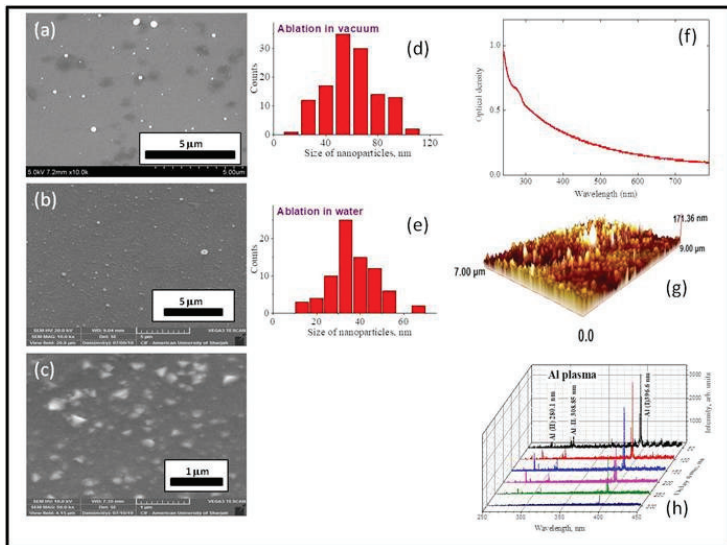
Fig. 4.27. Structural and spectral properties of Al based NPs. (a-c) SEM images of the Al based NPs produced by ablation of target using 10 ns pulses in different environment: (a) vacuum, (b) water, and (c) water (after 30 days). The corresponding histograms of the NPs size distributions are shown in (d) and (e) in the case of ablation in vacuum and water, respectively. (f) Absorption spectrum of Al based NPs suspension. (g) Atomic force microscopy image of Al NPs layer deposited during ablation in vacuum. (h) Variation of plasma emission (250-450 nm). UV spectra of Al plasma were collected at different delays from the beginning of ablation by nanosecond pulses. Reproduced from [46] with permission from Elsevier.

This absorption spectrum of the aluminium suspension demonstrates the increase of absorption of UV spectra in the vicinity of 275 nm. This peculiarity of absorbance points out to the presence of nanoparticles in this suspension. The difficulty in distinguishing this peak is related to the strong emission in the near UV region (340-400 nm, Fig. 4.27(f)), which masks the influence of the plasmonic resonance of Al based NPs. The motivation of these optical absorption studies is to demonstrate the presence of synthesized NPs in the liquid environment. Notice that the above-described morphology studies are based on the analysis of the

debris deposited on the Si or SiO$_2$ substrates either by direct ejection of laser plasma plume formed in air or by spin-coating of the suspension containing the products of laser ablation of aluminium in water. In the meantime, formation of NPs during laser ablation can be performed (a) during direct aggregation of ejected atoms in the vicinity of ablated area or (b) during the process of deposition on the substrates, when small agglomerates appear during some aging period. The observed peak of absorption spectrum at ~275 nm corresponds to the surface plasmon resonance of the spherical Al based NPs, which confirms their presence in the suspension.

The variation of plasma emission at vacuum conditions is shown in Fig. 4.27(h). The emission lines in the UV region were analyzed using laser-induced breakdown spectroscopy (LIBS) during 500 ns from the beginning of ablation, with a step of 50 ns. The incident fluence was taken to be optimal for the formation of NPs at vacuum conditions and roughly corresponded to 10 J/cm^2 also used in the numerical simulations. The intense lines in this spectral range [309 nm (Al I) and 397 (Al I) nm] almost disappeared after few hundred nanoseconds from the beginning of ablation.

4.4.2. Wettability variations of glasses under deposition of Al based NPs

Below we analyze the study of the wetting properties of the Al-based NPs films prepared by self-assembly of NP layers deposited on the glass surfaces. For the preparation of the film, the suspensions of the Al-based NPs formed in water by nanosecond and femtosecond pulses-induced ablation of bulk material were used. The layer after layer of NP suspension was deposited on the cleaned glass slide by the drop-casting method. Prior to the preparation of the new layer, the previous layer was completely dried in the air. A variable number of layers showed a change in the colour of the glass slides and also depicted a change in the wetting properties of the glass substrate. The wettability of Al-based NP layers deposited during ablation of aluminium in a vacuum was also analyzed. A drop shape analyzer was used for the contact angle measurements of the coated and uncoated glass surfaces.

As it was mentioned, SEMs showed a narrower distribution of NPs in the case of ablation in water compared with ablation in a vacuum. The NP sizes were in the range of 15-80 nm in the case of ablation in water, Fig. 4.27(e), and 20-110 nm in the case of ablation in a vacuum, Fig. 4.27(d). The formation of extremely rough nanostructured film during deposition

of NPs in vacuum became the reason for the superhydrophobic properties of Al NPs coatings and therefore these nanostructures yielded low adherence when they come in a contact with water. Atomic force microscopy was employed for the analysis of the topography of the NPs-coated surface, Fig. 4.27(g). The thickness of these coatings deposited in vacuum was ~150 – 200 nm.
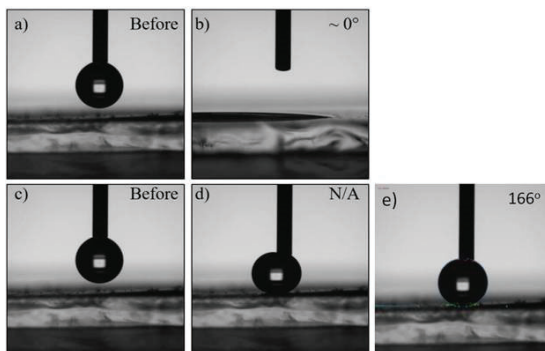
Fig. 4.28. Contact angle measurement of (a, b) Al based NPs suspension produced during ablation in water and deposited on the glass slides showing the superhydrophilic properties with a contact angle of nearly 0°. (c, d) Al NPs deposited on the glass slide by laser ablation in vacuum show an extremely superhydrophobic surface. (e) The image from which one can obtain the contact angle of at least not less than 166°, with the needle still in contact with the droplet. Reproduced from [46] with permission from Elsevier.

These studies showed that Al NPs deposited in a vacuum possess superhydrophobic properties irrespective of the coating thickness. The contact angle measurements on the deposited surfaces, which were almost transparent, showed their superhydrophobic response. The coating was not uniform. However, the contact angle remained the same at different regions of deposited glass. The below-reported contact angle measurements are the averaged values of the contact angle measurements at various coated regions of the glass.

The contact angle measurements were also carried out for different coating thicknesses when 1 to 20 layers of NPs suspension were dropped on the surface of glass followed by the drying procedure between each of the coating steps. A significant change in contact angle was observed after the application of 7 layers. 20 layers were also applied to understand the

change in contact angle. However, no significant change of contact angle was observed when the coating thickness was increased above 7 layers.

Figures 4.28(a) and 4.28(b) show the contact angle measurements of the pure glass surface filled with 7 layers of Al-based NPs synthesized during ablation in water. The deposited layers showed a variation in the wettability behaviour and contact angle of the cleaned glass surface from 44° to nearly 0°. The variation in contact angle depicts the superhydrophilic characteristics of the Al-based NPs formed during ablation in water and deposited on the glass slide as shown in Figs. 4.28(a) and 4.28(b). The time period between the moments when the water droplet gets in contact with the surface and disappears from it was less than 0.5 s.

The effect became completely opposite for the Al NPs deposited on the glass surface during laser ablation in a vacuum, Figs. 4.28(c) and 4.28(d). In that case, an extremely superhydrophobic surface of Al NPs was obtained. The effect is strongly water-repellent even when the water droplet is pushed against the Al NPs coatings. The water droplet remained stuck to the needle of the drop shape analyzer because of high repellence from the coating. It was estimated that this superhydrophobic surface had a contact angle greater than 150° with a roll-off angle less than 5°.

Figures 4.28(a) and 4.28(c) show the images of the water droplet before it makes contact with the studied surface. It was aimed to demonstrate the superhydrophilic and superhydrophobic response of deposited species with regard to the initial state of the unprocessed glass surface, therefore before and after contact situations are displayed in the case of the processed surface. In Fig. 4.28(b) the water droplet during contact with thin deposited layer spreads along the surface filled in with Al-based NPs suspension within < 0.5s because of strong hydrophilic response, probably due to presence of –OH functional groups, resulting in water contact angle close to 0°. Contrary to that, Fig. 4.28(d) shows the water droplet on the surface filled in with the Al NPs deposited in a vacuum. The droplet was pushed-retracted against the surface several times to land it on the surface for contact angle measurement. Thus surface contact angle cannot be quantitatively determined. In Fig. 4.28(e), the image is shown from which one can obtain the contact angle of at least not less than 166°, with the needle still in contact with the droplet that makes such measurements inaccurate, though these Al NPs formed in vacuum clearly provided the superhydrophobic response.

The observed variation of the wettability characteristics of the glasses coated with Al NPs during ablation at vacuum conditions can be used for self-cleaning of the surfaces and, particularly may provide an alternative transparent coatings solution for self-cleaning window glass of skyscrapers. In

that case, a superhydrophobic surface is created without the need for surface treatment by hazardous chemicals.

Moreover, for the Al bulk surface structured by the femtosecond and nanosecond pulses, the contact angle measurements showed a superhydrophilic characteristics of the droplet, as the water droplet immediately goes into the channels and microgrooves of the laser structured area because of the high affinity with water. Thus, a wide range of extreme wettability behaviour was observed for the different Al-based NPs formed from the same bulk material, as well as for the ablated material itself. The reasons for the different behaviour of deposited NPs still require further investigation and analysis for potential industrial applications. Some options in explanation of this phenomenon are discussed below.

Al-based NP suspension produced during ablation in water and deposited on the glass slides also showed superhydrophilic properties with a contact angle of nearly 0°, Fig. 4.28(b). This similarity with the above-mentioned conditions for Al bulk surface is probably related to the formation (in both cases) of cavities and other types of roughness supporting the filling of the water inside them. In the case of deposition of the nanoparticles during ablation of Al surface in a vacuum, the synthesized NPs are deposited on the glass substrate at a much higher velocity compared with a drop-casting method used in the former case. This may lead to the formation of a denser NP layer, without the holes, cavities, and other irregularities of the newly formed layer. Thus the superhydrophobic properties of nano- and microstructured surfaces can be explained by a modification of the roughness of the deposited surfaces. In that case, the variation of the wettability can be related to the alteration of the surface free energy.

Another consideration is related to the role of different types of synthesized NPs. In the case of the water environment, the formation of $Al(OH)_3$, $AlO(OH)$, and Al_2O_3 occurs. It is known that oxidation does happen in laser ablation of Al in water or air, and special efforts should be made to minimize the oxidation of the nanoparticles. The oxidation has a major effect on the nanoparticle formation on the ns time scale, their structure (e.g., larger core-shell particles or fully oxidized smaller clusters), and size distributions. Moreover, this process influences the wettability properties of the synthesized NPs as well.

Thus, the second possible explanation of the difference of Al-based NP coated surfaces' wettability can be related to the presence or absence of hydroxides on the deposited surface. As it was mentioned, during the laser ablation in liquid the newly formed surface reacts with water and produces

the aluminium hydroxide ($Al(OH)_3$), which is hydrophilic in nature. Meanwhile, the ablation of Al surface in vacuum conditions leads to deposition of primarily Al NPs, since no oxygen and water components interact with the ablating surface.

Thus, the laser-produced Al-based NP in a water environment undergoes oxidation and hydroxylation reactions because of the presence of H_2O molecules in the vicinity of newly formed particles. A possible reaction mechanism during the laser ablation in H_2O was given earlier in [51]. The presence of hydroxylated functional groups has a strong affinity towards the H_2O molecules due to their polar nature. The Al-based NPs formed in a water environment have terminal –OH groups, and these NPs once deposited on glass cover it completely during multiple deposition cycles. The terminal –OH groups on Al-based NPs show strong attraction towards the water and therefore make the newly developed surface superhydrophilic as shown in Fig. 4.28(b). Contrary to laser ablation of Al in water, direct deposition of Al NPs synthesized in vacuum during laser ablation showed the superhydrophobic response, Fig. 4.28(d). The reason is the absence of H_2O molecules during laser ablation in a vacuum that tends to change the functionality of the pure Al NPs. The absence of terminal hydroxylated functional groups in the case of Al NPs formed in a vacuum tends to have a non-polar response making it superhydrophobic.

One can see that there are two options explaining the observed wettability properties of NP-deposited surfaces. Since neither of these two assumptions has been precisely proven to be the main mechanism of wettability variations, the above consideration of observed phenomena of different behaviour of deposited NPs still requires further investigation.

4.4.3. Z-scan studies of the nonlinear optical properties of Al NPs

The motivation of the studies of the nonlinear absorptive and refractive properties of NPs, as well as their various optical properties, is based on their potential applications in optoelectronics, optical limiters, and photonics. Meanwhile, the analysis of the role of pulse duration during ablation of Al target on the coefficients of nonlinear absorption and nonlinear refraction of Al-based NPs has not been reported during previous studies of these species. A search of small-sized materials possessing strong nonlinear refractive and absorptive properties prompted analyzing the NP produced by nanosecond, picosecond, and femtosecond pulses.
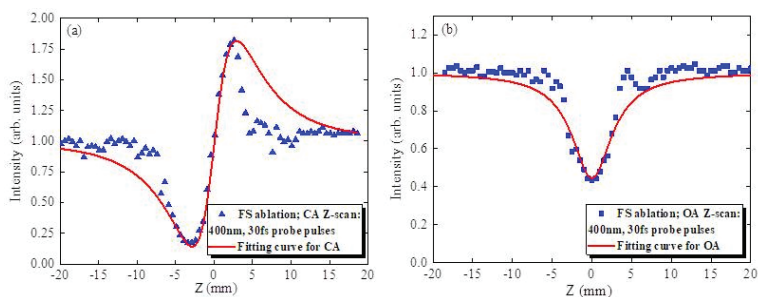
Fig. 4.29. (a) CA and (b) OA z-scans of suspensions measured using 400 nm, 30 fs pulses. The suspension was prepared by ablation of bulk aluminium in water using 30 fs pulses. Reproduced from [46] with permission from Elsevier.

Here we analyze the nonlinear optical properties of different Al-based NP suspensions prepared during ablation of bulk aluminium in water by nanosecond, picosecond, and femtosecond pulses using a z-scan scheme. The normalized transmittances of Al-based NPs suspensions were analyzed using the standard fitting procedure to determine their nonlinear absorption coefficients (β) and nonlinear refractive indices (γ). The optical nonlinearities of the aluminium-based NPs obtained by ablating Al bulk in liquid were analyzed using pulses with different durations (5 ns, 200 ps, and 30 fs).

Figures 4.29 show the CA and OA z-scans of samples using 400 nm, 30 fs pulses. The fitting of these curves allowed determining the nonlinear absorption coefficients and nonlinear refractive indices of three suspensions (generated by fs, ps, and ns pulses) using 400 nm, 30 fs pulses. The highest values of nonlinear optical parameters were observed in the case of the suspension produced by ablation of aluminium using picosecond pulses, while the other two suspensions showed three (femtosecond ablation) and five (nanosecond ablation) times smaller γ and β. The γ and β of the NP suspension produced by picosecond pulses were measured to be $\sim 10^{-13}$ cm^2 W^{-1} and 10^{-11} cm W^{-1}, respectively. Since the volume part of NPs in these suspensions was $\sim 10^{-4}$, the values of γ and β of Al-based NPs were estimated as $\sim 10^{-9}$ cm^2 W^{-1} and 10^{-7} cm W^{-1} correspondingly, which are among the highest values reported in this spectral region.

As it was mentioned, a mixture of different NPs was contained in suspensions (i.e. those containing pure Al, Al(OH)$_3$, AlO(OH), and Al$_2$O$_3$). It is difficult to distinguish the role of each of these components in

NP-contained suspension. However, whether those NPs are oxides or hydroxides, the main component responsible for the low-order nonlinear optical response is aluminium.

4.4.4. Discussion

This research covers different aspects of the applications of Al NPs produced by laser ablation of the surface of the aluminium. The logic behind combining two totally different aspects like wettability of NP-contained surface and nonlinearities of the same NPs is as follows. The applications of nanoparticles in nowadays science are too broad to cover even a few of them in a single set of studies. Two of those applications were chosen to demonstrate the scientific novelty in (a) wettability properties of the surfaces covered by synthesized *in-situ* small-sized species and (b) conversion of laser wavelength towards the extreme ultraviolet region using the same synthesized *in-situ* small-sized species, as well as a demonstration of their strong nonlinear refraction and absorption.

On one hand, this study reveals the possibilities for modification of the wettability of the Al-based NP coated glass. Only a few studies have demonstrated similar features due to deposited NPs of other species. Meanwhile, most wettability variation studies were performed by modifying the surface using laser irradiation. However, in the case demonstrated by these studies, the synthesized *in-situ* NPs cover the surface by well-developed drop casting or spin coating methods.

On the other hand, the study of the low- and high-order nonlinear optical properties of Al-based NPs is related to the practical and fundamental aspects of applications of the small-sized aggregates in different fields of nonlinear optics. It was demonstrated that these aggregates, being formed during the laser ablation of metal surface, serve as an efficient medium for high-order harmonics generation in the extreme ultraviolet range. Additionally, the nonlinear absorptive and refractive properties of NPs, as well as their various optical properties, can find their potential applications in optoelectronics, optical limiters, and photonics. Thus the whole set of these studies is linked with the applications and characterization of the Al NPs produced during the ablation of bulk Al targets.

As it was mentioned, two groups of NPs were among the studied samples, i.e. relatively "pure" Al NPs formed during ablation of the aluminium target in a vacuum and oxidized or hydroxide-contained Al NPs. The importance of consideration of the latter case is related to the

role of ingredients of synthesized NPs. In the case of a water environment, the formation of Al(OH)$_3$, AlO(OH), and Al$_2$O$_3$ NPs occurs on the exposing of a newly formed fresh metal surface to the chemical reactions with oxygen and water, while the laser irradiation significantly influences their relative content. In the case of femtosecond ablation, no Al(OH)$_3$ NPs were detected, while the composition was mainly a mixture of Al and Al$_2$O$_3$. Therefore, one can use the term "Al-based NPs" for each of these groups of nanoparticles synthesized in a water environment.

Various reactions at the Al NPs in the water environment can occur during laser ablation. These reactions lead to the formation of Al$_2$O$_3$ and Al (OH)$_3$ molecules under the conditions of growing localized temperatures, which has been discussed in [51]. It is known that oxidation does happen in laser ablation of Al in water or air, and special efforts should be made to minimize the oxidation of the nanoparticles. Particularly, an anionic surfactant stabilizer is used to suppress the aluminium oxide formation.

The oxidation may have a major effect on the long time scale of the nanoparticle formation, their structure (e.g., larger core-shell particles or fully oxidized smaller clusters), and size distributions. As it was stated, the water environment results in the narrower and more uniform size distribution of more or less spherical NPs (Figs. 4.27(a) and 4.27(b) in the case of vacuum and water, respectively). The aging led to the formation of the triangle and pyramidal NPs, Fig. 4.27(c). Due to the limited time scale, the formation of such structures cannot be predicted explicitly from the calculations but can be assumed to be attributed with a highly pronounced effect of the crystal structure from the point of energetically favourable positions of nucleating species, during the continuation of the NPs aggregation.

Below we address the superhydrophilic properties of the glass substrate with Al-based NPs synthesized in water and discuss its connection with the chemical properties of NPs. Aluminium nanoparticles formed at the water environment yield in the formation of aluminium hydroxide. The growth of local temperature at the ablated region and the presence of water as a surrounding environment act perfectly for a reaction to form Al(OH)$_3$. As a result of laser ablation, the Al-based NPs are formed, which are then converted into Al(OH)$_3$. The -OH terminal groups in alumina hydroxide demonstrate the superhydrophilic response as they have a high affinity towards the water.

Aluminium during ablation reacts by the following rout:

$$4Al + 3O_2 = 2Al_2O_3 \qquad\qquad (4.11)$$

$$2Al + 6H_2O = 2Al(OH)_3 + 3H_2 \qquad (4.12)$$
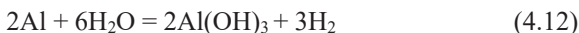
Those studies demonstrated the appearance of triangles and pyramids after some aging period. Annealing temperatures at 300 and 500 C facilitate the formation of triangular/pyramidal shape structures. It was proven that the ablation by picosecond pulses caused the appearance of a much larger concentration of triangle and pyramidal Al-based NPs compared with ablation by femtosecond pulses. The discussed study confirmed the small efficiency of triangles formation using the femtosecond ablating pulses. The structure composition in that case corresponded to $Al(OH)_3$. Thus, a possible mechanism of the formation of such structures, besides the crystal structure effect mentioned above, can be also substantially contributed with the surface chemistry and oxidation.

The wettability of solid substrates is governed by their surface free energy and surface geometrical structure. The superhydrophobic properties of nano- and microstructured surfaces can be explained by a modification of the roughness of the deposited coating. Control of the wetting properties of Al surfaces can protect them from corrosion. Without the surface roughness, water static contact angles on the Al surface before and after stearic acid modification were only about 48° and 90°, respectively. The formation of materials with tuneable wettability is important for applications ranging from antifouling to waterproofing surfaces.

It was shown in present studies that the resulting size, shape, and morphology of generated NPs generated are not only material properties dependent, but also are sensitive to the experimental conditions such as the incident fluence, the pulse duration, the laser wavelength, and surrounding medium. Of course, the theoretical approach did not account for the description of all the possible processes involved in the pulsed laser ablation in liquids (like chemical reactions, oxidation, and non-linear effects of the laser beam propagation in water). The detailed knowledge of the NPs formation mechanisms dependence on the irradiation conditions, however, allows for their productions of the desired properties. The discussed study is a demonstration of such a procedure. For this moment, based on simulation results and the experimental measurements one can conclude that by means of changing the pulse duration and fluence, one can trigger one or another mechanism (or a mixture of them) of the NPs generation. In other words, there exist optimal laser irradiation parameters for manufacturing the colloidal solutions with the desired size distribution and the mean value. This gives an opportunity for the NPs formation with predesigned properties that becomes the topic of future investigations.

References to Chapter 4

[1]   K.G. Stamplecoskie, J.C. Scaiano, V.S. Tiwari, H. Anis, Optimal size of silver nanoparticles for surface-enhanced Raman spectroscopy, J. Phys. Chem. C 115 (5) (2011) 1403-1409.

[2]   M. Darroudi, M. Ahmad, R. Zamiri, R. Abdullah, A. Ibrahim, N. Shameli, K. Shahril, M. Husin, Preparation and characterization of gelatin mediated silver nanoparticles by laser ablation, J. Alloys&Compounds 509 (4) (2011) 1301-1304.

[3]   M. Valverde-Alva, T. García-Fernández, M. Villagrán-Muniz, C. Sánchez-Aké, R. Castañeda-Guzmán. E. Esparza-Alegría. C. Sánchez-Valdés. J. Llamazares, C. Herrera, Synthesis of silver nanoparticles by laser ablation in ethanol: A pulsed photoacoustic study, Appl. Surf. Sci. 355 (11) (2015) 341-349.

[4]   V. Nikolov, R. Nikov, I. Dimitrov, N. Nedyalkov, P. Atanasov, M. Alexandrov, D. Karashanova, Modification of the silver nanoparticles size-distribution by means of laser light irradiation of their water suspensions, Appl. Surf. Sci. 280 (9) (2013) 55-59.

[5]   M. Darroudi, M. Ahmad, R. Zamiri, A. Abdullah, N. Ibrahim, A. Sadrolhosseini, Time-dependent preparation of gelatin-stabilized silver nanoparticles by pulsed Nd:YAG laser, Sol. Stat. Sci. 13 (3) (2011) 520-524.

[6]   R. Das, S. Nath, D. Chakdar, G. Gope, R. Bhattacharjee, Synthesis of Ag NPs and their optical properties, J. Exper. Nanoscien. 5 (3) (2010) 357-365.

[7]   D. Rativa, R. E. De Araujo, A.S.L. Gomes, Nonresonant high-order nonlinear optical properties of silver nanoparticles in aqueous solution, Opt. Express 16 (23) (2008) 19244-19254.

[8]   M. Mashayekh, D. Dorranian, Size-dependent nonlinear optical properties and thermal lens in silver nanoparticles, Optik 125 (19) (2014) 5612-5617.

[9]   R. A. Ganeev, M. Baba, A. I. Ryasnyansky, M. Suzuki, H. Kuroda, Characterization of optical and nonlinear optical properties of silver nanoparticles prepared by laser ablation in various liquids, Opt. Commun. 240 (4-6) (2004) 437-448.

[10] R. A. Ganeev, A. I. Ryasnyansky, A. L. Stepanov, T. Usmanov, Saturated absorption and reverse saturated absorption of Cu:SiO2 at $\lambda = 532$ nm, Phys. Stat. Sol. B 241 (3) (2004) R1-R4.

[11] M. López-Arias, M. Oujja, M. Sanz, R. A. Ganeev, G. S. Boltaev, N. K. Satlikov, R. I. Tugushev, T. Usmanov, M. Castillejo, Low-order harmonic generation in metal ablation plasmas in nanosecond and picosecond laser regimes, J. Appl. Phys. 111 (4) (2012) 043111.

[12] R. A. Ganeev, M. Suzuki, M. Baba, H. Kuroda, High-order harmonic generation from laser plasma produced by pulses of different duration, Phys. Rev. A 76 (2) (2007) 023805.

[13] H. Singhal, R. A. Ganeev, P. A. Naik, J. A. Chakera, U. Chakravarty, H. S. Vora, A. K. Srivastava, C. Mukherjee, C. P. Navathe, S. K. Deb, P. D. Gupta, High-order harmonic generation in a plasma plume of in situ laser-produced silver nanoparticles, Phys. Rev. A 82 (4) (2010) 043821.

[14] G. S. Boltaev, R. A. Ganeev, P. S. Krishnendu, S. K. Maurya, P. V. Redkin, K. S. Rao, K. Zhang, C. Guo, Strong third-order optical nonlinearities of Ag nanoparticles synthesized by laser ablation of bulk silver in water and air, Appl. Phys. A 124 (11) (2018) 766.

[15] Y.-P. Sun, J. E. Riggs, H. W. Rollins, R. Guduru, Strong optical limiting of silver-containing nanocrystalline particles in stable suspensions, J. Phys. Chem. B 103 (1) (1999) 77-82.

[16] R. A. Ganeev, A. I. Ryasnyansky, S. R. Kamalov, M. K. Kodirov, T. Usmanov, Nonlinear susceptibilities, absorption coefficients and refractive indices of colloidal metals, J. Phys. D: Appl. Phys. 34 (11) (2001) 1602-1610.

[17] R. A. Ganeev, A. S. Zakirov, G. S. Boltaev, R. I. Tugushev, T. Usmanov, P. K. Khabibullaev, T. W. Kang, A. A. Saidov, Structural, optical, and nonlinear optical absorption/refraction studies of the manganese nanoparticles prepared by laser ablation in ethanol, Opt. Mater. 33 (3) (2011) 419-423.

[18] R. Sato, M. Ohnuma, K. Oyoshi, Y. Takeda, Spectral investigation of nonlinear local field effects in Ag nanoparticles, J. Appl. Phys. 117 (11) (2015) 113101.

[19] G. K. Podagatlapalli, S. Hamad, S. P. Tewari, S. Sreedhar, M. D. Prasad, V. R. Soma, Silver nano-entities through ultrafast double ablation in aqueous media for surface enhanced Raman scattering and photonics applications, J. Appl. Phys. 113 (7) (2013) 073106.

[20] H. Sanchez-Esquivel, K. Y. Raygoza-Sanchez, R. Rangel-Rojo, B. Kalinic, N. Michieli, T. Cesca, G. Mattei, Ultra-fast dynamics in the nonlinear optical response of silver nanoprism ordered arrays, Nanoscale 10 (11) (2018) 5182-5190.

[21] H. Singhal, R. A. Ganeev, P. A. Naik, A. K. Srivastava, A. Singh, R. Chari, R. A. Khan, J. A. Chakera, P. D. Gupta, Study of high-order harmonic generation from nanoparticles, J. Phys. B: At. Mol. Opt. Phys. 43 (2) (2010) 025603.

[22] R. A. Ganeev, M. Suzuki, M. Baba, M. Ichihara, H. Kuroda, High-order harmonic generation in Ag nanoparticle-containing plasma, J. Phys. B: At. Mol. Opt. Phys. 41 (4) (2008) 045603.

[23] M. L. Naudeau, R. J. Law, T. S. Luk, T. R. Nelson, S. M. Cameron, J. V. Rudd, Observation of nonlinear optical phenomena in air and fused silica using a 100 GW, 1.54 μm source, Opt. Express 14 (13) (2006) 6194-6200.

[24] R. A. Ganeev, H. Singhal, P. A. Naik, J. A. Chakera, M. Kumar, P. D. Gupta, Fourth-order harmonic generation during parametric four-wave mixing in the filaments in ambient air, Phys. Rev. A 82 (4) (2010) 043812.

[25] Y. Jiang, Y. Ma, Z. Fan, P. Wang, X. Li, Y. Wang, Y. Zhang, J. Shen, G. Wang, Z.-J. Yang, S. Xiao, Y. Gao, J. He, Abnormal nonlinear optical properties of hybrid graphene-TiO_2 nanostructures, Opt. Lett. 43 (3) (2018) 523-526.

[26] S. I. Alnassar, E. Akman, B. G. Oztoprak, E. Kacar, O. Gundogdu, A. Khaleel, A. Demir, Study of the fragmentation phenomena of TiO2

nanoparticles produced by femtosecond laser ablation in aqueous media, Opt. Laser Technol. 51 (1) (2013) 17-23.

[27] J. S. Golightly, A. W. Castleman, V. Pennsyl, Analysis of titanium nanoparticles created by laser irradiation under liquid environments, J. Phys. Chem. B 110 (40) (2006) 19979-19984.

[28] A. H. Yuwono, J. Xue, J. Wang, H. I. Elim, W. Ji, Y. Li, T. J. White, Transparent nanohybrids of nanocrystalline TiO2 in PMMA with unique nonlinear optical behavior, J. Mater. Chem. 13 (6) (2003) 1475-1479.

[29] V. Gayvoronsky, A. Galas, E. Shepelyavyy, T. Dittrich, V. Y. Timoshenko, S. A. Nepijko, M. S. Brodyn, F. Koch, Giant nonlinear optical response of nanoporous anatase layers, Appl. Phys. B 80 (1) (2005) 97-100.

[30] C. C. Evans, J. D. B. Bradley, E. A. Martí-Panameño, E. Mazur, Mixed two- and three-photon absorption in bulk rutile (TiO2) around 800 nm, Opt. Express 20 (3) (2012) 3118-3128.

[31] L. Jyothi, R. Kuladeep, D. N. Rao, Solvent effect on the synthesis of cobalt nanoparticles by pulsed laser ablation: Their linear and nonlinear optical properties, J. Nanophot. 9 (1) (2015) 93088.

[32] R. A. Ganeev, A. I. Ryasnyansky, M. K. Kodirov, S. R. Kamalov, V. A. Li, R. I. Tugushev, T. Usmanov, Optical limiting in cobalt-doped polyvinylpyrrolidone, Appl. Phys. B 74 (1) (2002) 47-51.

[33] K. S. Rao, R. A. Ganeev, K. Zhang, Y. Fu, G. S. Boltaev, P. S. Krishnendu, P. V. Redkin, C. Guo, Laser ablation–induced synthesis and nonlinear optical characterization of titanium and cobalt nanoparticles, J. Nanopart. Res. 20 (10 (2018) 285.

[34] E. B. Barmina, E. Stratakis, C. Fotakis, G. A. Shafeev, Generation of nanostructures on metals by laser ablation in liquids: New results, Quantum Electron. 40 (1) (2010) 1012.

[35] J. Li, C. Liu, Z. Xie, Synthesis and surface plasmon resonance properties of carbon-coated Cu and Co nanoparticles, Mater. Res. Bull. 46 (5) (2011) 743-747.

[36] T. Karali, N. Can, L. Valberg, A. L. Stepanov, P. D. Townsend, Ch. Buchal, R. A. Ganeev, A. I. Ryasnyansky, H. G. Belik, M. L. Jessett, C. Ong, Optical properties and luminescence of metallic nanoclusters in ZnO:Cu, Physica B 363 (1-4) (2005) 88-95.

[37] H. Ahmad, N. E. Ruslan, M. A. Ismail, Z. A. Ali, S. A. Reduan, C. S. J. Lee, S. W. Harun, Silver nanoparticle-film based saturable absorber for passively Q -switched erbium-doped fiber laser (EDFL) in ring cavity configuration, Laser Phys. 26 (9) (2016) 095103.

[38] T. A. Chevychelova, I. G. Grevtseva, A. I. Zvyagin, M. S. Smirnov, O. V. Ovchinnikov, R. A. Ganeev, Nonlinear optical properties of Ag nanoparticles with and without silicon dioxide shell, Opt. Mater. 111 (11) (2021) 110583.

[39] A. Arbouet, N. Del Fattia, F. Vallee, Optical control of the coherent acoustic vibration of metal nanoparticles, J. Chem. Phys. 124 (14) (2006) 144701.

[40] A. Crut, P. Maioli, N. Del Fatti, F.Vallee, Time-domain investigation of the acoustic vibrations of metal nanoparticles: Size and encapsulation effects, Ultrasonics 56 (2015) 98-108.

[41] W. Huang, W. Qian, M. A. El-Sayed, The optically detected coherent lattice oscillations in silver and gold monolayer periodic nanoprism arrays: the effect of interparticle coupling, J. Phys. Chem. B 109 (40) (2005) 18881-18888.

[42] M. A. Mahmoud, D. O'Neil, M. A. El-Sayed, Shape- and symmetry-dependent mechanical properties of metallic gold and silver on the nanoscale, Nano Lett. 14 (2) (2014) 743−748.

[43] S. K. Maurya, A. Rout, R. A. Ganeev, C. Guo, Effect of size on the saturable absorption and reverse saturable absorption in silver nanoparticle and ultrafast dynamics at 400 nm, J. Nanomater. 2019 (2019) 9686913.

[44] R. A. Ganeev M. Suzuki, M. Baba, M. Ichihara, H. Kuroda, Low- and high-order nonlinear optical properties of Au, Pt, Pd, and Ru nanoparticles, J. Appl. Phys. 103 (6) (2008) 063102.

[45] A. Karimi, Z. Fakhroueian, A. Bahramian, N. P. Khiabani, J. B. Darabad, R. Azin, S. Arya, Wettability alteration in carbonates using zirconium oxide nanofluids: EOR implications, Energy Fuels 26 (2) (2012) 1028-1036.

[46] M. Iqbal, S. A. Khan, D. S. Ivanov, R. A. Ganeev, V. V. Kim, G. S. Boltaev, N. A. Abbasi, S. Shaju, M. E. Garcia, B. Rethfeld, A. S. Alnaser, The mechanism of laser-assisted generation of aluminum nanoparticles, their wettability and nonlinearity properties. Appl. Surf. Sci. 527 (14) (2020) 146702.

[47] E. G. Goh, X. Xu, P. G. McCormick, Effect of particle size on the UV absorbance of zinc oxide nanoparticles, Scripta Materialia 78-79 (2014) 49-52.

[48] C.-Y. Shih, M. V. Shugaev, C. Wu, L. V. Zhigilei, The effect of pulse duration on nanoparticle generation in pulsed laser ablation in liquids: Insights from large-scale atomistic simulations, Phys. Chem. Chem. Phys. 22 (13) (2020) 7077-7099.

[49] I. N. Saraeva, S. I. Kudryashov, A. A. Rudenko, M. I. Zhilnikova, D. S. Ivanov, D. A. Zayarny, A. V. Simakin, A. A. Ionin, M. E. Garcia, Effect of fs/ps laser pulsewidth on ablation of metals and silicon in air and liquids, and on their nanoparticle yields, Appl. Surf. Sci. 470 (3) (2018) 1018-1034.

[50] E. Stratakis, M. Barberoglou, C. Fotakis, G. Viau, C. Garcia, G. A. Shafeev, Generation of Al nanoparticles via ablation of bulk Al in liquids with short laser pulses, Opt. Express 17 (15) (20090 12650-12659.

[51] K. Zhang, D. S. Ivanov, R. A. Ganeev, G. S. Boltaev, P. S. Krishnendu, S. C. Singh, M. E. Garcia, I. N. Zavestovskaya, C. Guo, Pulse duration and wavelength effects of laser ablation on the oxidation, hydrolysis, and aging of aluminum nanoparticles in water, Nanomaterials. 9 (3) (2019) 767.

CHAPTER 5

MORPHOLOGICAL AND OPTICAL CHARACTERISTICS OF NANOPARTICLES

In this chapter, we describe the characteristics of nanoparticles. We discuss the systematic structural analysis of the CuO and Cu_2O nanostructures, which were obtained during ablation of Cu in water using various pulses (5 ns, 200 ps, and 30 fs), wavelength (1064 and 355 nm radiation of 5 ns pulses, 800 nm radiation of picosecond and femtosecond pulses) and energy (high and low fluence), using the scanning electron microscopy and spectroscopic techniques. The effects of pulse duration and wavelength on particles' formation and aging will be systematically analyzed. The stability of CuO/Cu_2O nanostructures was studied using SEM a few months after ablation of bulk Cu.

The ablation of Al targets in distilled water by 800 nm laser pulses of different durations (5 ns, 200 ps, and 30 fs) is analyzed along with the study of the influence of different wavelengths (1064 nm and 355 nm) of the heating radiation on this process. We analyze the morphology of NPs prepared under different pulse durations, which changes significantly over time. We discuss how the pulse duration influences the aging of NPs. In addition, the compositions of NPs obtained using different durations and wavelengths of heating pulses are found to vary significantly.

Finally, we analyze the influence of pulse duration (5 ns, 200 ps, and 60 fs), ablation energy (different energy gradients under picosecond pulse condition) and the temperature of water (high and low) on the process of ablation of the metal target (indium) with low hardness and melting point. The effect of these factors on the formation and aging of NPs was determined by absorption spectroscopy, scanning electron microscopy, transmission electron microscopy, and X-ray diffraction. The ablation of the Zn target, which had high hardness and melting point, in distilled water by pulses with different duration showed that Zn and ZnO NPs existed simultaneously. In addition, the size distribution range and stability of NPs are strongly dependent on the pulse duration used in ablation.

5.1. Structural variations during aging of the particles synthesized by laser ablation of copper in water

Pulsed laser ablation in liquid (PLAL) can be used to prepare metals and oxide micro/nanoparticles possessing different structure and compositions. PLAL provides a simple and efficient way to synthesize micro/nanoparticles compared to chemical methods. In addition, various controllable factors, such as pulse duration and type of liquid [1], allow modifying the composition, morphology, and structure of micro/nanoparticles. The discussed research has clearly shown that external experimental conditions can affect the properties of resulting oxide micro/nanoparticles through laser ablation. For example, the CuO particles from ablated bulk Cu in water using Q-switched pulsed laser (532 nm, 5 ns, 100 mJ/pulse) have been analyzed, and it was found that the increase of annealing temperature can reduce the size of particles [2]. Meanwhile, annealing also affects the band gap and other optical properties. The ablation by 120 fs, 780 nm radiation of the Cu target in acetone showed that both Cu and CuO particles were present in the colloidal solution [3]. These particles had spherical shape with a mean diameter of 9 nm. The optical absorbance carried out immediately after ablation has shown the presence of surface plasmon resonance (SPR) at 602 nm. The green colour of particles in acetone solution maintained stability even after a long time. Another group of studies using Nd:YAG laser (1064 nm, 7 ns) showed that Cu target ablated in water mainly leads to the formation of Cu_2O, while the products during ablation in ethanol are Cu particles [4]. However, if the ablation condition was changed to Nd:YAG laser, 532 nm, 10 ns, two kinds of stable oxides are formed in water: monoclinic CuO and cubic Cu_2O. In addition, the application of different solvents allows synthesizing of different types of composite particles. Generally speaking, many external conditions and their combinations bring uncertainty to the variations of the morphology and size of micro/nanoparticles during ablation, while providing the possibilities for more precise control of the ablation process to obtain particles with controllable morphology and size.

Below we discuss the systematic structural analysis of the CuO and Cu_2O nanostructures, which were obtained during ablation of Cu in water using various pulses (5 ns, 200 ps, and 30 fs), wavelength (1064 and 355 nm radiation of 5 ns pulses, 800 nm radiation of picosecond and femtosecond pulses) and energy (high and low fluence), using the scanning electron microscopy (SEM) and spectroscopic techniques [5]. The effects of pulse duration and wavelength on particles' formation and aging were systematically analyzed. Particles with uniform morphology

and larger sizes were synthesized. The stability of CuO/Cu_2O nanostructures was studied using SEM a few months after ablation of bulk Cu. It was found that the application of ultra-short pulses in ablation allows obtaining smaller-sized particles with narrower distribution, while the pulse wavelength has a decisive effect on the morphology of the particles.

5.1.1. Experimental arrangements

These studies were carried out using a focused pulsed laser to irradiate the surface of bulk Cu with a thickness of 3 mm, which was cleaned to remove the oxide film and stains on the surface. Cu target was kept in a quartz cell filled with distilled water. During ablation from the top side, the quartz cell was moved along X and Y directions to ensure that the ablation occurs at different places on the surface of Cu. Slow and uniform movement of the cell was maintained to ensure minimal impact on the liquid level, which was 25 mm above the target surface. The laser pulse, which was focused by a focal lens with f=150 mm, was irradiated from the top of the cell on the surface of the target. The laser beam focal length increases in water. The amount of additional focal length is directly proportional to the water height.

Experiments were accomplished using a regenerative amplifier, which provided the 800 nm pulses at repetition rate of 1 kHz and pulse durations of either 30 fs (laser energy: 0.56 mJ, scan speed: 5 mm/s during experiments) or 200 ps (laser energy: 0.56 mJ, scan speed: 5 mm/s during experiments). The nanosecond Nd: YAG laser provided 1064 nm pulses (as well as its third harmonic (λ=355 nm)) of 5 ns duration at 10 Hz repetition rate (laser energy: between 10 to 100 mJ, scan speed: 5 mm/s during experiments), which were also used in these studies. The influence of pulse energy on the ablation was analyzed using three pulse durations (5 ns, 200 ps and 30 fs pulses). The duration time of ablation was maintained at 30 minutes during each experiment.

The size, nanostructure, distribution, and morphology of particles obtained by PLAL were analyzed by SEM, thus allowing determining the change of morphology during the aging process. The chemical composition and microscopic structure of particles were analyzed by X-ray Diffraction (XRD) and Energy Dispersive Spectroscopy (EDS). The absorption spectroscopy was carried out to determine the band gaps and SPRs of particles in the water colloids.

Table 5.1. The parameters of experiments. Reproduced from [5] with permission from Springer.

	Nd: YAG laser		Ti:sapphire laser Picosecond pulses	Ti:sapphire laser Femtosecond pulses
Wavelength	1064 nm	355 nm	800 nm	800 nm
Pulse duration	5 ns		200 ps	30 fs
Repetition rate	10 Hz		1000 Hz	1000 Hz
Peak power	1×10^7 W		3×10^6 W	2×10^{10} W
Average power	0.54 W		0.56 W	0.56 W
Laser fluence	76 J/cm^2		0.79 J/cm^2	0.79 J/cm^2
Laser energy	54.0 mJ		0.56 mJ	0.56 mJ
Scan speed	5 mm/s		5 mm/s	5 mm/s
Spot size	~ 0.3 mm		~ 0.3 mm	~ 0.3 mm

The experimental parameters are shown in Table 5.1. The information presented in this table allows determining the role of different pulses in the ablation process, similarly to earlier presented data for ablation and formation of nanoparticles using pulses of different duration [6]. The purity of the Cu target used in this study was 99.99%, in accordance with the data provided by the manufacturer. According to the quality analysis report provided by the manufacturer, the Cu bulk contained some impurities. The types of impurity are given in the test report. Most of the impurities did not show in EDS because their content was extremely small, but some elements, such as Cl and K, showed very weak EDS peaks. In addition, there was a strong peak of Si because EDS was detected by using the silicon wafers to prepare the ablated samples. Moreover, there were three main sources of oxygen in EDS. Firstly, oxygen is the most abundant impurity in the Cu target according to the analysis report. Secondly, in order to improve the surface smoothness of the silicon wafer, a very thin oxide film is deposited on the surface of a silicon wafer, which was shown up in the EDS tests with silicon. Thirdly, there were oxygen components in copper oxide and cuprous oxide formed by oxidation of copper particles in air and liquid. The oxygen element presented in the EDS is a collective representation of many sources superimposed.

For some elements (especially impurity elements) only a weak single peak appeared during EDS measurements. The content of impurity elements in the sample was extremely low. When the EDS analysis was conducted on different positions of the sample, we found that the individual impurity elements appeared occasionally. The presence of the element with only one peak during the EDS measurements is also a common case in previous studies [7].

EDS supported the expected results. In [8], the authors have presented the EDS of CuO and Cu₂O nanostructures prepared with chemical methods which coincided with discussed results. The amount of the elements was measured using the EDS of the CuO films deposited on the surfaces of a silicon substrate. In the meantime, we analyzed the EDS of the pure silicon substrate.

5.1.2. Spectroscopy of colloidal suspensions

The initial colloidal solution containing particles prepared by ablation using different pulse duration (nanosecond (ns), picosecond (ps), femtosecond (fs)) showed green colour. However, the colour of a solution obtained by ps pulses was the deepest, while that of ns and fs was relatively light. The depth of colour of the colloidal solution depends mainly on the concentration of particles. It is worth noting that in the case of ns pulses with a 10 Hz repetition rate, the number of pulses acting on the target surface during the same time (30 min) was 100 times less compared with the case of ps pulses. In addition, the water level has a strong effect on the laser power at the 1064 nm wavelength. About 5.5% of the laser power will be lost during the propagation of 1064 nm radiation through a 2 mm thick water layer. A 25 mm thick water layer above the surface of the target was used, which weaken the energy of the laser pulses (1064 nm, 5 ns) on the target surface. The total amount of particles produced by ns pulses during the same ablation time was significantly lower than that in the case of ps pulses.

During ablation by fs pulses, strong white light was emitted when these pulses propagated through the liquid. The white light generation is a threshold effect, which depends on the power of the focused beam. This effect led to a decrease of pulse intensity on the target surface, resulting in lower efficiency of nanoparticles formation. As a result, the concentration of particles, in that case, was significantly smaller than in the case of ablation using ps pulses. Therefore, the efficiency of the synthesis of particles at the condition of ablation by ns and fs pulses during these experiments was significantly lower than that of ps pulses, which explained the lighter colour of suspensions in the former cases. After a few hours from ablation, the colloidal solutions of particles obtained by ns and ps pulses showed brown colour, while the change of the colour of a solution obtained by fs pulses was insignificant. Since then, colloidal solutions became extremely stable in colour.

The absorption spectra of suspensions perfectly reflected the temporal change of colour of the nanoparticles-contained suspensions. The

absorption spectra of the newly prepared colloidal solutions of particles were measured immediately after ablation [Fig. 5.1(a)]. The absorption spectra of the solution obtained by PLAL were compared using different pulse durations. Although the duration time of ablation was the same, the absorption of the sample obtained by ps pulses was significantly stronger than that of the other two (ns and fs). The difference in absorption spectra of particles obtained by various wavelengths (1064 and 355 nm of 5 ns pulses) correlated with the difference in the morphology and size of these particles, which was confirmed by SEM measurements (see the following subsection).
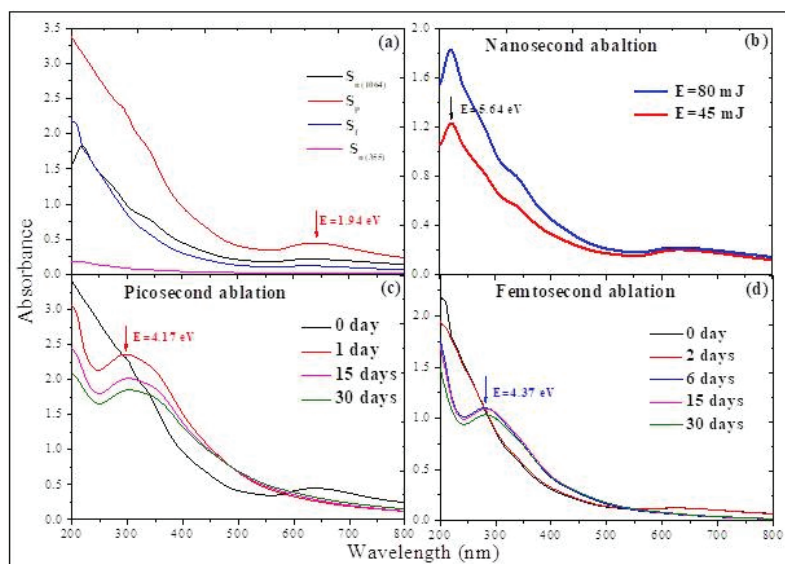
Fig. 5.1. Absorption spectra of the suspensions containing CuO/Cu$_2$O nanostructures synthesized by ablation in distilled water. (a) Spectra of suspensions obtained by various pulse durations (5 ns, 200 ps and 30 fs) and wavelengths (1064 and 355 nm in the case of 5 ns pulses). (b) Spectra of suspensions obtained at different energies of 1064 nm, 5 ns pulses. (c) Spectra of aged colloidal solutions obtained by ps pulses. (d) Spectra of aged colloidal solutions obtained by fs pulses. Reproduced from [5] with permission from Springer.

The absorption peak at λ=640 nm (E=1.94 eV) was observed in three samples [5 ns (1064 nm), 200 ps (800 nm), and 30 fs (800 nm)], which showed the highest intensity in the case of ps pulses. One can assume that

this absorption peak is related to the SPR of non-spherical Cu nanoparticles. It is worth mentioning that there are many different reports about the location of the absorption peaks of Cu particles, which were mainly attributed to the difference in the ablation conditions and the physical properties of nanoparticles.

During laser ablation of the copper, the change of the colour of the suspension was observed due to the formation of the nanoparticles of the copper. The colour of the suspension became green, which indicated stronger linear absorption in the near-infrared range. The transparency and loss of the ablation pulses energy were negligible at wavelengths of 800 nm and 1064 nm of the probe pulses (Fig. 5.1). In the case of ablation with 355 nm, the strong absorption of the ablation pulses energy led to the decreased concentration of the ablated copper nanoparticles (see Fig. 5.1(a), solid purple). As was mentioned, in the case of the femtosecond ablation the energy of ablating pulses was lost due to the white light generation starting from the surfaces of the cell and continuing inside the water. The conversion of the energy of ablating femtosecond pulses to white light generation led to the decrease of the energy of pulses on the surfaces of the bulk copper immersed in the distilled water for ablation of the copper nanoparticles.

In the case of 5 ns pulses (λ=1064 nm), ablation was carried out using two different energies [E=80 and 45 mJ), Fig. 5.1(b)]. Spectral measurements showed that the absorption of the colloidal solution obtained at higher energy (E=80 mJ) is stronger. The intensity of the absorption spectrum reflects the amount of the particles contained in the colloidal solution, that is, the volume of particles formation. The ablation efficiency of particles depends on the type of material used, the heat of vaporization, and laser power used. Higher pulse energy corresponds to higher laser power (at the same repetition rate, 10 Hz), resulting in a larger nanoparticle generation rate. Therefore, more nanoparticles can be produced at higher ablation energy (80 mJ), while the shapes of absorption curves in these two cases are similar to each other. Besides a broad absorption band located at λ=640 nm, there is a very strong absorption peak that appeared at λ=230 nm (E=5.64 eV) in the case of ablation by 5 ns, 1064 nm pulses. This peak (λ=230 nm) is related to the copper electrons band-to-band transition. The oxidation process under these conditions is extremely rapid. The interaction time between a single ns pulse and the target surface is relatively long. The less stable particles formed at these conditions easily interact with the surrounding environment, which leads to faster aging.

In the case of ps ablation, the UV spectrum of the initial colloidal solution of particles showed a wide "shoulder" at λ=640 nm. However, the

spectra significantly changed during the subsequent measurements [Fig. 5.1(c)]. The absorption peak at 640 nm disappeared, while a very strong absorption peak appeared near λ=300 nm (E=4.17 eV), which is caused by the Brillouin transitions of Cu_2O. This observation pointed out the formation of Cu_2O during aging. The spectra measured at the 2nd, 15th, and 30th days were similar to each other. Meanwhile, the colour of the colloidal solution was changed from green to brown. The species obtained at the beginning of ablation were mainly Cu nanoparticles, which led to the green colour of the colloidal solution. However, during aging, the particles reacted with oxygen in the solution to form CuO/Cu_2O shell during the aging process, which led to the change of colour from green to brown. This led to the change of absorption peak position.

The absorption peak located at λ=640 nm in the case of fs ablation was smaller than the one observed using ps pulses mainly due to the lower rate of particles synthesized by fs pulses [Fig. 5.1(d)]. Similar to the sample obtained by ps pulses, the common feature of the sample synthesized by fs pulses after several days of aging was a strong resonance peak at λ=300 nm. It is noteworthy that, compared with the former (ns and ps) regimes of ablation, the aging process in the case of fs ablation was relatively slow. On the second day after ablation, the colour of the colloidal solutions obtained by ns or ps pulses changed due to oxidation, and the absorption spectra also showed the corresponding changes. However, the absorption spectrum of the solution obtained by ablation using fs pulses did not show a significant difference during the first few days after ablation due to the slow oxidation process.

As it has been shown in the case of longer pulses (ns and ps), the plasma plume produced during ablation forms the nanoparticles. The longer interaction time between laser radiation and target surface caused longer heating. The internal structure of particles was determined by cooling and aggregation of the plume interacting with the external environment for a longer period. On the other hand, the particles synthesized under ultra-short pulse (fs) ablation did not participate in a similar heating/cooling process, which made those particles more stable. This probably was a reason why the colour and spectral curves of the colloidal solution changed in the case of ns and ps pulses, while the aging of a solution under fs pulses ablation was relatively slow and more stable. In addition, from the analysis of these spectra, one can infer a negligible absorption of the long-wavelength part of the spectrum, which means that in the case of 800 and 1064 nm relatively long ablating pulses the absorption in suspension was insignificant.

5.1.3. Morphology of particles

SEM was carried out to characterize the morphology, size, and distribution of particles obtained at different pulse durations and wavelengths. Taking into account the fact that the initial particles became oxidized during a very short time (a few hours), which led to unstable morphology, the analysis was mainly carried using the samples, where the nanoparticles completed the oxidation process and remained at stable conditions. The SEM images of particles obtained under different pulse durations are shown in Fig. 5.2. These studies demonstrated that pulse duration during ablation of Cu target in water plays a crucial role in the process of particles' formation, which resulted in the remarkable difference of the morphology and particle sizes of synthesized species.
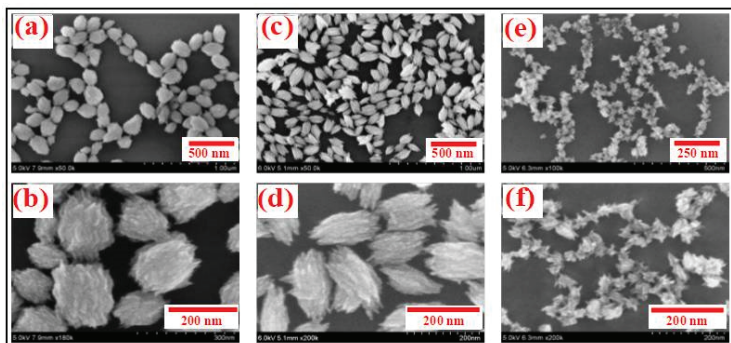
Fig. 5.2. SEM images of CuO/Cu_2O nanostructures obtained in distilled water using the pulses of different duration. (a-b) ablation using 5 ns, 1064 nm pulses; (c-d) ablation using 200 ps, 800 nm pulses; (e-f) ablation using 30 fs, 800 nm pulses. Reproduced from [5] with permission from Springer.

The particles obtained at some conditions, particularly during ablation by 800 nm, 200 ps pulses, showed the same morphology, and the particle sizes had a very good homogeneity. SEM images showed that the particles obtained by 200 ps pulses were smaller compared with the 5 ns case. The conclusion that the size of particles became smaller under the condition of shorter pulses ablation was further confirmed in the case of 30 fs pulses. In addition, the synthesized particles demonstrated a common feature. Their surface did not show a smooth and holistic structure but rather contained the aggregated filamentary structures.
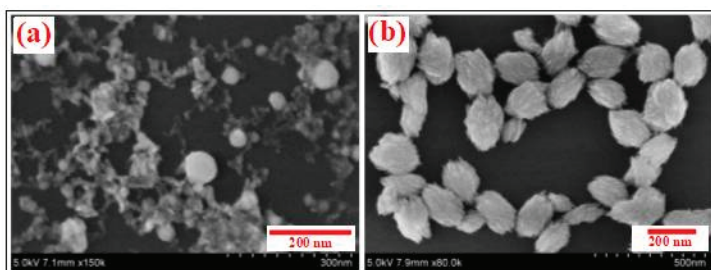
Fig. 5.3. SEM images of CuO/Cu₂O nanostructures obtained in distilled water using 5 ns pulses. (a) Ablation using 5 ns, 355 nm radiation. (b) Ablation using 5 ns, 1064 nm radiation. Reproduced from [5] with permission from Springer.

In order to analyze the effect of wavelength on the morphology of particles, the ablation of the Cu target was carried out using fundamental (1064 nm) and third harmonic (355 nm) pulses of Nd: YAG laser (t=5 ns). The images of particles synthesized at these conditions are shown in Fig. 5.3. In the case of 355 nm radiation, the morphology of particles always presented the regular spherical structure. Overall, the distribution of particle sizes was extremely broad [from a few nanometres to 100 nm, Fig. 5.3(a)]. It was found that there are no significant morphology differences between initial and aging particles. The ablation using 1064 nm, 5 ns pulses showed a completely different pattern. The particle size became larger, while the size distribution range was narrower compared with the former case [Fig. 5.3(b)]. In addition, the ablation was analyzed at different energies (45 and 80 mJ) of 5 ns, 1064 nm pulses, which showed no significant difference in the size and morphology of synthesized particles in these two cases.

The temporal variation/stabilization of particles during the aging process was analyzed using the sample obtained by 200 ps, 800 nm pulses. The SEM images at different periods from ablation are shown in Fig. 5.4. As was mentioned earlier, the particles in the colloidal solution obtained by PLAL rapidly oxidized during a short period (a few hours), which changes the colour of the solution from green to brown. After that, the colour of the solution became stable. The brown solution was analyzed by SEM, which showed that there was no obvious difference between the measurements at different periods from ablation. Thus the morphology and particle size of particles in brown solution maintained excellent stability.
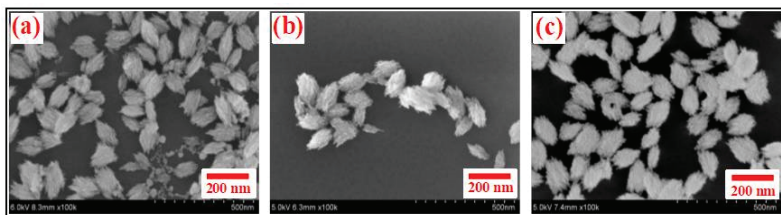
Fig. 5.4. Dynamics of CuO/Cu$_2$O particles' morphology variations after laser ablation of bulk Cu using 200 ps, 800 nm pulses. (a) Within 24 hours from ablation. (b) One month from ablation. (c) Four months from ablation. Reproduced from [5] with permission from Springer.

The influence of pulse duration on different metal targets is different. At the beginning of these experiments, it was not clear which pulse duration could ablate the copper target more efficiently. The results show that the morphology and particle size of nanoparticles obtained with various pulse durations vary during the ablation process. In the case of 5 ns, the difference in the wavelength of heating pulses (1064 and 355 nm) showed a significant effect on the morphology. Similarly, the effect of pulse duration (200 ps and 30 fs) in the ablation process was studied at 800 nm wavelength.

The wavelength dependence in the case of picosecond ablation was difficult to analyze due to the low conversion efficiency towards the second harmonic of 800 nm, 200 ps pulses. Due to the low energy of 400 nm pulses, the comparative analysis of the ablation of copper and the formation of nanoparticles in water using two wavelengths (800 and 400 nm) was not performed. On the other hand, the inefficiency in the application of the 355 nm, 5 ns pulses for ablation and formation of copper nanoparticles was demonstrated due to the strong linear absorption of the light at the wavelength of 355 nm.

The larger ablation threshold of copper can be related to its larger thermal depth as compared to aluminium and titanium. The large thermal depth of copper results in a lesser localization of the excitation energy. Thereby, it causes difficulties during the melting and evaporation of the copper surface. The difference between the ablation rates of metals in the visible and infrared ranges originates from the different optical and thermal proprieties of materials at these wavelengths.

In order to analyze the composition of particles, EDS of evaporated suspension was carried out. Apart from Cu and silicon, on which the samples were dried, there were some impurities. Among them, the

presence of potassium (K) and chlorine (Cl) was detected. The EDS in Fig. 5.5a shows all the elements in the studied sample. The sources of these elements are very clear. Silicon comes from the base used to measure EDS, while potassium and chlorine may come from the impurities in the Cu target. However, the important parameter here is the proportion between the basic elements of a sample (oxygen and copper).
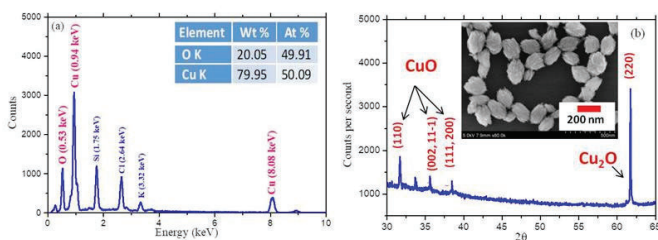
Fig. 5.5. (a) EDS and (b) XRD of the particles produced during ablation of bulk Cu using 200 ps, 800 nm pulses. Reproduced from [5] with permission from Springer.

Two main peaks of copper were located at 0.94 and 8.08 keV, respectively, while the peak attributed to oxygen appeared at 0.53 keV. The table embedded in Fig. 5.5a presents the parameters of two (O and Cu) elements. After removing impurities, only the relative atomic and weight parts of oxygen and copper are shown in the table. The comparative ratio of the atoms present in the sample should be 1:1 for CuO while the measurements showed 49.91:50.09, which is almost the same.

Structural analysis of particles obtained by 200 ps, 800 nm pulses was carried out by XRD. The results are shown in Fig. 5.5(b). All diffraction peaks were analyzed according to the standard monoclinic structures of Cu, Cu_2O, and CuO. There were three sharp peaks located at $2\theta = 31.75°$, $35.64°$ and $38.54°$, which corresponded to diffraction from the (110), (002, 11-1) and (111, 200) of CuO, respectively [9]. Meanwhile, a very strong peak appeared at $2\theta = 61.71°$, which corresponded to (220) of Cu_2O [10]. CuO and Cu_2O were also detected in the other samples, which were obtained by 5 ns (1064 and 355 nm) and 30 fs pulses. Notice that the XRD image shows that the copper oxide formed after aging exhibited a crystalline state. Additionally, Cu_2O has a self-oxidation process oriented to CuO [11].

5.2. Pulse duration and wavelength effects of laser ablation on the oxidation, hydrolysis, and aging of aluminium nanoparticles in water

Aluminium, a very active metal, can spontaneously react with oxygen or water from room temperature up to its melting temperature (660 °C) Normally, a dense oxide film (aluminium oxide, alumina, Al_2O_3) is formed by the reaction of Al with oxygen, which prevents other reactions. The chemical reaction between Al and water is so slow that it is virtually unobservable. Aluminium hydroxide $[Al(OH)_3]$, which will be formed at the initial stage, can entirely isolate the contact between Al and water. However, the chemical reactions are very different once one considers the nano- and macro-scale structures. In the case of nanoscale, studies have shown that morphology [12,13] and sizes of particles [14-16] have an impact on their chemical properties. Therefore, it is worth studying the dynamics of morphology and particle sizes of Al, aluminium oxide, and hydrolysates at the nanometre level.

The performance of materials at the nanoscale is totally different from their macroscopic performance. The mixture of Al powder and Al oxide powder can significantly improve the efficiency of hydrogen production. Due to the enormous industrial importance of hydrogen, there has been extensive research on Al–water systems, mainly including interactions with pure water systems, acid-based systems, oxide systems, and salt systems [17,18]. What these studies have in common is the destruction of the oxide layer to facilitate the continuation of the reaction. Particularly, the syntheses of Al and its oxide NPs by pulsed laser ablation in liquid (PLAL) can be considered to be an efficient, simple, and green method. In addition, this method has been widely used in the syntheses of other metal and oxide NPs [19,20]. However, many factors, such as the type of surrounding media, temperature of the liquid, laser pulse duration and fluence, the relative position of the focus and the target surface, adding a surfactant, and characteristics of targets [21-23], strongly influence the ablation processes in such a manner that the composition, morphology, and particle sizes of synthesized NPs show significant differences under different conditions.

In this subsection, the ablation of Al targets in distilled water by 800 nm laser pulses of different durations (5 ns, 200 ps, and 30 fs) is analyzed along with the study of the influence of different wavelengths (1064 nm and 355 nm) of the heating radiation on this process [24]. It is found that the morphology of NPs prepared under different pulse durations changes significantly over time. We discuss how the pulse duration influences the

aging of NPs. In addition, the compositions of NPs obtained using different durations and wavelengths of heating pulses are found to vary significantly.

5.2.1. Colour and spectral variations of ns-, ps-, and fs-induced Al nanoparticles suspensions

The experiment was accomplished by irradiating the Al target in distilled water with focused laser pulses. A sheet of bulk Al was polished and cleaned in anhydrous alcohol and then placed in a quartz cell ($30 \times 30 \times 30$ mm^3) filled with distilled water, which can be moved along the two directions. Laser pulses were focused by a 150 mm focal length lens on the surface of bulk Al. The beam diameter on the ablating surface was 0.3 mm.

The ablation was carried out using the Ti: Sapphire laser, which provided the 800 nm, 1 kHz pulses of 30 fs and 200 ps duration. The nanosecond laser ($\lambda = 1064$ nm, $\tau = 5$ ns, 10 Hz pulse repetition rate) and its third harmonic ($\lambda = 355$ nm) were also used for ablation. Laser ablation was carried out using 48 mJ, 0.56 mJ, and 0.68 mJ energies of ns (nanosecond, 1064 and 355 nm), picosecond (ps), and femtosecond (fs) pulses, respectively. Each ablation process lasted for 30 min. The synthesized NPs suspensions are designated as $S_{n(1064/355)}$, S_p, and S_f for 5 ns, 200 ps, and 30 fs ablation processes, respectively.

Sizes, macrostructure, and morphology of NPs were analyzed by scanning electron microscope, which allowed determination of the change of synthesized particles morphology during a long period. The composition and structure of NPs were determined by energy dispersive spectroscopy and X-ray diffraction. UV-vis-NIR absorption spectroscopy was used to determine the optical band gaps of suspensions and to monitor the number of NPs in the water colloids.

The ablation of Al in water under various conditions showed that pulse duration and wavelength have a close connection to the morphology, size, and composition of NPs, which were changed during some period after ablation. These studies showed that pulse duration significantly influences the modification of synthesized particles.

Thin layers of Al_2O_3 and $Al(OH)_3$ produced during the initial stages of the interaction of Al, oxygen, and water suppressed further interaction between those components. Laser irradiation destroyed those films and allowed the reactions to continue. In addition, the heating effect of laser-matter interaction also played a role in promoting the reaction. The favourable temperature range for producing $Al(OH)_3$ lies between room

temperature and 280 °C. Above 480 °C, Al_2O_3 becomes the most probable product of the reaction. Extreme conditions of reaction, such as high temperature and high pressure provided by laser radiation, play a decisive role during the process of ablation. It was shown previously that the external environment affects the self-organization process of bubbles in the corrosion process [25]. The plume induced by the laser rapidly cools down in the solution that led to the formation of NPs through agglomeration. Agglomeration not only influences the whole process of NPs formation but also plays an important role in the subsequent aging processes.

It was found during laser ablation studies that, without any surfactant or catalyst, Al_2O_3 and $Al(OH)_3$ coexist during the process of ablation, while pulse duration significantly influences their relative content. After polishing, the pure Al was placed in distilled water. It reacts rapidly with oxygen and water, forming a film containing Al_2O_3 and $Al(OH)_3$. The laser pulses destroy this film, re-expose pure Al, and allow further reactions between the above components. The pulse heating also promotes the reaction between them. Therefore, the NPs containing Al, Al_2O_3, and $Al(OH)_3$ should appear in the solution during ablation at the same time. This assumption has been proven during structural and morphology analysis of synthesized species.

To analyze the role of pulse duration during the formation of NPs, laser pulses with different durations were used to ablate the target. The influence of fundamental and third harmonic wavelengths on ablation was compared under ns ablation conditions. The suspensions obtained during ablation of Al bulk with variable pulse durations were slightly different in colour. The colloidal solution obtained under ablation by ns pulses showed milky white colour, while ps radiation caused the light gray colour, and the colloidal solution produced by fs pulses ablation showed a brown colour. In all of the above-mentioned cases, the solutions had the micro-emulsion consistency, and after a few days, the precipitation started to play an important role.

Absorption spectra of the colloidal solutions obtained by PLAL were measured immediately after ablation. The results are shown in Fig. 5.6a. The solutions exhibited large absorption in the ultraviolet range, and the edge of the absorption band extended towards the visible region so that the solutions had different colours. The suspension of NPs prepared by fs pulses showed a resonance peak located at $\lambda = 230$ nm ($E = 5.39$ eV, red curve), while there were no similar peaks in the case of application of the ns (dot-dashed curve) and ps (dashed curve) pulses.
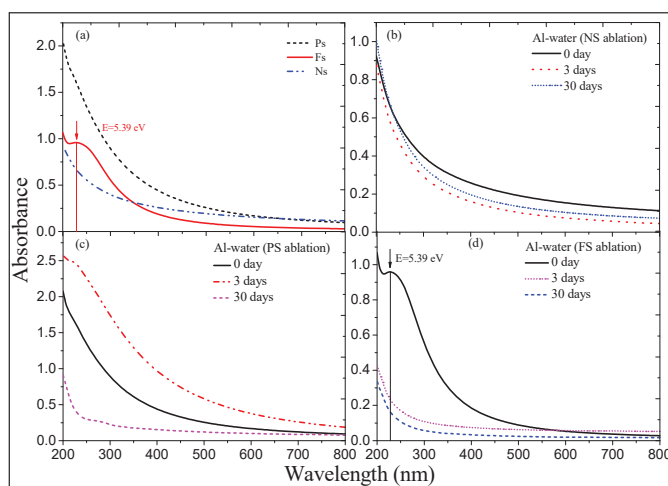
Fig. 5.6. Absorption spectra of Al nanoparticles (NPs) colloidal solutions. (a) Absorption spectra measured immediately after ablation using different pulse durations (Ns: 5 ns, 1064 nm, 10 Hz, 48 mJ; Ps: 200 ps, 800 nm, 1 kHz, 0.56 mJ; Fs: 30 fs, 800 nm, 1 kHz, 0.68 mJ). (b) Dynamics of absorption spectra of aged NPs in the case of ablation by ns pulses. (c) Absorption spectra variations in the case of ablation by ps pulses. (d) Variation of absorption of the NPs suspension prepared using fs pulses. Reproduced from [24] with permission from MDPI.

Earlier, 150 ps pulses of Nd:YAG laser were used to ablate the Al target in ethanol, and the colloidal solution had a similar absorption peak, which was explained as the product of ethanol decomposition [26]. Compared with their research, different pulse duration (30 fs) and solvent (distilled water) were used in this study, which showed the same peak of absorption. Therefore, the appearance of the peak can be considered independent of the pulse duration and solvent used, but rather attributed to the peculiarities of the products of ablation of Al target.

In addition, during ablation by fs pulses, a bright white light was emitted when ultra-short pulses passed through the liquid. Extremely high peak power led to stronger absorption of the laser radiation passing through the liquid, thus reducing the intensity at the target surface, which has earlier shown the low rate of NPs formation by fs pulses [26]. As a result, the absorption of these colloids was significantly reduced compared with the former case. The repetition rate of ns pulses (10 Hz) was significantly smaller, and the pulses acting on the bulk surface during the

same time were 100 times less compared with the ablation by fs or ps pulses. Therefore, the number of NPs generated by excitation of ns pulses was significantly lower, which led to significantly smaller absorption (dot-dashed curve).

The colloidal solutions were also analyzed 3 and 30 days after the ablation (Fig. 5.6b–d). The major changes in the morphology occurred mainly during the first few days after the ablation. Since then, the morphology and particle sizes remained basically stable, so no measurements of the absorption spectra of colloidal solutions during the stable period were carried out. The colloidal solution S_n did not show essential changes in the absorption spectrum (Fig. 5.6b). The stability of the absorption spectrum, in that case, corroborated the SEM studies of Al NPs (see the following subsection). Meanwhile, the absorption spectra of colloidal solutions S_p (Fig. 5.6c) and S_f (Fig. 5.6d) have undergone significant changes. The absorption of S_p was slightly increased on the third day and a "shoulder" appeared at $\lambda = 240$ nm ($E = 5.17$ eV) compared with the initial colloidal solution. This modification was mainly based on the difference in NPs' morphology. The absorption spectrum measured after 30 days was further modified, and the position of the shoulder became redshifted. The remarkable difference between the 3rd and the 30th days indicates that the morphological structure of particles is still changing at this stage. Other test results also showed that the colloidal solution obtained using ps pulses-induced ablation is the most surprising and complex. Spectroscopic measurements of the solution S_f showed that, after the third day, its properties became almost stabilized.

5.2.2. Morphology of synthesized Al NPs

SEMs of three groups of colloids were performed to determine the morphology, particle sizes, and distribution of NPs. For ns pulses, ablation was operated at two wavelengths (1064 nm and 355 nm). These studies allowed analyzing the influence of the wavelength of 5 ns ablation beam on the formation of NPs. SEM of ablation showed that the initial morphology of NPs was close to the regular spherical structure. The NP structures obtained under different wavelength conditions (1064 nm and 355 nm) did not distinguish them from each other.
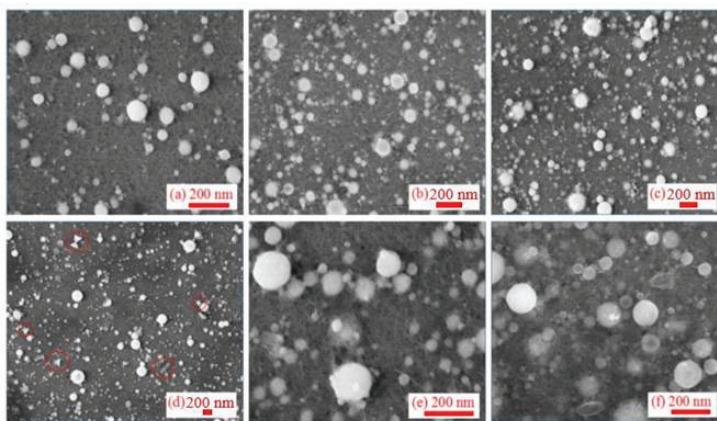
Fig. 5.7. SEMs of the colloidal solutions synthesized using ns, 1064 nm pulses and measured at different time intervals from ablation: (a) Less than 1 day after ablation, (b) 8 days, (c) 15 days, (d) 40 days, (e) 60 days, and (f) 90 days after ablation. Reproduced from [24] with permission from MDPI.

In the case of 1064 nm pulses, SEM images did not show a significant difference in morphology and particle sizes during the aging process for more than three months (Fig. 5.7). Compared with other metal NPs, the Al NPs obtained at these conditions of ablation did not show aggregation. On the 40th day (Fig. 5.7d), when the same colloidal solution of NPs was measured, it was found that the morphology of very few NPs presented the conical or rod-like structures (marked by red rings), while most of NPs showed the regular spherical shape.

In the case of ablation using 355 nm, 5 ns pulses, the initial shapes of NPs were similar to the case of ablation using 1064 nm radiation (Fig. 5.8). The size of particles significantly increased after 60 days of ablation. SEM studies of the newly synthesized NP solution showed the presence of a powdery structure uniformly distributed on the substrate of the silicon wafer. After 30 days, the surrounding powders aggregated and coagulated to form new particles with notably larger sizes. Smaller particles and colloids in liquids adhered to the surface of NPs and then coagulated with them (Fig. 5.8c). The NPs still have a spherical structure. Additionally, two months later, the test results showed that there were a few holes on the surfaces of some NPs, which had a doughnut-like structure (Fig. 5.8d).
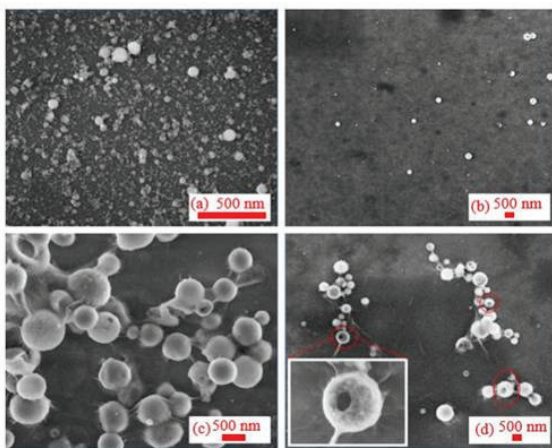
Fig. 5.8. SEM images at different periods after ablation by 355 nm radiation: (a) 1 day, (b) 20 days, (c) 45 days, and (d) 60 days after ablation. Reproduced from [24] with permission from MDPI.

The ablation of Al by ps pulses is a commonly used technique. However, the most interesting stage of the morphology dynamics at the conditions of ablation has not yet been analyzed. SEM images of NPs at different stages after ablation by ps pulses are presented in Fig. 5.9. SEM of initial NPs showed the spherical shapes and narrow particle size distribution. Some of them showed a structure similar to the red blood cells (Fig. 5.9a). Meanwhile, the morphology of NPs was notably changed during the following days. There were no transitional structures between initial (spherical) and subsequent (cone-shaped and triangle) morphologies. Therefore, one cannot think that structures like "red blood cells" can be considered as the precursors of the subsequent morphology variations.

Figure 5.9b shows a typical SEM image obtained 10 days after ablation, when the spherical particles were transformed completely into a large number of triangles and conical structures supplemented by a small number of rod-like NPs and very rare spherical structures (see marked red rings). In the subsequent SEM measurements, the conical and rod structures remained stable, while the spherical structures completely disappeared (Fig. 5.9c–f). Interestingly, many conical structures became joined in pairs to form bow-tie structures (Fig. 5.9b). This unique structure makes the number of free electrons located at the apex of the cone significantly larger than in other positions.

Results of ablation by fs pulses completely differ from the ps ablation. Although the initial NPs (Fig. 5.10a) were similar to those in the previous two cases (ns and ps pluses) and showed regular globules with a narrow range of particle size distribution, the influence of pulse duration became fully recognizable during the subsequent aging process (Fig. 5.10b–d). After a period of aging, its morphology presented the granular structures with uniform size distribution. Individual particles demonstrated the layered structure. Such a structure remained stable during the following three months of aging research.
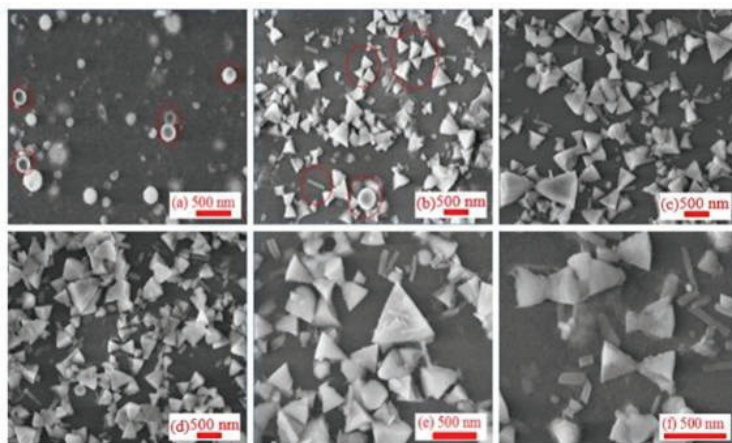
Fig. 5.9. SEM images of NPs at different stages after ablation by 200 ps, 800 nm, 0.54 mJ pulses, (a) 1 day, (b) 10 days, (c) 30 days, (d) 60 days, (e) 90 days, and (f) 100 days after ablation. Reproduced from [24] with permission from MDPI.

The life cycle of particles can be divided into three stages. (1) Formation stage (during ablation and within 24 h after ablation). Within a short time after ablation and during the process of ablation, the plume cooled down rapidly and formed the spherical NPs by aggregation. At this stage, the particles interact with the surrounding liquid environment, and the sizes, morphology, and composition of particles are still unstable. (2) Great change stage (a few days after ablation). This stage is a transitional period when NPs continue interacting with the surrounding environment and with each other, which causes the largest changes in their morphology. The sizes, morphology, and composition of NPs drastically vary during this stage, thereby gradually becoming more stable. (3) Stable stage (about

three months after the completion of the great change stage). This stage presents the final results of the ablation by pulsed lasers in the liquid environment. During this stage, the influence of external conditions on the ablation process, such as pulse duration and wavelength, diminishes. The duration of each stage of the same ablation process varies greatly. For the Al target, the influence of pulse duration and wavelength on the morphology and sizes of synthesized particles is very significant, especially in the subsequent aging processes. The sizes of NPs obtained by ultra-short pulses were remarkably smaller and more homogeneous.
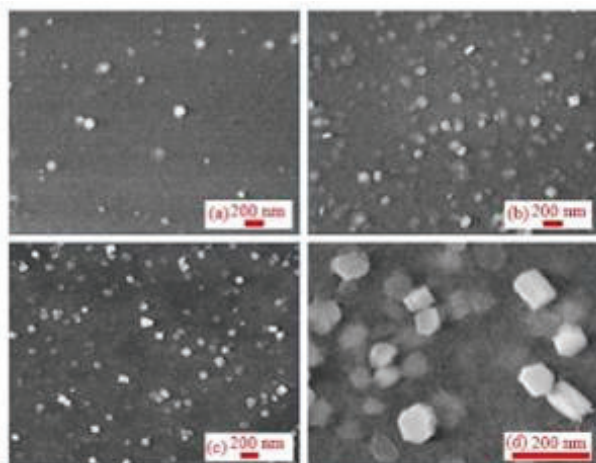
Fig. 5.10. SEM images of NPs at different stages after ablation by 30 fs, 800 nm pulses: (a) within 1st day, (b) after 20 days, (c) after 40 days, and (d) after 80 days from ablation. Reproduced from [24] with permission from MDPI.

EDS and XRD were carried out to further analyze the composition and structure of NPs obtained using different pulse durations and wavelengths. Considering the intense interaction between NPs and the surrounding environment during the formation and great change stages, the composition and structure of NPs are still unstable. Therefore, EDS and XRD were measured during the stable stage. Colloidal solutions were deposited and evaporated repeatedly in the air at room temperature onto the silicon wafer with an oxide film on its surface for EDS and XRD. The XRD of samples are shown in Fig. 5.11. The EDS test results of each sample are shown in Table 5.1.
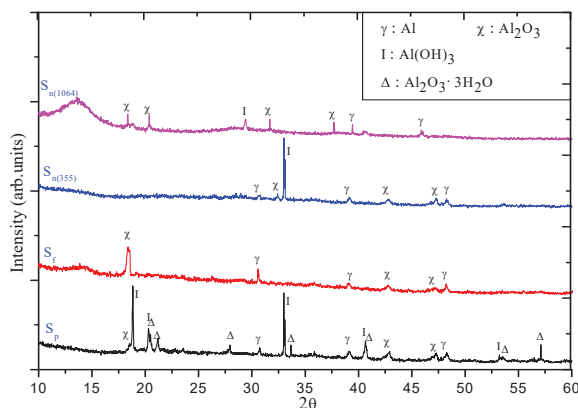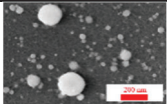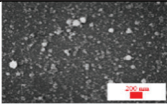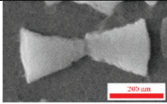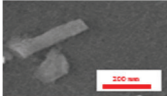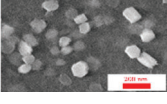
Fig. 5.11. XRD image of NPs prepared at different conditions. $S_{n(1064)}$: NPs obtained by 1064 nm, 5 ns pulses. $S_{n(355)}$: NPs obtained by ns pulses with 355 nm. S_f: NPs obtained by fs pulses. S_p: NPs obtained by ps pulses. Reproduced from [24] with permission from MDPI.

It was found during EDS and XRD studies of the ns-induced suspension that this composition includes Al, Al_2O_3, and $Al(OH)_3$. The peak intensity of each component is similar in the XRD images. In the case of 355 nm ablating pulses, $Al(OH)_3$ showed a very strong peak compared to those from Al and Al_2O_3. The EDS and XRD of the suspensions produced by 1064 nm and 355 nm radiation were completely different. In the case of ps pulses, the NPs mainly show two different morphologies, the conical shape dominated by Al_2O_3 $3H_2O$ and the rod shape dominated by $Al(OH)_3$.

In addition, Al still exists in NPs according to XRD. A specific morphology, such as conical shape, comprises Al_2O_3 $3H_2O$ as the main component, while the NPs do not exist in the state of a single crystal. Compared with the former case, XRD peaks of NPs obtained using ps pulses are more complex and stronger, including Al (marked by γ), Al_2O_3 (marked by χ), $Al(OH)_3$ (marked by I), and Al_2O_3 $3H_2O$ (marked by Δ). The main difference at fs ablation conditions is that the presence of $Al(OH)_3$ was not detected in the XRD image, probably due to weak intensity. Its composition was mainly a mixture of Al and Al_2O_3, and the content of Al_2O_3 was relatively larger.

Table 5.1. Summary of energy dispersive spectroscopy measurements. Reproduced from [24] with permission from MDPI.

	Wt %		At %		Type	Picture
	Al	O	Al	O		
S_n (1064 nm)	38.4	61.6	27	73	Al & Al_2O_3 & $Al(OH)_3$	
S_n (355 nm)	35	65	24.2	75.8	Al & Al_2O_3 & $Al(OH)_3$	
S_p	32.4	67.6	22.1	77.9	Al_2O_3 $3H_2O$	
	18	82	11.5	88.5	$Al(OH)_3$	
S_f	36.3	63.7	25.8	74.2	Al & Al_2O_3	

Compared with the same aging stage of NPs obtained by different ablation conditions, it is easy to find that the NPs prepared by ps pulses exhibit larger size after aging and self-assembly, while the shorter wavelength laser sources play a positive role in obtaining smaller particle size distribution in the case of nanosecond pulses. Meanwhile, the NPs obtained by ultrashort pulses have better uniformity in morphology and narrower particle size distribution. In addition, the XRD data exhibiting the presence of Al NPs mainly for fs ablation could be interpreted in terms of direct nanoparticle yield via phase-explosion mechanism, while for ns and ps ablation, laser–plume interaction could destroy parent ablation products until atoms and ions with the following recondensation.

5.3. Formation, aging, and self-assembly of regular nanostructures from laser ablation of indium and zinc in water

Metallic and metal oxide nanoparticles (NPs) with different morphologies and sizes will possess different characteristics, which effect has attracted a wide range of attention from material syntheses, to theoretical simulations and potential applications. Especially in the preparation of NPs, new synthetic methods and research results emerge endlessly, such as thermal decomposition, microwave radiation, pulsed laser deposition, and pulsed laser ablation in liquid [27-32]. PLAL has been highly praised because of its advantages of low cost, environmental friendliness, and simplicity. It is noteworthy that the physical properties of metal materials, hardness, melting, and boiling point, play an important role during the process of NPs' formation based on PLAL. Metals with different melting and boiling points will show different sensitivity to pulse intensity, which will produce completely different effects. This means that in the process of PLAL, there will be both similarities and individualities between different metals at the same operating conditions. In addition, the NPs obtained by PLAL exhibit obvious, efficient aging and self-assembly phenomena, which limits the stability of the initial NPs. But on the other hand, the study of the aging process and self-assembly phenomena will provide another way to prepare new functional materials.

From the point of view of physical properties, indium (In) with very low hardness (Mon's hardness: 1.2), and melting point (157^0), while zinc (Zn) with relatively high above indexes (Mon's hardness: 2.5, melting point 419^0) were selected as the research objects in this study. Furthermore, these metal and oxide NPs have a very wide range of applications. For example, indium and indium oxide (In_2O_3) NPs show great potentials in photoelectric and sensors because of their high transparency and metal-like conductivity [33-35]. Meanwhile, zinc and zinc oxide (ZnO) are widely used as piezoelectric materials. The great application value of ZnO in new devices, photoelectricity, and semiconductors are also the focus of attention of many scholars [36,37].

In this section, we analyze the influence of pulse duration (5 ns, 200 ps, and 60 fs), ablation energy (different energy gradients under picosecond pulse condition), and the temperature of water (high and low) on the process of ablation of a metal target, indium, with low hardness and melting point [38]. The effect of these factors on the formation and aging of NPs was determined by absorption spectroscopy, scanning electron microscopy, transmission electron microscopy, and X-ray diffraction.

Indium hydroxide (In(OH)$_3$) was found for the first time by studying the aging process of NPs. The ablation of the Zn target, which had high hardness and melting point, in distilled water by pulses with different duration showed that Zn and ZnO NPs existed simultaneously. In addition, the size distribution range and stability of NPs are strongly dependent on the pulse duration used in ablation.

Laser pulses of Nd: YAG laser and Ti:sapphire laser were focused by a 150 mm focal length lens on the surface of the metal targets, which were placed in a 30 mm quartz cell containing 10 mL of distilled water. The Nd: YAG laser provided the 5 ns, 1064 nm, 10 Hz pulses, and the Ti:sapphire laser provided the 200 ps, 800 nm, 1 kHz, and 60 fs, 800 nm, 1 kHz pulses. The experimental setup is shown in Fig. 5.12.
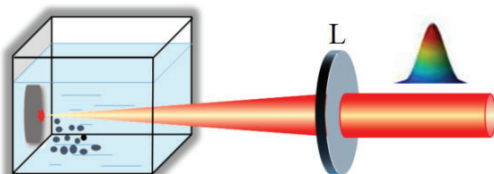
Fig. 5.12. Experimental layout for pulsed laser ablation in liquid environment. L: lens, f=150 mm. Reproduced from [38] with permission from Elsevier.

Indium (99.995%), as a metal with very low hardness and melting point, was studied in three different regimes, which allowed determining the influence of pulse duration (group of In-01), pulse energy (group of In-02), and temperature of the liquid (group of In-03) during the formation and aging of NPs. Zinc (99.995%), which had a higher hardness, melting point, was also used in these studies. The parameters of laser ablation of In and Zn are shown in Table 5.2.

The experiment was carried out in a super-clean room (temperature: 20℃). In order to analyze the effects of liquid with different temperatures during the ablation process, distilled water used is pre-heated or cooled to the desired temperature (80℃ and 4℃). Because of the short duration time of ablation, the experiment neglected the change of water temperature affected by room temperature during ablation. In addition, the obtained colloidal solution of NPs was stored in a transparent plastic centrifugal tube. The centrifugal tube was sealed, stored under room temperature and shading conditions for aging analysis.

Morphological and Optical Characteristics of Nanoparticles

Table 5.2. Parameters of laser ablation of In and Zn targets. Reproduced from [38] with permission from Elsevier.

Target	Group	Pulses	Sample	Pulse energy (mJ)	Fluence (J cm^{-2})	Intensity ($\times 10^{11}$ W cm^{-2})	Ablation time (min)	Temperature (^{0}C)
In	In-01	5 ns	In-ns	30	667	1.3	10	20
		200 ps	In-ps	0.54	12	0.6		
		60 fs	In-fs	0.54	12	2000		
	In-02	200 ps	In-ps01	0.53	12	0.6	15	
			In-ps02	0.45	10	0.5		
			In-ps03	0.29	6.4	0.32		
			In-ps04	0.25	5.6	0.28		
			In-ps05	0.15	3.3	0.17		
			In-ps06	0.04	0.9	0.05		
	In-03	200 ps	In-low	0.54	12	0.6	10	4
			In-high					80
Zn		5 ns	Zn-ns	102	2267	4.53	20	20
		200 ps	Zn-ps	0.54	12	0.6		
		60 fs	Zn-fs	0.87	19	3170		

5.3.1. Characterization of NPs suspensions obtained by indium ablation

The colloidal suspensions, which were obtained by different pulse durations, pulse energies, and water temperatures, were analyzed by absorption spectrometry, SEM, and TEM to determine the surface plasmon resonances (SPR), morphology, size, and distribution of NPs.

Indium, like a very soft metal (Mon's hardness: 1.2), with a low melting point (157°C), and its melting heat and evaporation heat are 3.263 kJ/mol and 231.5 kJ/mol respectively. Thus, indium is easily ablated.

The SEM studies of nanoparticle suspensions showed that the morphology and particle size of the initial NPs (all of the three groups, whether based on the difference of pulse duration, ablation energy, or water temperature) did not differ significantly, and had almost a spherical shape [Fig. 5.13(a)]. However, the morphology of these samples was drastically changed a few days after the ablation.
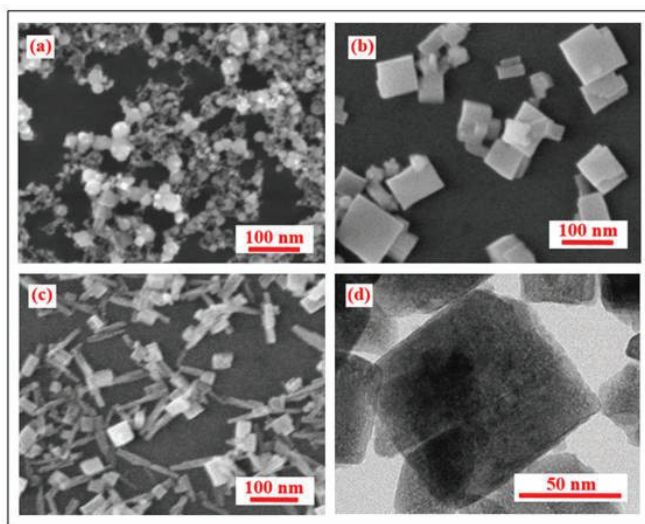
Fig. 5.13. SEM images of colloidal solution obtained by ablation of indium target. (a) SEM image of initial NPs obtained by ablation using picosecond pulses. (b) SEM image of the same suspension obtained by picosecond pulses after two days. (c) SEM image in the case of ablation by femtosecond pulses after two days. (d) TEM image of square-like NPs obtained using ablation by picosecond pulses. Reproduced from [38] with permission from Elsevier.

In the case of ablation by picosecond pulses, after several days of aging, the NPs changed to cubic and rectangular cuboids structures with a narrower size distribution, while a small amount of spheroid and rod-like particles still existed [Fig. 5.13(b)]. Variations of ablation energies and water temperatures have no significant effect on the subsequent aging and self-assembly process. Continuous SEM test results show that in the following two months, the morphology and particle size remained stable. That is to say, for In, the soft metal, ablation under picosecond pulses condition, whether the initial state of NPs or the subsequent aging and self-assembly process, the difference of ablation energy and surrounding water temperature does not have a visual impact on the results.

Due to indium having a very low ablation threshold, lower ablation energy is sufficient to produce the same effect as higher ablation energy. Therefore, in the range of 0.53 mJ to 0.04 mJ, there is no significant difference between different ablation energies. In addition, whether the water temperature is high or low during the experiment, the great temperature difference between the plume and the water always exists, which means that the temperature difference between the two samples (4 and 80°C) is insignificant compared with that of the plume.

The morphology and size of the NPs produced by nanosecond and picosecond pulses were basically the same [Fig. 5.13(b)], they all appear as cubic and rectangular structures. However, in the case of picosecond pulses, the same morphology was maintained for nearly two months, and then a gradual aggregation was observed.

In the case of nanosecond pulses the rectangular morphology held for less than half a month and then aggregated rapidly. The morphology was changed to the irregular structures, while the particle size further increased [Fig. 5.14(a)-(f)]. Meanwhile, the initial NPs, which were obtained by femtosecond pulses, were similar to the two former cases. But after a few days, the morphology became significantly different from a large number of cubic blocks. In the case of femtosecond pulses, a large number of rod-like structures and a small number of cubic blocks were observed, and their sizes were significantly reduced [Fig. 5.13(c)]. The morphology was stable for nearly three months, and then the structures aggregated.
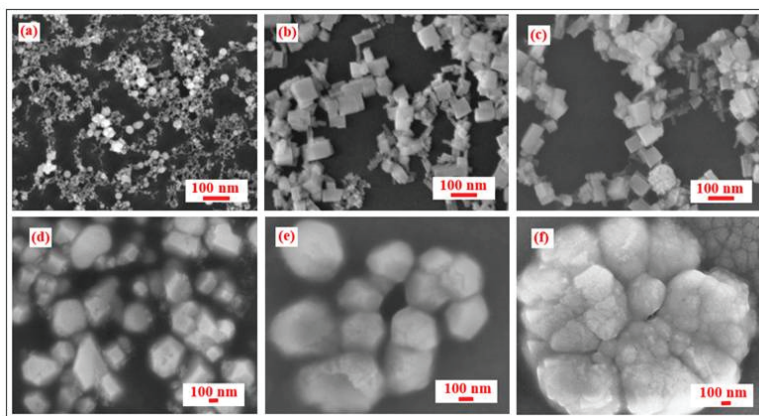
Fig. 5.14. SEM images of colloidal solution obtained by ablation of indium target. (a) SEM image of initial NPs obtained by nanosecond pulses. (b) SEM image after aging for three days. (c) SEM image after aging for ten days. (d) SEM image after aging for twenty days. (e) SEM image after aging for two months. (f) SEM image after aging for three months. Reproduced from [38] with permission from Elsevier.

Obviously, although the morphology and size of the NPs obtained by different pulse duration are identical in the initial state, the effect of pulse duration on the ablation process is gradually reflected in the subsequent aging process. Ultra-short pulses can not only obtain smaller NPs, but also maintain longer stability during the subsequent aging and self-assembly process.
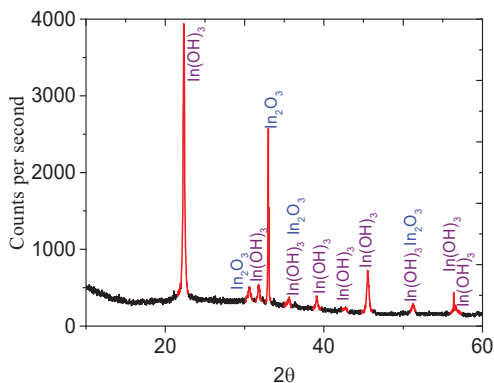
Fig. 5.15. XRD of NPs obtained by picosecond pulses after several days of aging. Reproduced from [38] with permission from Elsevier.

Indium can be easily ablated. A pulsed laser with different pulse duration or energy can achieve a similar ablation effect. Therefore, the initial NPs did not show a significant difference. However, the action time will be different between pulses with different durations and the target surfaces. The action time of a single pulse with 5 ns is much longer than that of 200 ps pulses. This means that the target has a longer time to absorb more energy when the nanosecond pulses act on it. Consequently, the NPs obtained by nanosecond pulses were relatively unstable and more prone to aggregation. Meanwhile, the properties of soft material and low melting point make this phenomenon more obvious. Ablation under ultra-short pulse condition (fs) is a completely different mechanism of action. In addition, the experimental results also show that the NPs were smaller and more stable during the aging process in the case of shorter pulses ablation.

The composition and structure of the NPs, which were produced by picosecond pulses, were analyzed after several days of aging by XRD. XRD showed that the particles consisted of In_2O_3 and, mainly, $In(OH)_3$ (Fig. 5.15). The large number of In_2O_3 meets the predictions and existing research results [39]. Indium is very active, from room temperature (20°C) to the melting point, indium can react with oxygen, forming a very thin oxide film on the surface. Bulk indium does not react with water, but the powdered indium, which is produced by pulsed laser, reacts slowly with water to form $In(OH)_3$ during dissociation of water molecules in the vicinity of the hot target. The thermal effect during ablation further promotes the oxidation of NPs. TEM images of particles, which were ablated by picosecond pulses, are shown in Fig. 5.13(d).
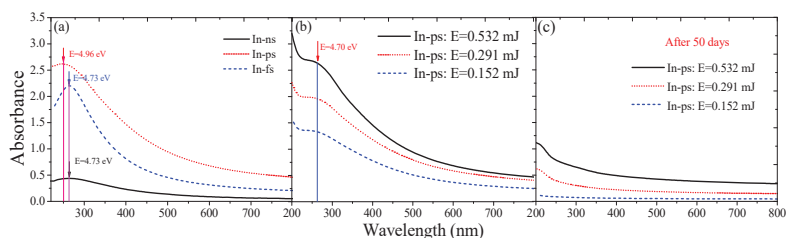
Fig. 5.16. (a) Absorption spectra of the NPs aqueous solutions synthesized using ablation by pulses with different durations. (b) Absorption spectra of initial NPs obtained by picosecond pulses with different energies. (c) Absorption spectra of NPs obtained by picosecond pulses at different energies after 50 days. Reproduced from [38] with permission from Elsevier.

The initial absorption spectra of the NPs suspensions obtained by pulsed laser ablation with different duration are shown in Fig. 5.16(a). The SPR peak was located at $\lambda = 262$ nm (E=4.73 eV) that is consistent with the SPR peak of indium NPs obtained by the chemical method. Reports show that the position of the SPR peak strongly depends on the solvents, morphology, and size of the NPs [40,41]. However, the absorption of the NPs suspensions obtained by picosecond and femtosecond pulses was significantly stronger than the case of nanosecond pulses, mainly because of the repetition rate of the former pulses (1 kHz) was significantly larger than that of the latter pulses (10 Hz). In addition, under the condition of a high repetition rate, secondary ablation is particularly obvious.

The absorption spectra of NPs suspensions obtained by picosecond pulses with different energy are shown in Fig. 5.16(b). Their spectra after 50 days from ablation are shown in Fig. 5.16(c). In the latter case, the SPR peak of suspensions is disappeared.

The height of the SPR peak depended on the laser energy during ablation [Fig. 5.16(b)]. Larger energy led to a higher concentration of small-sized particles during the same ablation time and to higher absorption along the whole spectral range. Meanwhile, the SEM images showed that the initial morphology and size of spherical particles obtained by different pulse energies were almost the same, and so were the positions of SPR.

With the passage of time, the change of particle morphology and composition leads to the change of absorption curve. The NPs obtained by pulsed laser ablation showed aging and self-assembly in the regular cubic structure after several days. Particularly, aging and self-assembly do not show any dependence on the energy used in ablation. Continuous SEM tests showed that the particles with this morphology and size can remain stable for about two months. Meanwhile, at this stage, the SPR peaks entirely disappeared from the absorption spectra [Fig. 5.16(c)].

5.3.2. Characterization of NPs suspensions obtained by zinc ablation

Zinc is a relatively hard metal (Mon's hardness: 2.5, melting point 419.5°C, melting heat: 7.322 kJ/mol, vaporization heat: 115.3 kJ/mol), so its ablation differed from the case of indium. In a short period of time after ablation, the morphology and particle size of NPs did not change significantly. However, the longer aging process changed their morphology gradually. All the particles of the initial stage had irregular fracturing morphology. Comparing the NPs obtained under different pulse duration,

one can find that the size and size distribution range of NPs are obviously dependent on the pulse duration used for ablation.

In the case of ablation by nanosecond pulses, the particle size distribution was extremely broad, ranging from several nanometres to nearly 100 nm [Fig. 5.17(a)]. The particle size distribution was relatively narrower at the condition of ablation by picosecond pulses ($10 \sim 50$ nm) [Fig. 5.17(b)]. This trend was more significant for femtosecond pulses [Fig. 5.17(c)].

The NPs produced by nanosecond pulses have larger particle sizes and broader distribution, while the NPs obtained by ultra-short pulses have smaller particle sizes with a narrower distribution. A single pulse with a longer pulse duration (5 ns) interacts with the metal target surface for a longer time, and the target absorbs more heat, providing conditions for the formation of larger particles, while, at shorter pulse ablation (200 ps), significantly lower time of acting allows synthesizing only small particles. Thus the overall size is smaller and the distribution shows narrower in the case of shorter pulses. Ultra-short pulses (60 fs) have no thermal effect on the target, their ablation mechanism is significantly different from that of the former, but the effect of pulse duration on ablation, i.e., the rule that shorter pulse duration allows for smaller NPs and narrower size distribution, is still valid and more obvious. Interestingly, after nearly two months of aging, these NPs showed a significant change in morphology presenting a cubic structure and a significant increase in particle size, which independently on the duration of the ablating pulses [Fig. 5.17(d)-(f)].
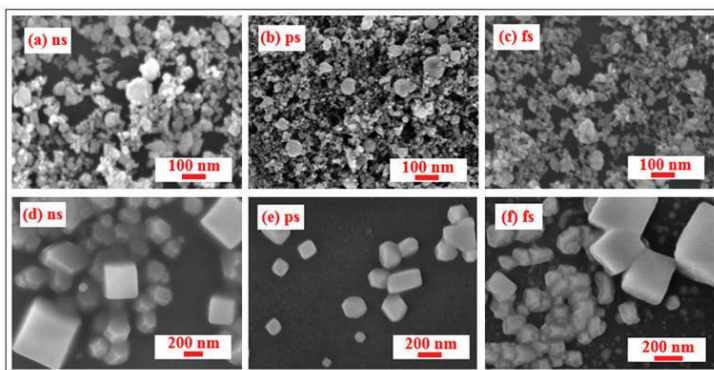
Fig. 5.17. SEM images of colloidal solution obtained by ablation of zinc target. SEM images of initial NPs (a-c) and after two months (d-f), which obtained by nanosecond pulses (a and d), picosecond pulses (b and e), femtosecond pulses (c and f). Reproduced from [38] with permission from Elsevier.

The absorption spectra of NPs suspensions produced using different pulse duration and their absorption spectra after 50 days are shown in Fig. 5.18. Compared to former (NPs suspensions obtained by indium ablation), suspensions obtained by zinc ablation showed two resonance peaks. The first peak was at $\lambda = 207 \sim 238$ nm ($E = 5.21 \sim 5.99$ eV). The second peak was at $\lambda = 337$ nm (E=3.68 eV) and is related to the absorption by ZnO [42]. These spectra confirmed the presence of both Zn and ZnO during ablation of zinc in a liquid environment in good agreement with [43]. The two resonance peaks in the initial state of the suspension show that ZnO particles are produced not during the aging, but simultaneously with zinc particles.

In addition to the formation of ZnO due to rapid oxidation during ablation, ZnO is also the final form of aging of zinc NPs. The colloidal solution has obvious white precipitation after a period of stationary, which promotes the formation of its aggregation. The aggregation phenomenon leads to a significant increase in particle size. In addition, ZnO has very large surface free energy, which makes them grow larger and agglomerate. The small redshift in the peak position after aging ($\lambda = 361$ nm, E = 3.43 eV) compared with the original peak position ($\lambda = 266$ nm, E = 4.66 eV), is explained by the change of composition of NPs from zinc to ZnO. Meanwhile, there are also effects of morphology and particle size.
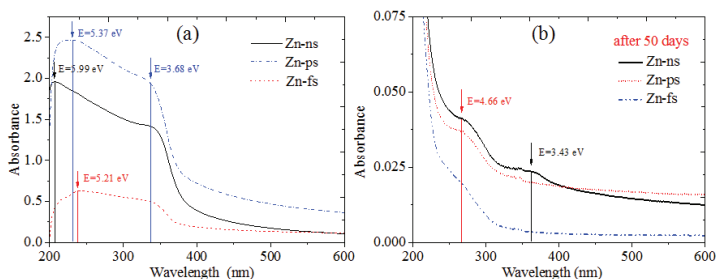
Fig. 5.18. Absorption spectra of the aqueous solutions of NPs synthesized at different pulse durations. (a) Absorption spectra of initial NPs. (b) Absorption spectra after 50 days. Reproduced from [38] with permission from Elsevier.

During the process of PLAL, various factors may affect the formation of NPs. However, the role of a specific factor in the ablation process varies greatly from target to target. They have both similarities and differences. The discussed studies showed that the pulse duration affects the particle

size of NPs, ultra-short pulses allowed to obtain smaller size NPs. While in the case of the indium target the pulse duration influences the stability of morphology during aging.

There are many factors affecting pulsed laser ablation in liquid. In addition to the pulsed laser, the physical properties of the used materials also have a significant impact, such as hardness, melting point, boiling point, etc. A key point of this study was to compare the characteristics of two metals with different hardness and melting points (indium with smaller hardness and melting point and zinc with larger hardness and melting point) under the same ablation conditions.

The experimental analysis shows that the simultaneous ablation of the aluminium-copper target does not produce special phenomena, no matter in morphology or particle size, compared with the separate ablation of the two targets when those showed the pyramidal and nanourchin-like morphologies of aged synthesized nanostructures. One can consider this process as just a simple mix of these two samples. The absence of new peculiarities, in that case, is also an expected result, since, in distilled water, the effect of pulsed laser can only cause plume to react with oxygen or distilled water, and form oxides or hydroxides. Meanwhile, the laser pulse action is not sufficient to cause other chemical reactions between the two metals (Al and Cu, or In and Zn). Therefore, the morphology and composition of nanoparticles formed by mixed ablation compared during previous studies showed that, in terms of ablation and morphology, there are no special changes with regard to the separate studies of these samples.

Indium target reacts with oxygen and water in the surrounding environment to form indium oxide and indium hydroxide micro- and nanoparticles during the ablation process. At a very short time after ablation, the synthesized structures modify to become cubic in morphology and cubic rods at femtosecond pulse ablation conditions. This morphology is not suitable for particle size statistics. Thus the comparison of nanostructures in the discussed case can be considered as intuitive, rather than quantitative, which is enough to illustrate the characteristics of particle size and morphology.

The nanoparticles obtained by ablation of zinc target show irregular granular shape. Although the size is different, the peculiarities of their formation can be clearly identified by comparing the particles obtained under different pulse conditions. For example, the average particle size of nanoparticles obtained under shorter pulse ablation appears to be smaller, which is a very intuitive and obvious phenomenon. After aging and self-assembly, the aggregation occurs between aged particles by forming large-

sized structures. These nanostructures reflect the difference between the nanoparticles obtained under variable ablating pulse conditions.

References to Chapter 5

[1] M. Castro-Lopez, D. Brinks, R. Sapienza, N. F. van Hulst, Aluminum for nonlinear plasmonics: resonance-driven polarized luminescence of Al, Ag, and Au nanoantennas, Nano Lett. 11 (11) (2011) 4674-4678.

[2] M. A. Gondal, T. F. Qahtan, M. A. Dastageer, Y. W. Maganda, D. H. Anjum, Synthesis of Cu/Cu2O nanoparticles by laser ablation in deionized water and their annealing transformation into CuO nanoparticles, J. Nanosci Nanotechn. 13 (8) (2013) 5759-5766.

[3] K. Furusawa, K. Takahashi, H. Kumagai, K. Midorikawa, M. Obara, Ablation characteristics of Au, Ag, and Cu metals using a femtosecond Ti:sapphire laser, Appl. Phys. A 69 (7) (1999) S359-S366.

[4] D. A. Goncharova, I. N. Lapin, E. S. Savelyev, V. A. Svetlichnyi, Structure and properties of nanoparticles fabricated by laser ablation of bulk metal copper targets in water and ethanol, Russian Phys J. 60 (4) (2017) 1197-1205.

[5] K. Zhang, R. A. Ganeev, G. S. Boltaev, C. Guo, Structural variations during aging of the particles synthesized by laser ablation of copper in water, Appl. Phys. A 125 (4) (2019) 698.

[6] A. Hamad, L. Li, Z. Liu, A comparison of the characteristics of nanosecond, picosecond and femtosecond lasers generated Ag, TiO 2 and Au nanoparticles in deionised water, Appl. Phys. A 120 (4) (2015) 1247-1260.

[7] B. Oktem, I. Pavlov, S. Ilday, H. Kalaycıoglu, A. Rybak, S. Yavas, M. Erdogan, F. Ilday, Nonlinear laser lithography for indefinitely large-area nanostructuring with femtosecond pulses, Nat. Photonics 7 (11) (2013) 897-901.

[8] J. Singh, G. Kaur, M. Rawat, A brief review on synthesis and characterization of copper oxide nanoparticles and its applications, J. Bioelectron. Nanotechnol. 1 (1) (2016) 9.

[9] S. Sun, X. Zhang, Y. Sun, S. Yang, X. Song, Z. Yang, Facile water-assisted synthesis of cupric oxide nanourchins and their application as nonenzymatic glucose biosensor, ACS Appl. Mater. Interfaces 5 (10) (2013) 4429-4437.

[10] R. K. Swarnkar, S. C. Sigh, R. Gopal, Effect of aging on copper nanoparticles synthesized by pulsed laser ablation in water: structural and optical characterizations, Bull. Mater. Sci. 34 (7) (2011) 1363-1369.

[11] S. Sun, X. Zhang, Y. Sun, J. Zhang, S. Yang, X. Song, A facile strategy for the synthesis of hierarchical CuO nanourchins and their application as non-enzymatic glucose sensors, RSC Adv. 3 (2013) 13712-13719.

[12] R. A. Ganeev, H. Singhal, P. A. Naik, J. A. Chakera, A. K. Srivastava, T. S. Dhami, M. P. Joshi, P. D. Gupta, Influence of C60 morphology on high-order harmonic generation enhancement in fullerene-containing plasma, J. Appl. Phys. 106 (10) (2009) 103103.

[13] T. Yamamoto, K. Machi, S. Nagare, K. Hamada, M. Senna, The relation between surface plasmon resonance and morphology of Ag nanodots prepared by pulsed laser deposition, Solid State Ion. 172 (1-4) (2004) 299-302.

[14] E. G. Goh, X. Xu, P. G. McCormick, Effect of particle size on the UV absorbance of zinc oxide nanoparticles, Scripta Mater. 78-79 (2014) 49-52.

[15] G.-H. Fan, S.-L. Qu, Z-Y. Guo, Q. Wang, Z.-G. Li, Size-dependent nonlinear absorption and refraction of Ag nanoparticles excited by femtosecond lasers, Chin. Phys. B 21 (4) (2012) 047804.

[16] K. Wang, H. Long, M. Fu, G. Yang, P. Lu, Size-related third-order optical nonlinearities of Au nanoparticle arrays, Opt. Express 18 (13) (2010) 13874-13879.

[17] S. Lee, A. Ahn, M. Y. Choi, Direct observation of aluminium ions produced *via* pulsed laser ablation in liquid: a 'turn-on' fluorescence study, Phys. Chem. Chem. Phys. 14 (2012) 15677-15681.

[18] Z.-Y. Deng, Y.-F. Liu, Y. Tanaka, J. Ye, Y. Sakka, Modification of Al particle surfaces by γ-Al2O3 and its effect on the corrosion behavior of Al, J. Am. Ceram. Soc. 88 (4) (2005) 977-979.

[19] J. M. J. Santillán, F. A. Videla, M. B. F. van Raap, D. C. Schinca, L. B. Scaffardi, Analysis of the structure, configuration, and sizing of Cu and Cu oxide nanoparticles generated by fs laser ablation of solid target in liquids, J. Appl. Phys. 113 (13) (2013) 134305.

[20] K. K. Kim, D. Kim, S. K. Kim, S. M. Park, J. K. Song, Formation of ZnO nanoparticles by laser ablation in neat water, Chem. Phys. Lett. 511 (1-3) (2011) 116120.

[21] R. M. Tilaki, A. I. Azad, S. M. Mahdavi, Stability, size and optical properties of silver nanoparticles prepared by laser ablation in different carrier media, Appl. Phys. A 84 (2006) 215-219.

[22] Y. Ishikawa, Y. Shimizu, T. Sasaki, N. Koshizaki, Preparation of zinc oxide nanorods using pulsed laser ablation in water media at high temperature, J. Colloid Interf. Sci. 300 (2) (2006) 612-615.

[23] R. A. Ganeev, M. Baba, A. I. Ryasnyansky, M. Suzuki, H. Kuroda, Characterization of optical and nonlinear optical properties of silver nanoparticles prepared by laser ablation in various liquids, Opt. Commun. 240 (4-6) (2004) 437-448.

[24] K. Zhang, D. S. Ivanov, R. A. Ganeev, G. S. Boltaev, P. S. Krishnendu, S. Singh, M. E. Garcia, I. N. Zavestovskaya, C. Guo, Pulse duration and wavelength effects of laser ablation on the oxidation, hydrolysis, and aging of aluminum nanoparticles in water, Nanomater. 9 (2019) 767.

[25] E. V. Barmina, P. G. Kuzmin, G. A. Shafeev, Self-organization of hydrogen gas bubbles rising above laser-etched metallic aluminum in a weakly basic aqueous solution, Phys. Rev. E 84 (4) (2011) 045302.

[26] E. Stratakis, M. Barberoglou, C. Fotakis, G Viau, C. Garcia, G. A. Shafeev, Generation of Al nanoparticles via ablation of bulk Al in liquids with short laser pulses, Opt. Express 17 (15) (2009) 12650-12659.

[27] J. F. Q. Rey, T. S. Plivelic, R. A. Rocha, S. K. Tadokoro, I. Torriani, E. N. S. Muccillo, Synthesis of In2O3 nanoparticles by thermal decomposition of a citrate gel precursor, J. Nanopart Res. 7 (2) (2005) 203.

[28] C. R. Patra, A. Gedanken, Rapid synthesis of nanoparticles of hexagonal type In$_2$O$_3$ and spherical type Tl$_2$O$_3$ by microwave irradiation, New J. Chem. 28 (2004) 1060-1065.

[29] D. Beena, R. Vinodkumar, I. Navas, G. Rajan, V. P. Mahadevan Pillai, Efficient photoluminescence from pulsed laser ablated nanostructured indium oxide films, Mater Sci Eng. B 174 (1-3) (2010) 59-65.

[30] D. Dorranian, S. Tajmir, F. Khazanehfar, Effect of laser fluence on the characteristics of Ag nanoparticles produced by laser ablation, Soft Nanosci. Lett. 3 (4) (2013) 37813.

[31] Y.-H. Chen, C.-S. Yeh, Laser ablation method: Use of surfactants to form the dispersed Ag nanoparticles, Colloid Surface A 197 (1-3) (2002) 133-139.

[32] T. Tsuji, D. H. Thang, Y. Okazaki, M. Nakanishi, Y. Tsuboi, M. Tsuji, Preparation of silver nanoparticles by laser ablation in polyvinylpyrrolidone solutions, Appl. Surf. Sci. 254 (16) (2008) 5224-5230.

[33] J. Gan, X. Lu, J. Wu, S. Xie, T. Zhai, M. Yu, Z. Zhang, Y. Mao, S. Chi, I. Wang, Y. Shen, Y. Tong, Oxygen vacancies promoting photoelectrochemical performance of In$_2$O$_3$ nanocubes, Sci. Rep. 3 (2013) 1021.

[34] S. Elouali, L. G. Bloor, R. Binions, I. P. Parkin, C. J. Carmalt, J. A. Darr, Gas sensing with nano-Indium Oxides (In2O3) prepared via continuous hydrothermal flow synthesis, Langmuir 28 (3) (2012) 1879-1885.

[35] F. Li, J. Jian, R. Wu, J. Li, Y. Sun, Synthesis, electrochemical and gas sensing properties of In2O3 nanostructures with different morphologies, J. Alloy Compd. 645 (2015) 178-183.

[36] Y. W. Heo, D. P. Norton, L. C. Tien, Y. Kwon, B. S. Kang, F. Ren, ZnO nanowire growth and devices, Mater. Sci. Eng. R Reports 47 (1-2) (2004) 1-47.

[37] K. Iwata, H. Tampo, A. Yamada, P. Fons, K. Matsubara, K. Sakurai, Growth of ZnO and device applications, Appl. Surf. Sci. 244 (1-4) (2005) 504-510.

[38] K. Zhang, R. A. Ganeev, G. S. Boltaev, P. V. Redkin, P. S. Krishnendu, C. Guo, Formation, aging and self-assembly of regular nanostructures from laser ablation of indium and zinc in water, Colloids Surf. A 584 (2020) 124016.

[39] N. Acacia, F. Barreca, E. Barletta, D. Spadaro, G. Currò, F. Neri, Laser ablation synthesis of indium oxide nanoparticles in water, Appl. Surf. Sci. 256 (22) (2010) 6918-6922.

[40] P. K. Khanna, K. W. Jun, K. B. Hong, J. O. Baeg, R. C. Chikate, B. K. Das, Colloidal synthesis of indium nanoparticles by sodium reduction method, Mater Lett. 59 (8-9) (2005) 1032-1039.

[41] F. Barreca, N. Acacia, E. Barletta, D. Spadaro, G. Currò, F. Neri, Small size TiO2 nanoparticles prepared by laser ablation in water, Appl. Surf. Sci. 256 (21) (2010) 6408-6412.

[42] Ü. Özgür, Y. I. Alivov, C. Liu, A. Teke, M. A. Reshchikov, S. Doğan, A comprehensive review of ZnO materials and devices, J. Appl Phys. 98 (4) (2005) 041301.

[43] P. Camarda, L. Vaccaro, F. Messina, M. Cannas. Oxidation of Zn nanoparticles probed by online optical spectroscopy during nanosecond pulsed laser ablation of a Zn plate in H2O, Appl. Phys. Lett. 107 (1) (2015) 013103.

CHAPTER 6

SIZE- AND SHAPE-DEPENDENT PROPERTIES OF NANOPARTICLES

In this chapter, we discuss the results of studying the optical, structural, and nonlinear optical characteristics of the gold nanoparticles (GN) suspensions prepared using the chemical technique. A systematic study of the third-order optical nonlinearities of the GN of four different sizes is analyzed. We also analyze the variable nonlinear optical response of these nanoparticles and discuss the optical limiting studies in GN suspension.

We discuss the synthesis of Cu NPs and self-aggregated CuO nanoellipsoinds (NEs) produced during laser ablation. We also analyze the change of the band gap of oxidized Cu NPs in water. This process leads to the formation of CuO NEs with 2.4 eV band gap due to the "bottom-up" aggregation of Cu NPs in deionised water. We discuss the influence of the band gaps of Cu NPs and CuO NEs on their nonlinear optical properties.

Finally, we analyze different nonlinear optical processes in the ZnO-containing nanostructured materials. We discuss the third-order nonlinear optical properties of ZnO nanoparticles synthesized during laser ablation of the bulk materials in the water environment using the 1064 nm, 5 ns heating pulses. Second-order optical nonlinearities of the thin films comprising ZnO nanocrystals, nanorods, and nanoparticles are analyzed by the second harmonic generation emitting from those nanostructures in the case of irradiation by 800 nm, 40 fs pulses. The suspension of ZnO nanoparticles shows the optical of fs pulses due to the nonlinear absorptive and refractive processes in these species.

6.1. Size-dependent off-resonant nonlinear optical properties of gold nanoparticles and demonstration of efficient optical limiting

Gold nanoparticles (GN) in the form of colloidal solutions were previously prepared using either chemical or laser ablation methods. The difference between these methods consists of different size characteristics

of the nanoparticles produced. In previous studies, dynamics of the spatial and nonlinear optical parameters of GN were noted, but the mechanisms responsible for these variations have not been clarified to a sufficient extent. Optical nonlinearities of GN were the subject of a number of studies during the past two decades. In particular, it has been shown that the nonlinear refractive index of the gold colloidal solution has a considerable value [1]. Those studies of gold aggregates at the wavelength of 532 nm, i.e. at resonance conditions with the SPR band of GN, have shown that the changes of the refraction index can be due to different physical mechanisms.

Saturable absorption (SA) and reverse saturable absorption (RSA) using the 532 nm excitation are two familiar nonlinear absorption types in metal nanoparticles [2]. SA and RSA are related to the decreasing and increasing in the absorption, respectively. For GN, the SA effect at resonance conditions (i.e. close to $\lambda = 530$ nm) can mainly be attributed to the ground-state plasmon bleaching of the intraband transition in the *s-p* conduction band at moderate pump intensities. As the SA bands belong to the visible range, the GNs possess the potential of Q-switchers for short pulses generation in this region [3]. Additionally, the RSA effect can be related to free-carrier absorption or two-photon absorption (2PA). The changes from a negative value of nonlinear absorption to a positive one with increasing pulse energy suggest that the primary nonlinear absorption in GN has been transformed from SA to RSA process, which can be useful for the optical limiting of propagating radiation.

Optical limiting (OL) is one of the potential applications of the materials' optical nonlinearities. It is aimed at protecting eyes and sensitive registration devices from damage. Previously, small-sized species, like nanoparticles and quantum dots, have shown advantages in their use for OL [4,5]. The mechanisms that cause OL have different origins. RSA, which takes place due to enhanced absorption from excited states, is responsible for OL in colloidal metal compounds [6,7] and fullerenes [8]. 2PA is responsible for OL in semiconductor structures [9]. Excited-state induced process is one of the main sources of optical nonlinearities, which has potential applications for OL [10]. Thus a search of the enhanced population of these states in the case of various nanoparticle solutions is worth continuing by using the size-related variations of their nonlinear optical response at off-resonant conditions. Additionally, a search of effective optical limiters at 800 nm is useful for practical applications.

The enhanced nonlinear optical properties of nanoparticles as compared to those of the bulk state make nanoscale particles more promising for

designing optoelectronic and microelectronic devices. In this connection, the growing interest in GN is related to their unique optical, morphological, and electronic properties that are based on the quantum-confinement effect [11]. Many types of studies for GN with different shapes (sphere, cube, octahedron, rod, etc.) have been carried out [12-18].

The above analysis shows that the optical nonlinearities of GN under 530 nm resonant conditions have been studied extensively. Meanwhile, the analysis of the off-resonant nonlinear optical behaviour of synthesized GN of different sizes at around 800 and 400 nm or even shorter wavelengths is of special importance. Some variations of the third-order nonlinear properties in GN have been found for wavelengths at around 800 nm [19]. Meanwhile, the role of spatial characteristics of nanoparticles at off-resonant conditions yet took attention during previous studies of GN. The size-dependent variations of nonlinear optical characteristics along with the strong nonlinear optical absorption of both large (>50 nm) and small (<20 nm) GN under 400 and 800 nm femtosecond pulses can be used for different applications, such as high-order harmonic generation in "optimally" prepared GN plasmas, optical limiting, and switching, etc.

In this section, we discuss the results of studying the optical, structural, and nonlinear optical characteristics of the GN suspensions prepared using the chemical technique. A systematic study of the third-order optical nonlinearities of the GN of four different sizes is analyzed. We also analyze the variable nonlinear optical response of these nanoparticles. Finally, we discuss the optical limiting studies in GN suspension [20].

6.1.1. Synthesis of GN suspensions and optical and nonlinear optical measurements

Gold nanoparticles can be synthesized by different methods. Since the optical, and especially nonlinear optical, properties are strongly governed by GN sizes, morphology, and surrounding environment, a modified preparation of the Turkevich citrate method [21] was chosen for the synthesis of four different sizes of nanoparticles. The sizes of the GN were controlled by quantitatively varying the addition of the trisodium citrate (stabilizing and reducing agent) to tetrachloroauric acid.

GNs were prepared by the reduction of tetrachloroauric acid ($HAuCl_4$) with trisodium citrate ($Na_3C_6H_5O_7$). The $HAuCl_4$ solution (1% 2 mL) and deionised water (48 mL) were heated until boiling. Then specific quantities of trisodium citrate along with deionised water (5 mL) were added quickly into this boiling mixture under vigorous stirring. The solution turned from yellow to wine-red colour and then the heating was

stopped after 15 minutes. The stirring was continued for 30 more minutes until the reaction mixture was cooled down. To prepare the GN suspensions of different sizes, 0.0143, 0.0285, 0.114, and 0.228 g of trisodium citrate were added during the process to stabilize and reduce the $HAuCl_4$ and to obtain a descending size distribution of GN. The particle size and the shape of prepared samples were determined using a scanning electron microscope (SEM) and a transmission electron microscope (TEM). The absorption measurements of samples were performed using a UV-Vis spectrophotometer. The optical spectra were measured in the range of 400 to 800 nm to detect the characteristic SPR and visible light absorption of GN suspensions.

The conventional z-scan scheme was used to study the off-resonant third-order nonlinear optical properties of GN suspensions (see the detailed description in previous chapters). The 800 nm, 60 fs pulses from Ti: Sapphire laser operating at 1 kHz repetition rate were focused using the 400 mm focal length spherical lens along the *z-axis* through which the GN suspension filled in a 2 mm thick silica glass cell was displaced. To generate the second harmonic pulses (λ=400 nm), a BBO crystal was used. The 200 ps pulses were also available from this laser by extracting part of uncompressed radiation. The spatial distribution of the focused beam was found to be close to the Gaussian shape with the 42 and 76 μm full widths at half maximum and $1/e^2$ maximum of intensity distributions respectively, which was defined using a CCD camera. The variations in the normalized transmittances of samples in the closed-aperture (CA) and open-aperture (OA) z-scan schemes were measured using a fast photodetector. The aperture sizes of the CA scheme (1.5 mm) allowed transmittance of ~10% of the radiation propagated through the samples.

This z-scan scheme was calibrated using a 1-mm-thick fused silica plate. The calculations using the fitting procedure allowed the definition of the nonlinear refractive index of this material at 800 nm to be $(3.0\pm0.7)\times10^{-16}$ cm^2 W^{-1}. This value is close to earlier reported measurements of the γ of fused silica at this wavelength (3×10^{-16} cm^2 W^{-1} [22], $(2.7\pm0.3)\times10^{-16}$ cm^2 W^{-1} [23]). The error bars ($\pm5\%$) of these measurements were the same during the entire course of the experiments. The error bars of the definition of the absolute values of γ and β were estimated to be $\pm25\%$ due to uncertainty in the measurements of the intensity of laser pulses in the focal plane. The OA and CA Z-scans were fitted using standard equations of the z-scan theory described in previous chapters.

6.1.2. Morphological and optical analysis of GN suspensions

The particle size distribution and the morphology of synthesized GN were determined from the SEM and TEM images [Fig. 6.1(a)]. The mean diameters of GN were found to be 64, 32, 17, and 13 nm in the case of the addition of a different amount of trisodium citrate to the mixture. It was distinctly observed that the increase of trisodium citrate led to a decrease of GN sizes, which has shown that the relative concentration of the precursor and the reducing agent strongly affect the nucleation and the growth progression of GN. For particles below 20 nm, the size distribution was comparatively homogeneous and the standard deviation from mean size was minimal. Electron microscopy of suspensions [Fig. 6.1(b)] demonstrated no changes in the size parameters of the nanoparticles occurring during two months period. The size distribution of GN remained stable as well.
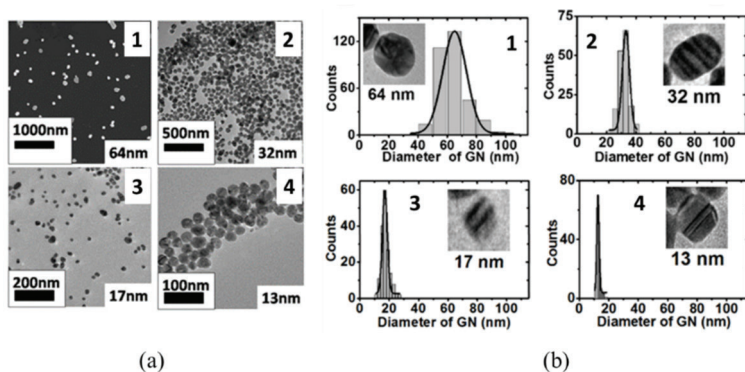
Fig. 6.1. (a) SEM image of (1) 64 nm GN. TEM images of (2) 32, (3) 17, and (4) 13 nm GN. (b) Histograms of corresponding nanoparticles and images of single GN. Reproduced from [20] with permission of the Optical Society of America.

The optical properties of GN show the characteristic absorption dominated by surface Plasmon resonance (SPR) peaks at 537, 528, 526, and 521 nm for particle sizes of 64, 32, 17, and 13 nm respectively (Fig. 6.2). For the metal nanoparticles, size controllability and surface tenability are essential. The electronic and optical properties exploited in their applications are highly dependent on the particle size and shape. The red shift is also accompanied by a broadening of the SPR band. The red shift

increased with the increase in particle size and is characterized by the appearance of a blue-colour solution. The absorption spectrum is determined by the localized surface plasmon resonance of the metal nanoparticles in the suspension. The broad range of particle sizes and shape distributions for 64 nm GN resulted in a notably broader absorption spectrum. The width and position of SPR were varied as a function of particle size and shape (see inset in Fig. 6.2).

As has been previously pointed out in a number of studies, the absorption spectra of GN can be controlled, to a considerable extent, by the parameters and methods of preparation of the nanoparticle-contained solutions. The positions of the SPR of these colloidal suspensions prepared by chemical methods correspond to the range of 530 - 550 nm, whereas, in the case of laser ablation, the peak of the SPR is slightly shifted toward shorter wavelengths due to the influence of small-sized particles. Variations of the absorption spectra of the chemically prepared GN were analyzed during two months and no significant changes were observed.
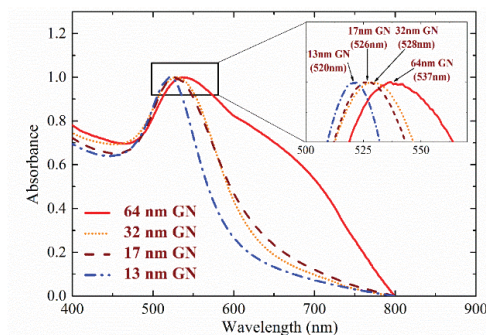
Fig. 6.2. Absorption spectra of different GN. Inset shows the enlarged area of the maximums of the SPR of different GN. Reproduced from [20] with permission of the Optical Society of America.

Previously, the aggregation and precipitation of GN were the main reasons for the variation of the optical and nonlinear optical properties of the nanoparticle suspensions obtained by chemical and laser ablation methods. Note that the nonlinear optical studies described in this paper were performed at the conditions of the stabilization of the size and spectral characteristics of the GN in the suspensions. The studies were carried out in the spectral regions corresponding to single (in the case of 400 nm radiation) and two-photon (in the case of 800 nm radiation)

absorption in the suspensions containing GN. These nanoparticles mostly showed spherical shapes. Notice that the absorption peak at around 527 nm corresponds to a commonly reported SPR of the spherical GN.

Once the sizes of nanoparticles increase, their peak of plasmon resonance will be tuned towards a longer wavelength and vice versa. One can use Mie and Drude theory to show that the sizes of GN can be calculated from their absorption spectra. The bandwidth of SPR has earlier been used [24] to estimate GN sizes according to the equation

$$\Delta\omega_{1/2} = \upsilon_F/R, \tag{6.1}$$

where $\Delta\omega_{1/2}$ is the half-width of the absorption band, R is the GN radius in nanometres, and F is the Fermi velocity of conduction electrons in gold (1.39×10^{15} nm/s). By applying this formula, which is useful for small particles ($R < 20$ nm), the diameter of GN in suspension was estimated (11 nm). This value is close to the direct measurements of the mean size of GN using the TEM images (13 nm).

6.1.3. OA z-scans

The main nonlinear optical process observed using the OA scheme at λ = 800 nm and related to the small-sized GN was the nonlinear absorption [Fig. 4(a)]. This process has earlier been associated with the RSA [25]. These OA Z-scans were obtained in the case of the suspensions containing 13, 17, and 32 nm nanoparticles. The values of the nonlinear absorption coefficients for these three GN suspensions were calculated to be 1.5×10^{-12}, 1.5×10^{-12}, and 2×10^{-12} cm W^{-1} respectively. These data were defined by the fitting procedure. The nonlinear absorption in these suspensions was also observed in the case of 400 nm pulses. In this case the process was also attributed to RSA [Fig. 6.3(b)]. The measured values of the nonlinear absorption coefficients attributed to RSA in these three GN suspensions were 1×10^{-11}, 1.5×10^{-11}, and 1.2×10^{-11} cm W^{-1} respectively, which are larger than in the case of longer wavelength pulses. No effect of the fused silica cell and water was observed up to $I_0 = 3\times10^{11}$ W cm^{-2}.

In the meantime, the SA was observed in the case of the suspension containing 64 nm GN by using both 800 and 400 nm pulses. Though the SA in the case of 800 nm pulses was relatively weak [$|\Delta T| \leq 0.075$, Fig. 6.3(a), upper curve], its influence was notably increased in the case of shorter wavelength (400 nm) pulses [$|\Delta T|\sim0.2$, Fig. 6.3(b), upper curve] even at significantly smaller intensity. This wavelength-dependent growth of SA is a commonly observed feature attributed to a larger cross-section

of the population of the excited states responsible for RSA in the case of shorter wavelength excitation.

The electric field polarizing a nanoparticle may substantially exceed the externally applied field. The most remarkable manifestation of this effect is related to the plasmonic properties, which enhance the nonlinear optical characteristics of the medium in the vicinity of the central wavelength of SPR, especially in the case of resonant excitation. This resonance can be considered in the framework of the model of collective oscillations of surface electrons in a nanoparticle. However, in discussed case (800 and 400 nm pulses) the excitation occurs far from the SPR band of GN (~530 nm). Thus the SA of GNs hardly could be attributed only to the influence of SPR, which is the coherent coupling between free electrons of the conduction band and the external electromagnetic field emitting at approximately similar wavelength [26].
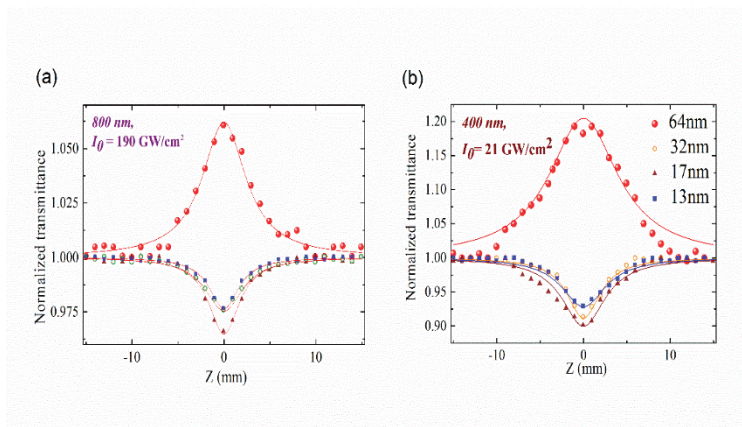
Fig. 6.3. OA z-scans of suspensions containing different GN using (a) 800 and (b) 400 nm, 40 fs pulses at the intensities of 1.9×10^{11} and 4.5×10^{10} W cm^{-2} in the focal plane. Reproduced from [20] with permission of the Optical Society of America.

Variation of 400 nm pulse energy strongly affected the z-scan of the suspension containing 64 nm GN and changed the role of SA. In Fig. 6.4, one can see the dependence of normalized transmittance on the position of the suspension containing 64 nm GN at different energies of 400 nm pulses. The absorption spectrum of this solution shows a broad linear absorption band centred at the wavelength of ~530 nm (Fig. 6.2, solid line). SA was steadily over passed by RSA with the growth of pulse energy from 38 to 410 nJ. Standard OA z-scan fitting allowed determining

sign and magnitude of positive and negative nonlinear absorption coefficients, as well as saturation intensity of this suspension.

One can see that SA, which dominates over RSA at relatively small energies of 400 nm pulses [E = 38 nJ, empty circles in Fig. 6.4(a)], becomes less pronounced at higher pulse energies ($E > 130$ nJ, see other curves) with regard to the growing RSA effect. This difference in the involvement of SA and RSA is clearly seen in the area close to the focal plane of the focusing lens (i.e. near z = 0 mm where laser radiation had the largest intensity). The gradual growth of pulse energy led to the appearance of a deeper valley and a larger decrease of normalized transmittance in the vicinity of z = 0 mm [down to $T \approx 0.6$; E = 318 nJ, filled triangles in Fig. 6.4(c)]. Finally, at E = 410 nJ, only RSA was dominated over the whole range of normalized transmittance variations [empty triangles, Fig. 6.4(d)]. The intensity of laser pulses at these conditions was close to the one at which the largest value of optical limiting can be achieved at λ = 400 nm (5×10^{11} W cm^{-2}).
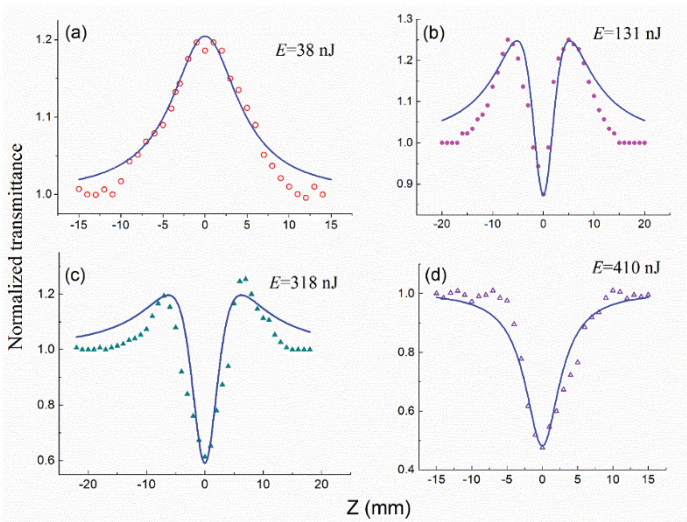
Fig. 6.4. OA Z-scans of the suspension containing 64 nm GN using 400 nm pulses of different energy. [(a) 38, (b) 131, (c) 318 and (d) 410 nJ]. Solid curves [(a) and (d)] are fitted with experimental data in accordance with the relations of phenomenological model of SA and Z-scan theory. Reproduced from [20] with permission of the Optical Society of America.

The nonlinear absorption coefficients at $\lambda = 400$ nm in the cases including SA and RSA were analyzed by the $\alpha(I) = \alpha_0 \times 1/(1 + I/I_{sat}) + \beta \times I = \alpha_{SA} + \alpha_{RSA}$ relation for intensity-dependent absorption coefficient. Here α_0 is the linear absorption coefficient, I is the intensity of laser pulse and I_{sat} is the saturation intensity. This absorption coefficient consisted of two parts: one related to saturable absorption (α_{SA}) and another related to reverse saturable absorption (α_{RSA}). Using this model one can find the saturation intensity ($I_{sat} = 4 \times 10^{11}$ W cm^{-2}) for used GN suspension. The β of this 64 nm GN suspension associated with RSA [Fig. 6.4(d)] was calculated to be 7×10^{-10} cm W^{-1} (at $\lambda = 400$ nm). One can estimate the β of nanoparticles to be 7×10^{-6} cm W^{-1} taking into account the volume part of 64 nm GN in the solution (10^{-4}). This strong RSA-associated nonlinear absorption was responsible for the optical limiting of 400 nm radiation.

A five-level model is used to interpret the RSA process. Such absorption in the medium requires the fulfilment of the following basic criteria: firstly, the material must have an excited-state absorption cross-section larger than the ground-state absorption cross-section, and secondly, the lifetime of the excited state must be long enough [in comparison with the pulse duration (t) of the laser radiation]. Each of the studied GN satisfies these criteria, which allow observation of such variations of normalized transmittance (T) of the GN suspensions, allowing an entire suppression of SA at the used conditions of experiments ($\lambda = 400$ nm, $t = 60$ fs, $E \approx 0.4 \mu$J).

Below we discuss the observation of different nonlinear absorption processes at 800 and 400 nm [Figs. 6.3 and 6.4]. One can see that, depending on particles sizes, the nonlinear absorption shows different signs (Fig. 6.3). SA was observed for larger-sized nanoparticles, while smaller-sized nanoparticles demonstrated TPA (in the case of 800 nm radiation) and RSA (in the case of 400 nm radiation). SA has been observed previously in various media (glasses doped with semiconductor nanoparticles, dyes, thin polythiophene films, etc.) in the IR, visible, and UV ranges. This process was analyzed at two wavelengths (800 and 400 nm) in the case of the suspension containing 64 nm nanoparticles. The parameter β can be represented by the ratio of the linear absorbance to the saturation intensity ($\beta = -\alpha/I_{sat}$). The theoretical dependence for 64 nm GN presented in Fig. 6.4(a) allowed defining $\beta = -4 \times 10^{-11}$ cm W^{-1}.

Earlier, a saturable absorption in similar media was reported in the case of 400 nm laser pulses [27]. Weak negative refraction and nonlinear absorption in GN using 792 nm radiation were demonstrated as well. Previous studies reported the values of saturated intensity and negative

nonlinear absorption coefficient of GN suspensions ($9{\times}10^9$ W cm^{-2} and $-8{\times}10^{-11}$ cm W^{-1} respectively) [28]. The appearance of SA in those studies was attributed to bleaching of the ground state at moderate intensities. Notice that the signs of nonlinear refractive indices and nonlinear absorption coefficients of GN were reported to be either negative or positive. Probably, this discrepancy can be attributed to the difference in the involvement of the local field of nanoparticles on the variation of the magnitude and sign of β and γ.

6.1.4. Optical limiting

OL materials based on noble metal nanoparticles are attractive, because gold and silver nanoparticles are easy to prepare, and they are highly soluble and stable in aqueous and organic solvents. The optical, nonlinear optical and optical limiting properties of gold and silver nanoparticles strongly depend on their size, shape, surrounding matrix, and solvent in which the nanoparticles are dissolved. Previously, considerable efforts have been focused on investigating the relationships between the OL and nonlinear optical properties of GN and their size and shape (nanostars, nanospheres, nanorods, nanoshells, bipyramidal, etc). In the case of nanosecond pulses, the GN exhibited intensity-dependent transformation from SA to RSA. Thus, the GNs were found to display strong OL properties in the case of relatively long and high-energy laser pulses [29]. The improved OL response in GN has earlier been discussed from the viewpoint of structural characteristics.
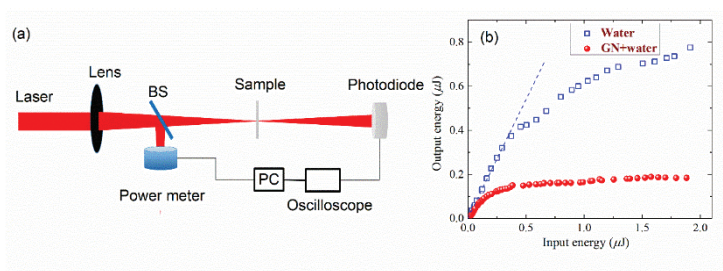
Fig. 6.5. (a) Setup for optical limiting studies. (b) Optical limiting of 800, 60 fs pulses in water and suspension containing 17 nm GN. Reproduced from [20] with permission of the Optical Society of America.

In discussed studies, the OL was demonstrated using the 800 nm, 60 fs pulses propagating through the suspension containing 17 nm GN in water.

This effect is attributed to RSA. The suspension was placed close to the focal plane of the 400 mm focal length lens. The energy of 800 nm pulses was gradually increased and the output radiation propagated through the 2-mm-thick cell containing GN suspension was measured [Fig. 6.5(a)]. The linear dependence between input and output pulses was maintained up to the input pulse energy of ~ 0.11 μJ [Fig. 6.5(b), filled spheres]. Further growth of input pulse energy led to OL of the energy of propagated laser radiation.

The energy of propagated pulse was stabilized at ~0.15 – 0.17 μJ. This process was maintained up to the input energy of 2 μJ above which stronger impeding processes worsened the propagation of laser pulses. A similar study in pure water showed no declination from the linear dependence up to $E_{output} \approx 0.35$ μJ of output radiation [Fig. 6.5(b), empty circles]. At these conditions, the coefficient of optical limiting induced suppression of propagating radiation in GN suspension compared to pure water was measured to be ~2.5. Further growth of input energy (i.e. above $E_{input} = 0.4$ μJ) led to the growing influence of white light generation in water and declination of E_{input}/E_{output} ratio from the linear dependence. Nevertheless, at the highest used input energy ($E_{input} \approx 1.9$ μJ) the ~4-fold suppression of output pulses in GN suspension compared to the pure water was achieved.

6.1.5. CA z-scans

The nonlinear refractive index of metal nanoparticles in different matrices may vary in a wide range and even change the sign, depending on the conditions of interaction, in particular, in resonant or nonresonant conditions. Under near-resonant conditions, the sign of nonlinear refractive index is determined by the ratio of the fundamental (or double) frequency of laser light and the SPR frequency of the nanoparticles. The conditions of experiments have corresponded to the nonresonant case. Even at these conditions, the sign of nonlinear refraction depends on the peculiarities of the experiment. Particularly, overheating of the samples by relatively strong 200 ps pulses led to negative nonlinear refraction of 800 nm, 1 kHz pulses, while weaker 60 fs pulses caused positive nonlinear refraction.

Figure 6.6 shows CA z-scans of the suspension containing 32 nm nanoparticles using different energies of 200 ps, 800 nm pulses. These z-scans exhibit different asymmetric peaks followed by a valley, which is a typical pattern for the thermal-lens-induced negative nonlinear refraction attributed to heat accumulation in the area of beam propagation. Similar z-

scans were observed in the case of other small-sized GN suspensions. This asymmetric pattern, together with the fact that the laser pulses strongly heat the suspension at a 1 kHz repetition rate, points out that the origin of the observed nonlinear refractive index is related to the thermal process. The pure water did not show such z-scans even at significantly larger energies of laser pulses.

In discussed case, the laser pulse interacts with the medium affected by the heating induced by the preceding pulse. The heat accumulation is due to 2PA or RSA and the low thermal conductivity of the medium. The laser-induced thermal lens effect occurs as energy absorbs from a laser beam, and it turns the medium into a lens for the same beam. The change of refractive index with temperature is caused by a decrease in the medium's density with increasing temperature. The refractive index will be changed with the change of the thermal lens effect in the GN-containing medium by varying the pulse energy. The characteristic time scale for heat dissipation is proportional to R^2 (R is the radius of nanoparticles) The characteristic time constant for heat dissipation depends on the surface area of the particle in accordance with relation $\tau(ps) = 0.64 \times R^2$ for R in nanometers [30]. The estimates show that the time necessary for the heat dissipation over the focused beam cross-section is ~1 ns, and, hence, it is important to take the heat accumulation into account when using radiation with the pulse repetition rate of 1 kHz at a relatively high pulse energy.
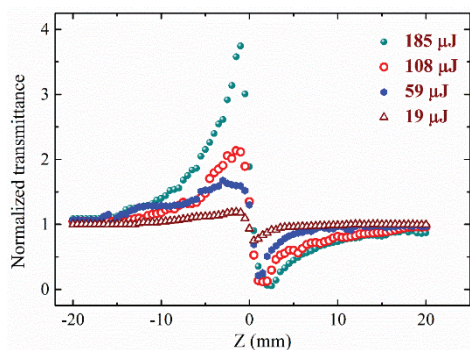
Fig. 6.6. CA z-scans of GN suspension using 800 nm, 1 kHz, 200 ps pulses of different energy. Reproduced from [20] with permission of the Optical Society of America.

To confirm the decisive role of the nonlinear absorption in the occurrence of the thermal effect one can note that the distance between

peak and valley (Δz_{p-v}), i.e. between the maximum and the minimum in the Z-scans, was close to 5 mm, which is equal to $1.2z_0$ (Fig. 6.6) since Rayleigh length for the focused beam was measured to be ≈4.2 mm. A relation $\Delta z_{p-v} \approx 1.2z_0$ for z-scan dependences in the case of the thermal effect caused by the nonlinear absorption is a sign of the fifth-order process, contrary to the case of third-order nonlinear refraction. In other words, firstly, the nonlinear process (either 2PA or RSA) causes the absorption, which further influences the nonlinear refractive properties of the medium at relatively high pulse energies.
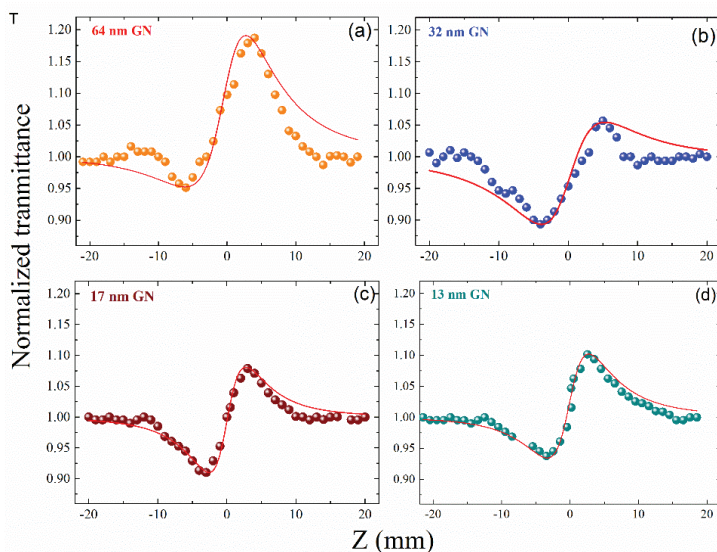
Fig. 6.7. CA z-scans of the nanoparticle suspensions containing (a) 64, (b) 32, (c) 17, and (d) 13 nm GN using 800 nm radiation. The energy of 800 nm, 60 fs pulses was 160 nJ. Reproduced from [20] with permission of the Optical Society of America.

The investigations of the dependence of ΔT_{p-v} on the pulse energy confirmed the decisive role of the 2PA-induced nonlinear absorption on the whole pattern of z-scans in the case of small-sized GN. The thermal-induced nonlinear refractive index of GN suspension was calculated to be $\gamma_T = -2 \times 10^{-9}$ cm^2 W^{-1} using the approach developed for nanoparticles dissolved in the water possessing relatively high thermal conductivity (0.6

WmK^{-1}). One can anticipate the growth of γ_T in the case of other liquids possessing lower thermal conductivity.
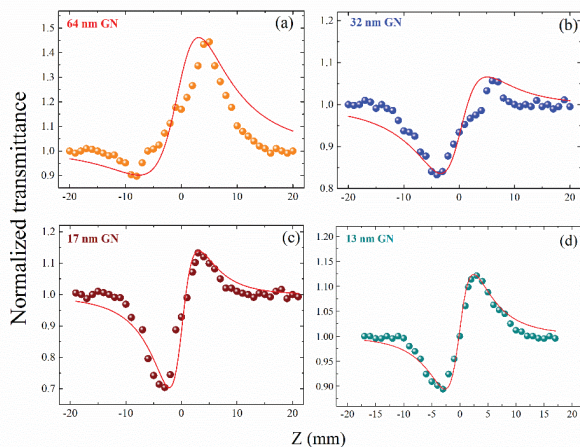
Fig. 6.8. CA z-scans of the nanoparticle suspensions containing (a) 64, (b) 32, (c) 17 and (d) 13 nm GN using 400 nm radiation. The energy of 400 nm, 60 fs pulses was 38 nJ. Reproduced from [20] with permission of the Optical Society of America.

Among different processes (intramolecular interaction, orientational Kerr effect, and electronic Kerr effect) contributing to the nonlinear refraction in the case of short laser pulses, the latter effect seems to be the determining one, especially in the case of femtosecond probe pulses. However, as it was shown in Fig. 6.6, under certain experimental conditions (relatively high pulse energy, longer pulse duration, higher pulse repetition rate, etc.), a considerable contribution to the nonlinear refraction can be also related to the thermal lens effect.

This effect can be caused by two processes. The first process is associated with the propagation of an acoustic wave arising due to the absorption of radiation in the medium. As studies showed, this process is an unimportant component, which does not influence the whole nonlinear refractive pattern of the studied samples. The second process consists of a change in the medium density caused by the accumulation of thermal energy in the absorbing region. It occurs in the case of low thermal conductivity of the medium and/or a high repetition rate of laser pulses. This process was responsible for observed negative nonlinear refraction in those studies. Similar experiments were also performed using the same

energies at a 10 Hz pulse repetition rate and did not observe the thermal lens effect. Indeed, the estimates showed that the relatively small temperature fluctuations do not obviously influence the refractive nonlinearities of the GN suspension.

Table 6.1. Calculated nonlinear optical characteristics of four GNs. Reproduced from [20] with permission of the Optical Society of America.

D	γ (cm^2/W) ($\times 10^{-10}$)	β (cm/W) ($\times 10^{-7}$)	γ (cm^2/W) ($\times 10^{-10}$)	β (cm/W) ($\times 10^{-7}$)
	λ=800 nm, t=60 fs, 1 kHz, E = 160 nJ		λ=400 nm, t=60 fs, 1 kHz, E = 38 nJ	
		OA		OA
64 nm	0.18	-0.7 (I_{sat}=5.7 $\times 10^{-12}$ W/cm^2)	-2.3	-2.7 (I_{sat}=4 $\times 10^{-11}$ W/cm^2)
32 nm	0.13	0.84	1	9
17 nm	0.14	0.59	2	7.2
13 nm	0.13	0.56	1.1	5.8

In the case of small energies of laser pulses, no accumulative effects occur at a 1 kHz repetition rate. Below we discuss the CA z-scans of four GN suspensions containing nanoparticles of different sizes using 800 nm, 160 nJ, 1 kHz, 60 fs pulses (Fig. 6.7). One can see that all suspensions showed the positive nonlinear refraction characterized by valley followed with a peak in the z-scan pattern. Both SA [Fig. 6.7(a)] and RSA [Fig. 6.7(b)] also influence these comparative CA z-scans, which was manifested by either larger peak or deeper valley. Similar measurements using significantly weaker 400 nm pulses (38 nJ, 1 kHz, 60 fs, Fig. 6.8) also showed positive nonlinear refraction, with negative and positive nonlinear absorption influencing the whole pattern of CA z-scans in the cases of the suspensions containing 64, 32 and 17 nm GN [Figs. 6.8(a) – 6.8(c)]. The use of a smaller pulse repetition rate at these experimental conditions resulted in similar results.

From Fig. 6.7, one can find that the distance between valley and peak (Δz_{v-p}), i.e. between the minimum and the maximum in the z-scans, was about 7.3 mm, which is close to $1.7z_0$. This relation ($\Delta z_{v-p} \approx 1.7z_0$) for z-scan dependences is a sign of a third-order process. The third-order nonlinear response of the studied suspensions mainly originates from pure electronic effects in nanoparticles. These electronic contributions are due to both intraband and interband transitions of gold. The first one corresponds to transitions within the conduction band and the second one corresponds to transitions from the upper levels of the filled d band to the levels above the Fermi level in the conduction band.

Previously, the influence of GN sizes on the third-order nonlinearity of PVA films was reported in Ref. [31]. Three samples of GN with different sizes were produced by the laser ablation method. They were used to produce GN doped PVA thin films. Using the z-scan technique, the nonlinear refractive index and nonlinear absorption coefficient of films were measured under the irradiation of the second harmonic of a low-power CW Nd:YAG laser. Results show that by decreasing the size of nanoparticles in the range of 9–20 nm, the nonlinear refractive index of Au doped PVA films decreases while their nonlinear absorption coefficient increases. The thermo-optical coefficient of samples was also calculated. Increasing the size of nanoparticles led to an increase in their thermo-optical coefficient.

The calculations of nonlinear refractive indices of GN suspensions were carried out using the standard fitting procedure. The γ at two wavelengths were calculated to be $\gamma_{800\ nm} = 1.4\times10^{-11}$ cm^2 W^{-1} and $\gamma_{400\ nm} = 2\times10^{-10}$ cm^2 W^{-1} (both for 17 nm GN suspension). The thermal-induced variation of nonlinear refraction in these conditions is minimal, contrary to the case shown in Fig. 6.6. Notice that thermal-induced processes may play important role in the case of high pulse repetition rate (MHz), as well. The calculated data of the nonlinear optical characteristics of different GNs are collected in Table 6.1.

6.2. Nonlinear optical characterization of copper oxide nanoellipsoids

The investigation of the nonlinear optical properties of metal oxides, such as Co_3O_4, V_2O_5, CuO, Fe_2O_3, Mn_3O_4, Cr_2O_3, has shown larger nonlinear responses compared to non-oxidized nanostructures [32,33]. Among the advantages of the metal oxides are the large optical nonlinearities ($10^{-8} - 10^{-7}$ esu), good thermal and chemical stability as well as mechanical strength. In particular, the copper oxide nanostructures

have the largest figure of merit based on the ratio of the magnitude of the optical nonlinearity to the linear optical absorption. The nonlinear optical properties of spherical copper nanoparticles doped in indium tin oxide matrix by ion implantation were studied in [34]. The $\chi^{(3)}/\alpha_0$ values for copper colloids were obtained to be of the magnitude of 10^{-12} to 10^{-11} esu cm. Meanwhile, no comparative analysis of the influence of band gaps on the nonlinear optical properties of CuO nanostructures was reported.

In this subsection, we discuss the synthesis of Cu NPs and self-aggregated CuO nanoellipsoinds (NEs) produced during laser ablation. We analyze the change of the band gap of oxidized Cu NPs in water. This process leads to the formation of CuO NEs with a 2.4 eV band gap due to the "bottom-up" aggregation of Cu NPs in deionised water. We analyze the influence of the band gaps of Cu NPs and CuO NEs on their nonlinear optical properties. The enhancement of the nonlinear refraction index of suspension and the red-shifted band gap of CuO NEs is observed [35].

6.2.1. *Morphology and linear optical responses of the samples*

The CuO NEs were synthesized from ablated Cu target in water using picosecond pulses. The output characteristics of the uncompressed pulses of this laser system were as follows: wavelength λ= 800 nm, pulse duration t= 200 ps, 1 kHz pulse repetition rate. The bulk Cu target with sizes $10\times10\times2$ mm^2 was immersed in a 20 mm thick quartz cell filled with deionised water. The focusing lens with 100 mm focal length was used for focusing laser radiation on the surface of the bulk copper target. The radiation fluence on the surface of the ablated target was measured to be 30 J cm^{-2}. The Cu was ablated for 30 min. The volume ratio of synthesized Cu NPs in suspension was estimated to be 1×10^{-4}. The target was moved to maintain the efficiency of laser ablation on the fresh surface of the Cu target. The suspension was rinsed during ablation to decrease the absorption of laser radiation in front of the surface of the copper target. No surfactants were added to the suspension to prevent the aggregation of nanoparticles. Copper nanoparticles were studied using TEM and SEM. The optical absorption of Cu NPs suspension was analyzed by a spectrometer. The oxidation of ablated suspension occurred during ablation. The stability of CuO NEs was controlled during the nonlinear optical studies of suspension. The morphology of Cu NPs in the water a few days after laser ablation was also analyzed.

Prior to carrying the study of third-order optical nonlinearities of CuO NEs the analysis of the morphological and linear absorptive characteristics of Cu NPs and CuO NEs was provided. In the case of Cu NPs, the broad

surface plasmon resonance peak was observed at 620 nm that was attributed to the presence of spherical nanoparticles (Fig. 6.9(a)). The green colour of Cu NPs suspension was attributed to the strong absorption near the infrared range of the spectrum. In the case of CuO NEs, the broad SPR peak was observed at 300 nm, which is a characteristic of these nanoellipsoids in deionised water. The increase in the band gap of the CuO NEs points out the quantum confinement effect arising due to the presence of the small nanoparticles and nanoellipsoids.

The volume ratio of small-sized nanostructures is the most important parameter in the quantum confinement effect. The red-shift of plasmonic peaks shows the growth of the sizes of nanostructures. In the meantime, the ratio of surface area to volume for the materials or substances containing nanoparticles has a significant effect on the optical properties of the material. It means that this ratio increases with a decrease in the radius of the spheres. The number of carriers increases with the blue shift of SPR. The enhancement of third-order nonlinearity can be explained by a high concentration of the carriers on the surfaces of CuO nanoellipsoids.

The band gaps were calculated based on the Tauc's model. The Tauc's model allows determining the band gap energies of Cu nanoparticles and CuO nanoellipsoids by extrapolation of the absorption spectra measured by spectrophotometer. Though the Tauc's plot extrapolation has been widely adopted for extracting bandgap energies of semiconductors, there is a lack of theoretical consideration for applying it for the nanocrystals. The optical transitions in CuO NEs have been formulated based on a purely theoretical approach. For α-Fe$_2$O$_3$, α-Cu$_2$V$_2$O$_7$, and monoclinic-BiVO$_4$ phases, the Automated Tauc Analysis methodology has been developed in Ref. [36]. This methodology was used for the extrapolation of the absorption spectra of CuO NEs to estimate the band gaps of these materials.

The optical band gaps of samples were estimated by fitting the equation

$$\alpha_0 h\nu = C(h\nu - E_g)^{1/2} \tag{6.2}$$

with the linear absorption spectra (see inset in Fig. 6.9(a)). Here h, ν and C are the Planck's constant, frequency, and constant, respectively. The band gaps of Cu NPs and CuO NEs were defined to be 3.5 and 2.4 eV.

The presence of CuO NEs was confirmed using X-ray diffraction spectroscopy (Fig. 6.9(b)). The atomic ratio of Cu to O was 1:1. The XRD of CuO nanoellipsoids has earlier been analyzed in Ref. [37], and showed the crystalline structure of these species. In those studies, the diffraction patterns were observed at 2θ = 31.7 (110), 35.49 (-111), 38.68 (111), and

61.45^0 (-123), which were assigned to the reflection lines from monoclinic CuO NEs. The discussed results were found to be in agreement with the reported diffraction patterns of CuO NEs from the above-refereed paper, thus confirming the crystalline structure of NEs.
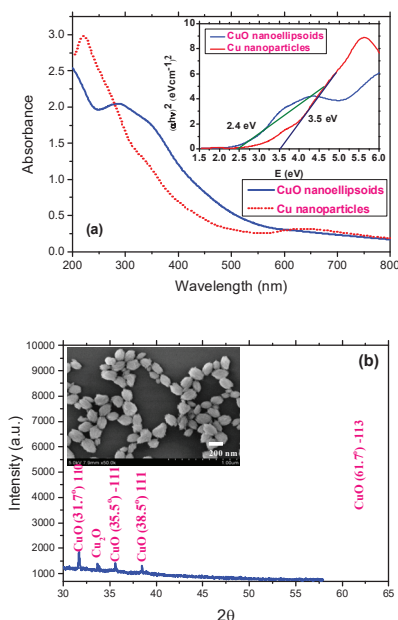
Fig. 6.9. (a) Absorption spectra of Cu nanoparticles during laser ablation using 200 ps, 800 nm pulses and self-aggregated CuO nanoellipsoids from Cu nanoparticles in the deionized water. (b) The XRD of CuO nanoellipsoids. Inset: SEM of CuO nanoellipsoids. Reproduced from [35] with permission of the Nature Research.

The inset in Fig. 6.9(b) shows the SEM of CuO NEs. The sizes of the orthogonal axes of these NEs were 150 and 200 nm. The statistics of the sizes of CuO NEs was analyzed using SEM and TEM of these nanostructures. The majority of NEs had sizes, which were equal to a=200 nm b=150 nm. The ellipticity of CuO NEs was equal to 0.75. The dispersion of sizes was 40 nm by a-axis and 30 nm by b axis. The ellipticity of NEs did not change during the change of the sizes of NEs.

The ellipticity of these particles was in the range of 0.7 - 0.75, which is relatively similar to the ellipsoidal particles.
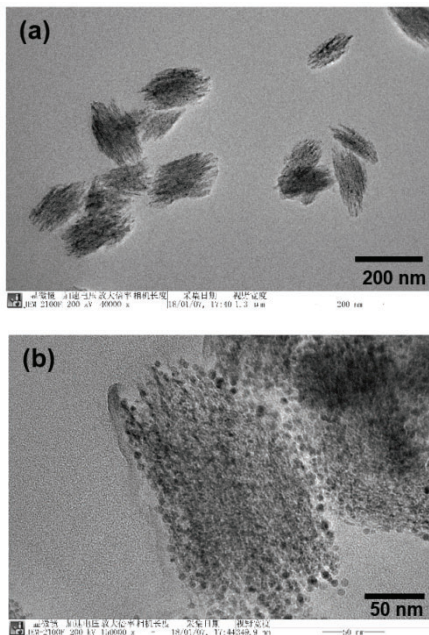
Fig. 6.10. TEM images of self-aggregated CuO NEs in water after laser ablation of bulk copper target using 800 nm, 200 ps heating pulses: (a) 200 nm scale, (b) 50 nm scale. Reproduced from [35] with permission of the Nature Research.

The morphology of CuO nanoellipsoids was studied three days after laser ablation of Cu target in water. For the first day the small-sized Cu nanoparticles, which caused the variation of the absorption spectra of fresh ablated samples, were observed. After three days the morphology of Cu NPs was changed. The synthesized CuO NEs were attached to each other to form the small CuO nanocrystals, which were identified by XRD peaks [Fig. 6.9(b)]. The most important parameters of nanostructures are their dimensions [38]. In the case of self-aggregated metal oxide nanoparticles, their sizes are distributed in a broad range.

The TEM images of CuO NEs were also analyzed [Fig. 6.10(a)]. The formation of copper nanoellipsoids can be explained by the "bottom-up"

approach. The aggregation based on this mechanism results in the formation of the single crystalline assemblies of CuO NEs containing a few hundred quantum dots. The small monocrystalline structures were observed, which aggregated during oxidation of Cu NPs in deionised water [Fig. 6.10(b)]. The formation of ellipsoids-like particles was observed (with the width of these particles in the range of 120–180 nm and the length 200–250 nm). The TEM images of these particles revealed the simultaneous presence of some grain-like particles [Fig. 6.10(b)], which were undetected in the SEM micrographs. The TEM image of a single NE clearly showed the roughness of the surface around the edges thus suggesting that these seeds were formed by the accumulation of other smaller-sized particles.

6.2.2. *Third-order nonlinear optical responses of the samples*

The z-scan method was used for the determination of the magnitude of the nonlinear optical parameters of Cu NPs and CuO NEs using the 60 fs fundamental (λ=800 nm) pulses, and its second harmonic generation (λ=400 nm) from Ti:S laser. Figure 6.11 shows the z-scans of CuO NEs suspension and the optical limiting (OL) in this suspension using the 800 nm, 60 fs probe pulses. In the case of CuO NEs suspension, the positive nonlinear refractive properties were observed in the field of femtosecond pulses with a 1 kHz repetition rate. (Fig. 6.11(a), filled squares).

The magnitudes of the nonlinear optical parameters (nonlinear refractive index (γ) and nonlinear absorption coefficient (β)) of the CuO NEs at λ=800 nm were determined to be γ =1.2×10^{-15} cm^2 W^{-1}, and β=1.0×10^{-10} cm W^{-1} (Fig. 6.11(a)). OA z-scan allowed analyzing the optical limiting properties of CuO NEs suspension at the wavelength of 800 nm, 60 fs pulses. The suspension was contained in 1-mm thick quartz cell. A linear transmittance of CuO NEs suspension was equal to 80 %. Figure 6.11(b) shows OL in CuO NEs suspension that was attributed to the two-photon absorption (2PA) measured by using the z-scans (Fig. 6.11(a), empty circles). The linear part of this dependence between output energy and input energy of 800 nm, 60 fs pulses in the OL curve was observed up to the energies of ~ 0.6 μJ (Fig. 6.11(b)). The deviation from linearity of this curve occurs with further growth of the input pulse energy from 0.6 to 1.6 μJ. Pure water was also studied in this energy range of propagated laser pulses and did not show the OL properties. The slope of linear fitting for pure deionised water at different input pulse energies was equal to 1.0, while the slope of linear fitting of CuO NEs at small energies was equal to 0.8. Further decrease of output energy was attributed to OL due to 2PA.

Notice that OL was not observed in the Cu NPs using 800 nm, 60 fs probe pulses at the same range of pulse energies as in the case of CuO NEs.
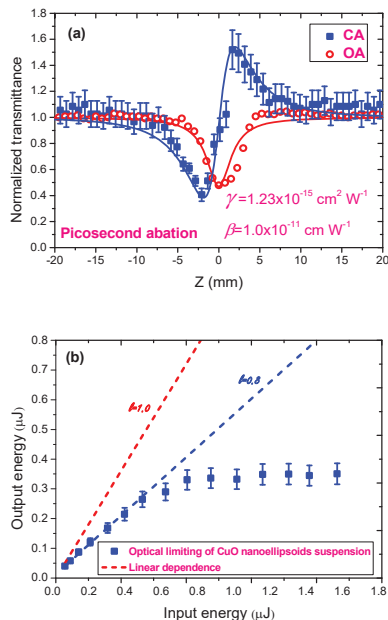
Fig. 6.11. (a) Z-scans using open-aperture (OA) and closed-aperture (CA) schemes. The Cu NEs were synthesized using ablation by the 800 nm, 200ps pulses. (b) Optical limiting curve of self-aggregated CuO NEs suspension with the same linear transmittance of 80% at 800 nm. Reproduced from [35] with permission of the Nature Research.

The comparative analysis of the nonlinear optical response of Cu NPs and CuO NEs suspensions was performed using the 400 nm radiation. Figure 6.12 shows the CA and OA Z-scan dependences of these suspensions. The nonlinear optical parameters of samples, measured using 400 nm, 60 fs probe pulses, are presented in Table 6.2. The four-fold increase of nonlinear refractive index in these two suspensions can be associated with the decrease of the band gap of CuO NEs. The band gap and refractive index are related to each other as follows:

$$n^4 E_g = 95\ eV \tag{6.3}$$

According to this relation, the refractive index of a semiconductor can be determined by knowledge of the energy band gap (E_g). This relation is based on the general assumption that all energy levels in a solid are scaled

down by a factor of $1/\varepsilon_{eff}^2$, where ε_{eff} is the effective dielectric constant of the samples.
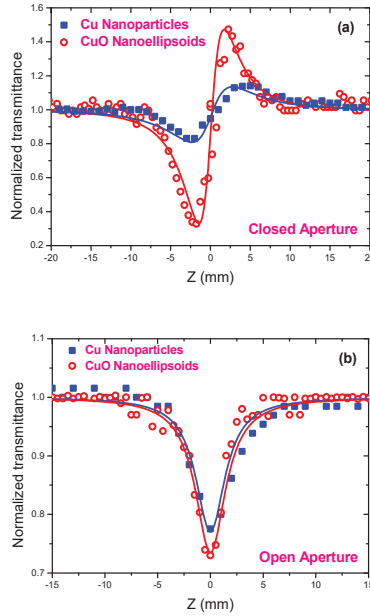
Fig. 6.12. Z-scans of copper NPs and copper oxide NEs suspensions (wavelength 400 nm, pulse duration 60 fs): (a) CA, and (b) OA Z-scans. Reproduced from [35] with permission of the Nature Research.

The relation between the 2PA coefficient and band gap was analyzed in [39]. It was shown that the 2PA varies as E_g^{-3}. This dependence can be represented by the following equation:

$$\beta_{2PA} = K\sqrt{E_p} F(2h\nu/E_g)/n^3 E_g^3 \qquad (6.4)$$

where K is a material-independent constant, n is the linear refractive index, and $E_p = 8P^2 m/h^2$ (where P is the Kane momentum parameter and m is the electron mass) is nearly material independent for a wide variety of semiconductors. This equation permits a prediction of 2PA coefficients of materials at different wavelengths. The function F, whose exact form depends on the assumed band structure, is a function only of the ratio of the photon energy $h\nu$ to E_g, which determines the states that

are optically coupled. In discussed case, the variation of the 2PA coefficient was observed due to different band gap energies of Cu NPs and CuO NEs.

Table 6.2. Nonlinear optical characteristics of the Cu nanoparticles and CuO nanoellipsoids. Reproduced from [35] with permission of the Nature Research.

Sample	Band gap (eV)	800 nm, 60 fs			400 nm, 60 fs		
		γ (cm^2 W^{-1})	β_{2PA} (cm W^{-1})	$\chi^{(3)}$ (esu units)	γ (cm^2 W^{-1})	β_{2PA} (cm W^{-1})	$\chi^{(3)}$ (esu units)
Cu NPs	3.5	-	-	-	1.5×10^{-15}	3.5×10^{-11}	6.0×10^{-10}
CuO NEs	2.4	1.23×10^{-15}	1.0×10^{-11}	1.2×10^{-9}	6.0×10^{-15}	3.8×10^{-11}	2.8×10^{-9}

The large third-order optical nonlinearities of spherical nanoparticles of the Cu$_{2-x}$S for strongly localized surface plasmon resonances (LSPR) absorption bands in the near-infrared region were investigated in [40]. The resonantly enhanced nonlinear susceptibility was observed in the vicinity of the LSPR peak, similar to the case of noble metal nanoparticles. The aim of this work was to show the variation of the third-order optical nonlinearities depending on the band gaps of Cu NPs and CuO NEs. The third-order nonlinear optical parameters of samples were compared with Cu$_{2-x}$S nanoparticles and showed the enhancement of the third-order nonlinearity of these nanostructures due to the influence of LSPR. In the case of 400 nm, 60 fs probe pulses the large nonlinear susceptibilities of CuO NEs were obtained (see Table 6.2). The nonlinear optical parameters of CuO NEs and Cu NPs were also compared at the same conditions. The aim of those studies was to show the advantages of CuO NEs compared with Cu NPs at the same wavelength of exciting laser radiation.

The pump-probe measurements were carried out to study the temporal response of the CuO NEs using 400 nm, 60 fs pulses. During these studies, the temporal response of the transient absorption profile of CuO NEs was not observed. Earlier, the transient absorption spectroscopy using an above band gap pump beam and below band gap probe beam to analyze the relaxation and recombination dynamics of the CuO nanocrystals at various pump fluencies was reported in [41]. They used the pulses of 1550 nm (1.6 eV) radiation as the probe beam and 780 nm (0.8 eV) radiation as the pump beam. In the meantime, the band gap of 50 nm CuO NPs was 1.5 eV. The three-time constants were reported in those studies. The first time constant varied with pump fluence from 330 fs to 630 fs, and was

attributed to momentum relaxation via carrier-carrier scattering in the valence band as well as exciton-exciton annihilation. The second time constant was unchanged at 2 ps and was attributed to the energy relaxation via carrier-phonon scattering within the valence band.

In discussed case, the probe and pump beam were higher than band gap of CuO NEs. The 800 nm, 60 fs pulses, and second harmonic generation of Ti:S laser at the 400 nm, 60 fs as a pump beam were also used, however, the temporal variations of the nonlinear optical response of NEs were not observed. The nonlinear refraction based on the Kerr nonlinearities depending on the band gaps of Cu NPs and CuO NEs was observed.

The main difference between the CuO NEs and CuO NPs is that CuO NEs have a 3D ellipsoidal shape, while CuO NP-contained nanosheets have a 2D sheet shape. 3D nanomaterials have tuneable properties, while 2D nanomaterials possess exceptional inherent properties. During those studies, the variation of the properties of self-aggregated CuO NEs originating from Cu NPs was observed. In the meantime, the 3D shape of CuO NEs can play an important role during the studies of the high-order nonlinearities of these species.

6.3. Low-order nonlinear optical studies of ZnO nanocrystals, nanoparticles, and nanorods

The optical limiting effect based on the third-order nonlinear optical properties of ZnO nanostructures has been analyzed in [42]. It was demonstrated that doping with different metals can improve the OL efficiency of ZnO. The third-order nonlinear optical properties and SHG in ZnO single crystals and nanomaterials (films, rods, wires, and crystals) have earlier been studied in [43-46]. The unusual shape of the angular dependence of SHG observed in those studies has been explained by various orientations of the polycrystalline structure in ZnO films. Recent studies have shown that the unique nonlinear optical properties of ZnO nanocrystals can be utilized in the nanoantennas for enhancement of the resonant SHG using the infrared femtosecond laser pulses [47].

In this section, we analyze different nonlinear optical processes in the ZnO-containing nanostructured materials [48]. We discuss the third-order nonlinear optical properties of ZnO nanoparticles synthesized during laser ablation of the bulk materials in the water environment using the 1064 nm, 5 ns heating pulses. Second-order optical nonlinearities of the thin films comprising ZnO nanocrystals, nanorods, and nanoparticles are analyzed by the second harmonic generation emitting from those nanostructures in the case of irradiation by 800 nm, 40 fs pulses. The suspension of ZnO

nanoparticles shows the OL of fs pulses due to the nonlinear absorptive and refractive processes in these species.

The laser ablation method, as well as the low temperature hydrothermal and chemical solution deposition methods, was used for the formation of ZnO nanostructures. The ZnO NPs were synthesized by ablation of the large-sizes (500 nm) ZnO nanocrystals in deionised water using the 1064 nm, 5 ns, 4 mJ, 10 Hz pulses. The laser beam was focused on the pressed tablet containing ZnO nanocrystals immersed in deionized water. The ablation was carried out for 10 min. The volume ratio of ZnO NPs in suspension was estimated to be 1×10^{-4}. The experimental arrangement for SHG measurements was as follows. The fs pulses ($\lambda=800$ nm, $\tau=40$ fs, and 1 kHz repetition rate; Ti: sapphire laser) passed through the neutral filters (NF) and then focused on different ZnO samples. The generated second harmonic (SH) yield was analyzed using the fibre spectrometer. The nonlinear optical parameters of species were analyzed using the standard z-scan technique.

6.3.1. Synthesis of samples

ZnO nanorods. ZnO nanorods were synthesized using the low-temperature hydrothermal method. Zinc nitrate hexahydrate ($Zn(NO_3)_2 6H_2O$) and hexamethyltetramine ($C_6H_{12}N_4$) were separately dissolved in the deionised water at room temperature and then mixed. The concentrations of both components were fixed at 0.1M. The mixture was stirred for 30 min, yielding a clear and homogenous solution. Then the indium tin oxide (ITO) film-coated substrates with a ZnO seeding layer were dipped into the solution and placed into the oven. The hydrothermal treatment was carried out at 90 °C for 5 h. Upon completion of the reaction, the samples were cooled down, washed in the deionised water several times, and dried in the air. Then zinc acetate dihydrate ($Zn(CH_3COO)_2 2H_2O$) was dissolved in pure ethanol at a concentration of 5mM. This solution was coated several times onto the substrates by a spin coater. The coated substrates were dried at room temperature and then annealed in air at 250 °C for 30 min. The annealed temperature (250 °C) was maintained above the decomposition temperature of zinc acetate particles in order to form the ZnO nanoparticles' seed layer. All chemicals were of analytical reagent grade.

ZnO nanocrystals. The ZnO nanocrystals were fabricated by the chemical solution deposition method [49]. 0.6586 g of zinc acetate dehydrate (Zn $(CH_3COO)_2 2H_2O$) was dissolved in a 30 ml methanol under vigorous stirring at room temperature. A 10 ml distilled water was then

added into the solution under stirring and was sonicated for 5 min. Sapphire and borosilicate glass substrates, being ultrasonically cleaned in acetone and methanol, were put into the bottom of the conical flask containing the above suspension. The conical flask was placed into a water tank at a constant temperature of 60 °C for 24 h. After the expiration of the ZnO particle deposition process, the flask with samples was taken out and cooled to room temperature. These samples were cleaned several times with methanol.

ZnO NPs. The UV-visible absorption spectroscopy and scanning electron microscopy were performed to characterize the suspensions after laser ablation of the tablet containing large ZnO nanoparticles. The UV and visible absorption spectra of NP suspensions were measured using the spectrophotometer. The SEM studies were carried out using the scatting electron microscope. The third-order nonlinearities of ZnO nanoparticle suspension were analyzed using the z-scan technique. For the comparative analysis of the second-order optical nonlinearities of the ZnO nanostructures possessing different shapes, the thin films containing ZnO nanoparticles from ablated solution were prepared using the spin-coating method.
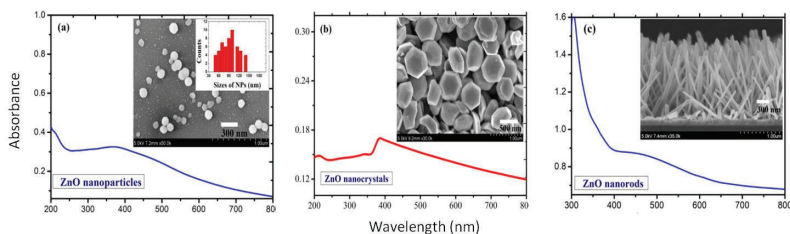
Fig. 6.13. Absorption spectra of ZnO nanostructures dispersed in deionised water: (a) ZnO nanoparticles, (b) ZnO nanocrystals (c) ZnO nanorods. Insets present the SEM images of samples. Reproduced from [48] with kind permission of The European Physical Journal (EPJ).

Figure 6.13a shows the absorption spectrum of the spherical ZnO NPs ablated in deionised water using the 1064 nm, 5 ns pulses. The surface plasmon resonance (SPR) for this NP suspension was located at 374 nm. It was observed that ZnO NPs showed the broadest SPR peak among the analyzed species. The broad SPR peak was attributed to the wide size distribution of spherical ZnO NPs in water (40 - 150 nm). Figures 6.13b and 6.13c show the absorption spectra of ZnO nanocrystals and ZnO nanorods. The corresponding SPRs of ZnO nanocrystals and ZnO

nanorods suspensions were located at 379 and 455 nm, respectively. These samples were chosen for the comparative analysis of the third-order optical nonlinearities of the ZnO nanostructures prepared by different methods. The thin films containing ZnO nanostructures were prepared for investigation of the second-order optical nonlinearities. The sizes of hexagonal ZnO nanocrystals were equal to 600 nm (inset in Fig. 6.13b). Inset in Fig. 6.13c shows the SEM image of ZnO nanorods. In the case of ZnO nanorods, the mean length and width of the single nanorods were approximately 2 μm and 50 nm, respectively. These nanorods possessed hexagonal shapes, while some spherical particles became attached to the centre of the structures.

6.3.2. Second harmonic generation and optical nonlinearities

In order to compare the SHG in ZnO nanostructures, the same energy of excitation pulse was kept during the whole set of experiments. Figure 6.14a shows the emission spectra from ZnO samples under excitation by 800 nm, 40 fs, 0.1 mJ pulses. The increase of pulse energy led to the appearance of white light generation on the surfaces of these samples. It was observed that these ZnO nanostructures emit the SHG radiation (λ=400nm) as well as provide the photoluminescence (PL) in the 500 - 700 nm range (Fig. 6.14b) under the excitation by 800 nm radiation.

The ZnO nanorods showed relatively strong SH emission, as well as a broader spectral range of PL, compared with ZnO nanocrystals and NPs at the same conditions of excitation. Moreover, these samples possess different peaks of photoluminescence, i.e. 585 nm (ZnO nanorods), 600 nm (ZnO nanoparticles), and 540 nm (ZnO nanocrystals), respectively. The shift of PL peaks was caused by the defects in the lattice of the ZnO crystal structure.

Figure 6.15 shows the dependence of the 400 nm radiation yield from different ZnO structures with respect to 800 nm pulse energies. The slopes of fitting lines in Fig. 6.15 correspond to 1.7, 1.9, and 2.0 that are close to the anticipated quadratic dependences between the fundamental and SH pulses. In the case of ZnO nanorods, the measured slopes of these dependencies in different ranges of pulse energies were changed from 1.7 to 2.5. A similar change of the slope has earlier been also observed in [50], which was explained by SHG or/and two-photon-induced luminescence (TPL).
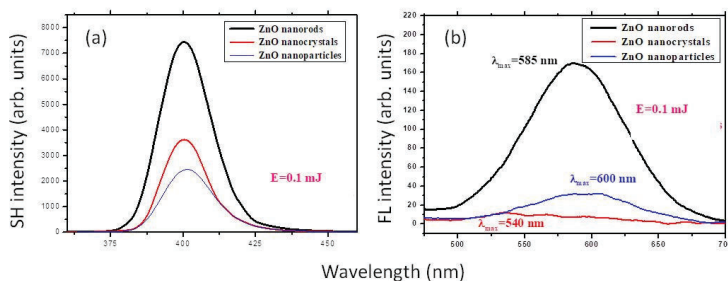
Fig. 6.14. (a) Spectra of second harmonic generation on the surfaces of ZnO nanostructures under irradiation by 800 nm, 40 fs pulses. (b) The comparative PL spectra of ZnO nanostructures excited by 800 nm, 40 fs pulses. Reproduced from [48] with kind permission of The European Physical Journal (EPJ).
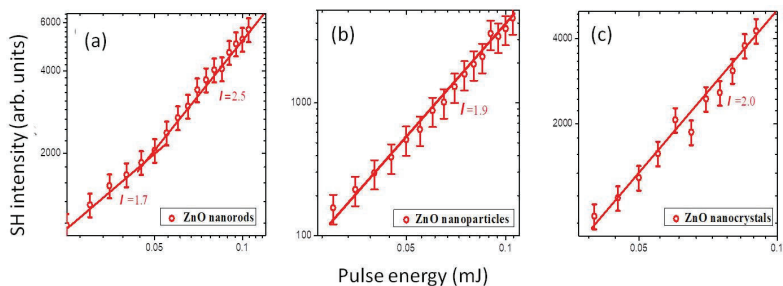
Fig. 6.15. The dependence of SH intensity (400 nm) on the energy of 800 nm pulse. (a) ZnO nanorods; (b) ZnO NPs; (c) ZnO nanocrystals. Reproduced from [48] with kind permission of The European Physical Journal (EPJ).

The analysis showed that the intensity of probe pulses was sufficient to observe the TPL in ZnO nanorods using the 800 nm, 40 fs pulses. In the meantime, TPL was not observed in ZnO nanoparticles and ZnO nanocrystals at the same excitation conditions. The four-fold enhancement of the intensity of SH was observed in ZnO nanorods compared to the intensity of SH in nanocrystals and nanoparticles. This difference in SH yields from the samples can be explained by the stronger local field effects in ZnO nanorods.

In the discussed study, the variations of OL properties were analyzed at different energies of the probe pulses. Figure 6.16 shows the absorptive

and refractive OL properties of ZnO NP suspension measured using the 800 nm, 40 fs pulses in the range of 0.5-1.6 µJ. The NP suspension was placed before the focal plane at the position of the valley of CA z-scan to measure the nonlinear absorption- and refraction-induced OL, respectively. In both cases, the limiting properties started to appear at ~0.47 µJ. It was observed that the nonlinear absorption-induced OL is more effective than the nonlinear refraction-induced OL. A lower threshold of nonlinear absorption-induced OL is attributed to the growing cross-section of reverse saturable absorption in ZnO nanoparticles. A similar process in pure water demonstrated notably lesser OL properties (Fig. 6.16, empty circles).
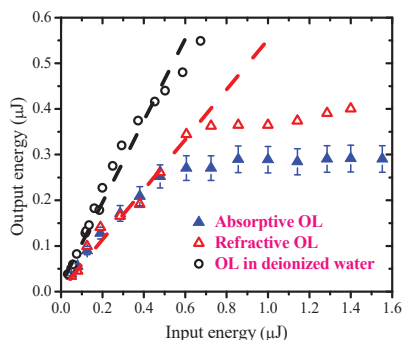
Fig. 6.16. Absorptive and refractive OL properties of ZnO NP suspensions in deionized water. Reproduced from [48] with kind permission of The European Physical Journal (EPJ).

The discussed studies revealed that the larger-sized NPs in ZnO suspension cause higher nonlinear absorption and hence stronger OL. The suspension containing 100 nm ZnO NPs demonstrated the OL effect caused by nonlinear absorption and nonlinear refraction in these nanostructures. In the case of refractive OL, the threshold of this process was higher than the threshold of absorptive OL at the same range of pulse energies (empty and filled triangles).

The optical nonlinearities of ablated ZnO NPs in water were studied using the z-scan technique using the 800 and 400 nm, 40 fs pulses (Fig. 6). It is seen from the absorption spectra shown in Fig. 6.13 that the 800 nm radiation is non-resonant with regard to the SPR of these NPs since there are no absorption peaks in the vicinity of this wavelength. Meanwhile, at 400 nm these NPs possess some notable absorption.
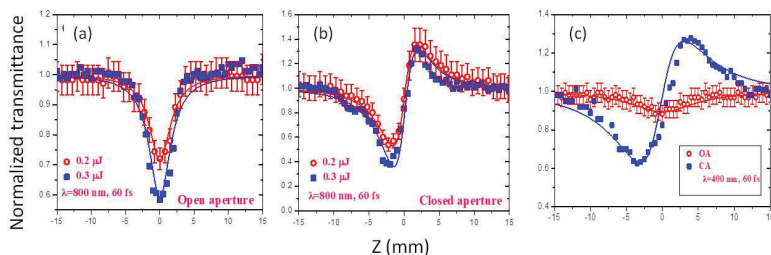
Fig. 6.17. (a) OA and (b) CA Z-scans of ZnO NPs suspension obtained using the 800 nm pulses of fs radiation at two probe pulse energies. (c) OA (open circles) and CA (filled squares) Z-scans of ZnO NPs suspension obtained using the 400 nm radiation. Reproduced from [48] with kind permission of The European Physical Journal (EPJ).

Table 6.3. Nonlinear optical parameters of ZnO NPs suspension. Reproduced from [48] with kind permission of The European Physical Journal (EPJ).

Parameters of probe pulses		Nonlinear optical parameters		
	Intensity (W cm^{-2})	β (cm W^{-1})	γ (cm^2 W^{-1})	$\chi^{(3)}$ (esu units)
800 nm	11.9×10^{10}	4.6×10^{-11}	1.6×10^{-15}	2.5×10^{-10}
400 nm	11.7×10^{10}	8.4×10^{-11}	4.3×10^{-15}	7.8×10^{-10}

Figure 6.17(a,b) shows the OA and CA measurements for ZnO NPs at different fs pulse intensities of 800 nm, 40 fs radiation. The nonlinear refraction and absorption coefficients remain approximately the same at different pulse energies (0.2 and 0.3 μJ). During the analysis of the third-order nonlinearities of ZnO NPs suspension, an asymmetric CA z-scan curve was observed at the highest energies of fs probe pulses caused by the growth of the nonlinear absorption in this suspension. The third-order nonlinear susceptibilities ($\chi^{(3)}$) of the suspension of ZnO NPs were determined using the fs 800 nm and 400 nm pulses.

The measured nonlinear optical parameters of ZnO NP suspension at corresponding pulse intensities are comprised in Table 6.3. The measurements showed the relatively high nonlinear absorption coefficient of ZnO NPs at 400 nm ($\beta = 8 \times 10^{-7}$) cm W^{-1} taking into account the 10^{-4} volume part of zinc oxide nanoparticles in the suspension. Other parameters of nanoparticle

suspension shown in this table could also be multiplied by 10^4 to determine the nonlinear optical characteristics of ZnO NPs.

These results obtained using 80 nm NPs were compared with those using smaller-sized ZnO NPs (40 nm). The 80 nm ZnO NPs suspension showed higher nonlinear optical parameters compared with the 40 nm NPs.

References to Chapter 6

[1]   S. C. Mehendale, S. R. Mishra, K. S. Bindra, M. Laghate, T. S. Dhami, K. S. Rustagi, Nonlinear refraction in aqueous colloidal gold, Opt. Commun. 133 (1-6) (1997) 273-276.

[2]   R. A. Ganeev, T. Usmanov, Nonlinear optical parameters of various media, Quantum Electron. 37 (7) (2007) 605-632.

[3]   D. Wu, J. Peng, Z. Cai, J. Weng, Z. Luo, N. Chen, H. Xu, Gold nanoparticles as a saturable absorber for visible 635 nm Q-switched pulse generation, Opt. Express 23 (18) (2015) 24071-24076.

[4]   L.W. Tutt, A. Kost, Optical limiting performance of C60 and C70 solutions, Nature 356 (6366) (1992) 225-226.

[5]   N. Venkatram, D. N. Rao, M. A. Akundi, Nonlinear absorption, scattering and optical limiting studies of CdS nanoparticles, Opt. Express 13 (3) (2005) 867-872.

[6]   W. Ji, H. J. Du, S. H. Tang, S. Shi, Nanosecond reverse saturable absorption in cubanelike transition-metal clusters, J. Opt. Soc. Am. B 12 (5) (1996) 876-881.

[7]   R. A. Ganeev, A. I. Ryasnyansky, M. K. Kodirov, S. R. Kamalov, T. Usmanov, Nonlinear susceptibilities, absorption coefficients and refractive indices of colloidal metals, J. Phys. D 34 (11) (2001) 1602-1610.

[8]   R. A. Ganeev, A. I. Ryasnyansky, M. K. Kodirov, T. Usmanov, Nonlinear optical characteristics of C 60 and C 70 films and solutions, Opt. Commun. 185 (4-6) (2000) 473-478.

[9]   M. Sheik-Bahae, A. A. Said, E. W. Van Stryland, High-sensitivity single-beam N2 measurements, Opt. Lett. 14 (17) (1985) 955-957.

[10] L.W. Tutt, T. Boggess, A review of optical limiting mechanisms and devices using organics, fullerenes, semiconductors and other materials, IEEE J. Quantum Electron. 17 (4) (1993) 299-338.

[11] G. Ramakrishna, O. Varnavski, J. Kim, D. Lee, T. Goodson, Quantum-sized gold clusters as efficient two-photon absorbers, J. Am. Chem. Soc. 130 (15) (2008) 5032-5033.

[12] Y. Yang, M. Nogami, J. Shi, H. Chen, G. Ma, S. Tang, Controlled surface-plasmon coupling in SiO2-coated gold nanochains for tunable nonlinear optical properties, Appl. Phys. Lett. 8 (8) (2006) 081110.

[13] I. Mirza, D. McCloskey, W. J. Blau, J. G. Lunney, Mechanism of large optical nonlinearity in gold nanoparticle films, Opt. Lett. 43 (7) (2018) 14551458.

[14] L. D. Boni, E. L. Wood, C. Toro, F. E. Hernandez, Optical Saturable absorption in gold nanoparticles, Plasmonics 3 (2008) 171.

[15] H. I. Elim, J. Yang, J. Y. Lee, J. Mi, W. Ji, Observation of saturable and reverse saturable absorption at longitudinal surface plasmon resonance in gold nanorods, Appl. Phys. Lett. 88 (8) (2006) 083107.

[16] K. S. Lee, M. A. El-Sayed, Dependence of the enhanced optical scattering efficiency relative to that of absorption for gold metal nanorods on aspect ratio, size, end-cap shape, and medium refractive index, J. Phys. Chem. B 109 (43) (2005) 20331-20338.

[17] X. Liu, X. Jia, M. Fischer, Z. Huang, D.R. Smith, Enhanced two-photon photochromism in metasurface perfect absorbers, Nano Letters 18 (10) (2018) 6181-6187.

[18] R. A. Ganeev, L. B. Elouga Bom, T. Ozaki, Enhancement of the high-order harmonic generation from the gold plume using the time-resolved plasma spectroscopy, J. Appl. Phys. 102 (7) (2007) 073105.

[19] J. T. Seo, Q. Yang, W. J. Kim, J. Heo, S. Ma, J. Austin, W. S. Yun, S. S. Jung, S. W. Han, B. Tabibi, D. Temple, Optical nonlinearities of Au nanoparticles and Au/Ag coreshells, Opt. Lett. 34 (3) (2009) 307-309.

[20] Y. Fu, R. A. Ganeev, P. S. Krishnendu, C. Zhou, K. S. Rao, C. Guo, Size-dependent off-resonant nonlinear optical properties of gold nanoparticles and demonstration of efficient optical limiting, Opt. Mater. Express 9 (3) (2019) 976.

[21] X. Ji, X. Song, J. Li, Y. Bai, W. Yang, X. Peng, Size control of gold nanocrystals in citrate reduction: the third role of citrate, J. Am. Chem. Soc. 129 (45) (2007) 13939-13048.

[22] K. Dota, J. A. Dharmadhikari, D. Mathur, A. K. Dharmadhikari, Third-order nonlinear optical response in transparent solids using ultrashort laser pulses, Appl. Phys. B 107 (3) (2012) 703-709.

[23] D. Blömer, A. Szameit, F. Dreisow, T. Schreiber, S. Nolte, A. Tünnermann, Nonlinear refractive index of fs-laser-written waveguides in fused silica, Opt. Express 14 (6) (2006) 2151-2157.

[24] M. A. Villegas, M. A. Garcia, J. Llopis, J. M. Fernandez Navarro, Optical spectroscopy of hybrid sol-gel coatings doped with noble metals, J. Sol-Gel Sci. Technol. 11 (3) (1998) 251-265.

[25] R. A. Ganeev, A. I. Ryasnyansky, A. L. Stepanov, T. Usmanov, Saturated absorption and reverse saturated absorption of Cu:SuO_2 at λ=532 nm, Phys. Status Sol. B 241 (3) (2004) R1-R4.

[26] K. Wang, H. Long, M. Fu, G. Yang, P.-X. Lu, Chin. Off-resonant third-order optical ninlinearity of Au nanoparticle array by femtosecond Z-scan measurement, Phys. Lett. 27 (12) (2010) 124204.

[27] S. K. Maurya, A. Rout, R. A. Ganeev, C. Guo, Effect of size on the saturable absorption and reverse saturable absorption in silver nanoparticle and ultrafast dynamics at 400 nm, J. Nanomater. 2019 (2019) 9686913.

[28] R. A. Ganeev, G. S. Boltaev, R. I. Tugushev, T. Usmanov, H. Kuroda, Nonlinear optical absorption and refraction in Ru, Pd, and Au nanoparticle suspensions, Appl. Phys. B 100 (3) (2010) 571-576.

[29] C. Zheng, J. Huang, L. Lei, W. Chen, H. Wang, W. Li, Nanosecond nonlinear optical and optical limiting properties of hollow gold nanocages, Appl. Phys. B 124 (1) (2018) 17.

[30] X. L. Zhang, Z. B. Liu, X. C. Li, Q. Ma, X. D. Chen, J. G. Tian, Y. F. Xu, Y. S. Chen, Transient thermal effect, nonlinear refraction and nonlinear absorption properties of graphene oxide sheets in dispersion, Opt. Express 21 (6) (2013) 7511-7520.

[31] T. Ghambari, D. Dorranian, Measurement of third order nonlinear susceptibility of Au nanoparticles doped PVA film, Opt. Spectrosc. 119 (5) (2015) 838-848.

[32] M. Ando, K. Kadono, M. Haruta, T. Sakaguchi, M. Miya, Large third-order optical nonlinearities in transition-metal oxides, Nature 374 (1995) 625-627.

[33] X. Zhu, J. Wang, D. Nguyen, J. Thomas, R. A. Norwood, N. Peyghambarian, Linear and nonlinear optical properties of Co_3O_4 nanoparticle-doped polyvinyl-alcohol thin films, Opt. Mat. Express 2 (1) (2012) 103-110.

[34] A. I. Ryasnyansky, B. Palpant, S. Debrus, R. I. Khaibullin, A. L. Stepanov, Nonlinear optical properties of copper nanoparticles synthesized in indium tin oxide matrix by ion implantation, J. Opt. Soc. Am. B 23 (7) (2006) 1348-1353.

[35] G. S. Boltaev, R. A. Ganeev, P.S. Krishnendu, K. Zhang, C. Guo, Nonlinear optical characterization of copper oxide nanoellipsoids, Scient. Rep. 9 (2019) 11414.

[36] S. K. Suram, P. F. Newhouse, J. M. Gregoire, High throughput light absorber discovery, Part 1: An algorithm for automated Tauc analysis, ACS Comb. Sci. 18 (11) (2016) 673-681.

[37] X. Zhang, S. Sun, J. Lv, L. Tang, C. Kong, X. Song, Z. Yang, Nanoparticle-aggregated CuO nanoellipsoids for high-performance non-enzymatic glucose detection, J. Mater. Chem. A 2 (26) (2014) 10073-100080.

[38] A. L. Stepanov, R. A. Ganeev, A. I. Ryasnyansky, T. Usmanov, Nonlinear optical properties of metal nanoparticles implanted in silicate glass, Nucl. Instrum. Meth. B 206 (2003) 624-628.

[39] N. M. Ravindra, P. Ganapathy, J. Choi, Energy gap–refractive index relations in semiconductors – An overview, Infra. Phys.& Techn. 50 (1) (2007) 21-29.

[40] Y. Hamanaka, T. Hirose, K. Tamada, T. Kuzuya, Plasmonic enhancement of third-order nonlinear optical susceptibilities in self-doped $Cu_{2-x}S$ nanoparticles, Opt. Mat. Express 6 (12) (2016) 3838-3848.

[41] B. Born, J. D. A. Krupa, S. Geoffroy-Gagnon, I. R. Hristovski, C. M. Collier, J. F. Holzman, Ultrafast charge-carrier dynamics of copper oxide nanocrystals, ACS Photon. 3 (12) (2016) 2475-2481.

[42] L. Irimpan, V.P.N. Nampoori, P. Radhakrishnan, Spectral and nonlinear optical characteristics of ZnO nanocomposites, Sci. Adv. Mater. 2 (2) (2010) 117-137.

[43] K.Y. Lo, Y.J. Huang, J.Y. Huang, Z.C. Feng, W.E. Fenwick, M. Pan, T.I. Ferguson, Reflective second harmonic generation from ZnO thin films: A study on the Zn–O bonding, Appl. Phys. Lett. 90 (16) (2007) 161904.

[44] R. Prasanth, L.K. van Vugt, D.A.M. Vanmaekelbergh, H.C. Gerritsen, Resonance enhancement of optical second harmonic generation in a ZnO nanowire, Appl. Phys. Lett. 88 (18) (2006) 181501.

[45] S.W. Chan, R. Barille, J.M. Nunzi, K.H. Tam, Y.H. Leung, W.K. Chan, A.B. Djurišić, Second harmonic generation in zinc oxide nanorods, Appl. Phys. B 84 (2006) 351-355.

[46] B. Kulyk, Z. Essaidi, J. Luc, Z. Sofiani, G. Boudebs, B. Sahraoui, Second and third order nonlinear optical properties of microrod ZnO films deposited on sapphire substrates by thermal oxidation of metallic zinc, J. Appl. Phys. 102 (11) (2007) 113113.

[47] N. Weber, M. Protte, F. Walter, P. Georgi, T. Zentgraf, C. Meier, Double resonant plasmonic nanoantennas for efficient second harmonic generation in zinc oxide, Phys. Rev. B 95 (20) (2017) 205307.

[48] A. Rout, G. S. Boltaev, R. Ganeev, K. S. Rao, D. Fu, R. Rakhimov, S. Kurbanov, S. Urolov, Z. Shaymardanov, C. Guo, Low- and high-order nonlinear optical studies of ZnO nanocrystals, nanoparticles, and nanorods, Eur. Phys. J. D 73 (2019) 235.

[49] S.S. Kurbanov, T.W. Kang, Effect of ultraviolet-illumination and sample ambient on photoluminescence from zinc oxide nanocrystals, J. Luminesc. 158 (2) (2015) 99-102.

[50] J. Dai, J. Zeng, S. Lan, X. Wan, S. Tie, Competition between second harmonic generation and two-photon-induced luminescence in single, double and multiple ZnO nanorods, Opt. Expess 21 (8) (2013) 10025-10038.

CHAPTER 7

THIRD HARMONIC GENERATION IN MONOPARTICLE- AND NANOPARTICLE-CONTAINED PLASMA MEDIA

Third harmonic generation (THG) in air and laser-induced plasmas (LIPs) using femtosecond pulses from Ti:sapphire class lasers is a well-studied process that allows determining the maximally available conversion efficiency of this nonlinear optical effect and diminishing the impeding mechanisms restricting this process [1-6]. THG allows the formation of ~266 nm sources of femtosecond pulses at the conversion efficiency from 800-nm class lasers of up to 10^{-3} [7-9] or even higher [10-13]. It can be increased by either varying the duration or the energy of driving pulses [14]. In the meantime, the decrease of THG conversion efficiency with the increase of the concentration of free electrons in the air was observed in [15].

Longer wavelength lasers allow observation of this process in the visible range, or even in the near and mid-IR ranges [16]. However, the application of these mid-IR sources does not allow achieving such relatively large conversion efficiencies due to the growing restricting mechanisms, which limit the number of photons of converted radiation. To increase the average power of such sources of coherent radiation in the shorter-wavelength range one has to apply high pulse repetition rate laser systems. Commonly used Ti:sapphire lasers do not allow operating with the rates above 1 kHz regime. The application of MHz sources of femtosecond pulses is also inefficient due to low pulse energies restricted by tens of nJ. In this connection, the millijoules-class Yb-doped fiber lasers ($\lambda \approx 1030$ nm) operating in the 100 kHz regimes can be considered as the suitable sources of driving pulses for THG ($\lambda \approx 343$ nm). This process has been studied in a few gases [17,18]. Moreover, these lasers are suitable for the fifth harmonic generation (FHG, $\lambda \approx 206$ nm).

The use of such lasers allows increasing the average third harmonic (TH) power by about two orders of magnitude, which becomes sufficient for various applications of these UV sources in spectroscopy,

photomodification of sensitive organic materials, photoluminescent studies of dyes and complex molecules, etc. These lasers can also be used for low-order nonlinear optical spectroscopy of LIPs generated on the surfaces of various materials. THG in LIP has already attracted attention due to its interesting features that allow determining plasma characteristics (concentration of electrons and plasma, presence of nanoparticles (NPs), determination of the optimal ablating materials for further expansion of generating harmonics towards the extreme ultraviolet region through high-order harmonics generation (HHG), etc.).

In this chapter, we discuss the study of the spatiotemporal profile of generated particles in various plasmas produced from bulk targets (C, Cr, In, Ni, Ag, CdS, and ZnS) using pulsed laser ablation and THG using 800 nm, 40 fs probe pulses. We also analyze the TH (λ=343 nm) and fifth harmonic (5H, λ=206 nm) generation produced in air and different LIPs by applying the Yb-doped fibre laser generating 37 fs, 100 kHz, 1030 nm, 0.5 mJ pulses.

7.1. Study of various material particles by third harmonic generation method based on laser pulse induced plasma

The clusters and nanoparticles have been recognized as the media possessing large optical nonlinearities. It has been proven that these multi-particle structures can be efficiently used for the generation of lower- and higher-order harmonics of ultrashort laser pulses. The harmonic generation (HG) can also be used as a characterization tool for the analysis of the composition of laser-induced plasmas. The spatiotemporal separation of emitted particles during the formation of plasma has made HG an effective technique to characterize them. There are few reports on the usage of THG as a characterization scheme [19-21] for the generated particles in plasma. This has been achieved by varying the arrival time of the probe pulses with respect to the heating pulses. The time-delay-based measurement of TH emission has shown the presence of the larger aggregates formed during LA, which can be also further analyzed during their deposition on the nearby substrates [22].

The discussed research analyzes the role of physical characteristics of the bulk target on THG in various plasmas using the variation of the delay between heating and probe pulses. An alternative approach of probing the ejected particle during plasma formation, other than time-delay-based measurements, is the measurement of the TH yield through the variation of the distance between the surface of the target and the probe pulses. Probing such particles in plasma through the measurement of TH can

determine the relationship between the mass and the velocity of the ejected particle during plasma creation similar to the delay-based measurements. THG is used as a probe mechanism to characterize the components of plasmas from various bulk targets such as graphite (C), silver (Ag), nickel (Ni), chromium (Cr), and indium (In), cadmium sulphide (CdS), and zinc sulphide (ZnS). THG in various plasmas is compared with the mass of the studied materials under vacuum conditions and in the air. Furthermore, we analyze the relative efficiency of THG in various plasmas, which were created using ns and ps heating laser pulses [23].

7.1.1. Experimental arrangements

All the bulk targets for the creation of plasma were used as purchased. C (99.9 %), Ag (99.95 %), Ni (99.95 %), Cr (99.95 %), and In (99.95 %) were chosen as the ablation targets. THG from wide band gap semiconductor materials, such as CdS (99.95 %), and ZnS (99.95 %), were also carried out in order to observe the influence of the ejected particle mass on THG.

The experimental setup for the THG study consisted of the regenerative amplifier operated at 800 nm with the pulses repetition rate of 1 kHz and 40 fs pulse duration. This system was seeded by Ti: sapphire oscillator (800 nm, 43 MHz, 60 nm bandwidth). Two different heating schemes were employed to perform THG in various targets. The first scheme [Fig. 7.1(a)] consisted of 200 ps heating pulses from the amplifier as heating pulses to create plasma plume from the target. The second scheme [Fig. 7.1(b)] consisted of 6 ns heating pulses at 1064 nm with a repetition rate of 10 Hz. The pulse width and beam diameter of the probe pulses at the position of the focusing lens were fixed at 40 fs and 20 mm, respectively. The beam diameters of ns and ps heating pulses were 5 and 7 mm respectively.

The arrival time of the fs probe pulse in the plasma area was fixed at 38 ns from the beginning of ablation by ps heating pulses. In the case of ns heating pulses, the arrival time of fs probe pulses with respect to heating radiation was controlled using a delay generator, which was operated using a trigger pulse from the amplifier running at 1 kHz. The heating pulses were focused on the targets using a 300 mm focal length lens, whereas the probe pulses were focused using a 500 mm focal length lens and propagated parallel to the surface of the target and perpendicular to the heating pulses. In the case of the ps heating scheme, the focus point of the fs probe beam was set to be 2 mm away from the focal point of the heating beam as shown in the inset of Fig. 7.1(a).
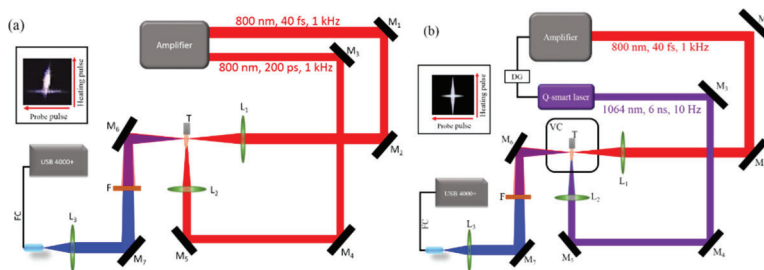
Fig. 7.1. Experimental setups for third-harmonic generation in (a) air and (b) vacuum conditions. M: mirrors, L: lenses, F: filter, T: target, VC: vacuum chamber, DG: delay generator. The insets show the spatial arrangements of the heating and probe laser pulses at the sample position in each schematic of the experimental setup. Reproduced from [23] with permission from Elsevier.

In the case of ns heating pulses, the focal points of both heating and probe pulses were set to be at the same point [see inset in Fig. 7.1(b)]. The energy of the heating pulses was fixed at 0.56 mJ for ps pulses and 3 mJ for ns pulses. The energy of probe pulses was varied by using a pair of a polarizer and a half-wave plate with a maximum employed energy of 0.5 mJ. The pressure in the vacuum chamber was kept at 0.1 Pa throughout the experiments for all samples. The generated TH radiation from the excited plasma was separated from the co-propagating fundamental beam using a prism and then was registered by a fibre spectrometer. The target sample was moved with constant speed to get the stable TH intensity. In order to establish the contribution of plasma species to the THG, the plasma spectra were collected using a 100 mm fused silica lens, which focused the plasma emission on the tip of the optical fibre interfaced with the spectrometer.

A systematic study was performed for the THG in various plasmas, where the dependence of the TH emission on the power of probe pulses, position of the target with respect to the probe pulses, and TH yield as a function of the arrival time of the probe pulses with respect to the heating pulses were carried out. The study consisted of two parts. The measurement of THG in the air was performed using the scheme shown in Fig. 7.1(a), whereas the schematic in Fig. 7.1(b) was used to study the time evolution of TH in various plasmas by varying the arrival time of probe pulses with respect to heating pulses.

7.1.2. THG from the metal plasmas produced in air

THG in the plasmas created on C, Ag, and Ni targets in the presence of air was carried out in order to compare the role of ejected particles based on their mass. Prior to the measurement of TH in respective plasmas, THG in the air was measured as a function of the probe pulse energy up to 0.5 mJ, which showed the cubic dependence of harmonic yield on the probe pulse energy. The intensity of TH from plasma was determined by subtracting the TH yield generated in the air from TH yield from plasma in the presence of air. As shown in Fig. 7.1(a), the wavelengths of the probe and heating pulses were kept at 800 nm with their respective pulse widths of 40 fs and 200 ps. The energy of the heating pulses was maintained at 560 µJ to create the plasmas. The arrival time of fs probe pulses was fixed at 38 ns after the beginning of plasma formation using ps heating pulses. The acquisition time for the TH collection was kept at 10 s. The surface of the bulk target was placed ~2 mm away from the axis of propagation of the probe pulse. The spatial arrangement of the probe and the heating pulses at the target position is shown in the inset of Fig. 7.1(a), which can anticipate a significant difference in TH intensity with the variation of the distance between the probe pulses and the target**.**

Figure 7.2 shows the variation of TH intensity as a function of the distance between the axis of propagation of probe pulses and the target (C, Ag, Ni) position. TH intensity dependences show similar behaviour with respect to the target position with maxima at ~2 mm for each of these targets. The trend in the TH intensity variations with this distance is related to the variation of heating laser fluence as the target moves away from the axis of probe pulse propagation due to the varying spot size of heating pulses on the target surface. The spot size variation changes the fluence of heating pulses on the target surface during ablation thus eventually producing the variable concentration of ejected particles during plasma movement towards the path of the probe beam. The major difference was seen for the case of carbon plasma, which allowed observation of TH up to almost 4 mm away from the target position. This difference in TH yields from different plasmas is attributed to the difference in the masses of the ejected particles, which are assumed to be lighter for C compared to the heavier masses of the ejected particles from Ag and Ni targets. In order to support the effect of the mass of the ejected particle on TH intensity, the comparison of TH intensities in C plasma with respect to other heavier metal targets was analyzed under vacuum conditions, which is discussed later.
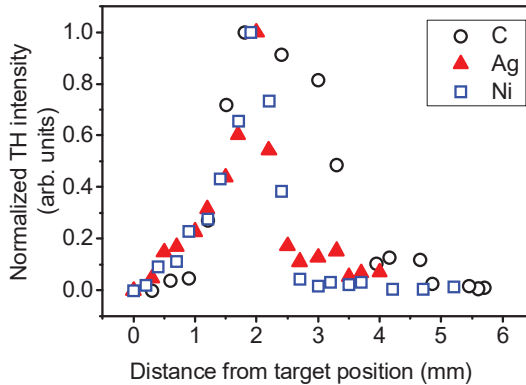
Fig. 7.2. TH intensity as a function of the distance between the axis of propagation of probe pulses and the C, Ag, and Ni surfaces at constant ps heating pulse energy (0.56 mJ) and fs probe pulse energy (0.045 mJ). Reproduced from [23] with permission from Elsevier.

Figure 7.3 shows the variation of TH intensity as a function of probe pulse energy at constant heating pulses energy of 0.56 mJ. The energy of probe pulses was varied between 5 µJ and ~70 µJ. The surfaces of the bulk targets were placed 2 mm away from the probe pulses propagation in order to measure the influence of the energy of these pulses on TH yield. The approximately cubic dependence of the yield of TH up to the probe pulse energy of 50 µJ was observed. The decrease of TH yield with an increase of the energy of probe pulses was observed in the case of Ag and Ni targets. This notable deviation from the cubic dependence can be attributed to the appearance of a large number of free electrons due to the interaction of intense fs probe pulses with the ejected particles during ablation, which led to the phase mismatch between the probe (800 nm) and TH (266 nm) waves in the plasma area. However, at this energy of probe pulses (70 µJ), TH in C plasma still showed the cubic dependence. This difference in the slopes of TH yields of three plasmas shows that the 70 µJ probe pulse energy employed for the generation of TH in carbon plasma was far from the threshold limit of the generation of a large number of free electrons. The absence of a decrease in TH intensity upon the increase of probe pulse energy beyond 50 µJ for C as compared to Ag and Ni, can be related to the ionization energies of used atoms, which is higher for C (11.26 eV) and relatively smaller for Ag (7.57 eV) and Ni (7.6 eV). Notice that the second ionization potentials of C, Ag, and Ni are 24.38 eV, 21.48

eV, and 18.48 eV, which also points out the smaller probability in further ionization of the former species.
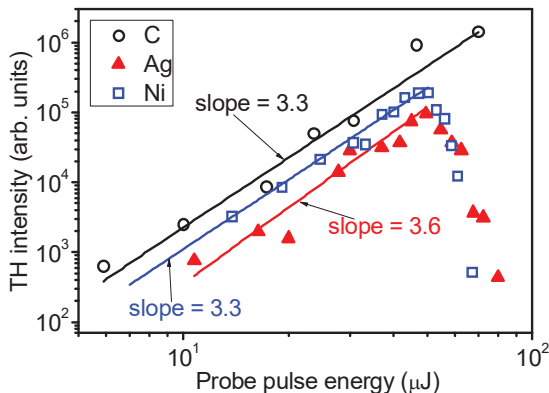
Fig. 7.3. TH intensity as a function of probe pulse energy at the constant ps heating pulse energy of 0.56 mJ on the surfaces of ablating C, Ag, and Ni targets. Reproduced from [23] with permission from Elsevier.

The employed intensity of 560 μJ, 200 ps heating pulses was ~6×10^10 W cm^-2. At this intensity of heating pulses, the degree of ionization was greater than 1.5 which indicates the appearance of free electrons in the created Ag and Ni plasmas [24]. Under these conditions, the plasma consists of singly charged ions with a small fraction of doubly charged ions. At the same time, the 50 μJ probe pulse energy corresponds to the peak intensity of ~2.7×10^14 W cm^-2. The appearance of free electrons at this intensity is mostly due to further ionization of singly ionized species rather than the ionization of neutral species in plasma plume [25,26]. The intensity provided by the probe pulses is close to the tunnel ionization threshold for the singly-charged Ag and Ni ions. However, the tunnel ionization threshold for singly-charged C ions is higher than the employed probe pulse intensity. Correspondingly, carbon plasma should demonstrate a lesser influence of free electrons on TH yield compared with Ag and Ni plasmas at similar conditions of experiments. As a consequence of this difference between the studied plasmas, in the latter two cases, the increase in free-electron density led to a decrease in the intensity of TH due to the phase mismatch of the probe and TH waves.

7.1.3. THG from metal plasma in the vacuum

In this subsection, THG study in various bulk targets, such as C, Cr, Ag, In, CdS, and ZnS, ablated under a vacuum pressure of 0.1 Pa is described. The schematic of experiments is shown in Fig. 7.1(b), where 1064 nm, ns heating pulses were used for LA to create the plasma plumes. The application of ns pulses for LA provided precise control over the time delay between the heating and probe pulses using the delay generator. Prior to these studies, TH yield from four plasmas (Ag, C, Cr, and In) at variable probe pulse energies was measured using the fixed heating pulse energy (3 mJ, Fig. 7.4).
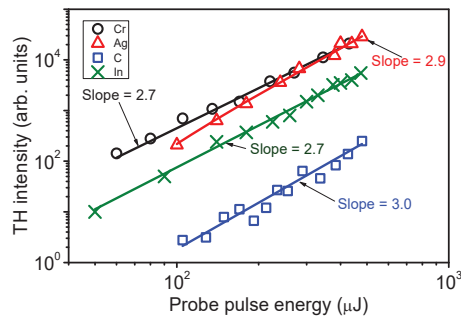
Fig. 7.4. TH intensity as a function of the energy of the probe pulses propagating through Ag, Cr, C, and In plasmas formed under vacuum conditions at the constant energy of ns heating pulse (3 mJ). Reproduced from [23] with permission from Elsevier.

The measurements of TH intensity were performed by setting the target position 0.6 mm away from the axis of probe pulses propagation. The variations of TH intensity in three plasmas showed approximately cubic dependences with the variation of probe pulses energy up to the maximum used pulse energies of 500 µJ. This observation allows concluding that the threshold limit for the generation of free electrons in those plasmas under vacuum conditions was far from maximal applied pulse energies, which has earlier been considered to be the dominating restricting factor at reasonably high energies of the probe pulses [27]. The THG efficiency was found to be maximal for Ag plasma, whereas C plasma showed the lowest efficiency.

Figure 7.5 shows the variations of TH intensity as the functions of the distance between the target and the probe pulses during ablation of Ag, Cr, In, and C targets at vacuum conditions. The generation of TH during ablation of C was observed up to ~ 4 mm away from the position of a

target, whereas, for the other three bulk targets, the TH intensity was achieved only up to the distance of 1 mm. This study reveals the characteristics of the particles, which were ejected during LA of different bulk targets and participated in THG. It was assumed that TH intensity depends on the distance between the probe pulses propagation and target (x) in accordance with the relation $I_{TH} \infty \, x^{-n}$, where n was considered to be dependent on the heating pulse intensity. From Fig. 7.5, TH intensity in the case of C and In was proportional to the distance from the target with the power low of n=-1.85 and -2.85 respectively. However, a completely different scenario was observed for the case of Cr and Ag plasmas, which showed two regions with different slopes (-1.15 and -5.9 in the case of Ag plasma, and -1.79 and -6.9 in the case of Cr plasma).
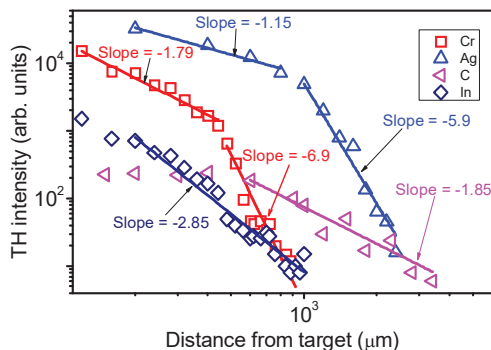
Fig. 7.5. TH intensity as a function of the distance between the surface of bulk target (Ag, Cr, In, and C) and fs probe pulses at the constant heating pulse energy (3 mJ) and probe pulse energy (0.5 mJ). Reproduced from [23] with permission from Elsevier.

TH intensity dependences at the distances close to target surfaces (up to ~0.6 mm) show a similar trend for all targets. As the distance from targets further increases, TH intensity decreases with two different regimes of x variations. This difference can be attributed to TH intensity changes due to both the density and the length of the nonlinear medium variations, which demonstrate the inverse relationship with each other as the ejected particles propagate away from the surface of the target. In order to understand the TH intensity variations with the growth of distance from the target, the statistical distribution of each group of particles during plasma formation should be analyzed, analogously to earlier reported studies [19]. The dependence of TH intensity on probe distance from the surface of the target has shown the presence of different species with

different masses and velocities during the formation of plasma that has a
direct impact on TH yield. This is largely governed by the motion of the
ejected particles away from the surface of the ablated target while
considering the energy conservation during LA. This leads to the
conclusion that during LA of the bulk target, lighter particles, such as C
and Ag, are responsible for TH at larger distances from the target.
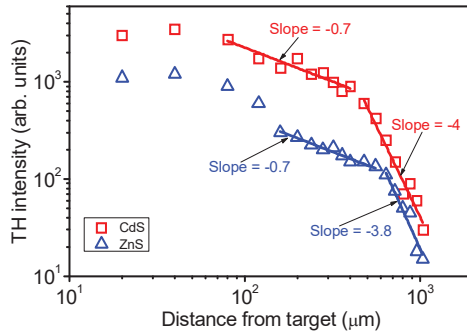
Fig. 7.6. TH intensity as a function of the distance between the surfaces of
bulk CdS and ZnS and femtosecond probe pulses at the constant pulse
energy of 3 mJ for ns heating pulses and 0.5 mJ for fs probe pulses.
Reproduced from [23] with permission from Elsevier.

Similar to TH intensity variation in Ag and Cr plasmas, the TH
intensity in CdS and ZnS plasmas shows a similar trend with the variation
of the distance between target and probe pulses (Fig. 7.6). In order to
explain TH intensity variations in all plasmas shown in Figs. 7.5 and 7.6,
the presence of two groups of particle clouds is assumed, which have been
observed previously in different materials [22]. Their presence can be
explained by the fact that the ablation of the outermost surface of targets
results in atomization, whereas the inner surface is mostly responsible for
the generation of molecules, clusters, and nanoparticles due to the
explosion and mechanical fragmentation processes. These atomic and
clustered clouds of particles move towards the probe beam with different
velocities, which was observed during THG studies. This peculiarity can
be the dominating factor for the TH intensity behaviour in the case of Ag,
Cr, CdS, and ZnS. From this trend of TH intensity variations, one can
observe the ejected cloud of particles containing few atom-sized clusters
or large nanoparticles during the creation of plasma, which move smaller
distances compared to the generated atoms and ions during the creation of
plasma.
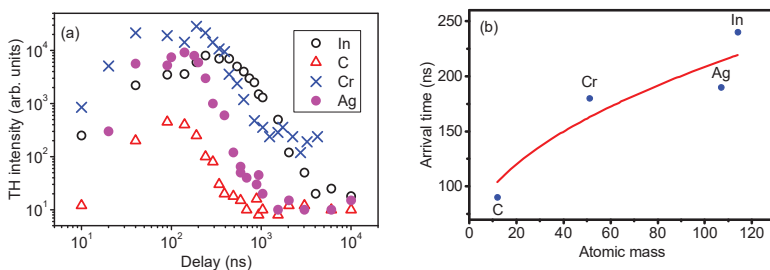
Fig. 7.7. (a) TH intensity as a function of the delay between the heating and probe pulses. (b) Arrival time of C, Cr, Ag, and In particle clouds at the area of propagation of the probe pulses when TH intensity maxima were observed. The solid curve represents the phenomenological fit of the relationship between the delay time and atomic mass ($t_d \propto M^{0.5}$). Reproduced from [23] with permission from Elsevier.

TH intensity was analyzed as a function of a time delay between the heating and probe pulses under vacuum conditions. In order to measure the dependence of TH intensity on the variation of the delay between the heating and probe pulses, the target sample was placed at the focus of the heating pulses and 0.6 mm away from probe pulses. The pulse energies of the heating and the probe pulses were maintained at 3 and 0.58 mJ respectively. The comparison of TH intensity at variable delay was carried out for C, Cr, Ag, and In plasmas. Figure 7.7(a) shows the modulation of TH yield with the variation of the delay between heating and probe pulses. TH intensity shows a similar trend with delay variations for all samples, with TH maxima observed at 90 ns (C), 180 ns (Cr), 200 ns (Ag), and 250 ns (In). The TH intensity decreases slowly after reaching a maximum as the delay time increases. The TH intensity variations at different delays are in good agreement with the earlier reported studies [22].

The TH intensity variations show that the atomic and ionic species are the dominant components responsible for harmonic generation at present conditions compared with the clusters and nanoparticles in different plasmas. The optical emission spectra of these species (see Fig. 7.9a) clearly indicate the atomization of bulk materials during heating by ns pulses. It is worth mentioning that the objective of this study is to look into the impact of the type of bulk materials on TH intensity variations. The delay times at which maximal yields of TH were achieved were correlated with their respective masses [Fig. 7.7(b)]. The atomic mass of the ablated target has a direct effect on the arrival time of the ejected particle at the probe pulse axis. Thus HG in plasmas provides an assessment of the particle size distribution for different materials.

The HG in plasma can provide information about the role of the complex composition of ablated species. The nature of HG emitters can be revealed by the evolution of harmonic yield towards the maximum at some specific delay from the beginning of laser ablation. This specific delay, at fixed heating pulse energy, can be used to characterize the propagation time required for cluster/molecules to reach the probe pulses axis. The components created during laser ablation can be characterized using their average arrival times [19], which can be assigned to different cluster sizes governed by conservation of average kinetic energy ($E=mv^2/2$). The relationship between employed energies and the masses of ejected particles allows determining the relation between the arrival time and the masses of ejected particles. The delay at which TH yield reaches its maximum should scale as a square root of atomic weight, e.g. $t_d \propto M^{0.5}$. It reflects that the lighter atoms and ions from the target surface will reach the probe pulse position before the heavier species.

Following this logic, due to the kinetic relation of particles movement, the large clusters/aggregates should appear in the laser-plasma interaction zone $M^{0.5}$ times later than single atoms and ions of respective materials. In other words, the appearance of the group of clusters in the interaction zone could be expected at delayed times compared to the lighter particles. In order to validate the relationship between the arrival time and the atomic masses of materials, the temporal evolution of the TH yield from various plasmas was analyzed, as shown in Fig. 7.7a. As mentioned above, the distance between target and femtosecond beam propagation in these experiments was maintained at ~0.6 mm. As expected, the arrival times for atomic and ionic species of Cr, In and Ag were $(M_{Cr}:M_C)^{0.5}$~1.27, $(M_{In}:M_C)^{0.5}$~3 and $(M_{Ag}:M_C)^{0.5}$~2.9 times longer compared with the optimal delay for C particles. This anticipated maximal yield of TH from respective plasmas was observed in the experiments as shown in Fig. 7.7b.

The evolution of TH intensity with the variation of delay between the heating and probe pulses has been studied theoretically and experimentally in [19,22], which have shown that the TH intensity variations at $t_d < 300$ ns are possibly due to the presence of ions and neutral atoms. The TH intensity variations at the delays greater than 300 ns can be attributed to the presence of clusters and nanoparticles in the plasma. It can be seen from the plasma spectra of all bulk targets that, under experimental conditions, the optical emission from plasma consists of the emission attributed to the respective ions [see Fig. 7.9(a)], which supports the argument that the initial variation of TH intensity with delay is mostly due to the presence of atoms and ions during plasma formation.
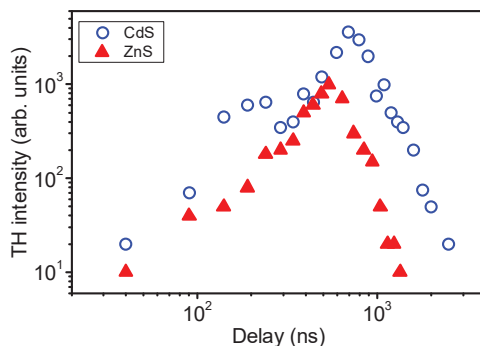
Fig. 7.8. TH intensities as the functions of the delays between ns heating and fs probe pulses in the case of CdS and ZnS plasmas. Reproduced from [23] with permission from Elsevier.

In order to validate the relationship between the arrival times of the ejected particles and their masses, TH intensity measurements during LA of the wide band gap semiconductors (CdS and ZnS) at different delays between the heating and probe pulses were performed. Figure 8 shows that TH intensities reach the maximums at the delays of 540 ns (ZnS) and 690 ns (CdS). This observation also supports the relationship between the arrival times and atomic masses, which predicts that the expected arrival time for CdS atoms, ions, or clusters is $(M_{ZnS}:M_{CdS})^{0.5} \sim 1.22$ times longer than the arrival time of ZnS species. TH in these plasmas was observed up to the delays of 2 μs that was in agreement with literature at the target distance of 0.6 mm from probe pulse position [21,22,28].
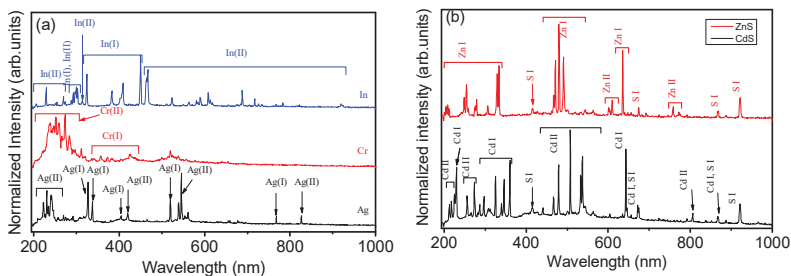
Fig. 7.9. Emission spectra of the studied plasmas excited by ns heating pulses (3 mJ). (a) Ag, Cr, and In. (b) CdS and ZnS. Reproduced from [23] with permission from Elsevier.

The optical emission spectra from the CdS and ZnS plasmas revealed the existence of atomic species such as Cd, Zn, S, and their respective ions in the plasma area [Fig. 7.9b]. The complex mixture of Cd(II) and Cd(I) was observed in the optical emission spectra of CdS plasma, whereas the emission spectra from ZnS plasma consisted dominantly on the emission lines attributed to Zn(I).

The TH intensity approaches its maximum at around 100-300 ns for C, Ag, Cr, and In, which is an earlier timescale compared to the timescales of 540 ns for CdS and 690 ns for ZnS. These time scales can be better explained by the fact that the created plasmas mostly contain two components. One consists of atoms and ions, which can possess the velocity at around 5×10^5 cm s^{-1}, and the other consists of clusters and nanoparticles with the respective velocities of 1×10^5 cm s^{-1}. The TH intensity variations in these semiconductor materials are probably due to the existence of large-sized clusters and nanoparticles, which mostly arrive on a longer time scale as compared to their respective atoms or ionic species. These measurements confirmed that, in semiconductor materials, THG is mostly due to the presence of their respective clusters, which arrive at a microsecond time scale as compared to their respective ions and atoms ejected during plasma formation.

7.2. Third and fifth harmonics generation in air and nanoparticle-containing plasmas using 150 kHz fibre laser

The limitation of THG conversion efficiency in the case of fibre chirped laser pulse amplification systems is that their pulse duration is usually limited to a few hundred femtoseconds. The use of such long pulses leads to ionization at the peak of the laser pulse, which causes an increase in phase mismatch between the interacting waves. Meanwhile, for pulses shorter than 100 fs, the intensity can be significantly increased, resulting in improved THG conversion efficiency. The use of 40 fs class lasers generating pulses with a repetition rate of ~100 kHz, can open up new opportunities in THG from air and LIPs by achieving large average fluxes of coherent UV radiation.

In this section, we analyze the TH (λ=343 nm) and fifth harmonic (5H, λ=206 nm) generation produced in air and different LIPs by applying the Yb-doped fibre laser generating 37 fs, 100 kHz, 1030 nm, 0.5 mJ pulses [29]. Different characteristics of these processes (power and density dependences, influence of impeding mechanisms, role of synthesized NPs in THG, variations of spectral modulation of driving and harmonic pulses,

etc.) are reported. We discuss and compare the formation of NPs-containing plasmas on the surfaces of aluminium, carbon, manganese, and titanium bulk species, as well as quantum dots (QDs) of metal sulphides as the media for low-order harmonics generation at different delays between the heating and driving pulses, using infrared 250 fs (1030 nm) and 5 ns (1064 nm) pulses. The role of NPs and QDs in the enhancement of harmonic yield will be discussed.

Ultrafast high-performance Yb-doped fibre laser was used in these studies. The first port of this laser provided 250 fs, 1030 nm, 50 – 150 kHz, 0.3 mJ pulses that were used for LIP formation. The second port provided 37 fs pulses (1030 nm, 50 – 150 kHz, ~1 mJ, 120 nm spectral width), which were used as driving radiation for THG and fifth harmonic generation (FHG) in air and plasma. The laser operated at 50 kHz – 20 MHz pulse repetition rate, however, the discussed studies were limited to 100 kHz regime. The 250 fs radiation from the first port was directed towards the vacuum chamber (Fig. 7.10) and focused using a 200-mm focal length spherical lens on the surface of the target into a spot of 0.3 mm size. The optimal fluence and intensity of 250-fs heating radiation on the target surface were $F = 0.5$ J cm^{-2} and $I_{hp} = 1.5 \times 10^{12}$ W cm^{-2}, respectively. At these conditions of ablation, the maximal yield of TH and 5H from different plasmas was observed.

The nanosecond pulses from Nd: YAG laser (5 ns, 1064 nm, 10 Hz, 5 mJ) were also used for ablation of targets using approximately the same fluence to compare the harmonic yield with regard to the ablation using femtosecond pulses. The arrival time of femtosecond pulses with respect to heating radiation was controlled using a delay generator, which was operated using a trigger pulse from the amplifier running at 100 kHz.
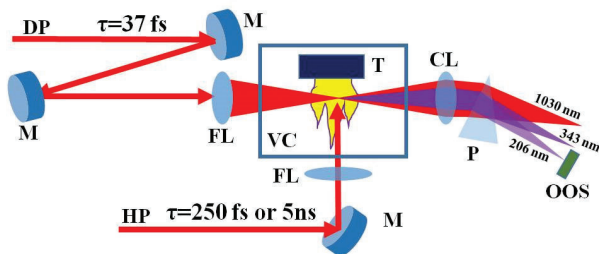
Fig. 7.10. Experimental setup for TH and 5H generation from air and plasmas. DP, driving pulse; HP, heating pulse; M, mirrors, FL focusing lenses; VC, vacuum chamber; T, target; CL, collecting lens; P, prism, OOS, Ocean Optics spectrometer. Reproduced from [29] with permission from Springer.

The radiation from the second port was delayed with regard to the one from the first port to propagate through the formed plasma at a maximal density of the ejected particles. This radiation was focused by a 400-mm focal length spherical lens inside the LIP. The pressure in the vacuum chamber was kept at 0.1 Pa throughout the plasma formation experiments for all samples. In the case of THG in air, the dependence of harmonic yield on the gas pressure in the chamber was analyzed. The confocal parameter of the focused radiation was 10 mm. The intensity of the driving pulses in the plasma area was maintained below 5×10^{14} W cm^{-2}. The optical delay line between 250 and 37 fs pulses was established to maintain the optimal delay for the used LIPs and for the 0.3 mm distance between the target surface and the optical axis of the driving pulses inside the vacuum chamber. In the case of harmonic generation from the air, the vacuum chamber was filled in with air at different pressures. The generated TH and 5H radiation from the air and plasma plume were separated from the co-propagating fundamental beam using a quartz prism and then registered by a spectrometer.

Titanium (Ti), aluminium (Al), carbon (C), and manganese (Mn) bulk targets, as well as Ag_2S, ZnS, and CdS QDs were used for ablation and plasma formation. The sizes of Ti, Al, and Mn targets were $5\times5\times2$ mm^3. The QDs were synthesized and immersed in gelatine to dry and insert in the vacuum chamber for further ablation. The samples were placed on a computer-driven 3D coordinate movement system. The target sample was moved with constant speed to get the stable harmonic intensity.

7.2.1. Low-order harmonics generation in air and various plasmas

Below we discuss the systematic study of the low-order harmonics generation in air and various plasmas using high pulse repetition rate femtosecond pulses. The dependences of the TH and 5H emission yield on the air pressure and power of driving pulses at different ratios of harmonic yields were determined. The ratios of harmonic yields from metals and air were compared at different conditions of these studies. The TH yield as a function of the arrival time of the driving pulses with respect to the heating pulses was analyzed. The THG by touching the solid target surface by the driving radiation was also analyzed. The morphology studies showed that, in most cases, the plasma consisted of the NPs produced during laser ablation of materials.

Figure 7.11(a) shows the spectra of TH and 5H measured at similar conditions of laser-air interaction (at 5W of the driving 37 fs pulses). One

can see the appearance of the broadened component in the shorter wavelength side of the third harmonic. Such a blue shift of harmonic is a characteristic of the harmonic generation when different impeding mechanisms influence this nonlinear optical process. This figure demonstrates the relatively narrow low-order harmonics, without any sign of plasma emission from the filaments in the air. This condition of filaments formation can be identified as the "optimal" from the point of view of the maximal harmonic yield and the absence of incoherent plasma emission. These experiments were carried out at 1/10th of atmospheric pressure (number of particles in cubic centimetre $N{\approx}2.6{\times}10^{18}$ cm^{-3}) to diminish the role of impeding processes (pulse broadening, self-phase modulation, extended filamentation, spatial disintegration of harmonics, etc.). The ratio of TH and 5H yields at these conditions was ~40:1. This ratio increased up to 200:1 at the normal air pressure ($N{=}2.6{\times}10^{19}$ cm^{-3}) due to worsened conditions of the phase matching for 5H with regard to TH.

This deterioration of the optimal relation between the phases of driving and converted waves mostly affected the higher-order harmonic (5H), which was 3 to 6 times weaker than in the case of the optimal laser-air interaction conditions. A smaller density of air ($N{=}5{\times}10^{17}$ cm^{-3} and below) allowed the generation of 5H without the influence of restricting factors. That is why the low-order harmonics from air and LIPs were compared using this range of particles concentration. Those comparative studies are presented below.
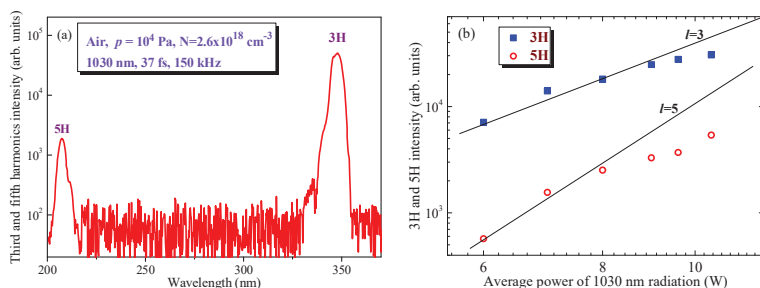
Fig. 7.11. TH and 5H generation in air. TH in the graphs corresponds to the third harmonic. (a) Spectra of harmonics at the air pressure of 10^4 Pa. (b) Power dependences for THG and FHG. The deviation from $l{=}3$ and $l{=}5$ slopes was observed at the average power of driving pulse above 8 W (see text). Reproduced from [29] with permission from Springer.

TH and 5H in the air were measured as functions of the driving pulse power up to 11 W of the average power of 100 kHz, 37 fs pulses. The energy of driving pulses was varied between 5 µJ and ~30 µJ. These dependencies showed the cubic and fifth-order slopes of harmonic yield on the driving pulse power [Fig. 7.12(b)] and were maintained at the pulse powers up to ~8 W after which the saturation and deviation from the cubic and fifth-order dependences were observed. This observation allows concluding that the threshold for the generation of free electrons in filamented air at P=8 W was far from the maximal applied pulse energies. The notable deviation from the expected dependences is attributed to the appearance of a large number of free electrons in filaments, which led to the phase mismatch between the 1030 nm, TH (343 nm), and 5H (206 nm) waves.
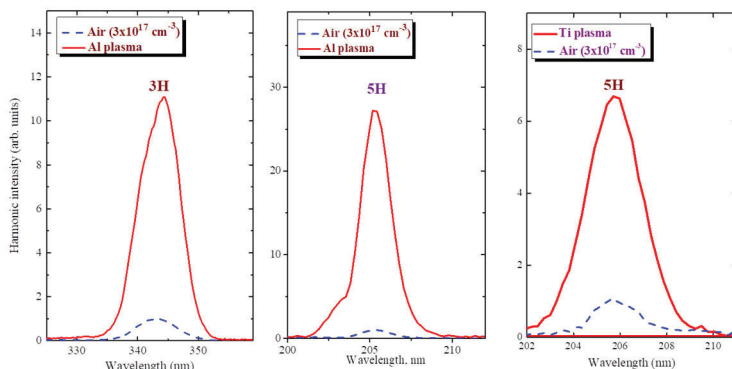
Fig. 7.12. TH (left panel) and 5H (central and right panels) spectra from Al (left and central panels) and Ti (right panel) plasmas. Dashed curves show the normalized spectra of TH and 5H generated from air at similar density as in the case of LPPs. Reproduced from [29] with permission from Springer.

Figure 7.12 shows the comparative studies of the (a) TH and (b) 5H in aluminium plasma and air at a similar density of particles (3×10^{17} cm^{-3}) in both media and at the intensity of driving pulses of 2×10^{14} W cm^{-2}. No special features in spectral variations of harmonics, like blue-shift, were observed at these conditions. The density of different plasmas has earlier been estimated using the code HYADES for the ablated materials during HHG at optimal conditions of plasma formation [30]. The harmonic yields from the air were normalized to be equal to 1. These measurements

showed the 11- and 27-fold enhancement of the TH and 5H yields, respectively, in this LIP with regard to the air at similar conditions of experiments. The stronger harmonic yield from LIPs is attributed to the appearance of the NPs synthesized *in situ* prior to the arrival of the driving femtosecond pulses in the area of interaction. Their presence in LIP was confirmed by the morphology studies of the deposited debris from the used LIPs.

Similar comparative studies of harmonics were carried out using other metal and QD LIPs. Particularly, the 5H yield from Ti plasma was 7 times stronger as compared with the 5H from the air at a similar density of these two media and equal intensities of the driving pulses [Fig. 7.12(c)]. Each of LIP demonstrated stronger harmonic yields with regard to harmonic generation in air.

The formation of optimal LIP at the moment of the driving pulse propagation through the studied ablated material is a crucial requirement for the generation of as strong as possible harmonics. The term "optimal" refers to the experimental conditions, which can be different for each ablating material, as well as the characteristics of converted and heated radiation. However, this term in each of those cases is related to the conditions when the maximal yield of harmonics can be achieved. Different parameters of such experiments play important role in the determination of the best conditions for optimal plasma formation (i.e. delay between the heating and driving pulses, fluence on the surface of ablating target, the intensity of driving wave in the plasma area, presence of the aggregates of evaporated material in LIP, etc.).

The delay between pulses allows determining the conditions when the femtosecond pulse propagates through the dense LIP spreading out from the surface at the specific velocity determined by the kinetics of plasma formation and the atomic weight of ablating material. The optimization of delay includes the determination of the time scale characterized by the distance from the target surface and the velocities of plasma components. Practically, one has to change the delay between the beginning of the plasma ignition process and the propagation of ultrafast laser pulse at the chosen distance from the target. By estimating the velocities of atoms and ions possessing the medium atomic weight, like Mn (55 amu), in the range of 2×10^3 m s^{-1} and by choosing the 0.2 mm distance from the target one can determine the time scale between the heating and driving pulses at which one can expect the maximal harmonic yield (~100 ns) when the central part of plasma cloud arrives in the area of driving beam propagation.

It was found that the maximal yield of TH in the case of manganese LIP can be achieved at ~80-100 ns delay [Fig. 7.13(a)]. Further increase of delay led to a gradual decrease of harmonic yield until it almost disappeared at >400 ns delay.

A scheme of nanosecond pulse heating and femtosecond laser pulse conversion has already been used for both high-order [31] harmonic generation studies. The advantage of this approach is related to the control of the delay between the heating nanosecond pulses and the driving femtosecond pulses over a wide range. Earlier, the demonstration of large particle formation in the atmosphere of noble gases allowed the THG not only from atoms and ions of carbon materials (at small delays) but also from their aggregates (at large delays) [32].

Manganese plasma, similar to Al and Ti LIPs, allowed the generation of TH emission, which was four times stronger with regard to THG in air. Meanwhile, the blueshift of the shorter-wavelength component of TH in the case of Mn LIP was observed during the increase in the intensity of driving pulses from 2×10^{14} W cm^{-2} to 4×10^{14} W cm^{-2} (Fig. 7.13(b), thin solid red curve).
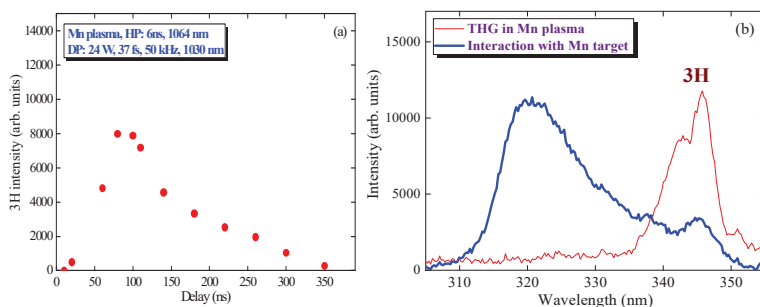
Fig. 7.13. Characterization of TH generating from Mn plasma. (a) Delay dependence between the beginning of ablation by nanosecond heating pulses (HP) and propagation of femtosecond driving pulses (DP) through the Mn LPP. (b) TH spectrum generated during propagation through the pre-formed Mn plasma (red thin solid curve) and during interaction of the wing of driving beam with Mn solid target without the formation of plasma by the heating pulses (blue thick solid curve). Reproduced from [29] with permission from Springer.

The TH emission was also observed without target ablation by heating pulse while minimizing the distance between the axis of driving

femtosecond beam propagation and the target surface. Once the spatial wing of the driving beam touches the Mn target along its whole length (5 mm), the TH is generated even without the formation of plasma by the heating pulse (Fig. 7.13(b), blue thick curve). The efficiency of this process was approximately 20 times lower than the THG from the preformed LIP. The maximums of TH yields in these two cases (THG in the preformed 0.3-mm thick plasma and during touching the target) were normalized to emphasize the difference in the TH spectra. In the latter case, a very strong, broadened, and blueshifted component at ~320 nm was dominated along the whole spectrum.
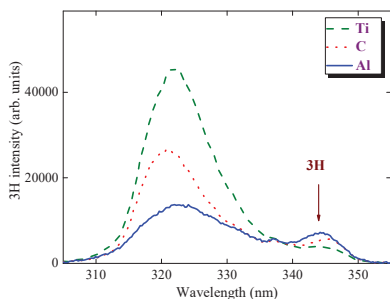
Fig. 7.14. TH spectra obtained during interaction of the wing of driving beam with Ti (green dashed curve), C (red dotted curve), and Al (blue solid curve) bulk targets. Reproduced from [29] with permission from Springer.

The same feature was observed in the case of other targets at similar conditions of experiments (Fig. 7.14, Ti, C, and Al), when the spectrum of harmonic radiation was also broadened and blueshifted. Notice that, at these conditions, the spectral variation of propagated laser radiation was notably smaller. One can assume that the strong 320 nm shoulder of TH emission was enhanced due to self-phase modulation of the generated UV pulse propagating through the excited extended plasma in the vicinity of the target.

The ablated and deposited debris from the carbon, titanium, and manganese bulk targets during ablation by 250 fs pulses contained the nano-sized particles. The smallest among them were the carbon NPs (~25 nm), while the mean sizes of Mn and Ti NPs were determined to be 50 and 100 nm, respectively (see SEM images and histograms of deposited Ti and Mn species, Fig. 7.15). Their formation and presence in the plasma plume can, to some extent, cause the enhancement of harmonic yield with regard to the atomic species of similar elemental consistency. There are several

methods for the formation of the nanoparticles, where complete control over size and shape were achieved depending on the material characteristics. They require some procedure and time to synthesize the NPs, which can later be used for different goals. In the meantime, the laser ablation technique provides the opportunity for the formation of NPs *in situ*, i.e. during the experiments sensitive to the presence of the small-sized species.

The *in-situ* formation of nano-sized species creates the conditions for laser-NPs interaction. Though yet confirmed for low-order harmonics, stronger HHG flux from clusters, QDs, and NPs with regard to the monomers has earlier been attributed to better conditions of the formation of harmonic emitters in the case of agglomerates formation and spreading, as well as to the specific properties of NPs, such as the ionization and recombination to the same ion of the cluster, to the neighbouring ions and to the whole cluster [33,34], allowing the increase of recombination cross-section of the electrons participating in HHG. Additionally, the enhancement of HHG in the presence of such structures can be explained by the higher nonlinear optical response of materials caused by the plasmonic properties of NPs.
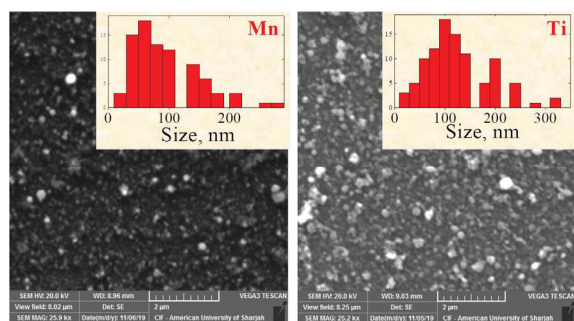
Fig. 7.15. SEM images of the deposited layers of Mn (left panel) and Ti (right panel) ablation. Histograms show the size distributions of Mn and Ti NPs. Reproduced from [29] with permission from Springer.

These NPs were generated during ablation by femtosecond pulses. Their sizes were distributed in a broad range. Most of the inner atoms of these structures, apart from outer atoms on the surface of NPs, do not participate in harmonics generation being screened by the neighbouring atoms. Thus one can expect the attractiveness of the smaller-sized aggregates for both THG and HHG. The examples of such already prepared aggregates are the QDs of metal sulphides. One can argue which

of multiparticle aggregates is most useful for the frequency conversion of the ultrafast laser pulses?

Being qualitatively divided by three groups (clusters with up to 10^3 atoms and dimensions less than 1 nm, QDs with up to 10^5 atoms and dimensions less than 5 nm, and large NPs with up to 10^8 atoms and dimensions up to 100 nm), each of them demonstrates both positive and negative features as the emitters of harmonics. Another important issue is the concentration of active centres of harmonic emission since as mentioned, in the case of large aggregates, only those atoms in the vicinity of NP surface can participate in harmonic emission. The latter issue is especially important in the case of HHG. In this connection, QDs demonstrating strong local-field-induced enhancement of the nonlinear optical properties can be considered as the most attractive species for efficient THG and HHG.
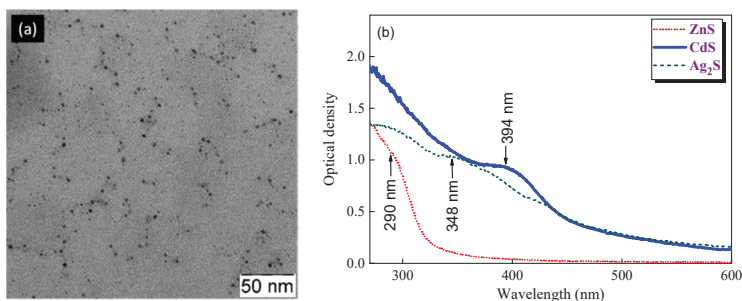
Fig. 7.16. (a) TEM image of Ag$_2$S QD. (b) Absorption spectra of metal sulphide QDs. Reproduced from [29] with permission from Springer.

The procedure for preparation of the metal sulfide QDs is reported elsewhere [35]. Briefly, the synthesis of QDs was carried out taking into account a number of criteria for their use to generate harmonics of ultrafast pulses. The first criterion is the formation (as a result of ablation of samples by femtosecond, picosecond, or nanosecond heating pulses) of a plasma cloud consisting of QDs, as well as atoms, ions, and clusters at the time of the passage of the converting femtosecond pulses above the target surface. The second criterion is the presence of the maximal concentration of QDs at the time of transmission of the femtosecond pulses through the plasma. The third criterion is the size characteristics of quantum dots. Previous studies of harmonic generation in multi-particle containing plasmas, as well as qualitative assessments, show that the most optimal sizes of such species should be in the range of 1 - 4 nm.

The synthesized samples of colloidal solutions of zinc, cadmium, and silver sulphides were further used to produce the solid targets for laser ablation and generation of harmonics. The method of increasing the filling factor of Ag_2S, ZnS, and CdS QDs in the stabilizing polymer (gelatine) was used to develop the solid samples of multi-particle species for laser ablation in vacuum and formation of the plasma torches containing a large amount of QDs required for efficient generation of harmonics.

The mean sizes of ZnS QDs measured using a transmission electron microscope (TEM) were 2 nm, while other species had mean sizes in the range of 1.7 to 2.0 nm (Ag_2S, Fig. 7.16(a)), and 3.0 to 3.2 nm (CdS). The optical spectra of these QDs (Fig. 7.16(b)) were significantly blue-shifted with regard to the bulk materials of similar elemental consistency.
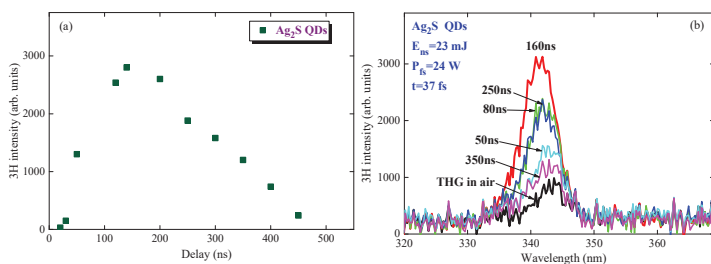
Fig. 7.17. THG in Ag_2S QD LPP. (a) Delay dependence between the beginning of ablation by nanosecond heating pulses and propagation of femtosecond driving pulses through the plasma. (b) Blue shift of TH spectrum at different delays between pulses. Reproduced from [29] with permission from Springer.

The atomic mass of the ablated target has a direct effect on the arrival time of the ejected particle at the axis of propagation of the driving pulse. THG in plasmas at different delays between heating and driving pulses provides an assessment of the particle size distribution for different materials. The components created during laser ablation can be characterized using their average arrival times, which can be assigned to different cluster sizes governed by conservation of average kinetic energy ($E=mv^2/2$). The delay at which TH yield reaches its maximum should scale as a square root of atomic weight, e.g. $t_d \propto M^{0.5}$. It reflects that the lighter atoms and ions from the target surface will reach the driving pulse position before the heavier species.

In order to validate this relationship, the TH intensity measurements during ablation of metal sulphide QDs-containing species at different

delays between the heating and driving pulses were performed. Figure 7.17a shows that TH yield reaches the maximums at the delays of 120 – 200 ns in the case of Ag_2S QDs. This observation supports the relationship between the arrival times and atomic or molecular masses, which predicts that the expected arrival time for Ag_2S species (ions or clusters) should be $(M_{Ag2S}:M_{Mn})^{0.5} \sim 1.7$ times longer than the arrival time of Mn species (80-100 ns). Thus, one can assume that the above kinetic rule properly explains the dynamics of material spreading out from the ablated target, once one analyzes the particles' movement during laser ablation at relatively moderate fluences (5 – 20 J cm^{-2}) of heating nanosecond pulses.
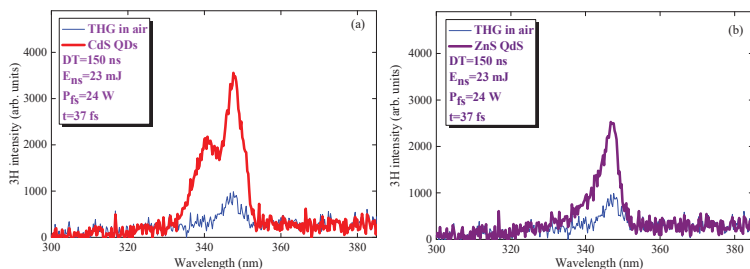
Fig. 7.18. THG in (a) CdS QD LIP and (b) ZnS QD LIP. Reproduced from [29] with permission from Springer.

TH from QD-containing LIPs was blue-shifted with regard to the central wavelength of this harmonic (343 nm). The blue shift was larger in the case of denser plasma (Fig. 7.17b). Particularly, the largest blue shift was observed in the case of the optimal delay between heating and driving pulses corresponding to the largest concentration of Ag_2S QDs along the axis of propagation of the driving pulses. Similar dependencies were observed in the case of CdS and ZnS QD LIPs (Fig. 7.18). In each of these cases, the TH yield was significantly (5 to 20 times) larger with regard to the TH generated in the air at similar concentrations of particles.

7.2.2. Analysis of the studies of the low-order nonlinearities

Previously, low-order harmonics from air and LIPs were performed using 10 Hz and 1 kHz class Ti: sapphire lasers. No THG studies in LIPs have been conducted using a laser operating at a pulse repetition rate above 1 kHz. Here the application of a 100 kHz class ytterbium fibre laser for THG and FHG in air and several plasma formations is analyzed. For the experiments presented here the fibre laser generating the 0.5 mJ, 100

kHz, 37 fs pulses was used for interaction with the nonlinear optical medium.

Below, we consider a possible explanation of the experimental observation of strong TH and 5H radiation from ablated solids, which is probably related to the cluster formation during laser ablation. Previously, it has been shown that in the case of the plasma plumes containing metal nanoparticles, those species demonstrate increased HHG conversion efficiency compared with the LIPs formed on the surfaces of bulk metal targets when they consist of atoms and ions [36]. Small aggregated particles can be formed in an ablation plume induced by ultrashort laser pulses. The ultrafast laser ablation has been proposed as the simplest method for generating small nanoparticles. Note that these conditions for the formation of NPs are unsuitable for effective plasma HHG since they provide a large number of free electrons, which leads to an increasing phase mismatch between the driving and harmonic waves, especially in the case of higher orders of harmonics.

The absolute measurements of the 343 nm yield from the air were performed using a power meter, which allowed determining the average power of generated UV radiation (~5 mW) at a 100 kHz pulse repetition rate. By knowing the experimental ratio of TH yields in air and Mn plasma (1:4) one can determine 20 mW as the average power of the TH generating in the latter medium. By assuming the energy of 343 nm photon (5.8×10^{-19} J) and the whole energy of 343 nm flux during 1 second (20 mJ) one can define the number of photons generating from Mn plasma during THG (3.4×10^{16}). Correspondingly, the average power of UV photons (3.61 eV, ~20 mW) allows determining the THG conversion efficiency in the case of 20 W driving pulses propagating through the manganese plasma (~10^{-3}).

Based on the experiments with different targets, one can conclude that overheating of the same spot worsens the conditions of stable plasma formation. The morphology of the heating spot did not remain unchanged during these experiments. At the same time, crater formation in the case of a movable target occurred after a significantly longer period compared to static targets. Once the target begins to move, the previously heated area cools down and can again be used for effective ablation and harmonic generation. This phenomenon was observed from many targets.

In the case of low-order harmonic generation, two perspectives can be considered: on one hand, it can be useful in the search for new efficient materials that will act as nonlinear media in THG processes. On the other hand, it is suitable as a diagnostic tool to characterize the species presented in LIP. Previous studies of harmonic generation in the laser plasmas containing NPs were conducted only using lasers with a relatively low

pulse repetition rate (from 10 Hz to 1 kHz). Since the average harmonic power increases with the repetition rate, it is highly desirable to maintain the concentration of NPs in the plasma during repeated irradiation of the cluster-containing ablation target. The search for methods to ensure a stable concentration of clusters in the plasma will increase not only the output of low- and high-order harmonics, but also the average power of the generated harmonics. At the same time, stable conditions of the nanoparticle plasma allow investigating the influence of various cluster properties, in particular surface plasmon resonance, on the efficiency of THG. The use of a laser with a high pulse repetition rate (100 kHz and above) is advantageous for the above studies since with an increase in the average power of the generated harmonics, less time is required to collect all the necessary data to compare the nonlinear optical properties of different plasmas.

Below we address the application of several nm-sized species to THG. QD-containing materials, in particular, QD based on metal sulphides, attract special attention due to their large low-order optical nonlinearities. In particular, various nonlinear optical processes can be induced in ZnS nanoparticles, which have become useful in photonics [37]. The coexistence of reverse saturable absorption and two-photon absorption in silver sulphide suggests that Ag_2S QDs could be a very promising nonlinear medium for photonic devices at different time scales if these semiconductor nanocrystallites are incorporated into the respective media while retaining the attractive properties of both components. Ag_2S QDs also demonstrate low-threshold optical limiting in the visible and near-infrared ranges [38].

The harmonic stability and plasma content were also considered in the case of experiments with high pulse repetition using different LPPs. The target could be moved along the vertical and horizontal axes using a computer-controlled three-axis transfer stage. In addition, the use of rotating targets would generate stable harmonics for at least 10^6 shots corresponding to ~20 minutes of instantaneous irradiation of a rotating target with a 1 kHz class laser. In the discussed case (100 kHz), this number of shots was executed in 10 seconds. It was able to observe the generation of harmonics for several tens of seconds while maintaining the correct position of the ablating spot and the corresponding movement of the target. The long-term stability of plasma harmonic generation at this pulse repetition rate still needs to be improved. However, the combined use of a rotating target and the movement of the heating beam spot along the height of the target being dragged up and down would further improve the stability of the harmonic output from 100 kHz lasers.

Once pointing out the influence of different parameters of such experiments on THG yield, one can emphasize the role of delay between heating and driving pulses. As it was mentioned, in the case of heating nanosecond pulses, the delay can be easily adjusted electronically using a digital generator. In the case of femtosecond heating pulses, this parameter was optimized using an optical delay line, which is less convenient but allows achieving a similar goal. The control of the delay between the heating nanosecond pulses and the driving femtosecond pulses over a wide range allowing the analysis of the role of slowly moving NPs seems the alone advantage, which distinguishes the process of heating by nanosecond pulses over femtosecond pulses.

References to Chapter 7

[1]   S. Backus, J. Peatross, Z. Zeek, A. Rundquist, G. Taft, M. M. Murnane, H. C. Kapteyn, 16-fs, 1-μJ ultraviolet pulses generated by third-harmonic conversion in air, Opt. Lett. 21 (9) (1996) 665-667.

[2]   R. A. Ganeev, M. Suzuki, M. Baba, H. Kuroda, I. A. Kulagin, Third harmonic generation in air by use of femtosecond radiation in tight-focusing conditions, Appl. Opt. 45 (4) (2006) 748-755.

[3]   F. Théberge, N. Aközbek, W. W. Liu, A. Becker, S. L. Chin, Tunable ultrashort laser pulses generated through filamentation in gases, Phys. Rev. Lett. 97 (2) (2006) 023904.

[4]   S. Suntsov, D. Abdollahpour, D. G. Papazoglou, S. Tzortzakis, Efficient third-harmonic generation through tailored IR femtosecond laser pulse filamentation in air, Opt. Express 17 (5) (2009) 3190-3195.

[5]   R. A. Ganeev, H. Singhal, P. A. Naik, J. A. Chakera, M. Kumar, P. D. Gupta, Fourth harmonic generation during parametric four-wave mixing in the filaments in ambient air, Phys. Rev. A 82 (4) (2010) 043812.

[6]   M. Stafe, C. Negutu, N. N. Puscas, Third harmonic from air breakdown plasma induced by nanosecond laser pulses, Appl. Phys. B 124 (6) (2018) 106.

[7]   H. Yang, J. Zhang, J. Zhang, L. Z. Zhao, Y. J. Li, H. Teng, Y. T. Li, Z. H. Wang, Z. L. Chen, Z. Y. Wei, J. X. Ma, W. Yu, Z. M. Sheng, Third-order harmonic generation by self-guided femtosecond pulses in air, Phys. Rev. E 67 (1) (2003) 015401.

[8]   F. Théberge, N. Aközbek, W. Liu, J.-F. Gravel, S. L. Chin, Third harmonic beam profile generated in atmospheric air using femtosecond laser pulses Third harmonic beam profile generated in atmospheric air using femtosecond laser pulses, Opt. Commun. 245 (1-6) (2005) 399-405.

[9]   R. A. Ganeev, G. S. Boltaev, R. I. Tugushev, T. Usmanov, M. Baba, H. Kuroda, Third harmonic generation in plasma plumes using picosecond and femtosecond laser pulses, J. Opt. 12 (5) (2010) 055202.

[10] E. V. Vanin, A. V. Kim, A. M. Sergeev, M. C. Downer, Excitation of ultrashort bursts of harmonics of the radiation during ionization of a gas by an intense light pulse, JETP Lett. 58 (1993) 900-903.

[11] A.B. Fedotov, N. I. Koroteev, M. M. T. Loy, X. Xiao, A. M. Zheltikov, Saturation of third-harmonic generation in a plasma of self-induced optical breakdown due to the self-action of 80-fs light pulses, Opt. Commun. 133 (1-6) (1997) 587-595.

[12] N. Aközbek, A. Iwasaki, A. Becker, M. Scalora, S. L. Chin, C. M. Bowden, Third-harmonic generation and self-channeling in air using high-power femtosecond laser pulses, Phys. Rev. Lett. 89 (14) (2002) 143901.

[13] M. L. Naudeau, R. J. Law, T. S. Luk, T. R. Nelson, S. M. Cameron, J. V. Rudd, Observation of nonlinear optical phenomena in air and fused silica using a 100 GW, 1.54 µm source, Opt. Express 14 (13) (2006) 6194-6200.

[14] M. López-Arias, M. Oujja, M. Sanz, R. A. Ganeev, G. S. Boltaev, N. K. Satlikov, R. I. Tugushev, T. Usmanov, M. Castillejo, Low-order harmonic generation in metal ablation plasmas in nanosecond and picosecond regimes, J. Appl. Phys. 111 (4) (2012) 043111.

[15] C. Rodríguez, Z. Sun, Z. Wang, W. Rudolph, Characterization of laser-induced air plasmas by third harmonic generation, Opt.Express 19 (17) (2011) 16115-16125.

[16] G. O. Ariunbold, P. Polynkin, J. V. Moloney, Third and fifth harmonic generation by tightly focused femtosecond pulses at 22 µm wavelength in air, Opt. Express 20 (2) (2012) 1662-1667.

[17] D. Kartashov, S. Ališauskas, A. Pugžlys, A. Voronin, A. Zheltikov, M. Petrarca, P. Béjot, J. Kasparian, J.-P. Wolf, A. Baltuška, Mid-infrared laser filamentation in molecular gases, Opt. Lett. 38 (16) (2013) 3194-3197.

[18] D. L. Weerawarne, X. Gao, A. L. Gaeta, B. Shim, Higher-order nonlinearities revisited and their effect on harmonic generation, Phys. Rev. Lett. 114 (9) (2015) 093901.

[19] M. Oujja, J. G. Izquierdo, L. Banares, R. de Nalda, M. Castillejo, Observation of middle-sized metal clusters in femtosecond laser ablation plasmas through nonlinear optics, Phys. Chem. Chem. Phys. 20 (2018) 16956-16965.

[20] R. de Nalda, M. Lopez-Arias, M. Sanz, M. Oujjaa, M. Castillejo, Harmonic generation in ablation plasmas of wide bandgap semiconductors, Phys. Chem. Chem. Phys. 13 (2011) 10755–10761.

[21] M. Sanz, M. Lopez-Arias, J.F. Marco, R. de Nalda, S. Amoruso, G. Ausanio, S. Lettieri, R. Bruzzese, X. Wang, M. Castillejo, Ultrafast laser ablation and deposition of wide bandgap semiconductors, J. Phys. Chem. C 115 (2011) 3203-3211.

[22] M. Sanz, R. de Nalda, J.F. Marco, J. G. Izquierdo, L. Banares, M. Castillejo, Femtosecond pulsed laser deposition of nanostructured CdS films, J. Phys. Chem. C 114 (2010) 4864-4868.

[23] S. K. Maurya, M. Venkatesh, R. A. Ganeev, C. Guo, Study of various material particles by third harmonic generation method based on laser pulse induced plasma, Opt. Mater. 98 (10) (2019) 109423.

[24] L.B. Elouga Bom, J.-C. Kieffer, R.A. Ganeev, M. Suzuki, H. Kuroda, T. Ozaki, Influence of the main pulse and prepulse intensity on high-order harmonic generation in silver plasma ablation, Phys. Rev. A 75 (2007) 033804.

[25] T. Ozaki, L.B. Elouga Bom, R. Ganeev, J.-C. Kieffer, M. Suzuki, H. Kuroda (2007). Intense harmonic generation from silver ablation, Laser Part. Beams 25 (2007) 321–327.

[26] R.A. Ganeev, H. Singhal, P.A. Naik, U. Chakravarty, V. Arora, J.A. Chakera, R.A. Khan, M. Raghuramaiah, S.R. Kumbhare, R.P. Kushwaha, P.D. Gupta. Optimization of the high-order harmonics generated from silver plasma, Appl. Phys. B 87 (2007) 243–247.

[27] G. Lambert, A. Andreev, J. Gautier, L. Giannessi, V. Malka, A. Petralia, S. Sebban, S. Stremoukhov, F. Tissandier, B. Vodungbo, P. Zeitoun, Spatial properties of odd and even low order harmonics generated in gas, Sci. Rep. 5 (2015) 7786.

[28] M. Oujja, I. Lopez Quintas, A. Benitez Canete, R. de Nalda, M. Castillejo, A.B. Canete, Harmonic generation by atomic and nanoparticle precursors in a ZnS laser ablation plasma, Appl. Surf. Sci. 392 (2017) 572-580.

[29] G. S. Boltaev, N. A. Abbasi, V. V. Kim, M. Iqbal, S. A. Khan, A. I. Zvyagin, M. S. Smirnov, O. V. Ovchinnikov, R. A. Ganeev, A. S. Alnaser, Third and fifth harmonics generation in air and nanoparticle-containing plasmas using 150 kHz fiber laser, Appl. Phys. B 126 (1) (2020) 76.

[30] L. B. Elouga Bom, J.-C. Kieffer, R. A. Ganeev, M. Suzuki, H. Kuroda, T. Ozaki, Influence of the main pulse and prepulse intensity on high-order harmonic generation in silver plasma ablation, Phys. Rev. A 75 (3) (2007) 033804.

[31] R. A. Ganeev, G. S. Boltaev, K. Zhang, P. V. Redkin, S. K. Maurya, M. Venkatesh, Z. Yu, V. V. Kim, C. Guo, Role of carbon clusters in high-order harmonic generation in graphite plasmas, OSA Continuum 2 (2019) 1510.

[32] I. Lopez-Quintas. M. Oujja, M. Sanz, M. Martín, R.A. Ganeev, M. Castillejo, Low-order harmonic generation in nanosecond laser ablation plasmas of carbon containing materials, Appl. Surf. Sci. 278 (2013) 33-37.

[33] T. D. Donnelly, T. Ditmire, K. Neuman, M. D. Perry, R. W. Falcone, High-order harmonic generation in atom clusters, Phys. Rev. Lett. 76 (14) (1996) 2472-2475.

[34] C. Vozzi, M. Nisoli, J.-P. Caumes, G. Sansone, S. Stagira, S. De Silvestri, M. Vecchiocattivi, D. Bassi, M. Pascolini, L. Poletto, P. Villoresi, G. Tondello, Cluster effects in high-order harmonics generated by ultrashort light pulses, Appl. Phys. Lett. 86 (11) (005) 111121.

[35] R. A. Ganeev, G. S. Boltaev, V. V. Kim, K. Zhang, A. I. Zvyagin, M. S. Smirnov, O. V. Ovchinnikov, P. V. Redkin, M. Wöstmann, H. Zacharias, C. Guo, Effective high-order harmonic generation from metal sulfide quantum dots, Opt. Express 26 (26) (2018) 35013-35025.

[36] H. Singhal, R. A. Ganeev, P. A. Naik, J. A. Chakera, U. Chakravarty, H. S. Vora, A. K. Srivastava, C. Mukherjee, C. P. Navathe, S. K. Deb, P.D. Gupta,

In-situ laser induced silver nanoparticle formation and high order harmonic generation, Phys. Rev. A 82 (4) (2010) 043821.

[37] Z. Zeng, C. S. Garoufalis, A. F. Terzis, S. Baskoutas, Linear and nonlinear optical properties of ZnO/ZnS and ZnS/ZnO core shell quantum dots: Effects of shell thickness, impurity, and dielectric environment, J. Appl. Phys. 114 (2) (2013) 023510.

[38] R. B. Martin, M. J. Meziani, P. Pathak, J. E. Riggs, D. E. Cook, S. Perera, Y.-P. Sun, Optical limiting of silver-containing nanoparticles, Opt. Mater. 29 (2007) 788-793.

CHAPTER 8

HIGH-ORDER HARMONICS GENERATION IN NANOPARTICLES

In this chapter, the application of tuneable NIR pulses for harmonic generation in the laser-produced plasmas containing Ag, Sn, C_{60}, and graphene nanoparticles is analyzed. The application of a two-colour pump of nanoparticles allows the generation of harmonics up to the thirties orders. We discuss a significant enhancement of harmonics in the case of the two-colour pump of nanoparticle-contained plasmas compared with a single-colour pump. We analyze the similarities and distinctions in the NIR-induced harmonic spectra from the ablations of nanoparticle and bulk targets.

We also discuss how harmonics obtained from Au NPs are affected by using the active substrate, which itself allows the generation of harmonics. The systematic experimental studies of the NPs formation during laser ablation and the HHG from Au NPs, Au bulk, and Au NPs deposited on paper and glass substrates are analyzed.

Finally, we discuss the studies of the formation of quasi-phase-matching in different plasma plumes produced by nanosecond, picosecond, and femtosecond pulses on the surfaces of materials allowing the formation of imperforated and perforated LIPs containing atoms, ions, and NPs. The optimization of quasi-phase-matching during HHG in such plasmas allows the formation of the groups of harmonics with the significant enhancement factors.

8.1. High-order harmonic generation in Ag, Sn, fullerene, and graphene nanoparticle-containing plasmas using two-colour mid-infrared pulses

To extend the applications of high-order harmonic generation (HHG) related nonlinear spectroscopy of various ablating materials one has to use the tuneable radiation, which allows the analysis of single harmonic enhancement by tuning the harmonic wavelength along the ionic resonances

possessing high oscillator strength. The optical parametric amplifiers of the white-light continuum in the near-infrared (NIR) and mid-infrared (MIR) ranges could be an excellent choice for these studies [1]. NIR and MIR pulses could also be extremely useful in the case of nanoparticle-containing plasmas since the main sources of harmonics in this medium are assumed to be the neutrals, contrary to the ablation of bulk materials. The use of metal nanoparticles [2] and carbon-containing nanoparticles (particularly, fullerenes and graphene) at these conditions would allow further analysis of the nonlinear optical properties of those species.

In this section, the application of tuneable NIR pulses (70 fs, 1300–1600 nm) for harmonic generation in the laser-produced plasmas containing Ag, Sn, C_{60}, and graphene nanoparticles is analyzed [3]. The application of a two-colour pump (TCP, NIR+H2) of nanoparticles allowed the generation of harmonics up to the thirties orders. We discuss a significant enhancement of harmonics in the case of the TCP of nanoparticle-contained plasmas compared with a single-colour pump (SCP). We also analyze the similarities and distinctions in the NIR-induced harmonic spectra from the ablations of nanoparticle and bulk targets.

8.1.1. Experimental arrangements for high-order harmonics generation

The experimental setup consisted of Ti:sapphire laser, travelling-wave optical parametric amplifier (OPA) of the white-light continuum, and high-order harmonic generation scheme using propagation of amplified signal pulse from OPA through the extended laser-induced plasma (LIP, Fig. 8.1a). The mode-locked Ti:sapphire laser pumped by diode-pumped, cw laser was used as the source of 803 nm, 55 fs, 82 MHz, 450 mW pulses for injection in the pulsed Ti:sapphire regenerative amplifier with pulse stretcher and additional double passed linear amplifier. The output characteristics of uncompressed radiation from this laser were as follows: central wavelength 810 nm, pulse duration 370 ps, pulse energy 4 mJ, 10 Hz pulse repetition rate. This radiation was further amplified up to 22 mJ in the homemade three passed Ti:sapphire linear amplifier. Part of amplified radiation with pulse energy of 5 mJ was separated from a whole beam and used as a heating pulse for homogeneous extended plasma formation using the 200 mm focal length cylindrical lens installed in front of the 5-mm long targets placed in the vacuum chamber. The intensity and fluence of the heating pulse on the target surface were varied up to 4×10^9 W cm^{-2} and 1.4 J cm^{-2}, respectively. The ablation area was 5×0.08 mm^2.

The output characteristics of Ti:sapphire laser were as follows: pulse energy 8 mJ, pulse duration 64 fs, 10 Hz pulse repetition rate, pulse bandwidth 17 nm, central wavelength 806 nm. This radiation pumped the OPA. Signal and idler pulses from OPA allowed tuning along the 1200–1600 nm and 1600–2600 nm ranges respectively. In discussed HHG experiments, the signal pulses were predominantly used, which were ~1.5 times stronger than the idler pulses. Most of the experiments were carried out using the 1 mJ, 70 fs signal pulses tuneable in the range of 1280–1440 nm, while some measurements of harmonic emission were carried out using the 1600 nm pulses mixed with 806 nm radiation. The spectral bandwidth of tuneable pulses was 45 nm. The intensity of the 1310 nm pulses focused by 400 mm focal length lens inside the extended plasma was 2×10^{14} W cm^{-2}. The OPA pulses were focused, 45 ns from the beginning of ablation, onto the extended plasma from the orthogonal direction, at a distance of ~200 μm above the target surface.

Most of the experiments were carried out using the TCP pump of LIP. The reasons for using the TCP instead of SCP were related to the small energy of the driving NIR signal pulses. The $I_H\propto\lambda^{-5}$ rule (I_H is the harmonic intensity and λ is the driving field wavelength) led to a significant decrease of harmonic yield in the case of the longer-wavelength sources compared with the 806 nm pump and did not allow the observation of strong harmonics even from the 1310 nm pulses, which had the highest energy. Because of this, the second-harmonic generation of the signal pulse was used to apply the TCP scheme (NIR+H2) for plasma HHG. The 0.5-mm-thick BBO crystal (type I, Θ = 21^0) was installed inside the vacuum chamber on the path of focused signal pulses (Fig. 8.1a). The conversion efficiency of H2 pulses was ~20%.

Silver, tin, graphene, and C$_{60}$ nanoparticles were used as the media for harmonic generation during propagation of the tuneable NIR+H2 pulses through the LIP produced on the surfaces containing these species. A detailed description of the morphological properties of these species will be presented in the following subsection. HHG from ablated nanoparticles and bulk targets of similar origin (5-mm long Ag, Sn, and graphite plates) was compared.

8.1.2. Morphology of the nanoparticle emitters of harmonics

Silver (99.95% purity, 20-30 nm), tin (99.9%, <100 nm), graphene (1–5 nm wrapped sheets), and fullerene (C$_{60}$, 98%) nanoparticle powders were used as the media for harmonic generation during propagation of the tuneable NIR+H2 pulses through the plasmas produced on the surfaces

containing these species. The nanoparticle powders were prepared as targets by mixing with cyanoacrylate-based glue and coating the surface of the 5×5 mm^2 glass substrate. Thus the material directly surrounding the nanoparticles was a polymer (epoxy glue), which has a considerably lower ablation threshold than the metallic bulk materials. The nanoparticle-carrying polymer begins to ablate at relatively low intensities, resulting in the lower laser intensity required for the formation of the optimal plasma medium for the HHG. This feature allowed for the easier formation of the optimum plasma conditions, which also resulted in better HHG conversion efficiency from the nanoparticle-containing plumes compared to those from the ablation of bulk targets (5-mm long Ag, Sn, and graphite plates). The glue without nanoparticles was ablated and did not show the harmonic generation during propagation of femtosecond pulses through the glue-containing plasma. The ablation of pure glue led mostly to the emission of incoherent radiation. The glass substrates also did not play any role in HHG.

To define more details about used nanoparticles the morphology of the above species before and after ablation was analyzed. Figure 8.1b (upper left panel) shows the transmission electron microscopy (TEM) images of debris at the optimal conditions of ablation. The length of black lines is 50 nm. The sizes of original graphene nanoparticles were distributed in a broad range of 10–80 nm. The plasma debris collected on the carbon grids placed nearby to ablation area was analyzed at the optimal and non-optimal conditions of plasma formation. These terms refer to the strong and weak harmonic yields from the graphene-contained plasma. The analysis of post-ablation conditions of the deposited debris can provide some information about the plasma components despite the possible difference between the composition of the plasma in its early stages and the deposited material, which can be modified due to the aggregation on the substrate.

To compare the dependence of the properties of the debris under different ablating conditions, the target was ablated using the 370 ps pulses of the Ti:sapphire laser at a repetition rate of 10 Hz using a variable fluency. The figure shows the material ejected upon ablation of graphene nanopowder at the above-mentioned conditions. The shapes of deposited material were similar to those of the initial clustered target, though the sizes of deposited clusters were smaller, probably due to the disintegration of large crumpled and wrapped sheets of graphene on the smaller parts. The monolayer, bilayer, trilayer, etc. nanosized chunks were observed depending on the conditions of ablation. In discussed studies, moderate laser ablation fluency (~0.7 J cm^{-2}) was used, which corresponded to the

conditions of efficient HHG. Ablation of the graphene-contained target by higher fluency (~2 J cm^{-2}) did not yield similar nanostructured deposits, but rather the groups of chaotically shaped large aggregates. The harmonic yield from the plasma produced using this high fluency of heating pulses was considerably weaker compared with the optimal conditions of ablation (0.7 J cm^{-2}). The use of higher ablation fluencies resulted in the formation of a large number of free electrons, which is a detrimental factor for the HHG due to the growing contribution of the latter species on the phase mismatch between the driving and harmonic waves. The presence of the larger amount of nanoparticles in the plasma did not compensate for the deteriorated phase relations between interacting waves caused by a significant amount of free electrons in the plasma plume.
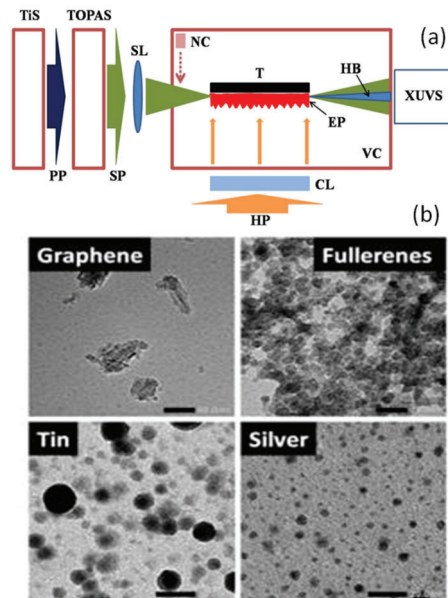
Fig. 8.1. (a) Experimental setup. TiS, Ti:sapphire laser; TOPAS, optical parametric amplifier; PP, pump pulse for pumping the optical parametric amplifier; SP, amplified signal pulse from OPA; HP, heating picosecond pulse from Ti:sapphire laser; SL, spherical lens; CL, cylindrical lens; VC, vacuum chamber; T, target; EP, extended plasma; NC, nonlinear crystal (BBO); HB, harmonic beam; XUVS, extreme ultraviolet spectrometer. (b) TEM images of ablated nanoparticles (see text). Reproduced from [3] with kind permission of The European Physical Journal (EPJ).

The upper right panel of Fig. 8.1b shows TEM images of fullerene agglomerates after ablation. Black markers correspond to 20 nm. The sizes of deposited agglomerates were estimated to be 3–5 nm. The mass-resolved spectra of the fullerene plasmas were analyzed using time-of-flight mass spectroscopy (TOFMS). The laser pulses were used to ablate the species at the fluencies corresponding to both efficient and inefficient HHG. To ascertain the presence of neutral species in the ablated plasma, an additional source of ionization should be used. Those TOFMS measurements did not reveal the presence of neutral clusters in the plasma, since there was no opportunity in post-ionization of the plasma plume. However, other studies (for example [4]) have indicated the presence of neutral carbon clusters at similar conditions of ablation.

Ablation of C_{60} at a weak fluence revealed the appearance of fullerene ions, while the strong signal from C_{26} clusters pointed out the preferable disintegration of the C_{60} molecule rather than its ionization. The growth of heating pulse fluence on the target surface considerably modified this pattern. While C_{26} still remained in the mass spectrum, a very strong signal from the C_{60} ion dominated the whole spectrum, together with the appearance of some particles containing clusters (C_{56}, and C_{58}). Moreover, two additional groups of clusters appear in the high-mass/charge range (from C_{108} to C_{118} and from C_{164} to C_{176}). The sodium and potassium lines appear from the substrate of ablating species.

The deposits generated upon laser ablation of the bulk graphite were also analyzed at the conditions that ensured the efficient harmonic generation in the ablation plume. Under the conditions of using the moderate fluencies, the collected deposits showed evidence of ~10–20 nm nanoparticles. Note that the formation of carbon nanoparticles by laser ablation of graphite at high fluencies of heating ultrafast pulses is a well-studied phenomenon. However, the use of high ablation fluencies results in the generation of a large number of free electrons, which is a detrimental factor for HHG due to the growing contribution of free electrons to the phase mismatch between the pump and harmonic waves. This explains why, under ablation conditions leading to nanoparticle production in the plume of some bulk metal targets, the HHG signals were extremely weak. In that case, the presence of nanoparticles in the plasmas formed on bulk materials does not compensate for the deteriorated phase relations between the interacting waves caused by over-ionization and the appearance of a large number of electrons. In the meantime, cluster formation during ablation of graphite occurs at rather low laser fluencies, which allowed the maintenance of the moderate level of electron concentration.

TEM image of tin nanoparticles after their ablation is shown in the bottom left panel of Fig. 8.1b (black line corresponds to 50 nm). The original nanoparticles were dissolved in methanol and rinsed. The drop of this suspension was dried and analyzed by TEM. The sizes of nanoparticles were in the range of 40–110 nm. The tin nanoparticles were presented in a sphere-like shape. The analysis of the ablated material, which was deposited on nearby glass plates, showed nanoparticles similar to the original ones. This observation confirmed the presence of tin nanoparticles in the plasma plume at the used fluencies of the heating pulse (0.8 J cm^{-2}). In most cases, both the original and deposited nanoparticles were individually isolated. The morphology of the debris deposited on the glass plates during ablation of bulk Sn targets was also analyzed. No nanoparticles were observed in that case at the heating pulse fluencies up to 1.5 J cm^{-2}. This observation points out the absence of nanoparticles and the presence of monomers in the plasma plumes at the conditions corresponding to the harmonic generation from the ablation of bulk metals.

TEM measurements of original silver nanoparticles showed that the maximum sizes of these particles corresponded to those provided by suppliers (~20–30 nm). However, the nanoparticles had broad inhomogeneous size distribution centred at ~20 and ~5 nm. The ablated species (at optimal ablation conditions corresponding to maximum HHG conversion efficiency) had smaller sizes, without indication of large (>10 nm) nanoparticles, with average sizes of 4 nm (Fig. 8.1b, right bottom panel; black line corresponds to 20 nm).

This morphology analysis confirmed the presence of nanoparticles in the LIP. Below we discuss the results of the studies of harmonic spectra from these nanoparticles using NIR+H2 pulses.

8.1.3. HHG in nanoparticles using NIR pump

The weak intensity of NIR pulses led to a significantly smaller harmonic yield compared with 806 nm pump pulses in the case of propagation through the ablation of bulk tin. The application of 0.8 mJ, 70 fs, 1420 nm SCP did not lead to the harmonic generation below 60 nm. In the case of the 1355 nm pump, weak harmonics up to H21 were observed (Fig. 8.2a, thin curve). The harmonic efficiency significantly increased once BBO crystal was introduced on the path of focused NIR pulses (Fig. 8.2a, thick curve). The enhancement factor, in that case, was 15×. Harmonics up to H34 ($\lambda = 41.8$ nm) were observed using NIR+H2 pulses (1420nm + 710 nm), with the notable enhancement of the H30 compared

with the lower-order harmonics (Fig. 8.2b, upper panel). In the case of Sn nanoparticle-containing plasma at the same conditions, the harmonics showed a similar pattern (Fig. 8.2b, second panel). The intensity of a whole harmonic spectrum, in that case, was ~5 times stronger compared with the case of bulk tin ablation. The tuning of NIR pulses from 1420 nm towards 1310 nm led to a decrease of enhanced single harmonic (H28) and the growth of lower-order harmonic yield (Fig. 8.2b, third panel). Note that the energy of 1310 nm pulses was ~1.2 times larger compared with the 1420 nm pulses.
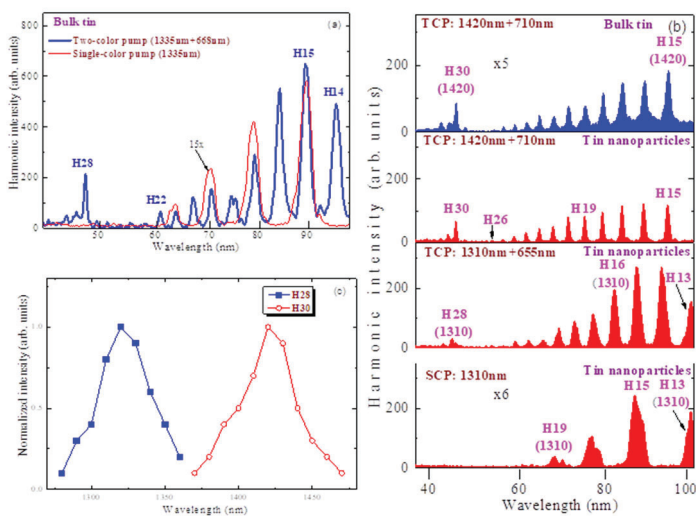
Fig. 8.2. (a) SCP- and TCP-induced harmonic spectra from ablated bulk tin. (b) Harmonic spectra in the cases of two-colour pump of bulk tin plasma (first panel, 1420 nm + 710 nm), tin nanoparticle plasma (second panel, 1420 nm + 710nm), tin nanoparticle plasma (third panel, 1310 nm + 655 nm), and single-colour pump of tin nanoparticle plasma (fourth panel, 1310 nm). Upper panel was multiplied by a factor of 5 for better comparison with harmonic spectra from nanoparticles (second panel). Bottom panel was multiplied by a factor of 6 for better comparison with harmonic spectra using TCP (third panel). (c) Variations of H28 and H30 yields during tuning the NIR pulses. Reproduced from [3] with kind permission of The European Physical Journal (EPJ).

These experiments showed that the harmonic efficiency for the separate order significantly depended on the detuning out of ionic resonances

responsible for such enhancement, while the stronger intensity of pump pulses (1310 nm + 655 nm) did not significantly influence this process. The removal of BBO from the path of NIR pulses at these conditions led to the generation of a few odd harmonics (Fig. 8.2b, fourth panel), without any enhancement of a single harmonic. The main aim to show these two bottom spectra was the demonstration of a small cut-off in the case of nanoparticles. This led to the absence of resonantly-enhanced harmonic in the vicinity of 47 nm. The bottom spectrum was collected during 6 seconds (i.e. during 60 laser shots) compared with the case of TCP (10 laser shots, third panel) to show that, even at larger collection time, no shorter-wavelength harmonic near resonance can be registered.

The ionic resonances, which influenced the enhancement of single harmonic in the case of bulk and nanoparticle ablations, corresponded to the wavelengths in the region of 47 nm and are associated with the influence of the transitions of Sn II ions. The H30 harmonic of 1420 nm + H2 TCP is close to some transitions between autoionizing and ground states of tin. The observed enhancement of this harmonic was attributed to its closeness with the $4d^{10}5s^25p\ ^2P_{3/2} \rightarrow 4d^95s^25p^2\ ^2D_{5/2}$ transition of the Sn II possessing large oscillator strength gf ($\lambda = 47.28$ nm, $gf = 1.43$; see also [5] regarding the theoretical calculation of gf). The discussed studies of ablated nanoparticles using the tuneable NIR pulses and their second harmonics allowed a fine-tuning of the resonance-enhanced harmonic and change of the order of this harmonic. The energy difference was a tuneable factor, which varied between 1.5 eV and 0 eV from both sides of the transition responsible for resonance enhancement.

The maximally enhanced harmonics generated in the Sn nanoparticle-contained plasma, for which both micro-processes and macro-processes were optimized to generate the highest photon yield, were tuned from H31 in the case of 1440nm+770nm TCP to H27 in the case of 1280nm+640nm TCP. In all these cases, the preceding harmonics were significantly suppressed compared with resonance-enhanced ones. In Fig. 8.2c, the dependence of H28 and H30 normalized intensities on the variation of NIR wavelength is shown.

Note that ablation of Sn nanoparticles using weak fluence (~0.5 J cm^{-2}) led to the generation of lower-order harmonics in the case of TCP and did not show the resonance enhancement in the region of strong ionic transition. This observation points out that in the case when ablation did not cause the appearance of ionized nanoparticles, the HHG occurs using the involvement of neutral particles leading to generation of lower-order harmonics, without the ionic resonance induced enhancement of single harmonic.
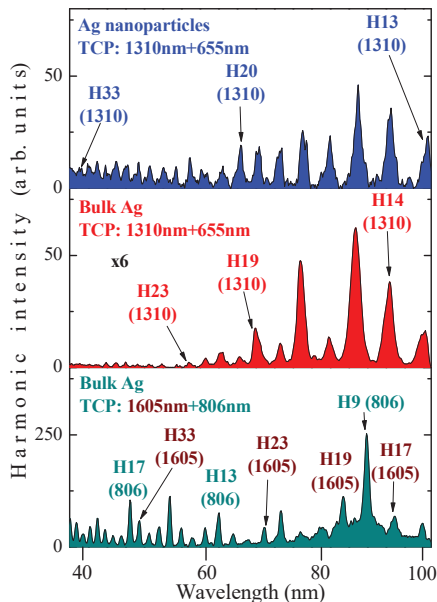
Fig. 8.3. Harmonic spectra in the cases of two-colour pump of silver nanoparticle-containing plasma (first panel, 1310 nm + H2), bulk silver plasma (second panel, 1310 nm + H2), and bulk silver plasma (third panel, 1605 nm + T:sapphire pulse). Middle panel was multiplied by a factor of 6 for better comparison with harmonic spectra from nanoparticles (upper panel). Reproduced from [3] with kind permission of The European Physical Journal (EPJ).

Similar studies of HHG using silver nanoparticles showed a featureless extended spectrum of equal odd and even harmonics using 1310nm+H2 TCP (Fig. 8.3, upper panel). The spectrum was extended towards the shorter wavelength region (up to the H56; not shown in this panel) compared with the ablation of bulk silver (Fig. 8.3, second panel). As in the case of bulk and nanoparticle Sn, the collection time for bulk Ag plasma-induced harmonics was six times larger than for the case of Ag nanoparticle plasma (60 and 10 shots respectively). The unequal collection times were chosen to show the HHG spectra at a similar Y-axis.

The difference in the spectra could be attributed to better conditions for the formation of a larger amount of harmonic emitters in the case of Ag nanoparticle ablation, as well as to specific properties of nanoparticles leading to stronger harmonic yield compared with atoms and ions. Specific properties of nanoparticles refer to those, which allow achieving the enhanced yield of harmonics from nanoparticle-contained medium compared with the atomic medium. In the case of gas nanoparticles (gas clusters) those include the involvement of different channels of harmonic generation, particularly, the ionization and recombination to the same ion of the cluster, to neighbouring ions, and to the whole nanoparticle [6]. These features, alongside the enhanced cross-section of recombination of the accelerated electron with the parent particle in the case of nanoparticles compared with the atoms, distinguish cluster-induced gas harmonics from the monomer-induced ones. The same is true for the nanoparticles appearing in the laser-induced plasmas. However, silver nanoparticles possess additional specific properties. Early studies of the low-order processes in Ag nanoparticles have revealed the enhancement of the nonlinear optical response in the case of using the wavelength of pump radiation (~800 nm), which was integer to the broadband plasmonic resonance (~400 nm) of these species. Particularly, the nonlinear susceptibility of Ag nanoparticles in this spectral region was enhanced compared with other spectral ranges [7]. The growth of nonlinear susceptibility was attributed to the growth of the matrix components of this parameter in the vicinity of plasmonic wavelength. One can suggest that a similar enhancement could be realized in the case of higher-order processes. The discussed study using a tuneable pump source could be a proof-of-concept for this assumption. A significant enhancement of lower-order harmonics (H9–H19) in clustered media compared with Ag monomers was reported in previous studies using 800nm-class lasers [8,9] thus confirming the above assumption.

The discussed study used the pump radiation, which was commensurate in some spectral regions with regard to the plasmonic wavelength of Ag nanoparticles (correspondingly 1280 nm and 420 nm, with a ratio of 3:1). To which extent this coincidence affects the nonlinear optical response of nanoparticle-contained plasma remains unclear. Even at these less favourable conditions, the harmonic yield from silver nanoparticle-contained plasma was significantly larger with regard to the monomer case, though no superior features of Ag nanoparticles compared with other metal particles were observed in the case of the NIR+H2 pump.

The application of another TCP (NIR + Ti:sapphire pulses) of orthogonally polarized pulses in the case of ablation of the bulk silver led

to the prevailing generation of harmonics from the stronger component (806 nm pulses). There were also the harmonics attributed to the combination of the wavelengths of two pumps, similar to the theoretical predictions of Ref. [10]. The third panel of Fig. 8.3 shows the harmonic spectrum from ablation of bulk Ag using 1605nm+806nm orthogonally polarized pulses. The harmonics were extended below the spectral region of consideration (37–103 nm) and represented three additional sum and difference frequencies between each odd harmonic originating from a stronger 806 nm pump. A similar pattern was also observed in the case of silver nanoparticle-contained plasma.
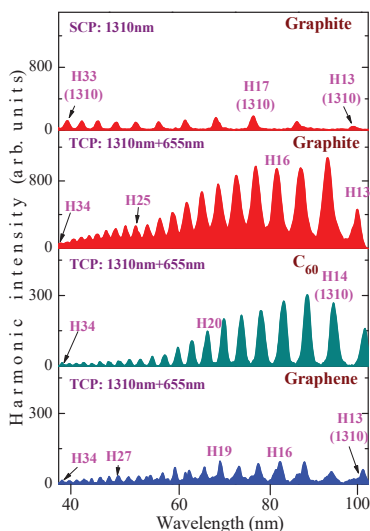
Fig. 8.4. Harmonic spectra in the cases of single-colour pump of graphite plasma (first panel, 1310 nm), and two-colour pumps of graphite plasma (second panel, 1310 nm + 655 nm), fullerene plasma (third panel, 1310 nm + 655 nm), and graphene plasma (fourth panel, 1310 nm + 655 nm). Reproduced from [3] with kind permission of The European Physical Journal (EPJ).

The extension of pump sources towards the longer wavelengths allows defining best conditions for the high-order nonlinear optical effects. Carbon-containing nanoparticles, particularly fullerene and graphene clusters, are the important species for the analysis of various processes

since the method of formation of the gaseous-like media containing the above clusters can provide the opportunity for the definition of their properties in different spectral regions. The advantages in using the tunable femtosecond pulses in the mid-infrared region include the analysis of the variation of nonlinear response with a variation of the photon energy of pump radiation. In the case of carbon species, this could be the chance to study nonlinear optical processes while keeping plasma components at the level when different mechanisms (i.e. nanoparticle-induced growth of HHG efficiency, resonance-induced enhancement of single harmonic, involvement of neutral and/or ionized clusters in HHG, etc.) can switch the spectral distribution of harmonics from one to another. TCP is also advantageous in that case since it allows both the enhancement of harmonic yield and the growth of frequency components in the spectral areas where the growth of harmonic efficiency is expected.

Graphene and fullerene plasmas demonstrated some specific nonlinear optical features compared with those observed in the case of bulk graphite ablation. The latter plasma was a rare case of an efficient medium for HHG using SCP (1310 nm; Fig. 8.4, upper panel). The harmonics up to the 43rd order (λ_{H43}=29.1 nm, E_c=42.6 eV) were observed once the system of registration was shifted towards the shorter wavelength region. Even this extension of harmonics did not follow well with the $E_c \propto \lambda^2$ rule [11] where E_c and λ are the cut off energy of harmonics and wavelength of pump radiation respectively. In the case of 806 nm pulses, at a similar intensity of driving radiation (2×10^{14} W cm^{-2}) it was possible generating harmonics up to the 19th order (λ_{H35}=42.4 nm, E_c = 29.2 eV) from graphite plasma. The above rule predicts the $(\lambda_{1310}/\lambda_{806})^2 \approx 2.6$-fold growth of harmonic cut off energy, while the experiment showed a factor of ~1.5.

Various processes could cause the inclination from the above rule, such as self-phase modulation, some difference in peak intensity caused by heterogeneity in the focal plane, involvement of different species for HHG, etc. Self-phase modulation has clearly been emphasized in those experiments by showing short-wavelength lobes near each harmonic in the case of graphite plasma (bottom panel of Fig. 8.4). This process occurs as modulation and growth of frequency components of the driving pulse propagating through the plasma. Note that the appearance of lobes was observed only in the case of carbon-contained components of plasma. Moreover, self-defocusing could be measured as well [12]. Thus the self-modulation of the laser field may influence the observed harmonic spectra. Note the growth of harmonic yield in the case of using the TCP of graphite plasma (Fig. 8.4, second panel; compare Y-axes of two upper panels),

similar intensities of odd and even harmonics, and gradual decrease of conversion efficiency for the shorter wavelength components.

Approximately the same cut offs were observed in the case of the TCP of graphene and fullerene particles (Fig. 8.4, two bottom panels). The application of SCP (NIR) led to a significant decrease in HHG conversion efficiency compared with bulk graphite ablation. The disadvantage in using these species was a decrease of harmonic yield with the growth of the number of shots on the same place of nanoparticle-contained targets. Because of this one needs to drag these samples up and down to keep the same harmonic yield from extended plasma. Nevertheless, even the low pulse repetition rate of the used system (10 Hz) allowed collecting a sufficient amount of data during the single set of measurements lasting 1 s.

The characteristic peculiarity of harmonic spectra from ablation of bulk graphite compared with C_{60} and graphene was the blue shift of harmonic orders (compare the wavelengths of H13 in the case of graphite, fullerene, and graphene ablations, Fig. 8.4) at the conditions of stronger ablation of the target (i.e. at the fluency of ~1 J cm^{-2}) leading to higher conversion efficiency. The shorter wavelength shift of harmonics at weaker (0.6 J cm^{-2}) excitation of graphite target was not observed. This feature has been analyzed previously in a few studies of carbon harmonics. Particularly, the origin of the shift of harmonics has been studied in Ref. [13] and was attributed to the influence of the self-phase modulation of the driving femtosecond pulse during propagation through the graphite plasma plume.

8.1.4. Discussion of HHG in NPs using NIR pump

Initially, studies of nanoparticle-induced harmonic generation were limited to exotic clusters of noble gases. The physical origin of this process in the gas clusters was mostly related to standard atomic harmonic generation, modified by the fact that the atoms in nanoparticles are close to each other. The increase of HHG conversion efficiency in those studies was attributed to the growth of the number of emitters. The cross-section of recombination of the accelerated electron with the parent particle in the case of nanoparticles is higher compared with atoms. Still debated, this enhancement was commonly observed in the ablation experiments. Moreover, even in the case of bulk silver ablation the appearance *in situ* of Ag clusters formed during over-excitation of the silver target also led to the growth of harmonic yield at extremely unfavourable conditions of plasma formation [14]. Note the easiness of comparison of these two groups of emitters in the case of plasma harmonic experiments compared with the gas harmonic case.

In both cases of ablation, the conditions of maximal harmonic yields from mono- and nanoparticle plasmas were analyzed. The issue of "larger densities" in the case of nanoparticle ablation also requires special consideration. Of course, local density (i.e. inside the nanoparticles) was significantly larger compared with plasma density ($\sim 10^{23}$ and 10^{17} cm^{-3}). However, one has to note that only outer atoms of clusters play important role in a harmonic generation. Furthermore, it is not clear how to compare the average densities of two plasmas from the point of view of their influence on the harmonic yield. The same can be said about the comparison of monomer- and cluster-induced HHG in gases.

The plasma species produced during nanoparticles ablation generate strong harmonics. It is the experimental fact, also proven in numerous previous experiments in various laboratories. Which species are responsible for that? Those are obviously not monomers, which commonly exhibit extended harmonic cut-off. What else may exist in plasma during ablation of nanoparticle-contained targets? The plasma may comprise nanoparticles, aggregates, disintegrated nanoparticles, small and large molecules, monomer neutrals, and ions. The emission spectra from such plasmas did not show the presence of the ions of silver monomers, though their presence could not be excluded. The ablation at the fluencies of ~1 J cm^{-2} allows keeping original nanoparticles in the plasma volume almost intact. TEM measurements of initial species and deposited material on nearby glass substrates have shown a similarity of their morphology, thus confirming the presence of nanoparticles in the plasmas during the propagation of femtosecond pulses. The distinction in the harmonic spectra from atoms- and nanoparticle-contained plasmas is another proof of the involvement of different emitters in the formation of harmonic spectra. In the former case, neutral nanoparticles are largely responsible for dominantly lower-order harmonic spectrum formation, while in the latter case, the monomer ions allow the extension of harmonic cut-off.

The comparative studies of HHG in the plasmas consisting of either nanoparticles or monomers showed that, at optimal experimental conditions, the former species provide stronger harmonic yield, thus pointing out the advanced properties of the large emitters of harmonics in the nanoparticle-containing plasmas. The cross-section of recombination of the accelerated electron with the parent particle in the case of nanoparticles is higher compared with the atoms. The uncertainty in the exact mechanism of the HHG from nanoparticles has previously been underlined in a few studies using gas clusters [15]. Among HHG mechanisms, the ionization and recombination to the same ion, to the neighbouring ions, and to the whole nanoparticle have been proposed.

The advantage of the studies of resonance-induced enhancement of harmonics using tuneable NIR+H2 pulses is the opportunity of fine-tuning this high-order nonlinear optical process for spectral enhancement of the harmonic yield. Another advantage is closely related to the analysis of the oscillator strengths of some ionic transitions of metal mono- and nanoparticles using the HHG approach. The oscillator strengths of ionic transitions could be defined from the absorption data of plasmas in the XUV, which has been demonstrated in numerous publications [16,17]. The discussed studies point out the relation of the proposed approach of tuneable enhanced harmonics with the analysis of *gf* of some transitions. This method cannot define the values of this parameter of ionic transitions but rather can point out the transitions possessing strong *gf*. And vice versa, the spectroscopy findings of the transitions possessing strong *gf* (which is itself a rather tough task) allow defining the potential plasmas where those transitions may cause the growth of nearby harmonic. These assumptions have found clear confirmation starting from the first observations of exceptionally strong single harmonic generating near In II transition (19.92 eV).

The demonstrated method of optimization of driving pulses for the resonance-enhanced HHG opens new opportunities for the harmonic generation of ultrafast pulses in the laser-produced plasma plumes and can be considered as a tool for various studies of different species (particularly large molecules and clusters) produced during laser ablation. The use of tuneable NIR TCP allows the analysis of the ionic states in plasmas and broadens the subjects of studies compared with presently used HHG in gases and plasmas using fixed wavelength sources.

Below we address the temporal and spatial walk-offs of two pump pulses in the plasma volume. A 0.5-mm-thick BBO causes a 26 fs delay of 1310 nm pulses with regard to 655 nm pulses due to small group velocity dispersion in this spectral region. The method of calculations is based on the definition of the delay of the fundamental wave $\Delta_{\text{cryst}} = d[(n^{\text{o}}_{\omega})_{\text{group}}/c - (n^{\text{e}}_{2\omega})_{\text{group}}/c]$ with respect to the H2 pulse (2ω) in this negative uniaxial crystal ($n^{\text{o}}_{\omega} > n^{\text{e}}_{2\omega}$). Here d is the crystal length, $c/(n^{\text{o}}_{\omega})_{\text{group}}$ and $c/(n^{\text{e}}_{2\omega})_{\text{group}}$ are the group velocities of the ω and 2ω waves in the BBO crystal, c is the light velocity, and n^{o}_{ω} and $n^{\text{e}}_{2\omega}$ are the refractive indices of the ω and 2ω waves. The method is described in Refs. [18]. The temporal overlap between two pumps in the plasma area was more than sufficient, assuming a large conversion efficiency of H2 (~20%). Previous two-color pump experiments in plasmas using 810 nm and H2 pulses at significantly smaller conversion efficiency (7%) in the 0.3-mm-long BBO causing 60 fs delay between pulses have shown a notable influence of second assistant

field leading to 50-fold growth of harmonic yield compared with single-colour pump. The use of extended plasma has further decreased the temporal walk-off between pulses.

The use of axial placement of thin BBO between the focusing lens and plasma allowed excluding the spatial walk-off as well as the dispersion-induced difference of the focal planes of NIR and H2 beams, so the spatial overlap was also satisfied the requirements of efficient interaction of two pumps in the plasma medium. The most important proof of the spatio-temporal overlap of two pump pulses in the plasma area is the dramatic growth of harmonic yield in the case of TCP compared with SCP. This amendment was achieved by the simple insertion of BBO on the path of NIR pulses, without any other change of experimental conditions.

The phase matching between fundamental and harmonic waves is another very important issue in the case of plasma harmonics, similarly to gas HHG experiments. To address this problem one has to analyze the dependence of harmonic yield (I_h) on the length of extended plasma (L_{plasma}) for different orders of harmonics. Once the $I_h(L_{plasma})$ dependence follows the quadratic rule along the whole range of plasma sizes the conclusion on the negligible influence of phase mismatch could be drawn. In other words, for the plasma lengths less than coherence length for specific harmonic order the phase mismatch becomes less influential impeding factor compared with other restricting mechanisms.

The issue of phase mismatch during HHG in extended plasmas has been carefully analyzed in Ref. [19]. The principles developed in those studies for excluding phase mismatch problems during plasma HHG were transferred in the discussed study. Specifically, the I_h (L_{plasma}) dependences were carefully analyzed in all used plasma species and found a negligible deviation from the quadratic rule at optimal ablation. The estimated plasma density ($\sim 10^{17}$ cm^{-3}) was not as high as the one at which one can expect the appearance of the phase mismatch between interacting waves caused by ionization of plasma particles. To keep these conditions the above-mentioned "optimal ablation" of targets was maintained. This term refers to the conditions when plasma properties (i.e. plasma density, electron density, incoherent plasma emission) allowed maximum yield of harmonics at the used sizes of plasma formations (5 mm). Contrary to that case, over-excitation of targets by strong fluencies of heating pulses led to the phase mismatch, which initially affected the highest orders and then, at further growth of heating pulse fluency, diminished the lower-order harmonic yield. In the meantime, to overpass the phase mismatch at those conditions, the quasi-phase-matching of modulated plasma has been developed [20], which was out of the scope of the discussed study.

One has to point out the importance of the influence of the plasma concentration on the phase-matching conditions. This parameter would be different for each case once the ablation conditions keep similar for all experiments. However, it was not the case of the discussed studies. The ablation conditions were kept, particularly by changing the heating pulse fluency, at such conditions that the phase mismatch in optimally prepared plasmas did not play a significant role. Furthermore, the large electron density rather than plasma density is instrumental for developing the non-optimal conditions for HHG. These electrons refer to those appearing during ionization of plasma species by fundamental pulse rather than the electrons appearing during target ablation. Thus plasma concentration being exceeded over some level causes the appearance of a large number of free electrons due to tunnel ionization by femtosecond pulses. The optimal ablation conditions were maintained to achieve the highest yield of harmonics from extended plasma taking into account the above consideration and optimal pulse duration of heating radiation. Regarding the width of the heating pulse, we would like refereeing to previous systematic studies of target ablation using pulses of different duration in a broad range varied between a few tens of femtosecond and a few tens of nanoseconds [21]. Those studies have demonstrated the optimal heating pulse duration for plasma harmonics (a few hundred picoseconds) while pointing out the fluence rather than the intensity of heating pulse as the main factor for the formation of suitable laser-produced plasma for HHG.

The discussed TCP studies using NIR+H2 pulses allowed the tuning of nonlinear optical processes using carbon-contained nanoparticles. Particularly, one can explore the use of giant broadband plasmonic resonances of those species at carefully maintained conditions of excitation of the carbon-contained clusters. This mechanism of harmonic enhancement has already been realized using a fixed pump source (800 nm) and fullerenes when the broad (10 eV FWHM) plasmonic resonance centred at 60 nm allowed the enhancement of H11-H15 [22].

While considering results of HHG using another method of TCP (i.e. mixture of 1605 nm and 806 nm pulses) in Ag nanoparticle plasma, we would like to note that these are not the odd and even harmonics of NIR pulses. Only a few studies of such kind of TCP have been reported [23,24]. The theory developed in those papers predicts a generation of attosecond pulses in such a configuration, whilst using multi-cycle pump pulses. At the used conditions (0.5 mJ pulses of 1605 nm signal wave of OPA and 3 mJ pulses of Ti:sapphire laser radiation) the assistant field seems the NIR radiation. The generated components of the spectrum are the sum and difference frequencies of 1605 nm and 806 nm waves

[E_{odd}(NIR)±E(806nm)], not the odd and even harmonics of 1605 nm radiation, though they seem similar to each other.

The relative polarization of the two pumps does not play a significant role. The parallel polarization of two pumps (while using idler pulses instead of signal pulses as the NIR waves) was used and did not show a significant difference compared with orthogonally polarized (i.e. signal and NIR) waves. Thus the message of these NIR+800nm experiments is the availability of high-order sum and difference frequency generation, which has never been studied (excluding the above-referred papers dealing with gas harmonics). The refereed studies, at approximately similar conditions of experiments (30 fs pulses, 1700 nm, and 800 nm pumps) have demonstrated the generation of 300 as pulses during HHG in argon gas. One can assume that similar pulse durations (i.e. shorter than 1 fs) could be realized in the discussed harmonic experiments, contrary to the case of conventional TCP.

All plasma samples from bulk materials showed a similar feature of less extended harmonic cut-off than one can expect from the $E_{cut\text{-}off} \propto \lambda^2$ rule for the longer wavelength pumps. The reason for this behaviour is the small intensity of fundamental NIR radiation, which prevented observation of higher-order harmonics. The energy of NIR pulses was ~6 times lower than the one of the 806 nm pump. This difference in harmonic yields was exaggerated by the $I_H \propto \lambda^{-5}$ rule, which for the 806 nm (6 mJ) and 1300-nm (1 mJ) pumps gives the drop of HHG conversion efficiency by a factor of at least ~80 in the latter case. That is why no extended harmonics were achieved from the single-colour NIR pulses. The situation was dramatically improved in the case of using the two-colour pump (NIR+H2, compare two bottom panels of Fig. 8.2b).

Note that, while the HHG during the two-colour pump of the plasma from bulk materials showed, to some extent, the extension of $E_{cut\text{-}off}$ compared with 806 nm pump, the use of nanoparticles did not lead to any extension of harmonic cut-off. This difference is directly related to the difference in the primary emitters of harmonics. As it was already mentioned, in the former case, the singly-charged ions were responsible for extended harmonic generation, while in the latter case, the neutral clusters were assumed to be involved in HHG. This difference in charge state of primary emitters caused the difference in E_c.

To compare these results with those obtained in the case of 800-nm-class lasers one has to maintain similar conditions of experiments. In the meantime, it is unclear how one can formulate the meaning "similar conditions" for the cases of 800-nm-class lasers and NIR+H2 pumps. How one can take into account the wavelength-dependent yield of harmonics

$(I_H \propto \lambda^{-5})$ and at the same time consider the use of both NIR and visible (H2) pulses? Past work on that matter [25] has analyzed the wavelength scaling and revealed some declination from the above rule (from $I_H \propto \lambda^{-5}$-λ^{-6} to $I_H \propto \lambda^{-3}$ - λ^{-4}).

8.2. High-order harmonic generation in Au nanoparticle-contained plasmas

The production of clusters in the laser plasma during ablation of various targets has a high probability, while their presence and concentration in the plasma volume, where the frequency conversion occurs, is yet to be confirmed directly. Analysis of post-ablation conditions of the deposited debris can provide information on the nature of those species, despite the differences between the composition of the plasma formed at its early stages and the deposited material (due to the influence of aggregation on the substrate). Further evidence of the cluster contribution to the enhancement of the harmonic generation comes from investigations of intense laser ablation of a target, which would give the assumptions regarding the participation of in situ generated nanoparticles.
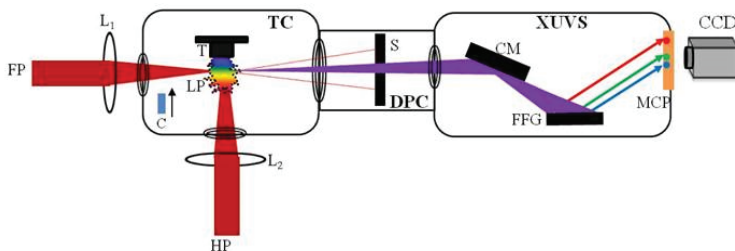
Fig. 8.5. Experimental setup for high-order harmonic generation in LPPs. FP, converting femtosecond pulses, HP, heating pulses; $L_{1,2}$, focusing lenses; TC, target chamber; T, target; C, BBO crystal; LP, laser plasma; S, slit; DPC, differential pump chamber; XUVS, extreme ultraviolet spectrometer; CM, cylindrical gold-coated mirror; FFG, flat field grating; MCP, micro-channel plate; CCD, CCD camera. Reproduced from [26] with permission from MDPI.

Gold nanomaterials have potential applications because their surface plasmon resonance affects the optical properties of materials. Here, we discuss how harmonics obtained from Au NPs are affected by using the active substrate, which itself allows the generation of harmonics [26]. The

systematic experimental studies of the NPs formation during laser ablation and the HHG from Au NPs, Au bulk, paper, and Au NPs deposited on paper and glass substrates are analyzed.

The experimental layout of HHG is shown in Fig. 8.5. 100 nm and 10 nm Au NPs (99.95% purity) were glued on the glass substrate and paper, respectively. Notice that ablated pure glue did not allow the generation of harmonics in LIP. The studied samples were ablated by nanosecond (1064 nm, 5 ns, 10 Hz), picosecond (800 nm, 200 ps, 200 Hz), and femtosecond (800 nm, 30 fs, 200 Hz) pulses. Both femtosecond (fs) and picosecond (ps) laser pulses were obtained from the same laser by separation of the part of uncompressed radiation (200 ps) before entering into the compressor stage. The delay between heating radiation (i.e., fs or ps pulses) and driving fs pulses (800 nm, 30 fs, 200 Hz) was varied in the range of 0–120 ns by using the optical delay line. The delay between heating nanosecond (ns) pulses and driving fs pulses was varied electronically between 0 and 10^5 ns using a delay generator. LIP was created by heating pulses, while the driving pulses were focused inside the plasma using a 500 mm focal length spherical lens from the orthogonal direction with regard to ablating pulse to generate harmonics. The diameter of focused driving femtosecond pulses was 64 μm. The energy (intensity) of driving pulses employed in this experiment was 0.5 mJ (4×10^{14} W cm^{-2}). The HHG experiments using TCP of LIP were carried out using the 0.2-mm thick β-barium borate (BBO) crystal, which was kept inside the vacuum chamber on the path of 800 nm pulses to generate a second harmonic (400 nm). The harmonic spectra were analyzed using an XUV spectrometer and collected by a CCD camera.

8.2.1. Comparison of harmonic emission from different plasmas containing gold nanoparticles

The low- and high-order nonlinear response of gold NPs prepared by the chemical method was analyzed in Ref. [27]. Particularly, the harmonics up to the 27th order (H27) were generated during the ablation of thin Au NP-containing films. The difficulties encountered during the application of these films were related to their small thickness (100 nm) leading to evaporation during a single shot, which required the constant movement of the destroyed film. In the discussed study, the commercially available Au NP powder, which can be attached to the surface of different materials (glass, paper) to form the NP multilayer sample with the rather large thickness (~1–2 mm), was used. The application of such samples allowed the maintenance of relatively stable harmonic emission for a

longer period of ablation. This amendment in handling the NP target, in turn, allowed better optimization of HHG and achieving the conditions for the generation of higher-order harmonics (up to H39). Additionally, HHG from the ablated bulk gold target was analyzed. These studies demonstrated the appearance of Au NPs in LIP at these conditions, which can also enhance the harmonic yield from such plasma.

HHG spectra were analyzed using the 1 s integration time of CCD. The employed repetition rates of ns, fs, and ps laser were 10, 200, and 200 Hz, respectively. Every single HHG spectrum was obtained from the fresh sample. The irradiation of the same spot of targets at a high pulse repetition rate caused the crater formation and degradation of plasma thus decreasing the stability of harmonic yield. Firstly, the stable harmonics generation was maintained by moving the position of the focal spot of heating radiation along the horizontal axis of the targets. The movement was accomplished manually and was restricted by the length of the targets (5 mm). At any movement of the plasma plume, it was positioned within the confocal parameter (8 mm) of the focused driving pulses. It was also possible to move the target along the vertical and horizontal axes using the computer-driven three-axis translating stage. However, the most advanced method was the application of the rotating target, which has earlier allowed stable harmonics generation at least for 10^6 shots corresponding to ~20 min of instant irradiation of the target by 1 kHz class laser [28]. The rotating speed in the range of 5–300 rpm did not influence the stability of harmonics. The application of the rotating target and the movement of the spot of the heating beam along the height of this target being dragged up and down would allow further improvement of the stability of harmonic yield.

Figure 8.6 shows the harmonics in the spectral range of 20–130 nm generated from the plasmas produced on the surface of different targets (Au bulk target, Au 100 nm nanoparticles, and Au 10 nm nanoparticles glued on paper). 5 ns, 1064 nm, 10 Hz, and 35 fs, 800 nm, 200 Hz laser pulses were used as the heating and driving pulses. These HHG spectra show the variations for different delays between the driving and heating pulses (from 100 to 7000 ns) at heating nanosecond and femtosecond pulse energies of 10 and 0.5 mJ, respectively. At smaller delays (<20 ns), the concentration of particles (neutral atoms, molecules, single charged ions, and NPs) was insufficient for HHG because the whole cloud of ablated particles possessing velocities of ~2 × 10^4 m s^{-1} cannot reach the spatial region of the driving beam, which propagated at the distance of 0.5 mm above the surfaces of the target. At larger delays (≥100 ns), the

concentration of the particles appearing on the path of the driving pulse became sufficient for the generation of harmonics.

The optimal delays allowing the generation of the maximal yield of harmonics were in the range of 150–400 ns for the ablated Au bulk, Au 100 nm NPs and Au 10 nm NPs on paper. At optimum delay, the harmonic range was extended up to H19 for Au bulk and Au 100 nm NPs, whereas it was H29 in the case of ablated Au 10 nm NPs on paper. An increase of the delay above the optimal values led to a gradual decrease in HHG efficiency. The harmonics were observed up to 600, 1000, and 7000 ns delays between the driving and heating pulses for the ablated Au bulk, Au 100 nm NPs, and Au 10 nm NPs on paper, respectively.
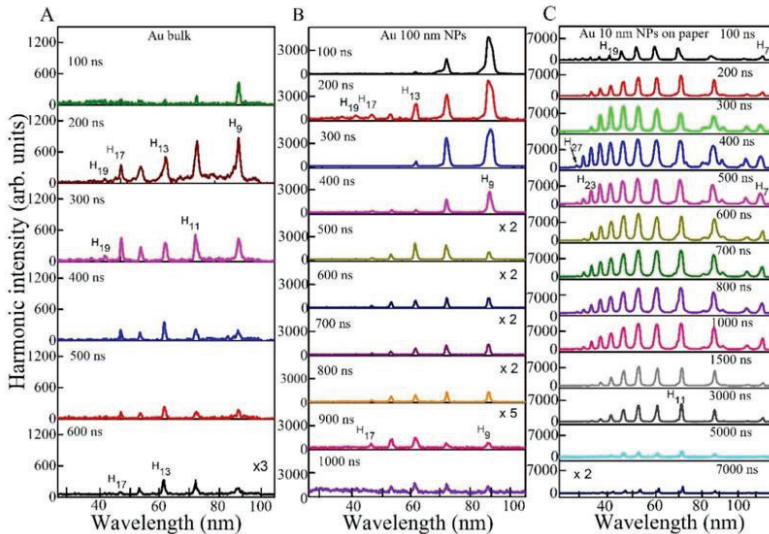
Fig. 8.6. Harmonics spectra from the Au plasmas produced on three targets at different delays between the heating and driving pulses. (A) Bulk Au, (B) Au 100 nm NPs, (C) Au 10 nm NPs glued on paper. Reproduced from [26] with permission from MDPI.

Figure 8.7 shows the comparative spectra of harmonics produced from the plasmas generated on the Au bulk, Au 100 nm NPs deposited on glass and Au 10 nm NPs on the paper at optimal delays between the heating and driving pulses. Some emission lines appeared in harmonic spectra and were attributed to the carbon present in the paper-containing target.

At 200 ns delay, the harmonic intensity obtained from ablated Au 10 nm NPs on paper was approximately three and 14 times stronger with regard to Au NPs on glass and Au bulk, respectively. However, at 500 ns delay, the harmonic yield from ablated Au 10 nm NPs on paper was further enhanced up to five and 40 times compared to Au 100 nm NPs on glass and bulk Au, respectively. No harmonic was observed in the case of heating of the pure glass surfaces at similar fluencies of heating pulses.

The weak harmonics appearing from paper plasma were attributed to the presence of the carbon atoms and ions in LPP. Previously, the presence of CI and CII in carbon-containing plasma led to efficient harmonics generation in such plasma formations [29-31]. The harmonics started from H11 and extended up to H29. Notice that the ablated Au 10 nm NPs on paper also demonstrated the harmonic range between H7 and H29, however, the intensities of H11, H13, H15, and H17 from the plasmas produced on the Au 10 nm NPs on paper were 40, three, four and five times stronger with regard to those from the ablated paper. The significant enhancement of HHG efficiency from Au NPs on paper is attributed to the influence of the surface plasmon resonance of Au NPs which causes stronger absorption of incident laser light resulting in a larger amount of Au during propagation of the driving pulses compared to other samples.
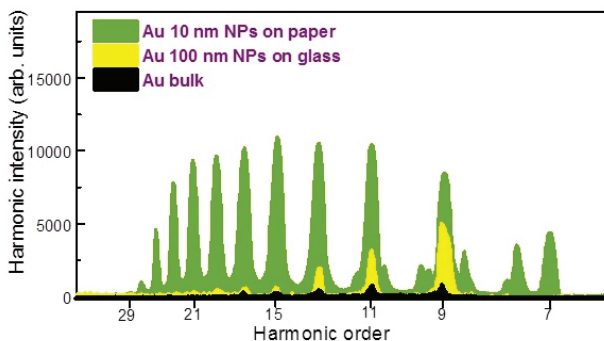
Fig. 8.7. Comparative harmonic spectra from ablated bulk Au (at 200 ns delay), Au 100 nm NPs (at 200 ns delay), and Au 10 nm NPs on paper (at 350 ns delay). Reproduced from [26] with permission from MDPI.

This finding is supported by the experimental measurements of the complex dielectric function of gold [32]. Localized surface plasmon resonance increases the local electrical field around the metal nanoparticle, which can in principle lead to effective decreasing of ionization potential. According to the three-step model of HHG, this decreased ionization

potential results in higher conversion efficiency for the low-order part of HHG plateau and at the same time causes the shortening of the cut off and plateau range. Additionally, local field enhancement is attributed to the collective motion of free electrons confined in narrowly localized regions, similar to that observed in colloidal nanoparticles exposed to an external electromagnetic field.

A method of HHG allowed exploiting the local field enhancement induced by plasmons within a metallic nanostructure consisting of bow-tie-shaped gold elements on a sapphire substrate [33,34]. HHG resulting from the illumination of plasmonic nanostructures with a short laser pulse of longer wavelength was also studied in [35]. It was demonstrated that both the confinement of electron motion and the inhomogeneous character of the laser electric field play an important role in the HHG process and lead to a significant increase in the harmonic cut off. Field enhancement of plasmon nanoparticles deposited on substrate leads to enhanced second and third harmonics generation, as well as higher-order harmonics, which was reported in several works [36-38].

In discussed case, the harmonic intensity obtained from ablated Au 10 nm NPs on paper was approximately three and 14 times stronger with regard to Au NPs on glass and Au bulk, respectively. The conversion efficiency of samples was estimated using the comparison with known results from other plasma. The conversion efficiency from previous measurements of harmonic generation in the plasmas produced on the surface of bulk Ag was reported to be 8×10^{-6} [39]. In the case of Au bulk plasma at similar conditions, the HHG conversion efficiency was almost ¼ with regard to ablated bulk silver. Hence the conversion efficiency of in Au plasma was estimated to be 2×10^{-6}. Therefore, the HHG conversion efficiency in the plasma produced on the Au NPs glued on paper was determined to be 3×10^{-5}.

8.2.2. Role of different parameters of driving and heating pulses on the HHG efficiency in Au NP containing plasmas

The sample's absorption and evaporation show insignificant wavelength dependences of employed 1064 nm (ns pulses) and 800 nm (ps and fs pulses) laser sources due to the closeness of their wavelengths. Meanwhile, pulse duration strongly influences the ablation and harmonic emission due to different time scales of interaction with samples.

The effect of heating pulse duration on HHG from ablated Au bulk target is presented in Figure 8.8a. Maximum harmonic intensity for ablated Au bulk target using ns heating pulses was observed at $E(\text{ns}) = 10$ mJ with

harmonics extended up to H21 (upper panel). Harmonic yield decreased at E(ns) > 10 mJ due to the growth of free electrons density and phase mismatch between interacting waves. In the case of ps and fs heating pulses (two bottom panels of Fig. 8.8a), harmonics extended up to H33. The intensities of harmonics in the case of heating ps and fs pulses were 5 and 4 times larger compared to the ns pulses induced ablation, while the driving pulse and heating pulse fluencies were smaller. This variation of HHG yield confirms the fact that heating pulse duration affects the harmonic yield and cut-off. Those studies confirm that LIP from bulk Au allows the generation of strong harmonics using short heating pulses. Laser ablation using ps and fs pulses allows the formation of relatively dense plasma, with regard to ns heating pulses while electron concentration was maintained at ~10% of the plasma concentration. To achieve a similar concentration of plasma with nanosecond heating pulse, one has to use stronger fluence, which causes the appearance of a notably larger number of free electrons. These electrons significantly suppress the conversion efficiency of harmonics [40].
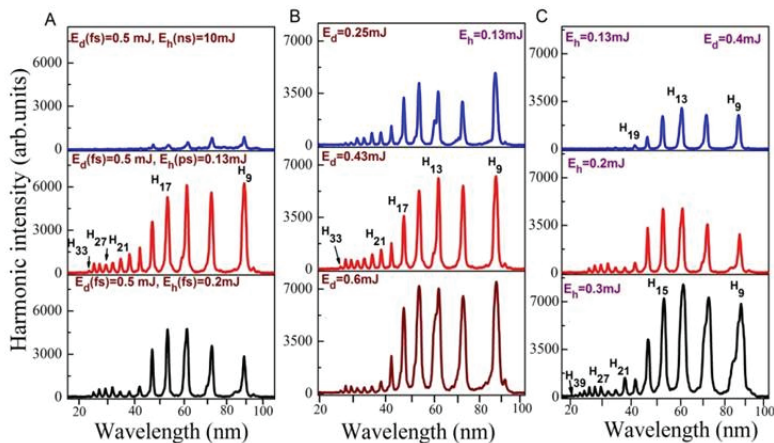

Fig. 8.8. Harmonics spectra from ablated bulk Au at (a) different energies of ns heating pulses, (b) different energies of fs driving pulses, and (c) different energies of ps heating pulses. Reproduced from [26] with permission from MDPI.

At similar fluence, (i) the concentration of free electrons is more in the laser plasma created by ns pulses with regard to fs and ps heating pulses,

and (ii) the density characteristics of plasma (i.e., the concentration of neutrals and single charged atoms) are high at fs and ps ablation with regard to the ablation using ns pulses. A high concentration of generated free electrons leads to self-defocusing and self-modulation of the driving laser pulses resulting in the phase mismatch between the driving and harmonic waves. Hence, the possibility of phase-mismatch using ns heating pulses is larger with regard to ps and fs heating pulses. Therefore, the efficient generation of the highest harmonics from the Au plasma produced by fs and ps heating pulse is attributed to better phase matching conditions between the driving pulses and harmonic waves compared with the ns-induced LPP.

Figures 8.8b and 8.8c show the variable harmonic intensities with respect to variation in the energies of heating and driving laser pulses. The harmonic intensity and harmonic range were increased with the growth in driving and heating pulse fluencies. These results illustrate that harmonics intensity and cut off produced from the plasma of Au bulk target strongly depend on the driving and heating pulse energies.

With the increase in heating pulse and driving pulse energies, the particle density and number of photons available for particle acceleration increase leading to the growth of harmonic yield and extension of harmonic cut off. The decrease in harmonic efficiency after crossing certain energy of heating pulses is due to the growth of free electrons density, which leads to the self-defocusing and self-modulation of fs pulse resulting in phase mismatch [41-43].

The diameter ($2w_0$) of the focused radiation was 64 μm. The corresponding Rayleigh length was $z_o = k(w_0)^2/2 = 4$ mm. Here, k is the wave number and w_0 is the beam waist radius. For the plasma length of 0.3 mm, the driving beam interacted with the plasma plume at the conditions of the plain wave propagation. The coherence length for mid-term harmonic ($q = 21$) (L_{coh}(mm) $\approx 1.4 \times 10^{18}(q \times N_e)^{-1}$ [44]) was equal to 2 mm at the concentration of free electrons $N_e = 3 \times 10^{16}$ cm^{-1} corresponding to 10% of plasma concentration (3×10^{17} cm^{-1}). At these conditions, no phase mismatch occurs, since the coherence length is larger than the size of the nonlinear medium. The over-excitation of the gold target causes the growth of free electrons concentration until the conditions when almost all particles became ionized. In that case, the coherence length decreases down to 0.2 mm, which caused the strong phase-mismatch between interacting waves inside the 0.3 mm long medium.

Figure 8.9a shows the harmonic spectra obtained from ablated Au bulk target using SCP of LIP and different heating laser pulse duration. The obtained harmonics were extended up to H33 in the case of the shortest

heating pulse duration. The harmonic cut-off was decreased in the case of TCP (H23, Fig. 8.9b) as compared to SCP (H31) due to the application of a shorter wavelength component of pumping radiation. The harmonic intensities obtained using TCP were two times stronger with regard to SCP (Fig. 8.9b), despite the small conversion efficiency of second-harmonic radiation in BBO (~2.5%) and a small ratio of 800 and 400 nm energies (1:40). It was suggested that TCP generates stronger harmonics because of the formation of the quasi-linear field, selection of a short quantum path component, which has a denser electron wave packet, and higher ionization rate compared with SCP [45]. TCP generated broader harmonics with regard to SCP due to self-modulation of the driving pulses in the plasma area (Fig. 8.9b). Figure 8.9c shows the harmonic spectra obtained from ablated Au bulk and Au 100 nm NPs using TCP geometry and ns heating pulses. One can see that ablated Au 100 nm NPs produced stronger harmonics as compared to ablated Au bulk target in the two-colour configuration as well.
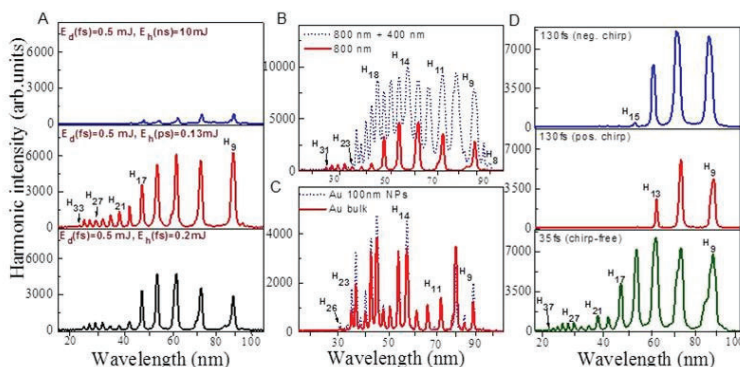
Fig. 8.9. Harmonics spectra from the plasma of bulk Au. (a) single-colour driving pulses (800 nm) and different pulse durations of heating pulses, (b) single- and two-colour (800 + 400 nm) driving pulses while using 0.2 mJ femtosecond heating pulses, (c) TCP of ablated bulk Au and Au 100 nm NPs, and (d) application of chirped laser pulses. Reproduced from [26] with permission from MDPI.

Figure 8.9d shows the effect of laser chirp on the generation efficiency of harmonics. The reduced harmonic cut off in the case of chirped laser pulses is attributed to the reduced intensity at a longer pulse duration. The harmonics were insignificantly red- and blue-shifted in the case of

positively and negatively chirped 130 fs laser pulses. The variation of the sign of laser chirp also affected the conversion efficiency of harmonics. The low-order harmonics (e.g., H9 and H11) were larger in the case of negatively chirped 130 fs pulses with regard to positively chirped pulses. The neutrals and ions present in plasma can be responsible for additional chirp-induced blue and red shifts. Particularly, self-phase modulation of laser pulses during propagation of the leading part of the laser pulse through the plasma containing neutral and ions might be the reason for the observed red-shift of harmonics. Previously, a similar scenario has been observed in Xe gas jet and LIP [46,47].
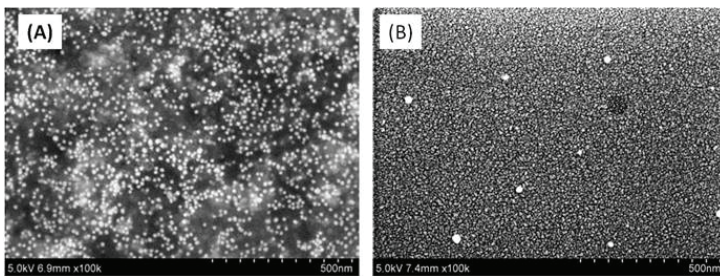
Fig. 8.10. SEM images of (a) deposited 10 nm NPs after ablation, and (b) deposited NPs synthesized during ablation of Au bulk target by 200 ps pulses. Reproduced from [26] with permission from MDPI.

SEM measurements of the deposited debris of 10 nm Au NPs (Fig. 8.10a) were carried out under laser ablation conditions corresponding to the optimal plasma formation for the highest yield of harmonics. The substrates (glass plates and silicon wafers) used to collect the deposited material were placed at a distance of 40 mm in front of the ablation area, and the debris was further analyzed by SEM. The mean size of deposited NPs (12 nm) was close to the NPs sizes measured prior to ablation (8–15 nm).

During ablation of a bulk target, under weak gold plasma formation conditions, the SEM images did not reveal the presence of nanoparticles in deposited debris with sizes above the microscope detection limit (3 nm). This was probably due to the small fluence (0.5 J cm^{-2}) of the heating 200 ps pulses on the target surface. Another pattern was observed upon ablation of the target using higher heating fluence (2 J cm^{-2}), which caused the appearance of small nanoparticles deposited onto a nearby substrate. At these conditions, the NPs appeared in the SEM images of the deposits,

with their mean size of ~5 nm, while some larger NPs of a mean size of about 20 nm and higher were also seen (Fig. 8.10b). One has to reiterate that these characteristics of debris were measured once obtaining them at the maximum HHG conversion efficiency. These morphological studies confirmed the presence of a large number of tiny NPs and a small amount of large NPs simultaneously deposited on the substrates under conditions of 'optimal' laser ablation. This observation points out the presence of synthesized NPs at the moment of femtosecond pulses propagation.

The concentration of these small NPs increased with the growth of heating pulse intensity. The production of nanoparticles by laser ablation of metallic targets is a well-studied phenomenon. However, the use of high ablation fluencies allowing the synthesis of a large amount of Au NPs resulted in the growth of free-electron concentration, which is a most detrimental factor in HHG due to the contribution to the phase mismatch between the driving and harmonic waves. This explains why, under ablation conditions leading to NP formation in the plume of bulk metallic targets, the HHG signals are weaker with regard to the ablation of already existing Au NPs on the target surface. In that case, the presence of NPs in the plasma does not compensate for the deteriorated phase mismatch conditions caused by over-ionization and the presence of a large number of electrons.

8.2.3. Analysis of NP morphology and HHG

The characterization of the gold nanoparticles being presented in LIP is an important component of morphology and HHG studies, though it is very difficult to properly determine some of those parameters. Below we address a few issues related to those experiments using Au NPs.

(1) Can the laser radiation destroy or modify Au NPs? Yes, it can. NPs can be disintegrated by the radiation of the heating pulses. The debris of deposited Au NPs was analyzed under the irradiation by ns, ps, and fs pulses. The mean size of NP debris was dominantly the same as of the initial NPs (10 and 100 nm), though the presence of the smaller-sized wing in the histogram of size distribution pointed out the appearance of disintegrated NPs. Their ratio was insignificant since Au NPs were ablated at the fluencies allowing evaporation of those particles without the notable modification of their structure. Stronger irradiation of targets led to the appearance of large aggregates and small NPs in the nearby substrates, alongside the decrease of HHG conversion efficiency attributed to a large concentration of free electrons.

(2) How much of them remained from pulse to pulse? As for the remained particles on the target surface, their concentration did not change, since only an insignificant part of NPs was ejected from the surface during a single shot. The problem of crater formation was resolved by moving the target surface either by dragging the sample up and down or by using the rotating targets or by both above methods.

(3) How many particles escaped into the plasma? To properly analyze and determine the amount of NPs ablated and appeared in the plasma area one has to carry out the accurate measurements of the weight of NP powder before and after ablation by a large number of pulses and then calculate how many particles escaped into the plasma during a single shot. Even this information is insufficient for the determination of the amount of NPs participating in HHG during the interaction with fs driving pulses since the plasma cloud had relatively large sizes (a few mm, in accordance with the observations of the emission of incoherent radiation of the plasma moving out from the surface) and an only small portion of them met the fs driving beam. How much NPs were inside the "tube" with the diameter ~64 μm (i.e., sizes of the focused driving beam) and length ~0.4 mm (diameter of spreading plasma at the distance of ~0.5 mm from the target surface) at the moment when the largest amount of them reaches the axis of propagation of the fs pulse remains unknown.

(4) What was their concentration? Here we can talk only about the averaged concentration of NPs in the plasma cloud at the moment of propagation of the driving fs pulses. Earlier, estimates and calculations using code HYADES of the density of ablated particles at the conditions suitable for efficient HHG were reported on the 2×10^{17} cm^{-3} concentrations of silver atoms and ions in the case of efficient HHG in Ag plasma [48]. The discussed studies were carried out at other experimental conditions (i.e., easier ablation and lower laser heating fluencies, formation of NP cloud, presence of different groups of NPs, etc.). It is also difficult to compare the concentrations of the homogeneous plasma containing separated atomic and ionic species and of the plasma containing ultrasmall "solid" species like NPs.

An explanation for intense harmonic generation from Au NPs could be the higher concentration of neutral atoms due to the presence of nanoparticles. Unlike single atoms and ions, whose density quickly decreases due to plasma expansion, the NPs retain densities that are close to their solid-state, while the distance between NPs in plasma jet is notably larger as compared with the distance between particles in atoms-containing LIPs. The concentration of atoms in solid species depends on its density and varies in the range of 10^{22}–10^{23} cm^{-3}. Combined with the

higher harmonic efficiency of neutral atoms compared with their ions, the neutral atoms within the NPs could generate high-order harmonics efficiently.

How many atoms in the nanoparticle become optimal for efficient generation of coherent extreme ultraviolet radiation using a whole ensemble of particles, which allow increasing the number of photons of high-order harmonics, remains a puzzle despite the fact that to date numerous experiments using the ablated NPs were conducted [49-51]. Qualitative assessments predict that the presence of the particles containing a few hundred to a few thousand atoms in the area of interaction with a strong laser field may lead to the maximal growth of generated harmonics. The comparative analysis of HHG spectra generated in the plasmas excited on the surfaces of pure paper and Au NPs-contained paper showed the advantages of ablated NPs-containing targets and the influence of these species on the enhancement of harmonic yield at the same conditions of the experiment.

8.3. Effects of laser-plasma formation on quasi-phase-matching of high-order harmonics from nanoparticles and atoms

Among different methods of harmonic enhancement, one can admit the formation of the quasi-phase-matching (QPM) conditions between the driving and generating waves during HHG [52-54]. This mechanism has been originally demonstrated in the visible range using solid materials [55]. Application of this concept in the case of the shorter-wavelength region requires the conditions when the absorption of generating harmonic waves becomes insignificant with regard to the enhancement of this radiation at the conditions when the transfer of energy from driving to harmonic waves occurs at similar phase velocities. QPM since then has been demonstrated in gaseous [56-59] and plasma [60,61] media. One of the approaches here is the division of an extended medium into groups of smaller media separated by a vacuum. In these parts of extended medium, the conditions of harmonics enhancement maintain along the whole length (so-called coherence length) of divided plasmas and gas media until the phase difference $\Delta\varphi$ between converting and converted waves becomes equal to π.

In the case of gas HHG, the conditions of separation of the extended medium onto the group of smaller-sized media were realized by the formation of a few gas jets separated from each other by a distance equal to the sizes of these jets. To form such jets, one has to drill the extended

tube containing gas in a few places along the direction of femtosecond beam propagation. The obstacle of this method is the limitation of QPM conditions for a group of harmonics at the used intensities of the driving pulse.

HHG in laser-induced allows the formation of variable conditions for QPM by using either extended perforated targets [62,63] or the application of multi-slit masks (MSM) placed in front of an ablating extended surface [64]. The manipulation of MSM geometry (i.e., sizes of slits, the distance between slits, number of slits, tilting of MSM, etc.) allows the formation of the plasma jets of different spatial and concentration characteristics. Most important among them is the variation of free electron concentration in each of the jets of this multi-jet plasma (MJP) structure. The tuning of free electron concentration can be performed by changing the fluence of heating radiation on the target surface, as well as by tuning the pulse duration of heating radiation in a broad range. Notice that previous plasma QPM studies were carried out using the picosecond pulses as the heating radiation for the formation of the optimal plasma configurations dominantly containing atoms and ions.

In the meantime, the application of heating laser pulses of different duration and nanoparticle-containing targets can drastically change the characteristics of LIP. These include the temperature of the plasma, ion and atom concentration, formation of clusters, quantum dots, NPs, and microparticles (MPs), excitation of plasma, electron concentration, etc. Particularly, the electron concentration significantly depends on the temporal characteristics of the ablating beam. Thus the studies of plasma QPM using the heating pulses of different duration in the case of nanoparticle-containing targets can clarify the ways for the creation of the "optimal plasma" allowing the most efficient enhancement of the groups of harmonics in different ranges of XUV by combining the concepts of QPM- and NPs-induced enhancement of HHG.

In this section, we discuss the studies of the formation of QPM in different plasma plumes produced by nanosecond (ns), picosecond (ps), and femtosecond (fs) pulses on the surfaces of materials allowing the formation of imperforated and perforated LIPs containing atoms, ions, NPs and MPs [65]. The optimization of QPM during HHG in such plasmas allowed the formation of the groups of harmonics with the enhancement factors exceeding 25×.

8.3.1. QPM scheme for HHG in LIP

The 30 fs, 800 nm, 1 kHz, and 200 ps, 800 nm, 1 kHz pulses were used as the femtosecond and picosecond heating radiation from Ti: Sapphire laser for plasma formation. Nd: YAG laser (5 ns, 1064 nm, 10 Hz) was synchronized with Ti: Sapphire laser and used as a source of nanosecond heating radiation. The insignificant difference in the wavelengths of ns (1064 nm) and ps/fs (800 nm) pulses does not cause different dynamics in the absorbance, heating, melting, and evaporation of used samples. The most important difference in the ablation is attributed to different timescales of the interaction of the heating pulses with the targets.

Both 30 fs and 200 ps pulses were generated from the same laser. 200 ps pulses were obtained by separation of the part of uncompressed radiation of this laser prior to entering the compressor stage. The delay between heating and driving pulses was adjusted by using the optical delay line for the latter pulses. The driving pulses were focused using a 400 mm focal length spherical lens in the plasma area, 0.3 mm above the target surface. The intensity of these pulses in the plasma area was 3×10^{14} W cm^{-2}.

An electronic delay between nanosecond and femtosecond pulses allowed applying sufficiently longer delays between two pulses compared with the optical delay technique. The delay between pulses was tuned using the delay generator. The synchronization of two laser sources, such as the most commonly used Ti: Sapphire and Nd: YAG lasers, may resolve, to some extent, the puzzle related to the enhancement of harmonics in the multi-atomic particles produced during ablation of the bulk materials or the targets initially containing these multi-atomic species. The main advantage of this approach is the control of the delay between the heating nanosecond pulses and the driving femtosecond pulses over a wide range between 0 and 10^5 ns, which assumes to be sufficient for analysis of the fast and slow components spreading out from the target in the laser-produced plasmas. The use of nanosecond Nd: YAG lasers as the sources of heating pulses may also offer some additional advantages compared with the commonly used picosecond pulses of the same repetition rate and wavelength as the driving sources. The application of nanosecond pulses to ablate the surface of targets allows the formation of less ionized and less excited plasma during a longer period of laser-matter interaction compared with picosecond pulses. This conclusion is based on the analysis of the nanosecond and picosecond ablation induced plasma emission in the visible and XUV ranges in the case of formation of the "optimal" plasmas leading to the generation of the highest harmonic yields. Notice that such plasmas formed by picosecond pulses have demonstrated stronger incoherent XUV emission. Additionally, Nd:

YAG lasers commonly operating at 10 Hz pulse repetition rate are more suitable for stable HHG in plasmas compared with the 1-kHz picosecond pulse ablation.

The heating pulses were focused using a 300-mm focal length cylindrical lens on the targets placed in the vacuum chamber to form the homogeneous extended plasmas (l = 5 mm, Fig. 8.11a). The spatial characterization of spreading plasma has shown that it moves out from the ablating surface as the cone with the diverging angle of 20^0. Thus the spatial characteristics of plasma at the distance of 0.3 mm from the target were almost the same as the sizes of heating radiation on the ablating surface (~0.3 mm).
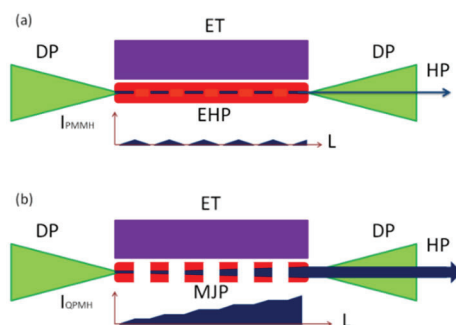

Fig. 8.11. Schemes for non-QPM and QPM during HHG in LIPs. (a) HHG in extended plasma. DP, driving femtosecond pulse; ET, extended target; EHP, extended homogeneous plasma; HP, harmonic pulse; I_{PMMH}, intensity of phase mismatched harmonic; L, length of plasma. (b) HHG in multi-jet plasma. MJP, multi-jet plasma. I_{QPMH}, intensity of the quasi-phase matched harmonic. Reproduced from [65] with permission from MDPI.

The intensity of heating pulses on the target surface was varied up to 6×10^{11} W cm^{-2} (in the case of fs pulses), 4×10^{9} W cm^{-2} (in the case of ps pulses), and $I = 1 \times 10^{9}$ W cm^{-2} (in the case of ns pulses). One can see a significant difference in the optimal intensities of heating pulses on the target surface exceeding two and a half orders of magnitude. Meanwhile, the difference in the optimal fluencies of these pulses (0.2, 0.8, and 5 J cm^{-2} in the cases of fs, ps, and ns pulses) was notably smaller compared with the difference in their intensities. Those experiments showed that the maintenance of the fluence of heating pulses in this range allows the formation of QPM conditions.

To produce MJP (Fig. 8.11b), MSM was installed between the cylindrical lens and the target. Three different MSMs were used to

produce variable plasma jets on the 5-mm long target. Most of the experiments were carried out using the MSM comprising 0.2-mm slits separated from each other at a distance of 0.2 mm. MSMs comprising 0.5-mm slits separated from each other at the distance of 0.5 mm and 0.8-mm slits separated from each other at the distance of 0.3 mm were also used. The 50 ns delay was introduced prior to propagation of the 30 fs, 800 nm driving pulses through MJP. The maximal intensity of driving pulses in the plasma area was 5×10^{14} W cm^{-2}. The generated harmonics were analyzed using an XUV spectrometer.

Boron NPs powder, silver MPs powder, and bulk silver sulphide were used as the targets. The samples were provided in the form of powders. The mean sizes of B NPs were 50 nm, with the range of size distribution between 30 and 90 nm. The mean sizes of Ag MPs were 70 µm, with the range of size distribution between 50 and 90 µm. The NPs and MPs had spherical shapes. The powdered MPs, NPs, and mixtures of MPs and NPs were pressed to form the tablets of 5-mm diameter using the electric hydraulic press machine.

Silver sulphide was also used as the target for ablation and QPM since this plasma provides the generation of harmonics of 800 nm lasers up to the fifty-fifth orders (H55, $\lambda\approx15$ nm). There are a few other species, such as silver, indium, and manganese, allowing the generation of harmonics in this spectral range. These targets have already been studied in previous plasma QPM studies. The generation of as many as possible harmonic orders is a crucial requirement for observation and tuning of the group of enhanced harmonics in the 50 – 90 eV range.

8.3.2. QPM in nanoparticles using femtosecond heating pulses

The first sample was the tablet containing boron nanoparticles and silver microparticles powders (B NPs + Ag MPs). Both boron and silver plasmas being ablated from bulk targets have shown harmonic generation greater than sixty orders. One could expect the enhancement of harmonic yield from the plasmas containing nanoparticles and microparticles of these elements to behave similarly to previous studies of nanoparticle-containing plasmas. The discussed studies confirmed that the conversion efficiencies of harmonics generated from these species were a few times larger than those from ablated bulk B and Ag. The reason for the application of the mixture of these two powders was to attempt to combine the attractive features of boron and silver emitters of harmonics; additionally, the formation of pressed tablets with suitable mechanical

properties allowing the maintenance of surface properties during ablation by pulses of different duration (5 ns, 200 ps, and 30 fs).

Initially, the harmonic generation was analyzed in the extended plasmas using pulses of different duration. The envelopes of harmonic spectra in each of those cases had plateau-like shapes demonstrating the gradual decrease of each next harmonic order. Among three heating pulse regimes, fs and ps pulses provided better harmonic conversion efficiencies, while ns pulses allowed the generation of weaker harmonics with the lower cut off. The example of the harmonic spectrum from extended 5-mm plasma produced by 200 ps pulses on the surface of the B NP + Ag MP tablet is shown in Fig. 8.12, while the shape of extended plasma on the target surface is presented in the inset to this figure.
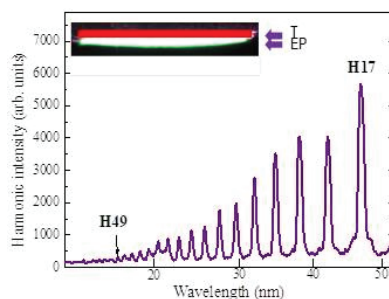

Fig. 8.12. Harmonic spectrum produced from extended B NP + Ag MP plasma. Inset: Image of extended plasma (EP) produced on the 5 mm long target (T) by focusing the 200 ps beam using cylindrical lens. Reproduced from [65] with permission from MDPI.

The spectrum of emitting radiation in the 15-50 nm range represented the set of harmonic orders, which were gradually decreased until the cut-off (H49). No significant enhancement of harmonics and cut off extension were obtained with the gradual growth of the length of LIP. The reason for this restriction in the growth of harmonic yield is as follows. At some point in the generating medium, the phase difference between the harmonic which arrived at that point, and the harmonic generated at that point reached π. Further increase of phase difference led to destructive interference of harmonics up to phase difference of 2π. The harmonic yield increases and decreases along the whole length of the medium with the periodicity equal to the so-called coherence length (L_{coh}). This pattern is illustrated in the $I_{PMMH}(L)$ curve (Fig. 8.11a). One can admit that, at these strongly phase mismatched conditions, an insignificant averaged

accumulation of harmonic yield can be expected. Correspondingly, no enhancement of harmonic yield can be expected at these conditions in spite of the extended length of the nonlinear optical medium.
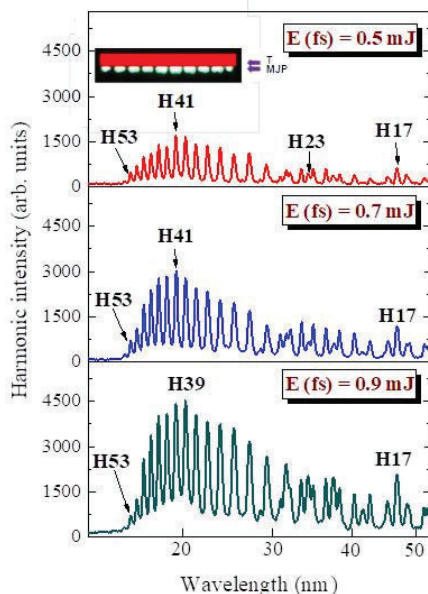
Fig. 8.13. Harmonic spectra from perforated B NP + Ag MP LIP obtained at different energies of driving femtosecond pulses (0.5 mJ: upper panel; 0.7 mJ: middle panel; 0.9 mJ: bottom panel). Maximally enhanced QPM harmonic (H41 or H39) was maintained at these conditions. Inset: shape of MJP produced on the target surface. Reproduced from [65] with permission from MDPI.

Then MSM was installed between the focusing cylindrical lens and target to produce the MJP containing ten 0.2-mm long jets separated from each other by 0.2 mm. The shape of this heterogeneous plasma formation is shown in the inset of Fig. 8.13. The plasma was formed using fs, ps, or ns heating pulses. The whole length of these MJPs was two times smaller than the length of extended imperforated plasma.

Initially, QPM conditions were analyzed in the case of MJP produced by fs pulses. Different energies of driving fs pulses (0.5, 0.7, or 0.9 mJ) were used. The 0.9 mJ heating fs pulses were used in each of these cases. The generated harmonics spectra at these three conditions of MJP formation are shown in Fig. 8.13.

One can see a drastic change of the envelope of the harmonic distribution obtained in the case of MJP (Fig. 8.13) with regard to the case of extended imperforated plasma (Fig. 8.12). Firstly, the harmonic yield in the longer-wavelength range was suppressed, while the shorter-wavelength harmonics became significantly enhanced. The enhanced harmonics were centred at around the thirty-ninth or forty-first orders (H39 or H41). These maximally enhanced harmonics (H_{qpm}) were almost the same in the case of three different energies of driving pulses since the concentration of the free carriers responsible for QPM for some specific harmonic order was equal for three regimes shown in Fig. 8.13 due to the same energy of heating fs pulses for three shown cases. The discussed experiments demonstrated that the role of free carriers appearing during propagation of driving femtosecond pulses through the plasma did not strongly influence the QPM conditions. The only difference in these three cases was the growth of the overall harmonic yield of QPM-enhanced harmonics and the broadening of the envelope of harmonic distribution centred at around H_{qpm}. Notice a similarity in the ratio between the enhanced harmonics in the shorter-wavelength range and the suppressed harmonics in the longer-wavelength range.

Thus, at the conditions when the maintenance of the heating pulse's energy does not significantly change the concentration of electrons, the maximal order of enhanced harmonics remained almost the same. Notice a significant decrease in the lower-order harmonics of these three spectra compared with the case shown in Fig. 8.12 when the harmonics were generated in the extended imperforated plasma. The additional lines in the longer wavelength parts of spectra correspond to the second and third orders of diffraction of the enhanced groups of harmonics, apart from a few of them, which were attributed to the notably decreased lower-order harmonics (H17 – H23).

QPM in LIP using spatial modulation of the medium is based on compensation of the phase mismatch $\Delta\varphi$ accumulated between the two fields with different frequencies (in HHG this is the driving field and its certain harmonics) when propagating in the dispersive medium. Commonly accepted understanding of optimal HHG QPM is that the multi-jet structure of plasma changes $\Delta\varphi$ from π at the exit from one jet to 2π at the beginning of another jet, so the separation between jets prohibits the destructive generation of harmonics with opposite directions of the electric field when $\pi < \Delta\varphi < 2\pi$. Notice that the transition from plasma jet to no-plasma interval is not as distinct as, for example, the boundary between the periodically poled crystal structures in classical QPM. The optical properties of no-plasma regions may also differ significantly from

properties of plasma jets, so we consider the possibility for HHG QPM to be sub-optimal, fulfilling a less strict condition. Namely, the change of the phase at the exit of the jet is not necessarily π, but the total phase change of a harmonic after passing one jet and one no-plasma region is $\cong 2\pi$, which one can call 2π QPM condition.

This 2π QPM condition is assumed to support the experimentally observed near-quadratic growth of HHG efficiency with the number of jets. The enhancement of harmonic yield, in that case, is illustrated in the $I_{QPMH}(L)$ curve shown in Fig 8.11(b). The yield of H_{qpm} gradually increases along the whole length of the perforated plasma thus achieving significant enhancement. Notice that in the case of a single jet, when other slits in MSM were shielded, the envelope of the harmonic spectrum was similar to the one shown in Fig. 8.12.

8.3.3. QPM in nanoparticles using picosecond and nanosecond

heating pulses

In the case of ps heating pulses, an even better pattern of QPM was observed for the narrower group of enhanced higher-order harmonics. Figure 8.14 shows the normalized spectra of the harmonics generated in B NP + Ag MP plasma. The upper panel corresponds to the extended imperforated plasma, and the two bottom panels correspond to the five 0.5-mm long lets and ten 0.2-mm long jets, respectively. The normalization of the intensity of the strongest harmonic to 1 allows the enhancement of the group of QPM harmonics to be clearly distinguished in different ranges of XUV with regard to the longer-wavelength region. The plateau-like harmonics in the case of 5-mm long plasma (upper panel) transform the group of enhanced harmonics at around H_{qpm} = H25 in the case of five 0.5mm long jets (middle panel). H_{qpm} then changed to H41 (i.e., similar to the case of ablation by fs pulses) once this MSM was replaced by the one containing 0.2mm slits (bottom panel).

The variation of H_{qpm} for different lengths of jets is attributed to the variation of L_{coh} of different harmonics. The larger H_{qpm} at the smaller length of the jet (l_{jet}) should satisfy the optimal phase-matched conditions at similar electron concentrations in the plasma plume. The relation between these parameters should follow the $H_{qpm} \times l_{jet} \infty \ const$ rule once a similar fluence of heating pulses irradiates the target. This rule stipulates the decisive role of plasma dispersion over other mechanisms leading to the variation of the difference between the phases of driving and harmonic waves. Notice that in the discussed case this relation does not exactly satisfy the observation of the maximally enhanced harmonics (H29 and

H41) for the two groups of plasma jets l_{jet} ratio of which was 0.5mm/0.2mm=2.5. Different impeding mechanisms and conditions of experiments, such as heterogeneity of plasma jets and their concentrations, role of clusters of different sizes on the dispersion of plasma, etc., can cause the deviation from the above relation.

Fig. 8.14. Normalized harmonic spectra from imperforated B NP + Ag MP LIP (upper panel), five 0.5 mm long jets (middle panel), and ten 0.2 mm long jets (bottom panel) obtained during ablation of target by 200 ps pulses. Reproduced from [65] with permission from MDPI.
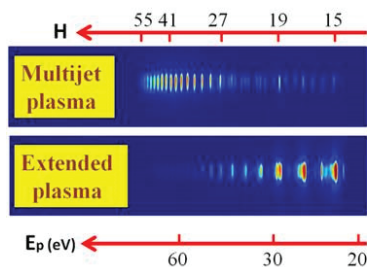
Fig. 8.15. Images of harmonic distribution along the XUV range in the case of silver sulphide plasma produced by ps pulses on the solid surface. Upper panel shows the case of 10-jet plasma obtained using the MSM comprising the 0.2 mm slits. Bottom panel shows the case of extended imperforated 5mm long plasma. H, harmonic orders; $E_p(eV)$, energy of photons. Reproduced from [65] with permission from MDPI.
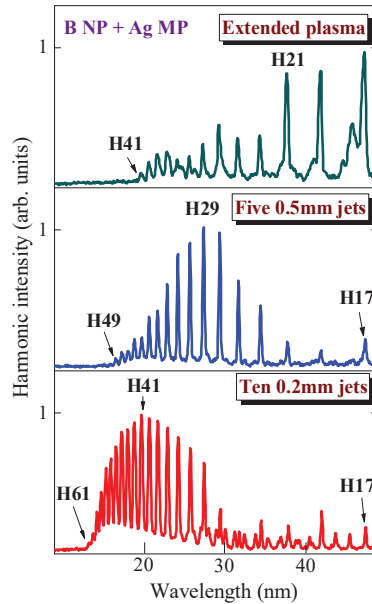

Fig. 8.16. Harmonic spectra from imperforated B NP + Ag MP LIP (upper panel), four 0.8 mm long jets (middle panel), and ten 0.2 mm long jets (bottom panel) obtained during ablation of target by 5 ns pulses. Dashed lines show the plasma emission. Reproduced from [65] with permission from MDPI.
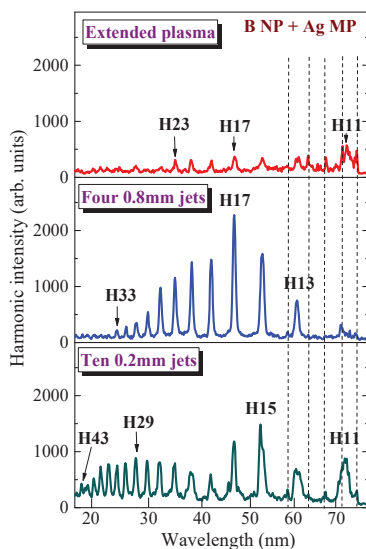
The comparison of the raw images of harmonics visually demonstrates the notable difference in the harmonic spectra produced in the imperforated and perforated plasmas. Figure 8.15 shows this comparison in the case of the plasma produced by picosecond pulses on the surface of silver sulphide in the cases of the absence (bottom panel) and presence (upper panel) of the MSM comprising the 0.2 mm slits. One can see a dramatic enhancement of higher orders and a significant suppression of the lower-order harmonics in the case of MJP with regard to extended plasma. Notice that higher harmonics (i.e., those above the 31st order) were barely seen in the case of extended plasma. The enhancement factor of H41 in the case of MJP was calculated to be 27×.

Quite another pattern appeared in the case of perforated plasma produced by ns pulses on the surface of the pressed tablet containing the mixture of Ag microparticle and B nanoparticle powders (Fig. 8.16). The HHG efficiency and harmonic cut-off significantly decreased in the case of extended imperforated plasma produced by 5 ns pulses (Fig. 8.16, upper panel) compared with the ps and fs cases. The perforation of plasma using the masks containing 0.2 and 0.8 mm slits caused the formation of QPM conditions at around H17 and H29 respectively (Fig. 8.16, middle and bottom panels). One can see a lesser difference between the envelopes of these harmonic spectra compared with the cases of ablation by fs and ps pulses. The enhancement factors of H_{qpm} (H17 and H29) in the case of these two MJP configurations produced by ns pulses were smaller compared with those achieved during ablation by shorter pulses.

8.3.4. Analysis of QPM in NPs at different conditions of plasma formation

The main goal of discussed studies was the demonstration of the conditions when NPs- and MPs-contained plasmas satisfy the formation of QPM for different groups of harmonics. The presence of atoms of the same consistency, which obviously existed in LIP due to, for example, partial disintegration of ablating NPs and MPs, is less influential with regard to much denser low-dimensional species. Previous studies revealed the fulfilment of the QPM concept in the case of the presence of atoms and ions in the plasma area. The discussed studies have demonstrated that the presence of molecular and low-dimensional species in plasma can also lead to the formation of the QPM conditions.

During those studies, no variations of heating pulse energy on the surface of NP/MP target leading to variations in particle concentration were analyzed, since this issue has been earlier reported in [66]. Some

indirect analysis of the influence of particle concentration on QPM was carried out by varying the fluence of heating pulses, either fs or ps and ns. However, it is almost impossible to maintain the consistency of similar plasma conditions in these three cases. Notice that particle concentration is not a crucial issue in the QPM concept. The most important component influencing the QPM conditions in LIPs is the concentration of electrons. To analyze this influence, one has to fix the concentration of harmonic emitters. Otherwise, it would be difficult to distinguish different processes affecting QPM in plasma.

The plasma at appropriate conditions of ablation of solid targets contains the nanoparticles aggregated from atoms. It has been confirmed during numerous studies of the debris deposited on a nearby surface. Meanwhile, the formation of these NPs strongly depends on the experimental conditions, such as the material of target, pulse duration, and fluence of heating radiation, etc. The analysis of the role of NPs and MPs in QPM becomes questionable once the bulk materials became ablated due to the instability of appearance of these low-dimensional structures in the area of driving pulse propagation. To resolve this problem, the targets, which have already contained the low-dimensional species, such as commercially available NPs and MPs, were prepared and then properly ablated those targets to form the LIPs containing these species. This concept allowed maintaining NPs and MPs in plasmas without their drastic disintegration. The presence of these species in LIP has been proven by SEM analysis of the debris of ablated material containing approximately the same species with almost similar sizes as the NPs and MPs attached to the target.

Below we address the difference in the harmonic enhancement observed in the discussed studies using variable conditions of plasma formation. Ablation by fs and ps pulses allowed the formation of relatively dense plasma ($>5\times10^{17}$ cm^{-3}), while electron concentration was maintained at ~10% of the plasma concentration. The influence of these free electrons on the phase mismatch between interacting waves can be compensated for by the formation of the multi-jet configuration of ablated material when the length of each plasma jet corresponded to L_{coh} of some higher-order harmonic and a few surrounding harmonic orders. These QPM conditions allowed the generation of the group of enhanced harmonics in the XUV region. Another situation occurs in the case of target ablation by ns pulses. To achieve a similar concentration of plasma one has to use stronger fluence, which causes the appearance of a notably larger amount of free electrons. These electrons significantly suppress the conversion efficiency of harmonics. At these conditions, the application of the QPM concept did

not allow harmonic enhancement similar to those attained during ablation of the target by shorter pulses.

The electron density in plasmas is one of the central issues in the QPM concept. Meanwhile, this method itself can provide valuable information using the relation between the electron concentration in plasma, maximally enhanced harmonic at QPM conditions, the wavelength of the driving field, and the sizes of a single plasma jet in MJP configuration. The previous study [67] has revealed that this method of determination of the electron concentration in the low-dense, low-ionized laser-produced plasma using the nonlinear optical process of HHG of ultrashort pulses at the conditions of QPM of driving and harmonic waves is quite reliable and can be compared with the calculations of this parameter using code HYADES.

In discussed case, the electron density of used LIPs can also be defined using the QPM relation. The coherence length (measured in millimetres) at the conditions of using the 800-nm driving laser could be presented as $L_{coh} \approx 1.4 \times 10^{18}/H_{qpm} \times N_e$. Here N_e is the electron density in the plasma jets measured in cm^{-3}. This simple formula allows defining the electron density by knowing the coherence length, which is equal to the length of the single jet at the conditions of QPM in MJP, and the maximally enhanced harmonic order. In discussed case, the electron density in silver sulphide plasma was calculated to be 1.7×10^{17} cm^{-3} in the case of 0.2-mm-long jets and at the maximally enhanced harmonics centred at around the 41st order (Fig. 8.15).

Additional diagnostics are required to define the consistency of LIPs. Though it is extremely difficult to provide the time-of-flight mass spectroscopy measurements alongside the operating HHG facility, some estimates have been reported during previous studies of carbon-contained clusters using ToFMS, which revealed their presence in plasma at the moment of propagation of the driving wave [68]. Another diagnostic confirming the presence of low-dimensional species in the plasmas is based on the analysis of the debris of deposited material on the nearby substrates. The observation of low-dimensional species using SEM of these substrates confirmed the presence of boron NPs and silver MPs in the plasmas.

References to Chapter 8

[1]   C. Hutchison, R. A. Ganeev, M. Castillejo, I. Lopez-Quintas, A. Zair, S. J. Weber, F. McGrath, Z. Abdelrahman, M. Oppermann, M Martín, D. Y. Lei, S. A. Maier, J. W. Tisch, J. P. Marangos, Comparison of high-order harmonic generation in uracil and thymine ablation plumes, Phys. Chem. Chem. Phys. 15 (29) (2013) 12308-12313.

[2]   R. A. Ganeev, M. Suzuki, S. Yoneya, H. Kuroda, Resonance-enhanced harmonic generation in nanoparticle-containing plasmas, J. Phys. B 48 (16) (2015) 165401.

[3]   R. A. Ganeev, M. Suzuki, H. Kuroda, High-order harmonic generation in Ag, Sn, fullerene, and graphene nanoparticle-containing plasmas using tuneable two-colour mid-infrared pulses, Eur. Phys. J. D 70 (2016) 21.

[4]   E. A. Rohlfing, Optical emission studies of atomic, molecular, and particulate carbon produced from a laser vaporization cluster source, J. Chem. Phys. 89 (10) (1988) 6103-6112.

[5]   G. Duffy, P. van Kampen, P. Dunne, 4d→5p transitions in the extreme ultraviolet photoabsorption spectra of Sn II and Sn III, J. Phys. B 34 (15) (2001) 3171.

[6]   H. Ruf, C. Handschin, R. Cireasa, N. Thiré, A. Ferré, S. Petit, D. Descamps, E. Mével, E. Constant, V. Blanchet, B. Fabre, Y. Mairesse, Inhomogeneous high harmonic generation in krypton clusters, Phys. Rev. Lett. 110 (8) (2013) 083902.

[7]   Y. Hamanaka, A. Nakamura, H. Hayashi, and S. Omi, Dispersion curves of complex third-order optical susceptibilities around the surface plasmon resonance in Ag nanocrystal–glass composites, J. Opt. Soc. Am. B 20 (6) (2003) 1227-1232.

[8]   R. A. Ganeev, M. Suzuki, M. Baba, M. Ichihara, H. Kuroda, High-order harmonic generation in Ag nanoparticle-contained plasma, J. Phys. B 41 (4) (2008) 045603.

[9]   R. A. Ganeev, L. B. Elouga Bom, T. Ozaki, Comparison of high-order harmonic generation from various cluster- and ion-contained laser plasmas, J. Phys. B 42 (5) (2009) 055402.

[10] P. Lan, E. J. Takahashi, K. Midorikawa, Optimization of infrared two-color multicycle field synthesis for intense-isolated-attosecond-pulse generation, Phys. Rev. A 82 (5) (2010) 053413.

[11] P. B. Corkum, Plasma perspective on strong field multi-ionisation Phys. Rev. Lett. 71 (13) (1993) 1994-1997.

[12] R. A. Ganeev, M. Suzuki, M. Baba, H. Kuroda, Analysis of the nonlinear self-interaction of femtosecond pulses during high-order harmonic generation in laser-produced plasma, J. Opt. Soc. Am. B 23 (7) (2006) 1332-1337.

[13] R. A. Ganeev, H. Singhal, P. A. Naik, I. A. Kulagin, P. V. Redkin, J. A. Chakera, M. Tayyab, R. A. Khan, P. D. Gupta, Enhancement of high-order harmonic generation using two-color pump in plasma plumes, Phys. Rev. A 80 (3) (2009) 033845.

[14] H. Singhal, R. A. Ganeev, P. A. Naik, J. A. Chakera, U. Chakravarty, H. S. Vora, A. K. Srivastava, C. Mukherjee, C. P. Navathe, S. K. Deb, P.D. Gupta, In-situ laser induced silver nanoparticle formation and high order harmonic generation, Phys. Rev. A 82 (4) (2010) 043821.

[15] V. Véniard, R. Taïeb, A. Maquet, Atomic clusters submitted to an intense short laser pulse: A density-functional approach, Phys. Rev. A 65 (1) (2001) 013202.

[16] G. Duffy, P. Dunne, The photoabsorption spectrum of an indium laser produced plasma, J. Phys. B 34 (6) (2001) L173-L178.

[17] H. Kjeldsen, F. Folkmann, B. Kristensen, J. B. West, J. E. Hansen, Absolute cross section for photoionization of Mn+ in the 3p region, J. Phys. B 37 (6) (2004) 1321-1330.

[18] G. Lambert, J. Gautier, C. P. Hauri, P. Zeitoun, C. Valentin, T. Marchenko, F. Tissandier, J. P. Goddet, M. Ribiere, G. Rey, M. Fajardo, S. Sebban, An optimized kHz two-colour high harmonic source for seeding free-electron lasers and plasma-based soft X-ray lasers, New J. Phys. 11 (8) (2009) 083033.

[19] R. A. Ganeev, M. Suzuki, H. Kuroda, Advanced properties of extended plasmas for efficient high-order harmonic generation, Phys. Plasmas 21 (5) (2014) 053503.

[20] R. A. Ganeev, M. Suzuki, H. Kuroda, Quasi-phase-matching of high-order harmonics in multiple plasma jets, Phys. Rev. A 89 (3) (2014) 033821.

[21] R. A. Ganeev, M. Baba, M. Suzuki, S. Yoneya, H. Kuroda, Low- and high-order harmonic generation in the extended plasmas produced by laser ablation of zinc and manganese targets, J. Appl. Phys. 116 (24) (2014) 243102.

[22] R. A. Ganeev, L. B. Elouga Bom, J. Abdul-Hadi, M. C. H. Wong, J. P. Brichta, V. R. Bhardwaj, T. Ozaki, High-order harmonic generation from fullerene using the plasma harmonic method, Phys. Rev. Lett. 102 (1) (2009) 013903.

[23] E. Takahashi, P. Lan, O. D. Mücke, Y. Nabekawa, K. Midorikawa, Infrared two-color multicycle laser field synthesis for generating an intense attosecond pulse, Phys. Rev. Lett. 104 (23) (2010) 233901.

[24] E. Takahashi, P. Lan, O. D. Mücke, Y. Nabekawa, K. Midorikawa, Attosecond nonlinear optics using gigawatt-scale isolated attosecond pulses, Nat. Commun. 4 (2013) 2691.

[25] P. Lan, E. Takahashi, K. Midorikawa, Wavelength scaling of efficient high-order harmonic generation by two-color infrared laser fields, Phys. Rev. A 81 (6) (2010) 061802.

[26] M. Venkatesh, R. A. Ganeev, D. S. Ivanov, G. S. Boltaev, V. V. Kim, L. Jingguang, I. N. Zavestovskaya, M. E. Garcia, C. Guo, High-order harmonics generation in Au nanoparticles-contained plasma, Nanomater. 10 (2020) 234.

[27] A. Rout, G. S. Boltaev, R. A. Ganeev, Y. Fu, S. K. Maurya, V. V. Kim, K. S. Rao, C. Guo, Nonlinear optical studies of gold nanoparticle films, Nanomater. 9 (2019) 291.

[28] C. Hutchison, R. A. Ganeev, T. Witting, F. Frank, W. A. Okell, J. W. G. Tisch, J. P. Marangos, Stable generation of high-order harmonics of femtosecond laser radiation from laser produced plasma plumes at 1 kHz pulse repetition rate, Opt. Lett. 37 (11) (2012) 2064-2066.

[29] L. B. E. Bom, Y. Pertot, V. R. Bhardwaj, T. Ozaki, Multi-µJ coherent extreme ultraviolet source generated from carbon using the plasma harmonic method, Opt. Express 19 (4) (2011) 3077-3085.

[30] R. A. Ganeev, P. A. Naik, H. Singhal, J. A. Chakera, M. Kumar, U. Chakravarty, P. D. Gupta, Use of carbon containing materials for efficient high order harmonic generation with femtosecond pulses, Opt. Commun. 285 (2012) 2934-2941.

[31] R. A. Ganeev, C. Hutchison, T. Witting, F. Frank, W. A. Okell, A. Zaïr, S. Weber, P. V. Redkin, D. Y. Lei, T. Roschuk, T.; S. A. Maier, I. López-Quintás, M. Martín, M. Castillejo, J. W. G. Tisch, J. P. Marangos, High-order harmonic generation in graphite plasma plumes using ultrashort laser pulses: a systematic analysis of harmonic radiation and plasma conditions, J. Phys. B 45 (16) (2012) 165402.

[32] R. L. Olmon, B. Slovick, T. W. Johnson, D. Shelton, S.-H. Oh, G. D. Boreman, M. B. Raschke, Optical dielectric function of gold, Phys. Rev. B 86 (23) (2012) 235147.

[33] S. Kim, J. Jin, Y.-J. Kim, I.-Y. Park, Y. Kim, S.-W. Kim, High-harmonic generation by resonant plasmon field enhancement, Nature 453 (2008) 757.

[34] I.-Y. Park, S. Kim, J. Choi, D. H. Lee, Y.-J. Kim, M. F. Kling, M. I. Stockman, S.-W. Kim, Plasmonic generation of ultrashort extreme-ultraviolet light pulses, Nature Phot. 5 (2011) 677-681.

[35] M. F. Ciappina, S. S. Aćimović, T. Shaaran, J. Biegert, R. Quidant, M. Lewenstein, Enhancement of high harmonic generation by confining electron motion in plasmonic nanostructures, Opt. Express 20 (2012) 26261-26271.

[36] K. Chen, C. Durak, J. R. Heflin, H. D. Robinson, Plasmon-enhanced second-harmonic generation from ionic self-assembled multilayer films, Nano Lett. 7 (2007) 254-258.

[37] Z. Dong, M. Asbahi, J. Lin, D. Zhu, Y. M. Wang, K. Hippalgaonkar, H.-S. Chu, W. P. Goh, F. Wang, F. Z. Huang, Second-harmonic generation from sub-5 nm gaps by directed self-assembly of nanoparticles onto template-stripped gold substrates, Nano Lett. 15 (2015) 5976-5981.

[38] R. A. Ganeev, Controlling single harmonic enhancement in laser produced plasmas, J. Appl. Phys. 121 (13) (2017) 133108.

[39] R. A. Ganeev, M. Baba, M. Suzuki, H. Kuroda, High-order harmonic generation from silver plasma, Phys. Lett. A 339 (1-2) (2005) 103-109.

[40] R. A. Ganeev, G. S. Boltaev, S. Y. Stremoukhov, V. V. Kim, A. V. Andreev, A. S. Alnaser, High-order harmonic generation during different overlaps of two-colored pulses in laser-produced plasmas, High-order harmonic generation during different overlaps of two-colored pulses in laser-produced plasmas, Eur. Phys. J. D 74 (2020) 199.

[41] R. A. Ganeev, Harmonic generation from partially ionized plasma, J. Opt. Soc. Am. B 31 (9) (2014) 2221-2231.

[42] C.-J. Lai, F. X. Kärtner, The influence of plasma defocusing in high harmonic generation, Opt. Express 19 (23) (2011) 22377-22387.

[43] R. A. Ganeev, On- and off-axis studies of the quasi-phase-matching-enhanced harmonics generated in the multi-jet laser-produced plasmas, J. Phys. B 49 (9) (2016) 095402.

[44] C. Kan, N. H. Burnett, C. E. Capjack, R. Rankin, Coherent XUV generation from gases ionized by several cycle optical pulses, Phys. Rev. Lett. 79 (16) (1997) 2971-2974.

[45] I.J. Kim, G. H. Lee, S. B. Park, Y. S. Lee, T. K. Kim, C. H. Nam, T. Mocek, K. Jakubczak, Generation of submicrojoule high harmonics using a long gas jet in a two-color laser field, Appl. Phys. Lett. 92 (2) (2008) 021125.

[46] F. Brandi, F. Giammanco, W. Ubachs, Spectral redshift in harmonic generation from plasma dynamics in the laser focus, Phys. Rev. Lett. 96 (12) (2006) 123904.

[47] R. A. Ganeev, L. B. E. Bom, J.-C. Kieffer, T. Ozaki, Systematic investigation of resonance-induced single harmonic enhancement in the extreme ultraviolet range, Phys. Rev. A 75 (6) (2007) 063806.

[48] L. B. E. Bom, J.-C. Kieffer, R. A. Ganeev, M. Suzuki, H. Kuroda, T. Ozaki, Influence of the main pulse and prepulse intensity on high-order harmonic generation in silver plasma ablation, Phys. Rev. A 75 (3) (2007) 033804.

[49] R. A. Ganeev, C. Hutchison, M. Castillejo, I. Lopez-Quintas, F. McGrath, D. Y. Lei, J. P. Marangos, Ablation of nanoparticles and efficient harmonic generation using 1 kHz laser, Phys. Rev. A 88 (3) (2013) 033803.

[50] M. Wöstmann, P. V. Redkin, J. Zheng, H. Witte, R. A. Ganeev, H. Zacharias, High-order harmonic generation in plasmas from nanoparticle and mixed metal targets at 1-kHz repetition rate, Appl. Phys. B 120 (1) (2015) 17-24.

[51] R. A. Ganeev, G. S. Boltaev, K. Zhang, P. V. Redkin, S. K. Maurya, M. Venkatesh, Z. Yu, V. V. Kim, C. Guo, Role of carbon clusters in high-order harmonic generation in graphite plasmas, OSA Continuum 2 (5) (2019) 1510-1523.

[52] A. Paul, R. A. Bartels, R. Tobey, H. Green, S. Weiman, I. P. Christov, M.M. Murnane, H. C. Kapteyn, S. Backus, Quasi-phase-matched generation of coherent extreme-ultraviolet light, Nature 421 (6918) (2003) 51-54.

[53] X. Zhang, A. L. Lytle, T. Popmintchev, X. Zhou, H. C. Kaptayn, M. M. Murnane, O. Cohen, Quasi phase matching and quantum path control of high harmonic generation using counterpropagating light, Nature Phys. 3 (4) (2007) 270-285.

[54] A. Bahabad, M. M. Murnane, H. C. Kapteyn, Quasi-phase-matching of momentum and energy in nonlinear optical processes, Nature Phys. 4 (8) (2010) 570.

[55] M. M. Fejer, G. A. Magel, D. H. Jundt, R. L. Byer, Quasi-phase-matched second harmonic generation: tuning and tolerances, IEEE J. Quantum Electron. 28 (11) (1992) 2631-2654.

[56] J. Seres, V. S. Yakovlev, E. Seres, C. H. Streli, P. Wobrauschek, C. H. Spielmann, F. Krausz, Coherent superposition of laser-driven soft-X-ray harmonics from successive sources, Nature Phys. 3 (12) (2007) 878.

[57] A. Pirri, C. Corsi, M. Bellini, Enhancing the yield of high-order harmonics with an array of gas jets, Phys. Rev. A 78 (1) (2008) 011801.

[58] V. Tosa, V. S. Yakovlev, F. Krausz, Generation of tunable isolated attosecond pulses in multi-jet systems, New J. Phys. 10 (2) (2008) 025016.

[59] T. Fok, Ł. Węgrzyński, M. Kozlova, J. Nejdl, P. W. Wachulak, R. Jarocki, A. Bartnik, H. Fiedorovicz, High-order harmonic generation using a multi-jet gas puff target, Photonics Lett. Poland 6 (1) (2014) 14.

[60] R. A. Ganeev, G. S. Boltaev, V. V. Kim, M. Venkatesh, A. I. Zvyagin, M. S. Smirnov, O. V. Ovchinnikov, M. Wöstmann, H. Zacharias, C. Guo, "High-order harmonic generation using quasi-phase matching and two-color pump of the plasmas containing molecular and alloyed metal sulfide quantum dots," J. Appl. Phys. 126 (19) (2019) 193103.

[61] M. Wöstmann, L. Splitthoff, H. Zacharias, Control of quasi-phase-matching of high-harmonics in a spatially structured plasma, Opt. Express 26 (11) (2018) 14524.

[62] R. A. Ganeev, M. Suzuki, H. Kuroda, High-order harmonic enhancement using the quasi-phase-matching in laser plasma, High-order harmonic enhancement using the quasi-phase-matching in laser plasma, JETP Lett. 99 (7) (2014) 368-372.

[63] R. A. Ganeev, M. Suzuki, S. Yoneya, H. Kuroda, Quasi-phase-matching induced enhancement of the groups of high-order harmonics generating in various multi-jet plasmas produced using perforated targets and modulated heating pulses, Laser Phys. 24 (11) (2014) 115405.

[64] R. A. Ganeev, V. Tosa, K. Kovács, M. Suzuki, S. Yoneya, H. Kuroda, Influence of ablated and tunneled electrons on the quasi-phase-matched high-order harmonic generation in laser-produced plasma, Phys. Rev. A 91 (4) (2015) 043823.

[65] R. A. Ganeev, G. S. Boltaev, V. V. Kim, C. Guo, Effects of laser plasma formation on quasi-phase matching of high-order harmonics from nanoparticles and atoms, Nanomater. 9 (2019) 572.

[66] R. A. Ganeev, A. Husakou, M. Suzuki, H. Kuroda, Application of mid-infrared pulses for quasi-phase-matching of high-order harmonics in silver plasma, Opt. Express 24 (4) (2016) 3414-3420.

[67] R. A. Ganeev, M. Suzuki, S. Yoneya, H. Kuroda, Electron density measurements using high-order harmonic generation in laser-produced plasmas, Appl. Phys. B 121 (3) (2015) 307-313.

[68] I. Lopez-Quintas, M. Oujja, M. Sanz, A. Benitez-Cañete, C. Hutchison, R. de Nalda, M. Martin, R. A. Ganeev, J. P. Marangos, M. Castillejo, Characterization of laser-induced plasmas of nucleobases: Uracil and thymine, Appl. Surf. Sci.302 (2014) 299-302.

CHAPTER 9

HIGH-ORDER HARMONICS GENERATION IN CLUSTERS AND QUANTUM DOTS

In this chapter, we analyze a scheme of nanosecond pulse heating and femtosecond laser pulse driving for high-order harmonics generation (HHG). The main advantage of this approach is that one can control the delay between the heating nanosecond pulses and the driving femtosecond pulses over a wide range. The application of nanosecond pulses to ablate the surface of targets allows the formation of less ionized and excited plasma during a longer period of laser-matter interaction compared with picosecond pulses. This approach is important in the case of the ablation of the small-sized species for HHG.

The coexistence of reverse saturable absorption and two-photon absorption in silver sulphide suggests that Ag_2S quantum dots (QDs) could be a very promising nonlinear medium for photonic devices in different time scales if these semiconductor nanocrystallites are incorporated into appropriate media while retaining the attractive features of both components. The Ag_2S QDs also demonstrate low-threshold optical limiting in the visible and near-IR ranges. A search for new applications of QDs is an important task for the optical community. The interesting idea is to find the optimal conditions in the application of such QDs as effective emitters of the high-order harmonics of femtosecond pulses for the development of efficient sources of coherent extreme ultraviolet (XUV) radiation. We discuss the harmonics generation in QDs using electronically driven delays between the heating and driving lasers.

Different aspects of the application of low-dimensional aggregates for efficient HHG in plasma media have yet to be analyzed. These unexplored concepts include (a) the application of two driving waves with different polarizations for the harmonic generation, (b) a modulation of the spatial shape of the aggregate-containing media to apply the quasi-phase-matching concept for harmonic enhancement in different ranges of the extreme ultraviolet, (c) a modification of the structure of aggregates for determining the role of morphology properties on the frequency conversion of infrared

pulses in such structures, etc. In this connection, the laser-produced plasmas provide a wider range of options than the gaseous media for variation of the properties of aggregates-containing media. We analyze HHG from laser-produced plasmas containing QDs of metal sulphides using different approaches, including a two-colour pump, application of single and alloyed QDs, and quasi-phase-matching of interacting waves. This approach allows determining the optimal methods for further enhancing HHG efficiency and analyzing the properties of harmonic emitters.

9.1. Role of carbon clusters in high-order harmonic generation in graphite plasmas

The earlier reported studies of HHG from gases and during ablation of cluster and nanoparticle targets have revealed the advantages of using such species for frequency conversion in the XUV range. Larger cross-section of recombination, the possibility of recombination of the accelerated electron with parent multi-particle through either recombination with the same atom or neighbouring atom, or the multi-particle as a whole were considered as the most probable reasons in enhancing high-order harmonic yield from such clustered plasmas. However, there has been no study in optimizing the delay between heating and driving pulses in the microsecond timescale assuming the hypothesis of the slower velocities for larger-sized species. Notice that, even without this optimization, the harmonic yields from ablated multi-particle targets are higher than from ablation of bulk targets of the same material leading to the formation of single atomic/ionic plasmas. Here the meaning of multi-particle target refers to the one containing the clusters, quantum dots, or nanoparticles glued on the surface of different substrates.

The most probable reason for harmonic enhancement was attributed to the appearance of small clusters in the area of femtosecond pulse propagation at relatively small optical delays. Their appearance in that area was assumed once estimating their velocities and delays between the beginning of ablation and propagation of femtosecond pulse at the fixed distance above the target surface. Particularly, for most HHG experiments, these distances were maintained at ~0.2 mm, while the delay for each target was chosen to be 20 to 80 ns depending on the atomic weight of the elements comprising different targets. Particularly, the maximal harmonic yield from ablated graphite has earlier been achieved at ~30 ns, which allows calculating the velocity of atoms and ions spreading out from the target ($\sim 6 \times 10^3$ m s^{-1}). At the same time, ablation of the fullerenes

comprising 60 atoms of carbon led to a similar "optimal delay" at which maximal yield of harmonics was achieved. Correspondingly, one could assume the similarity in the velocities of carbon single atoms and C_{60} at the conditions of ablation using picosecond heating pulses. A similar feature has also been observed in the case of carbon nanotubes.

Another important concept allowing the enhancement of harmonic yield is the application of the two-colour pump (TCP) of generating medium when two fields simultaneously participate in the HHG process. This concept has earlier been demonstrated in the case of gases and ablated bulk materials. Earlier studies of HHG in gases have anticipated that stronger harmonics generation in the case of TCP was possible due to the formation of a quasi-linear field, selection of the short quantum path component, which has a denser electron wave packet, and higher ionization rate compared with single-color pump (SCP) [1]. The orthogonally polarized second field can also be responsible for the modification of the trajectory of an accelerated electron from being two-dimensional to three-dimensional which may lead to the removal of the medium symmetry. With suitable control of the relative phase between the fundamental and second harmonic radiation, the latter field enhances the short path contribution, resulting in a clean spectrum of harmonics. One can expect that TCP of clusters can further enhance the harmonic yield even at small ratios of second and first waves' intensities provided the sufficient overlap of these two fields in the medium under consideration.

In this section, we further discuss a scheme of nanosecond pulse heating and femtosecond laser pulse driving for HHG [2]. The synchronization of two laser sources, such as the most commonly used Ti: sapphire and Nd:YAG lasers, may resolve, to some extent, the puzzle related to the enhancement of harmonics in the multi-atomic species produced during ablation of the bulk materials or the targets initially contained multi-atomic components. The main advantage of this approach is that one can control the delay between the heating nanosecond pulses and the driving femtosecond pulses over a wide range between 0 and 10^5 ns, which assumes to be sufficient for analysis of the fast and slow components spreading in the laser-produced plasmas. The use of nanosecond Nd:YAG lasers as the sources of the heating pulse may also offer some additional advantages compared with the commonly used picosecond pulses of the same pulse repetition rate and wavelength as the driving sources. The application of nanosecond pulses to ablate the surface of targets under consideration may allow the formation of less ionized and excited plasma during a longer period of laser-matter interaction compared with picosecond pulses. This conclusion is based on the analysis of the

nanosecond and picosecond ablation induced plasma emission in the visible and XUV ranges in the case of formation of the "optimal" plasmas leading to the generation of the highest harmonic yields. Notice that such plasmas formed by picosecond pulses have demonstrated stronger incoherent XUV emission. Additionally, Nd:YAG lasers commonly operating at 10 Hz pulse repetition rate are more suitable for stable HHG in plasmas compared with 1-kHz picosecond pulse ablation, though in the latter case some tricks such as target rotation can partially mitigate the stability of 1-kHz coherent short-wavelength sources.

The first attempts in frequency conversion at such conditions were reported in the case of the studies of the lowest-order harmonic generation from the ablated carbon-containing materials [3]. The third harmonic (TH) in the laser plasmas produced on the surfaces of different materials was analyzed using the delays ranging between a few tens nanosecond to a few hundred microseconds between a 7-ns heating pulse and a 17-ns driving pulse, both of 1064 nm in wavelength. The observation of TH emission, though extremely weak, at the microsecond timescale of delays allowed concluding that the process of third-harmonic generation (THG) occurs not only from atoms and ions of carbon materials at small delays but also from their aggregates at large delays.

This approach is extremely useful for the analysis of multi-atomic systems as the media for HHG. In this section, we discuss the HHG in graphite plasma using a broad range of delays between a 5-ns heating pulse and a 40-fs driving pulse. We analyze the advantages of using nanosecond pulses for plasma formation to achieve the efficient HHG compared with picosecond pulses induced ablation. The TCP concept of laser-clusters interaction demonstrates the advantages in the generation of odd and even harmonics. This approach allows determining the optimal delay between the heating and driving pulses for both atoms and multi-particle aggregates and to generate harmonics from those species. The discussed studies show that small carbon clusters arrive at the area of interaction with femtosecond beam notably earlier than one can expect assuming the kinetic consideration when the components are assumed to reach thermodynamic equilibrium during the expansion. Those observations allow concluding that all carbon clusters acquire from the very beginning similar kinetic energy and spread out of the surface with the velocity approximately similar to the one that possesses a single carbon atom ablating from the bulk material.

9.1.1. Experimental

Here we discuss two groups of experiments, which were carried out to analyze the role of carbon clusters in harmonic generation by studying the influence of delay between heating and driving pulses on the frequency conversion of the latter pulses. Initially, we analyze TH yield from graphite plasma, and then we discuss the generation of high-order harmonics depending on the delay, fluence of heating pulse, driving pulse energy, SCP, and TCP of laser-produced plasma.
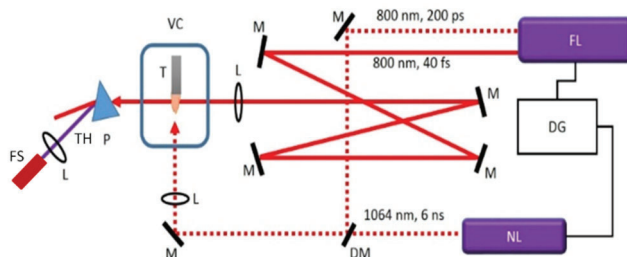

Fig. 9.1. Third harmonic generation arrangement. FL, femtosecond laser; NL, nanosecond laser; DG, digital generator; M, mirrors; DM, dichroic mirror; L, lenses; VC, vacuum chamber; T, target; P, prism; TH, third harmonic emission; FS, fiber spectrometer. Reproduced from [2] with permission from the Optical Society of America.

In the case of THG studies the laser radiation (λ=800 nm, τ=40 fs, 1 kHz) was focused by a 400 mm focal length lens at a distance of 0.6 mm above the target surface on the plasma produced by ablation in the vacuum chamber of bulk graphite using picosecond (1 kHz, 800 nm, 0.5 mJ, 200 ps) or nanosecond (10 Hz, 1064 nm, 5 mJ, 5 ns) pulses (Fig. 9.1). The beam waist diameter of the focused femtosecond radiation was 76 μm. The spectral characteristics of TH radiation (λ=266 nm) were analyzed by a spectrometer. To create a plasma plume using picosecond pulses, a pulse was split from the Ti: sapphire laser by a beam splitter before the compression of the fundamental uncompressed pulse. This radiation was focused on the target to heat it and to produce plasma either in vacuum or air conditions. The diameter of the ablation zone was adjusted to be approximately 0.25 mm. An optical delay between heating (picosecond) and driving (femtosecond) pulses was varied between 5 and 60 ns, while an electronic delay between nanosecond and femtosecond pulses allowed

to apply sufficiently longer delays between the two pulses (i.e. up to 10^5 ns).

The graphite plasma was also used for HHG (Fig. 9.2). The femtosecond pulse propagated through the plasma 30 ns from the beginning of target irradiation by 200 ps or 5 ns heating pulses. This delay between heating and pump pulses was proven to be optimal for HHG in graphite plasma at the used geometry of experiments when the 800 nm driving femtosecond pulses were focused onto the plasma from the orthogonal direction, at a distance of 0.2 mm above the target surface, contrary to the TH studies when this distance was maintained at 0.6 mm.
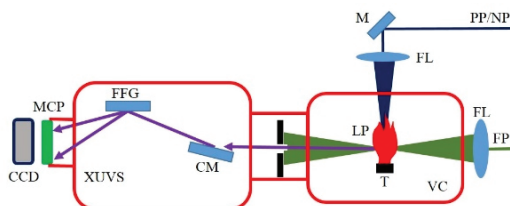

Fig. 9.2. Setup for high-order harmonic generation. FP, converting femtosecond pulses, PP/NP, picosecond or nanosecond heating pulses; FL, focusing lenses; VC, vacuum chamber; T, target; LP, laser plasma; XUVS, extreme ultraviolet spectrometer; CM, cylindrical gold-coated mirror; FFG, flat field grating; MCP, microchannel plate; CCD, CCD camera. Reproduced from [2] with permission from the Optical Society of America.

The harmonic yield was maximized by adjusting the position of the target with regard to the optical axis of propagation of the driving femtosecond pulses and by varying the focusing position relative to the plasma. The harmonic emission was directed to the XUV spectrometer, which contained a cylindrical mirror and a 1200 grooves/mm flat field grating with variable line spacing. The XUV spectrum was recorded by a micro-channel plate (MCP) with a phosphor screen, which was imaged by a CCD camera.

Some of the experiments were carried out using a two-colour pump of graphite plasma. The reason for using TCP instead of a single-colour pump was related to earlier demonstrated advantages of this approach in generating the odd and even harmonics, as well as larger efficiency of harmonic yield. TCP using the 800 nm radiation as the first field and 400 nm radiation as the second field was applied to carry out the comparative analysis of TCP and SCP schemes. The 0.4-mm-thick barium borate crystal (BBO, type I) was installed inside the vacuum chamber on the path

of focused the 800 nm pulse. The conversion efficiency of H2 pulses (λ=400 nm) was ~5%. The overlap of these two pulses in the plasma area was sufficient for observation of the role of the second orthogonally polarized field influencing the whole process of HHG due to small group velocity dispersion in the thin BBO crystal.

Ablation of graphite in most of these HHG experiments was carried out using nanosecond pulses from Nd:YAG laser as well. Similar to TH studies, two lasers were synchronized with each other. The harmonic yield was analyzed using the electronically variable delay between the heating and driving pulses.

9.1.2. Third harmonic generation

The motivation for THG prior to HHG in the clustered medium is related to two factors. Firstly, the analysis of different plasma species using this lower-order nonlinear optical process is less complex compared with the HHG-based approach from the point of view of determining the most suitable and efficient media, as well as the most efficient conditions for a harmonic generation. Secondly, the coincidence of the optimal delays between heating and driving pulses in the cases of lowest harmonic generation and HHG can provide additional information to determine the relationship between the velocities of singly-atomic and multi-atomic species in plasmas.

Prior to the study of the frequency conversion in the graphite plasma, THG in the air with variable driving pulse energy was performed which showed the anticipated cubic dependence of harmonic yield on the laser energy. THG in the air was carried out in order to calibrate the experimental setup and estimate TH conversion efficiency from carbon-containing plasma with regard to a similar process in air.

Two sets of experiments were performed for the THG study in the graphite plasma produced in a vacuum. In the first case, the 200 ps pulses were used as heating radiation to create C plasma. In the second case, 5 ns heating pulses were used for target ablation. The objective was to optimize the target position, the heating pulse energy, the delay between pulses, and the driving beam focal position to achieve the maximum TH yield from C plasma. These studies revealed the preference in the application of nanosecond pulses for plasma formation to achieve higher conversion efficiency compared with picosecond heating pulses.

Figure 9.3(a) shows, how TH yield from C plasma increases with the growth of the driving pulse energy. Variation of TH intensity showed approximately cubic dependence by increasing the driving 40 fs pulse

energy up to 500 μJ. An increase in the free-electron density was likely the limiting factor for the harmonic yield in early experiments with laser plasmas [4]. So the search for the formation of "optimal" plasma from the point of view of larger conversion efficiency towards the shorter wavelength region is required, thus prompting to analyze TH efficiency variations at different energies of heating nanosecond pulses. In discussed experiments, the TH intensity was gradually increased with the growth of heating 5 ns pulses up to 3 mJ [Fig. 9.3.(b)].
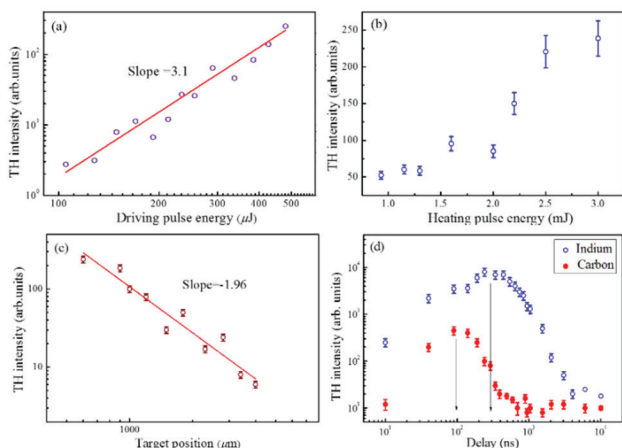

Fig. 9.3. (a) TH intensity as a function of driving pulse energy. No saturation of cubic $I_{TH}(E_{DP})$ dependence was observed along the whole range of variations of the driving pulse energy. (b) Influence of nanosecond heating pulse energy on the TH yield. (c) TH intensity as a function of the distance between graphite target and axis of femtosecond beam. The measurements were carried out up to 4 mm from the target surface. (d) Dependence of TH yield from graphite plasma on the delay between heating nanosecond pulse and driving femtosecond pulse (filled circles). Similar dependence is also shown in the case of indium plasma (empty circles). Arrows show the delays at which maximal TH yields were observed. The driving beam was focused at the distance of 0.6 mm above the target in all of these experiments excepting of these shown in (c). The delay between the heating and driving pulses was maintained at 100 ns during these experiments except of (d). Reproduced from [2] with permission from the Optical Society of America.

Harmonic intensity considerably depended on the distance between the optical axis of the driving beam and graphite surface due to the variations

of plasma concentration above the target at a fixed delay. Figure 9.3(c) shows the variation of TH intensity as a function of the distance between the target and the optical axis of the femtosecond pulse. TH from plasma was observed up to the distance of ~4 mm away from the graphite target. It has been demonstrated earlier that the distribution of spreading species during ablation is controlled by their longitudinal velocity and strongly depends on input fluence [5]. The distribution of different species during ablation has a direct influence on the TH intensity that resulted in the maximal harmonic yield close to the target surface. The variation of TH intensity at different distances between the optical axis of the driving beam and the target surface (x) was approximately close to reciprocal quadratic dependence [$I_{TH} \propto x^{-n}$, $n=1.96$] at the nanosecond pulse fluence of 4 J cm^{-2}. Notice that parameter n can be varied by changing conditions of experiments, in particular the fluence of heating pulses. The delay between the heating and driving pulses was maintained at 100 ns during the THG experiments presented in Fig. 9.3(a-c), which was optimal assuming the 0.6 mm distance between the target and the optical axis of the femtosecond beam.

Previous studies of laser ablation of graphite have revealed the typical characteristics of the expanding plasma species (average velocity 1.5×10^3 m s^{-1}) for ablation with 532 nm, 10 ns pulses at fluencies of the order of 3 J cm^{-2} [6]. The measured mass distribution presented in [6] revealed the presence of C_5 to C_{25} species. Those carbon clusters, as has also been shown in other studies, have the largest population in the graphite plasma among other clusters. It was assumed that they may be a reason for such attractive features as the more efficient harmonics generation with regard to similar processes in single atomic/ionic media. In the meantime, large nanoparticles do not participate in the process of HHG, but rather may serve as the sources of the formation of smaller clusters during different stages of laser ablation due to partial disintegration of large multi-particle species during heating, melting, and evaporation. These stages of laser-matter interaction may cause the formation of notably smaller clusters containing a few tens of carbon atoms. Meanwhile, the remaining parts of large nanoparticles do not participate in the harmonic generation, but rather deposit later on the nearby surfaces. Thus the performance of nanomaterials for the applications in harmonic generation depends on their distribution and size at the moment of propagation of the femtosecond pulses through the plasma plume. Hence the precise control over the dynamics of their appearance in the plasma is essential.

The temporal evolution of TH yield from C plasma was analyzed by varying the delay between the nanosecond pulses inducing ablation and

the driving laser pulses [Fig. 9.3(d), filled circles]. The distance between target and femtosecond beam propagation in these TH experiments was maintained at ~0.6 mm. The maximal TH yield was observed at ~100 ns from the beginning of ablation. To prove the concept that this optimization depends on the mass of the particles participating in a harmonic generation a heavier target (indium) ablated at a similar fluence of heating pulses and other similar experimental conditions was used. A similar kinetic energy $E=mv^2/2$ can characterize the arrival of plasma components from different materials ablated at identical conditions. Correspondingly, one can expect the arrival of indium ions and atoms in the area of interaction with the driving beam at $(M_{In}:M_C)^{0.5}$~3 times longer delay with regard to carbon particles taking into account the ratio between atomic weights of these two targets ($M_{In}:M_C\approx9$).

This anticipated maximal yield of TH from indium plasma was observed in experiments when the highest TH efficiency was achieved at ~300 ns from the beginning of ablation of the indium target [Fig. 9.3(d), empty circles]. Thus, one can assume that this rule works properly for the dynamics of material spreading once one analyzes the movement of the particles during laser ablation at relatively moderate fluencies (2–10 J cm^{-2}) of heating nanosecond pulses.

9.1.3. High-order harmonics generation

XUV emission spectra of carbon plasma at different regimes of graphite ablation in the range of 30 – 130 nm are shown in Figures 9.4(a) and 9.4(b). Either picosecond (upper panel) or nanosecond (middle panel) pulses were used for laser ablation (Fig. 9.2). Various emission lines attributed to CII – CIII ions were identified and used for calibration of the XUV spectrometer. These conditions of ablation were unsuitable for efficient HHG due to the presence of a large number of free electrons preventing optimal phase relations between the driving and harmonic waves. The nanosecond pulses induced ablation was chosen for further analysis of HHG from different species of graphite plasma since in that case, contrary to ablation by picosecond pulses, it was possible to analyze the delay-dependent harmonic emission a the delays between heating and converting pulses ranging between 0 and 5×10^4 ns.

Lesser excitation of graphite target by nanosecond pulses allowed the formation of plasma suitable for a harmonic generation [Fig. 9.4(c)]. Odd harmonics of 800 nm radiation up to 23rd order (H23) were observed. It is worth noting that the discussed observations of harmonic spectra did not show a simultaneous presence of plasma emission from high-charged

particles in the studied spectral range (30–130 nm) that confirming that these experiments were carried out at a soft ablation regime of the carbon-containing target. The absence of the plasma emission associated with the higher-charged ions at these conditions was accomplished by the moderate excitation of graphite. The driving pulse at $I \approx 2 \times 10^{14}$ W cm^{-2} also did not cause the appearance of strong ionic emission from the higher-charged carbon ions.
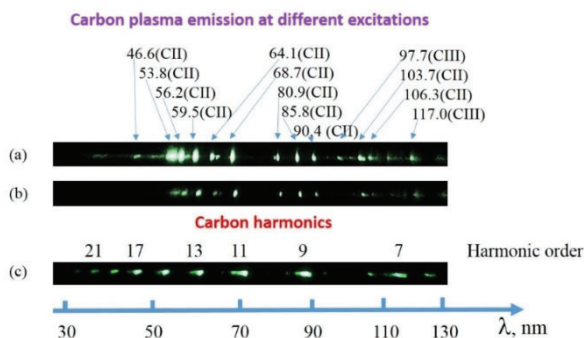

Fig. 9.4. Raw images of plasma and harmonic spectra. (a) Graphite plasma emission using picosecond pulses induced ablation. (b) Graphite plasma emission using nanosecond pulses induced ablation. (c) Harmonic spectra using single-colour pump (800 nm) of C plasma at 30 ns delay between heating and driving pulses. The fluence of heating pulses on the target surface was maintained at 5 J cm^{-2}. The distance between the target and the axis of propagation of the driving beam was 0.2 mm. Reproduced from [2] with permission from the Optical Society of America.

The important peculiarity of these plasma emissions and harmonics studies was the proximity of some ionic transitions of carbon with the wavelengths of harmonics, particularly strong CII transitions (53.8 and 59.5 nm) and 15th and 13th harmonics (53.3 and 61.5 nm) respectively. Neither enhancement nor suppression of these harmonics generated in graphite plasma was observed. These studies showed that the proximity of strong emission lines and harmonics did not necessarily lead to a variation of the harmonic yield.

The reason for presenting the experimental data as the images appearing on the screen of the computer rather than the line-outs of HHG spectra is justified by better viewing of obtained data and a clear definition of the difference between the plasma and harmonic spectra. The goal of this group of studies was the qualitative determination of the influence of

different conditions of ablation on the plasma emission and the harmonics conversion efficiency rather than the quantitative measurements of harmonics in the plasmas. Also notice that visual analysis of the raw images of harmonics and plasma emission allows distinguishing these sources of XUV radiation by their divergences. The vertical dimensions of the raw images of plasma emission, which characterize its divergence, were a few times larger compared with those of harmonics. An additional advantage of this method of data presentation is a direct demonstration of the insignificant role of emission lines in the harmonic conversion efficiency. The approximately plateau-like shape of harmonics distribution remained unchanged in spite of the coincidence of plasma emission limes and some harmonics orders.

The λ-axis in Fig. 9.4 is shown on the basis of the calibration of the XUV spectrometer for distinguishing the distribution of harmonics along the short-wavelength region. The saturated images were intentionally chosen to present the spectra for better viewing. Note that the unsaturated images were used for the line-outs of the HHG spectra.

The next set of HHG studies was performed using two orthogonally polarized driving beams. The 0.4mm thick BBO crystal was inserted on the path of 800 nm radiation inside the vacuum chamber that allowed the generation of 400 nm pulses (H2) while maintaining sufficient temporal and spatial overlap of 800 and 400 nm pulses in C plasma. Even small conversion efficiency (~2%) of 400 nm radiation allowed the generation of the lower-order even harmonics alongside the odd ones (Fig. 9.5). The even harmonics generation up to H14 (see middle panel) were achieved. A relatively small yield of lower-order harmonics in these spectra (H6 to H9) was caused by the weaker sensitivity of MCP in the range of the wavelengths above 100 nm. The use of different fluencies of heating nanosecond pulses ranging between 5 and 9 J cm^{-2} led to variations of generated spectra.

The conversion efficiency of odd harmonics in the case of TCP was approximately three times higher than in the case of SCP. One can see that even at a very small ratio of 400 and 800 nm pulse energies (1:20) the influence of weak field was sufficient to strongly modify the whole harmonic spectrum.

The application of two-colour sources for HHG has also another advantage. It allows the two-fold increase of the number of generated harmonics, which in turn may lead to the observation of the resonance-induced enhancement of single components of those multi-harmonic sources. The latter process is mostly related to the ionic transitions of various materials possessing high oscillator strengths. In the case of

graphite plasma, no enhancement of even harmonics was observed, while in the case of indium plasma H12 was notably enhanced alongside H13 due to proximity with the ionic transition possessing large oscillator strength [7].
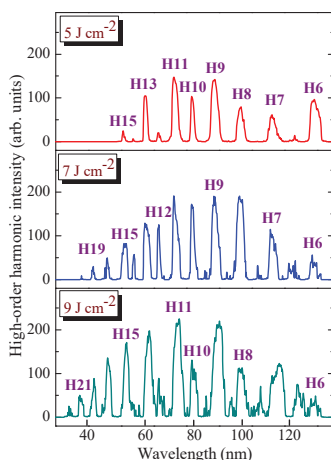

Fig. 9.5. Harmonic spectra using the two-colour pump (800nm+400nm) at different fluencies of nanosecond pulses on the target surface. One can see some red shift of odd harmonics at highest fluence while even harmonics remained at fixed wavelengths. Reproduced from [2] with permission from the Optical Society of America.

In the case of stronger excitation of carbon plasma, the small red shift of odd harmonics was observed, while even harmonics were not shifted due to notably weaker energy of 400 nm radiation compared with 800 nm pulses (bottom panel of Fig. 9.5). Previous reports on gas HHG experiments have shown a distinct difference between the HHG spectra driven by negatively and positively chirped pulses, which was related with both the influence of the dynamically induced negative chirp and the positive chirp induced by strong laser radiation and the ionized medium due to the self-phase modulation of the laser pulse [8]. Notice that the red-shift of chirp-free pulses in the case of dense plasmas has already been reported in the case of plasma harmonics studies [9].

Different scenarios can be involved in the case of clustered media in regards to the observed red shift of odd harmonics with higher intensities of the nanosecond ablating pulse. This process might be related to the Kerr

effect, electron-ion recombination, and ion expansion, and cluster formation. The latter mechanism seemed consistent with the experimental findings. The chirp-induced red and blue shifts were explained by the model including both atoms and ions. The neutrals were assumed to be responsible for the blue shift, while the ions were the main reason for the red shift. The red shift can also be attributed to the self-phase modulation (SPM) of the laser pulse during the propagation of the leading part of the pulse through the medium consisting of neutrals and singly charged ions. As one can see, the broader spectra of odd harmonics (Fig. 9.5, bottom panel) from C clusters can also be attributed to the influence of SPM, leading to the red shift of those harmonics.

The heating radiation intensity on the target surface was maintained at 2×10^9 W cm^{-2}. The particles density in plasma was estimated using the hydrodynamic code HYADES [10] to be a few units of 10^{17} cm^{-3}. The ionization potentials of carbon atoms and singly charged ions are equal to 11.25 and 24.38 eV, respectively. Thus such plasma mainly consists of excited neutral atoms and singly ionized carbon. Notice that the presence of excited atoms and ions can increase a nonlinear optical response of laser-produced plasma.
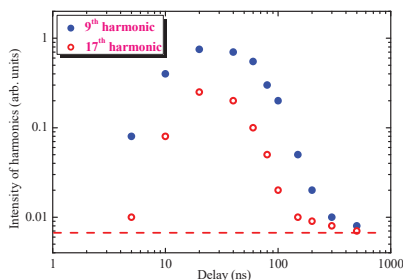

Fig. 9.6. Dependences of H9 and H17 yields on the delay between nanosecond and femtosecond pulses. Dashed line shows the threshold of registration of harmonic emission. Reproduced from [2] with permission from the Optical Society of America.

A typical dependence of the 9th and the 17th harmonics intensities on the delay between pulses is presented in Fig. 9.6. At the initial stages of plasma formation and spreading out of the target surface, i.e. at the delays less than 10 ns, the concentration of neutrals and singly charged ions is insufficient to produce a measurable amount of harmonic photons since the whole ensemble of particles possessing the velocities of $\leq 1\times10^4$ m s^{-1} cannot reach the optical axis of the propagation of driving beam, which

was ~0.2 mm above the graphite surface in present experiments. The increase of delay up to 10 to 50 ns caused the appearance of a large number of carbon atoms and ions, as well as light clusters, along the path of the femtosecond beam that allowed maximizing the yield of harmonics. The increase of delay above 50 ns led to a decrease of HHG efficiency. A similarity in the delay dependence for H9 and H17 was reported in those studies. The harmonics almost disappeared from XUV spectra once the delay exceeded 300 ns. The attempts to observe the harmonic emission in the microsecond time scale of delays were unsuccessful.

9.1.4. Role of clusters in HHG

Clusters play important role in the modification of the harmonic spectra generated in different media. In the case of clusters, the cross-section of recombination of the accelerated electron with the parent particle is higher compared with the atoms [11]. In the meantime, the experiments with gas clusters have revealed some difficulties in disentangling the harmonics produced by different species (monomers and clusters of different sizes). The uncertainty in the exact mechanism of the HHG from clusters has previously been underlined in [12].

Laser ablation of carbon has been proven to be a versatile method for the synthesis of clusters, which allowed characterization and dynamics of the multi-particle species formation [13]. The authors of [14] have concluded that the appearance of clusters during ablation is a result of clusters' ejection from the target and collision-related aggregation in the expansion of the plume. The growth of clusters is based on the addition of many neutral carbon species to the ions in a stepwise fashion. The processes that can cause the formation and disintegration of multi-atomic species include photomechanical ejection, liquid phase ejection, and fragmentation, homogeneous nucleation and decomposition, heterogeneous decomposition, etc. [15].

A detailed understanding of the basic physical processes governing the composition of carbon ablation and the reliable methods for controlling the plume species became a necessity for the selection of the optimal plasma conditions for HHG. The following arguments supporting the explanation of higher yield of harmonics from such plasmas were considered: (i) carbon species allow the formation of multi-particle clusters during laser ablation, which can enhance HHG yield, (ii) the first ionization potential of carbon is high enough to prevent the appearance of high concentration of free electrons, (iii) the graphite target allows easier generation of a relatively dense carbon plasma and the production of phase-matching

conditions for a lower-order harmonic generation. The carbon-containing materials like graphite, fullerenes, and carbon nanotubes have proven that, at optimal ablation conditions, they can be considered as attractive plasma media for efficient harmonic generation in the 40–80 nm spectral range using the femtosecond laser pulses [16].

To define the role of clusters in a variation of the nonlinear optical response of medium during frequency conversion of ultrashort pulses one has to analyze both lowest- and higher-order harmonic generation conditions. As already mentioned, the necessity in lowest-order harmonic generation studies is as follows. It provides a guide for the selection of the targets suitable for the efficient generation of short-wavelength coherent radiation using different delays between heating and driving pulses [17]. This method also allows the application of low-order harmonic generation for plasma diagnostics, which is less complex compared with the HHG-based method. The additional assumption for strong harmonics generation from clusters and nanoparticles compared with single atoms or ions could be the higher concentration of neutral atoms inevitably accompanying the presence of aggregated multi-atomic species. It was suggested in [18] that small carbon clusters play an important role in the generation of high-order harmonics of plasmas. A similar conclusion was made in [19] with regard to TH emission. It was underlined that harmonics generation in plasmas, when performed with full temporal delay control and under conditions of spatial segregation typical of laser ablation plasmas, provides a method to qualitatively assess cluster size distributions for different materials and irradiation conditions.

In graphite, the ablation plasma plume may contain various species of carbon, i.e. neutrals and ions, small molecules, clusters, aggregates, etc., which can contribute to harmonic generation to various extents. It is important to determine their presence in the region, where the driving laser pulse interacts with the expanding plasma. In particular, the production of clusters in the laser-plasma during laser ablation of various targets has a high probability, while their presence in the plasma area where the frequency conversion occurs was yet to be confirmed directly.

Earlier, the analysis of carbon cluster composition of the ablation plume produced by nanosecond laser pulses for HHG was accomplished by time-of-flight mass spectroscopy (ToFMS) [20], which confirmed the presence of carbon clusters ranging from C_5 to C_{25}. The attempts to find higher mass clusters failed, though they were searched for over a long range of delays up to a few µs between the onset of laser ablation and the switching on the triggering pulse in ToFMS. Earlier studies of carbon plasma have also shown that the 4n+3 clusters in $C_5 - C_{25}$ range had a

higher abundance than neighbouring ones [21]. The conclusion was made that those clusters (C_7, C_{11}, C_{15}, and C_{19}) could be considered as the most effective emitters of harmonics.

The harmonic generation in such plasma can prove or disapprove the role of the complex composition of ablated species in the former process. A signature revealing the nature of the emitters could be the growth of harmonics emission arising at some specific delay from the beginning of ablation. This delay may characterize the time of propagation of the clusters from the target's surface to the optical axis of ultrashort pulse propagation. It was suggested in [22] that if the components could be assumed to reach thermodynamic equilibrium during the expansion so that a similar average kinetic energy $E = mv^2/2$ could characterize all plasma components, the average arrival times could be assigned to different cluster sizes. However, this formula rather determines the condition of the similar velocities for the atoms and multi-atomic systems of similar elements, like carbon and fullerene. A similar assumption can be applied to atoms and ions of different materials, which was confirmed during the comparative THG studies using indium and graphite plasmas. The delay at which TH reaches its maximum intensity should scale as a square root of atomic weight, as was demonstrated in present studies [Fig. 9.3(d)]. The ejection of lighter atoms and ions from the target surface does not allow them to reach the axis of the driving beam earlier as compared with heavier species.

The large clusters like C_n should appear in the laser-plasma interaction zone $n^{0.5}$ times later compared with single atoms and ions of carbon. In other words, the appearance of the group of C_7–C_{19} clusters in the interaction zone could be expected at delays of 2.7 to 4.4 times later compared to the C_1 particles. However, this scenario does not happen, since no enhancement of harmonics occurred at these delays (90 – 140 ns). The discussed studies showed that carbon clusters arrive at the area of interaction with femtosecond beam notably earlier than one can expect assuming the above kinetic equation. In other words, from the very beginning, all atoms in clusters acquire similar kinetic energy and spread out of the surface with a velocity approximately equal to the one of a single atom of carbon.

Below, we address the difference in the expected and actual optimal delays between heating and driving pulses in the case of graphite-ablated plasma. In the case of a thermalized ablation plume, i.e. at very slow heating conditions, the average arrival times can be assigned to different cluster sizes. Another situation occurs in the case of the fast, either nanosecond or picosecond, ejection of energy in the tiny area of the target.

In that case, the delay between heating and driving pulses at which the harmonic yield reaches its maximum should scale as a square root of the atomic or molecular weight of the constituents. The additional studies revealed that, for bulk gold ablation, the maximum high-order harmonic yield from single gold atoms and ions occurred at a delay of about 180–300 ns. Meantime, the ablated 20-nm Au nanoparticles allowed efficient generation at about 200–350 ns delay, which is approximately equal to the delay in the case of Au atoms and ions. Furthermore, attempts to observe HHG at the delays of up to 50 µs, i.e., at the expected delay for thermalized larger nanoparticles, did not show any harmonic emission. Thus, the discussed studies demonstrate that clusters, quantum dots, and relatively small nanoparticles arrive in the area of interaction with the femtosecond laser beam notably earlier than one would expect assuming the thermalized regime of evaporation. In other words, all multi-atomic species acquire, from the very beginning, similar kinetic energy and spread out from the surface with velocities approximately similar to those of the single atoms and ions ablating from bulk material. This conclusion reconciles the similarity in the optimal delays for HHG from the plasmas produced on the bulk target leading to evaporation of atoms and ions and on the targets containing nanoparticles of the same material.

The velocities of the multi-atomic carbon clusters, which assume to be the main and most efficient emitters of third and higher-order harmonics, are estimated by knowing the "optimal" delays for highest harmonic yields in both cases ($\sim$ 100 and $\sim$25 ns) and the distances from targets in these two groups of experiments (0.6 and 0.2 mm). These particles possessed the 6×10^3 and 8×10^3 m s^{-1}. One can see a similarity of the velocities determined from the two groups of experiments using different facilities.

9.2. Effective high-order harmonic generation from metal sulphide quantum dots

The quantum dots containing materials, particularly sulphide-based quantum dots (QDs), have attracted special attention due to their large low-order optical nonlinearities [23,24]. Various nonlinear optical processes can be induced in the ZnS nanoparticles, which became useful in photonics [25-27]. The coexistence of reverse saturable absorption and two-photon absorption in silver sulphide suggests that Ag_2S QDs could be a very promising nonlinear medium for photonic devices in different time scales if these semiconductor nanocrystallites are incorporated into appropriate media while retaining the attractive features of both components. The Ag_2S QDs also demonstrate low-threshold optical limiting in the

visible and near-IR ranges [28-30]. A search for new applications of QDs is an important task for the optical community. The interesting idea is to find the optimal conditions in the application of such QDs as effective emitters of the high-order harmonics of femtosecond pulses for the development of efficient sources of coherent XUV radiation. In this section, we discuss the harmonics generation in QDs using electronically driven delays between the heating and driving lasers [31].

9.2.1. Preparation of QD-containing targets and scheme of experiments

Improving the efficiency of HHG in a plasma containing QDs requires solving two problems: (1) developing the methods for the synthesis of metal sulphides QDs, followed by the formation of solid-state materials containing large concentrations of these species, and ensuring the stability of the morphology of vaporized materials under laser ablation, and (2) optimizing the process of converting the wavelength of laser pulses during the HHG in a laser-plasma containing such multi-particles.

The synthesis of QDs was carried out taking into account a number of criteria for their use to generate harmonics of ultrashort pulses. The first criterion is the formation (as a result of ablation of samples by either picosecond or nanosecond heating pulses) of a plasma cloud consisting of QDs, as well as atoms, ions, and clusters at the time of the passage of the converting femtosecond pulses above the target surface. The second criterion is the presence of the maximal concentration of QDs at the time of transmission of the femtosecond pulses through the plasma. The third criterion is the size characteristics of quantum dots. Previous studies of harmonic generation in multi-particle containing plasmas, as well as qualitative assessments, show that the most optimal sizes of such species should be in the range of 1 - 4 nm.

Synthesis of colloidal QDs of ZnS and CdS was carried out by mixing the $CdBr_2 \times 4H_2O$, $ZnBr_2 \times 4H_2O$, and thioglucolic acid (TGA) in the required proportions. The corresponding salts of cadmium and zinc bromide were dissolved in water (200 ml) and then the TGA was added. Then the 50 ml of Na_2S aqueous solution (1.3 mM) was injected into the prepared solution. The synthesized colloidal solution of QDs was dissolved by adding ethanol to a 50% solution, centrifuged, and re-dissolved in water. The cleaning procedure was repeated several times. A similar procedure was used for the synthesis of Ag_2S QDs.

The synthesized samples of colloidal solutions of zinc, cadmium, and silver sulphides were further used to produce the solid targets for laser

ablation and generation of harmonics. A new method of increasing the filling factor Ag_2S, ZnS, and CdS QDs in the stabilizing polymer was developed to form solid samples of multi-particle species for laser ablation in vacuum and formation of the plasma torches containing a large amount of QDs required for efficient generation of harmonics. The method is based on the compatibility of synthesized colloidal QDs and gelatin, as well as the possibility of increasing the concentration of QDs during centrifugation in the presence of acetone. Gelatine's property of high filling ability as a polymer and the possibility of drying such samples to a solid-state are among the advantages of this method. The preparation of solid tablets was accomplished in the following sequence: the prepared concentrated solution of QDs was introduced into the gelatine melted at a temperature of 40-50 ^0C using intensive stirring and then the suspensions were dried at a temperature of 80 ^0C for 24 hours to a solid-state and then placed for further vacuum drying where they were kept for 10 days. Control of the obtained samples was carried out by analysis of their luminescence, which was compared with the luminescence of the same QDs in TGA.
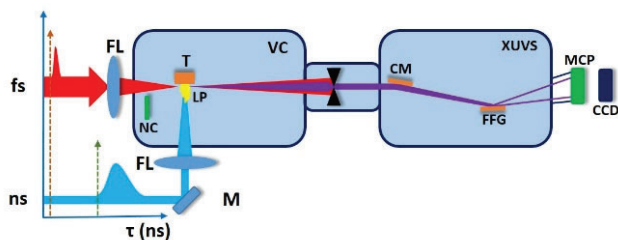

Fig. 9.7. High-order harmonic generation setup. fs, converting femtosecond pulses, ns, heating nanosecond pulses; FL, focusing lenses; VC, vacuum chamber; T, target; NC, BBO crystal; LP, laser plasma; XUVS, extreme ultraviolet spectrometer; CM, cylindrical gold-coated mirror; FFG , flat field grating; MCP, microchannel plate; CCD, CCD camera. Reproduced from [31] with permission from the Optical Society of America.

Synchronization of two laser sources, such as the most commonly used Ti: sapphire femtosecond laser and Nd: YAG nanosecond laser, may resolve, to some extent, the puzzle related to the observation of the enhancement of the harmonics generating in the plasmas produced during ablation of multi-particle media. The main advantage of this approach is the possibility to electronically drive the delay between heating nanosecond and driving femtosecond pulses in a broad range. Additionally, the use of

radiation from the nanosecond Nd: YAG lasers offers advantages in plasma formation compared with previously used picosecond pulses. The application of nanosecond pulses to ablate the targets allows the formation of less ionized and less excited plasma during a longer period of laser-matter interaction compared with the picosecond pulses. Nd: YAG lasers commonly operate at a 10 Hz pulse repetition rate, which is more suitable for stable HHG in plasmas compared with 1 kHz ablation, though in the latter case some strategies, such as target rotation [32], allowed, to some extent, improvement of the stability of 1 kHz coherent short-wavelength sources.

The details of the experimental setup are presented in the previous section. Briefly, the metal sulphide QD plasmas were used for HHG. The driving femtosecond pulses (800nm, 1 kHz) propagated through the plasma at different delays from the beginning of target irradiation by nanosecond heating pulses (1064 nm, 10 Hz). The variable delay ($0 - 10^6$ ns) between 5 ns heating pulses and 30 fs driving pulses was established to generate harmonics in plasma at the used geometry of experiments when the 800 nm femtosecond pulses were focused onto the plasma area from the orthogonal direction with regard to ablating radiation, at a distance of ~200 μm above the target surface (Fig. 9.7). Additionally, the harmonic yield was maximized by adjusting the position of the target with regard to the optical axis of propagation of the driving femtosecond pulses and by varying the focusing position of this radiation with regard to the plasma. The harmonic emission was directed to the XUV spectrometer containing a cylindrical mirror and a 1200 grooves/mm flat field grating with variable line spacing. The XUV spectrum was recorded by a micro-channel plate (MCP) with a phosphor screen, and the harmonics were imaged by a CCD camera.

HHG in QDs was also analyzed using the two-colour pump of plasma. The reason for using the TCP instead of the single-colour pump was related to the advantages of this approach in the generation of odd and even harmonics in gases and plasmas, as well as larger efficiency of harmonic yield in the former case. The TCP using 800 nm radiation as the first field and 400 nm radiation as the second field was applied to carry out the comparative analysis of TCP and SCP schemes. The 0.4-mm-thick BBO crystal (type I) was installed inside the vacuum chamber on the path of the 800 nm radiation to generate a second harmonic (H2). The conversion efficiency of H2 pulses (λ=400 nm) was relatively low (~4%). However, due to small group velocity dispersion in the thin BBO crystal, the overlap of these two pulses in the plasma area was sufficient to

determine how the weak second orthogonally polarized field influences the whole process of HHG in QDs.

9.2.2. Characterization of QDs

The originality of the general approach to increase the HHG efficiency is based on the choice of quantum confined multi-atomic particles to facilitate an increase of the nonlinear optical response of the plasma medium. Qualitatively, an increase of the cross-section for the recombination of accelerated electrons with the multi-particle species with increasing size of the parent particle can be expected. However, this assumption is valid only for certain sizes of multi-particle species. A further increase of the number of atoms or molecules in the particle leads to conditions where the atoms or molecules located inside the particle become completely shielded and thus eliminated from the three-step process of HHG, i.e., ionization, acceleration, and recombination. In other words, the internal atoms and molecules do not supply electrons for acceleration and recombination. Thus, the optimal size of the particles is one of the most important characteristics in order to achieve an increase in the efficiency of harmonic generation. Moreover, its importance rises with the increasing order of the generated harmonics. Early studies carried out in gases and plasmas have shown an increase of HHG intensity using clusters containing up to 1000 noble gas atoms, as well as using nanoparticles containing tens of thousands to a few million atoms. It turned out that the optimal number of atoms in the particles seems to lie in an intermediate size region. If one divides the aggregates into three categories like clusters (0.1 - 1 nm), QDs (1 - 6 nm), and nanoparticles (10 - 100 nm), then the second group seems to be the most promising for HHG. The QDs synthesized in this work are satisfying this criterion.

Samples of colloidal QDs were characterized by x-ray diffraction, transmission electron microscopy (TEM), optical absorption, and luminescence spectroscopy. The composition of the particles was determined by x-ray and electron diffraction. The dispersion of the particle sizes was determined by statistical data analysis of the TEM images of the QDs. TEM also provided information on the morphology of the QDs. The analysis of the structure, phase composition, and morphology of the samples allowed improvements to the synthesis techniques.
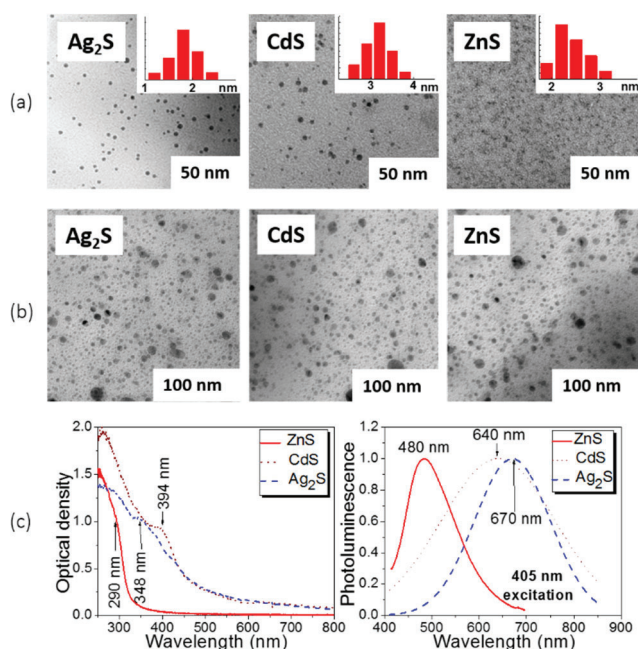
Fig. 9.8. (a) TEM images of synthesized metal sulphide QDs. (b) TEM images of the Ag$_2$S, CdS and ZnS QDs ablated at the 10 mJ energy of heating nanosecond pulse and deposited on nearby glass and silicon substrates. (c) Spectra of (left graph) optical absorption and (right graph) photoluminescence of synthesized QD. Reproduced from [31] with permission from the Optical Society of America.

TEM images of synthesized metal sulphide QDs are shown in Fig. 9.8(a). The size distribution is shown in the inset as histograms. From the histograms, one can conclude that Ag$_2$S QDs show mean sizes in the range of 1.7 to 2.0 nm, CdS QDs about 3.0 to 3.2 nm, and ZnS QDs about 2 to 2.2 nm diameter. The morphological studies reveal that Ag$_2$S QDs condensate in a monoclinic lattice, while CdS and ZnS QDs condensate in a cubic lattice and Ag$_2$S QDs in a monoclinic lattice. Figure 9.8(b) presents images of the QDs ablated by 10 mJ and 5 ns pulses and deposited on nearby substrates. The collected particles confirm the presence of metal sulphide QDs within the plasma plume. The sizes of deposited particles were larger than those of the original ones. Optical absorption and photoluminescence spectra are shown in Fig. 9.8(c). The spectra were significantly blue-shifted with regard to the bulk materials of

similar materials. The CdS, ZnS and Ag$_2$S QDs were embedded in gelatine with about 20% weight and prepared in the form of 5×5×3 mm plates.

9.2.3. Harmonic generation in QDs

Figure 9.9 shows high-order harmonics generated from these QDs in the spectral range of 20 – 120 nm. HHG at different delays between the heating and driving pulses from 100 to 2000 ns is shown for pulse energies of 4 and 0.4 mJ, respectively. At initial stages of plasma formation and spreading out from the target, i.e., at delays less than 50 ns, the concentration of particles (neutrals and singly charged ions) was insufficient for HHG since the whole ensemble of particles possessing velocities of ~2×10^4 m s^{-1} cannot reach the spatial region of the driving beam. At larger delays (above 100 ns) sufficient amounts of QDs appeared in the path of the femtosecond beam which allowed the generation of harmonics. The optimal delay was different for three QD plasmas studied. At about 400, 300, and 250 ns the highest harmonic yield was observed for Ag$_2$S QD (atomic weight 247.8 amu), CdS QD (144.5 amu), and ZnS QD (97.5 amu), respectively.
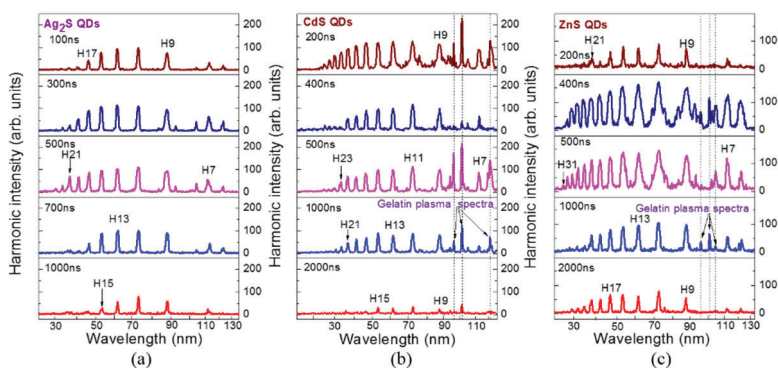

Fig. 9.9. Harmonic spectra from QD-containing plasmas [(a) silver sulfide QDs, (b) cadmium sulphide QDs, (c) zinc sulfide QDs] at different delays between heating and driving pulses. Dash-dotted lines show the plasma elision attributed to overexcited gelatine. Reproduced from [31] with permission from the Optical Society of America.

Notice that the use of a carbon plasma (atomic weight 12 amu) yielded maximal harmonic intensity at a significantly smaller delay of 30 ns between the heating and driving pulses using similar pulse energies. It should also be mentioned that harmonics generated from pure gelatin were almost one order of magnitude lower than those observed from the QDs. The harmonic cut-off is higher for lighter QD species, e.g., at the 31st harmonic for ZnS while Ag_2S showed the 25th as the highest harmonic. A further increase of the delay for each of these plasmas led to a gradual decrease of the HHG efficiency. The harmonics almost disappeared once the delay exceeded 2 to 3 μs. No harmonics were observed at delays up to 50 μs.
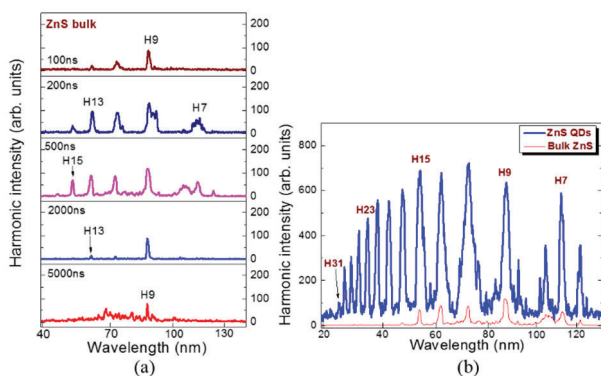

Fig.

9.10. (a) Harmonic spectra from the plasmas produced on the bulk ZnS surface at different delays between heating and driving pulses. The bottom panel was obtained at stronger excitation of the target (10 mJ). One can see the plasma emission lines from bulk zinc sulphide. (b) Comparison of harmonic distribution and intensities in the case of ablation of the QD (thick curve) and bulk (thin curve) ZnS targets at 500 ns delay between the heating and driving pulses. The weight part of QDs in gelatine (20%) is taken in to account for comparison of HHG at similar concentrations of plasmas. Reproduced from [31] with permission from the Optical Society of America.

Experiments using bulk targets of the same materials led to similar dependencies of the harmonic yield on the delay between the heating and driving pulses. These experiments showed that independently of whether molecules or QDs spread out from the target surface of the same material they appear in the area of the femtosecond beam approximately at the

same time. Figure 9.10(a) shows the harmonic generation in the laser-produced plasma after ablation of bulk ZnS by 4 mJ pulses. The harmonic yield maximizes at about 200 – 500 ns delay.

Figure 9.10(b) shows a comparison of the harmonic yield in the case of ablation of bulk and QD-containing ZnS targets. It is obvious that the QD plasma yield significantly stronger harmonics which also extend to higher orders. In the case of QD-containing plasma, the harmonics extended to ~50 eV (25 nm) or 31st order, while for the plasma produced from bulk ZnS the highest generated harmonic order was the 16th corresponding to a photon energy of ~26 eV (47 nm). The weight concentration of ZnS QDs in gelatine (0.2) was taken into account to carry out the comparison of the HHG spectra produced from atomic and multi-particle plasma. The overall ratio of intensities of the lower-order harmonics generated in these two plasmas was ~7.
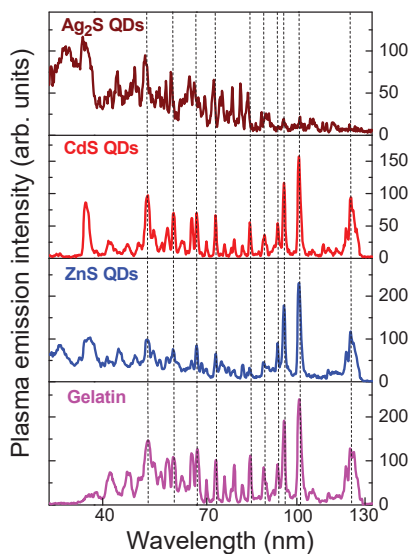

Fig. 9.11. Plasma emission spectra of Ag₂S, CdS and ZnS QDs in gelatin (three upper panels) and pure gelatin (bottom panel). Dash-dotted lines show similar emission in all four plasmas. Reproduced from [31] with permission from the Optical Society of America.

Figure 9.11 shows the plasma emission spectra of Ag₂S, CdS, and ZnS QDs in gelatine (three upper panels) and pure gelatine (bottom panel)

using larger energy of heating pulses (15 mJ). The majority of lines belong to gelatine emission, except the shorter-wavelength part of this spectrum. Most of the lines can be assigned to the emission from ionized carbon, as expected for gelatine. Those in the range of 45 – 90 nm seem mostly related to the C II emission. Probably, the existence of singly charged carbon caused the harmonic generation in pure gelatine plasma. These spectra underline that the metal sulphides were weakly excited and ionized during ablation. This condition of "mild" ablation, when the existing density of free electrons in the plasma does not prevent the formation of the phase-matching conditions between the waves of the driving and harmonic fields, is a prerequisite for efficient HHG. Notice that the conditions of ablation, when the plasma emission shown in Fig. 9.11 dominates in the XUV spectra, are unsuitable for efficient HHG due to the presence of a large number of free electrons which prevent an optimal phase relation between the driving and harmonic waves.

Less excitation of the QD-containing targets (4 mJ) allowed the formation of plasmas suitable for a harmonic generation. Odd harmonics of 800 nm radiation up to H25, H29, and H31 were achieved using Ag_2S, CdS, and ZnS QD plasmas, respectively (see Fig. 9.9). The appearance of strong harmonic emission did not coincide with the plasma emission from highly charged particles in the studied spectral range (20–120 nm), which confirms that these experiments were carried out at a soft ablation regime of QD containing targets. The driving pulse [$I \approx (2\text{-}5)\times10^{14}$ W cm^{-2}] also did not cause the appearance of strong ionic emission from higher charged molecules and QDs.

A final set of HHG studies was performed using two orthogonally polarized driving pulses. A 0.4 mm thick BBO crystal inserted inside the vacuum chamber on the path of the 800 nm fundamental radiation allowed the generation of 400 nm pulses while maintaining sufficient temporal and spatial overlap of 800 and 400 nm fields in the preformed plasmas. Notice that even only a small conversion efficiency (~5%) into the 400 nm radiation allowed the generation of the lower-order even harmonics alongside the odd ones (Fig. 9.12, dash-dotted curves). The even harmonics generated up to H14. The seemingly relatively small yield of low-order harmonics (H6 to H9) was caused by a weaker sensitivity of the MCP detector for wavelengths above 100 nm.

The conversion efficiency of even harmonics in the case of TCP was higher than of odd harmonics in the case of SCP, despite very low pulse energy of the 400 nm radiation with respect to the 800 nm one (~1:20). In the case of two-colour pumping stronger harmonics generation is possible due to the formation of a quasi-linear field, the selection of the short

quantum path component which has a denser electron wave packet, and a higher ionization rate compared to SCP.
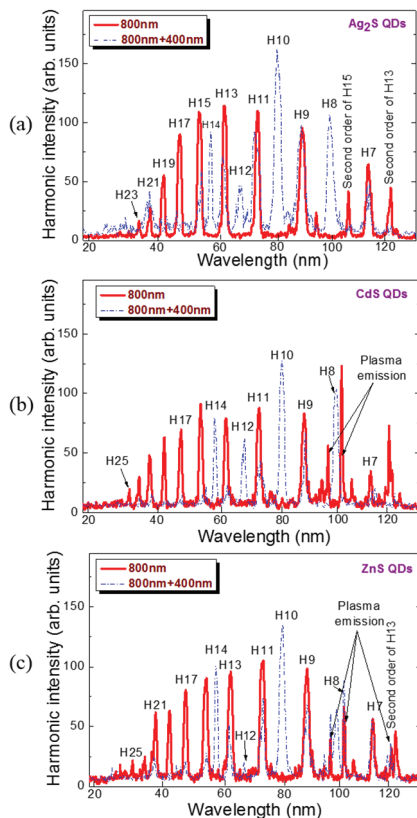

Fig. 9.12. Two-colour (800 nm + 400 nm, dash-dotted blue line) and single-colour (800 nm, full red line) pump induced harmonic spectra from Ag$_2$S (upper panel), CdS (middle panel), and ZnS (bottom panel) QDs at optimal delays between the heating and driving pulses for each species. Reproduced from [31] with permission from the Optical Society of America.

The orthogonally polarized second field also participates in the modification of the trajectory of the accelerated electrons from being two-dimensional to three-dimensional, which may lead to a removal of the

medium symmetry. With suitable control of the relative phase between the fundamental and the second harmonic radiation, the latter field enhances the short path contribution, resulting in a clean spectrum of harmonics. One can see that even at a very small ratio of 400 and 800 nm pulse energies the influence of the weak field was sufficient to strongly modify the whole harmonic spectrum compared to the single-colour pumping case.

Notice the relatively weaker H12 compared to H10 and H14. This heterogeneity in the even harmonic yields was caused by group velocity dispersion in the 0.4mm thick BBO crystal, which causes a notable delay between the 400 and 800 nm pulses at the output of the crystal in the case of 30fs pulses. Each 0.1 mm of BBO causes ~19fs delay between the driving (800 nm) and second harmonic (400 nm) waves. Only a small part of the second harmonic remains within the pulse duration of the driving fundamental 800 nm pulse. This causes a further decrease in the influence of the second harmonic field on the whole pattern of harmonic distribution. On the other hand, this second harmonic pulse generates relatively strong low-order odd harmonics: $H5_{400nm}$ which corresponds to $H10_{800nm}$, and $H7_{400nm}$ which corresponds to $H14_{800nm}$, see Fig. 9.12. An introduction of either positive or negative chirp in the femtosecond pulses by varying the distance between gratings in the compressor led to an increase of the pulse duration and a better overlap of the two orthogonally polarized pulses in the plasma. However, in that case, a decrease in the intensity of the driving pulse led to a general decrease of the whole harmonic yield.

The peculiarity of the gelatine plasma emission and TCP-induced harmonic spectra was the proximity of some ionic transitions of gelatine with the wavelengths of even harmonics, see H8 and the nearby emission lines of gelatine lines in the case of CdS QD (Fig. 9.12, middle panel) and ZnS QD (Fig. 9.12, bottom panel) plasmas. Neither enhancement nor suppression of this harmonic generated in both plasmas was observed. These studies showed that the proximity of strong emission lines and harmonics does not necessarily lead to a variation of the harmonic yield.

The estimates of conversion efficiency were carried out using the comparison with known results from other plasmas). In the case of silver plasma at similar conditions, almost equal conversion efficiencies with regard to ZnS in the range of 40-110 nm were achieved. By knowing the conversion efficiency from previous measurements of harmonic generation in the plasmas produced on the surface of bulk Ag (4×10^{-6}), the conversion efficiency in ZnS QD plasmas (which was 7 times higher than in bulk ZnS plasma) was estimated to be $\sim3\times10^{-5}$.

9.2.4. *Analysis of HHG in QDs*

The discussed experiments have two key features: ablation by nanosecond pulses and QDs-containing targets. So, the observed enhanced HHG conversion efficiency can have three origins: HHG from QDs, HHG from larger concentrations of neutral atoms, and HHG enhancement due to the interaction of QDs with atoms. Present studies show that particles with sizes of the order of a few nanometres can effectively generate high-order harmonics. HHG directly from QDs has not yet been studied theoretically, but a simulation of HHG from small clusters showed the increased HHG yield under the assumption of possible recombination of an electron on different atoms in the cluster. The cut off harmonics were also enhanced much more strongly than the plateau harmonics, which is in good agreement with discussed experimental results in the case of ZnS QDs (Fig. 9.10). The local enhancement of the electric field near larger nanoparticles also increases the intensity of cut off harmonics generated from the surrounding atoms [33].

Early experiments with larger nanostructures [carbon nanotubes, nanoparticles of metals and semiconductors, and other agglomerates of relatively large sizes (20-80 nm)] have shown both merits and drawbacks of this method for increasing the HHG efficiency. An increased recombination cross-section of the parent particle with the accelerated electron which, in the case of relatively large particle sizes, may result in an increased number of harmonic emitters is accompanied by a reduced number of atoms located on their surface. In traditional gas HHG, therefore, fewer atoms are involved in the generation of the harmonics because the atoms located inside the nanoparticles are unlikely to participate in HHG. As a consequence, the amount of harmonic generation processes per single atom falls short for large nanoparticles.

A similar average kinetic energy $E = mv^2/2$ could characterize all plasma components of the same elemental composition. Thus the average arrival time assigned to the particles containing different amounts of identical molecules will be approximately the same. The discussed studies have confirmed this assumption. The difference in "optimal" delays between heating and driving pulses is related to the difference in the velocities of particles, which depends on the atomic masses of the components of molecules. One can expect from this assumption the arrival of ZnS ions, atoms, and QDs in the area of interaction with the driving beam at $(M_{Ag2S}:M_{ZnS})^{0.5} \sim 1.59$ times earlier with regard to Ag_2S-containing particles taking into account the ratio between the atomic weights of these two molecules ($M_{Ag2S}:M_{ZnS} \approx 2.54$). Once one compares the "optimal"

delays for these two species, their ratio (400 ns : 250 ns = 1.6) becomes close to the above estimates. Thus, one can assume that the above rule properly explains the dynamics of material spreading out from the ablated target, once one analyzes the particles' movement during laser ablation at relatively moderate fluencies $(5 - 20 \text{ J cm}^{-2})$ of heating nanosecond pulses.

An increase of the recombination cross-section for QDs with respect to atoms or single molecules can enhance the HHG efficiency in multi-particle plasmas. An additional cause for strong harmonics generation from QDs compared to single atoms or ions could be the higher concentration of neutral metal sulphide molecules inevitably accompanying the presence of multi-particle species. The QDs present the extreme case of solid-state density in a very small volume. Compared to solids, they still do not absorb all the HHG radiation produced inside them due to their very small thickness. QDs can further improve phase-matching conditions for harmonics generated from atoms and ions using compensation of free-electron dispersion of the driving pulse by dispersion of clusters.

A new method for the analysis of multi-particle plasma formations using two laser sources for the HHG in the laser ablation can be considered as a promising approach to materials science. Its application will expand the possibilities of optimizing HHG in laser-induced plasma plumes, allow the implementation of new approaches to the study of large molecules and clusters undergoing ablation, and will significantly increase the range of objects of the study compared to HHG in gases. Thus, the method presented is not only an alternative approach in generating stronger coherent XUV radiation but rather can serve as a tool for various spectroscopic and analytical applications.

9.3. High-order harmonic generation using quasi-phase-matching and two-colour pump in the plasmas containing molecular and alloyed metal sulphide quantum dots

Recent studies of QDs have shown that particles with sizes of the order of a few nanometres can effectively enhance the nonlinear optical response and, in particular, generate high-order harmonics. HHG directly from QDs has not yet been studied theoretically, but a simulation of HHG from small clusters [34] showed an increased HHG yield under the assumption of possible recombination of an electron on different atoms in the cluster. Though the mechanisms of the enhancement of the harmonic yield in such multi-particle systems are still debatable, the studies have confirmed the potential of these species for both enhancing the coherent extreme ultraviolet flux and understanding the fundamental aspects of laser-multi-

particle interaction [35]. The probable explanation for this HHG enhancement in gas and plasma multi-particle media is due to the larger recombination cross-section for multi-atomic particles leading to higher HHG efficiency. Additionally, the growing recombination of the accelerated electrons with the same or neighbouring atoms, or with the multi-atomic particles, may also be, to some extent, the reason for the observed growth of harmonic yield from clusters and nanoparticles.

Laser-produced plasma produced on the surfaces of bulk materials attracts attention due to various processes occurring during the harmonic generation in this medium [36-44]. Meanwhile, different aspects of the application of low-dimensional aggregates for efficient HHG in plasma media have yet to be analyzed. These unexplored concepts include (a) the application of two driving waves with different polarizations for the harmonic generation, (b) a modulation of the spatial shape of the aggregate-containing media to apply the quasi-phase-matching concept for harmonic enhancement in different ranges of the extreme ultraviolet, (c) a modification of the structure of aggregates for determining the role of morphology properties on the frequency conversion of infrared pulses in such structures, etc. In this connection, the laser-produced plasmas provide a wider range of options than the gaseous media for variation of the properties of aggregates-containing media.

In this section, we analyze HHG from laser-produced plasmas containing QDs of metal sulphides using different approaches, including a two-colour pump, application of single and alloyed QDs, and quasi-phase-matching of interacting waves [45]. This study allows determining the optimal methods for further enhancing HHG efficiency and analyzing the properties of harmonic emitters.

9.3.1. *Experimental arrangements*

Colloidal $Cd_{0.5}Zn_{0.5}S$ QDs were prepared through the mixing of $CdBr_2$, $ZnBr_2$, thioglycolic acid, and Na_2S at the ratio of 1:1:2:2 at 40 °C. The synthesized $Cd_{0.5}Zn_{0.5}S$ QDs were centrifuged with adding ethanol and acetone and then again dissolved in water. After cleaning the suspension obtained the gelatine was added to this suspension. The concentration of QDs amounted to about 40% of the mass of gelatine. This method was based on the compatibility of synthesized colloidal QDs and gelatine, as well as the possibility of increasing the concentration of QDs during centrifugation in the presence of acetone. The mean sizes of $Cd_{0.5}Zn_{0.5}S$ QDs were 2 nm, while the other species had mean sizes in the range of 1.7 to 2.0 nm (Ag_2S), and 3.0 to 3.2 nm (CdS). The optical spectra of the

suspensions of these QDs were significantly blue-shifted with regard to the bulk materials of similar materials. The $Cd_{0.5}Zn_{0.5}S$, CdS, and Ag_2S QDs embedded in gelatine were prepared in the form of 5×5×3 mm plates. The solid targets containing the mixtures of gelatine and synthesized samples of colloidal solutions of cadmium, cadmium-zinc, and silver sulphides were then ablated in a vacuum chamber using the cylindrical focusing optics to produce 5 mm long laser-produced plasmas where HHG was carried out. This method allowed the formation of plasmas containing a large amount of QDs leading to an enhancement of the harmonic yield with regard to the ablation of bulk materials of the same elemental components. The silver sulphide bulk targets with the same composition as the QDs were also used to compare HHG in single atomic/ionic and QD species.
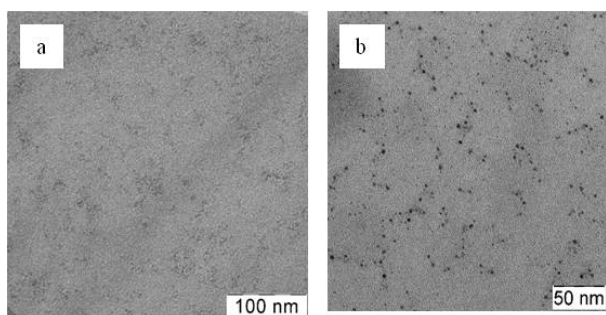

Fig. 9.13. TEM images of (a) deposited debris from ablated bulk Ag_2S and (b) deposited debris from ablated Ag_2S QDs. Reproduced from [45] with permission from the American Institute of Physics.

TEM image of deposited debris from bulk Ag_2S is shown in Fig. 9.13a. No measurable NPs were observed since the deposited debris presented a thin molecular film. These morphology studies confirmed that the emission of harmonics, in that case, occurred from the molecular components of the plasma rather than from the multi-particle associates aggregated during ablation of bulk silver sulphide at relatively mild conditions of ablation (i.e. at a fluence of the heating nanosecond pulses of ~100 J cm^{-2}). This image was taken at optimal fluence for the ablation of this target. The term "optimal" (as in any other case) refers to the maximal yield of harmonics from laser-produced plasma. Stronger ablation of bulk Ag_2S caused a sharp decrease of the harmonic conversion efficiency, while no difference in the debris with the previous case was detected.

Further enhancement of the fluence (above 250 J cm^{-2}) caused the appearance of large associates of silver sulphide (~ a few micrometers) among the debris, probably caused by blast-induced evaporation of large bullets from the bulk surface. For comparison the image of deposited Ag$_2$S QDs used during HHG studies is shown (Fig. 9.13b). The sizes of deposited QDs were almost similar to those from the initial QDs.

Femtosecond laser pulses (800 nm, 30 fs, 1 kHz) were employed for HHG during propagation at a distance of ~200 μm above the target surface through the QD-containing laser-produced plasmas (Fig. 9.14a). A scheme of heating nanosecond pulses and driving femtosecond pulses from different laser sources was used for HHG in plasmas. The ablation of QDs was carried out by nanosecond laser pulses (1064 nm, 5 ns, 10 Hz).An electronic delay between nanosecond and femtosecond pulses allowed to apply sufficiently long delays between two pulses compared with the optical delay technique. The delay between pulses was tuned using an electronic delay generator.

The most important parameters during plasma HHG studies are the fluence of heating pulses and the intensity of driving pulses. The fluence of heating pulses on the surface of metal sulphide QD targets was varied between 1.5 and 3 J cm^{-2} depending on the used samples. The difference in the optimal fluences allowing the strongest emission of harmonics was attributed to different conditions of plasma formation in the case of the three used QD samples. The optimal fluence of nanosecond heating pulses in the case of ablation of bulk Ag$_2$S target was notably higher (~100 J cm^{-2}) due to the larger threshold of ablation of the solid sample compared with the gelatine containing quantum dots. The intensity of driving 800 nm pulses did not exceed 4×10^{14} W cm^{-2}. Larger intensities of driving pulses caused strong plasma emission and a decrease of the harmonic yield, probably due to the appearance of a large number of free electrons leading to a phase mismatch between the harmonic and driving waves. Stronger ablation fluences (~10 J cm^{-2}) caused the saturation of the harmonic yield, which was also followed by a modulation of the spectra of lower-order harmonics.

The harmonic emission was analyzed using an extreme ultraviolet spectrometer composed of a vertical slit, a gold-coated cylindrical mirror, a 1200 lines/mm flat field grating, a microchannel plate, and a CCD camera. The grating separated the harmonic orders by mapping the wavelength onto the horizontal axis of the microchannel plate and the CCD camera, which recorded the intensity of harmonics on the phosphor screen of the microchannel plate.

HHG in QDs was carried out using a single-colour pump or two-colour pump of the laser-induced plasmas to determine the highest harmonic yield in different extreme ultraviolet ranges. For the two-colour pump, the fundamental at 800 nm and its second harmonic were used. A 0.2 mm thick barium borate (BBO) crystal was installed inside the vacuum chamber into the path of the 800 nm radiation to generate the second harmonic (Fig. 2a). The conversion efficiency of second-harmonic pulses ($\lambda = 400$ nm) was relatively small (~3%). Due to the small group velocity dispersion in the thin BBO crystal, the temporal overlap of the two driving pulses in the plasma area was sufficient for efficient generation of the odd and even harmonics in the longer-wavelength range of extreme ultraviolet.
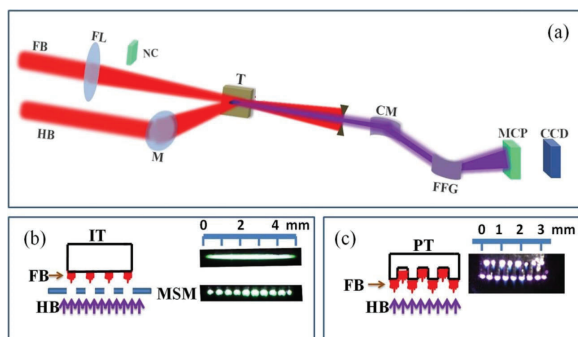

Fig. 9.14. (a) Experimental setup for HHG in laser-produced plasmas. FB, femtosecond beam; FL, focusing lens; NC, nonlinear crystal (BBO); HB, heating beam; M, mirror; T, target; CM, cylindrical mirror; FFG, flat field grating; MCP, microchannel plate; CCD, charge coupled device. (b) Formation of multi-jet plasma on the extended flat target. FB, femtosecond beam; HB, heating beam; IT, extended flat target; MSM, multi-slit mask. Insets: images of extended plasma (upper panel) and multi-jet plasma (bottom panel). (c) Formation of multi-jet plasma on the mechanically structured target. FB, femtosecond beam; HB, heating beam; PT, structured target. Inset: image of plasma jets from the structured target. Reproduced from [45] with permission from the American Institute of Physics.

The formation of quasi-phase-matching for driving and harmonic waves in laser-produced plasmas was analyzed by variation of the morphology of extended QD-containing plasmas using spatially structured heating beams. To create heterogeneous spatial heating of targets the multi-slit masks installed in front of the targets were used, which allowed

the formation of multi-jet plasmas containing different numbers of jets depending on the number of slits in the multi-slit mask (Fig. 9.14b).

Metal sulphide QD plates mechanically structured with steps of 0.3 mm distance and irradiated by a cylindrically focused heating pulse, were also used for HHG. The shape of such a target is shown in Fig. 9.14c. The depth of the grooves of the Ag_2S QD- and $Cd_{0.5}Zn_{0.5}S$ QD-containing surfaces was 2 mm. The plasma was formed on the upper and bottom parts of the target surface, as shown in the image of plasma jets. The driving pulse propagated through the plasma jets formed on the upper part of the target surface. The plasma jets formed on the bottom parts of the targets did not participate in the harmonic generation since they reach the axis of propagation of the driving beam only a few hundred nanoseconds after the beginning of the ablation when the femtosecond pulse has already passed through the plasma. This separation of the upper and bottom parts of the plasma jets has earlier allowed the formation of a nonlinear optical medium, which matches the requirements of quasi-phase-matching.

9.3.2. Single-colour pump

Harmonic spectra from QDs were analyzed at different energies of driving 800-nm, 30-fs pulses. Figures 9.15a and 9.16b show two groups of spectra generated in laser-produced plasmas containing $Cd_{0.5}Zn_{0.5}S$ and CdS QDs. Both harmonic cut-off and intensity gradually increased with an increase of the 30 fs pulse energy from 0.3 to 0.93 mJ. The deviation of the growth of harmonic cut-off on the driving pulse energy from the relation predicted by the three-step model of HHG is attributed to the saturation of harmonic yield, which also affected and saturated the intensity dependence of low harmonics. The application of pure gelatine as the ablation target did not yield similar harmonic intensities as in the case of QD-containing targets, though some weak harmonics mostly attributed to the influence of carbon ions on the HHG process appeared in the long-wavelength range of the extreme ultraviolet.

An interesting feature of the metal sulphide QD-induced harmonic spectra is that, at stronger ablation, the spectral width of harmonics becomes two to three times broader compared with those generated in the plasmas containing the monomolecular species of similar material. The intensities of the ablation and driving pulses are crucial for optimizing the HHG from metal sulphide QDs. The 1.5- to 3-fold increase of the intensity of the driving pulse led to an insignificant extension of the harmonics (Fig. 9.16), which is a sign of HHG saturation in the medium. Moreover, at relatively high femtosecond laser intensities, a decrease in the harmonic

output was observed, which can be ascribed to the phase mismatch as a result of higher free electron density.
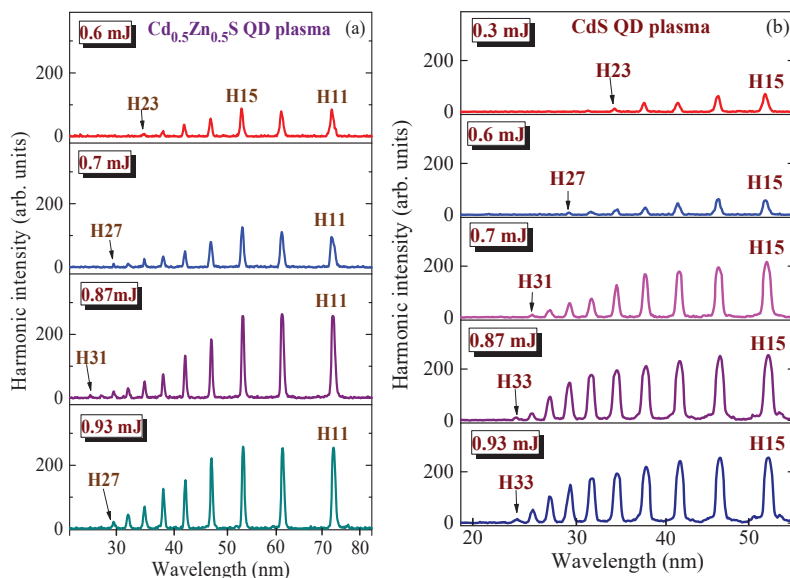

Fig. 9.15. Harmonic spectra from (a) $Cd_{0.5}Zn_{0.5}S$ and (b) CdS QD plasmas measured at different energies of driving pulses. Reproduced from [45] with permission from the American Institute of Physics.

A similar phenomenon is observed when the ablation pulse on the surface of QD-rich targets is increased above the optimal value for a harmonic generation. This reduction in harmonic intensity can be attributed to phenomena such as the fragmentation of QDs, an increase in free-electron density, and self-defocusing, similarly to earlier observed saturation of HHG in the multi-atomic systems like fullerenes.

The growth of the concentration of the harmonic emitters in the case of either QDs or single molecules plays an important role in the enhancement of HHG. The simplest way to achieve this is an increase of the heating pulse fluence, which in the discussed case was performed by increasing the pulse energy at similar geometrical conditions of ablation. Saturation of the harmonic yield in some of these cases was followed by a modulation of the spectra of lower-order harmonics. Figure 9.16 shows the harmonics generated in the Ag_2S QD plasma formed at the intensity $I =$

2×10^9 W cm^{-2} of the nanosecond heating pulses, which were almost three times stronger than the one used at optimal conditions allowing the maximal yield of harmonics.
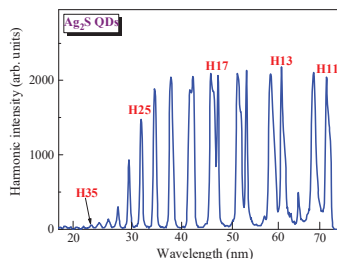

Fig. 9.16. HHG in the Ag$_2$S QD plasma formed at intensity $I = 2 \times 10^9$ W cm^{-2} of nanosecond heating pulses. Reproduced from [45] with permission from the American Institute of Physics.

Such a variation of the harmonic spectrum was mostly determined by the modulation of the fundamental spectrum. An extension of the harmonic spectral distribution toward the blue side was observed. One can see the notable modulation of the lower orders of harmonics (H11 – H19). Each of these orders was separated into two parts, which led to the appearance of the strong lobes on the shorter-wavelength side. The decrease of the driving pulse intensity by the introduction of a positive and negative chirp in incompletely compressed pulses using the tuning of the grating in the compressor stage of the used laser caused the disappearance of the modulation and broadening of harmonics. No significant influence of self-phase modulation on the spectral distribution of harmonics was expected at these experimental conditions [relatively low-density plasma $(3 \times 10^{17}$ cm$^{-3})$ and moderate laser intensities], which restrict the possibility of the influence of a strongly ionized medium on the phase characteristics of the driving and generating waves.

A highly ionized medium, with an electron density higher in the center than in the outer region, acts as a negative lens, leading to a defocusing of the laser beam in plasma and hence to a reduction in the effective harmonic generation volume. In addition, the rapidly ionizing medium modifies the temporal structure of the femtosecond laser pulse. This process can be responsible for the broadening and splitting of the harmonics (Fig. 9.16).

The influence of the long trajectory of accelerated electrons in the laser-produced plasma can also play important role in the appearance of

different wavelength components of harmonic spectra. This process has been analyzed in [46] where the images of harmonic distribution have demonstrated the components induced by long trajectories of electrons, which were clearly seen out of the axial line of harmonic distribution. Those measurements were taken at the conditions allowing the analysis of the divergence of harmonics. Notice the prevailing appearance of the longer-wavelength component of harmonics over the shorter-wavelength one. These signatures of different quantum paths show that rings attributed to long electron trajectory appear exclusively when the plasma is placed before the focus, in accordance with theoretical predictions discussed in [47] and experimental observations in gas HHG [48,49].

9.3.3. Two-colour pump

Below we address the two-colour pump of QD plasma. The orthogonally polarized second field in the case of a two-colour pump participates in the modification of the trajectory of the accelerated electrons from being two-dimensional to three-dimensional, which may lead to a removal of the medium symmetry. This two-colour pump-induced enhancement of harmonics has earlier been realized through generation of 400 nm radiation in a separate channel with further mixing with 800 nm radiation in gases, as well as through direct generation of the second harmonic in thin BBO crystals followed by focusing of two co-propagating beams in gases and plasmas [50-52].

Here we discuss HHG in the case of the single-color pump (Fig. 9.17, upper panel) and two-colour pump (Fig. 9.17, bottom panel) using Ag_2S QDs. When applying a 0.4-mm thick BBO for second harmonic generation (400 nm) some high-order harmonics (H12, H16, H20) were notably weaker than other odd and even harmonics of the fundamental radiation due to insufficient temporal overlap of both waves in the plasma region. This heterogeneity in the harmonic intensity distribution was caused by the delay between 800 and 400 nm waves introduced by group velocity dispersion in BBO. The application of a thinner crystal (0.2 mm) allowed the generation of a relatively homogeneous intensity distribution of all harmonics, though the odd harmonics of 400-nm radiation were still stronger than other harmonics (Fig. 9.17, bottom panel), since even this thin crystal caused an ~40 fs delay between the maxima of the two 30 fs driving pulses. Correspondingly, the pulse overlap in the plasma region was relatively small. Nevertheless, even this weak overlap of both 400 and 800 nm pulses rated as 1:30 by its energies was sufficient for a strong modification of the harmonic spectrum.
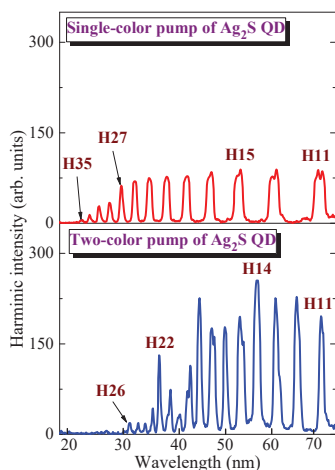
Fig. 9.17. Comparison of HHG in the case of (a) single-colour pump and (b) two-colour pump of Ag2S QD laser-produced plasma using a 0.2 mm thick BBO. Reproduced from [45] with permission from the American Institute of Physics.

Two peculiarities were observed during these comparative studies. In the case of two-colour pump the harmonic cut-off decreased compared with single-colour pump (H26 and H35, respectively, see bottom and upper panels of Fig. 9.17), probably due to the application of the shorter wavelength component of the pumping radiation. In the case of single-colour pump, the harmonics were broadened and each of the lower orders had a shorter-wavelength component (upper panel) due to self-modulation of the driving pulse in the plasma region. Meanwhile, the harmonics in two-colour pump were spectrally narrower.

The insertion of thin BBO crystal in the path of driving pulse led to some important changes in the plasma-laser interaction. The orthogonally polarized beam of second harmonic modifies the trajectory of accelerated electron. Probably, the relatively weak second harmonic does not play important role in the ionization dynamics. Thus the modification of the trajectory of electrons, as well as the decrease of the role of longer trajectory in harmonic yield, causes the enhancement of the yield of harmonics at relatively small addition of the second field. Since the joint influence of two trajectories of electrons may result in the broadening (and splitting) of harmonic spectrum, the diminishing of the role of the long

trajectory in the case of two-colour pump excludes, to some extent, this mechanism of harmonic broadening and splitting. In other words, the harmonics in two-colour configuration become as narrow, as one can expect from the initial spectrum of the driving field.

Finally, it is worth noticing that the 3% conversion efficiency into the second harmonic in two-colour pump experiments excludes its strong influence on ionization dynamics and suggests that the role of the second harmonic is a modification of electron trajectories during the HHG process, which can be considered as the main effect induced by the 400 nm field.

9.3.4. Structured plasma

Below we address HHG in spatially structured plasmas containing metal sulphide QDs for the realization of quasi-phase-matching between the driving and harmonic waves. This concept may successfully be applied when the absorption of generated harmonics in the extreme ultraviolet region is small compared to the enhancement of this radiation due to quasi-phase-matching. Quasi-phase matching has previously been demonstrated in gaseous [53,54] and plasma [55] media. One of the approaches here is the division of an extended medium into groups of narrow media separated by a vacuum. In these parts, the conditions of harmonics enhancement are maintained along the whole coherence length, i.e., until the phase difference $\Delta\varphi$ between converting and converted waves becomes equal to π.

In the case of laser-produced plasmas produced on the surfaces of bulk metals (Ag, In, etc.), the conditions of quasi-phase-matching are determined by the presence of a suitable concentration of free electrons in a single jet of multi-jet plasmas. One can expect the fulfilment of the basic rule for quasi-phase-matching at the conditions when the plasma dispersion assumes to be a dominant mechanism of phase mismatch, which stipulates the relation between the jet sizes and maximally enhanced harmonic ($H_{qpm} \times l_{jet} \propto const$). The ablation of bulk materials with spatially structured heating pulse allows the formation of spatially structured plasma where the boundaries of jets distinguish the areas of presence and absence of electrons. This difference in electron concentrations inside the plasma jet and the inter-jet space allows the formation of quasi-phase-matching for the group of harmonics and the driving radiation.
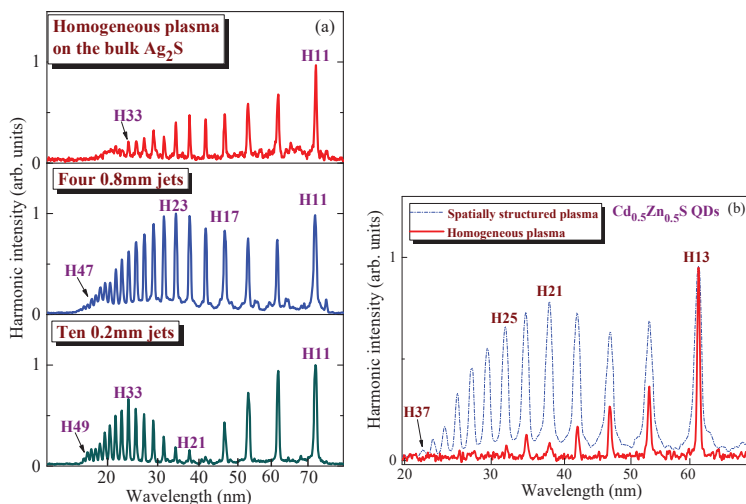
Fig. 9.18. Comparison of quasi-phase matching in the case of ablation of (a) bulk (Ag_2S) and (b) QD ($Cd_{0.5}Zn_{0.5}S$) targets. (a) Upper panel shows the gradually decreased harmonics from extended plasma produced on the surface of bulk Ag_2S target. Application of multi-slit masks with different sizes of slits (0.8 and 0.2 mm) led to generation of the groups of enhanced harmonics centred at around H23 (middle panel) and H33 (bottom panel). (b) Solid curve shows the gradually decreased harmonic spectrum in the case of extended plasma produced on the target containing $Cd_{0.5}Zn_{0.5}S$ QDs. Dash-dotted curve demonstrates the quasi-phase matching conditions for the group of harmonics at around H21 in the case of four 0.8 mm long jets. Reproduced from [45] with permission from the American Institute of Physics.

The results presented in Fig. 9.18a show the formation of quasi-phase-matching conditions in the case of Ag_2S bulk target ablation via multi-slit mask. One can clearly see a difference in the envelopes of the harmonics distribution in the cases of an extended flat (upper panel) and spatially structured plasma (lower two panels). An enhancement of higher orders in the case of multi-jet plasmas compared to the extended flat plasma is observed. Notice that higher harmonics, i.e., those above the 33rd order, were barely seen in the case of the extended plasma. The enhancement factor of H41 in the case of multi-jet plasmas was calculated to be close to 30×. Another important feature of this process in the case of multi-jet

plasmas produced on the surface of bulk material is the relatively narrow envelope of the group of enhanced harmonics comprising nine harmonic orders (H25 – H41, lowest panel).

A similar extreme ultraviolet intensity pattern appeared in the case of ablation of the mixture of $Cd_{0.5}Zn_{0.5}S$ QDs (see scheme shown in Fig. 9.14b) and gelatine with and without the application of multi-slit mask (Fig. 9.18b). Ablation of such targets at relatively high fluence allowing the formation of dense plasma probably did not follow with the presence of a large number of free electrons. Another reason of the diminished role of quasi-phase-matching in the former case is the observation of lower cut-off with regard to the ablated bulk Ag_2S. Quasi-phase matching in plasmas differs from the plateau-like distribution of harmonics mostly when the constituents of the plasma allow the generation of harmonic orders greater than forty or even fifty. Meantime, the studied QDs did not demonstrate the extended cut-off harmonics, thus diminishing the chances of formation of quasi-phase-matching conditions (compare the dash-dotted curve of Fig. 9.18b and the middle panel of Fig. 9.18a).

The scheme of quasi-phase-matching where the driving femtosecond beam interacts only with the top surface of a mechanically structured target (Fig. 9.14c) did not show a modulation of the intensity envelope of the generated harmonics similar to the one presented in Fig. 9.18b. Though the conditions of laser-produced plasma modulation were preserved for the propagating beam, the phase modulation between driving and harmonic waves was insufficient to allow quasi-phase-matching in the shorter wavelength region of the extreme ultraviolet, probably due to the influence of free electrons appearing in the area between plasma jets.

9.3.5. Discussion

The interaction of multi-particle species with a strong laser field was firstly analyzed in the media comprising the clusters containing a few thousand of atoms of noble gases [56,57]. The specific properties of clusters, quantum dots, and nanoparticles refer to those, which allow achieving the enhanced yield of harmonics from the multi-particle medium compared with an atoms-containing medium. In the case of gas clusters, those include the involvement of different channels of harmonic generation, particularly, the ionization and recombination to the same ion of the cluster, to the neighbouring ions, and to the whole cluster. These processes differ from the case of atoms and may either enhance or diminish the high-order nonlinear optical response of the medium depending on the sizes of nanoparticles. Meanwhile, the enhanced cross-

section of recombination of the accelerated electron and parent particle may naturally lead to the growth of the harmonic yield. In the case of significantly larger parent particles containing thousands to millions of atoms, the larger sizes of former species decrease the probability of missing the interaction with the accelerated electron, which returns during the second half of the cycle towards the emitters of electrons. In other words, large sizes of parent particles allow capturing the returning electron with a higher probability. However, there are some limits in this concept, which point out the existence of an optimal size of multi-particles associated with the maximal yield of harmonic emission.

The main advantage of the HHG in laser-produced plasmas from QDs is the higher efficiency compared to a gas jet and a bulk target. The harmonic generation efficiency was analyzed in the case of ablated CdS bulk plate, CdS QDs, as well as compared with HHG from argon gas. Those studies have demonstrated a 3- to 5-fold stronger harmonic yield in the latter case. Present experiments using metal sulphide-containing plasmas also showed a stronger harmonic yield from ablated CdS and CdS QD targets compared to the argon gas at similar concentrations of gas and plasma media. These comparative experiments were carried out using a narrow gas flow from a stainless steel needle with an inner diameter of 0.3 mm and the CdS and CdS QD plasma plumes of the sizes of 0.3 mm at similar energies of the driving pulses. The 4× (in the case of ablated bulk CdS) and 10× (in the case of ablated CdS QDs) prevalence of the conversion efficiency from plasma media compared with the gas medium was observed at similar conditions of experiments.

Ablation by nanosecond laser pulse most probably would lead to some disintegration of QDs due to avalanche ionization and Joule heating, leading to the presence of both QDs and single molecular species in the plasma plume. It is not clear if HHG solely happens from neutral QDs and nanoparticles/clusters generated due to ablation or it happens in charged species and ions. The electron density of such plasmas has never been measured. The work function for CdS QDs is about 5.2 eV. For Ti:sapphire laser pulses at 800 nm wavelength and the energy of quanta 1.55 eV this would mean essentially four-photon ionization.

Most probably HHG, in that case, can be considered as a sum of harmonic emissions from different emitters. To study the integrity of QDs in the plasma plume, the plasma conditions were optimized for maximal harmonic yield using the CdS QD target. Then the plasma debris was deposited on a fused silica substrate placed near the target. The TEM analysis of debris showed that the deposition contains the QDs with approximately the same sizes as the original species (Fig. 9.13b). This

result suggests that, for the low-excitation regime of plasma formation (i.e., for heating pulse intensity of about 8×10^8 W cm^{-2}), the ablated QDs keep their morphology within the plasma until the intense femtosecond pump arrives in the area of interaction.

The discussed observations give a rough pattern of the ablation and HHG from QD targets. The material around the QDs is dried gelatine, which has a lower ablation threshold than metal sulphide materials. Therefore, the gelatine starts to ablate at relatively low intensities, carrying QDs with it, resulting in the lower heating pulse intensity required for the ablation and evaporation of the target. It was found that the HHG from metal sulphide multi-atomic particles started to be efficient at considerably smaller heating pulse intensities [$(3–6)\times10^8$ W cm^{-2}] compared with the case of bulk metal sulphides [$(1–3)\times10^{10}$ W cm^{-2}]. This range of optimal intensities ($(3-6)\times10^8$ W cm^{-2}) corresponds to a fluence of $1.5 – 3$ J cm^{-2} in the case of 5 ns pulses. The spectrum broadening and splitting are observed at the fluence 10 J cm^{-2} (Fig. 9.16), which corresponds to the intensity of 2×10^9 W cm^{-2} for 5 ns heating pulses.

These studies showed the modulation of the lower orders of harmonics leading to the formation of the blue-shifted components. This process can be attributed to the self-phase modulation and chirping of the fundamental radiation propagating through the dense nonlinear medium. The decrease of the driving pulse intensity significantly lowered the modulation of harmonic spectra. The plasma density was estimated to be 3×10^{17} cm^{-3}. Usually, self-phase modulation is related to a nonlinear response of the neutral medium. Once one assumes ionization nonlinearity originating from the highly nonlinear field ionization process, the nonlinear interaction will lead first of all to a strong blue shift in the spectrum of the laser pulse. Meanwhile, the interesting structure of the spectrum in Fig. 9.16 is unlikely can be explained just by self-phase modulation induced by propagating driving pulses and plasma dispersion. Further studies require for determining the origin of such modulation of generating spectra. For example, the measurement of the spectrum of the transmitted fundamental pulse would unequivocally determine the relative role of self-phase modulation and ionization nonlinearity in the HHG spectrum evolution.

The process of harmonic broadening and splitting most often was reported as a consequence of using driving pulses possessing intensities above some threshold level. Meanwhile, plasma plume is a specific and more sophisticated target than gas, which initially possesses some amount of free electrons, which themselves may cause the modulation of the harmonic spectrum. This means that the spectral features of HHG depend not only on the intensity of the driving pulses but also on the intensity of

heating pulses. The observations of strong modulation and splitting of lower-order harmonics confirm this assumption.

Notice that almost no harmonics were generated in the case of pure gelatine ablation at similar conditions of HHG experiments. Only a few extremely weak lowest order harmonics from the gelatine plasma were observed at relatively strong ablation conditions (i.e. at the heating pulse intensity of 3×10^{10} W cm^{-2}). The harmonic generation efficiency, in that case, was calculated to be not more than 6×10^{-7}, while the same parameter in the case of QD-contained plasmas was almost two orders of magnitude larger (4×10^{-5}).

The quasi-phase matching concept used in discussed study broadens the range of applications of the specific relations between the fundamental wave and the waves of harmonics in different regions of the extreme ultraviolet. The basics of this concept were initially demonstrated in the case of gas media and further developed during the last few years while using plasma plumes. The crucial point for the realization of quasi-phase-matching in the latter medium is a formation of such a plasma configuration that allows the manipulation between the phases of the group of harmonics and fundamental radiation, leading to the tuning of the phase matching between them during propagation through the group of the plasma jets possessing variable spatial modulation. One of the most useful techniques to form such conditions is the separation of the extended plasma produced during focusing of the heating pulse by the cylindrical lens into a group of equidistant plasma jets. Such multi-jet plasma allows a significant enhancement of a group of harmonics, while other harmonics become suppressed. Another method of multi-jet plasma formation is the application of the perforated ablating target.

The discussed studies show that spatially modulated plasma containing quantum dots can also be considered as the efficient medium for the demonstration of the quasi-phase-matching concept (Fig. 9.18b). The enhancement of harmonics exceeding a factor of 10, especially for those above the 25th order (compare the dotted and solid curves in this spectral range), clearly points out the decisive role of the optimized relation between the phases of those harmonics and the driving pulse propagating through the QD-containing plasma. Notice that neither strong harmonics nor quasi-phase-matching effect was observed in the case of ablation of the pure gelatine.

The concepts of plasma high-order harmonic generation in laser-produced plasmas, quasi-phase-matching in multi-jet plasma, the two-colour pump of plasma, and harmonic enhancement in nanoparticle/quantum dot plasmas are not new. However, it was the first time when all those

concepts of the amendment of harmonic generation from QDs were combined in a single set of studies. The physics behind the observed difference of harmonic emission from monomers and multi-particle associates is as follows. Stronger harmonic flux from QDs with regard to the monomers could be attributed to better conditions of the recombination of accelerated electrons with harmonic emitters in the case of metal sulphide QDs ablation and spreading, as well as to specific properties of QDs, which, as was mentioned, include the ionization and recombination to the same ion of the cluster, to the neighbouring ions, and to the whole cluster. The effectiveness of HHG in the presence of such structures can be attributed to the plasmonic properties of nanoparticles and quantum dots leading to the involvement of the local fields in the enhancement of the nonlinear optical response of the medium.

One can assume that quantum dots are small-sized nanoparticles, which at specific conditions of excitation can demonstrate the quantum effect when local fields can enhance the nonlinear optical response of the medium. The comparison of HHG using QDs and nanoparticles of the same elemental consistency is a straightforward way to judge the role of the quantum effect. However, these comparative experiments can be barely realized due to experimental obstacles. The synthesis of larger-sized metal sulphide structures was problematic due to sedimentation prior to aggregation of the large particles (>10 nm). Meanwhile, the synthesized particles had sizes of 2-3 nm, which ideally matched the appearance of the structures allowing observation of the quantum properties and local field enhancement. Thus one can expect an influence of these processes on the HHG during discussed experiments.

There are still a lot of issues that have to be clarified in the case of the application of the used QDs for HHG. It remains a puzzle how the chemical composition, crystal structure, and spatial scales of the QDs affect the HHG efficiency and the cut-off frequency. There remain also other questions regarding the charge state of this plasma medium, which could be resolved only by using time-of-flight mass spectrometry. Particularly, are the QDs charged before the pump pulse comes? How many electrons are ionized under the high-intensity pump pulse from each QD? What are the exact ionization potentials of the chosen QDs and how do they affect the HHG cut off?

References to Chapter 9

[1]   I.J. Kim, G. H. Lee, S. B. Park, Y. S. Lee, T. K. Kim, C. H. Nam, T. Mocek, K. Jakubczak, Generation of submicrojoule high harmonics using a long gas jet in a two-color laser field, Appl. Phys. Lett. 92 (2) (2008) 021125.

[2]   R. A. Ganeev, G. S. Boltaev, K. Zhang, P. V. Redkin, S. K. Maurya, M. Venkatesh, Z. Yu, V. V. Kim, C. Guo, Role of carbon clusters in high-order harmonic generation in graphite plasmas, OSA Continuum 2 (5) (2019) 1510-1523.

[3]   I. Lopez-Quintas, M. Oujja, M. Sanz, M. Martin, R. A. Ganeev, M. Castillejo, Low-order harmonic generation in nanosecond laser ablation plasmas of carbon containing materials, Appl. Surf. Sci. 278 (2013) 33-37.

[4]   Y. Akiyama, K. Midorikawa, Y. Matsunawa, Y. Nagata, M. Obara, H. Tashiro, K. Toyoda, Generation of high-order harmonic using laser-produced rare-gas-like ions, Phys. Rev. Lett. 69 (15) (1992) 2176-2179.

[5]   X. W. Li, W. F. Wei, J. Wu, S. L. Jia, A. C. Qiu, The influence of spot size on the expansion dynamics of nanosecond-laser-produced copper plasmas in atmosphere, J. Appl. Phys. 113 (24) (2013) 243304.

[6]   W. R. Creasy, J. T. Brenna, Large carbon cluster ion formation by laser ablation of polyimide and graphite, Chem. Phys. 126 (2-3) (1988) 453-468.

[7]   R. A. Ganeev, M. Suzuki, M. Baba, H. Kuroda, T. Ozaki, Strong resonance enhancement of a single harmonic generated in extreme ultraviolet range, Opt. Lett. 31 (11) (2006) 1699-1701.

[8]   H. T. Kim, I. J. Kim, D. G. Lee, K.-H. Hong, Y. S. Lee, V. Tosa, C. H. Nam, Optimization of high-order harmonic brightness in the space domains, Phys. Rev. A 69 (3) (2004) 031805.

[9]   R. A. Ganeev, M. Suzuki, P. V. Redkin, M. Baba, H. Kuroda, Variable pattern of high harmonic spectra from a laser-produced plasma by using the chirped pulses of narrow-bandwidth radiation, Phys. Rev. A 76 (2) (2007) 023832.

[10] A.M. Rubenchik, M. D. Feit, M. D. Perry, J. T. Larsen, Numerical simulation of ultra-short laser pulse energy deposition and transport for material processing, Appl. Surf. Sci. 127-129 (2) (1998) 193-198.

[11] E. S. Toma, P. Antoine, A. de Bohan, H. G. Muller, Resonance-enhanced high-harmonic generation, J. Phys. B 32 (1999) 5843-5852.

[12] V. Veniard, R. Taıeb, A. Maquet, Atomic clusters submitted to an intense short laser pulse: A density-functional approach, Phys. Rev. A 65 (1) (2001) 013202.

[13] F. Bourquard, A.-S. Loir, C. Donnet, F. Garrelie, n situ diagnostic of the size distribution of nanoparticles generated by ultrashort pulsed laser ablation in vacuum, n situ diagnostic of the size distribution of nanoparticles generated by ultrashort pulsed laser ablation in vacuum, Appl. Phys. Lett. 104 (10) (2014) 104101.

[14] T. E. Itina, K. Gouriet, L. V. Zhigilei, S. Noël, J. Hermann, M. Sentis, Mechanisms of small clusters production by short and ultra-short laser ablation, Appl. Surf. Sci. 253 (19) (2007) 7656-7666.

[15] H. O. Jeschke, M. E. Garcia, K. H. Bennemann, Theory for the ultrafast ablation of graphite films, Phys. Rev. Lett. 87 (1) (2001) 015003.

[16] L. B. Elouga Bom, Y. Pertot, V. R. Bhardwaj, T. Ozaki, Multi-μJ coherent extreme ultraviolet source generated from carbon using the plasma harmonic method, Opt. Express 19 (4) (2011) 3077-3085.

[17] M. López-Arias, M. Oujja, M. Sanz, R. de Nalda, R. A. Ganeev, M. Castillejo, Generation of low-order harmonics in laser ablation plasmas, Molec. Phys. 110 (15-16) (2012) 1651-1657.

[18] R. A. Ganeev, Involvement of small carbon clusters in the enhancement of high-order harmonic generation of ultrashort pulses in the plasmas produced during ablation of carbon-contained nanoparticles, Opt. Spectrosc. 123 (3) (2017) 351-364.

[19] M. Oujja, J. G. Izquierdo, L. Bañares, R. de Nalda, M. Castillejo, Observation of middle-sized metal clusters in femtosecond laser ablation plasmas through nonlinear optics, Phys. Chem. Chem. Phys. 20 (25) (2018) 16956-16965.

[20] R. A. Ganeev, C. Hutchison, T. Witting, F. Frank, W. A. Okell, A. Zaïr, S. Weber, P. V. Redkin, D. Y. Lei, T. Roschuk, S. A. Maier, I. López-Quintás, M. Martín, M. Castillejo, J. W. G. Tisch, J. P. Marangos, High-order harmonic generation in graphite plasma plumes using ultrashort laser pulses: a systematic analysis of harmonic radiation and plasma conditions, J. Phys. B 45 (16) (2012) 165402.

[21] A.Kaplan, M. Lenner, C. Huchon, R. E. Palmer, Nonlinearity and time-resolved studies of ion emission in ultrafast laser ablation of graphite, Appl. Phys. A 92 (4) (2008) 999-1004.

[22] R. de Nalda, M. Lopez-Arias, M. Sanz, M. Oujja, M. Castillejo, Harmonic generation in ablation plasmas of wide bandgap semiconductors, Phys. Chem. Chem. Phys. 13 (22) (2011) 10755-10761.

[23] L. W. Liu, S. Hu, Y. P. Dou, T. H. Liu, J. Q. Lin, Y. Wang, Nonlinear optical properties of near-infrared region Ag2S quantum dots pumped by nanosecond laser pulses, Beilstein J. Nanotechnol. 6 (1) (2015)1781-1787.

[24] G. S. Boltaev, B. Sobirov, S. Reyimbaev, H. Sherniyozov, T. Usmanov, M. S. Smirnov, O. V. Ovchinnikov, I. G. Grevtseva, T. S. Kondratenko, H. S. Shihaliev, R. A. Ganeev, Nonlinear optical characterization of colloidal solutions containing dye and Ag_2S quantum dot associates, Appl. Phys. A 122 (2016) 999.

[25] P. Kumbhakar, M. Chattopadhyay, A. K. Mitra, Nonlinear optical properties of doped ZnS quantum dots, Int. J. Nanosci. 10 (1) (2011) 177-180.

[26] Z. Zeng, C. S. Garoufalis, A. F. Terzis, S. Baskoutas, Linear and nonlinear optical properties of ZnO/ZnS and ZnS/ZnO core shell quantum dots: Effects of shell thickness, impurity, and dielectric environment, J. Appl. Phys. 114 (2) (2013) 023510.

[27] H. Linnenbank, Y. Grynko, J. Förstner, S. Linden, Second harmonic generation spectroscopy on hybrid plasmonic/dielectric nanoantennas, Light: Sci. Appl. 5 (1) (2016) e16013.

[28] R. B. Martin, M. J. Meziani, P. Pathak, J. E. Riggs, D. E. Cook, S. Perera, Y.-P. Sun, Optical limiting of silver-containing nanoparticles, Opt. Mater. 29 (7) (2007) 788-793.

[29] R. Karimzadeh, H. Aleali, N. Mansour, Thermal nonlinear refraction properties of Ag2S semiconductor nanocrystals with its application as a low power optical limiter, Opt. Commun. 284 (9) (2011) 2370-2375.

[30] O. V. Ovchinnikov, M. S. Smirnov, A. S. Perepelitsa, T. S. Shatskikh, B. I. Shapiro, Optical power limiting in ensembles of colloidal Ag2S quantum dots, Quantum Electron. 45 (12) (2015) 1143-1150.

[31] R. A. Ganeev, G. S. Boltaev, V. V. Kim, K. Zhang, A. I. Zvyagin, M. S. Smirnov, O. V. Ovchinnikov, P. V. Redkin, M. Wöstmann, H. Zacharias, C. Guo, Effective high-order harmonic generation from metal sulfide quantum dots, Opt. Express 26 (26) (2018) 35013-35025.

[32] C. Hutchison, R. A. Ganeev, T. Witting, F. Frank, W. A. Okell, J. W. G. Tisch, J. P. Marangos, Stable generation of high-order harmonics of femtosecond laser radiation from laser produced plasma plumes at 1 kHz pulse repetition rate, Opt. Lett. 37 (11) (2012) 2064-2066.

[33] M. F. Ciappina, S. S. Aćimović, T. Shaaran, J. Biegert, R. Quidant, M. Lewenstein, Enhancement of high harmonic generation by confining electron motion in plasmonic nanostrutures, Opt. Express 20 (24) (2012) 26262-26274.

[34] J. R. Vázquez de Aldana, L. Roso, High-order harmonic generation in atomic clusters with a twodimensional model, J. Opt. Soc. Am. B 18 (3) (2011) 325-330.

[35] H. Ruf, C. Handschin, R. Cireasa, N. Thiré, A. Ferré, S. Petit, D. Descamps, E. Mével, E. Constant, V. Blanchet, B. Fabre, Y. Mairesse, Inhomogeneous high harmonic generation in krypton clusters, Phys. Rev. Lett. 110 (8) (2013) 083902.

[36] H. Singhal, V. Arora, B. S. Rao, P. A. Naik, U. Chakravarty, R. A. Khan, and P. D. Gupta, Dependence of high-order harmonic intensity on the length of preformed plasma plumes, Phys. Rev. A 79 (2) (2009) 023807.

[37] R. A. Ganeev, V. V. Strelkov, C. Hutchison, A. Zaïr, D. Kilbane, M. A. Khokhlova J. P. Marangos, Experimental and theoretical studies of two-color pump resonance-induced enhancement of odd and even harmonics from a tin plasma, Phys. Rev. A 85 (2) (2012) 023832.

[38] Y. Pertot, S. Chen, S. D. Khan, L. B. Elouga Bom, T. Ozaki, Z. Chang, Generation of continuum high-order harmonics from carbon plasma using double optical gating, J. Phys. B 45 (7) (2012) 074017.

[39] S. Haessler, V. Strelkov, L. B. Elouga Bom, M. Khokhlova, O. Gobert, J.-F. Hergott, F. Lepetit, M. Perdrix, T. Ozaki, P. Salières, Phase distortions of attosecond pulses produced by resonance-enhanced high harmonic generation, New J. Phys. 15 (1) (2013) 013051.

[40] N. Rosenthal, G. Marcus, Discriminating between the role of phase matching and that of the single-atom response in resonance plasma-plume high-order harmonic generation, Phys. Rev. Lett. 115 (13) (2015) 133901.

[41] M. A. Fareed, V. V. Strelkov, N. Thiré, S. Mondal, B. E. Schmidt, F. Légaré, T. Ozaki, High-order harmonic generation from the dressed autoionizing states, Nature Commun. 8 (2017) 16061.

[42] M. Wöstmann, L. Splitthoff, H. Zacharias, Control of quasi-phase-matching of high-harmonics in a spatially structured plasma, Opt. Express 26 (11) (2018) 14524-14537.

[43] Z. Abdelrahman, M. A. Khohlova, D. J. Walke, T. Witting, A. Zair, V. V. Strelkov, J. P. Marangos, J. W. G. Tisch, Chirp-control of resonant high-order harmonic generation in indium ablation plumes driven by intense few-cycle laser pulses, Opt. Express 26 (12) (2018) 15745-15758.

[44] M. A. Fareed, V. V. Strelkov, M. Singh, N. Thiré, S. Mondal, B. E. Schmidt, F. Légaré, T. Ozaki, Harmonic generation from neutral manganese atoms in the vicinity of the giant autoionization resonance, Phys. Rev. Lett. 121 (2) (2018) 023201.

[45] R. A. Ganeev, G. S. Boltaev, V. V. Kim, M. Venkatesh, A. I. Zvyagin, M. S. Smirnov, O. V. Ovchinnikov, M. Wöstmann, H. Zacharias, C. Guo, High-order harmonic generation using quasi-phase matching and two-color pump of the plasmas containing molecular and alloyed metal sulfide quantum dots, J. Appl. Phys. 126 (19) (2019) 193103.

[46] R. A. Ganeev, C. Hutchison, T. Siegel, A. Zaïr, J. P. Marangos, Quantum path signatures in harmonic spectra from metal plasma, Phys. Rev. A 83 (6) (2011) 063837.

[47] M. B. Gaarde, F. Salin, E. Constant, P. Balcou, K. J. Schafer, K. C. Kulander, A. L'Huillier, Spatiotemporal separation of high harmonic radiation into two quantum path components, Phys. Rev. A 59 (2) (1999) 1367.

[48] A.Zaïr, M. Holler, A. Guandalini, F. Schapper, J. Biegert, L. Gallmann, U. Keller, A. S. Wyatt, A. Monmayrant, I. A. Walmsley, E. Cormier, T. Auguste, J. P. Caumes, P. Salières, Quantum path interferences in high-order harmonic generation, Phys. Rev. Lett. 100 (14) (2008) 143902 (2008).

[49] M. Holler, A. Zaïr, F. Schapper, T. Auguste, E. Cormier, A. Wyatt, A. Monmayrant, I. A. Walmsley, L. Gallmann, P. Salières, and U. Keller, Ionization effects on spectral signatures of quantum-path interference in high-harmonic generation, Opt. Express 17 (7) (2009) 5716-5722.

[50] I.J. Kim, C. M. Kim, H. T. Kim, G. H. Lee, Y. S. Lee, J. Y. Park, D. J. Cho, C. H. Nam, Highly efficient high-harmonic generation in an orthogonally polarized two-color laser field, Phys. Rev. Lett. 94 (24) (2005) 243901.

[51] J. Mauritsson, P. Johnsson, E. Gustafsson, A. L'Huillier, K. J. Schafer, M. B. Gaarde, Attosecond pulse trains generated using two color laser fields, Phys. Rev. Lett. 97 (1) (2006) 013001.

[52] R. A. Ganeev, H. Singhal, P. A. Naik, I. A. Kulagin, P. V. Redkin, J. A. Chakera, M. Tayyab, R. A. Khan, P. D. Gupta, Enhancement of high-order harmonic generation using two-color pump in plasma plumes, Phys. Rev. A 80 (3) (2009) 033845.

[53] J. Seres, V. S. Yakovlev, E. Seres, C. H. Streli, P. Wobrauschek, C. H. Spielmann, F. Krausz, Coherent superposition of laser-driven soft-X-ray harmonics from successive sources, Nature Phys. 3 (2007) 878-883.

[54] A.Pirri, C. Corsi, M. Bellini, Enhancing the yield of high-order harmonics with an array of gas jets, Phys. Rev. A 78 (1) (2008) 011801.

[55] R. A. Ganeev, M. Suzuki, H. Kuroda, Quasi-phase-matching of high-order harmonics in multiple plasma jets, Phys. Rev. A 89 (3) (2014) 033821.

[56] T. D. Donnelly, T. Ditmire, K. Neuman, M. D. Perry, R. W. Falcone, High-order harmonic generation in atom clusters, Phys. Rev. Lett. 76 (4) (1996) 2472.

[57] C. Vozzi, M. Nisoli, J.-P. Caumes, G. Sansone, S. Stagira, S. De Silvestri, M. Vecchiocattivi, D. Bassi, M. Pascolini, L. Poletto, P. Villoresi, G. Tondello, Cluster effects in high-order harmonics generated by ultrashort light pulses, Appl. Phys. Lett. 86 (11) (2005) 111121.

SUMMARY

In this book, we discussed various subjects related to the nonlinear optics of nanostructured materials. We analyzed recent studies of large molecules, clusters, quantum dots, and nanoparticles as media for the demonstration of the morphological, optical, and nonlinear optical properties of nanostructured systems. To summarize the main achievements described in the present book, we consider each species involved in discussed studies.

Dyes. We have analyzed the nonlinear absorption of a few dyes using short (40 ps) and long (10 ns) laser pulses. The two-photon absorption and saturated absorption of the dyes of different classes (thiazine (thionine), xanthene (erythrosine), and carbocyanine (3,3'-di-(γ-sulfopropyl)-4,4',5,5'-dibenzo-9-ethylthiacarbocyaninebetaine pyridinium salt, DEC)) were measured at the wavelengths of 1064 and 532 nm. The concurrence of saturable absorption (SA) and two-photon absorption (2PA) was analyzed and various models of SA were compared. The reverse saturable absorption (RSA) plays an insignificant role compared with 2PA. Thus most of the discussed studies in dyes can be interpreted as the manifestation of 2PA or SA+2PA rather than RSA or SA+RSA processes. The processes of 2PA could be useful for optical limiting. In the materials with a strong nonlinear effect, such as dyes, the absorption of light increases with intensity such that beyond a certain input intensity the output intensity approaches a constant value.

Thin films. The comparative study of the third-order nonlinear optical processes in thin perovskite films using short infrared pulses was discussed. The perovskite films possess strong nonlinear absorption compared with the highest reported values for other thin structures. We have discussed the observation of photoluminescence (PL) emission from MAPbBr$_3$ film and analyzed the nonlinear optical origin of this process in the case of 800 nm pulses. In particular, we analyzed studies of the γ and β of MAPbBr$_3$, MAPbCl$_3$, and MAPbI$_3$ thin (~200 nm) films using 40 fs, 800 nm pulses. Those films have demonstrated large values of nonlinear absorption coefficients (up to 5×10^{-7} cm W^{-1}) and moderate values of nonlinear refractive indices ($\leq 3\times10^{-12}$ cm^2 W^{-1}). The values of nonlinear absorption coefficients are comparable and even higher than the best-reported data for thin films, suggesting that organometallic perovskites are

promising materials for optical switching, optical limiting, and bistability applications. SA and TPA in the case of the MAPbI$_3$ film demonstrated both positive and negative nonlinear absorption. The results using different perovskites can be interpreted as the manifestation of 2PA or SA+2PA processes in the case of 40 fs pulses. The processes of 2PA in perovskites could be useful for optical limiting. PL from MAPbBr$_3$ film demonstrated the quadratic dependence of emission intensity on the intensity of 800 nm probe pulse, thus showing the crucial role of 2PA in this process. Those studies have shown that strong nonlinear optical properties, especially nonlinear absorption, of some CH$_3$NH$_3$PbX$_3$ perovskites can fulfil the potential for using these compounds in optoelectronics. The discussed studies revealed large (compared to newly emerged all-inorganic perovskites) nonlinear absorption in three films. Those values are in the upper range of reported data for 2PA absorption coefficients (10^{-6} to 10^{-8} cm W^{-1}). As for the nonlinear refraction related to the electronic Kerr effect, this process was rarely observed in the case of MAPbX$_3$ perovskites, contrary to all-inorganic species, such as CsPbX$_3$. We discussed the measurements of nonlinear refraction in two perovskites, with γ in the range of 10^{-12} cm^2 W^{-1}. Notice that these parameters were one to two orders of magnitude larger compared to the all-inorganic perovskite films. Overall, methylammonium lead iodide perovskite films have shown to be highly nonlinear optical materials, possessing strong third-order nonlinearity.

We have described the methods for the preparation of the gold nanoparticles (NP) contained thin film by evaporation of the Au NP suspension, which was synthesized by laser ablation. The Au NP thin film was characterized using the UV-visible absorption spectra and SEM analysis. We have discussed the demonstration of the strong nonlinear absorption (8.9×10^{-6} cm W^{-1}) in this film at 400 nm. The thin film exhibited a switch from SA to RSA at stronger excitation. The relaxation time of SA was measured to be 1.6 ps.

The nonlinear optical properties of Ag$_2$S quantum dot (QD) thin films were analyzed using the open-aperture (OA) and closed-aperture (CA) z-scan technique and theoretical fitting allowing calculation of the nonlinear absorption coefficient (4×10^{-5} cm W^{-1} for the 80 nm thick film in the case of 400 nm probe pulses). The nonlinear absorption coefficients and nonlinear refractive indices of 80 and 500 nm thick films were significantly larger than for the Ag$_2$S QDs suspension. In the case of transient absorption measurements, the two distinct characteristic time constants of 150 fs and 245 fs were obtained for the films of different thicknesses.

Perovskites. We have discussed an enhancement of the Raman signal from single-crystal $MAPbCl_3$. The enhancement factor was estimated to be on the order of 10^5. The UV-Vis spectrum studies were used to corroborate that a resonance process occurs at the interface between the molecules and the single crystal surface under 532 nm laser excitation. It was suggested that charge transfer is the most likely mechanism responsible for the observed enhancement, as the plasmon resonances are ruled out. This phenomenon also provides a new molecule sensitized single-crystal perovskite used for photo-electronic detection study combined with Raman technique.

We have analyzed the femtosecond laser micromachining technology application, which allows achieving a variety of morphology (ripples, micro-nano protrusion, micro-nano rods, or network) on the surface of MBSC material by changing laser intensity and scan speed to enhance its fluorescence. Moreover, the femtosecond laser micromachining technology does not change the material composition and distribution, which could be proved by the small displacement of the characteristic vibration peak in Raman spectrum, the uniform distribution of elements in the EDS mapping, and the slight red shift of the fluorescence centre wavelength, but only changes the morphology on the surface of MBSC to improve fluorescence properties. The mechanism of fluorescence enhancement is mainly due to the existence of large specific surface area and grain boundary of the micro-nano structures with many micro-nano protrusions realized enhanced light absorption and fluorescence emission by breaking the long-distance electron transmission and reducing the total reflection probability. This discovery provides a new strategy to form multiple morphologies on the surface of MBSC by simple and easy-controlled femtosecond laser micro-machining technology. This could be applied in the micro-nano pattern etching and integrated nano-display, etc. Moreover, the discussed study also shows a novel method that could enhance the fluorescence of MBSC effectively without changing the material composition, thus providing a promising technique for the application of MBSC in light-emitting devices.

The comparative study of absorptive optical limiting properties of Al, Ti, Co, Ni, Zn, Ag, Sn, In, W, Au NPs, and Ag_2S quantum dots as well as $CsPbBr_3$ and $CsPbI_2Br$ perovskites, has been analyzed in the case of 60 fs, 800 nm pulses. It was observed that nanoparticles of smaller sizes possess comparatively strong optical limiting properties. The magnetic NPs and perovskites nanocrystals show comparatively higher nonlinear absorption coefficients, which can be used for optical limiting. Among the reported

NPs, QDs and perovskites, Au NPs, Sn NPs, Ag_2S QDs, and $CsPbBr_3$ show the higher optical limiting properties.

Laser-synthesized NPs. We have analyzed the Ag NPs prepared during the ablation of bulk silver in deionised water using different wavelengths and durations of heating pulses. Their structural, optical, and low-order nonlinear optical parameters were determined. The joint appearance of nonlinear optical refraction and absorption was analyzed using the 1064 nm, 5 ns, and 800 nm, 60 fs probe pulses. The study of the nonlinear optical parameters of Ag NPs in the resonant and quasi-resonant conditions using 400 nm, 60 fs pulses have shown the presence of SA and RSA. The nonlinear absorption coefficient of suspensions was as high as 3.0×10^{-5} cm W^{-1} at the wavelength of 1064 nm. The Ag NP suspension has demonstrated outstanding optical limiting properties in the case of 355 nm, 5 ns probe pulses. Nonlinear refraction showed the change of sign with a variation of the wavelength and duration of laser pulses.

The nonlinear optical properties of small-sized nanoparticles are related to the quantum confinement effect. Particularly, in the case of semiconductor nanoparticles, one has to take into account the variation of the band gap with the change of nanoparticles sizes. In discussed case, the increase of the nonlinear refractive index for 50 nm Ag NPs with regard to smaller sized NPs using 800 nm, probe pulses was observed. Meanwhile, in the case of 400 nm probe pulses, the reverse case was observed. The lifetime of excited plasmon for Ag NPs at 400 nm was measured to be 2.5 ps, which can be assigned to the electron-phonon relaxation time. The excited-state absorption cross-sections of Ag NPs at different wavelengths were determined.

Titanium and cobalt nanoparticles were synthesized using laser ablation technique in different liquid solvents (water, toluene, and ethylene glycol) using 200 ps pulses. We have discussed the structural and nonlinear optical properties of Ti and Co NPs in these suspensions. Studies of optical limiting of suspensions showed that they could be considered as effective limiters of 800 nm, 60 fs pulses. The origin of this process was analyzed using different experimental conditions. The third-order nonlinear optical properties of NPs were studied using the 60 fs pulses at two wavelengths. Ti and Co NPs showed SA and 2PA at 800 nm and RSA at 400 nm. At 800 nm in the case of CA z-scans, the joint influence of nonlinear refraction and SA was observed for Ti NPs in water and toluene, whereas nonlinear refraction and positive absorption were dominated in the ethylene glycol solution containing these NPs. The Ti and Co NPs showed positive nonlinear refraction at both 800 and 400 nm.

The Ti NPs ablated in water demonstrated the SA in the case of 355 nm, 5 ns pulses at lower energies, and RSA at larger energies.

Morphological and optical characteristics of nanoparticles. The laser ablation of Cu target in distilled water using different durations, wavelengths, and energies of heating pulses was analyzed. The experimental results have shown that colloidal solutions obtained at different conditions comprise CuO and Cu_2O. It was found that the colloidal solution obtained by ablation will be oxidized during a very short time, which changes the colour of the solution from green to brown. It was also demonstrated that, under ultra-short pulse ablation conditions, the oxidation rate of suspension is slower and the particles are more stable. The pulse duration has a decisive influence on the morphology of synthesized particles, and there is a corresponding relationship between them. Ultra-short pulses allow the synthesis of smaller-sized particles, which means that the decrease of pulse duration directly promotes the decrease of produced particle sizes. In a small range of pulse energy variations, the change of pulse intensity has no significant effect on the morphology and size of the particles. When the same pulse duration was used, the morphology of particles depends on the wavelength of used radiation.

The ablation of Al bulk in distilled water using pulsed lasers with different pulse durations and wavelengths was systematically analyzed. The experimental results have shown that almost all of the ablation products obtained at different conditions contain Al, Al_2O_3, and $Al(OH)_3$. It was found that the dynamics of NPs formation and modification can be divided into the formation, great change, and stable stages. The final shapes of NPs presented at the stabilization period after aging are analyzed using optical and morphology methods. The initial NPs prepared by various pulse durations (5 ns, 200 ps, and 30 fs) showed regular spherical structures. Under the condition of 5 ns pulses with 1064 nm, morphology and particle size were similar during the aging process. The main components were the mixtures of Al, Al_2O_3, and $Al(OH)_3$. Meanwhile, in the case of ns, 355 nm pulses, aggregation during aging significantly increased the sizes of NPs. Those NPs mainly consisted of $Al(OH)_3$ with a small amount of Al and Al_2O_3. The NPs obtained by ablation using ps pulses exhibited conical structures dominated by $Al_2O_3 \cdot 3H_2O$ and rod-like structures dominated by $Al(OH)_3$. Compared with the former (ns) case, NPs with small size and uniform distribution were obtained during ablation using ps pulses. The main components of these NPs were Al and Al_2O_3. The application of fs pulses led to the formation of granular NPs.

The NPs produced in distilled water by pulsed laser ablation of two metals (In and Zn) with different hardness and melting points were analyzed. The influence of pulse duration, pulse energy, and temperature of liquid on the formation, aging, and self-assembly of NPs was reported. In the case of indium with a very low melting point, pulse energy and water temperature have little influence on the formation and the subsequent aging process of NPs. The initial state of NPs obtained under different pulse duration is identical in size and morphology. However, the effect of pulse duration on ablation is reflected in the aging and self-assembly process. The NPs obtained by ultra-short pulses have smaller sizes, narrower distribution, and better stability. In addition, a large amount of $In(OH)_3$ in the pulsed laser ablation of indium exists in distilled water, and the regular $In(OH)_3$ and In_2O_3 nanostructure can be obtained by aging and self-assembly process. In the case of zinc with higher hardness and melting point, the influence of pulse duration on the formation of NPs is shown in the variation of particle size. The NPs ablated by nanosecond pulses showed a broad particle size distribution while having smaller particle sizes and narrow distribution by femtosecond pulses. At this point, it is basically consistent with indium. In addition, it was found that ZnO and zinc NPs simultaneously appeared during the ablation process. The existence of ZnO is not simply due to subsequent aging, but rather the inevitable result and final form of the aging process of zinc NPs. The morphology and size of the NPs prepared by PLAL were stable for approximately two months, after which gradual aggregation was observed. Aggregation stability is influenced by the pulse duration and physical properties of the metal target.

We have analyzed the nonlinear absorption and refraction in the solution of Ag_2S quantum dots and dyes using 40 ps pulses. The nonlinear refractive indices, nonlinear absorption coefficients, and third-order nonlinear susceptibilities of the Ag_2S quantum dots with various dyes (erythrosine, thionine, DEC, triquinolilmethane) were measured. The influence of dyes' nonlinearities on the whole pattern of the z-scans of quantum dot solutions, as well as the application of different molar fractions of dyes and intensities of probe radiation (1064 nm and 532 nm), were analyzed. The processes occurring in the components of such samples were quite different. However, among the mechanisms involved in the case of QDs and different dyes, the Kerr-induced self-interaction, excited state saturation, reverse saturates absorption, and multi-photon absorption played crucial roles in the variation of the refractive indices and absorption of these media. The observed positive sign of the nonlinear refraction of the associates of Ag_2S QDs and some dyes was discussed and

attributed to the latter components. The simultaneous appearance of saturated and nonlinear absorption was observed in the case of QDs:triquinolilmethane samples and attributed to the joint influence of the nonlinearities of QDs and dyes. The nonlinear absorption of 1064 nm pulses attributed to QDs could be related to TPA and/or three-photon absorption ($\beta \approx 5 \times 10^{-12}$ cm W^{-1}). The nonlinear absorption of 532 nm pulses caused by QDs ($\beta \approx 8 \times 10^{-11}$ cm W^{-1}) was attributed to both RSA and TPA. The observed nonlinear refraction ($\gamma = 4 \times 10^{-16}$ cm^2 W^{-1}) was related to the nonlinearities of some dyes.

Size- and shape-dependent properties of nanoparticles. The gold nanoparticles (GN) have been of significant importance due to their use for surface-enhanced Raman scattering. We analyzed four groups (with the sizes of 13, 17, 32, and 64 nm) of GN of different sizes at 400 and 800 nm using the 60 fs pulses propagating through the GN suspensions. The plasmonic resonance of GNs is far from 800 nm. We discussed the optical, structural, and nonlinear optical characteristics of the GN suspensions synthesized by the chemical method. Their nonlinear refractive indices, nonlinear absorption coefficients, and saturated intensities were measured. We analyzed the optical limiting of 800 nm, 60 fs pulses in 17 nm GN suspension and showed approximately four-fold limitation of propagated pulses with regard to the pure water. The competition of saturable and reverse saturable absorption in the case of 800nm pulses was studied at different energies of laser pulses.

The nanorods, nanocubes, and nanoparticles of the same metal show completely different properties. That is the reason why many groups are working to develop different methods of synthesis of metallic nanoparticles and particularly GN. The discussed study was aimed at the search of size-dependent nonlinear optical properties of GN at 400 nm (i.e. near the plasmonic resonance) and 800 nm (i.e. out of the plasmonic resonance). The calculation of the β in the case of RSA (7×10^{-6} cm W^{-1}) in GN is among the largest reported so far for the metal nanoparticles. The intensity-dependent transformation from saturable absorption to reverse saturable absorption and excellent optical response indicate that the small-sized GN can be considered as a potential candidate in passive mode-locking and eye/device protection against powerful lasers.

The properties of Cu NPs and CuO nanoellipsoids (NEs) synthesized during the laser ablation process of the bulk copper target in deionised water using 800 nm, 200 ps pulses were analyzed. The self-aggregation of Cu NPs to the CuO NEs led to the change of the band gaps of these nanostructures. The nonlinear optical studies of these suspensions have shown that the nonlinear refractive properties of CuO NEs depend on the

band gap. The increase of the nonlinear refractive index by decreasing the band gap of CuO nanostructures was discussed. The nonlinear refractive index and nonlinear absorption coefficient of suspensions at the wavelength of 800 nm, 60 fs probe pulses were determined to be 1.23×10^{-15} W cm^{-1} and 1.0×10^{-11} W cm^{-1}.

We have discussed different nonlinear optical processes in ZnO nanostructures. We have analyzed the second- and third-order nonlinear optical properties of ZnO nanorods, nanocrystals, and NPs using z-scan and second-order harmonic generation techniques. The second harmonic generation as a function of input laser intensity (800 nm) for different ZnO nanostructures was studied. The reported four-fold increase of the intensity of the second harmonic in ZnO nanorods compared to the ZnO nanoparticles and ZnO nanocrystals was analyzed at the same conditions of excitation using 800 nm, 40 fs pulses. The third-order nonlinear optical properties of ZnO NPs suspensions were studied using 800 nm and 400 nm, 60 fs pulses, and the nonlinear refractive indices and nonlinear absorption coefficients of NPs were determined. The optical limiting based on the nonlinear absorption and refractive properties of NPs suspensions was demonstrated.

Third harmonic generation in nanostructures. We have analyzed the nonlinear optical response of nickel nanoparticles prepared using nanosecond, picosecond, and femtosecond pulse induced ablation in deionized water, as well as the lower-order harmonic generation in the plasma containing these nanoparticles. We have discussed the third harmonic generation in nickel nanoparticle-containing plasma using 60 fs pulses at 800 nm. This study has shown that a longer pulse duration of ablating radiation results in larger third harmonic generation efficiency. Therefore, the laser ablation technique can provide efficient control over third-order optical nonlinearities, which can be modified by controlling the nanoparticle size formation during laser ablation.

The application of a high pulse repetition rate laser allowed increasing the average power of the low-order harmonics generating in air and different plasmas. We have analyzed the generation of the third and fifth harmonics of 37 fs pulses using carbon, boron, manganese, and titanium nanoparticle-contained laser-produced plasmas using a 100 kHz class laser. The fluxes of the third harmonic (343 nm) in the plateau region were estimated to be 8×10^{15} and 3×10^{16} photons/s in the case of air and manganese plasma, respectively. We also analyzed the third harmonic generation in quantum dot plasmas and the increase of the average power of coherent ultraviolet harmonics from plasmas by two orders of magnitude compared with previously used 1 kHz lasers.

THG in various plasma targets was studied using nanosecond and picosecond heating pulses in both vacuum and air. The third harmonic (TH) from various plasmas was used as a probe to characterize the components of the plasma. TH intensity has shown the cubic dependence on the probe pulse energy in both air and vacuum. It was observed in the case of THG in the air that, at the high intensity of probe pulses, TH intensity decreases, which is an indication of free electrons generation in air. TH intensity variations with the distance between the target and the probe pulses reveal the nature of the ejected particles during ablation under vacuum conditions, which was not observed during THG in air. TH intensity measurements with the change of the distance between the target surface and probe pulses position have shown the significant contribution of the smaller-sized particles along with ions and atoms compared to the heavier particles. The modulation of TH intensity with the variation of delay between the heating and probe pulses is attributed to the influence of the masses of ejected particles in accordance with the relation $t_d \propto M^{0.5}$. Among the studied materials under vacuum conditions, the relative TH conversion efficiency is larger for Ag plasma compared to the other species. It was shown that THG in metal plasmas is governed by the atomic or ionic species, contrary to the wide band gap semiconductor materials where TH was generated by the small-sized clusters and nanoparticles. TH maxima were observed at the delays in the range of 100-300 ns for metal plasmas as compared to 500-700 ns for semiconducting materials. This difference in optimal delays has revealed that the ejected particles from metal targets move faster compared to heavier targets. This study can be generalized to a variety of different materials as the sources of plasma for THG depending on the delay and spatial spreading of the plasma expansion.

High-order harmonics generation in nanoparticles. We have analyzed the application of tunable mid-infrared pulses ranging between 1300 nm and 1600 nm for harmonic generation in the laser-produced plasmas containing Ag, Sn, C_{60}, and graphene nanoparticles. We have compared the harmonic spectra from nanoparticles with those from the plasmas produced on the bulk targets of the same consistency (silver, tin, graphite). The application of a two-colour pump of nanoparticles (mid-infrared pulses + second harmonic) allowed the generation of equal odd and even harmonics up to the thirties orders. In some particular cases, we have compared different two-colour pump (TCP) schemes (NIR+H2 and NIR+806nm) and observed additional spectral components in the latter case. Resonance enhancement of single harmonic was observed in the Sn nanoparticle-containing plasma. The tuning of pump radiation allowed the

analysis of the nonlinear response of the clustered media in different spectral ranges. The demonstration of equal odd and even harmonic generation in nanoparticle-containing plasmas using tuneable NIR source and its second harmonic, as well as 800 nm pump, can be useful for producing an efficient source of short-wavelength ultra-short pulses for various applications and studies of the properties of harmonic emitters. This method of nanostructured material analysis can be considered one of the most important applications of HHG. The demonstrated approach adds new insight in the applications of plasma harmonics for nonlinear spectroscopy, which yet been demonstrated using gas harmonics, excluding the spectroscopy of benzene. One can suggest that the proposed method could be further developed in other two- (NIR+800nm) or three- (signal+idler+800nm) colour pumps of laser-produced plasmas, which may lead to the generation of attosecond pulses using multi-cycle pump sources.

We analyzed the harmonic generation from Au NPs. The 5- and 40-fold enhancement of harmonic yield was obtained from ablated Au NPs on paper as compared with ablated Au NPs on glass and Au bulk targets. The harmonic cut offs obtained from ablated Au NPs on paper, Au NPs on glass, and Au bulk target were 29th, 21st, and 21st orders, respectively, in the case of nanosecond heating pulses. In addition, the effects of heating pulse duration, TCP, and laser chirp on harmonic yield were studied in Au NP-contained LPPs. The enhanced harmonic intensity was obtained from ablated Au bulk target by decreasing the heating pulse duration. The application of picosecond and femtosecond heating pulses for plasma formation allowed the generation of 5 and 4 times stronger harmonics with regard to the nanosecond heating pulses. The harmonic cut offs were 33rd and 39th orders in the case of picosecond and femtosecond heating pulses, respectively. The enhanced harmonic intensity was demonstrated from ablated Au bulk target by applying TCP (800 nm + 400 nm) of LPP. Two-fold enhancement of harmonics was observed using TCP of ablated Au bulk target with regard to SCP. Negatively chirped 130 fs pulses enhanced 9th and 11th harmonics with regard to chirp-free (35 fs) and positively chirped 130 fs pulses. Performed MD-based simulations of NPs formation at different pulse durations and the incident fluencies supported the experimental measurements and revealed the main driving mechanisms responsible for the size and morphology of the generated particles.

The application of NPs and quasi-phase-matching plays an important role in the enhancement of high-order harmonics of ultrashort laser pulses. We have analyzed various regimes of nanoparticle plasma formation for the creation of conditions for maximal QPM-induced enhancement of the

groups of harmonics in the extreme ultraviolet (XUV). Laser plasmas were formed on the surfaces of NPs- and microparticles-contained targets using ablation by nanosecond, picosecond, and femtosecond pulses. Different conditions of laser-plasma formation (extended and perforated plasma) and variable concentrations of free electrons in these three cases of laser ablation led to modifications of QPM conditions. We have analyzed novel approaches in the optimization of QPM at the conditions of laser ablation of NPs and MPs by pulses of different durations. The formation of QPM conditions using femtosecond and picosecond heating pulses during HHG in such plasmas allowed the growth of conversion efficiency of the groups of harmonics with the enhancement factors exceeding 25× in different ranges of XUV, contrary to less efficient QPM in the case of nanosecond pulses induced ablation.

High-order harmonics generation in clusters and quantum dots. We have discussed the role of small carbon clusters, which inevitably appear during graphite ablation, in the generation of high-order harmonics. The advantage of the proposed method for laser ablation and delay-dependent study of harmonic emission during ablation of graphite target is that plasma formation in double-laser configuration of HHG experiments could be efficiently applied for a variation of the delay between heating and driving pulses using electronic methods. It can also be applied for other clustered targets to determine the best conditions for HHG in such plasmas. We have analyzed the advanced properties of the carbon plasma produced by nanosecond pulses as a medium for efficient low- and high-order harmonic generation. The role of $C_5 - C_{25}$ clusters in the enhancement of harmonic generation efficiency has been analyzed. Those HHG studies have demonstrated that these carbon clusters appearing during ablation of graphite influence HHG efficiency at the delays similar to those at which single carbon atoms and ions arrive in the area of femtosecond beam propagation. The discussed studies have shown that such clusters commonly appearing during time-of-flight mass spectroscopic studies of carbon ablation strongly influence the harmonics yield and thus could be considered as the sources of efficient harmonics in the 40-100 nm spectral range.

We have discussed the possibility and conditions of using quantum dots as efficient emitters for high-order harmonics generation by 30 fs pulses using optimally delayed heating and driving laser pulses. We further have analyzed methods for the aqueous synthesis of Ag_2S, ZnS and CdS QDs that enable, by their size and dispersion, as well as their structural properties, the effective generation of harmonics in plasma plumes. The study of the morphological properties of the samples

demonstrated the formation of ZnS and CdS QDs with mean sizes of 2-3.2 nm in a cubic lattice, and of Ag_2S QDs with mean sizes of 1.7-2.0 nm in a monoclinic lattice, all with a weight fraction of about 20-25% in gelatin. A comparison of HHG using QDs and ablation of solid-state targets for the same materials (Ag_2S, ZnS, and CdS) was analyzed. In the case of QDs, the conversion efficiency into harmonics is higher despite the lower concentration of these species in the plasma compared to the concentration of molecules and ions for bulk ablation. The observed increase of HHG conversion efficiency could be caused by a larger concentration of harmonic emitters and the specific properties of QDs, particularly their plasmonic properties. The maximum HHG conversion efficiency is achieved much earlier than one would expect from the kinetic model of QDs spreading out from the target surface. Therefore similar velocity distributions of molecules and QDs of these metal sulphides are assumed in the ablation process.

We have analyzed the harmonic generation during the propagation of 800 nm, 30 fs pulses through the plasmas containing Ag_2S, CdS, and $Cd_{0.5}Zn_{0.5}S$ QDs. The self-phase modulation of lower-order harmonics and an intensity-dependent saturation of the harmonic yield were discussed. The application of two-colour pumping allowed the generation of almost equal odd and even harmonics using a 0.2-mm thick barium borate crystal, while the application of a thicker (0.4 mm) crystal for second harmonic generation caused a weaker temporal overlap of the two driving fields (800 and 400 nm) in the metal sulfide QD plasma area. Finally, the studies of quasi-phase-matching conditions in spatially structured plasmas produced by either structuring the heating beam or the surface of the ablating target showed the formation of a group of enhanced shorter wavelength harmonics, though this process was less pronounced compared to the formation of a structured plasma on the surface of bulk metal sulphides.

All the above-discussed studies allowed the demonstration of new approaches in the formation and characterization of non-spherical nanostructures. The advanced approach in applications of quantum dots for the amendments of the nonlinear optical response of thin films and laser-induced plasmas and demonstration of high-order harmonics generation in nanostructured plasmas provides tools for optical analysis of recently developed nanostructures. The developments in this field of nanoscience are rapidly changing to follow the needs and requirements of this area of research. One can expect further achievements in this direction in the nearest future.

INDEX